AFIT/GSE/ENY/93D-1

PROTOTYPE SPACE FABRICATION PLATFORM
THESIS

James A. Bessel, Captain, USAF
James M. Ceney, Captain, USAF
David M. Crean, Captain, USAF
Edward A. Ingham, Captain, USAF
David J. Pabst, Captain, USAF

AFIT/GSE/ENY/93D-1

REPORT DOCUMENTATION PAGE

Form Approved
OMB No. 0704-0188

1. AGENCY USE ONLY (Leave blank)	2. REPORT DATE	3. REPORT TYPE AND DATES COVERED
	December 1993	Master's Thesis

4. TITLE AND SUBTITLE
PROTOTYPE SPACE FABRICATION PLATFORM

5. FUNDING NUMBERS

6. AUTHOR(S)
James A. Bessel, Capt, USAF
Edward A. Ingham, Capt, USAF
James M. Ceney, Capt, USAF
David J. Pabst, Capt, USAF
David M. Crean, Capt, USAF

7. PERFORMING ORGANIZATION NAME(S) AND ADDRESS(ES)
Air Force Institute of Technology, WPAFB OH 45433-6583

8. PERFORMING ORGANIZATION REPORT NUMBER
AFIT/GSE/ENY/93D-1

9. SPONSORING MONITORING AGENCY NAME(S) AND ADDRESS(ES)
Franklin B. Mead, Jr.
OLAC PL/RKFE
9 Antares Road
Edwards AFB, CA 93524-7680

10. SPONSORING MONITORING AGENCY REPORT NUMBER

11. SUPPLEMENTARY NOTES

12a. DISTRIBUTION/AVAILABILITY STATEMENT
Approved for public release; distribution unlimited

12b. DISTRIBUTION CODE

13. ABSTRACT (Maximum 200 words)
Current plans for constructing large structures in space entail fabricating the primary components, such as truss segments, on the ground and assembling them in space. This process requires an exorbitant number of support missions, and methods to minimize the number must be considered. Whenever the space shuttle is launched, its external tank is jettisoned and destroyed prior to reaching orbit. This aerospace grade aluminium structure can be carried into orbit and utilized extrnsively. The Prototype Space Fabrication Platform (SFP) fabricates aluminum materials, reduced from external tanks, into functional trusses. The trusses are strong and can be used as the primary components for future structures in space. The fabrication process produces a continuous truss allowing the end user to determine the length. The SFP can fabricate the same amount of truss from one external tank as four dedicated shuttle missions can deliver in the cargo bay. The SFP utilizes electrodynamic propulsion, via shielded coils, for maneuvering. The novel propulsion system facilitates a versatile payload transportation and delivery capability. The SFP can continuously track a target from all directions. The tracking system is ideal for docking since plume impingement is not a concern. With the assistance of remote manipulators, the SFP can deliver a payload in a wide variety of orientations. Under most conditions, the remote manipulator and maneuvering commands originate from ground workstations. Required manned presence is greatly reduced, and the time when the space shuttle is off station is effectively utilized. The logistical complications, currently inhibiting advancement in space, can be eliminated.

14. SUBJECT TERMS	15. NUMBER OF PAGES
space propulsion, space manufacturing, spacecraft docking, electrodynamic propulsion, large space structures, remote manipulators	493
	16. PRICE CODE

17. SECURITY CLASSIFICATION OF REPORT	18. SECURITY CLASSIFICATION OF THIS PAGE	19. SECURITY CLASSIFICATION OF ABSTRACT	20. LIMITATION OF ABSTRACT
Unclassified	Unclassified	Unclassified	UL

AFIT/GSE/ENY/93D-1

PROTOTYPE SPACE FABRICATION PLATFORM

THESIS

Presented to the Faculty of the Graduate School of Engineering
of the Air Force Institute of Technology
Air University
In Partial Fullfillment for the Degree of
Master of Science in Systems Engineering

James A. Bessel, Captain, USAF
James M. Ceney, Captain, USAF
David M. Crean, Captain, USAF
Edward A. Ingham, Captain, USAF
David J. Pabst, Captain, USAF

December 1993

Preface

The purpose of this study was to establish the technical feasibility of a space fabrication platform that produces functional trusses from aluminum materials salvaged from a space shuttle external tank in orbit. The utilization of electrodynamic propulsion for orbital maneuvering was also a key feature of the design.

We wish to thank our advisor, Dr. Curtis Spenny, and our committee members, Dr. William Bailey, Capt. Chris Hall, and Capt. Robert Canfield for their assistance.

Finally, we wish to thank our families for their patience and support.

GSE-93D

Table of Contents

List of Figures

List of Tables

Abstract

Current plans for constructing large structures in space entail fabricating the primary components, such as truss segments, on the ground and assembling them in space. This process requires an exorbitant number of support missions, and methods to minimize the number must be considered.

Whenever the space shuttle is launched, its external tank is jettisoned and destroyed prior to reaching orbit. This aerospace grade aluminum structure can be carried into orbit and utilized extensively. The Prototype Space Fabrication Platform (SFP) fabricates aluminum materials, reduced from external tanks, into functional trusses. The trusses are strong and can be used as the primary components for future structures in space. The fabrication process produces a continuous truss allowing the end user to determine the length. The SFP can fabricate the same amount of truss from one external tank as four dedicated shuttle missions can deliver in the cargo bay.

The SFP utilizes electrodynamic propulsion, via shielded coils, for maneuvering. The novel propulsion system facilitates a versatile payload transportation and delivery capability. The SFP can continuously track a target from all directions. The tracking system is ideal for docking since plume impingement is not a concern. With the assistance of remote manipulators, the SFP can deliver a payload in a wide variety of orientations.

Under most conditions, the remote manipulator and maneuvering commands originate from ground workstations. Required manned presence is greatly reduced, and the time when the space shuttle is off station is effectively utilized.

These and other capabilities of the SFP can be used to significantly enhance the construction of future structures. The logistical complications, currently inhibiting advancement in space, can be eliminated.

Prototype Space Fabrication Platform

I. Introduction

1.1 Design Study

A group design study was conducted at the Air Force Institute of Technology. The design group consisted of five Air Force officers enrolled in the Systems Engineering graduate degree program. The study was motivated by the problem developed in the next two sections.

1.2 Problem Description

Despite current apprehension over expanding America's space program, there is a significant demand for large structures in space. Effective methods to meet this demand must be considered. One possible avenue is to utilize the expended external tank of the space shuttle in low Earth orbit. If each shuttle mission carried the external tank into orbit, modified tanks could provide materials for the construction of numerous large space structures. Dedicated fabrication platforms could reduce the external tanks and re-fabricate the materials into components required for the construction. The utility of these fabrication platforms would be increased if they possessed transportation and delivery capabilities. Electrodynamic propulsion and attitude control could provide the precise maneuvering and control necessary to accommodate these features.

After researching the problem, the design group summarized the task into one problem statement:

> Utilize the external tanks from space shuttle missions and the concepts of electrodynamic propulsion to support the construction of large structures in space.

The group concluded that a space platform capable of fabricating trusses from external tanks with a delivery system driven by electrodynamic propulsion would illustrate effective means for the fabrication of large structures in space. An in-depth feasibility study for the development of a prototype space fabrication platform (SFP) is detailed in the report that follows.

1.3 Objectives

A list of objectives was developed to assist in directing the study. The objectives are to design a prototype space platform that:

- fabricates trusses for use in the construction of large structures in space
- utilizes external tank raw materials in the truss fabrication process
- utilizes electrodynamic propulsion for platform maneuvering
- possesses transportation capability
- possesses delivery capability

1.4 Scope

The development of a prototype space fabrication platform first requires a solid technical foundation. The intent of this study is to establish the technical feasibility of an SFP. Whenever multiple solutions to a particular problem in designing the SFP existed, the best solution was chosen based on technical merit. Immediate product availability and monetary costs did not influence the study. This completed technical feasibility study will serve as a basis for comparing the potential benefits of an SFP against product availability, cost, and the many other ramifications associated with its implementation.

1.5 Report Outline

In Chapter 2, the motivation for the SFP study is provided. The need for constructing large space structures is presented as well as the concepts of utilizing space shuttle external tanks and electrodynamic propulsion. The design study's solution to supporting the construction of large space structures with a truss producing space fabrication platform is developed. Potential growth applications of the platform are presented.

In Chapter 3, an overview of the study is delivered. Systems engineering techniques are used to define the requirements of the SFP and the decision making processes. Summaries of the SFP design, capabilities, and assembly plan are introduced to provide a foundation for the remainder of the report.

In Chapter 4, the work of a previous design study that is integral to the SFP study is briefly described. The previous study developed components and procedures for salvaging material from the expended external tank of the space shuttle. Critical components and procedures of the design study are reviewed. External tank material salvage and pre-processing operations required for SFP truss production are also described.

In Chapter 5, the SFP truss making process is detailed. Raw material salvaged during external tank reduction is combined to produce square trusses. All the processes necessary for truss production are discussed.

In Chapter 6, the basic theories of electrodynamic propulsion are developed. The concept of shielded coil electrodynamic propulsion is detailed, and an optimal linear control system, that utilizes electrodynamic propulsion for controlling the SFP, is discussed. The controllability requirement for the SFP, which sizes the SFP and dictates the specifications for the control elements, is explained.

In Chapter 7, the calculations for the power requirements of the SFP are described. The equations presented allow for an iterative design process. Based on

given available power, operational power scenarios are developed which outline the major capabilities of the SFP.

In Chapter 8, a conceptual analysis of the remote manipulator systems planned for SFP assembly and mission ready operations is delivered. The remote manipulators are categorized into two systems: the servicing system and the docking system. Both are heavily influenced by the remote manipulators proposed for Space Station Freedom and the proven remote manipulator system of the space shuttle. The docking system also utilizes the attributes of the electrodynamic propulsion system to provide a unique and impressive docking capability.

In Chapter 9, a conceptual sequence that illustrates the assembly of the SFP is delivered. The tradeoffs on how the SFP is built are discussed and an eight mission overview of the actual assembly is provided.

In Chapter 10, operational missions and SFP capabilities are discussed. The events in which an external tank is recovered, reduced, converted to the truss product, and then transported and delivered are covered in detail. The SFP's capabilities and its advantages over conventional systems are also discussed.

In Chapter 11, the critical design issues for the SFP are presented. The chapter supports the decisions made during the design process by expounding on issues that arose during the design study. Sections of the chapter are referenced throughout the report to provide increased detail on a subject without interrupting continuity in the body of the report.

In Chapter 12 the report is concluded. Recommendations for further research in the area are provided.

II. Motivation

2.1 Introduction

Before designing a fabrication platform, the guiding concepts must be thoroughly understood. This chapter identifies the need for large space structures. It provides a short introduction to the concepts of utilizing an external tank in space and propelling a vehicle with electrodynamic propulsion. The general idea of a space fabrication platform is presented, and future growth applications are addressed.

2.2 Large Space Structures

In the 1960's, the need for research in space promoted the production of a space station. Today, many needs, including research, are calling for not just a space station, but *numerous* large structures in space capable of fulfilling a variety of roles. Five of these needs will be identified, and ways to accommodate them will be discussed.

2.2.1 Alternative Energy. Large space structures are needed to conserve and augment the world's limited fossil fuel supplies. The amount of solar energy that reaches the earth is 20,000 times the total energy currently used by man (29:4). It could be harnessed in many ways. The most popular is via solar collectors. A large array of collectors at geostationary orbit would be in direct view of the Sun 99% of the year and could provide the Earth with abundant quantities of energy (11:1239). A solar collector array for this use is large. A Boeing design has a surface area of 112 km^2 and requires approximately 1300 km of truss (13:103).

Other solar energy capturing methods have also been considered. Large reflectors in space could direct light or heat during night or cold conditions. In February of 1993, a Russian satellite reflected a 4 km wide light beam from space onto Europe for six minutes (86:20). The potential agricultural and industrial benefits from this

technology are enormous, as well as the assistance it could provide during disaster relief operations.

2.2.2 Telecommunications. Large space structures are needed for improved telecommunications. Because of satellites, the ability to access data, computers, and other people anywhere in the world is becoming commonplace. Unfortunately, the demand for more communication satellites is leading to crowding of the geostationary orbit and the frequency spectrum (29:2). Many communication satellites could be replaced with just a few large geostationary platforms integrating all their individual functions with shared antennas.

2.2.3 Material Processing. Large space structures are needed for improved material processing. The consequences of processing without gravity and in a vacuum are far reaching. Materials that are difficult or impossible to produce on earth, because of the measures taken to control the environment, could easily be produced in space. For example, liquid and molten material could be processed without the use of a solid container. This would eliminate (29:4):

- problems with contamination and spontaneous physical processes caused by contacting the container walls
- problems attributed to processing highly corrosive materials
- restrictions in processing temperatures

Large material processing platforms could ease current demands for materials needed today, and accommodate future demands for materials yet to be created.

2.2.4 Spaceborne Service. Large space structures are needed to assist other space vehicles. A site in space for refueling, assembling, or repairing would have many advantages. for example, launches originating from Earth — which devote much of their payload to fuel for achieving orbit — could be minimized. It is highly

likely a manned Mars probe will be assembled and fueled on board a structure in space before departing for Mars (9:317). Also, inoperative satellites or satellites destined for deep space could be repaired or "last chance" checked for problems (29:7).

2.2.5 Spaceborne Construction. Finally, building on all the previous needs, large space structures are needed to construct other large space structures. Just like large construction projects require support facilities in remote locations on earth, similar facilities will be required in space. These facilities will provide (29:7):

- stable construction platforms
- habitation modules
- storage facilities
- machine shops
- communication centers

The needs just identified do not exhaust the list. They represent a cross-section of the many needs being generated by advancements in technology. This design study is motivated by these needs. A large space platform that directly or indirectly accommodates them is developed.

2.3 Space Fabrication Platform

The numerous large space structures proposed in the previous section require multiple launches for multi-staged assembly. At one time NASA was planning for approximately 20 space shuttle missions to build Space Station Freedom (78:1). To enhance the feasibility of producing structures in space, the launch support requirement must be minimized. This design study will develop a platform which fabricates trusses from space shuttle external tanks to support the construction of large space structures.

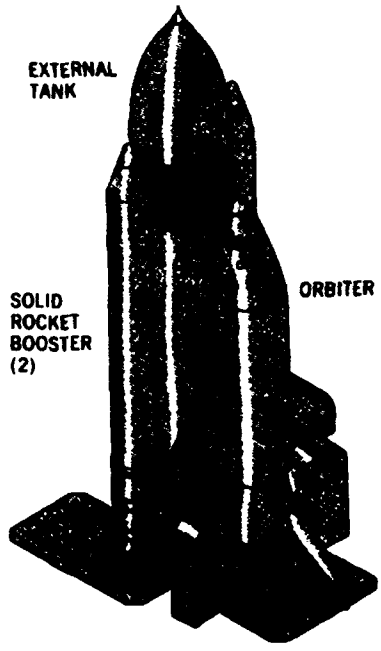

Figure 2.1 The space shuttle before launch with the external tank (ET) and solid rocket boosters attached (28).

2.3.1 Space Shuttle External Tanks. "The external tank is currently the only non-reusable portion of the Space Transportation System" (80:1)(see Figure 2.1). It is intentionally jettisoned into either the Indian or Pacific Ocean just prior to the space shuttle achieving orbit. The jettison occurs because the external tank is not currently used in space and is considered unwanted debris. When it is jettisoned, the orbiter and external tank both have 98% of the energy required to enter orbit. In fact, an alternate launch trajectory, called a direct injection, allows this to occur with no additional fuel costs (28:1–14)(see Figure 2.2).

There are many ways the external tank could be utilized in space. For example, its role as a container for 730,000 *kg* of propellants could easily be continued with minor modifications. After a direct injection, the external tank still has 7,000 *kg* of residual fuels remaining (28:1). This alone would provide significant support to other spacecraft already established in space.

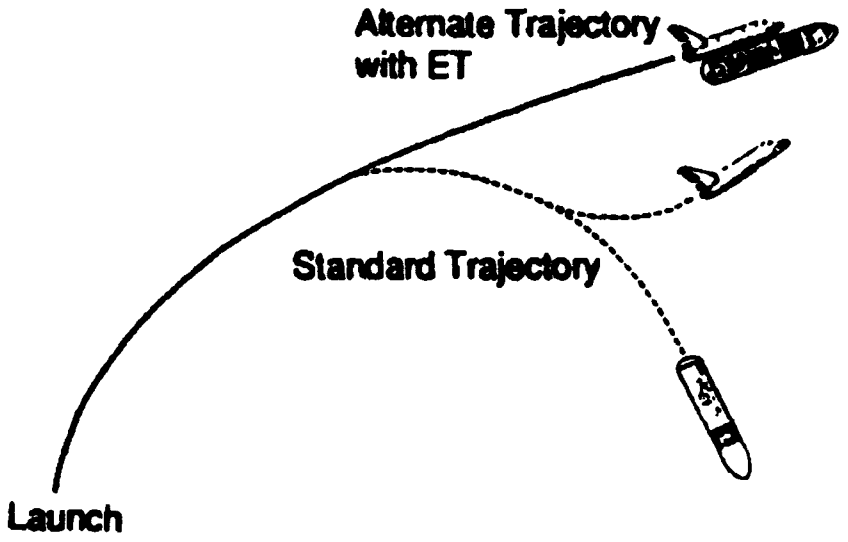

Figure 2.2 Space shuttle launch trajectories. The space shuttle keeping an external tank into orbit instead of jettisoning it into the Ocean (28).

The usefulness of the external tank is not limited to fuel storage. It could be adapted to store other liquids, gases, equipment, or even people. Also, it is made from 24,000 *kg* of aerospace grade aluminum. Intact, it is far more rigid than any structure currently in space and could serve as a backbone for the construction of other space structures. Dismantled, it could provide large quantities of construction materials. For example, trusses — which are primary components to most space structures — could be produced from these materials.

In 1990, a systems engineering group at the Air Force Institute of Technology designed a system for transforming the external tank into raw material while in low Earth orbit. The study demonstrated how assorted lengths of aluminum I-beam and flat plate could be salvaged. It was called *An Aluminum Salvage Station for the External Tank* (ASSET) (31).

The SFP design study uses aluminum raw material — recovered from external tanks by ASSET salvage procedures — for the production of trusses. Because the ASSET concepts are critical to this study, they are reviewed and modified for

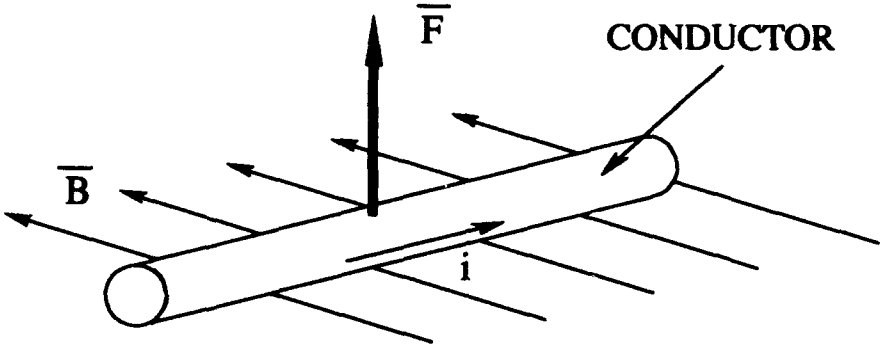

Figure 2.3 The defection force experienced by a conductor with a current flowing through it in a magnetic field.

specific applications in Chapter IV and Appendix A. The platform will also have the capability to transport and deliver the completed trusses to other sites where they can be utilized. The maneuvering capability of the SFP will be achieved with electrodynamic propulsion.

2.3.2 Electrodynamic Propulsion. When a current flows through a conductor in a magnetic field, $\overline{B}$, it experiences a transverse deflection force (see Figure 2.3). The magnitude and direction of the force, $\overline{F}_B$, is given by (32:539):

$$\overline{F}_B = i\overline{L} \times \overline{B} \tag{2.1}$$

i = current

$\overline{L}$ = length and direction of the conductor

$\overline{B}$ = magnitude and direction of the magnetic field

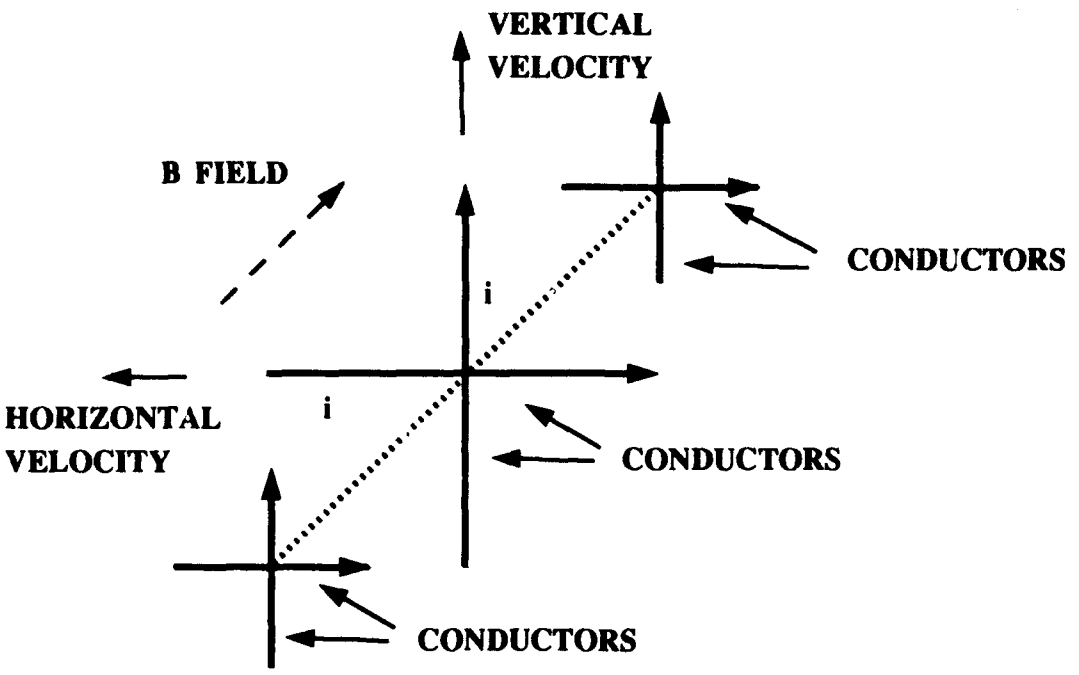

Figure 2.4 A rigid conductor electrodynamically propelled space vehicle configured for maximum control in the magnetic field.

In 1965, Drell, Foley, and Ruderman proposed running a current through a long conductor in the Earth's magnetic field to produce thrust for a vehicle in space (22). In 1992, a thesis at the Air Force Institute of Technology developed a space vehicle using this propulsion technique. It was called *A Precision Orbital Tracking Vehicle* (POTV) (49). The vehicle was composed of rigid orthogonal conductors sized and situated to provide multi-axis thrust and attitude control in the Earth's magnetic field. (see Figure 2.4).

Electrodynamic propulsion is ideal for situations requiring low or moderate levels of thrust over long periods of time (81:2). Orbit transfer, station keeping, stand-off, and attitude control — the maneuvering requirements of the SFP — are prime applications. If the power source for the propulsion system is solar generated, fuel requirements are minimal, and if the current in the conductors is variable, thrust

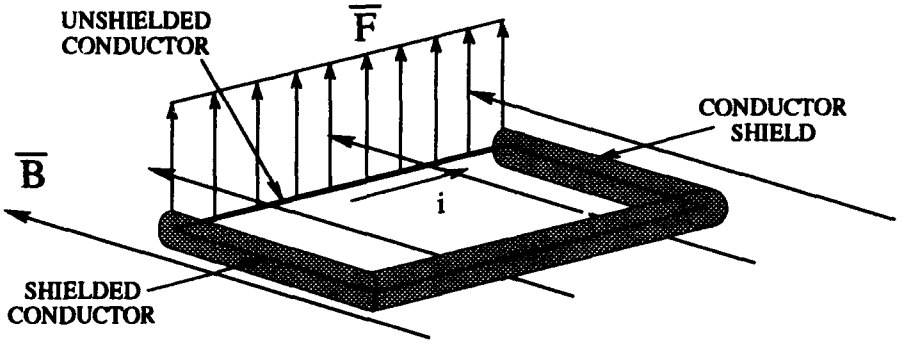

Figure 2.5 A single coil partially shielded by a magnetic shield. The return portion of the coil does not experience an external force.

can be variable. For these reasons, electrodynamic propulsion was adapted to propel the SFP.

As the concept of electrodynamic propulsion has developed, the task of driving current through a conductor in space has become an area of emphasis. Research on an approach that has provided encouraging interim results utilizes a partially shielded conductor coil (48). The coil closes the circuit. This minimizes the resistance involved in driving the current. Also, the shield removes the return portion of the coil from the magnetic field. This inhibits the shielded portion of the conductor from experiencing an opposite direction force. Figure 2.5 illustrates a partially shielded single coil. These desirable characteristics ultimately work to reduce the size requirements of space vehicles utilizing electrodynamic propulsion. For this reason, this technology is incorporated into the SFP. Shielded coil electrodynamic propulsion

is thoroughly developed in Chapter VI and implied when addressing electrodynamic propulsion for the remainder of this report.

2.4 Growth Potential

The study concentrates on developing an SFP that fabricates and delivers trusses only. However, with these capabilities satisfied, expanded roles could be considered. For example, once the SFP is complete, the external tank it receives could be delivered intact to a site that needs it. It could also be modified while on the SFP for a particular capability. Converting it to a habitation module, storage facility, or contained work area would be feasible.

The modified tank could still be delivered to a site, or — if the SFP was designed for it — could remain attached to the SFP. With this potential, the SFP by itself could become a construction facility capable of providing:

- a stable construction platform
- habitation modules
- storage facilities
- machine shops
- communication centers

With appropriate design considerations, the SFP could grow into any of the large space structures cited in Section 2.2.

2.5 Summary

This chapter identified the requirement for large structures in space and suggested utilizing the space shuttle external tank to support their construction. The potential uses of the external tank were presented. The concept of creating a platform that fabricates trusses, made from external tank raw materials, and utilizes

electrodynamic propulsion was developed. The potential of the platform to deliver completed trusses or modified tanks, or become any one of the large space structures identified in the beginning of the chapter was proposed.

III. System Overview

3.1 Introduction

This chapter is intended to assist the rest of the report by providing insight to the desired outcome of the SFP study. An overview of the fundamental decision drivers and resulting SFP design is presented. The chapter is divided into two sections: SFP design requirements and SFP overview. With the problem identified in Chapter 1, and the motivation established in Chapter 2, the SFP design requirements can be generated. The influence of these requirements and resulting SFP specifications are then summarized.

3.2 Requirements

Requirements for the SFP were developed *by the group* to satisfy the objectives listed in Section 1.3 and establish technical feasibility. The requirements were organized into needs, alterables, and constraints as defined by Sage (72:79–83). The Sage format greatly assisted in focusing the design study.

3.2.1 Needs. Needs are required, useful, or desired features designed into a system (72:79). The needs identified for the SFP are:

- a truss product that enhances the construction of large structures in space
- a truss product that utilizes the raw materials of the space shuttle external tank
- a delivery capability
- a maneuvering system that utilizes electrodynamic propulsion
- a versatile payload capability
- a versatile stand-off envelope

- a versatile orbit envelope
- an open work area for mission ready operations

3.2.2 Alterables. Alterables are the factors, pertaining to the needs, which can be changed during the design of a system (72:81). The alterables identified for the SFP are:

- the truss product shape and dimensions
- the welding method for truss fabrication
- the delivery method
- the payload capacity
- the stand-off envelope
- the orbit envelope
- the electrical power generation method
- the platform assembly plan
- the components of the platform prefabricated on Earth
- the manning requirements
- the command and control locations

3.2.3 Constraints. Constraints are the limitations under which the needs must be satisfied or the range over which the alterables can be varied (72:82). The constraints identified for the SFP are:

- the primary source of material for the truss product will be the space shuttle external tank
- the primary propulsion method will be electrodynamic
- the maximum usable electrical power will be 82 kW

- the maximum conductor temperature of the electrodynamic propulsion system will be 438°C (allows a safety factor of 1.5 from the minimum melting point of the materials used in the propulsion system)
- the maximum time required for a 200 km orbital altitude change will be less than 20 *days*
- the minimum payload capacity will be 30,000 kg
- the stand off-envelope will be from 0 to at least 40 m around a target's center of mass
- the orbit inclination envelope will be between 0° and 28.5°
- the orbit altitude envelope will be between 300 and 500 km

The SFP is a prototype platform. Any change in the needs, alterables, or constraints could change the final design but still establish technical feasibility of the concept. Recall, the needs, alterables, and constraints for this study were developed *by the group* to best demonstrate the technical feasibility of an SFP; this does not imply they are the only needs, alterables, and constraints that could accomplish the same task. Chapter XI analyzes the effects of designing to alternative needs, alterables, and constraints.

3.2.4 Decision Making. The decision making process used throughout this study can be characterized as discrete judgement. As mentioned in Section 1.4, solutions were chosen based on technical merit without the influence of product availability or monetary cost. The metrics used (mass, size, power, etc.) in design tradeoffs were based on situational appropriateness and vary between tradeoffs.

The flow of the report is to introduce possible design tradeoffs as they occur in their respective chapters and immediately identify the best solution. Usually, the tradeoff analysis is deferred to the design sensitivities chapter at the end of the

report. The desire is for the body of the report to maintain a logical progression towards the final SFP design.

3.3 Overview

This section summarizes the final design developed in the remainder of the report. Its purpose is to assist with continuity while reading the individual areas of consideration that were analyzed in the design process. Details of the decisions made during the design process are addressed in Chapter XI.

3.3.1 Configuration. Figure 3.1 illustrates the final configuration of the SFP. It is influenced by all the needs, alterables, and constraints, but dominated by the need for delivery and maneuvering capabilities.

The ultimate purpose of the SFP is to support construction in space. To accomplish this, the SFP product — trusses — has to be readily available to the end user. The SFP possesses an open work area, remote manipulator systems (docking and servicing systems), and a maneuvering system to facilitate delivery of the truss product.

After some reflection, it can be seen that the manipulation of $\overline{F}_B = i\overline{L} \times \overline{B}$ for six degrees-of-freedom mandates conductors in three orthogonal directions, as well as augmentation thrusters parallel to the B-field and an attitude torque generation system. The layout of the SFP accommodates these requirements with main, cross, and orthogonal integrated trusses that house conductors, four augmentation thrusters, and a coiled conductor integrated truss unit housing attitude control elements. The use of electrodynamic propulsion for maneuvering capability significantly influences the design of the SFP.

Solar dynamic power modules were incorporated with the existing ASSET photovoltaic arrays and placed at the ends of cross integrated trusses. The solar dynamic power modules possess higher power to mass ratios than the photovoltaic

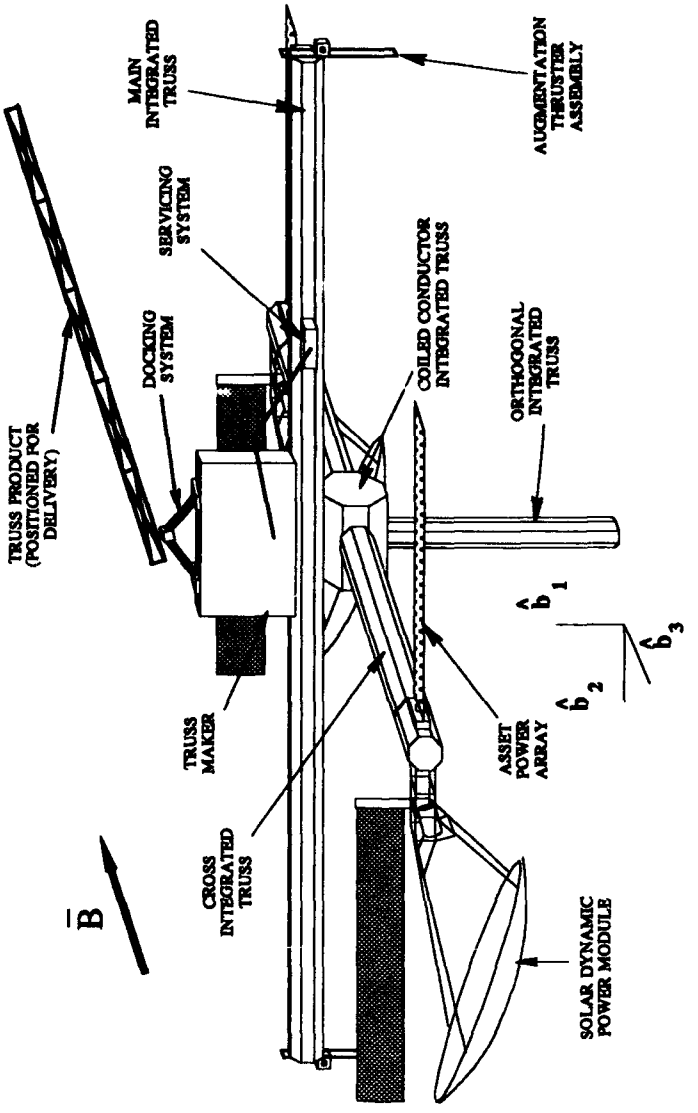

Figure 3.1 The final design of the SFP

Truss Product	
Dimensions	$1.0 \times 1.0 \times$ (variable) m
Mass/Length	$5.25\ kg/m$
Welding Method	Laser
Axial Stiffness	$3.774 \times 10^7\ N$
Bending Stiffness	$9.135 \times 10^6\ N \cdot m^2$
Torsional Stiffness	$1.103 \times 10^6\ N \cdot m^2$
Production Rate	$77\ m/hour$

Table 3.1 Truss Product Specifications.

arrays. They also possess thermal energy storage elements that provide power during eclipse operations, and eliminate the need for additional batteries. The position of the solar power systems on the SFP is required for unobstructed orientation with the Sun at all attitudes.

There are no habitation modules on the SFP; all manning requirements are satisfied by space shuttle visitations. Remote manipulators and ground control are used extensively throughout assembly and mission ready operations.

3.3.2 Truss Product Characteristics. Trusses are produced by a truss maker on the SFP. Specifications of the trusses are listed in Table 3.1. They are strong and compliment the construction of future structures in space. The truss maker produces continuous trusses allowing the end user to determine the length. The SFP can fabricate the same amount of truss from one external tank as four dedicated shuttle missions can deliver in the cargo bay.

3.3.3 Platform Capabilities. The electrodynamic propulsion system provides a precise and versatile transportation and delivery capability for the truss product. The SFP can continuously track a target in R-bar, V-bar, Z-bar (see Figure 3.2). The maximum R-bar stand-off capability is 82 m — SFP center of mass to target center of mass. The tracking system is ideal for docking since plume im-

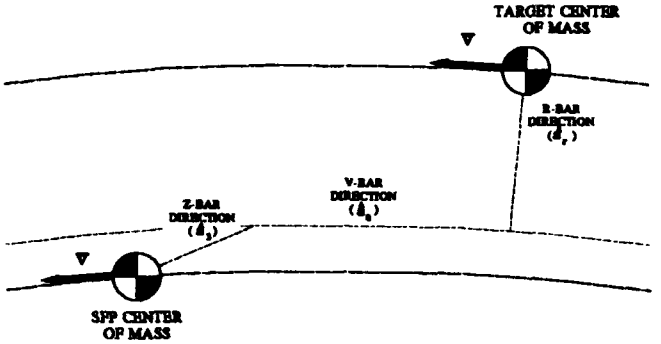

Figure 3.2 R-bar, V-bar, and Z-bar tracking. R-bar is defined along the radial direction, V-bar is defined along the orbit path direction, and Z-bar is defined along the out of plane direction.

pingement is not a concern. With the assistance of the remote manipulator systems, the SFP can deliver the truss product in a wide variety of orientations.

The electrodynamic propulsion system also provides an effective gross orbital maneuvering capability. The SFP can orbit anywhere from 300 to 500 *km* in altitude and traverse this 200 *km* envelope in less than 12 *days*. It is capable of orbit inclinations between 0° and 28.5°.

In most cases, the remote manipulator and maneuvering commands originate from ground workstations. Permanent manning is not required, and the time when the space shuttle is off station is effectively utilized.

The capabilities of the SFP addressed in this section highlight the design study. They are summarized in Table 3.2

3.3.4 Platform Assembly. Chapter IX describes the SFP assembly process. It is briefly explained here to further assist with the system overview. The assembly will begin by using an ASSET dismantled external tank for station keeping and power. A consolidated truss maker and a segment of the SFP main integrated

SFP	
Dimensions	$50.0 \times 64.3 \times 38.3\ m$
Mass	79,309 kg
Primary Propulsion	Electrodynamic
Power Source	Solar Dynamic & Photovoltaic
Permanent Manning Requirement	None
Primary Command and Control Source	Ground
Orbital Altitude Envelope	300–500 km
Orbital Inclination Envelope	0–28.5 °
Maximum Payload	31,300 kg
Maximum Acceleration Rate	$10.3 \times 10^{-5}\ m/s^2$
Minimum Time for 200 km Altitude Change	11.9 $days$
Maximum R-bar Stand-off Range	82 m
Maximum Continuous Usable Power	82 kW
Standard Mission Avg Power	44.9 kW
Propulsion Efficiency	87%

Table 3.2 The final design specifications for the SFP.

truss will be brought into orbit by the space shuttle. The truss maker, mounted to the main truss segment, will be attached to the external tank. Additional main truss segments will be delivered on subsequent space shuttle missions and attached to the previous truss segments until the main integrated truss is complete. Once complete, the main integrated truss will house conductors that can assist with station keeping, using ASSET power. The next shuttle mission will deliver a coiled conductor integrated truss for attitude control. The coiled conductor integrated truss mounts to the side opposite the truss maker on the main integrated truss. In addition to attitude control, it also establishes mounting points for the cross integrated trusses and the orthogonal integrated truss. The cross trusses and orthogonal truss are delivered by the space shuttle and assembled in segments similar to the main truss. The cross trusses house conductors for electrodynamic propulsion and also provide locations for solar power systems. When the orthogonal integrated truss is installed, it will provide the final conductors required to complete the electrodynamic propulsion system.

IV. Material Salvage and Pre-Processing Operations

4.1 Introduction

An Aluminum Salvage Station for the External Tank (ASSET) was the result of a systems engineering design study to develop possible techniques for transforming the space shuttle external tank into a source of construction material at low Earth orbit (31:xxii). The beginning of this chapter briefly describes ASSET and ASSET salvage operations. Additional ASSET information is provided in Appendix A. References (31) and (80) are the primary sources for ASSET. The remainder of the chapter addresses the external tank material salvage and preprocessing requirements for accommodating the SFP.

4.2 ASSET General Description

ASSET is a station in low Earth orbit where external tanks are reduced to raw material. The structure of ASSET is a partially reduced external tank (see Figure 4.1). The external tank is brought into low Earth orbit — as described in Section 2.3.1 — on a dedicated ASSET shuttle mission. During the mission, reduction equipment is set up inside the external tank to begin the salvage operation. Two hydrazine boost/deboost modules are attached to the external tank for altitude and attitude control (31:5.38). Photovoltaic arrays are added to provide electrical power for the boost/deboost modules, avionics, lights, cameras and reduction equipment.

The LH_2 tank section of the external tank is the source of material for the salvage operations (see Figure 4.2). Reduction equipment cuts composite sections of I-beams, flat plates, and spray-on foam insulation (SOFI) from the skin of the LH_2 tank. Figure 4.3 illustrates the potential source of I-beams and flat plate with an exploded view of the LH_2 tank. A primary cutter tracks along the I-beams inside the LH_2 tank cutting out the composite sections with an electron beam (see Figure 4.4). The primary cutter and the cut out composite sections are maneuvered with a robot

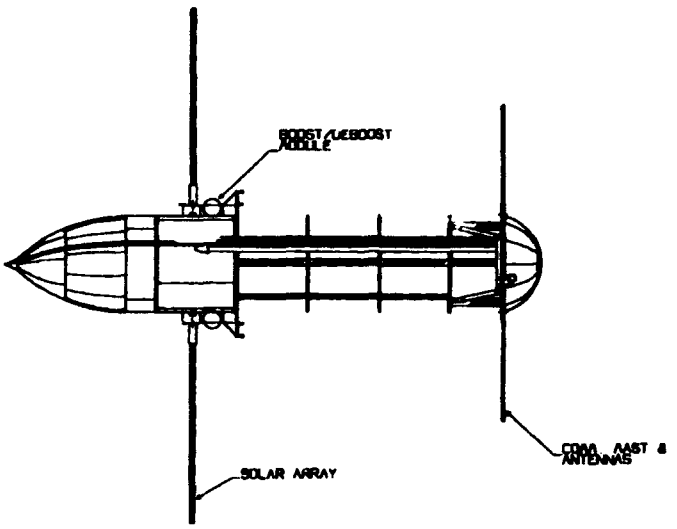

Figure 4.1 ASSET. The facility is produced from the external tank of the first space shuttle mission dedicated to ASSET (31).

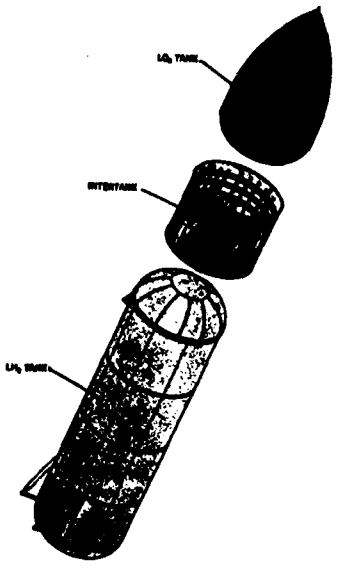

Figure 4.2 The external tank is composed of the LO_2 tank, the intertank, and the LH_2 tank. The LH_2 tank is the source of material for the salvage operations (31).

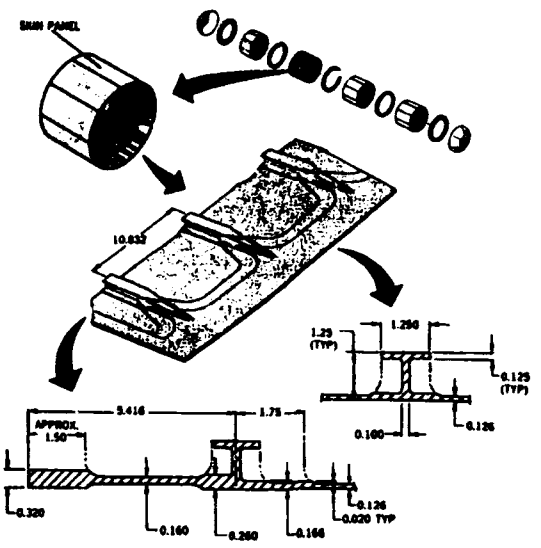

Figure 4.3 **tnkblow** An exploded view of the LH_2 tank. The potential source for I-beams and flat plates between them can be readily seen in the lower illustrations. Dimensions for this figure are in *inches*.

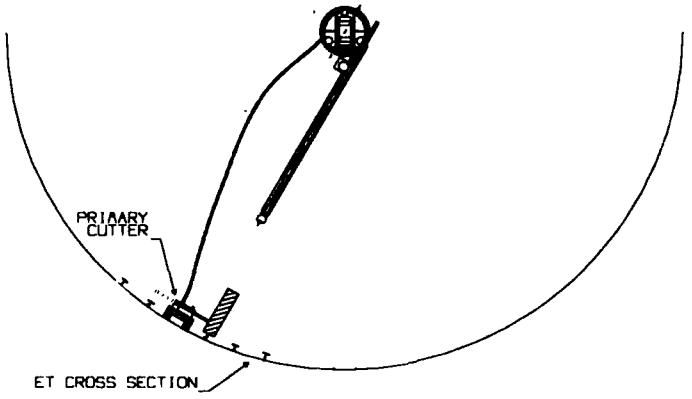

Figure 4.4 Cross-section of an LH_2 tank during ASSET salvage operations. The primary cutter tracks I-beams inside the LH_2 tank to cut out a composite section of skin with an electron beam. The primary cutter and the cut out composite sections are maneuvered with a robot arm on a centerline track inside the LH_2 tank (31).

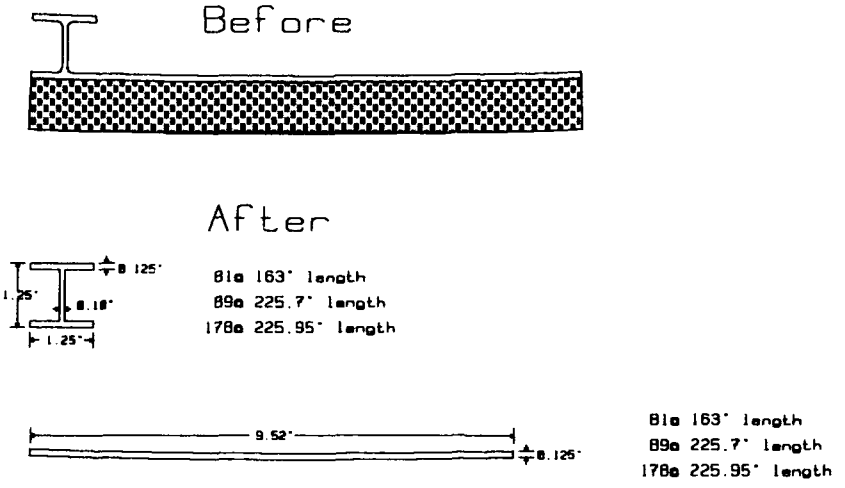

Figure 4.5 Cross-section of a composite section of LH_2 tank skin before and after workstation processing. The SOFI is removed and the I-beam is separated from the flat plate. Dimensions for this figure are in *inches* (31).

arm on a centerline track inside the LH_2 tank. The composite sections are carried to a workstation. At the workstation, the SOFI is removed, and the I-beam is cut from the flat plate. Figure 4.5 identifies a composite section before being processed by the workstation and the resulting I-beam and flat plate after workstation processing.

Ninety-four percent of the raw material produced by ASSET salvage operations comes in two shapes and two lengths:

- 81 flat plates 4.140 m long
- 267 flat plates 5.715 m long
- 81 I-beams 4.140 m long
- 267 I-beams 5.715 m long

All flat plates are 24.18 cm wide and 0.32 cm thick with a radius of curvature of 420.40 cm. All I-beams are 3.18 cm wide and 3.18 cm tall with a web thickness of 0.25 cm and a flange thicknesses of 0.32 cm.

Once the first external tank is made into ASSET, the study proposes that subsequent external tanks are docked with the ASSET for reduction. The reduction equipment is transferred to the new external tank, and the LH_2 tank is salvaged into more raw material. Afterwards, the reduction equipment and raw material product are transferred back to ASSET, and the remainder of the reduced external tank is detached and programmed to deorbit.

To accommodate an ASSET dedicated mission, the external tank must be modified on the ground. The significant ASSET external tank modifications are listed as follows (31:5.4):

- deactivate tumble valve
- install a disarm feature on the range safety system
- install an LO_2 and LH_2 tank depressurization capability.
- install hand rails and foot restraints within the LH_2 tank to assist extra vehicular activity (EVA)
- install a centerline track in the LH_2 tank for the ASSET robot arm
- install a handle on the aft manhole cover
- install bar codes, for indexing, on the major ring frames
- pre-tap holes for workstation mounts
- pre-tap holes for brackets and lights on the major ring frames
- modify the intertank to access power and power conditioning systems

4.3 Modifications to ASSET Equipment and Procedures

The SFP possesses a truss maker (see Section 5.3) that uses the raw materials produced during ASSET type salvage operations to create continuous trusses of variable lengths. For ASSET, the raw materials are cut into shapes and lengths which optimize ASSET's cutting and storage operations. However, before the SFP

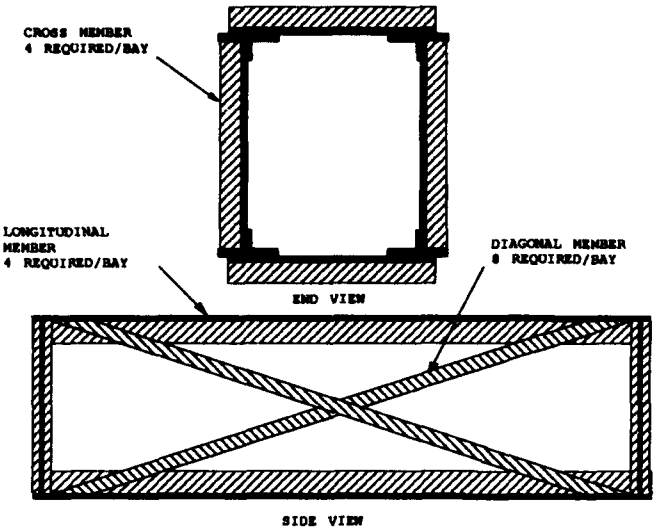

Figure 4.6 End and side view of a single bay of SFP produced truss (not to scale).

truss maker can use the raw materials for truss fabrication, modifications to the salvage operations are required. The raw materials must be cut into SFP truss maker required shapes and lengths. Once the materials are appropriately sized, they must be prepared for use by loading them into storage/feed magazines. As the name implies, the magazines not only store the raw materials but eventually *feed* the SFP truss maker. See section 11.5 for the specific quantities and configurations of the raw materials required for truss construction.

Two SFP fabricated truss configurations were considered as possible options for utilizing ASSET raw material. Selection of the final SFP fabricated truss configuration is described in Section 11.5. The members which make up a truss section are identified in Figure 4.6. Material and physical properties of the SFP produced truss are discussed in Appendix B. The necessary processes and tools to fabricate the SFP truss from external tanks are discussed in the remaining sections.

4.3.1 External Tanks. The SFP assembly originates from an already established, SFP modified, ASSET. When the SFP is mission ready, subsequent

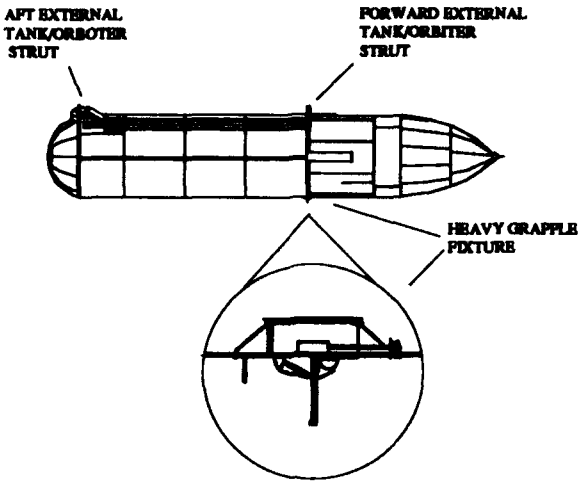

Figure 4.7 An external tank modified with a heavy grapple fixture opposite the forward external tank/orbiter strut. The lower illustration in the figure is an enlarged side view of a heavy grapple fixture. The heavy grapple fixture will be grappled by the SFP during docking.

external tanks replace the original external tank for more salvage operations. The SFP requires an additional ground modification to all the external tanks it processes. A heavy grapple fixture is installed on the intertank opposite the forward external tank/orbiter strut (see Figure 4.7). The heavy grapple fixture is used for docking the SFP with an external tank (see Section 8.3). For SFP assembly reasons, the first ASSET used to construct the SFP requires an additional heavy grapple fixture displaced 45° from the primary heavy grapple fixture (see Figure 4.8).

4.3.2 Primary Cutter. To eliminate storage and debris concerns, the primary cutter is reprogrammed for SFP operations to only cut out the material required for truss fabrication. The unused material remains attached to the external tank. SFP truss fabrication design decisions are discussed in Section 11.5. The primary cutter cuts out the 267 composite sections that are 5.715 m long, but only the I-beam portions of the 81 composite sections that are 4.140 m long. Additionally, the ends of the flat plates on the 5.715 m composite sections are cut at an angle.

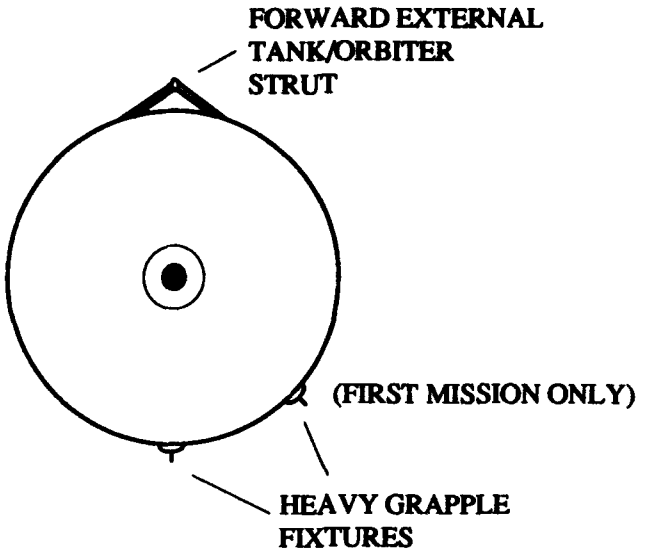

Figure 4.8 A cross-section view of the external tank modified with heavy grapple fixtures. The heavy grapple fixture offset 45° is only required for the first ASSET used in SFP assembly.

Originally, ASSET cut out 81 composite sections from the external tank in the form of 4.140 m long I-beams attached to 24.18 cm wide flat plates. However, the SFP truss maker requires only the 81 I-beams and not the flat plates. The I-beams are cross members for the truss product. To accommodate this requirement, the primary cutter only cuts out the I-beams from the 4.140 m long composite sections. The flat plate material remains attached to the external tank (see Figure 4.9).

The angle cut of the flat plates is necessary to eventually create diagonal truss members. The angled ends of the diagonal members allow a tight fit during the truss fabrication process. They also provide a larger surface area for weld attachment of the diagonal member to the truss longitudinal member (see Figure 4.10). Figure 4.11 illustrates the reprogrammed cuts on the 267 5.715 m composite sections. The angle cut is accomplished by reprogramming the path of the primary cutter. For the SFP truss maker, the desired angle is 12.8°.

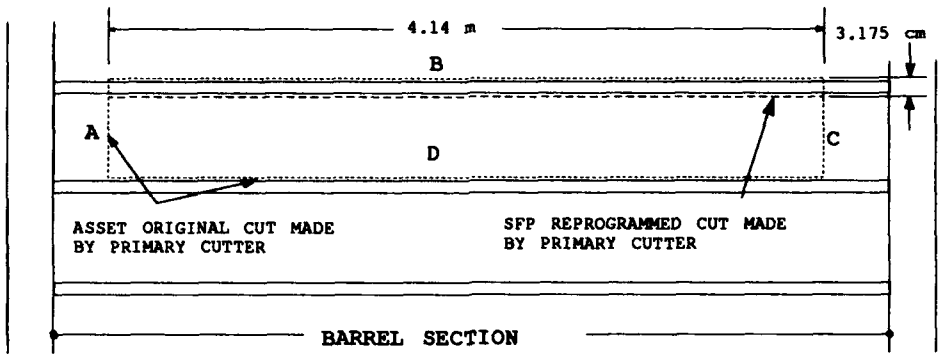

Figure 4.9 The primary cutter is reprogrammed to travel 3.175 *cm* during its cross cut of the 4.140 *m* composite sections. This produces 81 4.140 *m* I-beams. The flat plate originally cut during this same process remains attached to the external tank. Salvaging the material in this manner eliminates the problem of storing the excess flat plate material.

4.3.3 Workstation. In the original ASSET salvage operations, the robot arm carries a composite section of skin to a workstation for SOFI removal and separation of the I-beam and flat plate (see Figure 4.12) (31:5.23). At the workstation, the SOFI stripper uses a rotating wire wheel to cut the SOFI from the aluminum skin. Then, an electron beam cutter cuts the I-beam from the skin creating a separate I-beam and a flat plate. Figure 4.5 shows the material before and after processing through the workstation.

Figure 4.13 illustrates the modified workstation to support the SFP. After SOFI removal, the flat plate material from the composite sections is cut into five equal width strips and the I-beams are sliced down the center of the web to form two T-beams. To accomplish this, the workstation is modified by the addition of seven laser beam cut heads connected to a laser beam cutting system. Figure 4.14 is an end view of the rack of seven laser beam cut heads in the workstation. The ASSET electron beam cutter is eliminated. The reasons for selecting laser technology over

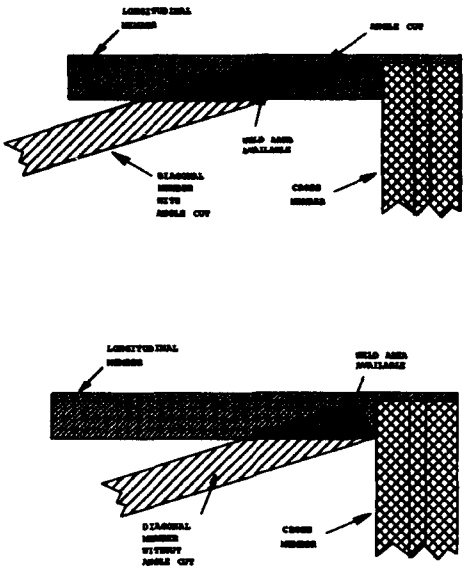

Figure 4.10 In the top illustration, an angled cut allows a proper fit for the diagonal truss member in the truss product and also provides a larger surface area for weld attachment. The bottom illustration shows how a poor fit occurs without the angled end of the diagonal truss member.

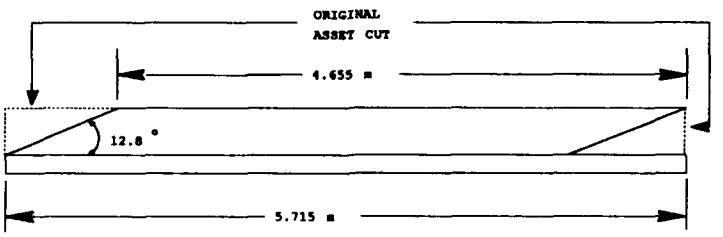

Figure 4.11 The primary cutter is reprogrammed to produce an angle cut, required later by the SFP truss maker, on the diagonal truss member.

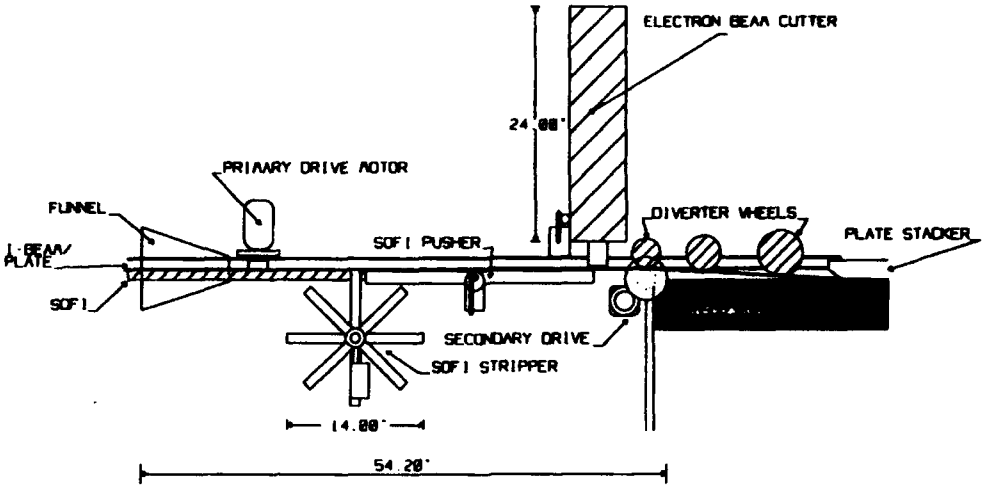

Figure 4.12 Side view of the ASSET workstation. The workstation removes the SOFI and separates the I-beam from the flat plate (31).

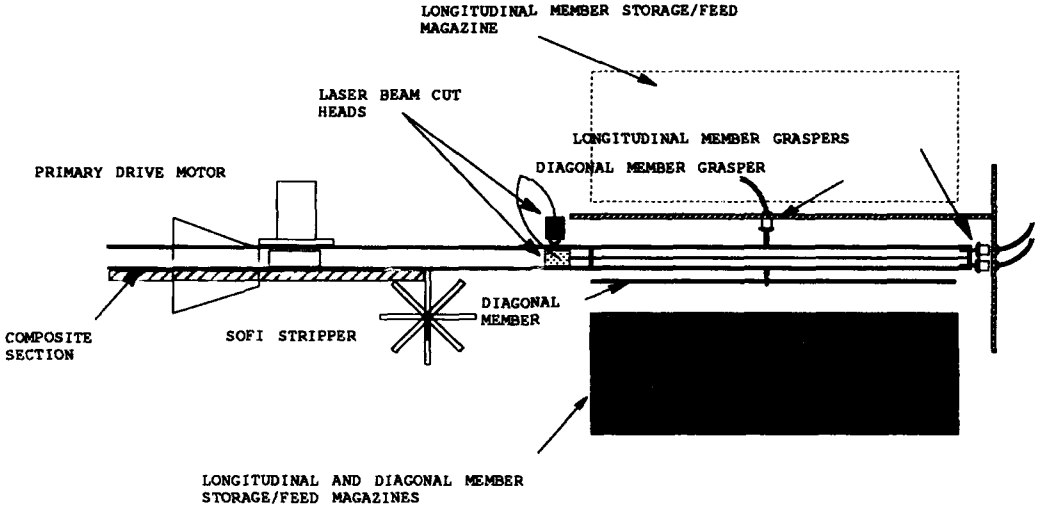

Figure 4.13 Side view of the ASSET workstation, modified to support the SFP.

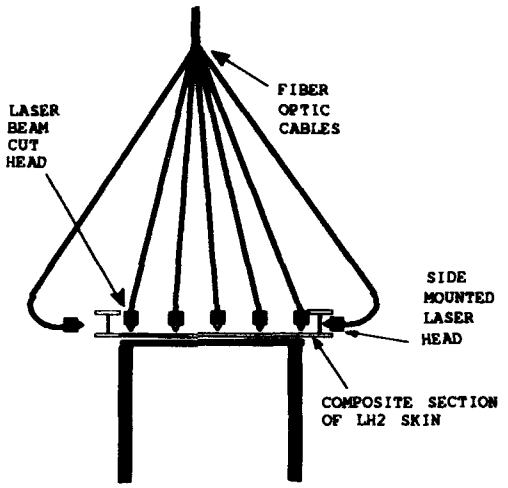

Figure 4.14 An end view of the seven laser beam cut heads in the modified ASSET workstation. The dotted I-beam represents the capability to operate on composite sections with the I-beam on the opposite side.

electron beam technology are discussed in Section 11.6. This same laser technology is also used during the SFP truss fabrication phase described in Section 5.3.

Five of the laser beam cut heads are attached above the workstation and serve two functions: they separate the I-beam from the flat plate material in the 5.715 m long composite sections, and they slice the 5.715 m flat plates lengthwise. As described earlier, the latter function is to produce diagonal members for the truss product. The two side mounted laser beam cut heads also serve two functions: they slice the web of the I-beam material lengthwise to produce T-beams, and they cut the 4.140 m T-beam material cross-wise to form equal length (1.035 m) T-beams. The 5.715 m and 1.035 m T-beams are the longitudinal and cross members of the truss product respectively. A side mounted laser beam cut head is required on both sides of the workstation because the primary cutting procedure produces composite sections with alternating I-beam side locations.

4.3.3.1 Side Mounted Laser Beam Cut Heads. As the composite section is driven past the side mounted laser beam cut head, the I-beam is sliced

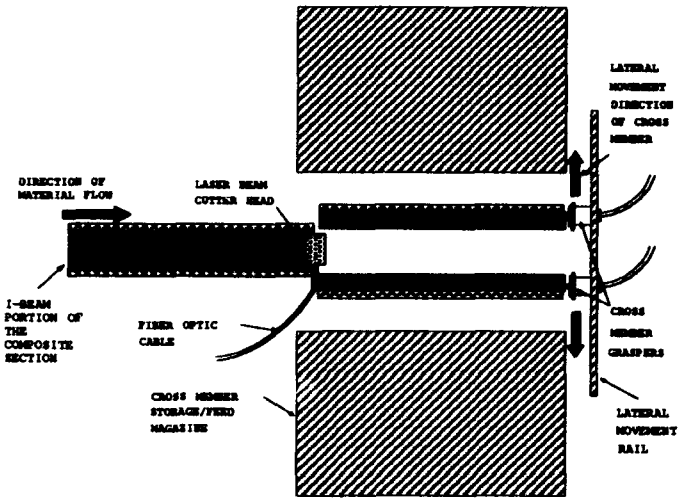

Figure 4.15 Side view of the I-beam on a composite section being driven through a side mounted laser beam cut head. In this particular illustration, the resulting T-beams are being cross cut into 1.035 m lengths and will serve as the cross members of the truss product.

down the center of the web to form two T-beams (see Figure 4.15). For cross member production, the 4.140 m composite sections are driven 1.035 m, the drive stops, and the two T-beams are grasped by the cross member graspers. Then, the side mounted laser beam cut head translates orthogonally to cut the T-beams cross-wise. Upon completion of the cross-wise cut, the side mounted laser beam cut head returns to its original position, the drive resumes moving, and cutting continues in the lengthwise direction. The cross-wise cut is accomplished three times for every piece of 4.140 m I-beam fed into the workstation. This produces 648 truss cross members that are 1.035 m long.

As soon as the cross-wise cut is made, the cross member graspers translate and load the cross members into cross member storage/feed magazines (discussed at the end of this section). The cross member graspers then return to their original positions and await the next pair of T-beam members.

The cross-wise cut is unnecessary when salvage operations shift to longitudinal truss member production. EVA crews extend the workstation distance between the laser beam cut heads and the graspers to accommodate the 5.715 m composite sections and bring in longitudinal member storage/feed magazines to replace the cross member storage/feed magazines. The longitudinal members are loaded into magazines in exactly the same way as the cross member magazines. This produces 534 5.715 m longitudinal members.

The process of T-beam cutting and magazine loading is accomplished on either side of the workstation. This means four magazines, two on each side of the workstation, are required during material processing. Magazine height was a concern due to the 91 cm diameter manhole each magazine was required to pass through to gain external tank entry. Therefore, a total of 12 cross member magazines are used to store the 648 cross members. By increasing the number of magazines, the height of the cross member storage/feed magazine is reduced to 85 cm. The width of the cross member storage/feed magazine is 8 cm.

Similar height concerns for the longitudinal member storage/feed magazines were alleviated by again using 12 magazines for storage. The height of the magazine was thus reduced to 71 cm. The width of the longitudinal member storage/feed magazines is also 8 cm.

The magazines are changed out by EVA crews. Full magazines are placed on a rack inside the external tank and will be removed by the remote manipulator servicing system after the salvage operations are complete. The servicing system is described in Section 8.2.

4.3.3.2 Top Mounted Laser Beam Cut Heads. As the 5.715 m composite sections are driven past the rack of five top mounted laser beam cut heads, the flat plates are cut into five equal width strips (see Figure 4.16). The five diagonal members generated by this operation are already the proper length due to the repro-

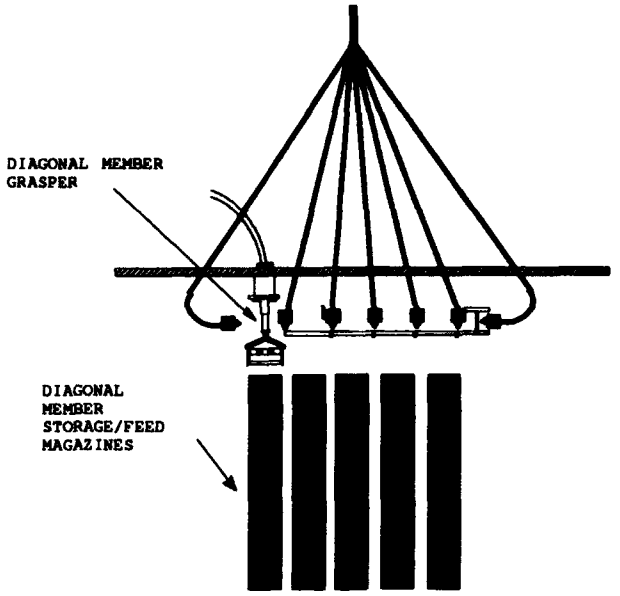

Figure 4.16 A rack of five top mounted laser beam cut heads cut lengthwise through the salvaged flat plate material to create five equal width strips and separate the flat plate from the I-beam.

grammed cut pattern of the primary cutter. Two centimeters prior to completing the lengthwise cut on the forward most diagonal member, the drive stops. A diagonal member grasper then grasps the end of each diagonal member about to be separated. Because the flat plate is cut at an angle, the diagonal members are separated in sequence versus simultaneously. Once grasped, the rack of five laser beam cut heads translates to cut the last 2 *cm* of the lengthwise cut to complete the diagonal member separation. The diagonal member grasper extends the separated diagonal member to a position for loading into a diagonal member storage/feed magazine. The loading process is the same as that described for the cross and longitudinal storage/feed magazines. When the diagonal member is loaded into the magazine, the diagonal member grasper resets over the next diagonal member to be separated. The rack of laser beam cut heads then translates back to the position where the simultaneous cuts were completed, and the drive/cutting procedures resume.

Eight diagonal member storage/feed magazines are loaded one magazine at a time. When five magazines are full, EVA crews change out the full magazines and place them on the rack inside the external tank for servicing system removal. The diagonal storage/feed magazine height is 52 *cm*.

4.3.4 Storage/Feed Magazines. The storage/feed magazines used to store and eventually feed individual truss members to the SFP truss maker, are modified versions of the magazines designed during the General Dynamics *Space Construction Automated Fabrication Experiment Definition Study* (12:2.130). In the General Dynamics case, the truss members were pre-loaded on the ground and eventually fed the General Dynamics truss maker in space. For a description of the General Dynamics truss maker, see Section 5.2 and (12). In the case of the SFP study, the magazines have been modified to allow loading in space as well as feeding the truss members to the SFP truss maker. This is not a major modification to the original concept and requires only that the top and bottom of the magazine be accessible (see Figure 4.17). The top is used for loading truss members, while the bottom is used for feeding truss members to the SFP truss maker.

Although three different size magazines are required for the three types of SFP truss members, the operation of all three are basically the same. The only difference is a pusher device added to the longitudinal member storage/feed magazine. This is required for feeding material into the SFP truss maker. The magazines are also fitted with dextrous grappling fixtures for eventual SFP servicing system grasping and maneuvering.

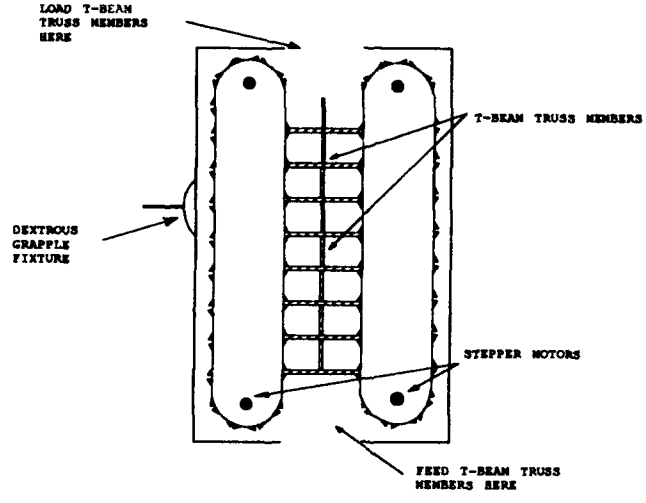

Figure 4.17 Side view of a cross member storage/feed magazine. The magazine is representative of the three different storage/feed magazines used on the SFP.

V. Truss Making

5.1 Introduction

The SFP is designed to fabricate versatile trusses which are basic elements for the construction of other space structures. Therefore, a literature survey was conducted to determine whether this type of operation had ever been conceived and to what extent it had been carried out.

During the late 1970's and early 1980's, much attention was paid to the possibility of placing large space structures into orbit. These structures were to be either built on Earth first and then deployed in space, or manufactured in space from raw materials brought from Earth.

The structures to be built on Earth were to be manufactured in such a way as to require as little volume as necessary in order to maximize use of the shuttle payload bay. Once in orbit however, these condensed packages would be deployed by different methods such as unfolding or unfurling into their final configuration. Even though ingenious methods for condensing and deploying these types of structures were envisioned, numerous shuttle launches would still be required to create a space structure of significant magnitude. Further, their structures did not possess great rigidity.

The structures to be manufactured in orbit using raw materials brought from Earth required new and innovative construction techniques before being considered feasible. Even though the complexity of the problem was compounded by virtue of the harsh environment of space, the benefit was the possibility of deploying in one shuttle mission what would take other methods multiple shuttle flights. It is this second, more complex space manufacturing method discussed in this design study.

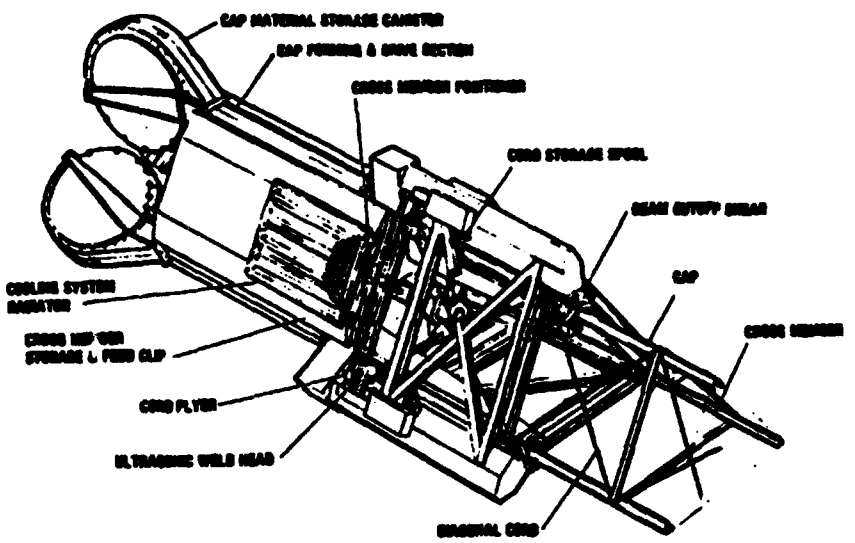

Figure 5.1 The General Dynamics truss builder automatically produces a truss constructed of three formed caps, joined to channel shaped cross members. It is stabilized with six zig-zag plyed tension cord diagonals (12:2-36).

5.2 Background

General Dynamics Convair Division and Grumman Aerospace Corporation accomplished independent studies outlining a method of manufacturing continuous truss sections in space. Truss sections are the basic building blocks of large space structures (i.e., platforms, space stations, solar power satellites, etc.) and therefore a valuable space construction commodity.

The General Dynamics truss building machine (see Figure 5.1) was designed during the *Space Construction Automated Fabrication Experiment Definition Study* and the truss building machine by Grumman (see Figure 5.2) was designed during the *Space Fabrication Design Study.* Ground versions of both machines were designed and manufactured. Each demonstrated the capability to automatically manufacture continuous truss sections. Although subtle differences existed between the two designs, the final product of each machine looked very similar (see Figures 5.3 and 5.4).

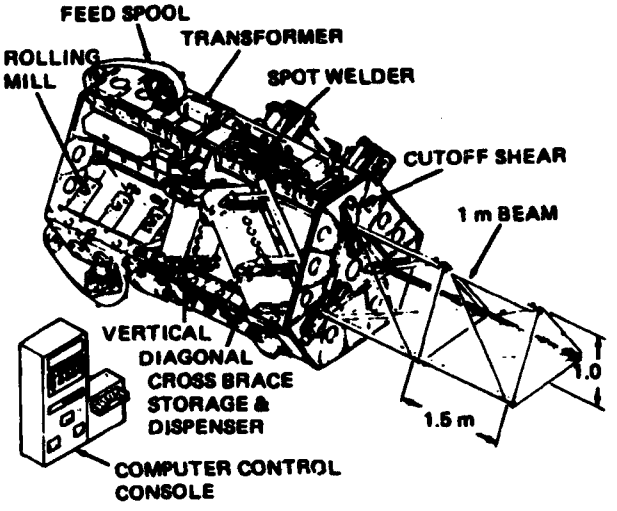

Figure 5.2 The Grumman truss builder is three identical machines arranged around a common axis. Each has its own coiled supply of material used for longitudinal cap formation. Pre-formed cross braces are supplied from cannisters attached to the machine. Some are at right angles, and some are inclined with respect to the cap members (43).

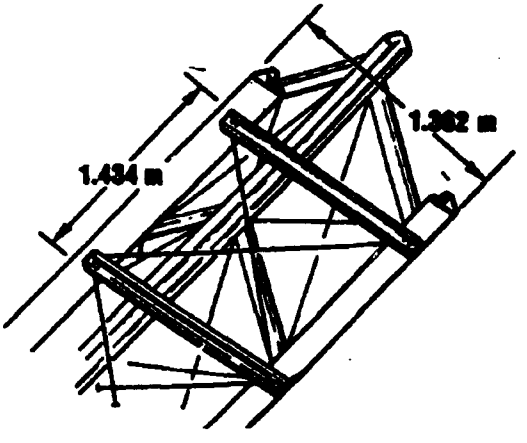

Figure 5.3 The triangular truss produced by the General Dynamics truss builder used zig-zag plyed tension cord as its diagonal bay support (7).

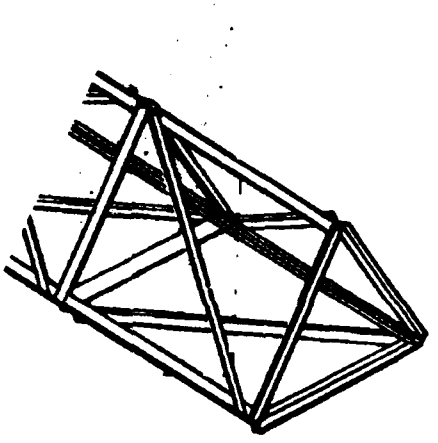

Figure 5.4 The triangular truss produced by the Grumman truss builder used preformed channel braces for its diagonal members (43).

5.2.1 General Dynamics Truss Machine. The General Dynamics machine was designed to go into orbit via the space shuttle and carry with it all materials required to manufacture truss sections. The space manufactured truss was constructed of three formed caps. These caps were joined to channel shaped cross-members and stabilized with six zig-zag plyed tension cord diagonals. Fabrication of the truss required the following processes (12:2-36):

- raw material storage
- material heating
- longitudinal cap forming
- truss drive
- diagonal cord application
- cross member application
- truss cutoff

Each of these processes is described briefly in the following sections.

5.2.1.1 Material Storage. Raw material for the truss maker was pre-processed and stored in a condensed form for use in space. Flat strip material for the caps was stored on three separate rolls (see Figure 5.1). Each roll could hold approximately 200 m of 0.0775 cm thick composite strip material and could be replaced by another roll when depleted.

5.2.1.2 Material Heating. The flat strip material for the caps was fed through a heating section in preparation for forming. The heating section applied heat only to bend zones. The zones were heated to the plastic state prior to entering the forming section. Applying heat to the material at the bend zones only, provided significant energy savings.

5.2.1.3 Longitudinal Cap Forming. The General Dynamics' patented *rolltrusion* process was used to form the heated flat strip material into the desired cross sectional shape (see Figure 5.5). On exit from the forming process, the cap sections were cooled before exposure to loads.

5.2.1.4 Truss Drive. The truss was moved through the fabrication process and deployed into space by a drive mechanism on each cap member. The drive mechanism also provided the force necessary to extract the cap material from storage and pulled it through the forming process.

5.2.1.5 Diagonal Cord Applicators. As the truss advanced through the fabrication process, the diagonal cord members were plyed across each face of the truss. The cords were properly tensioned and positioned for attachment. Final attachment of the tensioned diagonal cord members was accomplished at the same time as the cross members. This procedure is discussed in the next section.

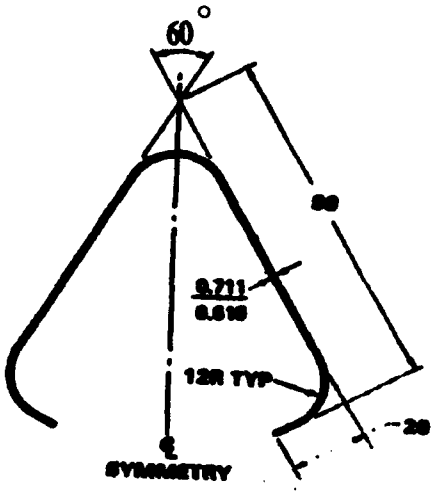

Figure 5.5 Cap sections formed by the General Dynamics patented *rolltrusion* process (12).

5.2.1.6 Cross Members. Prefabricated cross members were stacked closely together and stored in a clip mechanism. The clip had a belt fed mechanism designed to advance the stack, one member at a time. The cross members were positioned by a swing arm handler mechanism. When the cross members were positioned and the cords properly tensioned and positioned, one of six ultrasonic weld heads, equipped with a multiple-tipped weld horn, spot-welded the truss elements. The spot welding process captured each cord within a weld joint, between a cap and cross member.

5.2.1.7 Truss Cutoff. Once the desired length of truss had been produced, three guillotines cut through the three beam cap members. The finished truss was then ready to be utilized as required.

5.2.2 Grumman Truss Machine. The Grumman truss making machine was also designed to carry into orbit all materials required to manufacture truss sections in orbit. The Grumman truss maker employed three cap forming machines

arranged around a common axis. Each machine was complete with the storage, heating, forming, cooling, and drive sub-functions required to continuously process strip material into the desired cap shape. The three cap sections emerged from one end of the machine parallel to each other, 1 m apart to form the longitudinal corner sections of a triangular truss (43:34).

Just as in the General Dynamics design, pre-formed cross braces were supplied from magazines attached to each face of the machine. The magazines supplied cross braces at right angles to the caps. These cross braces were then induction welded to the longitudinal cap members.

The Grumman truss maker diverged from the General Dynamics truss maker by using a longer version of the cross brace as the diagonal member instead of crossed cord material. Grumman accomplished this by attaching, at an angle, an additional storage magazine to each face to supply the material (43:35).

5.3 SFP Truss Making

Direct application of either of the above truss makers for the SFP is not possible primarily because raw material thickness is too great to make heat forming practical. A discussion of this and other decisions related to truss making is located in Section 11.4. However, several aspects of the truss making processes described earlier find direct application in the SFP truss making machine (see Figure 5.6).

The SFP truss maker also has some unique features not found in the truss makers described earlier. These unique features are:

- the four sides of the truss maker must be accessible by the SFP servicing system which is described in Section 8.2
- the truss maker rides on rails along the main integrated truss and is necessary for center of mass considerations which are described in Section H

- the top of the truss maker is the mounting point for the docking and delivery system and is described in Section 8.8

In general, the SFP truss maker shown in Figure 5.6 begins truss fabrication when longitudinal T-beams are feed into the truss maker at one end and welded into continuous longitudinal members. The continuous longitudinal members are then indexed through the truss maker — stopping and starting at prearranged stations to receive cross and diagonal member attachment. The indexing process required to move the truss through the truss maker is such that cross and diagonal members are all welded to the longitudinal members during one stop. An additional stop is required and occurs to allow the formation of the continuous longitudinal members. Therefore, during normal operation, only two stops per truss maker cycle are required. Finally, once the desired length of truss has been fabricated, grapple fixtures are attached and the completed truss is cut and stored for future use. The remainder of this chapter is devoted to a complete description of the SFP truss making machine.

Simplicity of design and operation was the primary consideration in developing the tools and automated truss maker concept. This was necessary to achieve high reliability. For normal operations, no manned interface is necessary. Fabrication of the SFP truss sections requires the following processes:

- telerobotic manipulation of material storage/feed magazines
- feeding longitudinal T-beam from storage/feed magazines
- truss drive and guide wheel mechanism
- butt welding T-beams to form continuous longitudinal members
- application of cross members to continuous longitudinal members
- application of diagonal members to continuous longitudinal members
- application of dextrous grapple fixtures to truss

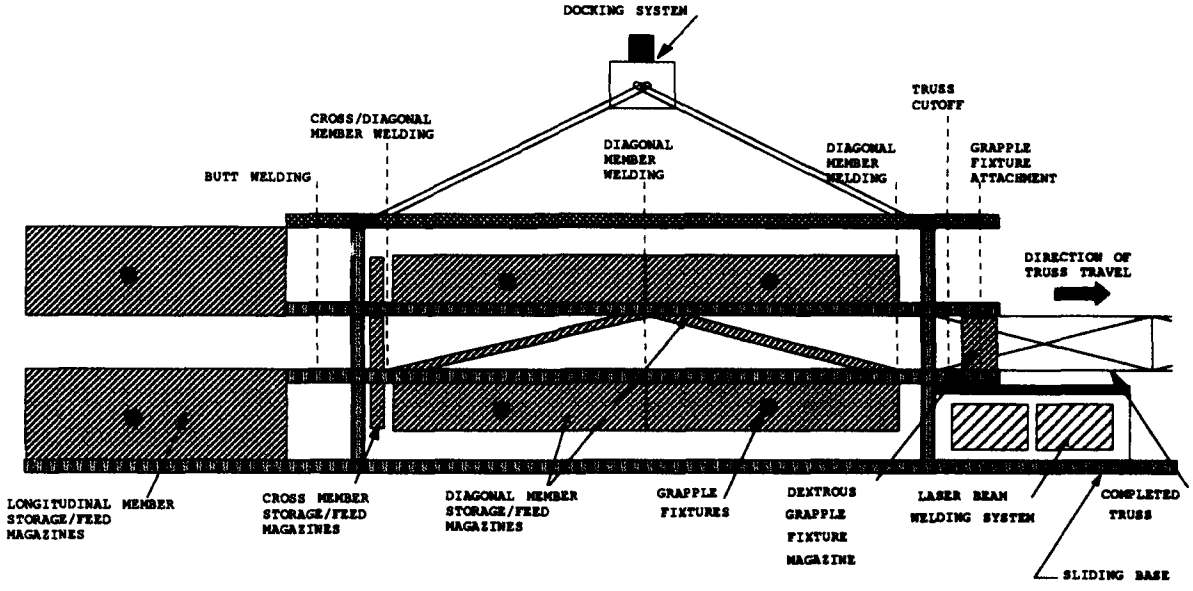

Figure 5.6 The SFP truss maker automatically fabricates continuous square trusses.

- cutoff of completed truss
- manipulation of completed truss sections

5.3.1 Manipulation of Storage/Feed Magazines. Thirty-two truss member storage/feed magazines are loaded during the ASSET salvage operation and must be moved from the ASSET facility to the SFP. The storage/feed magazines are equipped with dextrous grapple fixtures to allow the SFP's servicing system to grapple them. The truss member storage/feed magazines always reside in the same location in the ASSET facility. Therefore, a pre-planned, automated operation for grappling and maneuvering them into place on the SFP is envisioned.

The first four cross and longitudinal storage/feed magazines are attached to the SFP truss maker. There are a total of eight diagonal member storage/feed magazines. All eight of these magazines are required by, and attached to, the SFP truss maker. This leaves 16 additional truss member storage/feed magazines, eight containing longitudinal members and eight containing cross members. These 16 storage/feed magazines are maneuvered one at a time to their storage position under the main integrated truss (see Figure 5.7). Storage racks for the specific purpose of holding these spare storage/feed magazines are built into the underside of the main integrated truss. Extra storage racks are built into the underside of the main integrated truss to store empty storage/feed magazines.

5.3.2 Feeding Longitudinal T-Beams from Magazines. The truss fabrication process starts when four longitudinal T-beam magazines simultaneously eject one member each (see Figure 5.8). Longitudinal members are made available when the magazine feed belts are advanced one step. This delivers one longitudinal member into position for ejection. Once in position, a pusher mechanism guides the member out of the magazine to waiting drive wheels. The pusher then returns to its starting position until the next member is required by the truss maker.

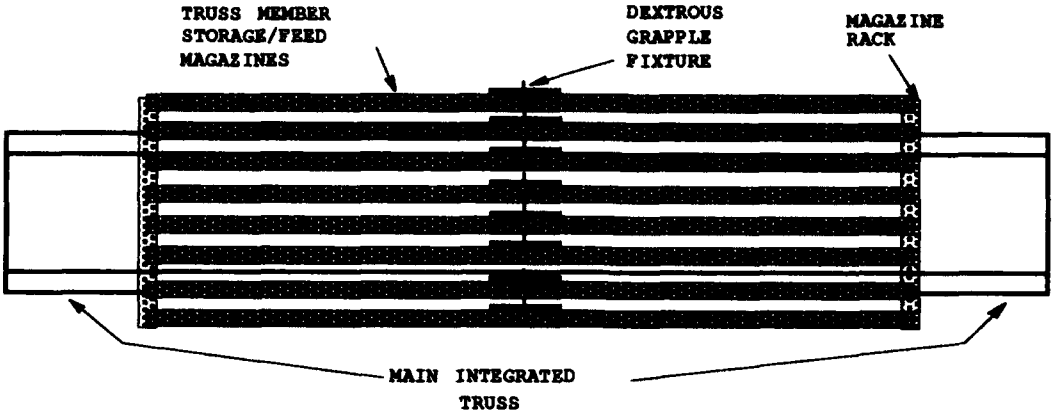

Figure 5.7 Bottom view of stored truss member storage/feed magazines. Sixteen loaded storage/feed magazines are stored below the main integrated truss until needed by the truss maker. Magazines are maneuvered one at a time to their storage position by the SFP's servicing system.

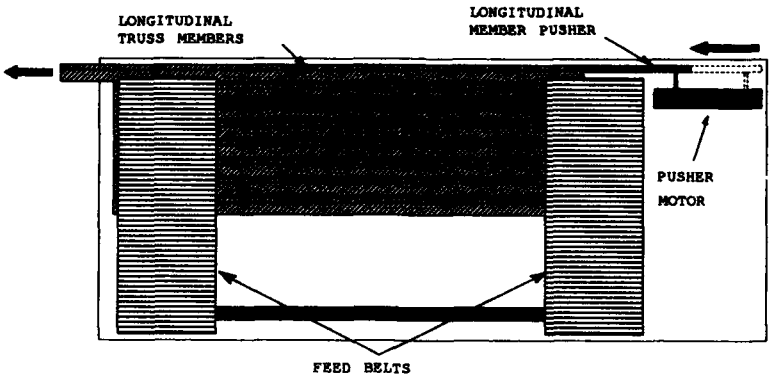

Figure 5.8 Side view of the SFP longitudinal member storage/feed magazine (not to scale). Stepper motors in the magazine shift the T-beam members into position one member at a time. Then the pusher drives the T-beam out of the magazine, thus *feeding* the SFP truss maker longitudinal truss members.

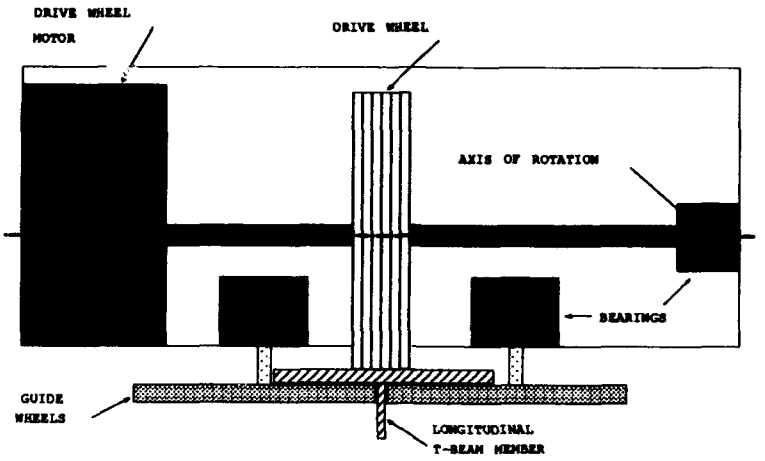

Figure 5.9 End view of one of the eight SFP truss maker drive wheels. The drive wheels push the truss through the SFP truss making process.

5.3.3 Truss Drive and Guide Wheel Mechanism. There are four SFP truss maker drive sections. Each drive section contains two friction drive wheels (see Figure 5.9) and eight guide wheels (see Figure 5.10). The drive wheels provide the necessary force to push the truss through the truss maker. The guide wheels provide support and guidance for the truss as it moves through the truss maker. The drive sections are located at the end of the SFP truss maker where the longitudinal truss members are fed by their storage/feed magazines.

When a longitudinal member is fed to the truss maker, it is engaged by the first drive wheel. The first drive wheel pushes the longitudinal member until it is engaged by the second drive wheel. Both drives push the longitudinal member until only the second drive wheel is in contact with the longitudinal truss member (see Figure 5.11). When this occurs, the second drive wheel stops the end of the longitudinal member when it is centered in the longitudinal member butt welding section.

Next, another longitudinal member is ejected by the storage/feed magazine. The first drive wheel engages it and pushes it until it is butted against the previous

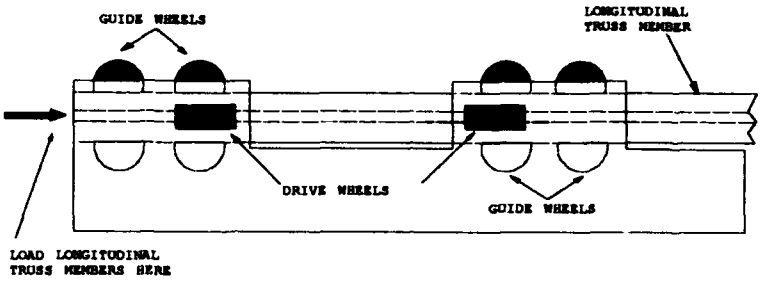

Figure 5.10 Top view of drive wheels housed in the SFP truss maker drive section. Drive wheels provide the necessary force to push the truss through the truss fabrication process while guide wheels provide support and guidance.

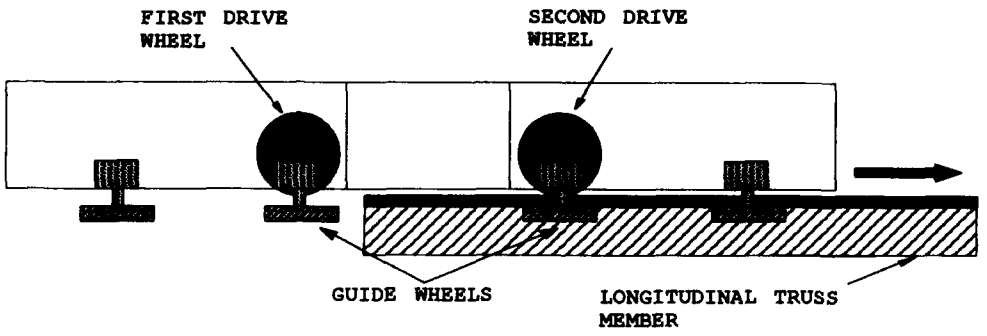

Figure 5.11 Side view of the SFP drive wheels pushing the truss through the SFP truss making process.

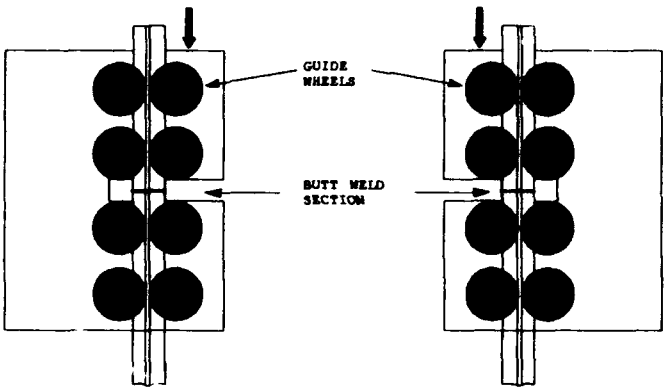

Figure 5.12 The drive wheels push the longitudinal truss members into the butt welding section. The drive wheels stop and hold the longitudinal members during the welding process.

longitudinal truss member still being held by the second drive wheel (see Figure 5.12). The process just described occurs simultaneously at all four truss drive sections. The longitudinal truss members are now in position for the butt welding process described in Section 5.3.4.

After butt welding is accomplished, the drive wheels push the now continuous longitudinal members into position for cross and diagonal member attachment. A new set of guide wheels are placed to allow attachment of truss cross members without interfering with the process. An inside set of guide wheels would interfere with cross and diagonal member attachment and is therefore eliminated. The outside guide wheels are shaped to hold the longitudinal truss members by their edges (see Figure 5.13 and 5.14). Pressure applied to the truss by the outside set of guide wheels provides support for the truss as it moves through the truss maker.

5.3.4 Butt Welding of T-Beams. Laser beam weld heads, one positioned over the butted surfaces and another positioned to the side of the butted surfaces, are

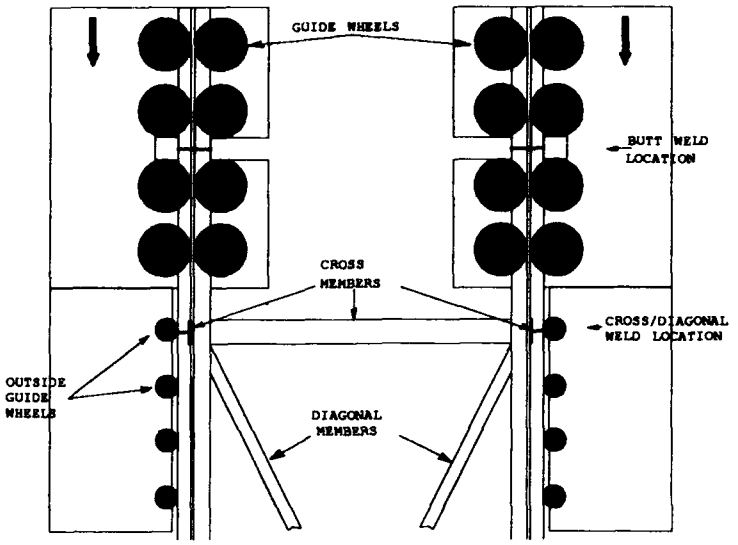

Figure 5.13 The SFP truss maker guide wheels, in combination with the drive wheels, hold the longitudinal members in place for the butt welding process.

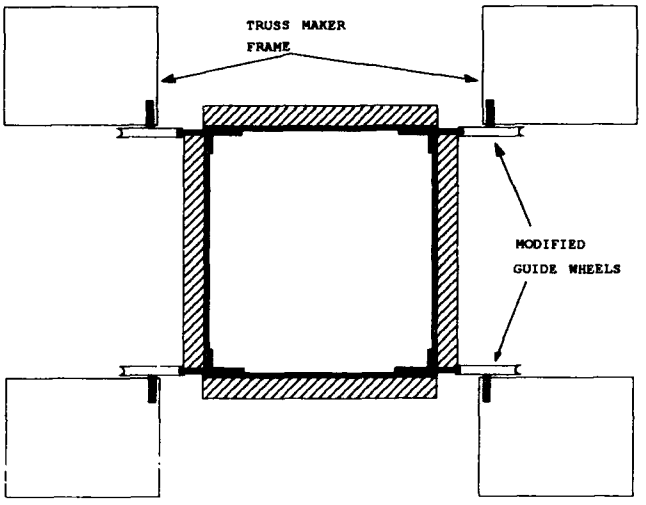

Figure 5.14 Outside guide wheels guide the truss through the SFP truss making process without interfering in the welding process.

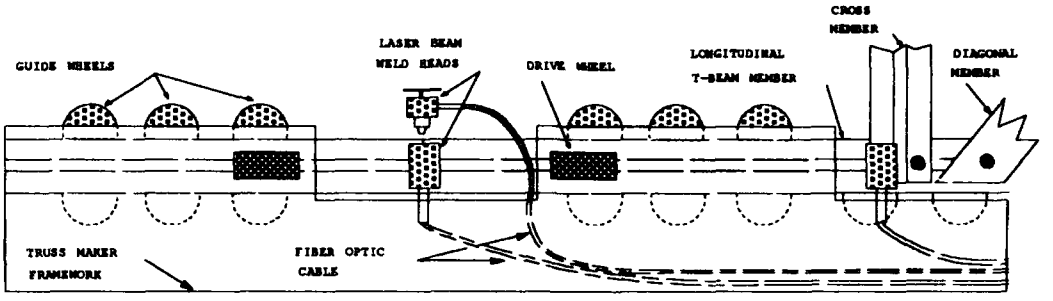

Figure 5.15 Top view of one of the truss maker's drive sections. The SFP laser beam welding system butt welds longitudinal truss members. The members are driven and held in place for welding by eight drive wheels, two for each longitudinal SFP truss maker drive section.

activated when the drive wheels have stopped. The weld heads move orthogonally across the abutting surfaces until a weld joint is formed. The weld heads are attached to the truss maker laser beam welding system via fiber optic cables. The fiber optic cables are laced inside the SFP truss maker framework to avoid possible interference problems cables on the outside of the truss maker might pose. Laser beam weld heads are attached to the ends of the fiber optic cables which exit the truss maker framework at the weld head locations (see Figure 5.15). The welding system used by the SFP truss maker applies multiplexing laser beam technology described in Section 11.7. The laser beam welding system is located at the end of the truss maker (see Figure 5.6). Welding is accomplished in a sequential, as opposed to simultaneous, manner. This means that no two weld heads ever operate at the same time. This versatile, multiplexing feature of the welding system keeps the truss maker power requirements low. The truss maker requires a maximum of 7 kW of power — 5 kW for the laser beam welding system and 2 kW reserved for truss maker command and control.

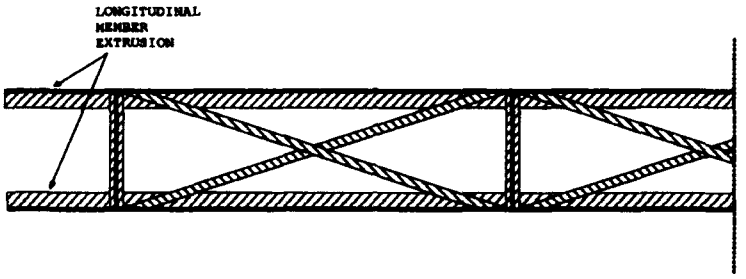

Figure 5.16 Side view of the 2 m extrusions on SFP fabricated trusses.

5.3.5 Application of Cross Members. The first longitudinal truss members are driven approximately 2 m beyond the cross member storage feed magazines. By driving the members beyond this first cross member attachment point, four longitudinal extrusions are created (see Figure 5.16). The extruded ends of the finished truss are intended for customer application of terminating quadpods (see Figure 5.17). Quadpods provide the desirable capability of centroidal connecting joints. Centroidal truss attachments are preferred over other types of truss joining, such as truss overlap, because of the avoidance of eccentric loads at the joints (10:15). However, centroidal attachments are only one possible technique for joining trusses in space.

With the longitudinal members properly positioned, cross member storage/feed magazines (see Figure 5.18) advance the magazine feed belts one step. Awaiting cross member graspers receive the cross members from the magazines (see Figure 5.19). The grasping operation is performed via a scissors-type clamp driven by redundant hold drive motors similar to the one used by the General Dynamics truss maker (12:2.130) (see Figure 5.20). Sensing the grasped cross member, the

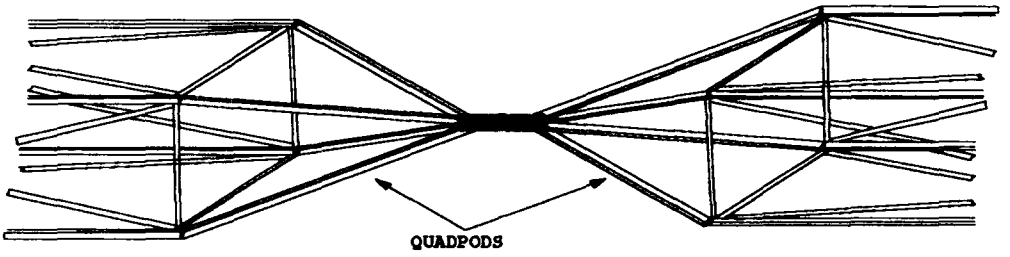

Figure 5.17 Conceptual drawing of truss terminating quadpods. Quadpods are not the only truss joining technique but they do avoid eccentric loads at joints while some other joining techniques do not (10:15).

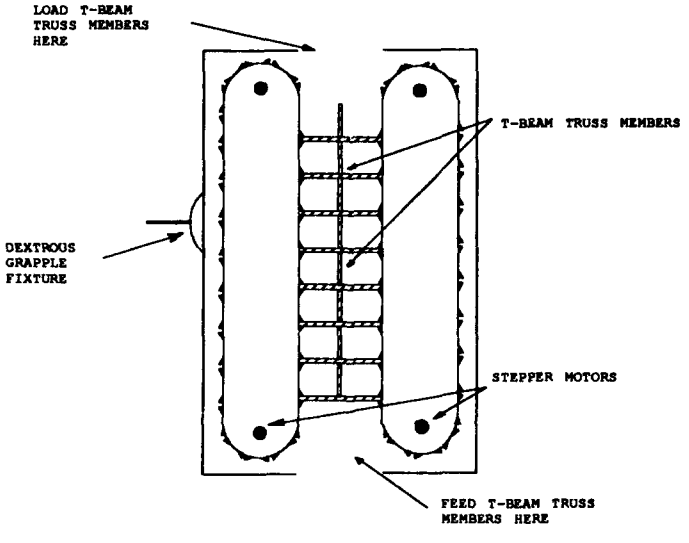

Figure 5.18 End view of the cross member storage/feed magazine. The cross member magazine feeds 1.035 m long T-beam members to awaiting cross member graspers.

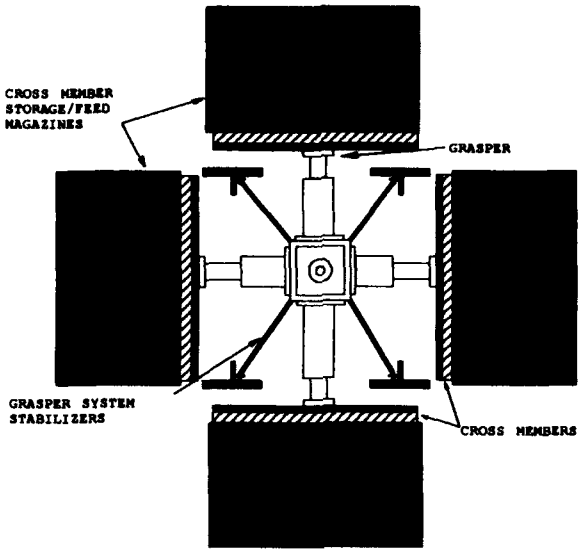

Figure 5.19 End view of the cross member storage/feed magazines providing a cross member for each cross member grasper.

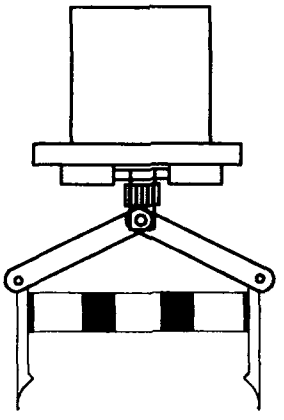

Figure 5.20 Finger mechanisms are used to grasp members as they are fed from storage magazines.

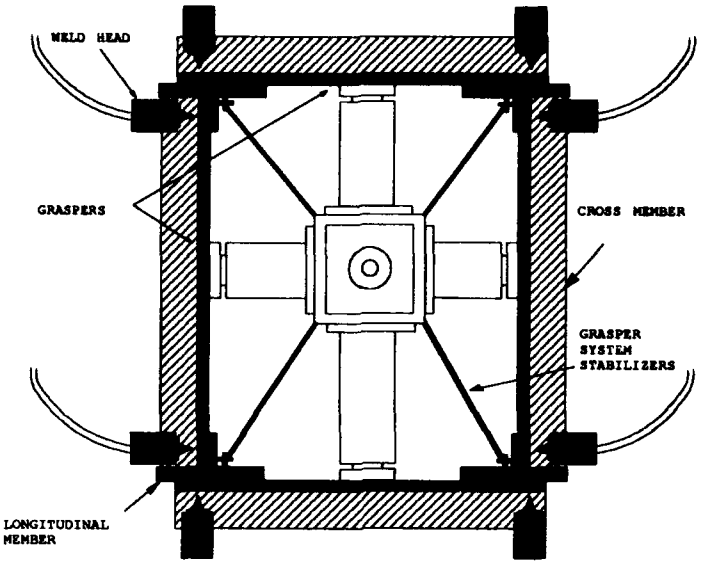

Figure 5.21 The SFP cross member graspers grasp, translate, and hold members while welding occurs.

grasper drive is activated causing the grasper arm and grasped cross member to translate inward toward the continuous longitudinal members.

Grasper system vibrations are damped out by stabilizers attached to the grasper system. Wheels are fixed to the ends of the stabilizers and ride against the inside of the longitudinal members (see Figure 5.19). The stabilizers are required to prevent misalignment of truss members during the grasping and welding process.

When the cross members are in proper welding position, the laser beam weld heads move into position (see Figure 5.21). The cross member storage/feed magazines are set back 10 *cm* from the truss maker to allow the laser beam weld heads access. Finally, the weld sequence is activated and the cross members are sequentially welded to the longitudinal members.

5.3.6 Application of Diagonal Members. Diagonal members are fed, grasped, positioned, and welded to the longitudinal truss members via a process similar to that of the vertical truss cross members. However, the diagonal truss

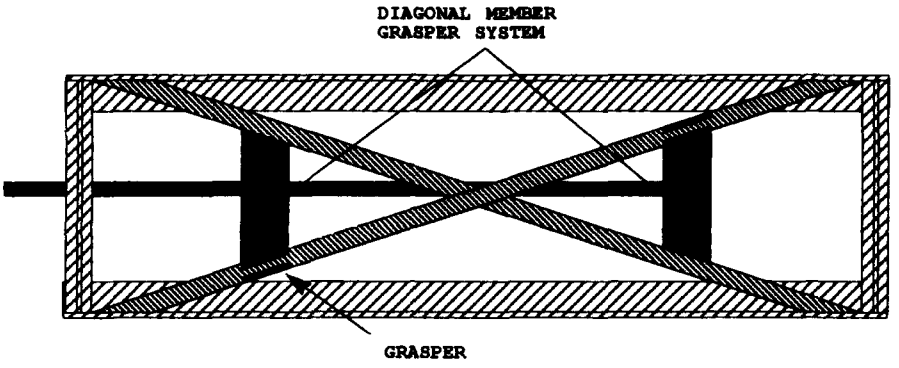

Figure 5.22 Side view of a diagonal truss member being held in position by graspers. The two grasping devices provide diagonal member stability during the welding process.

members require two grasper devices for their grasping system (see Figure 5.22). The two graspers are located at both ends of the diagonal storage/feed magazine and provide stability during the welding process. Two crossed diagonals per bay are required on each side of the truss. This configuration requires two separate stations for mounting diagonal members to prevent interference between diagonals during installation (see Figure 5.6). The crossed diagonals are attached in two stages. First, the diagonal storage/feed magazine releases one diagonal member to awaiting graspers. The diagonal member is held in place by the two graspers and welded to the longitudinal truss member. The truss is then driven one bay length and stopped. The second truss diagonal is then fed, positioned, and welded to complete one truss bay. The completed truss bay is driven unimpeded out the end of the SFP truss maker (see Figure 5.6). This process is repeated until the desired length truss is completed or raw material is exhausted.

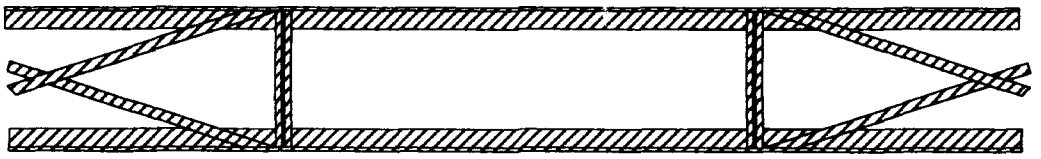

Figure 5.23 Side view of the last truss bay fabricated before the cutoff process. Longitudinal extrusions are generated by cutting through the middle of the bay. The extrusions can be used for quadpod application.

An exception to the truss diagonal member application process just described, occurs immediately prior to the truss cutoff process described in Section 5.3.8. The last truss bay fabricated before the truss cutoff process is created with no diagonals (see Figure 5.23). By creating a truss bay with no diagonals, the longitudinal extrusions for the attachment of quadpods can be formed by cutting through the middle of the bay.

5.3.7 Application of Dextrous Grapple Fixtures. Before the truss is cut, at least two dextrous grapple fixtures are attached to opposite sides of the completed truss section. More dextrous grapple fixtures can be attached at any point along the truss if required

The grapple fixtures, minus guide posts, are stacked in their own storage magazines. The guide posts are not initially attached to the stored grapple fixtures. This allows compact storage of the grapple fixtures in their storage/feed magazines. The grapple fixture storage/feed magazines feed the devices in the same fashion as the

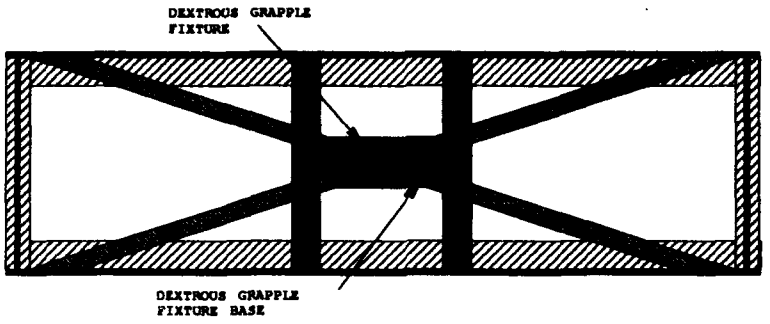

Figure 5.24 Side view of the truss bay with the dextrous grapple fixture attached. The SFP servicing system grapples the grapple fixture prior to truss cutoff.

other SFP storage/feed magazines. The grapple fixtures are fed into place and held against the outside of the completed truss. Weld heads then move into place and weld the grapple fixtures to the longitudinal members of the truss (see Figure 5.24).

Grapple fixture guide posts are stored in an upright position on the outside of the grapple fixture storage/feed magazines. The guide posts are detached from the storage/feed magazines and attached to the grapple fixtures by the grapple fixture guide post removal and replacement tool. See Section 8.2 for a description of SFP servicing system tools available. Once the dextrous grapple fixtures are firmly fixed to the truss and the guide posts have been attached, the SFP servicing system grapples one of the two dextrous grapple fixtures and holds the truss in position for cutoff.

5.3.8 Cutoff of Completed Truss. Four laser beam cutters cut the finished truss from the truss still being fabricated in the truss maker. The laser beam cut heads cut the truss at the center of the bay with no diagonals. This produces an

approximately 2 m extrusion on both the truss being cut and the truss still in the truss maker.

The four laser beam cutters begin the cutting process by moving orthogonally across the flange of the longitudinal member. After the flange has been cut, the laser beam cut heads stop cutting and move around to the side of the longitudinal members. The ability to move the laser beam cutters while holding the workpiece in this fashion is one of the advantages of laser beam technology and is discussed in Section 11.7. After this rotational movement, the laser beam cutters are now in position to cut orthogonally across the web of the longitudinal members. When all four longitudinal members have been cut, the SFP servicing system maneuvers the completed truss to either its storage position or the docking system for customer hand off. The SFP docking system is described in Section 8.3. The truss remaining the truss maker is the beginning of the next truss to be produced.

5.3.9 Manipulation of Completed Truss Sections. The SFP servicing system grapples one of the two dextrous grappling fixtures attached to the completed truss. The truss is then moved to a storage rack attached to the orthogonal integrated truss (see Figure 5.25). The truss storage racks are equipped with dextrous latching devices for attachment to the second SFP fabricated truss grapple fixtures. The SFP servicing system maintains a positive lock on its truss grapple fixture until the storage rack mates with the second truss dextrous grapple fixture. Once firmly secured by the storage rack, the servicing system releases its grapple fixture. The truss remains locked parallel to the storage rack until it is required by an end user.

When a truss section is required, the SFP servicing system grapples a free truss dextrous grapple fixture. Once positive lock has been achieved, the truss storage rack releases the lock on its grapple fixture. The servicing system maneuvers the truss to the SFP docking system. The SFP docking system mates with the free truss dextrous grapple fixture. When the docking system has positive lock on the truss,

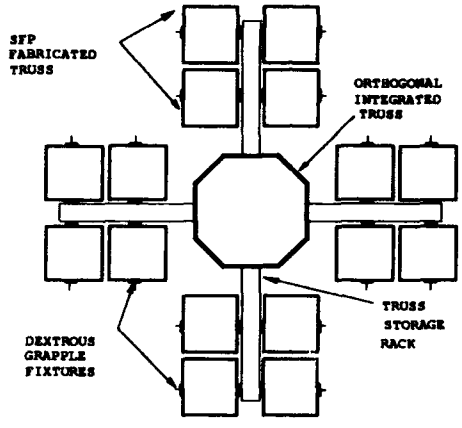

Figure 5.25 End view of SFP's orthogonal truss and truss storage rack. Completed truss sections are maneuvered to their storage position via the SFP's servicing system which grapples one of the two truss grapple fixtures. Truss sections are stored parallel to the orthogonal integrated truss. The storage rack is equipped with dextrous latching devices for mating with the second truss grapple fixture.

the SFP servicing system releases its grapple fixture. Finally, the docking system, in conjunction with the SFP's precision standoff capability, hands the truss section off to the end user.

VI. Shielded Coil Electrodynamic Propulsion

6.1 Introduction

Recent work by Spenny and Lawrence (81) and by Lawrence (49) has shown electrodynamic propulsion to be a possible method of propulsion for large space platforms. This design study applies the initial work done by Spenny and Lawrence in this area, and the initial work done by Ladouceur on the shielding of current-carrying conductors (48), to develop a shielded coil electrodynamic propulsion system for a prototype space fabrication platform (SFP). Electrodynamic propulsion relies on the interaction of a current through a wire with an external magnetic field. Depending on the configuration of the wire and the magnetic field, the interaction can be used to generate forces and torques. These forces and torques can be used for propulsion and attitude control.

An iterative design approach is used to evaluate and modify a proposed design configuration to achieve an SFP capable of meeting the requirements outlined in Section 3.2. The iterative design approach uses vehicle controllability as the basis for evaluating a proposed design. For a proposed design, a linear quadratic regulator based controller is developed. This controller is then used in computer simulations to determine the forces required to perform specific maneuvers. From these forces the vehicles design parameters, such as current carrying capacity, required power, conductor size, etc., can be determined. This process is repeated until a satisfactory design is developed. Once the final SFP design is determined, its performance can be analyzed.

Development of the electrodynamic propulsion system requires the combining of a number of basic concepts with the performance specifications to achieve a satisfactory platform design. The next section provides a discussion of these concepts.

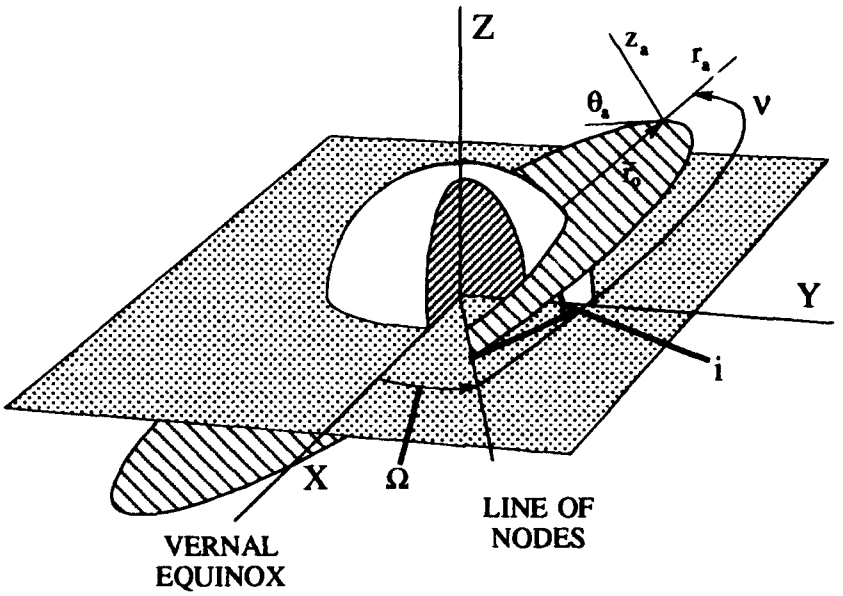

Figure 6.1 The orbital reference frame with the origin translated for clarity to a point on the orbit path.

6.2 Basic Concepts

Before developing the shielded coil electrodynamic propulsion system for the SFP, some basic concepts such as coordinate systems, forces and torques due to currents in magnetic fields, modeling of the Earth's magnetic field, and equations of motion for the SFP must be discussed. These concepts provide the foundation for the iterative design process for the SFP.

6.2.1 Coordinate Systems. Throughout the design process, a number of coordinate systems or reference frames are used. For satellites orbiting the Earth, a suitable inertial reference frame is the geocentric-equatorial coordinate system — the $\hat{i}$-frame. Another inertial coordinate system, the Earth-centered inertial coordinate system is also used — this is the $\hat{e}$-frame. The use of the dipole model for the Earth's magnetic field requires the use of the Greenwich-equatorial reference frame — the $\hat{g}$-frame. An orbital reference frame (see Figure 6.1) — the $\hat{a}$-frame — and body-

centered reference frame — the $\hat{b}$-frame — are required to describe the position and orientation of the SFP. A detailed discussion, as well as diagrams of these reference frames is contained in Appendix C.

6.2.2 Magnetic Field Generated Forces and Torques. One of the objectives of this design study is to use electrodynamic propulsion. Electrodynamic propulsion relies on the interaction of a current through a conductor with the Earth's magnetic field to produce forces. In order to understand how this is applied to the SFP, some basic concepts must be understood. This section presents the background of how the current/magnetic field interaction works.

6.2.2.1 Force Law. A charge, q_0, moving in a magnetic field, $\overline{B}$ (or B-field), will, in general, experience a sideways deflecting force that causes it to take a spiral path. If the velocity, $\overline{v}$, of the charge and the force, $\overline{F}_B$, are determined by observing the path, the magnitude and direction of $\overline{B}$ can be derived by satisfying the relation (32:538–540):

$$\overline{F}_B = q_0 \overline{v} \times \overline{B} \tag{6.1}$$

For direction considerations, the cross product assumes the right hand rule.

A current can be thought of as an assembly of moving charges. Because a magnetic field exerts a sideways force on a moving charge, it will also exert a sideways force on a conductor carrying a current. This is governed by the equivalent expression:

$$\overline{F}_B = i\overline{L} \times \overline{B} \tag{6.2}$$

where i is the current and $\overline{L}$ is the direction and length of the conductor (see Figure 6.2). This study will refer to Equation 6.2 as the *force law.* The *force law* concept will be used extensively for producing thrust.

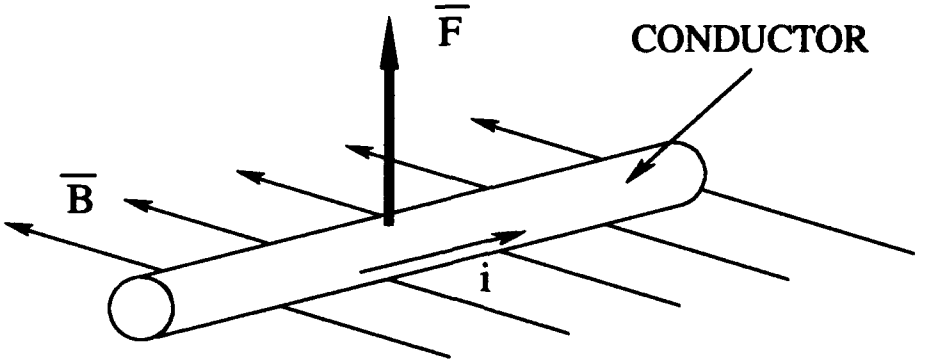

Figure 6.2 A conductor in a magnetic field with a current flowing through it experiences a force normal to the plane made by the conductor and the vector direction of the magnetic field.

6.2.2.2 Two Parallel Conductors. With a similar derivation method to the *force law*, it can be shown that a conductor carrying a current exerts forces on a charge a distance, r, away (32:557–559). A B-field, obeying the right-hand rule, is created by the conductor and has the magnitude:

$$B = \frac{\mu_0 i}{2\pi r} \tag{6.3}$$

where μ_0 is the free space permeability constant:

$$\mu_0 = 4\pi \times 10^{-7} \frac{tesla \cdot m}{A}$$

The units of $\overline{B}$ are *tesla* (T), where:

$$1\ T = 1\ \frac{N}{A \cdot m}$$

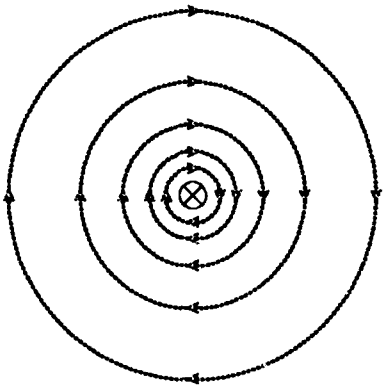

Figure 6.3 The cross section of a B-field created by a conductor carrying a current. The higher concentration of circles represents higher B-field magnitude.

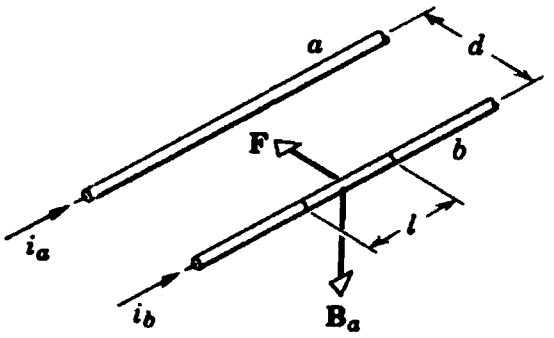

Figure 6.4 Two parallel conductors with currents in the same direction. Forces are generated that cause the conductors to attract.

Experiments have shown the B-field created by a conductor resembles Figure 6.3 in direction and magnitude. The higher magnitude of the B-field is associated with the higher concentration of circles.

Experiments have also shown that two parallel conductors will exert forces on each other. This can be seen by using Equation 6.3 to determine the B-field created by one conductor at the distance between the conductors and then using the *force law* (Equation 6.2) to determine the force (due to the generated B-field) experienced by the other conductor. Figure 6.4 provides a graphic example. Since the same situation occurs for the first conductor due to the second, conductors with currents

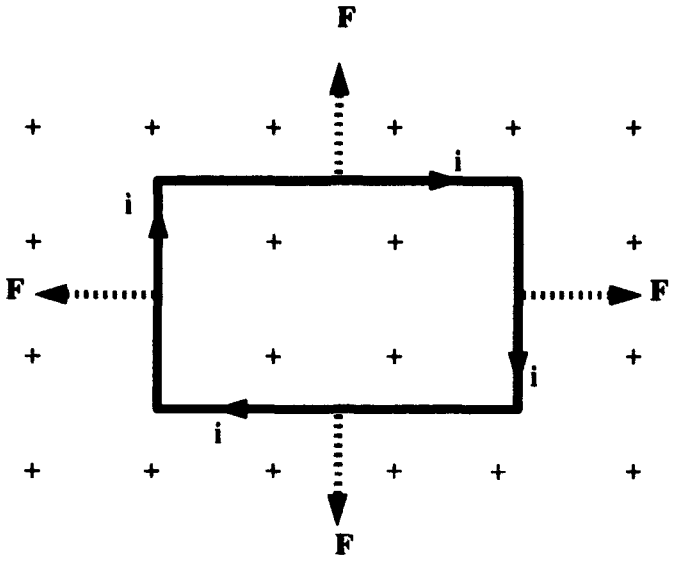

Figure 6.5 A continuous conducting current loop orthogonal to the B-field (going into the page) will experiences forces directed outward.

in the same direction attract and conductors with currents in the opposite directions repel.

6.2.2.3 Conductor Loops. A closed conductor loop in an external B-field with a current flowing through it also experience forces governed by the *force law* (32:541–543). Figure 6.5 shows a rectangular conductor loop orthogonal to an external B-field. The B-field vector is directed into the page. The conductors parallel to each other have currents in opposite directions and repel each other to create *hoop tension* which tries to open the loop. In addition to the repelling forces, outward forces generated by the influence of the external B-field and defined by the *force law* exist. If the loop is displaced as in Figure 6.6, the outward forces are off the line of action and create a net torque which rotates the loop back to an orthogonal position. Notice that all the forces concerned are equal and opposite. The loop does not experience any translation. These attributes apply to circular conductor loops as well, and lend themselves to attitude control applications.

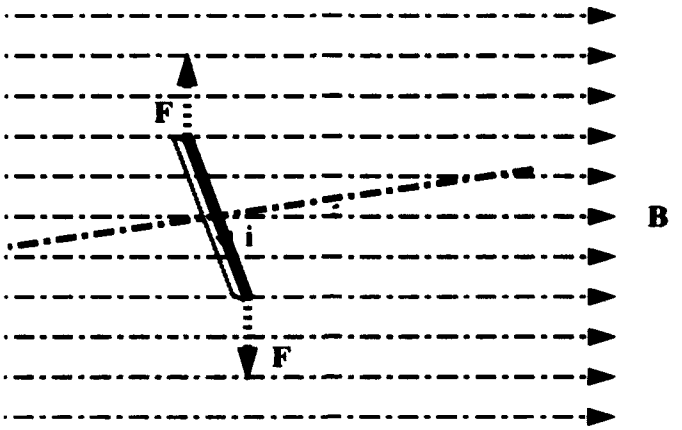

Figure 6.6 The forces experienced by a continuous current loop in a B-field create a torque that drives the loop to a position orthogonal to the field.

Another desirable aspect of multiple conducting loops is that they can be coiled. Every turn, n, of the coil will experience the same forces as previously described. This effectively increases the forces and torques involved by a factor of n without increasing i. This allows a large single loop to be collapsed into a small coiled loop which can help reduce support structure mass and size. The torque discussed above can be calculated from

$$\overline{\tau} = \overline{niA} \times \overline{B} \tag{6.4}$$

where A is area of the loop and the vector direction is defined along the normal of the area, in the direction of the current flow. Electric motors function on this basic operating principle (32:542). The use of conductor loops and coils for attitude control and performance enhancement will be incorporated into the SFP.

6.2.2.4 Shielding. Producing thrust with the *force law* (Equation 6.2) can theoretically be accomplished in two ways. One way is to drive current through a conductor and into the ionosphere via plasma contactors at both ends (63:120–121). This conceptually treats the entire conductor/ionosphere combination as a closed circuit (see Figure 6.7). In June 1993, an experiment performed from a Delta II

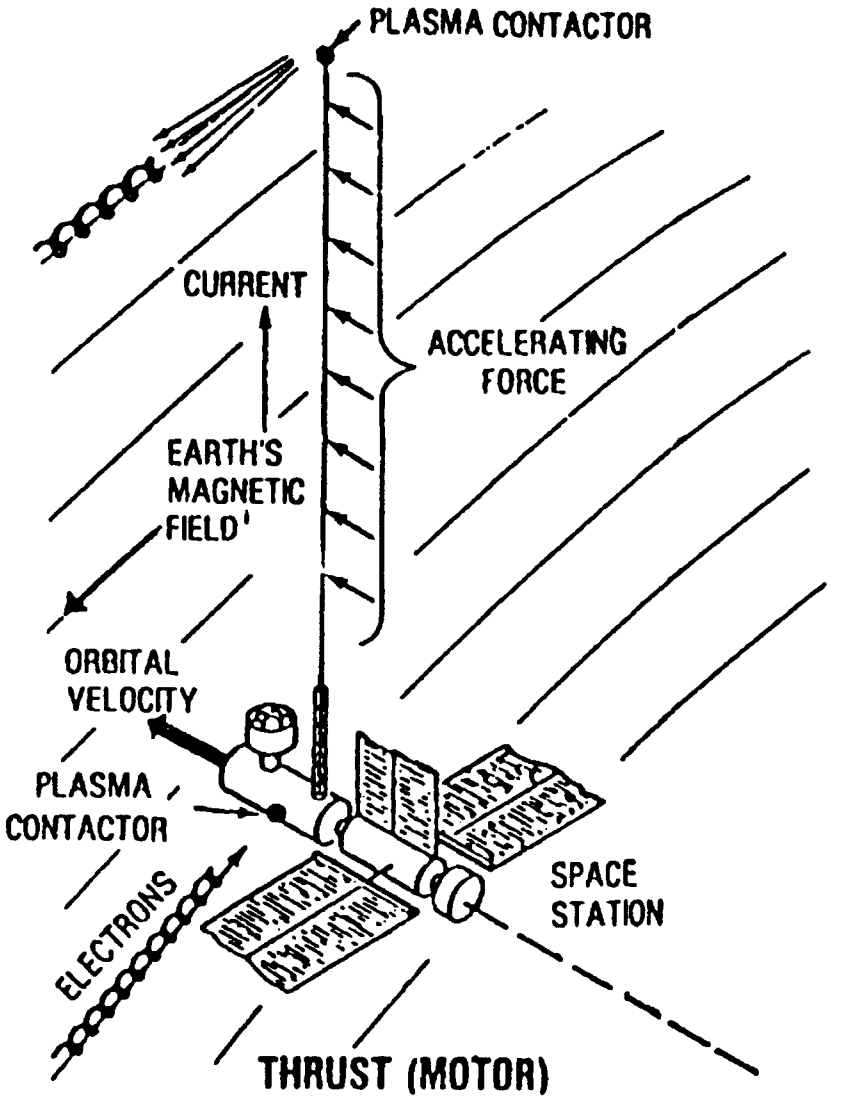

Figure 6.7 An electrodynamic tether with plasma contactors for creating a closed circuit with the ionosphere (63).

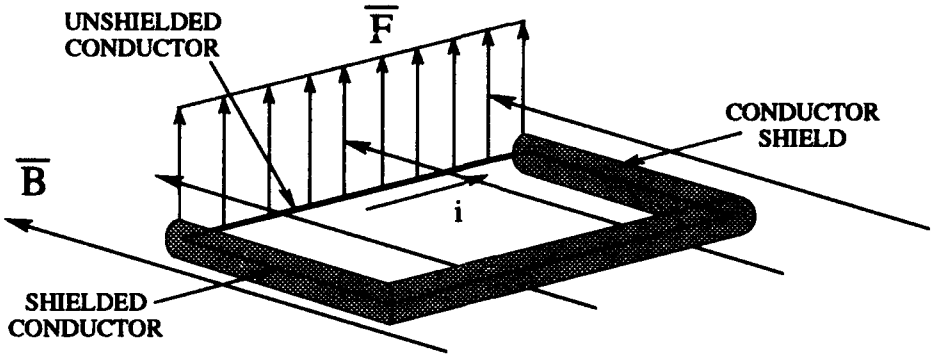

Figure 6.8 A continuous conductor loop with a portion shielded.

launch measured a current on a tether using plasma contactors to close the electrical circuit through the ionosphere (25:3).

Another potential method is to shield a portion of a continuous conductor loop. Theoretically, the current inside the shielded portion of the conductor loop would be unable to interact with both the B-field of the Earth and the B-field of the unshielded portion. Torque would be eliminated, and the current in the unshielded portion would produce translational thrust (see Figure 6.8). Thrust, $\overline{F}_B$, produced by the unshielded portion of the conductor could be increased by simply increasing the number of turns, n, in the conductor loop as described in Section 6.2.2.3. The original force equation would become:

$$\overline{F}_B = ni\overline{L} \times \overline{B} \tag{6.5}$$

Notice that thrust can be increased by increasing n without increasing $\overline{L}$ or i.

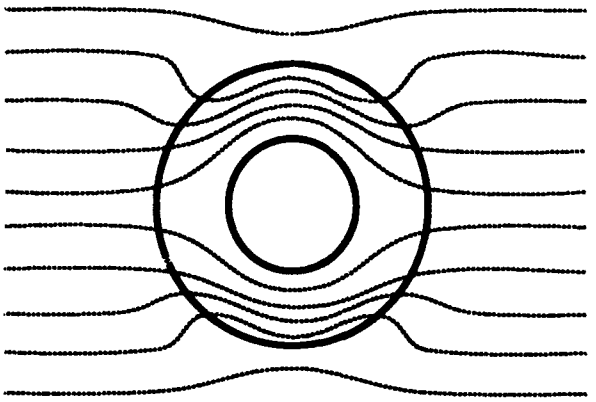

Figure 6.9 The effects of a high magnetic flux permeability shell on an external B-field (53).

In addition to the thrust advantages, shielded conductor loops would not rely on the ionosphere to complete the circuit. As mentioned, plasma contactor devices are used to close the electrical circuit of the previously proposed electrodynamic system. The resistance of this configuration has been estimated to be as high as 20 *ohms* (Ω) (63). This high resistance requires that a large power system be used. With conductor loops, the use of shielding allows closed electrical circuits to be on-board the platform, rather than closing them through the ionosphere. This makes plasma contactors unnecessary, and the only resistance would be internal to the closed circuit itself. Research on magnetic shielding for this application is on-going (48).

Conceptually, magnetic shielding is simple. A ferromagnetic material of high magnetic flux permeability is made into a shell (a cylindrical shell for this application) which surrounds part of the conductor. In a B-field, most of the magnetic flux is concentrated in the shell, thus reducing its interaction with the current flowing in the shielded conductor (53:67–68). Figure 6.9 shows a cylindrical shell in a B-field. It is important to realize that a B-field generated by the current in the conductor is concentrated in the shell as well. In (48), it is shown that the shield is only

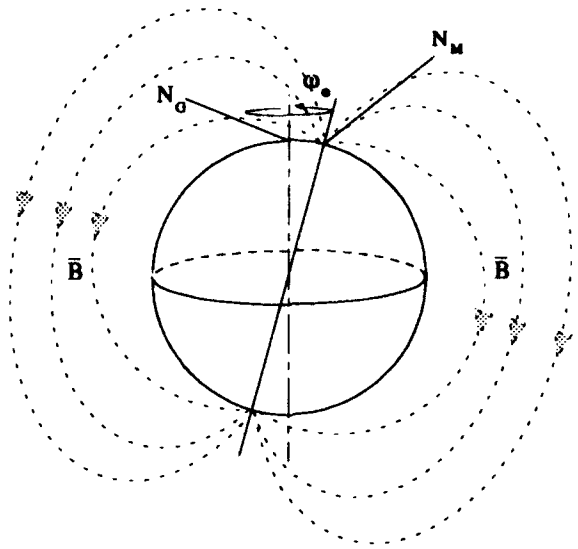

Figure 6.10 The dipole axis is offset 11.5° — N_G is the geographic north pole and N_M is the magnetic north pole.

subjected to a small torque in the force shielding process. An in-depth review of shielding theories and properties can be found in (48), (53), and (54).

6.2.3 Earth's Magnetic Dipole Model. As a first approximation, the Earth's magnetic field, $\overline{B}$, can be modeled as a dipole; the model is that of a sphere uniformly magnetized along the direction of the dipole axis (see Figure 6.10).

The simple dipole model for the Earth is a field centered around the dipole axis which cuts the Earth's surface at the austral (south) dipole pole, located at 78.5° S–111° E, and the boreal (north) dipole pole 78.5° N-69° W; this orientation yields the smallest cumulative error between the Earth-centered dipole model and the actual magnetic field (84:33). As can be seen from the location of the magnetic poles, the axis of the dipole model does not coincide with the Earth's rotation axis, the displacement angle being 11.5°.

While not used for this study, spherical harmonic analysis has been used to develop a more accurate mathematical model for the magnetic field. The more

accurate model has been used to define the eccentric dipole model. The origin of the eccentric dipole model results from displacing the origin of the centered dipole model 342 *km* in the direction of 6.5°N-161.8°E. This changes the coordinates of the austral dipole pole to 76.2°S-120.9°E and the boreal dipole pole 80.0°N-82.8°W. The error of this dipole model is only about ten percent (84:36).

The geomagnetic field, up to an altitude of 2,000 *km*, may be represented by the gradient of a scalar magnetic potential (77:2-21) — this is the simple dipole model for the Earth. The field is then defined as

$$\overline{B} = -\overline{\nabla} V \tag{6.6}$$

where V is the scalar magnetic potential. V, is defined as

$$V = \frac{\overline{M} \cdot \overline{r}}{r^3} \tag{6.7}$$

where $\overline{M}$ is the vector magnetic moment, $\overline{r}$ is the vector distance from the center of the dipole, and r is the magnitude of $\overline{r}$. The form of this relation, derived in detail in Appendix D, is given as:

$$\overline{B} = \frac{M}{r_o^3} \left[2\, m_1\, \hat{a}_r - m_2\, \hat{a}_\theta - m_3\, \hat{a}_3 \right] \tag{6.8}$$

where:

$$\begin{aligned}
m_1 &= c\Phi_0 \left[cvc\left(\Omega - \Theta_g - \Lambda_0\right) - svcis\left(\Omega - \Theta_g - \Lambda_0\right)\right] + s\Phi_0 svsi \\
m_2 &= c\Phi_0 \left[-svc\left(\Omega - \Theta_g - \Lambda_0\right) - cvcis\left(\Omega - \Theta_g - \Lambda_0\right)\right] + s\Phi_0 cvsi \\
m_3 &= c\Phi_0 sis\left(\Omega - \Theta_g - \Lambda_0\right) + s\Phi_0 ci \\
\overline{r}_o &= \frac{a\left(1-e\right)}{1 + e\cos\nu}\, \hat{a}_r
\end{aligned}$$

and

$c \equiv cos$

$s \equiv sin$

$M \equiv$ magnitude of the magnetic dipole

$\Phi_0 \equiv$ latitude of the dipole model's austral pole

$\Lambda_0 \equiv$ longitude of the dipole model's austral pole

and from Appendix C

$\nu \equiv$ true anomaly along orbit path

$\Omega \equiv$ right ascension of the ascending node

$\Theta_g \equiv$ Greenwich sidereal time

$i \equiv$ orbit plane inclination

$a \equiv$ semi-major axis of an elliptic orbit

$re \equiv$ eccentricity of a conic orbit

It is important to note that all three elements of $\overline{B}$ are nonlinear and time-variant. Since the Earth's magnetic field is fixed with respect to the Earth, the field expressed in the orbital reference frame varies proportionately to the Earth's rotation rate; this is seen by the presence of Θ_g in m_1, m_2, and m_3 in terms of Equation 6.8. The time variance is compounded by changes occurring at orbit rate as well. The presence of ν in the m_1 and m_2 terms indicates these terms vary at orbit velocity as well. Finally, there is a constant term in m_3, which accounts for the average north/south orientation of $\overline{B}$. While the time variance makes analysis more complex, it also allows for the Earth's magnetic field to be used to change all six of the classic orbit elements (63:168–169).

6.2.4 Modeled Forces and Torques. The iterative design process used in this study uses a dynamics model of the SFP to determine the platform's design parameters. This requires the development of a dynamics model that is simple enough to be solved, yet contains enough fidelity so as to provide meaningful information.

With this in mind, it is important to consider what forces and torques act on an orbiting satellite.

6.2.4.1 Modeled Forces. A number of external forces can act on an orbital vehicle. Among these forces are gravity, aerodynamic drag, magnetic field effects, non-spherical Earth effects, radiation pressure, meteoroidal impacts, and non environmental forces, such as mass expulsion; however, this list is not exhaustive. For the purposes of this study, the only external forces that will be included are gravity, aerodynamic drag, and magnetic field effects. Gravity and aerodynamic drag are environmental forces to be overcome, while the magnetic field effects are used for propulsion.

The force of gravity is described by (93:24):

$$\overline{F}_g = -\frac{Gm_1m_2}{r^3}\overline{r} = -\frac{GM_\oplus M_{tot}}{r^3}\overline{r} \tag{6.9}$$

where G is the universal gravitational constant, $M_\oplus$ is the mass of the Earth, M_{tot} is the mass of the SFP, $\overline{r}$ is the position vector of the SFP relative to the Earth, and r is the magnitude of $\overline{r}$.

The force due to aerodynamic drag is given by:

$$\overline{F_d} = -\frac{1}{2}\frac{M_{tot}\rho V_r}{\beta}\overline{V_r} \tag{6.10}$$

where

ρ = the atmospheric density

$\overline{V}_r$ = the velocity of the SFP relative to the atmosphere

V_r = the magnitude of $\overline{V}_r$

β = the ballistic coefficient (94:65)

While, the magnitude of the aerodynamic drag force is negligible compared to the force due to gravity, and is therefore not expected to significantly affect the gross

motion of the SFP in the short term, relative to the forces produced by the propulsion system, aerodynamic drag is significant, and cannot be neglected.

6.2.4.2 Modeled Torques. A number of external forces can contribute to the total external torque acting on an orbiting vehicle. As before, gravity, aerodynamic drag, magnetic field effects, and non-environmental forces can all apply torques to an orbiting vehicle. It is reasonable to expect that if the aerodynamic drag force is strong enough to be considered in the relative translational equations of motion, it should be included in the relative rotational equations as well. However, the SFP's configuration shown in Figure 3.1 is symmetric across the $\hat{b}_1\hat{b}_2$ plane. The majority of the presented area of the SFP is a result of the solar dynamic power modules and the ASSET photovoltaic arrays. Because of symmetry and the fact that the $\hat{b}_2$-axis is essentially aligned with the velocity vector, the aerodynamic drag is assumed to cause no torque about the $\hat{b}_1$-axis in this orientation. The remainder of the area is small and near the center of mass; it is assumed that the drag torque generated by this area is negligible. It is also assumed that there are no drag effects due to assymetries in component drag coefficients. The result is that aerodynamic drag effects are negligible in the relative rotational equations of motion, and for the purposes of this study, gravity and magnetic field effects will be the only forces included in the analysis.

An examination of Equation 6.9 shows the force due to gravity changes with the distance between the two bodies. This change can generate a torque on an orbiting vehicle, in this case the SFP. Assuming the SFP's principal body axes are aligned with the $\hat{b}$-frame axes, the approximate component gravitational torques are given by Wiesel (93:146-147) as:

$$\overline{M}_g = 3\frac{GM_\oplus}{r^5}\left[R_2R_3\left(C-B\right)\hat{b}_1 + R_1R_3\left(A-C\right)\hat{b}_2 + R_1R_2\left(B-A\right)\hat{b}_2\right] \quad (6.11)$$

where R_1, R_2, and R_3 are the components of $\overline{r}$ expressed in the $\hat{b}$-frame, and A, B, and C are the principal moments of inertia of the vehicle in the $\hat{b}_1$, $\hat{b}_2$, and $\hat{b}_3$ directions respectively.

6.2.4.3 Unforced Relative Equations of Motion. Six equations of motion are required to completely describe the position and orientation of the SFP. Since the iterative design process chosen for this study requires the dynamics model to be expressed as a system of linear, first-order, differential equations, a number of assumptions and linearizations must be incorporated into the equations of motion. They include:

- assume the SFP is a rigid body
- assume the true anomaly rate of change is constant
- neglect other than first order terms in the relative position and velocity components
- assume the atmosphere is fixed to the earth and can be described by an exponential model
- assume small angle approximations for yaw, roll, and pitch

Three of the six equations of motion are translational equations. They describe the movement of the SFP's center of mass relative to the inertial reference frame. While the equations of motion must be derived relative to the inertial frame, it is convenient to express them in the orbital reference frame shown in Figure 6.1. The three translation directions are the $\hat{a}_r$, $\hat{a}_\theta$, and the $\hat{a}_z$ directions. Assuming the SFP is a rigid body (see Appendix E), the translational equations of motion are derived from the form of Newton's second law:

$$\overline{F} = M_{tot}\overline{a} \tag{6.12}$$

where $\overline{F}$ is the sum of all external forces acting on the SFP, M_{tot} is the total mass of the SFP, and $\overline{a}$ is the acceleration of the SFP with respect to inertial space (52:406-408). In deriving the expression of Equation 6.12 for the SFP, the vehicle's center of mass (i.e. the origin of the $\hat{b}$-frame) will actually be a small distance away from the orbital reference point in the $\hat{a}$-frame. For the scope of this study, the reference point is assumed to be in a circular orbit. This allows for the development of the relative equations of motion for the SFP in the vicinity of a point in a circular reference orbit.

The remaining three equations of motion are the rotational equations. They describe the rotation of the body about the center of mass. The rotational equations of motion can be found by equating the sum of the applied torques, $\overline{M}$, to the rate of change of the angular momentum, $\overline{H}$ (93:109). Thus, with respect to the inertial frame,

$$\overline{M} = \dot{\overline{H}} \tag{6.13}$$

Assuming the SFP is a rigid body, the angular momentum is defined by

$$\overline{H} = \tilde{I}\overline{\omega} \tag{6.14}$$

and can be used if the reference frame is attached to the body, thus making the mass moment of inertia tensor, $\tilde{I}$, a constant. However, the time derivative required in Equation 6.13 must be taken with respect to the inertial frame. Thus, Equation 6.13 can then be expressed as:

$$^{b}\overline{M} = \tilde{I}^{b}\dot{\overline{\omega}}^{bi} + {}^{b}\overline{\omega}^{bi} \times \tilde{I}^{b}\overline{\omega}^{bi} \tag{6.15}$$

where $^{b}\overline{\omega}^{bi} = \omega_a\hat{b}_1 + \omega_b\hat{b}_2 + \omega_c\hat{b}_3$ is the angular velocity of the body frame with respect to the inertial frame. Aligning the $\hat{b}$-frame with the SFP's principal axes results in

a diagonal moment of inertia matrix

$$\tilde{I} = \begin{bmatrix} A & 0 & 0 \\ 0 & B & 0 \\ 0 & 0 & C \end{bmatrix}$$

Solving Equation 6.15 for the individual elements gives the standard Euler's equations (35:95)

$$\hat{b}_1: \quad A\dot{\omega}_a + (C - B)\omega_b\omega_c = {}^bM_1 \tag{6.16}$$

$$\hat{b}_2: \quad B\dot{\omega}_b + (A - C)\omega_a\omega_c = {}^bM_2 \tag{6.17}$$

$$\hat{b}_3: \quad C\dot{\omega}_c + (B - A)\omega_a\omega_b = {}^bM_3 \tag{6.18}$$

These are coupled, nonlinear, first order differential equations.

Equations 6.16 - 6.18 can be used to derive the last three equations of motion in terms of the yaw, pitch, and roll of the $\hat{b}$-frame. Thus, the angular velocity of the $\hat{b}$-frame, with respect to the $\hat{i}$-frame, must be defined in terms of ψ, θ, and ϕ.

By developing expressions for the linear and angular accelerations due to gravity and aerodynamic drag, and substituting the results into Equations 6.12 and 6.16 - 6.18, the dynamics model used for this study can be found. This process is described in detail in Appendix F. The process results in six equations of motion, given by:

$$\delta\ddot{r} - K\delta\dot{r} - 2nr_o\delta\dot{\nu} - 3n^2\delta r + K\delta\omega r_o\delta\nu + K\omega_2\delta z = 0 \tag{6.19}$$

$$r_o\delta\ddot{\nu} + 2n\delta\dot{r} + Kr_o\delta\dot{\nu} - K\delta\omega\delta r - K\omega_1\delta z - K\delta\omega r_o = 0 \tag{6.20}$$

$$\delta\ddot{z} - K\delta\dot{z} - K\omega_2\delta r + K\omega_1 r_o\delta\nu + n^2\delta z - K\omega_2 r_o = 0 \tag{6.21}$$

$$A\ddot{\psi} + n(C - B - A)\dot{\phi} + n^2(C - B)\psi = 0 \tag{6.22}$$

$$B\ddot{\phi} + n(A + B - C)\dot{\psi} + 4n^2(C - A)\phi + 3n^2\frac{(C - A)}{r_o}\delta z = 0 \tag{6.23}$$

$$C\ddot{\theta} - \frac{3}{2}\frac{nC}{r_o}\delta\dot{r} + 3n^2(B - A)\theta - 3n^2\frac{(B - A)r_o\delta\nu}{r_o} = 0 \tag{6.24}$$

completely describe the position and orientation of the SFP, in the neighborhood of the reference point, for small yaw, pitch, and roll angles when *no forcing functions are applied* (such as the propulsion/control system).

6.2.4.4 Steady State Equations of Motion. The primary use of the relative equations of motion is to design a controller to perform steady state tracking relative to a reference point. The controller design is then used to determine specific design parameters for the SFP. Some insight into the platform's required capabilities can be gained by considering the relative equations of motion under steady state conditions. Under steady state conditions:

$$\delta\dot{r} = \delta\ddot{r} = r_o\delta\dot{\nu} = r_o\delta\ddot{\nu} = \delta\dot{z} = \delta\ddot{z} = 0$$
$$\dot{\psi} = \ddot{\psi} = \dot{\phi} = \ddot{\phi} = \dot{\theta} = \ddot{\theta} = 0$$

Substituting these values into Equations 6.19 - 6.24 gives:

$$F_{\delta r_{ss}} = M_{tot}\left[-3n^2\delta r + K\delta\omega r_o\delta\nu + K\omega_2\delta z\right] \tag{6.25}$$
$$F_{r_o\delta\nu_{ss}} = M_{tot}\left[-K\delta\omega\delta r - K\omega_1\delta z - K\delta\omega r_o\right] \tag{6.26}$$
$$F_{\delta z_{ss}} = M_{tot}\left[-K\omega_2\delta r + K\omega_1 r_o\delta\nu + n^2\delta z - K\omega_2 r_o\right] \tag{6.27}$$
$$M_{\psi_{ss}} = A\left[n^2(C-B)\psi\right] \tag{6.28}$$
$$M_{\phi_{ss}} = B\left[4n^2(C-A)\phi + 3n^2\frac{(C-A)}{r_o}\delta z\right] \tag{6.29}$$
$$M_{\theta_{ss}} = C\left[3n^2(B-A)\theta - 3n^2\frac{(B-A)r_o\delta\nu}{r_o}\right] \tag{6.30}$$

A few conclusions can be drawn from these equations. First, excluding drag effects, a standoff in the radial direction requires three times as much force as a standoff of the same distance in the out-of-plane direction; a standoff along the orbit path requires no force (when drag is excluded). Second, drag effects require steady forces be applied in both the path and out-of-plane directions to stay at a fixed point, even

if the SFP is at the reference radius. Steady state forces are required in the radial direction only if the SFP is not at the reference radius. If the SFP is not at the reference radius, the steady state forces are required due to the vector component of the drag force that is tangent to the orbit path at the SFP's center of mass. Third, steady state moments are required to hold a yaw, roll, and/or pitch attitude. If the SFP is standing off along the orbit path or out-of-plane, steady state moments are required to maintain any fixed attitude.

6.3 Platform Design Process

6.3.1 Introduction. The this study uses an iterative design process to develop a satisfactory design for the SFP. The process takes a proposed design, develops a dynamics model for that design, and then uses a linear system based controller to determine specific design parameters. Once a satisfactory design is obtained, the controller is used to help evaluate the design's performance.

6.3.2 The Iterative Design Process. The first step in the iterative design process (see Figure 6.11) is to propose a general design for the SFP. This consists of determining the number of translation control conductor elements and the number of attitude control conductor elements. The specific configuration of these elements must also be specified.

Once the proposed design is specified, forcing functions for the equations of motion (Equations 6.19 - 6.24) must be developed. These forcing functions are incorporated into the equations of motion, which are then formed into a linear system of first-order differential equations. These equations are incorporated into a MATLAB (65) program (see Section G.1). This program — the *time-history design program* — is used to design a linear quadratic regulator based controller. In the program (see Figure 6.12 for a diagram of the program's flow), specific design parameters, such as vehicle payload, individual conductor lengths, number of turns

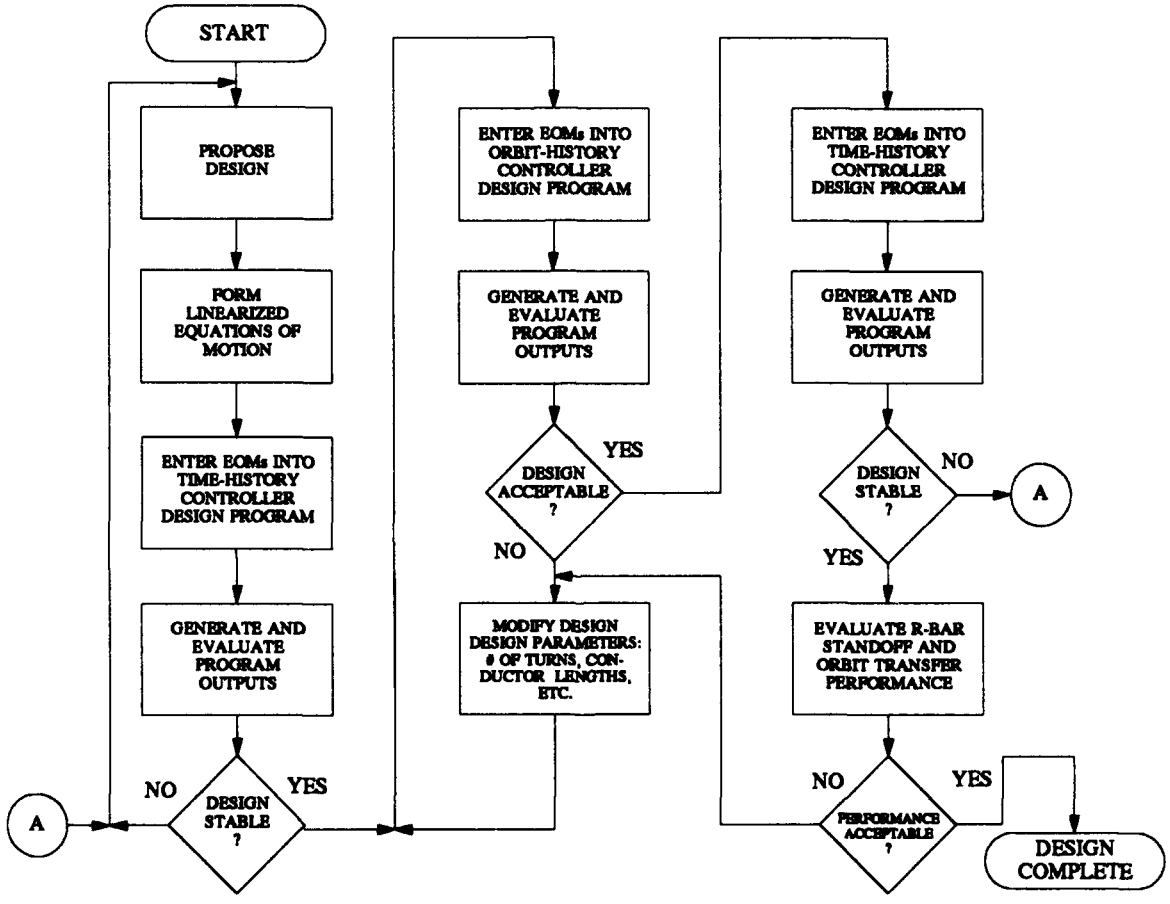

Figure 6.11 The iterative design process flow begins with a proposed design, evaluates its stability, and provides data used to determine design parameters.

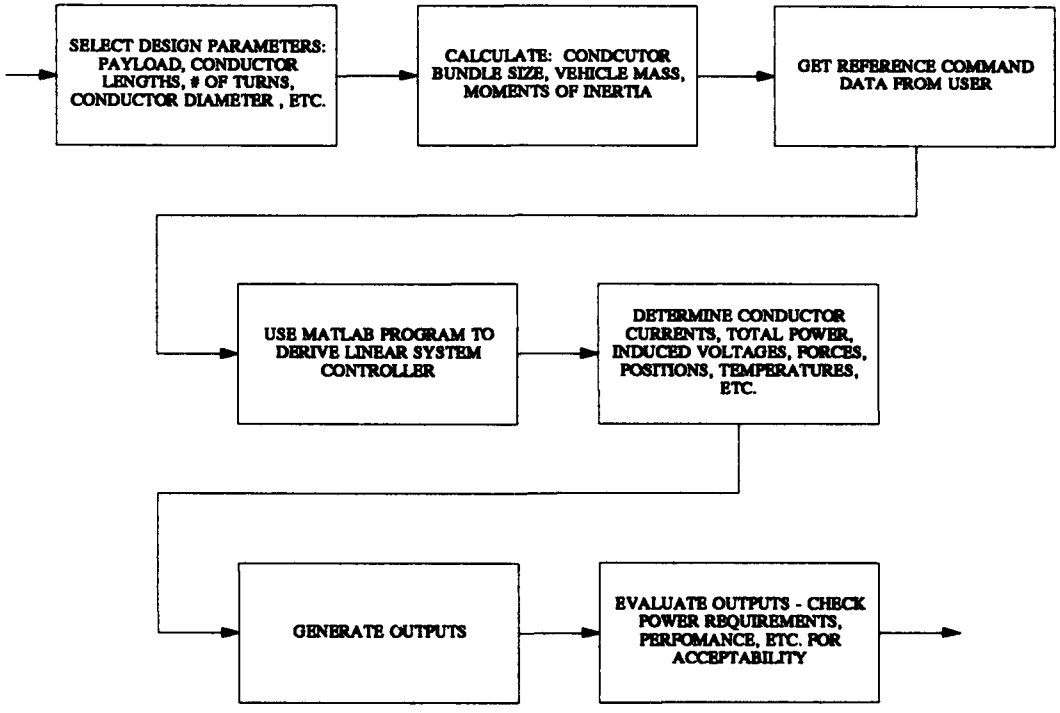

Figure 6.12 The design program is used to assess a proposed design's stability and performance characteristics, such as total power required and individual conductor current load.

on an individual conductor, the individual conductors diameter, and the thickness of the magnetic shield are entered. From this information, the program calculates the vehicle's mass and mass moments of inertia. This information is then used to determine the coefficients of the equations of motion. The user enters a reference command that fixes the location (altitude, inclination, and right ascension of the ascending node of the reference orbit, the true anomaly of the reference point, the distance between the SFP's center of mass, and the reference point) and attitude (thc angular orientation of the SFP with respect to the orbital reference frame) of the SFP. Using this reference command data, the program derives a linear quadratic regulator based controller for the derived equations of motion. The controller is then used to run a time-based simulation. The simulation is used to assess the stability, over time, of the proposed design. If the design is determined to not have the stability characteristics desired, the process is repeated with a new proposed design.

Once a proposed design with satisfactory stability characteristics is obtained, a modified version of the time-history design program — *orbit-history design program* — is used to determine specific design parameters. The same equations of motion are used, but the operation of the program is changed to simulate the platform moving through its orbit. The same controller derivation process is followed, but the controller program (see Section G.5) is called iteratively by a driver program. Each time the driver calls the modified controller design program, a new reference position is passed to it. The design program then passes back such data as the required power, the currents in the control elements, and conductor core temperatures (the program can be modified to pass virtually any of the calculated data back to the driver program for analysis). By calculating the changes in the true anomaly and other time variant parameters that affect the coefficients of the equations of motion, this iterative process can be used to approximate the movement of the SFP through its orbit. The data generated by this process can be used to assess the characteristics

for the proposed design. Any changes required are made and the process is repeated until an acceptable design is determined.

After an acceptable design is determined, its stability is rechecked. If the design is no longer stable, the process is started all over after any necessary changes are made. If the design is stable, the performance of the proposed design is evaluated using the orbit-history design program and the *orbital transfer analysis program* (see Section O). The programs are used to assess such performance characteristics as total power required, individual conductor currents, conductor core temperatures, stand-off capability, payload capability, and time-to-climb (descend) for orbit transfer. If the performance characteristics are not acceptable, the design parameter determination process is repeated with new parameters. The overall process is repeated until an acceptable design is obtained. Once an acceptable design is obtained, the design process is complete.

The following sections review the iterative design process for the final design of the SFP. The process begins with the performance requirements levied on the platform and is followed through to the final design of the SFP.

6.3.3 Design Constraints and Considerations. Section 3.2 described a number of factors which influence the final design of the SFP's electrodynamic propulsion system. The factors to be satisfied, or that constrain the design in some way, are:

- a maneuvering system that utilizes electrodynamic propulsion with maximum power requirement of 77 kW (of the 82 kW available) and a maximum conductor core temperature of 438.0 $^{\circ}C$
- a delivery capability
- a versatile payload capability with a capacity of at least 30,000 kg

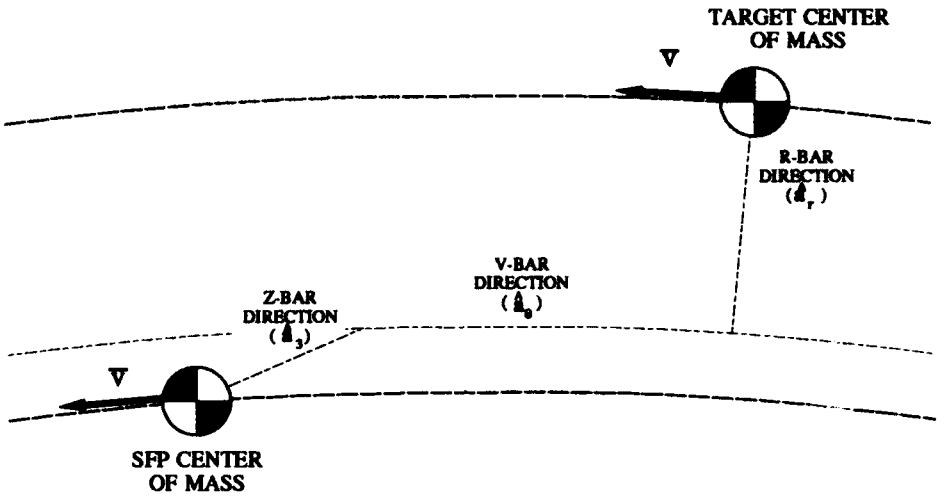

Figure 6.13 R-bar is defined along the radial direction, V-bar is defined along the orbit path direction, and Z-bar is defined along the out of plane direction.

- a versatile stand-off capability with an envelope from 0 m to at least 40 m around the reference point, at inclinations from 0° to 28.5°, and at altitudes from 300 km to 500 km
- an open work area for mission ready operations

Since the controllability of the SFP is used to determine the detailed design of the platform, the factors listed above must be incorporated into the controllability analysis. Since these are very general requirements, it is possible that a number of different designs could meet these requirements. To limit the scope of the search for a design for the SFP a specific maneuver was selected to be used as the performance characteristic to which the SFP would be designed. Because of the high demand on the performance of the propulsion system, an R-bar stand-off maneuver (see Figure 6.13) was selected as the single function the SFP would be designed to perform

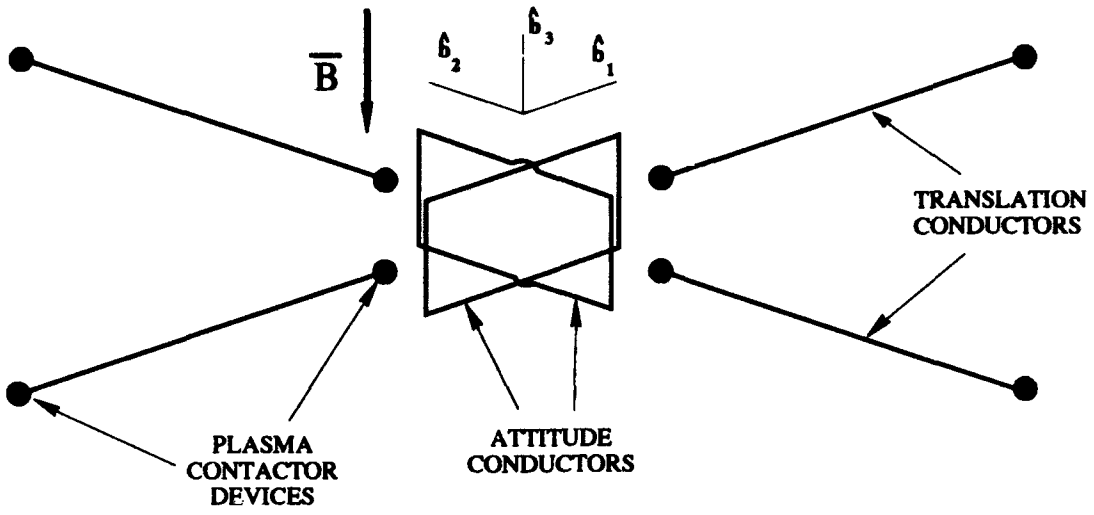

Figure 6.14 The POTkV consists of six conductors; four closed through the ionosphere via plasma contactor devices (shaded circles), and two on-vehicle closed circuit loops.

(see Section 11.2). To begin the iterative design process, a conceptual design for performing this maneuver is needed.

6.3.4 Conceptual Design. The Spenny and Lawrence propose a large orbital fabrication platform with an electrodynamic propulsion system consisting of six conductors (81:1–2). Four of these conductors are arranged in pairs along each in-plane axis (see Figure 6.14). By passing independently controlled currents through these conductors, they are used to generate the thrusting forces described by

$$\overline{F}_B = i\overline{L} \times \overline{B} \tag{6.31}$$

Each of these straight conductors uses plasma contactor devices to close their electrical circuits through the ionosphere. The other two conductors are closed circuit loops. These loops are closed on the vehicle itself, as opposed to closing them through the ionosphere as is the case with the straight conductors. By passing independently

controlled currents through them, these closed conductor loops generate attitude control torques as described by

$$\overline{\tau} = \left(\overline{niA}\right) \times \overline{B} \tag{6.32}$$

Even though the conductors can be operated independently, Spenny and Lawrence point out that the nature of Equation 6.31 precludes using electrodynamic propulsion to provide thrust control parallel to the B-field. A pair of opposing electric thrusters were added to provide the necessary thrust capability. The study also indicates that the straight conductors must be used for pitch control. Equation 6.32 shows that a conductor loop could not be used for pitch control since the torque would have to be parallel to $\overline{B}$. However, pitch can be controlled by differential application of the straight conductors.

There are two main drawbacks to this proposed design. The first is the required size for R-bar stand-off (see Figure 6.13). The sizes analyzed for the POTkV range from 275 m (with a current of 500 A and a stand-off of 100 m), to 1,700 m (with a current of 125 A and a stand-off of 100 m). With conductors of these lengths, the rigidized truss requirement becomes difficult to achieve. The other drawback is power. Because of the closure through the ionosphere (estimated to be 1–20 Ω), the power required was estimated to range from 63 kW to 1.25 MW. Power levels this high are hard to achieve. One easy way to reduce the power is to make the conductors longer, thus reducing the resistive power loss. However, this increases the rigidized truss problem described above.

The basic design of the SFP incorporates much of Spenny and Lawrence's design, but provides some solutions to its problems. The Earth's magnetic field effects will be used for propulsion, relying on the application of Equations 6.31 and 6.32. Unlike Spenny and Lawrence's design, however, partially shielded conductor loops with a large number of turns as suggested in Section 6.2.2.4, will take the place of the

long straight conductors with plasma contactor devices. Five such conductors will be used in the SFP for translation control. The single-turn conductor loops Spenny uses for attitude control will be replaced by tightly wound coiled conductors with a large number of turns. The coiled conductors operate under the principles discussed in Section 6.2.2.3. Five such tightly wound coils will be used on the SFP. Since it is not possible to generate thrust or torque parallel to $\overline{B}$, augmentation thrusters are used to provide the needed thrust capability, and split straight conductors are used to provide the needed torque capability. The addition of the two extra straight and three extra coiled conductors are to insure that there are no singularities in the attitude control of the SFP and to preserve the symmetry of the vehicle as much as possible.

In order to satisfy the basic propulsion system requirements and the system design constraints and considerations, a number of designs were considered. Figure 6.15 shows the layout of the ten conductor elements of the SFP. Figure 6.16 shows the configuration of the SFP — including the integrated trusses, the truss maker, the power modules and arrays, and the docking/delivery system — in an R-bar orientation. Using these two figures, it can be seen that conductors C_1 and C_2 are housed in the main integrated truss, conductors C_3 and C_4 are housed in the cross integrated truss, conductor C_5 is housed in the orthogonal integrated truss, and coiled conductors C_6, C_7, C_8, C_9, and C_{10} are housed in the coiled conductor integrated truss. The next section develops the forcing functions for the electrodynamic propulsion system defined by Figure 6.15.

6.3.5 Forced Equations of Motion. The ten multiple turn conductors described above — five long straight loop conductors and five tightly coiled conductors — are used to provide forcing functions for the SFP's relative equations of motion (Equations 6.19 - 6.24). Table 6.1 shows how each conductor is mathematically described in terms of the number of turns in the conductor, n_i, the current through the conductor, i_i, for the straight conductors, the length of the conductor

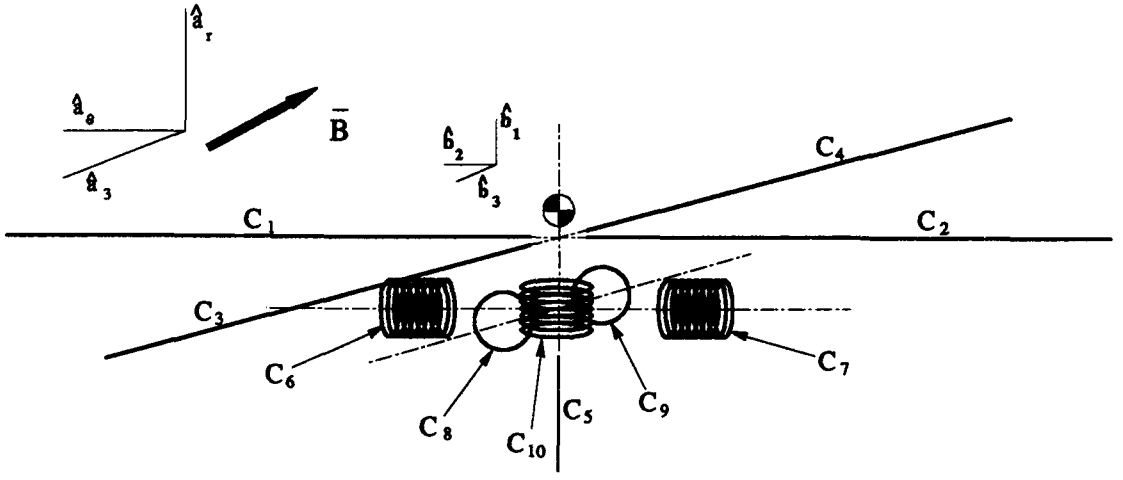

Figure 6.15 Straight conductors along each body axis provide translation control. Coiled conductors along each body axis provide attitude control.

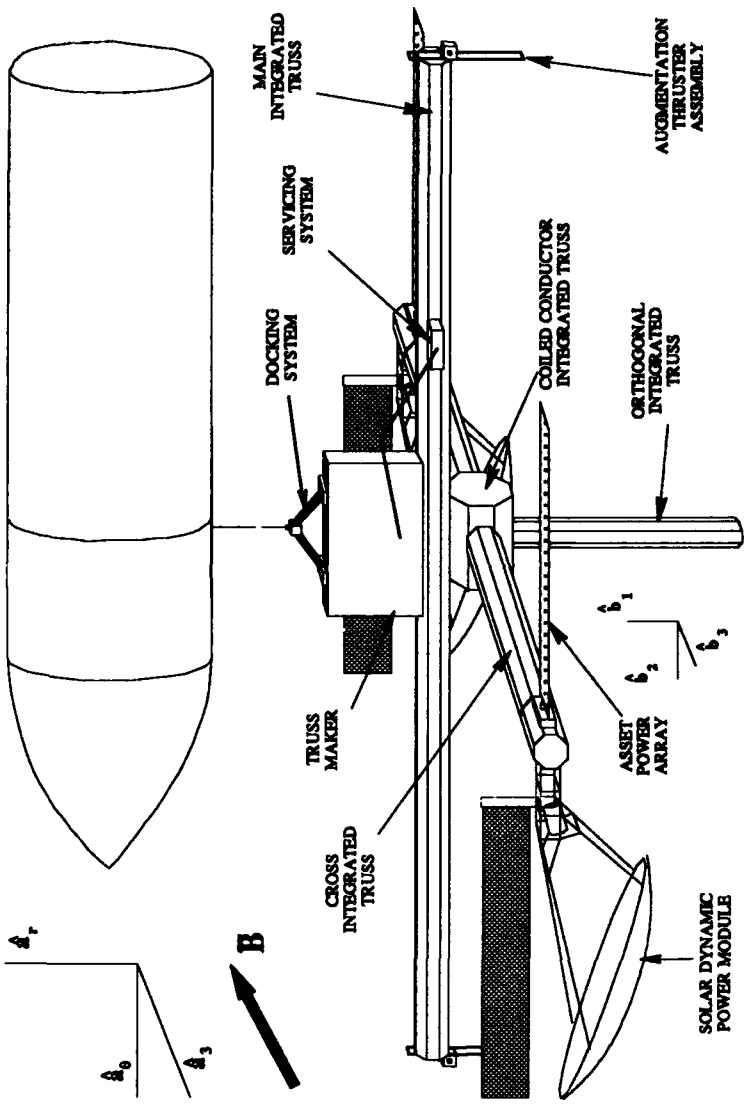

Figure 6.16 The SFP consists of three orthogonal integrated trusses, housing five partially shielded conductors loops, and an integrated truss housing five unshielded conductor coils.

Conductor	Description	Conductor	Description
C_1	$n_1 i_1 L_1 \hat{b}_2$	C_6	$n_6 i_6 A_6 \hat{b}_2$
C_2	$n_2 i_2 L_2 \hat{b}_2$	C_7	$n_7 i_7 A_7 \hat{b}_2$
C_3	$n_3 i_3 L_3 \hat{b}_3$	C_8	$n_8 i_8 A_8 \hat{b}_3$
C_4	$n_4 i_4 L_4 \hat{b}_3$	C_9	$n_9 i_9 A_9 \hat{b}_3$
C_5	$n_5 i_5 L_5 \hat{b}_1$	C_{10}	$n_{10} i_{10} A_{10} \hat{b}_1$

Table 6.1 The mathematical descriptions of the SFP's conductor elements, where n is the number of turns, i is the current, L is the length of the conductor, and A is the cross sectional area of the coiled conductor.

assembly, L_i, and for the coiled conductors, the cross-sectional area of the coiled conductor, A_i. The descriptions in Table 6.1 are used to implement Equation 6.31 to determine the translational force generated by each straight conductor and to implement Equation 6.32 to determine the torque generated by each coiled conductor.

To begin the development of the forcing functions for the equations of motion, Equation 6.31 is rewritten to account for multiple conductors and the augmentation thruster's thrust, F_{th}:

$$\begin{aligned} \overline{F}_B &= \sum_i \left(n_i i_i \overline{L}_i \times \overline{B} \right) + \overline{F}_{th} \\ &= \sum_i \left(\overline{n i L_i} \right) \times \overline{B} + F_{th} \hat{b}_3 \end{aligned} \tag{6.33}$$

where F_{th} is the thrust of the augmentation thrusters. Considering the conductors listed in Table 6.1, the first term in Equation 6.33 is found to be

$$\begin{aligned} {}^b\overline{niL} &= \sum_i n_i i_i {}^b\overline{L}_i \\ &= (n_5 i_5 L_5)\,\hat{b}_1 + (n_1 i_1 L_1 + n_2 i_2 L_2)\,\hat{b}_2 + (n_3 i_3 L_3 + n_4 i_4 L_4)\,\hat{b}_3 \\ &= (niL_5)\,\hat{b}_1 + (niL_1 + niL_2)\,\hat{b}_2 + (niL_3 + niL_4)\,\hat{b}_3 \end{aligned} \tag{6.34}$$

and is expressed in the $\hat{b}$-frame. However, since $\overline{B}$ and the translational equations of motion are expressed in the $\hat{a}$-frame, Equation 6.34 must also be expressed in the

$\hat{a}$-frame. Using the linearized version of Equation C.11 to transform Equation 6.34 and $\overline{F}_{th}$ to the $\hat{a}$-frame,

$$\begin{aligned}
{}^{a}\overline{niL} &= R^{ab}_{linear}\, {}^{b}\overline{niL} \\
&= [niL_5 - \theta(niL_1 + niL_2) + \phi(niL_3 + niL_4)]\,\hat{a}_r + \\
&\quad [\theta(niL_5) + (niL_1 + niL_2) - \psi(niL_3 + niL_4)]\,\hat{a}_\theta + \\
&\quad [-\phi(niL_5) + \psi(niL_1 + niL_2) + (niL_3 + niL_4)]\,\hat{a}_3 \\
&= IL_1\hat{a}_r + IL_2\hat{a}_\theta + IL_3\hat{a}_3 \qquad (6.35)
\end{aligned}$$

and

$$\begin{aligned}
{}^{a}\overline{F}_{th} &= R^{ab}_{linear}\, {}^{b}\overline{F}_{th} \\
&= \phi F_{th}\hat{a}_r - \psi F_{th}\hat{a}_\theta + F_{th}\hat{a}_3 \qquad (6.36)
\end{aligned}$$

Equations 6.8, 6.35, and 6.36 can now be used to solve Equation 6.33:

$$\begin{aligned}
{}^{a}\overline{F} &= \left[\frac{M}{r_o^3}(-IL_2m_3 + IL_3m_2) + \phi F_{th}\right]\hat{a}_r + \\
&\quad \left[\frac{M}{r_o^3}(2IL_3m_1 + IL_1m_3) - \psi F_{th}\right]\hat{a}_\theta + \\
&\quad \left[\frac{M}{r_o^3}(-IL_1m_2 - 2IL_2m_1) + F_{th}\right]\hat{a}_3 \qquad (6.37)
\end{aligned}$$

The component parts of this expression form the forcing functions of the relative translational equations of motion:

$$\hat{a}_r: \quad \cdots = \frac{M}{M_{tot}r_o^3}(-IL_2m_3 + IL_3m_2) + \frac{\phi F_{th}}{M_{tot}} \qquad (6.38)$$

$$\hat{a}_\theta: \quad \cdots = \frac{M}{M_{tot}r_o^3}(2IL_3m_1 + IL_1m_3) - \frac{\psi F_{th}}{M_{tot}} \qquad (6.39)$$

$$\hat{a}_3: \quad \cdots = \frac{M}{M_{tot}r_o^3}(-IL_1m_2 - 2IL_2m_1) + \frac{F_{th}}{M_{tot}} \qquad (6.40)$$

It is important to note the forcing functions for the $\hat{a}_r$ and $\hat{a}_\theta$ equations have terms which are always non-zero — due to the presence of the m_3 components of $\overline{B}$ — and are thus always controllable. However, since the $\hat{a}_3$ equation only has the sinusoidal m_1 and m_2 components of $\overline{B}$, there is a possibility that the first term of the right hand side of Equation 6.40 can go to zero. Without the augmentation thrusters, this term does in fact cycle through zero as can be seen by considering the controllability of the final linear system. Without the augmentation thrusters included, the controllability matrix (discussed in Section J.2) has a rank defect of one. As a result, without the augmentation thrusters, the system is not completely controllable. This makes sense from a physical standpoint since it is impossible for *any* purely electrodynamic propulsion system to generate thrust parallel to the B-field.

The remainder of the forcing functions are determined from the application of Equation 6.32. It is rewritten to account for multiple coiled conductors, split translational conductor pairs, and augmentation thrusters:

$$\overline{\tau} = \sum_i \left({}^b\overline{niA}_i \times {}^b\overline{B} \right) + \sum_i \left({}^b\overline{r}_i \times \left({}^b\overline{niL}_i \times {}^b\overline{B} \right) \right) + {}^b\overline{r}_{th} \times {}^b\overline{F}_{th} \tag{6.41}$$

where all vectors are expressed in the $\hat{b}$-frame and ${}^b\overline{r}_i$ is the vector position of the center of force of the ith conductor.

Considering the conductors listed in Table 6.1, ${}^b\overline{niA}_i$ in the first term of Equation 6.41 is found to be:

$$\begin{aligned} {}^b\overline{niA} &= \sum_i {}^b\overline{niA}_i \\ &= (n_{10}i_{10}A_{10})\,\hat{b}_1 + (n_6 i_6 A_6 + n_7 i_7 A_7)\,\hat{b}_2 + (n_8 i_8 A_8 + n_9 i_9 A_9)\,\hat{b}_3 \\ &= (niA_{10})\,\hat{b}_1 + (niA_6 + niA_7)\,\hat{b}_2 + (niA_8 + niA_9)\,\hat{b}_2 \end{aligned} \tag{6.42}$$

In order for the forcing torques to be useful in Equations 6.22 – 6.24, $\overline{B}$ must be expressed in the $\hat{b}$-frame. Using the linearized version of rotation matrix from the

Conductor	CF Position
C_1	$\frac{1}{2}L_1\hat{b}_2$
C_2	$-\frac{1}{2}L_2\hat{b}_2$
C_3	$-\left(h_{mit}+\frac{1}{2}h_{ccit}\right)\hat{b}_1+\frac{1}{2}L_3\hat{b}_3$
C_4	$-\left(h_{mit}+\frac{1}{2}h_{ccit}\right)\hat{b}_1-\frac{1}{2}L_4\hat{b}_3$
C_5	$-\left(h_{mit}+h_{ccit}+\frac{1}{2}L_5\right)\hat{b}_1$

Table 6.2 The center of force positions for each straight conductor. h_{mit} is the height of the main integrated truss, and h_{ccit} is the height of the coiled conductor integrated truss.

$\hat{a}$-frame to the $\hat{a}$-frame to transform Equation 6.8, ${}^b\overline{B}$ is found to be:

$$\begin{aligned} {}^b\overline{B} &= \frac{M}{r_o^3}\left[(2m_1-\theta m_2+\phi m_3)\,\hat{b}_1+(-2\theta m_1-m_2-\psi m_3)\,\hat{b}_2+\right. \\ &= \left.(2\phi m_1+\psi m_2-m_3)\,\hat{b}_3\right] \end{aligned} \tag{6.43}$$

The first term of Equation 6.41 can now be expanded as:

$$\begin{aligned} \sum_i\left({}^b\overline{niA_i}\times{}^b\overline{B}\right) &= \frac{M}{r_o^3}\left[(niA_6+niA_7)\,(2\phi m_1+\psi m_2-m_3)-\right. \\ &\quad \left.(niA_8+niA_9)\,(-2\theta m_1-m_2-\psi m_3)\right]\hat{b}_1+ \\ &\quad \frac{M}{r_o^3}\left[(niA_8+niA_9)\left[(2m_1-\theta m_2+\phi m_3)-\right.\right. \\ &\quad \left.\left.(niA_{10})\,(2\phi m_1+\psi m_2-m_3)\right]\right]\hat{b}_2+ \\ &\quad \frac{M}{r_o^3}\left[-(niA_6+niA_7)\,(2m_1-\theta m_2+\phi m_3)+\right. \\ &\quad \left.(niA_{10})\,(2m_1-\theta m_2+\phi m_3)\right]\hat{b}_3 \end{aligned} \tag{6.44}$$

The second term can also be expanded at this point. The ${}^b\overline{r}_i$ terms are the positions of the center of force for each individual straight conductor. Table 6.2 describes the position of the center of force for each straight conductor. Using the data from

Table 6.2 and Equations 6.34 and 6.43, the second term of Equation 6.41 is found:

$$\sum_i \left({}^b\overline{r}_i \times \left({}^b\overline{niL}_i \times {}^b\overline{B}\right)\right) =$$

$$\frac{M}{r_o^3}\left[\left(-\frac{1}{2}n_1 i_1 L_1^2 + \frac{1}{2}n_2 i_2 L_2^2 - \frac{1}{2}n_3 i_3 L_3^2 + \frac{1}{2}n_4 i_4 L_4^2\right)\left(2m_1 - \theta m_2 + \phi m_3\right)\right]\hat{b}_1 +$$

$$\frac{M}{r_o^3}\left[\left(-\frac{1}{2}n_3 i_3 L_3^2 + \frac{1}{2}n_4 i_4 L_4^2 + n_5 i_5 L_5\left(h_{mit} + h_{ccit} + \frac{1}{2}L_5\right)\right)\left(-2\theta m_1 - m_2 - \psi m_3\right)\right]\hat{b}_2 +$$

$$\frac{M}{r_o^3}\left[\left(-\frac{1}{2}n_1 i_1 L_1^2 + \frac{1}{2}n_2 i_2 L_2^2 + n_5 i_5 L_5\left(h_{mit} + h_{ccit} + \frac{1}{2}L_5\right)\right)\left(2\phi m_1 + \psi m_2 - m_3\right)\right]\hat{b}_3 \qquad (6.45)$$

where h_{mit} is the height of the main integrated truss and h_{ccit} is the height of the coiled conductor integrated truss. The third term in Equation 6.41 accounts for any torque generated by the operation of the augmentation thrusters. With the expectation that the force generated by the thrusters will be of the same order of magnitude as the highest forces generated by the electrodynamic propulsion system, the elimination of any such torque is desirable. To achieve this, the thrusters must be aligned with the center of mass of the SFP. Because of variable payloads, the center of mass moves over the range

$$-4.39\,\hat{b}_1\,m \;\leq\; \overline{r}_{cm} \;\leq\; +1.20\,\hat{b}_1\,m$$

from a reference point defined as the intersection between the orthogonal integrated truss axis and the top the main integrated truss (see Appendix H for the analysis of this required shift). The truss maker moves along the top of the main integrated truss to keep the vehicle's center of mass in the $\hat{b}_1\hat{b}_3$-plane. The augmentation thrusters must be able to track the shifting center of mass as it shifts along the $\hat{b}_1$-axis. To do

so, they are mounted on movable platforms at the ends of the main integrated truss. They point along the $\pm\hat{b}_3$ direction, away from the center of mass. See Appendix I for a more detailed discussion of the tracking requirement and thruster capability. The moment-arm of the thruster, ${}^b\overline{r}_{th}$, is then always zero, thus eliminating any thruster-generated moment, and the third term of Equation 6.41 drops out of the equation.

Equation 6.41 can now be solved to obtain the forcing functions for the rotational equations of motion. The right hand sides of Equations 6.22 - 6.24 then become:

$$\begin{aligned}
\hat{b}_1 \cdots &= \frac{M}{r_o^3}\left[\left(-\frac{1}{2}n_1 i_1 L_1^2 + \frac{1}{2}n_2 i_2 L_2^2 - \frac{1}{2}n_3 i_3 L_3^2 + \frac{1}{2}n_4 i_4 L_4^2\right)(2m_1 - \right. \\
&\quad \theta m_2 + \phi m_3) + (niA_6 + niA_7)(2\phi m_1 + \psi m_2 - m_3) - \\
&\quad \left.(niA_8 + niA_9)(-2\theta m_1 - m_2 - \psi m_3)\right] \qquad (6.46) \\
\hat{b}_2 \cdots &= \frac{M}{r_o^3}\left[\left(-\frac{1}{2}n_3 i_3 L_3^2 + \frac{1}{2}n_4 i_4 L_4^2 + n_5 i_5 L_5\left(h_{mit} + h_{ccit} + \frac{1}{2}L_5\right)\right)(-2\theta m_1 - \right. \\
&\quad m_2 - \psi m_3) + (niA_8 + niA_9)(2m_1 - \theta m_2 + \phi m_3) - \\
&\quad \left.(niA_{10})(2\phi m_1 + \psi m_2 - m_3)\right] \qquad (6.47) \\
\hat{b}_3 \cdots &= \frac{M}{r_o^3}\left[\left(-\frac{1}{2}n_1 i_1 L_1^2 + \frac{1}{2}n_2 i_2 L_2^2 + n_5 i_5 L_5\left(h_{mit} + h_{ccit} + \frac{1}{2}L_5\right)\right)(2\phi m_1 + \right. \\
&\quad \psi m_2 - m_3) + \left(-n_3 i_3 L_3 - n_4 i_4 L_4\left(h_{mit} + \frac{1}{2}h_{ccit}\right)\right)(2m_1 - \\
&\quad \theta m_2 + \phi m_3) + (niA_6 + niA_7)(-2m_1 + \theta m_2 - \phi m_3) + \\
&\quad \left.(niA_{10})(-2\theta m_1 - m_2 - \psi m_3)\right] \qquad (6.48)
\end{aligned}$$

where the m_3 terms with coefficients of one will be the primary control elements for each equation due to the presence of the constant term within m_3. Inspection of the $\hat{b}_3$ equation shows the necessity of splitting the conductor housed in the main integrated truss into two elements. The forces generated by conductors C_1, C_2, and C_5 are the primary pitch control elements. If conductors C_1 and C_2 were not split, C_5 would be the only nominal pitch control element. However, further consideration

of the $\hat{a}_\theta$ equation shows that C_5 is also the primary control element for movement along the orbit path in proximity of the reference point. To insure the SFP can achieve the desired control capabilities, it is necessary for all six equations of motion to have separate control elements that provide the primary control authority. To achieve this, the conductor housed by the main integrated truss was split into two control elements. This allows C_1 and C_2 to provide pitch control, while C_5 provides translation control along the orbit path. Conductors C_3, C_4, C_8, and C_9 do not provide any primary thrust or attitude capability, but are retained to prevent the SFP from getting "stuck" in a singularity of the force and/or the torque laws.

The forcing functions for all six equations of motion have now been derived. With the augmentation of the thrust and rotational capabilities, the SFP has full control of all relative position and attitude elements, and can therefore be considered to have full six degree-of-freedom control capability.

6.3.6 Linear System State Space Representation. The equations of motion provide the dynamics model of the SFP's behavior that is used to develop an SFP design that gives full control over the position and orientation of the SFP while achieving the operational capability goals. The method chosen to combine these two tasks was to use the controller design process outlined in the POTkV study (81:4–5) in an iterative scheme. In order to use this process, the equations of motion must be converted to a state space representation. The state space representation is checked for controllability and observability. Based on the state space representation, a linear systems controller is designed using a linear quadratic regulator and a prefilter. The state space open loop system is then converted to a closed loop system using full state feedback. Appendix J provides a detailed discussion of this process.

6.3.7 Time-History Analysis. Once the dynamics model is converted to a state space representation, the model is incorporated into the time-history analysis program. Specific design parameters, such as vehicle payload, individual conduc-

Resistance	84.000	$\mu\Omega/m$
Mass	0.839	kg/m
Melting Temperature	657	$°C$

Table 6.3 Properties of a two centimeter insulated aluminum conductor (20).

tor lengths, number of turns on an individual conductor, the individual conductors diameter, and the thickness of the magnetic shield are entered into the program.

Asbestos insulated aluminum wire with a 2 cm diameter was chosen for the conductor material for the SFP's electrodynamic propulsion system (see Table 6.3). At this diameter, aluminum wire has approximately twice the resistance of copper wire but weighs 70% less (20). Due to heat transfer considerations, the maximum current allowed is dictated by a maximum conductor core temperature of $438.0°C$ ($219°C$ below the melting point of aluminum which provides a factor of safety of 1.5). In a worst case scenario, no more than 99 turns of the conductor are required to generate enough force to maneuver the platform. The conductors are bundled into a 99 conductor element cable and shielded with one shield. A heat transfer analysis of the shielded cable can be found in Appendix K.

Using these parameters, a magnetic shield was developed to provide shielding over one half of a conductor loop. A 10.14 mm thick shield will provide the necessary shielding to allow the use of closed conductor loops (see Appendix L) for both translation and attitude control. Spenny's work assumed the use of plasma contactor devices to close the current loops through the ionosphere — a very expensive (in terms of power) method for using electrodynamic propulsion. Using magnetic shielding will allow the use of closed conductor loops which will result in significantly lower power requirements.

The time-history analysis program uses the design parameter information to calculate the vehicle's mass and mass moments of inertia, which allow the coefficients of the equations of motion to be determined. The user enters a reference command

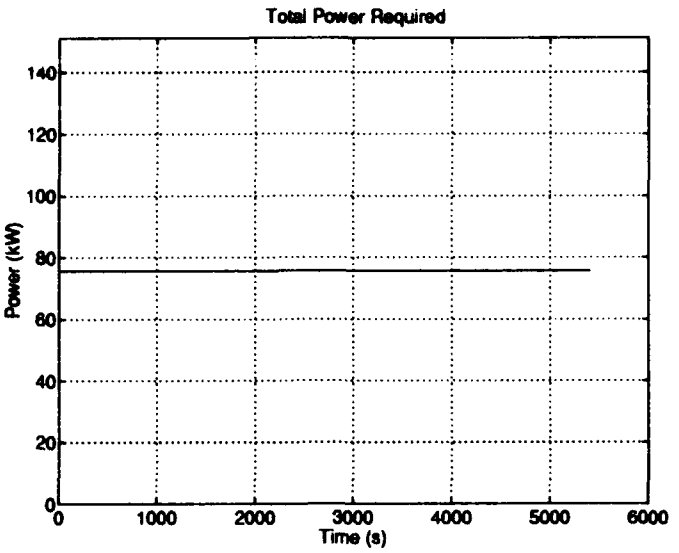

Figure 6.17 Time history of the total power required for a stable controller design.

that fixes the location (altitude, inclination, and right ascension of the ascending node of the reference orbit, the true anomaly of the reference point, the distance between the SFP's center of mass, and the reference point) and attitude (the angular orientation of the SFP with respect to the orbital reference frame) of the SFP. The program uses the dynamics model, a user-specified reference command, and proposed design parameters (vehicle size, conductor length, etc.) to derive a a linear quadratic regulator based controller. A time-based simulation of the controller is run to assess the stability properties, over time, of the proposed design. For a specific point in an orbit, with a stand-off reference command, the controller's outputs should be constant. This equates to a flat, horizontal line an a plot of power, for example, versus time, as can be seen in Figure 6.17 When the outputs demonstrate this behavior, the controller is assumed to be stable over time. See Section M.1 for a complete set of time-based plots and data outputs for the final platform design.

If the proposed design does not have the stability characteristics desired, the design is modified. The new dynamics model for the modified design is then de-

veloped, incorporated into the time-history design program, and evaluated. This process is repeated until a design with satisfactory stability characteristics is found. When such a design is found, the orbit-history design program is then used to determine the specific design parameters for the platform.

6.3.8 Orbit-History Analysis. Once determined to be stable, the proposed design must be evaluated to see if it meets the performance requirements. This evaluation is accomplished using a modified version of the time-history design program and a driver program which form the orbit-history design program. The dynamics model used in the time-history design program is incorporated into this program in the same fashion as previously described.

The driver program passes all the reference command and orbit position information to the sub-program. The driver contains a loop structure that is used to generate a discrete simulation of the SFP moving through its orbit. The sub-program then uses that information to generate a new controller (in the same fashion as the time-history design program), which allows the determination of new control information, such as total power required, individual conductor currents, etc. This data is then passed back to driver program (the program can be modified to pass virtually any of the calculated data back to the driver program for analysis). The data is then processed by the driver program to generate plots. The plots show how such parameters as total power required, individual conductor currents, conductor core temperatures, and thrust required change with position in the orbit. Figure 6.18 shows how the total power required for the electrodynamic propulsion system varies with orbital position. The effective time interval shown is one full revolution of the Earth.

The data generated by this process can be used to assess the characteristics for the proposed design. If any of the constraints are violated — too much power is required, a conductor core temperature is too high, etc. — the proposed design

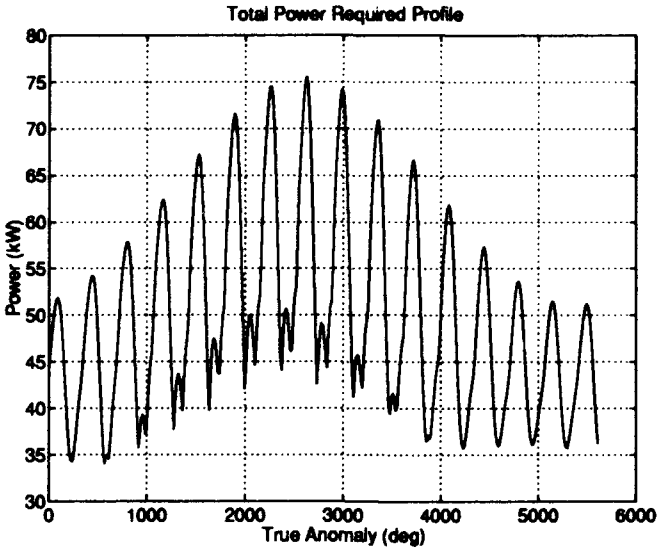

Figure 6.18 Orbit-history design program plot of total power required versus true anomaly.

parameters are changed and the program is re-run. This process is repeated until an acceptable design is obtained. Section M.2 shows the complete set of orbit-based plots for the final platform design performing the design R-bar standoff maneuver.

6.3.9 Final Design Characteristics. The final design of the SFP is a function of the performance/operational requirements levied upon the vehicle. Different requirements would most likely have resulted in a different final design (see Section 11.2 for more discussion). However, the final design is well suited to the performance/operational requirements discussed in Section 3.2. Table 6.4 lists the basic characteristics of the final platform design. Table 6.5 lists the dimensions, number of turns, and mass of each conductor, as well as the size of the individual conductor elements, and the thickness of the *Netic* shield.

The platform was designed to perform R-bar standoff, but must perform other maneuvers as well. The other primary function performed by the propulsion system

Description	Mass (kg)	Dimensions ($\hat{b}_1\, m$	×	$\hat{b}_2\, m$	×	$\hat{b}_3\, m$)
External Tank Payload	31,300	8.42	×	46.88	×	8.42
Truss Maker	3,000	5.0	×	10.0	×	2.0
Main Integrated Truss	1,000	2.0	×	50.0	×	2.0
Cross Integrated Truss	1,200	2.0	×	2.0	×	60.0
Orthogonal Integrated Truss	540	27.0	×	2.0	×	2.0
Coiled Conductor Integrated Truss	195	4.3	×	4.86	×	4.3
Solar Dynamic Power Module (2)	11,899	21.4	×	7.8	×	18.0
ASSET Photovoltaic Array (2)	7,194	20.6	×	3.0	×	10.3
Augmentation Thruster Assemblies	2,200	4.0	×	2.0	×	2.0
Augmentation Thruster Fuel	2,000					
Servicing System	5,000					
Salvage Equipment	2,000					
Miscellaneous Equipment	12,000					

Table 6.4 The estimate or calculated mass and dimensions of the major components of the final design of the SFP. Note that the dimensions for the solar dynamic power modules and ASSET photovoltaic arrays is based on them pointing upward toward the delivery system.

Conductor	Mass (kg)	Dimensions ($diameter$	×	$length$	×	$turns$)
C1	17,530	23.16 cm	×	25.0 m	×	99
C2	17,530	23.16 cm	×	25.0 m	×	99
C3	234	2.0 cm	×	25.0 m	×	1
C4	234	2.0 cm	×	25.0 m	×	1
C5	3,846	12.58 cm	×	27.0 m	×	21
C6	5,255	3.8 m	×	0.28 m	×	137
C7	5,255	3.8 m	×	0.28 m	×	137
C8	7	3.8 m	×	0.02 m	×	1
C9	7	3.8 m	×	0.02 m	×	1
C10	19,064	3.8 m	×	1.8 m	×	497
Single Conductor Wire Diameter		2.0 cm				
Netic Shield Thickness		10.14 mm				

Table 6.5 The mass, length, diameter, number of turns for each conductor element. Also listed is the size of the individual conductor wires and the thickness of the *Netic* shielding.

is orbit transfer. While orbit transfer is not the primary capability driving the design, how well the task can be accomplished is certainly important.

6.3.10 Orbit Transfer Analysis. The iterative design process required the use of a linearized representation of the SFP's equations of motion. The equations of motion for gross orbit maneuvers — orbit transfers — do not require such a formulation. In fact, some of the secondary effects lost by linearization are important to assessing the performance during an orbit transfer. The development of the nonlinear equations of motion is similar to that of the relative equations of motion; as such, only an abbreviated discussion is included here.

Using the SFP design determined through the iterative design process, an analysis was undertaken to establish the performance of the vehicle during an orbital transfer. The analysis provides the basis for mission time lines, transfer power requirements, and demonstrates the effects of the changing B-field.

For the POTV, Lawrence performed a simple analysis for an orbital transfer (49:5.1). He assumed the Earth's B-field has constant magnitude and constant relative orientation with respect to the vehicle. Applying these assumptions to the *force law* results in constant thrust from the propulsion system. Assuming a constant thrust, Lawrence analyzed the approximate time needed to transfer from a lower altitude orbit to a higher altitude orbit. The approximation used is valid for a low thrust vehicle whose thrust is constant (93:89). However, this approximation is not valid for an orbit transfer analysis which includes a time varying B-field. To perform the time variant analysis, a MATLAB program was used to numerically integrate the vehicle's equations of motion. The analysis is performed in the Earth centered inertial (ECI) coordinate system. Numerical integration is used to more accurately represent the changing B-field's impact on the vehicle's motion.

The previous analysis needed the SFP's relative equations of motion to be linear. The orbit transfer analysis does not require this restriction. As a result,

some of the elements of the equations of motion will change. Prior to performing the orbit transfer analysis, the SFP's gross equations of motion need to be modified.

6.3.10.1 Orbit Transfer Equations of Motion. The same forces incorporated into the relative equations of motion — gravity, aerodynamic drag, and magnetic field effects — are used to develop the nonlinear equations of motion to be used for the orbit transfer analysis. As before, gravity and aerodynamic drag are the retarding forces to be overcome, and the magnetic field effects are used for propulsion.

The dominant force acting on the SFP is due to the Earth's gravitational field. Modeling the Earth as a sphere of uniform density, the potential function for the field is

$$V_g = -\frac{GM_\oplus}{r} \tag{6.49}$$

where r is the magnitude of the length of the vector distance from the center of the Earth to the center of mass of the SFP. The acceleration of the vehicle due to this potential field is:

$$\begin{aligned} \overline{a}_g &= -\overline{\nabla} V \\ &= -\frac{GM_\oplus}{r^3}\overline{r} \end{aligned} \tag{6.50}$$

The SFP is a low thrust vehicle. Its performance is significantly impacted by aerodynamic drag forces. The acceleration due to aerodynamic drag is:

$$\overline{a}_d = -\frac{1}{2}\frac{\rho V_r}{\beta}\overline{V_r} \tag{6.51}$$

where, as before, ρ is the density of the atmosphere, $\overline{V_r}$ is the relative velocity of the SFP with respect to the atmosphere, and β is the ballistic coefficient.

The propulsive force generated by the SFP is given by the *force law* as:

$$\overline{F_p} = i\overline{L} \times \overline{B} \tag{6.52}$$

where i is the current through the conductor, L is the length of the conductor, $\overline{B}$ is the Earth's magnetic field. The unit vector describing the direction of $\overline{L}$ will be $\hat{L}$ and its orientation changes with respect to the $\hat{a}$-frame changes. Since $\overline{B}$ is fixed to the Earth, and rotates with it, it is time varying in the $\hat{e}$-frame. As a result, $\overline{B}$ is given as:

$$\begin{aligned}
\overline{B}\left(\overline{M}(t), \overline{r}(t)\right) = & -\left(\frac{M_1(t)}{r(t)^3} - \frac{3\left(\overline{M}(t)\cdot\overline{r}(t)\right)}{r(t)^5}x(t)\right)\hat{e}_1 \\
& -\left(\frac{M_2(t)}{r(t)^3} - \frac{3\left(\overline{M}(t)\cdot\overline{r}(t)\right)}{r(t)^5}y(t)\right)\hat{e}_2 \\
& -\left(\frac{M_3(t)}{r(t)^3} - \frac{3\left(\overline{M}(t)\cdot\overline{r}(t)\right)}{r(t)^5}z(t)\right)\hat{e}_3
\end{aligned} \tag{6.53}$$

where $x(t)$, $y(t)$, and $z(t)$ are the components of $\overline{r}(t)$ along the $\hat{e}_1$, $\hat{e}_2$, and $\hat{e}_3$ directions respectively.

The resulting acceleration due to the SFP's electrodynamic propulsion system is:

$$\overline{a}_p = \frac{iL\left(\hat{L} \times \overline{B}(\overline{r}, t)\right)}{M_{tot}} \tag{6.54}$$

6.3.10.2 Orbit Transfer Thrust Control. To transfer from a circular orbit to a higher altitude, coplanar, circular orbit, the original orbit is made elliptical. The semi-major axis, a, is increased until the perigee of the elliptical orbit is tangent to the original orbit, and the apogee is tangent to the desired orbit. When the desired altitude is reached, the orbit is recircularized. The most efficient way to perform these maneuvers is to apply all forces in the orbit plane. However, the electrodynamic propulsion system generates out-of-plane forces while generating propulsive forces.

To minimize changes to the inclination and longitude of the right ascension of the ascending node of the SFP's orbit, the out-of-plane forces must be minimized.

In Equation 6.52, the length of the conductor is fixed and $\overline{B} = \overline{B}\left(\overline{M}(t), \overline{r}(t)\right)$; only the current, i, and direction the conductor is pointing, $\hat{L}$, can be changed. Because $\overline{F_p}$ is perpendicular to the direction of $\overline{B}$, the conductor should be pointed to minimize the out-of-plane forces being generated by the propulsion system. The magnitude of $\overline{F_p}$ is controlled by changing both i and $\hat{L}$, and is maximized for a given current when $\hat{L}$ is perpendicular to $\overline{B}$.

Desired Thrust Direction. For a nearly impulsive propulsion system, the optimum energy transfer between two coplanar circular orbits was determined by Hohmann (93:71). A change in velocity, $\Delta\overline{v}$, is generated in the velocity direction, $\hat{v}$. This places the spacecraft into an elliptical orbit whose perigee is tangent to the original orbit at the maneuver, and whose apogee is tangent to the desired orbit. At apogee, another $\Delta\overline{v}$ is applied, again in the velocity direction, to circularize the orbit (see Figure 6.19). This optimization can be explained by the orbital energy equation:

$$\frac{v^2}{2} - \frac{\mu}{r} = -\frac{\mu}{2a} \tag{6.55}$$

Equation 6.55 shows that total energy must be increased in order to increase orbital radius. The only practical method of increasing the total energy is to increase v. An acceleration will induce a $\Delta\overline{v}$. Because $\overline{v}$ and $\Delta\overline{v}$ are both vectors, the largest total velocity ($\overline{v} + \Delta\overline{v}$) will result when both vectors are co-linear, pointing in the same direction. Therefore the greatest increase in orbital radius results from the thrust being applied in the velocity vector direction. Based on this, the SFP should be oriented to generate the maximum thrust along the orbit velocity direction.

Orientation of the Conductor. For a low inclination orbit, the average orientation of $\overline{B}$ is nearly perpendicular to the orbit plane throughout the

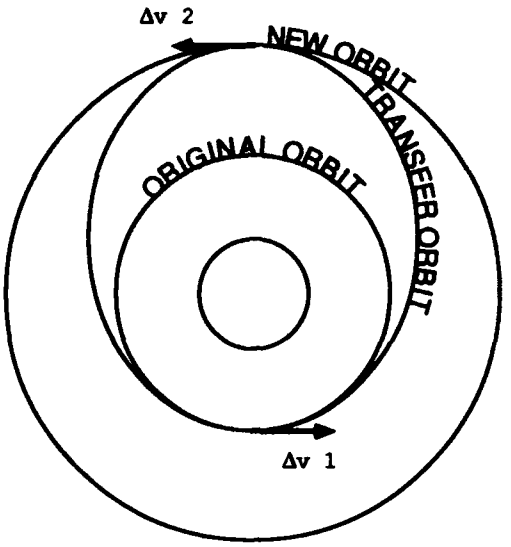

Figure 6.19 The Hohmann transfer is the most efficient coplanar orbit transfer in total Δv.

complete orbit. In his analysis of the POTV's orbit transfer performance, Lawrence suggested using a conductor aligned with the radius vector to generate a propulsive force that is generally in the velocity vector direction (49:5.2). For his analysis, Lawrence assumed $\overline{B}$ was constant and fixed the orientation of the vehicle so that its main conductor was perpendicular to both $\overline{B}$ and the velocity vector. Because the actual orientation of $\overline{B}$ varies with time, it is not always perpendicular to the velocity and radius vectors. As a result, the component of $\overline{F_p}$ in the velocity vector direction may not be maximized. Despite this problem, this type of analysis is simple to implement. For the analysis in this study, this method (Method 1) is compared to one where $\overline{B}$ is not assumed to be constant.

An alternative to fixing the direction of the conductor in the radial direction is to orient the conductor so that it is orthogonal to both $\overline{B}$ and the velocity vector. The resulting propulsive force is then in the plane defined by $\overline{B}$ and the velocity vector. It also provides the maximum acceleration in the velocity vector direction. For low inclinations, the angle between propulsive force and the velocity vector is

small. This type of analysis provides better performance, and is only marginally more difficult. The time varying $\overline{B}$ analysis is Method 2.

A comparison of Method 1 and Method 2 is made in Appendix N. The comparison shows that Method 2 is the most efficient orbit transfer method. Consequently, Method 2 is used for the all orbit transfer calculations.

6.3.10.3 Control for Rendezvous. At the conclusion of an orbital transfer, the SFP will rendezvous with some orbiting target. Generally this will entail matching the target's inclination and line of nodes and then circularizing the orbit to match true anomalies, ν. Conceptually, this requires applying a suitable force to recircularize the orbit at the appropriate time to achieve the desired final conditions. The calculation of force application time and the exact sequence of force applications is assumed to be achievable, but is not included. However, the general methods of controlling the SFP for rendezvous can be discussed.

Perturbations in the inclination and line of nodes can be controlled through occasional reorientation of the main conductor to provide sufficient out-of-plane thrusting to make corrections. As indicated in Section 6.2.3, higher order terms of the B-field, not included in this analysis, can be useful for making such corrections. The augmentation thrusters can be used as well.

The SFP's orbital eccentricity, e, is close to zero throughout the transfer. This is the basis of the constant low thrust transfer approximation. At any time during the transfer, if the propulsion system is turned off, the orbit of the SFP would be nearly circular. Figure 6.20 shows the velocity of the SFP during a transfer. Also plotted on Figure 6.20 is the circular orbit velocity, v_c, at the SFP's altitude. When approaching the target altitude, power should be adjusted so that the SFP reaches the target altitude at t_f. The oscillations of the SFP's velocity about the velocity to maintain a circular orbit should allow maneuver scheduling that uses a minimum

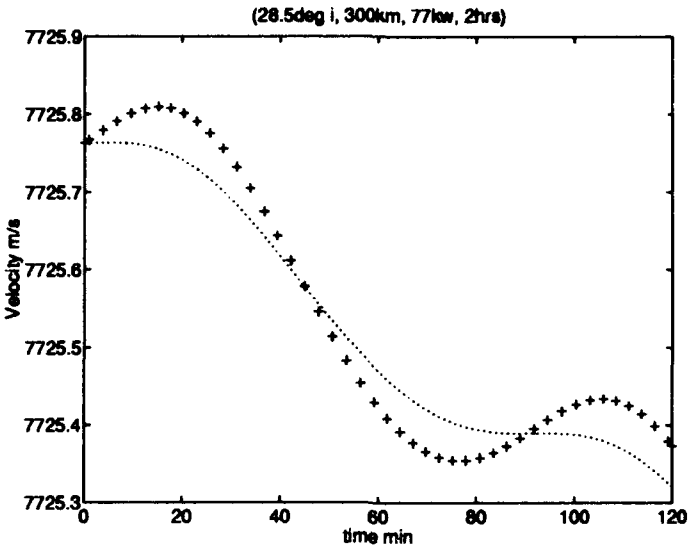

Figure 6.20 The SFP's velocity (—) oscillates about circular orbit velocity (···); control of propulsion power can be used to correctly time the intersections of the velocity curves.

amount of power to reduce the acceleration to zero. This would allow placing the SFP within the precision maneuvering controller's operating envelope.

6.3.10.4 Orbit Transfer Performance. In order to estimate the SFP's performance, a variety of numerical integrations were run using orientation Method 2 (see Appendix O). The general characteristics were demonstrated in a baseline run of 2 *days* with power limited to 77 *kW*. The initial conditions are the same as previously defined.

6.3.10.5 Altitude Changes. The baseline performance shows the SFP, carrying an external tank payload, increased altitude by 21.33 *km* in 2 *days* (see Figure 6.21). The small variations in the curve are a result of a cycle of exchange of kinetic energy for potential energy (altitude), a near circularization, and then a gain in kinetic energy. The state is always nearly a circular orbit. The long term trend in Figure 6.21 appears linear, but closer inspection reveals that SFP's transfer rate is

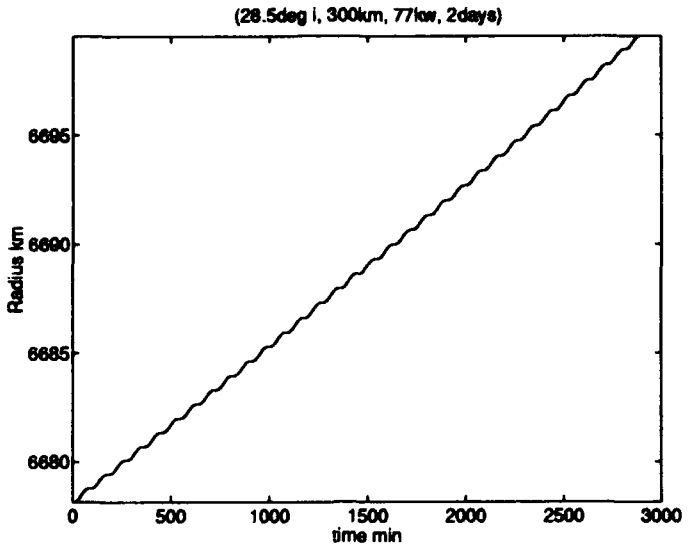

Figure 6.21 The SFP raises 21.33 *km* during the first 2 *days* of a transfer from a 300 *km* to 500 *km* orbit.

Initial Altitude *km*	$\dot{r}_{LT}$ *km/day*	$\dot{i}_{LT}$ $_\circ$*/day*	Max $\Delta\Omega$ $10^{-3\circ}$
300	10.67	0.012	2.00
400	12.70	0.012	2.00
500	14.00	0.012	2.00

Table 6.6 Change in performance with changes in starting altitude. For 28.5° inclination starting orbits, the climb rate of the SFP increases with altitude, while other changes remain relatively constant.

slowly increasing. This is due to the drop in aerodynamic drag as altitude increases (see Figure 6.22). As the vehicle's altitude increases, current generally increases to compensate for the general decrease in the strength of the B-field. However, power lost to resistance also increases. These trends were verified by performing the runs at different initial altitudes. Runs with higher starting altitudes (see Table 6.6) displayed higher daily transfer rates, mainly due to a two order of magnitude drop in aerodynamic drag.

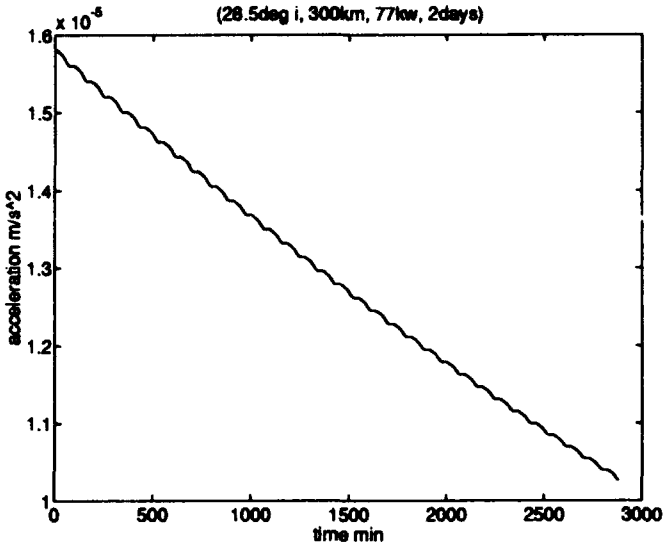

Figure 6.22 Aerodynamic drag versus time. During the transfer, the acceleration due to aerodynamic drag decreases. This decrease results from the increase in altitude.

The transfer rate of 10.67 *km/day* can be used for simple estimates for the time to reach desired altitudes from a 300 *km* orbit. For simple approximations it provides a conservative estimate, and avoids using the long and complex numerical integrations required for more accurate estimates.

Inclination Changes. A change in inclination results from the components of the out-of-plane thrust and drag forces. The effect of these out-of-plane forces is to alter the direction of the angular momentum vector. This changes the inclination and line of nodes. In the course of a normal closed orbit, the positive and negative changes in inclination generally cancel. However, with the SFP's increase in altitude, there is not a complete cancellation and a long term trend develops. The function is complicated by Earth's magnetic dipole not being aligned with the Earth's axis while it rotates with the Earth. As a result, the inclination changes by approximately $0.012°/day$ (see Figure 6.23); this includes the changes due to decreasing aerodynamic drag. The rate is essentially constant with respect

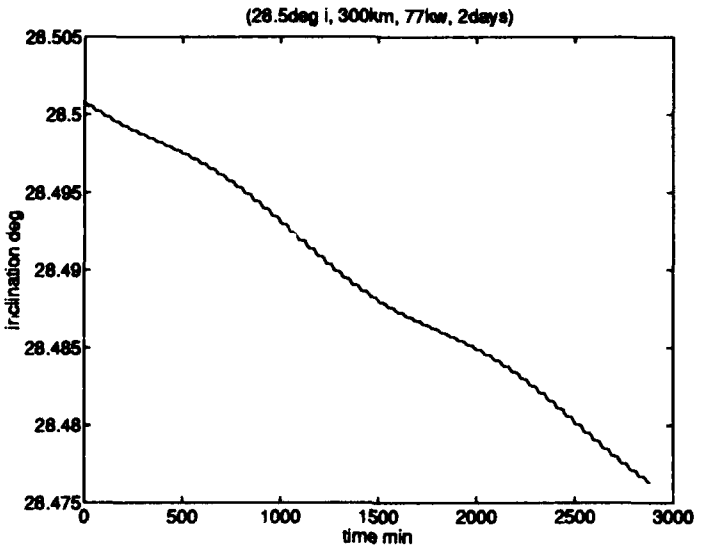

Figure 6.23 The SFP's inclination decreases by approximately $0.012°/day$.

to altitude (see Table 6.6). The short term trends can be seen in Figure 6.23. The long term cycle in Figure 6.23 is due to Earth's rotation.

The electrodynamic propulsion system can be used periodically to cancel inclination change at the sacrifice of longer mission times. These changes are possible because of the variations in the B-field as discussed previously. If the mission requires more timely corrections to inclination changes than can be made using the B-field, the augmentation thrusters must be used. For an impulsive inclination change maneuver at the relative line of nodes, the Δv required is given by (93:74):

$$\Delta v = 2v \sin \frac{\Delta i}{2} \tag{6.56}$$

At 500 km, the Δv is approximately 40 m/s for a 0.3° inclination change. This requires engines whose thrust is similar to the ASSET boost/deboost engines. Because of the fuel used to perform such maneuvers, it is preferable to take the additional time to use the B-field.

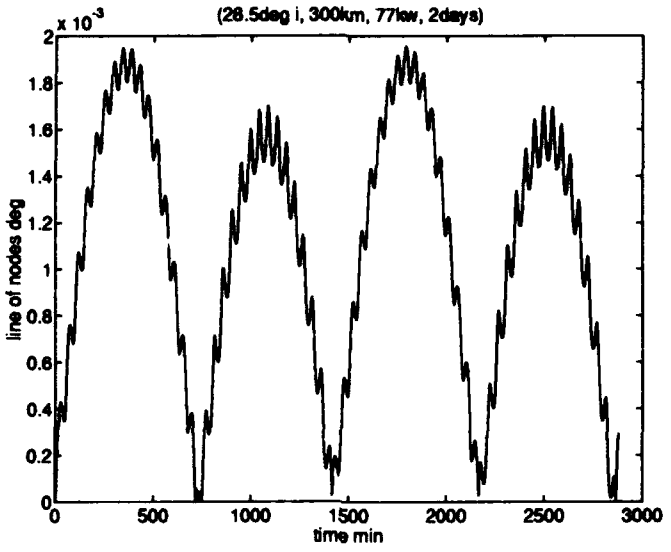

Figure 6.24 Through 2 *days*, $|\Omega|$ varies about zero.

Changes in Ascending Node Right Ascension. The out-of-plane forces also cause changes in the line-of-nodes. A plot of the absolute value of the line-of-nodes, $|\Omega|$, demonstrates the change is small and periodic about zero (see Figure 6.24). A very small trend still exists because of the increasing altitude.

The Earth's oblateness causes a greater change in Ω, with the orbit plane precessing at the rate:

$$\dot{\Omega} = -\frac{3nJ_2r_\oplus^2}{2a^2\left(1-e^2\right)^2}\cos i \tag{6.57}$$

where n is the mean motion, J_2 characterizes Earth's oblateness ($J_2 = 0.001082$, and is determined using spherical harmonic analysis), $r_\oplus$ is the radius of the Earth, a is the semi-major axis, e is the eccentricity, and i is the inclination. For the initial condition orbit, $\dot{\Omega} = 7.45°/day$.

SFP Mission Performance. Numerical integrations were executed for the SFP in three possible operating configurations:

- SFP baseline state: 77 *kW* of power with an external tank payload.

Target Altitude *km*	Time *days*	Δi *deg*	Max $\Delta\Omega$ 10^{-3}°	Comments
300	0.00	0.000	2.00	Starting altitude
360	5.62	0.067	2.00	ASSET maximum altitude
460	15.00	0.180	2.00	Space Station Freedom altitude
500	18.74	0.225	2.00	

Table 6.7 The baseline SFP can reach a 500 *km* altitude in less than 19 *days* from an initial orbit of 300 *km* and 28.5° inclination.

Target Altitude *km*	Time *days*	Δi *deg*	Max $\Delta\Omega$ 10^{-3}°	Comments
300	0.00	0.000	0.00	Starting altitude
360	12.00	0.132	1.68	ASSET maximum altitude
460	32.00	0.352	1.68	Space Station Freedom altitude
500	40.00	0.440	1.68	

Table 6.8 With 68 *kW* of power, the SFP can reach a 500 *km* altitude in 40 *days* from an initial orbit of 300 *km* and 28.5° inclination.

- Reduced power state: 68 *kW* of power with an external tank payload.
- No payload state: 77 *kW* of power with no payload.

The results were used to make linear approximations of critical mission planning factors (see Tables 6.7, 6.8, and 6.9). As discussed previously in Section 6.3.10.5, these estimates are conservative. Because the climb rate increases with altitude, the

Target Altitude *km*	Time *days*	Δi *deg*	Max $\Delta\Omega$ 10^{-3}°	Comments
300	0.00	0.000	0.00	Starting altitude
360	3.59	0.061	2.70	ASSET maximum altitude
460	9.58	0.163	2.70	Space Station Freedom altitude
500	11.98	0.204	2.70	

Table 6.9 With no payload, the SFP can reach a 500 *km* altitude in less than 12 *days* from an initial orbit of 300 *km* and 28.5° inclination.

time required to reach the target altitudes is less than the stated times. However, the additional time will probably be needed to:

- correct the inclination
- correct the line of nodes
- recircularize the orbit
- correct the true anomaly

Efficiency. In comparison to other space propulsion systems, the advantage of shielded coil electrodynamic propulsion is that it uses no propellant other than that used by the augmentation thrusters. Unfortunately, this advantage also makes comparing electrodynamic propulsion with other conventional propulsion systems difficult. The specific impulse, I_{sp}, cannot be used since it is directly related to exhaust velocity of the propellant. There is no way to compare shielded coil electrodynamic propulsion in this manner.

A different definition of efficiency must be considered for the SFP — output power divided by input power:

$$\eta = \frac{P_o}{P_i} \tag{6.58}$$

Because useless out-of-plane forces are produced by the shielded coil electrodynamic propulsion system, this definition must be modified. The output power must be multiplied by the percent of the total force generated that is used to increase the velocity along the velocity vector:

$$\eta = \frac{P_o}{P_i} \cdot \frac{\overline{F_p} \cdot \overline{v}}{|F_p|} \tag{6.59}$$

This efficiency can be compared directly against rocket engine thrust efficiency, defined as the thrust power divided by the input power (40:2).

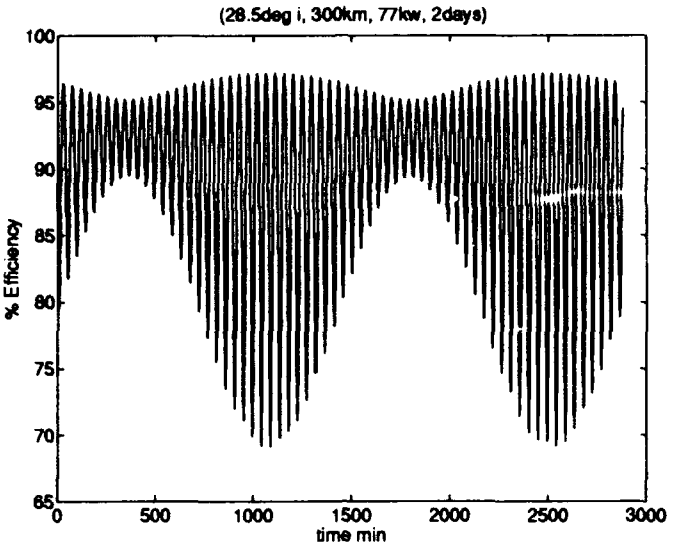

Figure 6.25 The efficiency of the electrodynamic propulsion system varies with $\overline{B}$ and i; the average during the baseline run was approximately 87%.

The efficiency of the shielded coil electrodynamic propulsion system varies with the B-field and applied current, i. The B-field affects both the output power and the percent of useful force. Waste heat generated by the shielded coil electrodynamic propulsion increases by the square of the current. Therefore the propulsion system is more efficient at lower currents.

The peak efficiency for the SFP during the baseline run (see Figure 6.25) is approximately 97%, while the average efficiency is approximately 87%. The shielded coil electrodynamic propulsion system ranks the highest in output/input efficiency when the peak efficiency is considered. The average value compares very well with other space propulsion systems (see Table 6.10). Note that the thruster with the highest output/input efficiency, the hydrazine EHT, has the lowest I_{sp}. This indicates it is less fuel efficient than other systems.

Thruster	η (%)	I_{sp} (s)
Hydrazine EHT	90	300
Shielded Coil Electrodynamic Propulsion	87	NA
Hydrazine Arcjet	35	500
Teflon PPT	5	840
Xenon SPT	55	1600
Xenon Ion Engine	65	3000
Xenon Ion Engine	78	10000

Table 6.10 Efficiencies of various propulsion systems (40:2). The shielded coil electrodynamic propulsion system ranks second.

VII. Electrical Power

7.1 SFP Power Requirements

The ultimate success of the power system is its ability to produce large quantities of power over long periods of time with a minimum investment in mass. Power management of the SFP can be broken down into several distinct segments. Power must be provided to the following systems: propulsion, truss making, servicing, external tank reduction operations, command and control and miscellaneous power management. Chapter X lists the various operational modes of the SFP. From these, a worst case scenario for power usage can be drawn. Early in the study, it became apparent that this worst case would be related to propulsion, specifically during *R*-bar maneuvering. The SFP is designed so that currents flowing in various conductors interact with the Earth's magnetic field to produce a net force on the vehicle. From the equations of motion outlined in Section 6.2.4 the forces required to propel the SFP are determined. Using the equations provided in the following sections of this chapter, the currents in each of the SFP conductors can be determined from the required forces. Once the currents are known, the power required can be determined. Once a power level is chosen, the above scheme can be used to specifically design a vehicle.

Obviously, more power available allows for greater currents in the conductors. The greater currents can be used to generate greater forces, resulting in a more capable SFP. There are some constraints in the actual selection of a power system that must be considered. The tradeoff analysis that led to the selection of the SFP power system is located in Section 11.8. The result of this analysis was the selection of a 70 kW solar dynamic closed Brayton cycle power system. Added to this 70 kW is the 12 kW of power provided by the ASSET photovoltaic arrays for a total of 82 kW of available power. A description of this design is included in the next section. Note

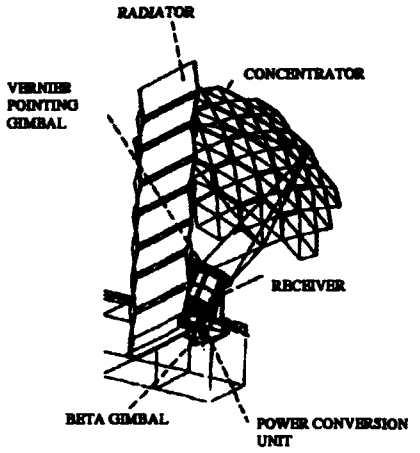

Figure 7.1 Space Station Freedom solar dynamic power module. The main components are shown including the concentrator, the receiver, the radiator, and the interface structure (89).

that the description provided is the actual design from Space Station Freedom. The SFP design differs slightly in a few areas that will be annotated later in Section 7.3.

7.2 Space Station Freedom Solar Dynamic Power Module

The solar dynamic power module (SDPM) consists of three major assemblies: the solar concentrator, the radiator and the closed Brayton cycle (CBC) power generation assembly. The SDPM is shown in Figure 7.1. The SDPM was designed so that two modules could be transported in one shuttle mission (8:321). The system masses are shown in Table 7.1. These assemblies must be mounted outboard on the cross integrated truss to allow for pointing and sun alignment of the assembly. This will be accomplished with the following: 1) An alpha joint in the integrated cross truss will allow orbital sun tracking about the SFP's $\hat{b}_3$-axis. A more complete description is provided in Section 9.2. 2) A beta joint between each power module and the truss will permit rotation about an axis normal to the truss for seasonal sun

Subsystem	Mass kg
Receiver	1752
Radiator	1529
Concentrator	1485.5
Power Control Unit	807.4
Structure	375.5
TOTAL	5949.4

Table 7.1 Space Station Freedom solar dynamic system masses.

tracking. 3) Two axis joints are provided for fine pointing the concentrator relative to the sun and the receiver (66:2).

The SDPM does not have a steady state performance condition. Performance is transient due to variations in orbital altitude, position in orbit (in sun or eclipse), seasonal variation in solar insolation and degradation of the collector performance (8:325). To meet the net power output of 25 kW the gross electrical power at the alternator must be a minimum of 32.15 kW.

7.2.1 Solar Concentrator. The solar concentrator is an offset parabolic design consisting of 19 hexagonal truss panels with triangular facets mounted within the hexes and is shown in Figure 7.2 (8:320). The concentrator focuses the solar energy into the receiver located at its focal point. This configuration minimizes shadowing and permits the SDPM center of mass to be located near the truss structure minimizing potential dynamic and control problems. The concentrator structure is connected to the module by six struts mounted on a two axis gimbal which is driven by redundant actuators for pointing and control. Approximately 30 meters of truss are necessary to allow the concentrator assembly to swivel on the beta gimbal without encountering any obstructions and to prevent any shadowing by other portions of the SFP.

7.2.2 Radiator. The radiator accepts the waste heat rejected by a working fluid through the use of a gas coolant liquid (Flourinal FC-75). The radiator package

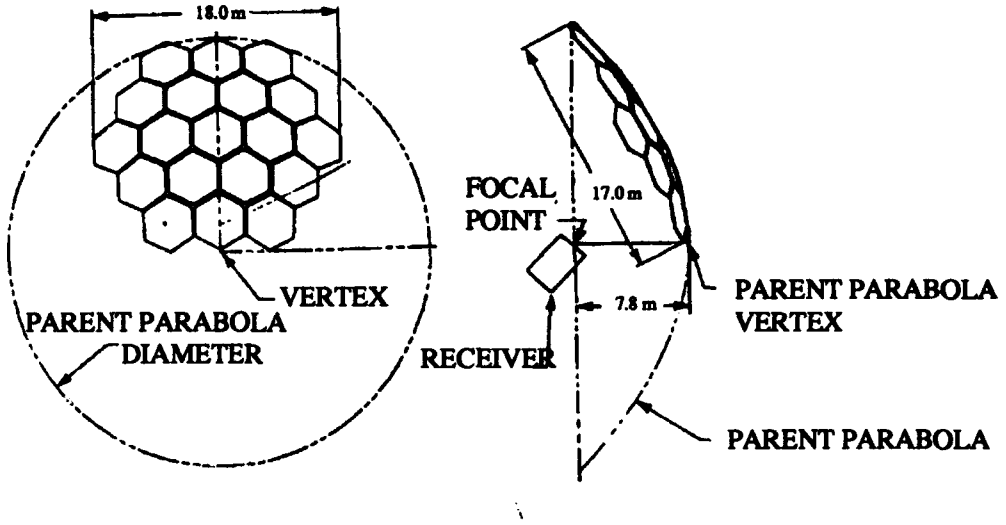

Figure 7.2 The solar dynamic concentrator is an offset parabola with 19 hexagonal panels (73).

consists of eight panels $2.3 \times 8\ m$. Deployment is accomplished by a scissors type mechanism similar to the one used on Skylab's arrays (see Figure 7.1).

7.2.3 Power Generation Assembly. The CBC operates with a helium xenon, $He-Xe$, mixture he ed in the receiver heat exchanger and expanded through a turbine which provides the shaft power to drive the compressor and generator. Most of the gas exiting the turbine is recycled by the recuperator and used to preheat the gas entering the receiver. Other components include a controller and an accumulator. The actual size of the Space Station Freedom design is shown in Figure 7.3 and an overall view of the power conversion unit can be seen in Figure 7.4. This CBC power conversion unit is a derivative of the well known, technically mature, gas turbine cycle used for auxiliary power units on military and commercial aircraft.

7.2.3.1 Receiver. The concentrated solar flux is admitted through a 43.2 *cm* diameter aperture in the receiver face. The receiver contains 82 tubes carrying the working fluid that absorbs solar energy (see Figure 7.5). These tubes

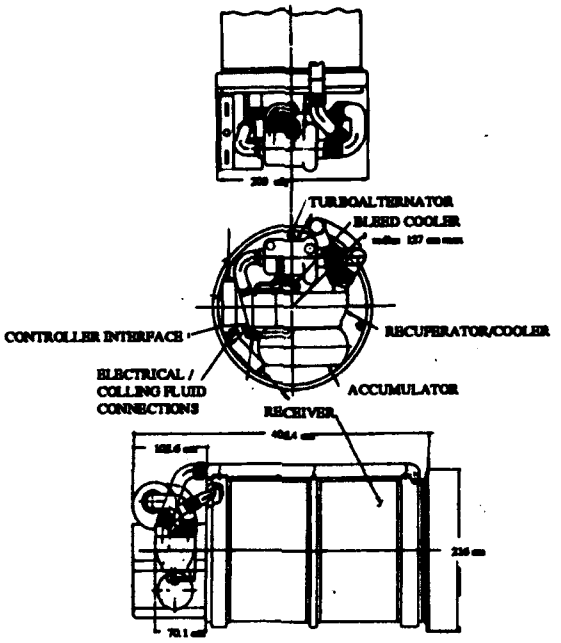

Figure 7.3 Dimensions of the power generation assembly — an approximate 4 *m* long by 1 *m* wide barrel (73).

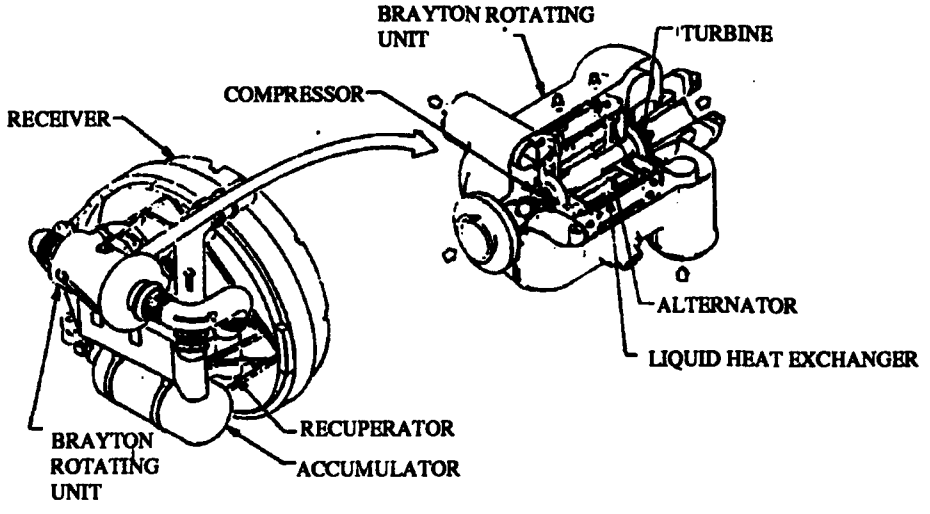

Figure 7.4 Power conversion unit. Figure shows the relative size of the unit in relation to the receiver (73).

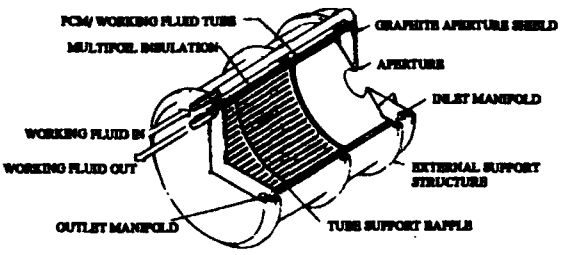

Figure 7.5 Solar dynamic power module receiver. Solar flux enters the receiver through the aperture and heats the working fluid flowing through the tubes as shown (73).

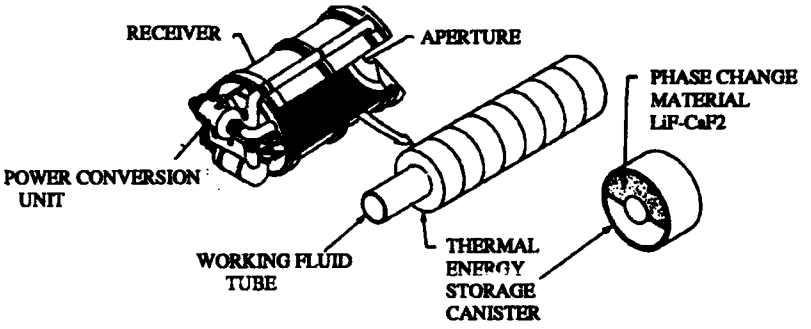

Figure 7.6 Solar dynamic power module receiver with a view of the working fluid tubes and the salt containment canisters (73).

are surrounded by canisters containing a salt. The salt is a eutectic mixture of lithium fluoride-calcium di-fluoride, $LiF - CaF_2$, that operates as a phase change material (see Figure 7.6 for an illustration of the canisters). The latent heat of fusion of this salt provides thermal energy storage for use during the eclipse portion of the orbit. During sunlight the salt approaches a fully liquid state. During eclipse it begins to solidify. In this state the temperature remains fixed at $767°C$ and is used to heat the working fluid (85:247). The containment canisters of the salt are structurally designed to minimize the highly predictable long term creep and the actual design lifetime is in excess of 30 years (8:323).

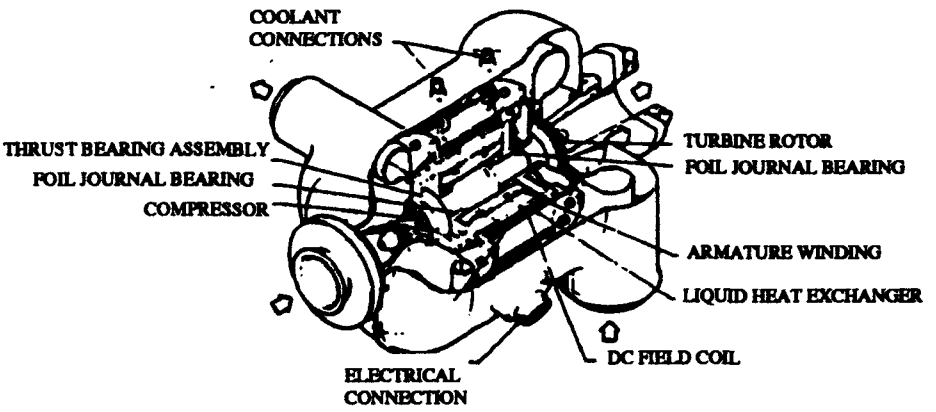

Figure 7.7 Turbomachinery of the power conversion unit. The working fluid passes through the unit turning the turbine and generating electricity (73).

Speed	32,000 *rpm*
Compressor diameter	16.51 *cm*
Turbine diameter	19.43 *cm*
Alternator rotor Diameter	12.12 *cm*

Table 7.2 Turbomachinery design specifications. Note the small size of the actual rotating parts.

7.2.3.2 Turbomachinery. The Turbomachinery involved in the unit are a radial compressor, solid alternator rotor, and a radial flow turbine suspended on compliant foil bearings that use the inert working gas as the lubricant (8:324) (see Figure 7.7). Pneumatic separation of the bearings from the rotor results in no metal-to-metal contact thereby increasing the lifetime. The rotor is the only continuously moving part in the power system. The turbine and compressor ratios are low, less than two to one, allowing very rugged, single stage aerodynamic wheels. Some specifications are included in Table 7.2.

7.2.3.3 Recuperator. The recuperator is a gas-to-gas heat exchanger which recovers energy from the turbine exhaust to heat the compressor discharge

flow prior to final heating in the receiver (see Figure 7.4). This has three beneficial results:

- a reduction in the amount of heating required in the receiver reducing the necessary size of the concentrator
- a reduction in the quantity of thermal energy storage for the eclipse
- a reduction in the amount of waste heat to be rejected reducing the size of the radiator (8:324)

7.2.4 Controller. The controller maintains a constant speed on the turbomachine by a parasitic load radiator which dissipates any excess power. This is accomplished by sensing the alternators frequency. Power generated varies based on how the receiver and the power conversion unit accommodate solar flux. At an inclination of 28.5°, this power ranges from 33.15 kW in a 300 km orbit to 36.42 kW in a 500 km orbit (8:324).

7.3 SFP Solar Dynamic Power Module

The SFP operation showed a need for power levels in excess of 50 kW; therefore, two Space Station Freedom modules would not be enough. Two CBC solar dynamic power modules providing 35 kW each were chosen to augment ASSET power to bring the total power available to the SFP to 82 kW. The 35 kW modules chosen are the same basic configuration as the previously described Space Station Freedom modules with the following exceptions: LiF salt is the thermal energy storage medium, the turbine inlet temperature is increased (1,086 K versus 1,006 K), the concentrator structure is made lighter, and some other masses are changed due to modifications made to accommodate the new thermal energy storage medium (89:19).

LiF has a 32% greater heat of fusion potential than $LiF - CaF_2$ (Space Station Freedom salt) but, this advantage is partially offset by a 16% higher specific

Subsystem	Mass kg
Receiver	1255
Radiator	1471
Concentrator	845
Power Control Unit	1010
Structure	486
TOTAL	5067

Table 7.3 SFP Solar dynamic system weights.

volume (89:309). A higher fraction of efficiency is realized due to the melting temperature of LiF being $79°K$ greater than that $LiF - CaF_2$. This higher temperature forces different materials to be used in the construction of the receiver. Different alloys actually resulted in a reduction in receiver mass as shown in Table 7.3. In general most of the receiver design is identical to the Space Station Freedom receiver except for the wall thickness and material, aperture area, and aperture shield thickness (89:61).

The largest reduction in weight over the Space Station Freedom design came in the concentrator. The SFP concentrator has the same shape and size, but the supporting structure was made lighter with new materials. The higher concentration ratios necessary for higher temperature operation in the receiver required smaller reflective segments in the truss hex design (89:54).

This 35 kW design provides 22% more power than the Space Station design with only the minor changes stated above. The higher cycle performance was due to the increased operating temperature. The size of the module is virtually unchanged but a benefit of new materials provided a weight reduction.

7.4 SFP Power Demand Calculations

The two module design of the SFP provides 70 kW which adds to the 12 kW provided by the ASSET arrays. This 82 kW must be distributed to the previously mentioned systems. The SFP was designed around this available power constraint.

The actual power demands of the SFP are related to propulsion, truss making and a variety of 'base power' items. How the actual power demands were determined is discussed in the following sections.

7.5 Power for Propulsion

The power necessary for propulsion alone can be broken into three main modes of operation:

- orbit transfer
- orbit maintenance (overcoming aerodynamic drag)
- R-bar maneuvering

In the orbit transfer mode of operation, conductors *C1* and *C2* are positioned in the radial direction to provide thrust and are the primary power drain during this operation. For simple orbit maintenance, conductor *C5* is oriented in the radial direction to provide counteracting thrust — the primary power drain. In the case of R-bar maneuvering, all conductors interact with the Earth's magnetic field to one degree or another depending on the exact orientation of the SFP. All conductors must then be considered in the power analysis. The MATLAB programs discussed in Chapter VI were used to calculate power requirements for the R-bar and orbit transfer maneuvers.

7.5.1 Power for Orbit Transfer. There are two possible methods to calculate the power requirements for an SFP orbit transfer. The first is through the force on the platform. Recall from Section 6.2.2.4 that the force on the conductor is given as:

$$\overline{F} = ni\overline{L} \times \overline{B} \tag{7.1}$$

The rate of orbital energy increase or decrease (depending on the direction of the current flow) is (55:343):

$$P = \overline{F} \cdot \overline{V} \tag{7.2}$$

where P is the power, and V is the velocity. This approach assumes that the current flow and conductor length are known quantities. In designing the SFP, these quantities were unknown initially. They depend upon the required capabilities and configuration of the SFP.

The second method for power determination uses Equation 7.1 along with the following analysis. These equations were used iteratively as part of the SFP design process.

The voltage induced across a straight conductor moving through a uniform magnetic field is (63:119):

$$V_{ind} = \overline{E}_{ind} \cdot \overline{L} = (\overline{v} \times \overline{B}) \cdot \overline{L} \tag{7.3}$$

$\overline{E}_{ind}$ = the electrical field induced across the conductor
$\overline{v}$ = the velocity of the conductor relative to the magnetic field
$\overline{B}$ = the magnetic field
$\overline{L}$ = the effective length of the conductor

The induced voltage is a function of orbit altitude, inclination, position in orbit, and position of the orbit plane with respect to the geomagnetic field. If the SFP is unpowered, current flows strictly due to the voltage induced by the platforms orbital motion through the Earth's magnetic field. A complete, closed circuit allows this current to flow. In the case of an unpowered SFP, induced current flows downward for eastward orbital motion to produce a braking force on the vehicle in accordance with Equation 7.1. To operate the system as a thruster, a high voltage dc power supply is required to provide a voltage greater than the voltage induced in the wire

by the magnetic field. This will force the current to flow upward and provide a thrusting force.

The velocity in the preceding equation is the vehicle orbital velocity minus the velocity of the co-rotating magnetic field (49:C.1). For a circular, equatorial orbit this is approximated as:

$$v = \sqrt{\frac{GM_{\oplus}}{r}} - \omega_{\oplus} r \tag{7.4}$$

G = the gravitational constant

$M_{\oplus}$ = the mass of the Earth

r = the orbital radius

$\omega_{\oplus}$ = the Earth's rotational angular velocity

For low inclination orbits this equation is approximately correct and can be used for illustrative purposes. Note that no voltage is induced if the conductor is perpendicular to the induced electric field. When the induced electric field is parallel to $\overline{L}$ the induced voltage is (49:C.1):

$$V_{ind} = (\sqrt{\frac{GM_{\oplus}}{r}} - \omega_{\oplus} r) BL \tag{7.5}$$

Assuming that the length of the conductor (in the case of orbit transfer, conductors *C1* and *C2*) can be oriented to be perpendicular to the B-field, and the velocity direction throughout the orbit, then the induced voltage will be the scalar product shown above. Concept development studies have shown the induced voltage can vary from a minimum of 113 V/km to a maximum of 207 V/km at an orbital altitude of 500 km (59:463). These values are even greater at altitudes below 500 km. This induced voltage must be overcome by the power supply if a thrusting force is desired. Using the circuit illustrated in Figure 7.8 and Kirchoff's voltage law, this can be expressed as:

$$V_{ps} = V_{ind} + iR_w \tag{7.6}$$

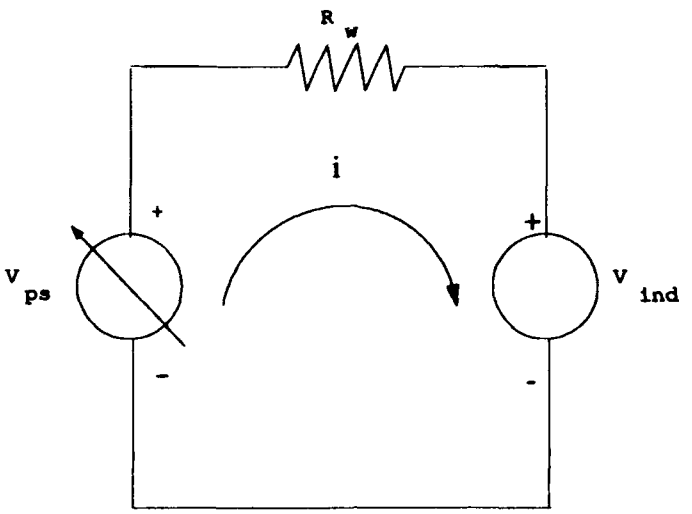

Figure 7.8 Equivalent circuit for thrusting operations of the SFP utilizing just conductors $C1$ and $C2$. Note that current flows upward in an orbital sense due to the fact that V_{ps} is greater than V_{ind}.

V_{ps} = the power supply voltage

V_{ind} = the induced voltage across the conductor

i = the current flowing through the conductor

R_w = the total electrical resistance of the conductors $C1$ and $C2$

R_w, the $C1$ and $C2$ conductors' total resistance, is the total length of the conductors times the resistance per unit length of the material. Prior to this study, most work in this area concentrated on the return circuit loop flowing through the Earth's ionosphere. The resistance of the ionosphere as well as that of the necessary plasma magneto generators or passive emitters/collectors is not well known or modeled (55:357). This uncertainty has been avoided by the shielding concept which allows the return loop to remain aboard the SFP. This makes the resistance of the circuit just the resistance of the wire.

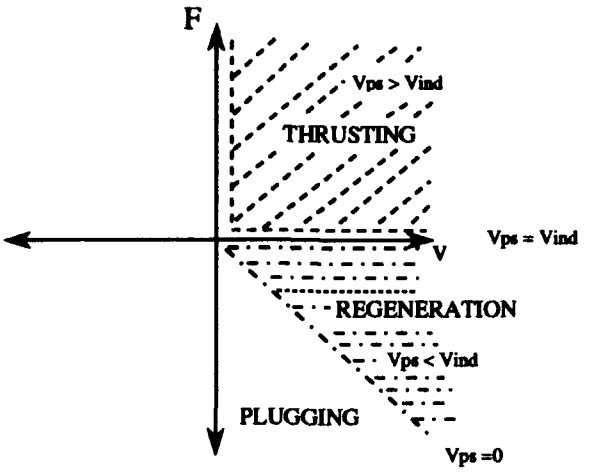

Figure 7.9 A force versus velocity plot for the operation of the SFP. When V_{ps} is greater than V_{ind}, current flows in the conductor in the direction for a thrusting force (THRUSTING region). If V_{ps} is less than V_{ind}, current flows in the conductor in the direction for a drag force (REGENERATION region). If V_{ps} is connected in the same direction as V_{ind}, current flows in the conductor in the direction for a larger drag force (PLUGGING region).

The power that must be supplied to operate the system as a thruster is given by:

$$P_{ps} = iV_{ind} + i^2R_{tot} = iV_{ps} \tag{7.7}$$

The sizing of the conductors was based on using a maximum power of approximately 77 kW (82 kW minus 5 kW for base power).

An analogy can be drawn between the SFP operation and the operation of a dc motor. In Figure 7.9, force versus velocity is plotted for varying voltages. This is similar to torque versus rotor angular speed in a dc motor. When the voltage of the power source is greater than V_{ind}, current will flow in the direction that produces a thrust force on the SFP. The magnitude of this thrust depends on how much greater V_{ps} is than V_{ind}. If $V_{ps} = V_{ind}$, then no thrust or drag force is produced and no power is expended since no current is flowing.

Up to this point, the discussion has been focused on thrusting and thereby increasing the SFP's altitude in orbit. If a decrease in orbit is required, a net negative force (opposite the velocity direction) must be applied to the SFP. To accomplish this, current must flow downward in conductors $C1$ and $C2$. If V_{ps} is less than V_{ind}, then current will attempt to flow in the direction that produces a drag force on the SFP. This situation could cause problems if the power supply is connected directly to the circuit as shown in Figure 7.8. Some type of intermediate energy storage/release device would be necessary in this case, to allow for this reverse current flow. Normal power supplies do not allow for a reverse current mode. Because of the naturally generated current from V_{ind}, this vehicle would be a far more efficient generator than a thruster. The problem is that power generation takes the energy from the orbit by producing a drag force. Storing this energy for any significant period of time would take an extremely large battery mass. This option was not considered in the design study. For completeness, a discussion of this possibility is included in the following paragraph.

If a battery storage device were present, then the magnitude of the drag will depend on how much less V_{ps} is than V_{ind}. If V_{ps} equals zero, the current will flow simply due to V_{ind}. The mode of operation, $0 \leq V_{ps} \leq V_{ind}$, can be labeled 'regeneration' since orbital energy is being converted to electrical energy and has the potential to be stored and used later. Current, in this case, will be in the drag direction and has the capability to be quite large if V_{ps} is much less than V_{ind}. If the direction of the power supply voltage is reversed to cause current to flow in the drag direction, then the power supply voltage and the induced voltage would be cumulative and would cause very large current flows in the drag direction. This mode of operation is called 'plugging' and is unachievable with the SFP design due to the high current flows. It is also unnecessary since the SFP could decay its orbit in a sufficient period of time due strictly to V_{ps} being less than V_{ind}.

The final SFP design does not use this variable voltage battery storage method to power the conductors during thrust and drag operations. It was decided instead to use dynamic braking in which additional resistance is switched into the circuit to replace the power supply. This however, has the potential for heat transfer problems if the current is not modulated correctly. The SFP is designed so that the core temperature of the shielded wire never exceeds $438.0°C$. This restriction was placed so that the danger of melting the conducting wires was never approached. The analysis of this heat transfer problem is discussed in Appendix K. The current flow that corresponds to this temperature is 300 A. Operation in the drag mode, due to V_{ind} alone, makes some type of resistance necessary to keep current flow under this level. The voltages induced by motion through the magnetic field would cause current flows much greater than this limit if opposed by only the resistance of the wire. For example, in a 300 km equatorial orbit, Equation 7.5 yields an induced voltage of 1,927 $volts$. Using $V_{ind} = iR_w$ yields a current of over 2,300 A for the SFP. This is almost an order of magnitude greater than the SFP design constraint. Therefore a switch is provided to take the power supply out of the circuit for drag operations and connect a variable bank of resistors in its place. This is illustrated in Figure 7.10. A variable resistor is needed to modulate the current flow as the B-field changes. A minimum resistance of 5.59 Ω, in addition to the resistance provided by the conductor wires themselves (0.84 Ω), is necessary to modulate the current below 300 A at an altitude of 300 km. The SFP uses a variable resistance bank that modulates the current flows from 0.1 to 300 A in conductors $C1$ and $C2$. At higher altitudes these resistances will be less due to the decrease in induced voltage. Therefore the minimum resistance necessary will be lower than the value stated for 300 km. The actual resistance needed for modulation of current varies from 20,000 Ω down to approximately 1 Ω over the altitudes of 300–500 km. The forces corresponding to these values vary from 0.027 N up to 80.19 N at 300 km and 0.009 N up to 28.81 N at 500 km.

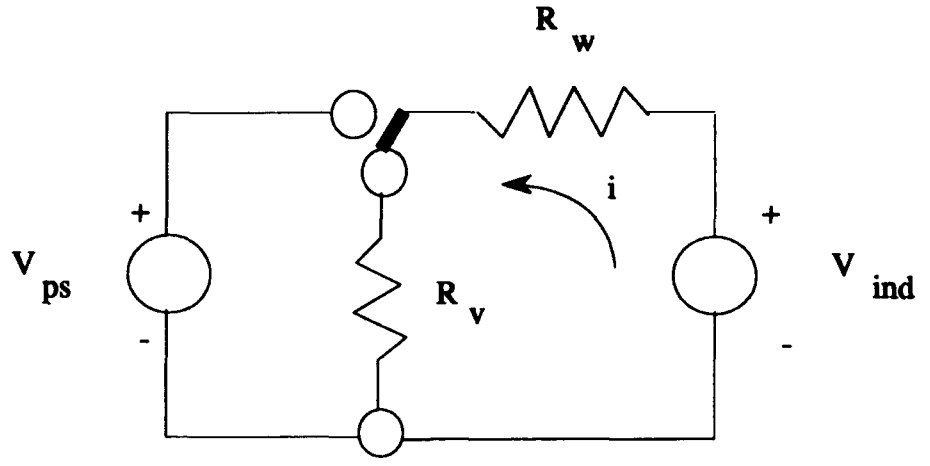

Figure 7.10 Equivalent circuit for orbit transfer drag maneuvering operations of the SFP utilizing conductors $C1$ and $C2$. A switch is provided to take the power supply out of the circuit and replace it with a variable resistance, R_v. This allows for modulation of current flows.

7.5.2 Power for R-bar Maneuvering. R-bar maneuvering used the same analysis as described in the previous section with the exception that all conductors were included in the model. For a typical R-bar maneuver, conductor $C5$ is in the radial direction, and is the primary contributor to any induced voltage problems due to the orbital velocity of the vehicle. With varying degrees of roll, pitch and yaw, other conductors can place a significant component of their length in the radial direction and can therefore greatly increase power requirements through larger induced voltages. It was recognized early in the design process that this situation would drive the major power concerns of the study. Figure 7.11 provides an illustrative circuit diagram that will help explain the power situation for an R-bar maneuver. Although some individual conductors have current flowing in the drag direction, the overall force necessary causes a thrusting current out of the power supply. This situation is unique to R-bar maneuvering. The opposite direction currents being generated by dragging conductors can then be used in thrusting conductors, reducing the overall power demand.

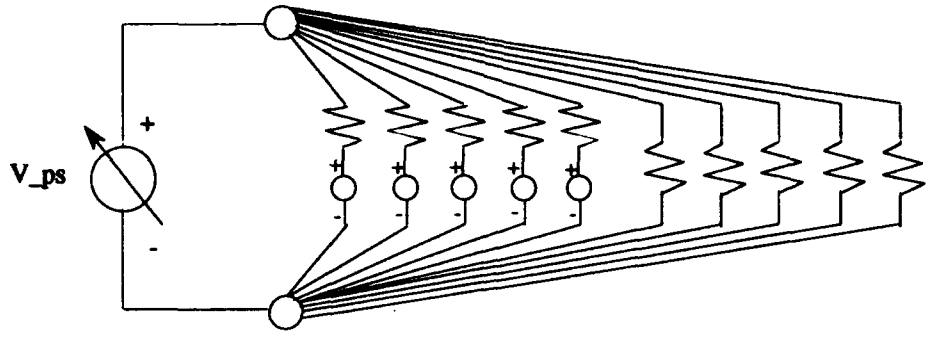

Figure 7.11 Equivalent circuit for R-bar maneuvering operations of the SFP utilizing conductors $C1$ through $C10$. Conductors $C1$ through $C5$ can have induced voltages because they are partially shielded. They are the first five loops shown in the above figure. Conductors $C6$ through $C10$ cannot have induced voltages because they are totally unshielded coils. They are the second five loops shown in the above figure and are modeled as simple resistances.

7.5.3 Orbit Maintenance. At 300 *km*, aerodynamic drag losses cause the SFP to decrease its orbit 14 *km* over a four day period. This is a worst case profile of the SFP. Refer to Section 6.2.1 for a complete discussion and analysis of this subject. The nominal configuration of the SFP is with conductor $C5$ in the radial direction. Overcoming drag at 300 *km* (the lowest operational altitude) costs 15.0 *kW* of continuous power for an inclination of 28.5° and 13.8 *kW* for an equatorial orbit. The power drain for orbit maintenance reduces as the SFP gains altitude due to the reduction in drag. This is counteracted however, by a reduction in the strength of the B-field. At 500 *km* (the highest operational altitude), the necessary power to overcome drag forces is 14.5 *kW* and 13.2 *kW* for 28.5° and equatorial orbits respectively. At this altitude drag forces would decrease an unpowered SFP's altitude by only 3 *km* in a four day period.

7.6 Truss Maker and Other Equipment Power

The power required to run the following is included in this section:

- truss maker — welder, drive wheels, graspers, etc.
- SFP servicing system
- control and communications
- miscellaneous

The truss maker and its associated equipment use 7 kW when operating at the maximum rate. The SFP servicing system takes a maximum power of 2 kW. The docking system is modeled as utilizing up to 2 kW during docking operations. Since the docking system will be utilized for only a short period of time, this amount can be included with the servicing system power drains. A base power will be needed for teleoperation, communications links, lights and cameras as well as other miscellaneous needs. Due to the complexity of the SFP, 5 kW of power is reserved for this need.

7.7 Overall SFP Power Usage

It is difficult to quantify the exact power being drawn by an SFP subsystem at any instant in time. Its fabrication capability means that it operates in a diverse and dynamic manner. As such, rather than provide a detailed list of power drains, a worst case analysis will be used. In other words the power used at theoretical maximum usage of the particular subsystems will be added together to give a total demand.

It was determined during the ASSET study that actual salvage of material from an external tank should occur at an altitude of 300 km and would require approximately five days. Power concerns for the SFP during reduction operations is summarized in Table 7.4. During salvage operations, power concerns are related to external tank reduction, base power concerns, and orbit maintenance. This requires 34 kW of power, leaving 48 kW available. If necessary the truss maker could be

SFP System	Power Used kW
Reduction Equipment	12
Command, Control and Communications	5
Servicing System	2
Orbit Maintenance	15
TOTAL	34

Table 7.4 Power concerns for the SFP during salvage operations at 300 km.

operated concurrently with external tank reduction. This would be done as material becomes available and would drain an additional 7 kW from the power supply.

Subtracting out the 5 kW of base power leaves a total of 77 kW available for propulsion to accomplish an orbit transfer or an R-bar maneuver. This is an adequate amount of power to achieve the required performances and capabilities outlined in Section 3.2. With conductors $C1$ and $C2$ in the radial direction, an orbit transfer, with a full payload of one external tank, from 300-500 km can be accomplished in 18.74 *days* for an inclined orbit of 28.5°. Without an external tank it takes just 11.98 *days*. These are constant power transfers; the current is modulated to maintain this power level as the B-field changes. If time to transfer is not critical, the power available for propulsion can be reduced and other activities can be undertaken. In other words, trusses can be made while enroute to their final destination. Truss making uses 7 kW of power for a time period of approximately 2 *days*. This would leave 70 kW for propulsion for the first 2 *days* and thereafter 77 kW. This would not significantly affect the stated time to transfer.

For an orbit reduction, only the 5 kW of base power is used by the SFP. All forces on the vehicle are provided by the induced currents flowing in conductors $C1$ and $C2$. If modulated to a constant flow of 100 A the transfer from 500 to 300 km would take only 15 *days*. If run at 300 A, transfer would occur in only 3 *days*, but heat transfer problems could possibly occur in the resistor for this level.

7.8 Power Summary

The result of the power survey and trade off analysis was a 70 *kW* closed Brayton cycle that augments the 12 *kW* of available ASSET power. This 82 *kW* of power available was metered to the various subsystems of the SFP. This level of power greatly influenced the actual design process of the SFP discussed in Section 6.3.

VIII. Remote Manipulators

8.1 Introduction

The assembly and mission ready operations of the SFP depend heavily on remote manipulators. This chapter conceptually identifies the two manipulator systems for the SFP: the servicing system and the docking system. Both systems are derived from the components of the proposed mobile servicing system developed for Space Station Freedom by SPAR Canada. The Space Station Freedom system is a natural extension of the already proven shuttle remote manipulator system.

When applicable, the component associated with the Space Station Freedom system will be identified to assist in the explanation of the component proposed for the SFP. Many of the operating limits and procedures for the Space Station Freedom system are still in the design phase. Those operating limits and procedures that have been resolved serve only as realistic guidance for their use in this application. They do not limit the SFP systems in this conceptual analysis. Future engineering for specific applications on the SFP is required.

8.2 Servicing System

8.2.1 Purpose. Similar to the mobile servicing system of the Space Station Freedom (42:7.2), the servicing system of the SFP will play a predominant role in:

- construction and assembly
- maintenance and servicing
- monitoring and inspecting
- truss making
- payload handling
- EVA support

8.2.2 Components and Procedures. The servicing system consists of two independent manipulator systems *primarily assigned* to each side of the main integrated truss. A complete manipulator system is comprised of the following primary components:

- a mobile base
- a heavy manipulator
- a dextrous manipulator

The two ends of the heavy manipulator possess heavy latching devices. A heavy latching device is an end effector for grappling heavy grapple fixtures. Figure 8.1 utilizes a Space Station Freedom illustration to identify the primary components of one SFP manipulator system and the associated grappling mechanisms.

Figure 8.2 utilizes an illustration of a Space Station Freedom power and data grapple fixture to identify a heavy grapple fixture for the SFP. The heavy grapple fixture is made up of two components: a circular base with a 0.65 m radius, and a screw on guide post with a 0.27 m length. On Space Station Freedom, the grapple fixture is designed to withstand moments of 4,270 $N \cdot m$ and loads of 1,000 N (82:D.11-D.15). Figure 8.3 identifies a heavy latching device in a pre-grapple or post-grapple position.

The result of grappling a heavy grapple fixture is the rigidization of the heavy manipulator to an object. The object may be a payload or a structure secured to the SFP (anything with a heavy grapple fixture). If the appropriate electrical connectors have been installed in the grapple fixture, power, data, and video can be transmitted for controlling the heavy manipulator. In figure 8.1, one latching device of the heavy manipulator is grappled to a heavy grapple fixture on the mobile base and the other latching device is grappled to a heavy grapple fixture on the dextrous manipulator. The words *primarily assigned* were chosen because the heavy latching devices on each end of the heavy manipulator can grapple any heavy grapple fixture associated

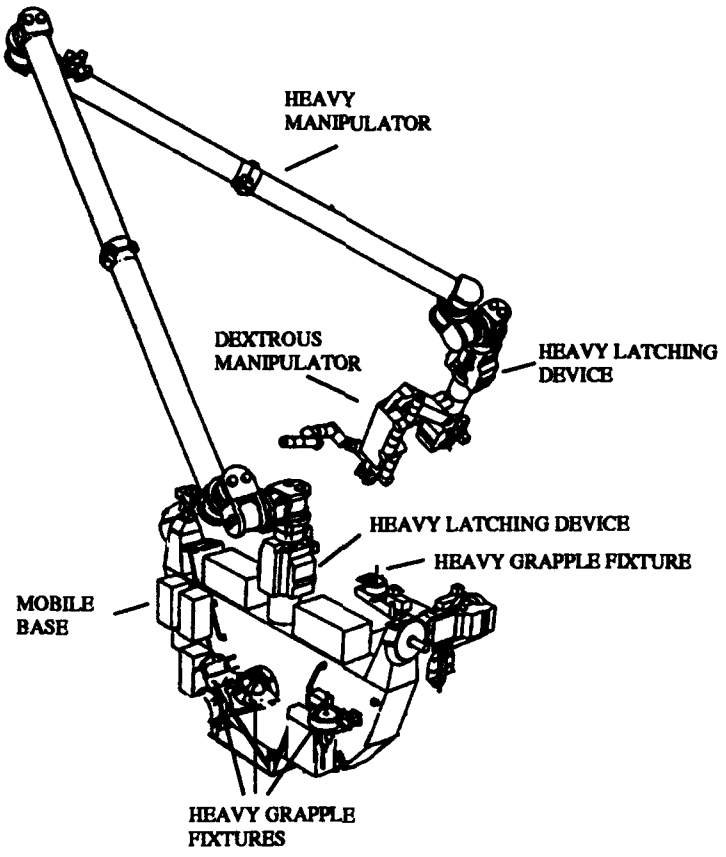

Figure 8.1 One complete manipulator system. The servicing system of the SFP consists of two independent manipulator systems primarily assigned to each side of the main integrated truss (82).

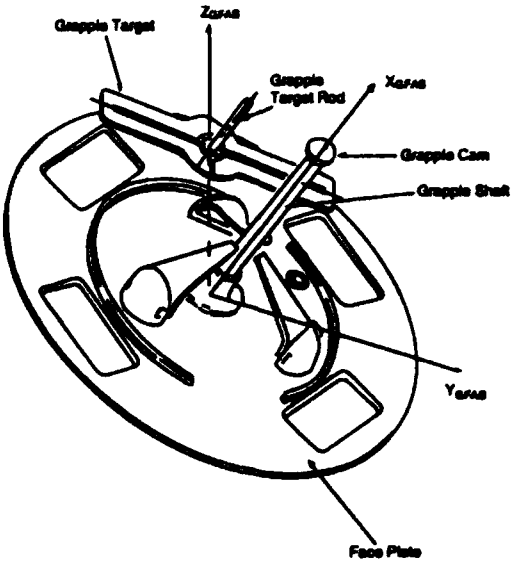

Figure 8.2 The heavy grapple fixture provides a grasp area and guide post for a heavy latching device. When integrated with the appropriate electrical connectors, it can facilitate the transmission of power, data, and video for controlling a manipulator (82).

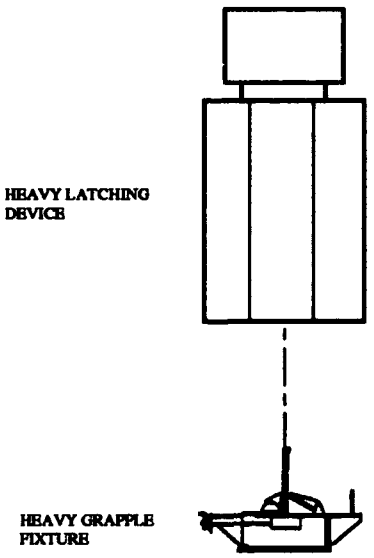

Figure 8.3 A heavy latching device in a pre-grapple or post-grapple position.

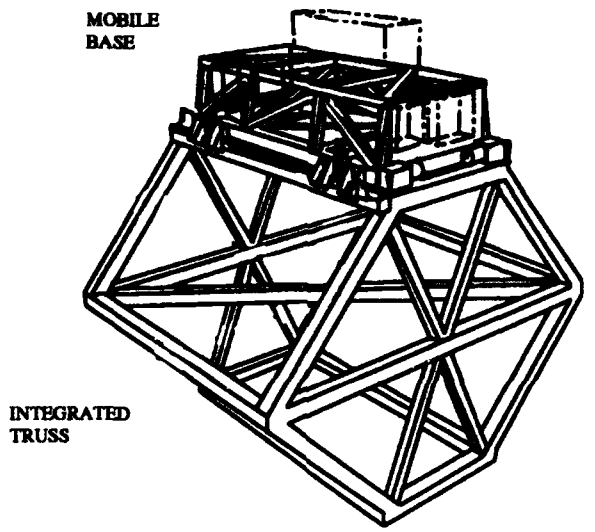

Figure 8.4 The Space Station Freedom mobile base attached to its integrated truss. The remainder of the manipulator system can be mounted to the mobile base, and the entire system can traverse the length of the integrated truss (82).

with the SFP. There is no requirement for the heavy manipulator to remain grappled to the mobile base or to the dextrous manipulator.

8.2.2.1 Mobile Bases. Mobile bases for the SFP are attached to rails on the integrated trusses. Figure 8.4 is a Space Station Freedom illustration of a mobile base attached to an integrated truss. With a heavy manipulator grappled to a mobile base, and a dextrous manipulator grappled to the heavy manipulator, the manipulator system is capable of traversing the entire length of an integrated truss. It can perform or assist with work anywhere within its expanded reach.

There are four mobile bases planned for the SFP: one on each side of the main integrated truss and one on each of the cross integrated trusses. They will provide the two heavy manipulators and two dextrous manipulators with mobility throughout the platform. When a manipulator system is configured on the main integrated truss, it will primarily assist with truss making operations, and when a

manipulator system is configured on a cross integrated truss, it will primarily assist with power system servicing.

Similar to the mobile remote servicer base and the mobile transporter of the Space Station Freedom (61:341), the mobile base of the SFP provides:

- an EVA workstation for direct control of the grappled manipulators
- an umbilical for external control of the grappled manipulators
- space for storing dextrous manipulator tools
- attachment points for transporting payloads
- cameras and lighting for automatic tracking and grappling
- cameras and lighting fo monitoring and inspecting operations

8.2.2.2 Heavy Manipulators. The heavy manipulators of the SFP are identical to the Space Station Freedom remote manipulator in appearance and functions (see Figure 8.5). They are 17.6 m serial linked manipulators with seven rotary joints. Three wrist joints are clustered at each end and one elbow joint is in the middle. From the elbow joint out to the heavy latching device on each wrist, they are completely symmetrical and identical in functions. Because of the previously described capability to transmit power, data, and video information through the heavy grapple fixtures into the heavy latching devices, appropriately placed and electrically configured heavy grapple fixtures can command a heavy manipulator to *walk* around the SFP.

As the name implies, the heavy manipulator is designed for manipulating heavy objects. Heavy objects associated with the SFP are objects with a mass in excess of 1,000 kg. The Space Station Freedom remote manipulator is being designed to manipulate payloads as massive as 136,000 kg (71:34). Also similar to Space Station Freedom applications (79:38-39), the heavy manipulator of the SFP has the capability to grapple heavy payloads and transport them across the platform via the

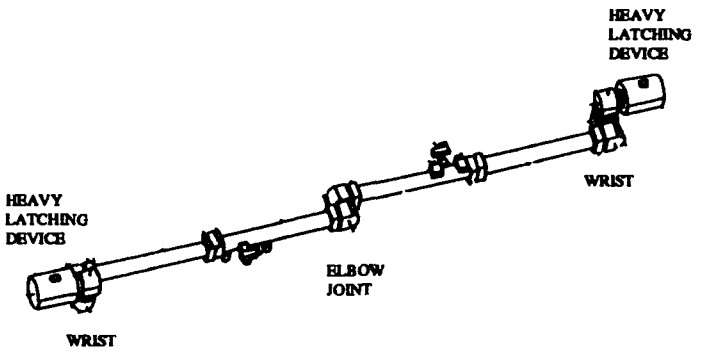

Figure 8.5 One 17.6 m heavy manipulator with seven joints. It is symmetrical about the elbow joint and can grapple any heavy grapple fixture (82).

mobile base. It can extend the reach and subsequent capabilities of the dextrous manipulator, and it can carry a suite of cameras and lighting for automatic tracking and grappling, or monitoring operations.

8.2.2.3 Dextrous Manipulators. The dextrous manipulators of the SFP are modeled after the special purpose dextrous manipulator of the Space Station Freedom (see Figure 8.6). Each manipulator consists of a base, an articulated body, two seven degree of freedom arms, and a head with cameras and lights. The base section has a heavy grapple fixture on one end to allow grappling with the heavy manipulator. The other end of the base section has a fully functional heavy latching device of its own. This gives a heavy manipulator the capability to grapple objects via the base of the dextrous manipulator. The dextrous manipulator can work on the heavy objects while they are attached in this fashion. If a heavy grapple fixture is appropriately configured with electrical connectors, and a dextrous manipulator is grappled to it, the dextrous manipulator can be commanded through the heavy

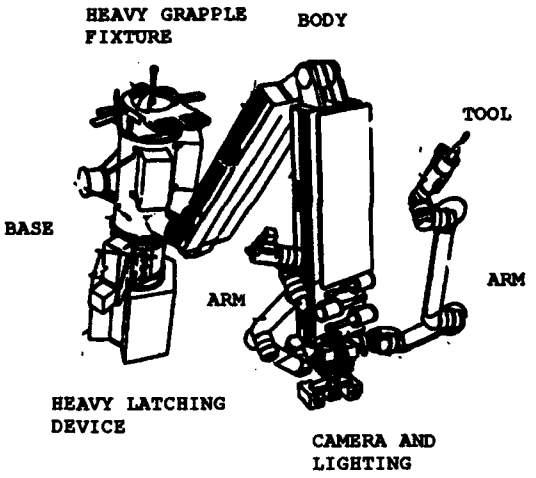

Figure 8.6 One dextrous manipulator. It can grapple any heavy or dextrous grapple fixture and/or be grappled by the latching device of a heavy manipulator (61).

grapple fixture. It does not have to be grappled with a heavy manipulator or a mobile base.

The body of the dextrous manipulator can fold or unfold to allow access to difficult work areas. It also serves as a storage rack for the many tools that can be attached to the manipulator arms. The proposed tools for the dextrous manipulators are:

- dextrous latching device
- non-standard grasping device
- socket drive
- grapple fixture guide post removal and replacement tool

The dextrous latching device facilitates grappling an object with a dextrous grapple fixture. This feature allows a dextrous manipulator to transport low mass objects (objects less than 1,000 kg) or rigidize with objects to increase precision for

work with the other manipulator arm. When precision is required, one arm acts as a stabilizer for the other. The dextrous grapple fixture is identical to the heavy grapple fixture in appearance and ultimate function. It is lighter and smaller than a heavy grapple fixture, and does not have electrical connectors. The dimensions of the dextrous grapple fixture are a 0.30 m radius base, and a 0.10 m guide post length.

The non-standard grasping device gives a dextrous manipulator a limited capability to grasp an object, or an area of an object, that does not have a dextrous grapple fixture. It resembles a small vice grip in appearance and function.

The socket drive allows the dextrous manipulator to manipulate a standard head bolt.

The grapple fixture guide post removal and replacement tool screws the guide post in and out of both the heavy and dextrous grapple fixture. It is used extensively in the truss making process for handling and storing items — including the truss product itself.

Additional or modified tools can be developed to assist in future operations. Similar to the special purpose dextrous manipulator of the Space Station Freedom (79:35), the dextrous manipulator of the SFP will have the following capabilities:

- connecting/disconnecting utilities
- attaching/detaching interfaces and covers
- mating/demating connectors
- removing/replacing components
- manipulating hinged mechanisms such as panels and doors
- providing lighting and cameras for EVA crews
- providing lighting and cameras for automatic tracking and grasping

- providing lighting and cameras for monitoring and inspecting operations

The dextrous manipulators, combined with heavy manipulators and mobile bases, define the SFP servicing system. Its capabilities make it an integral part of assembly and mission ready operations for the SFP.

8.2.3 Control. The mobile servicing system for Space Station Freedom will be controlled from an EVA workstation at the base of the remote manipulator, a workstation inside the shuttle, or a workstation inside its habitation modules (42:7.6). There are no plans to control the Space Station Freedom mobile servicing system from the ground. Because the SFP does not have habitation modules, its servicing system will be controlled from an EVA workstation, a shuttle workstation, or — to a limited extent — a ground workstation.

When controlling from the ground, there will be time delays of up to 10 *sec* between ground control inputs and servicing system responses (36:78). This significantly hinders operations that require real time feedback like grasping a moving object with a manipulator. However, carefully preplanned automated operations can be accomplished without complications. Inspections for maintenance, transportation of payloads, and preprogrammed grapples are not unreasonable applications (36:80). The designed capability to command any manipulator from any electrically configured heavy grapple fixture also enhances the feasibility of controlling from remote locations, such as the ground. Section 11.3 provides further analysis of SFP manning and control issues.

The requirements for the servicing system workstations in space are: video monitors, two three degree-of-freedom hand controllers (one translational and one rotational), and manipulator selection switches (see Figure 8.7). Control systems internal to the workstations must transform six axis control inputs into the proper commands for seven jointed manipulators. They will be augmented by six axis force/torque sensors in all the manipulator wrists. The sensors feedback force and

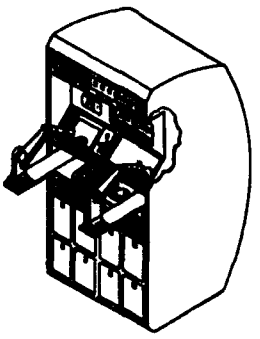

Figure 8.7 Possible configuration for a servicing system workstation. The workstation could be located on the ground or in a space shuttle (61).

torque information during contact with objects. Additional ground workstation requirements include a world model of the work site stored in memory for collision avoidance and trajectory planning.

8.3 Docking System

8.3.1 Purpose. In rendezvous terminology, ***docking*** identifies the use of on-board propulsion systems to join the docking ports of any two orbiting vehicles. The term ***berthing*** refers to accomplishing the same task by using a robotic arm to control the relative motion of the vehicles. Space Station Freedom planners prefer berthing over docking because relative velocities and impact loads between the vehicles are considerably reduced and the adverse affects of plume impingement from the propulsion systems do not exist (88:120).

The following procedures describe the berthing process currently planned for the rendezvous of a space shuttle and Space Station Freedom (18:28). When the shuttle reaches a position where the remote manipulator of Space Station Freedom

Closing Velocity	$0.005 \pm 0.001\ m/s$
Lateral Velocity	$\pm\ 0.002\ m/s$
Pitch, Roll, and Yaw Angular Velocity	$\pm\ 0.1\ deg/s$
Lateral Misalignment	$\pm\ 0.040\ m$
Pitch, Roll, and Yaw Angular Misalignment	$\pm\ 1.5\ deg$

Table 8.1 The docking contact requirements for Space Station Freedom and the European space plane (Hermes) (87:14).

can grapple the shuttle grapple fixture, the relative velocity between the shuttle and Space Station Freedom is reduced as close as possible to zero (simulation has shown typical values of .007 m/s). After achieving this position, the attitude control systems of both the shuttle and Space Station Freedom are inhibited, placing both in free drift. At that time, the remote manipulator operator of Space Station Freedom has approximately five minutes to capture the space shuttle grapple fixture before the two bodies drift out of the manipulator's range. Free drift for both the shuttle and Space Station Freedom is required to minimize the loads on the remote manipulator during berthing. Although serial linked manipulators are highly flexible, they are relatively weak, especially when they are in motion (50:6). After capture, approximately 12 more minutes of free drift are necessary to maneuver and rigidize the two bodies (4).

If grappling capabilities do not exist between Space Station Freedom and a different arriving vehicle — as is the case for the planned European Space Plane (Hermes) — docking agreements mandate stringent operational requirements. Table 8.1 identifies the contact requirements for the docking of Space Station Freedom and Hermes (87:14). Note that the maximum closing velocity allowed (0.006 m/s) is less than the typical minimized relative velocities achieved by the space shuttle in the previously described berthing simulations (0.007 m/s).

Both the planned berthing procedures and alternative docking requirements for Space Station Freedom have undesirable attributes. The berthing procedures

are complicated by the capabilities of the remote manipulator, and the docking requirements are difficult to achieve with conventional propulsion systems. The electrodynamic propulsion system of the SFP provides solutions to these problems. Electrodynamic propulsion is continuous and variable. With the tracking capability of the designed controller — demonstrated in Appendix M — relative velocities and impact loads can be minimized for safe docking. Also, electrodynamic propulsion eliminates the plume impingement problem. With docking achievable, remote manipulator berthing procedures are not required.

A simple remote manipulator has been developed to assist with SFP docking applications. Its purpose is to:

- enhance the delivery envelope of the SFP
- grapple arriving external tanks
- secure external tanks to the SFP

8.3.2 Components and Procedures. The docking system has three degrees-of-freedom (one translational and two rotational). It consists of a scissor extender — driven by a power screw and mounted above the truss maker — with a two degree of freedom heavy duty wrist at its apex. The wrist serves as a platform for a heavy/dextrous latching device (see Figure 8.8). Although the power screw and wrist configuration is relatively low in flexibility, it can be designed for strength. The latching device can grapple any object with a heavy or dextrous grapple fixture.

Despite the limited flexibility, three degrees-of-freedom designed into the docking system will enhance the delivery envelope of the SFP. Payloads with grapple fixtures built into them — like trusses — can be extended and rotated to arrive at a target in a desired orientation without changing the attitude of the SFP (see Figure 8.9). The procedure will be to rigidize the docking system once the desired orientation is achieved, and dock the payload to the target with the precision elec-

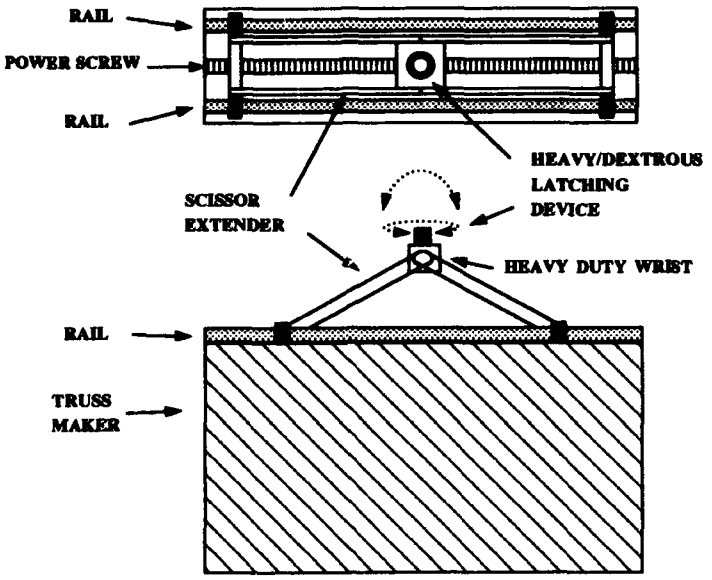

Figure 8.8 The docking system permanently mounted on the truss maker. The heavy latching device can grapple a dextrous latching adaptor for dextrous grappling capabilities.

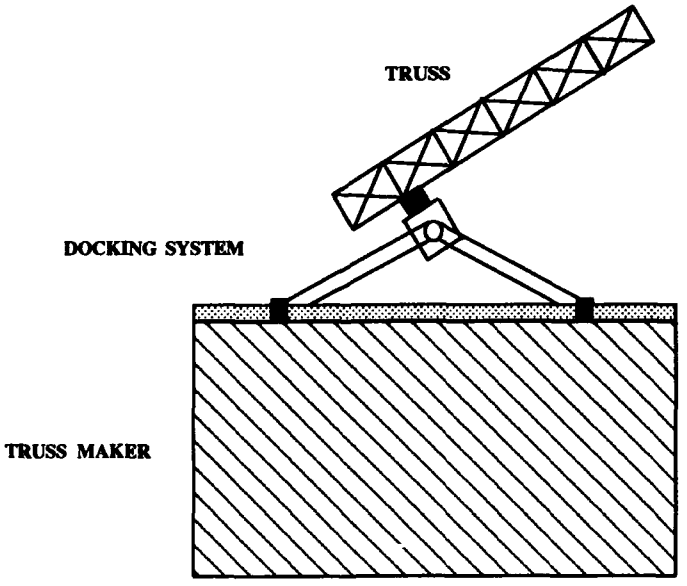

Figure 8.9 The docking system delivering a truss at a desired orientation.

trodynamic propulsion system of the SFP. Because of the docking system strength, inhibiting the target attitude system prior to docking will not be required.

In the case of receiving an external tank, the procedure will be similar. As described in Section 4.3, the external tank will be modified with a heavy grapple fixture prior to launch. The space shuttle will carry the external tank into orbit and serve as its attitude control system until rendezvous. At orbit altitudes, a separated external tank will remain stable for a small period of time without an attitude control system, but studies have shown a shuttle attached to an external tank will insure its stability (1). Section 11.9 provides further analysis on this subject. At the rendezvous position, the SFP will maneuver the extended rigidized docking system to grapple the heavy grapple fixture of the external tank. The shuttle will then release the external tank, and the docking system will completely retract the external tank to a secured position flush with the truss maker.

8.3.3 Control. The docking procedures can be implemented from the control locations of the servicing system: an EVA workstation, a shuttle workstation, or — under preplanned automated operations — a ground workstation. The shuttle workstation for the servicing system will also incorporate SFP maneuvering capabilities to execute docking procedures. Maneuvering the SFP, via the electrodynamic propulsion system, for docking requires real time feedback and will not occur from the ground. It is feasible for an advanced target — like a large telecommunication platform — to posses and operate a space shuttle type workstation as well. In this scenario, the SFP could be flown to the vicinity of the platform, and a delivery product could be positioned for delivery, via ground control. Then, control commands from a habitation module on-board the telecommunications platform could complete the remainder of the docking procedure.

The docking system combined with the electrodynamic propulsion system define the docking components and their capabilities. This combination facilitates simple, reliable docking procedures that are truly unique to the SFP.

IX. SFP Assembly

9.1 Introduction

This chapter includes a basic truss design and a conceptual sequence illustrating a method to bring the SFP to an operational mode in as few shuttle missions as possible. The final SFP design is shown in Figure 9.1. An illustration of the conductors within each integrated truss is shown in Figure 9.2. Complete assembly of the SFP can conceivably be accomplished in eight shuttle missions. After these eight missions, the SFP will be fully operational and can accept an external tank for reduction on every subsequent shuttle mission.

9.2 Truss Considerations and Design

Due to the total length of the main, cross and orthogonal integrated trusses (137 m), the question of how these trusses are designed, built and placed into orbit comes to mind. It was originally thought that SFP produced trusses could be used to construct the entire platform. The feasibility of such a concept was quickly negated for several reasons. First, the need to place a large bundle of wire inside the truss would be a difficult EVA task for an astronaut. Second, the wire bundles, shielded and unshielded, must be separated by at least 1 m to prevent magnetic interference (reference Appendix L). This would require attaching the conductors to the outside of the SFP trusses causing a significant amount of interference with other equipment. Third, the necessity of providing rails on the outside of the trusses so the SFP servicing system can traverse the entire length of the platform would be a time consuming EVA task. These rails would have to be attached to the SFP truss after its manufacture and could only be attached to the two sides without the previously mentioned conductors present. Fourth, power distribution equipment, batteries and any other miscellaneous equipment would be difficult to attach internally (the only space available with the rails and conductors occupying the external faces of the

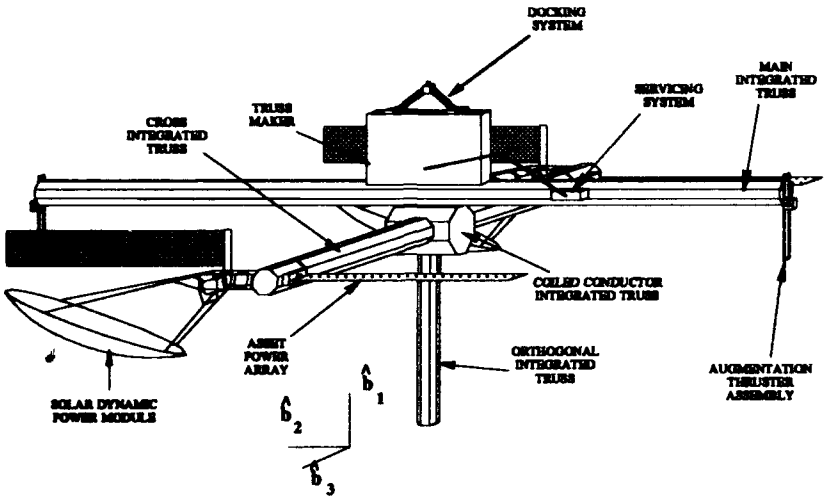

Figure 9.1 An illustration of the final design of the SFP. The main, cross, orthogonal and coiled conductor integrated trusses as well as the solar dynamic power modules, augmentation thrusters, and truss maker must all be carried into orbit by the space shuttle.

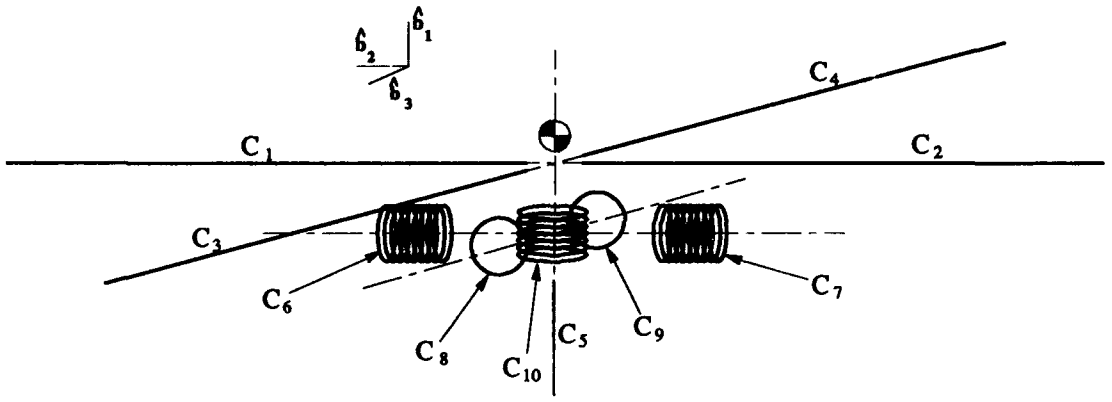

Figure 9.2 Layout of the conductors that must be located within the confines of the integrated truss structures.

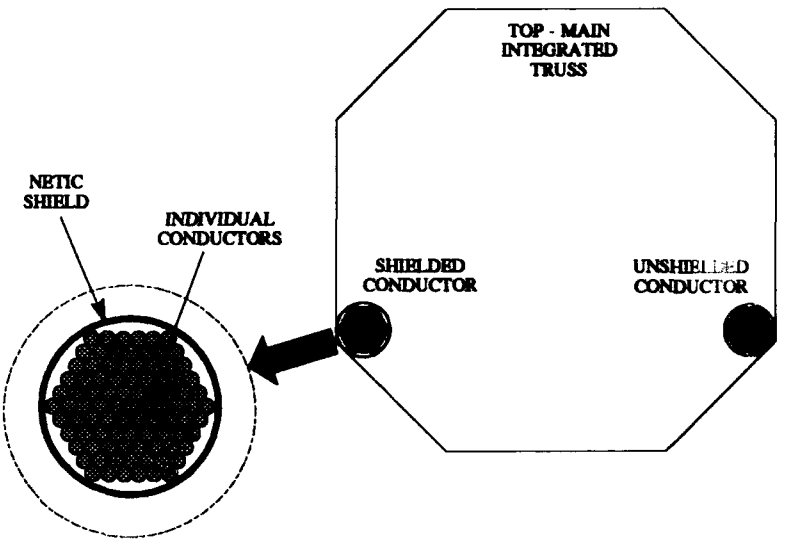

Figure 9.3 Cross-section of an integrated truss.

truss) to the SFP trusses by astronauts. This led to the conclusion that using SFP fabricated trusses to build the platform was infeasible and it would be easier to manufacture integrated trusses on Earth and assemble them in orbit with the assistance of the space shuttle and crew.

A similar conclusion was made by the designers of Space Station Freedom. Space Station Freedom trusses were originally designed to be assembled from pieces by EVA astronauts. A massive redesign effort culminated in the design of a pre-integrated truss structure (69:1). The pre-integrated structure has the advantages of simple orbital construction and gives the capability for ground checkout and verification of truss segments prior to launch. In addition, the pre-integrated truss is complete with all the necessary subsystems, utilities and mechanisms. Simplifying construction, minimizing EVA and verifying truss segments prior to launch are three very beneficial attributes the SFP trusses should have. As such, the decision was made to adopt an integrated truss structure for the assembly of the SFP.

A cross-section of an SFP integrated truss is shown in Figure 9.3 The shielded

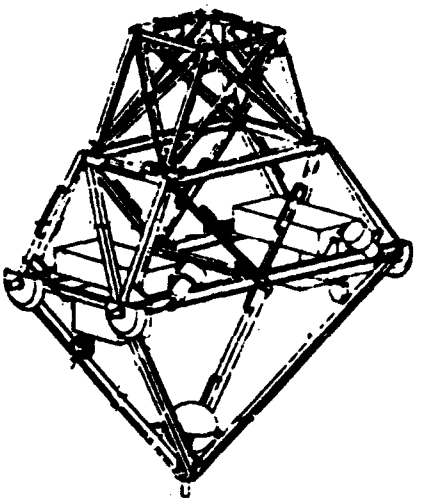

Figure 9.4 The unpressurized berthing adapter. This adapter is left with the orbiting vehicle. It provides a berthing mechanism that the shuttle arm can grapple and mount into its cargo bay (70).

and unshielded portions of the conductor coil are attached to the inside of the integrated truss structure. This provides sufficient separation between the conductors and allows for the placement of other equipment within the confines of the truss.

Space Station Freedom pre-integrated truss structure is assembled in the following manner (69:3): Assembled sections of truss are completely outfitted and checked on the ground. They are left intact and fitted into the shuttle cargo bay for launch. Upon reaching orbit, the truss section is attached to neighboring sections. An unpressurized berthing adapter (shown in Figure 9.4) is attached and left with the first segment (70:6). On subsequent missions, the shuttle berths with the orbiting segments via this device. The shuttle manipulator arm grapples the unpressurized berthing adapter and fixes it to a mounting device within the shuttle cargo bay. Additional truss segments can then be attached with the shuttle manipulator arm. The actual segment to segment attach mechanism consists of a capture latch, to hold the segments together in relative alignment, followed by motorized connecting bolts

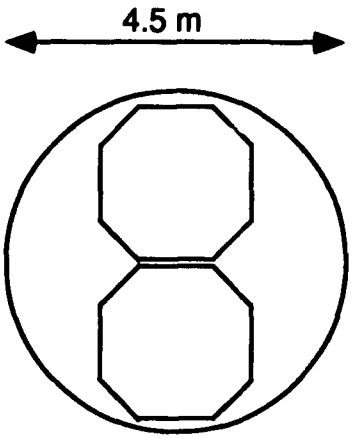

Figure 9.5 Layout of the basic integrated truss design of the SFP located within the confines of the space shuttle cargo bay (70).

engaged at each mating longeron (70:8). The same basic assembly process is used to construct the SFP from integrated trusses.

The design of the SFP integrated truss is influenced by a variety of factors. The space shuttle cargo bay imposes the following restrictions upon any structure — a maximum 4.5 m diameter and 13.7 m length (70:2). The actual length of the shuttle bay is 18.3 m but, the unpressurized berthing adapter and other miscellaneous equipment occupies a portion of the bay nearest the shuttle nose. If a 4.5 m diameter truss was used for the SFP a minimum of ten shuttle missions would be needed to just bring the trusses into orbit. Since the only significant restriction on truss design was the necessity to have the shielded and unshielded conductor portions 1 m apart, a 2 m octagonal truss design was chosen. This meant that 2 segments could be carried per mission and the number of missions for just truss work was reduced to five. An illustration of the basic truss shape within the confines of the space shuttle cargo bay is shown in Figure 9.5. It was also decided to construct the SFP integrated trusses from the same aluminum alloy as Space Station Freedom — Al-2219 (69:9). A finite element model of a basic truss structure is analyzed within Appendix E. The

main, cross and orthogonal trusses all share the same basic design with the minor exceptions outlined in the following paragraphs.

The main integrated truss (50 m in length and housing conductors *C1* and *C2*) has rails on all four flat faces. This allows for two mobile bases to be placed on opposing sides of the truss, the truss maker on top and the unpressurized berthing adapter on the bottom. Mobile bases and heavy manipulator arms on opposing sides provide the capability to reach both sides of an external tank when it is seated atop the truss maker. The rail on the top allows the truss maker assembly to move for the purpose of center of mass management. The bottom rail allows the unpressurized berthing adapter to move so the shuttle can berth at various points. This is extremely useful during the construction phase of the SFP.

The cross integrated trusses (30 m in length with either conductors *C3* or *C4* depending on which side it is) need only one rail on any side. This allows a mobile base to be placed on each cross truss. A heavy manipulator can then transfer from a mobile base on the main truss to a mobile base on the cross truss. This is necessary so the servicing system can access and build the solar dynamic power modules and ASSET photovoltaic arrays. Note that the first 25 m of the cross truss houses the conductors, while the remaining 5 m is to ensure clearance for the power systems and house a rotary joint. A solar alpha rotary joint is located between the two sections of cross truss so the power module and arrays are able to remain inertially oriented and track the sun throughout an orbit (70:9). The joint allows for 360° of rotation while providing structural and electrical continuity between segments and is illustrated in Figure 9.6.

The orthogonal integrated truss (27 m in length housing conductor *C5*) does not have any rails. It does contain an attachment rack to store the trusses produced by the SFP. The rack is described in Section 5.3.9.

The coiled conductor integrated truss (4.3 m in diameter by 4.86 m in length housing conductors *C6* through *C10*) does not share the same basic design as the

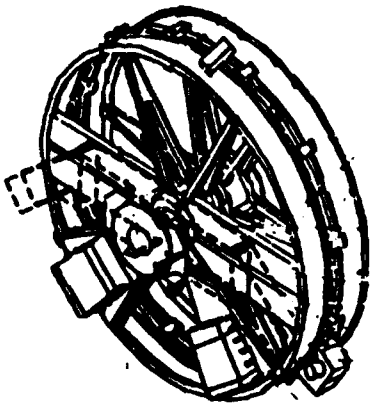

Figure 9.6 The solar alpha rotary joint that allows the power subsystem to remain inertially oriented and track the sun throughout the orbit.

others. A larger structure was necessary to house the coiled conductors and to allow for attachment points. These points allow for easy connection of the cross and orthogonal trusses.

9.3 Assembly of the SFP

The following section describes the conceptual assembly of the SFP. It contains a mission by mission synopsis which outlines the major events taking place.

9.3.1 Mission 1. The payload for mission 1 includes 17 m of integrated truss, the truss maker's frame and all truss making associated equipment. Refer to Figure 9.7 for the discussion of this mission. To begin the mission, the space shuttle approaches and matches the ASSET vehicle orbit and starts assembling the above listed components (see Figure 9.7a). Similar to the assembly plans of Space Station Freedom, the sections of truss are attached to the berthing adaptor and translated over the shuttle's nose so the next section can be attached (see Figure 9.7b and c). Due to shuttle bay size, the 17 m truss is brought in two sections— a 13.5 m length and a 3.5 m length. The 13.5 m section is attached to the berthing adapter via the

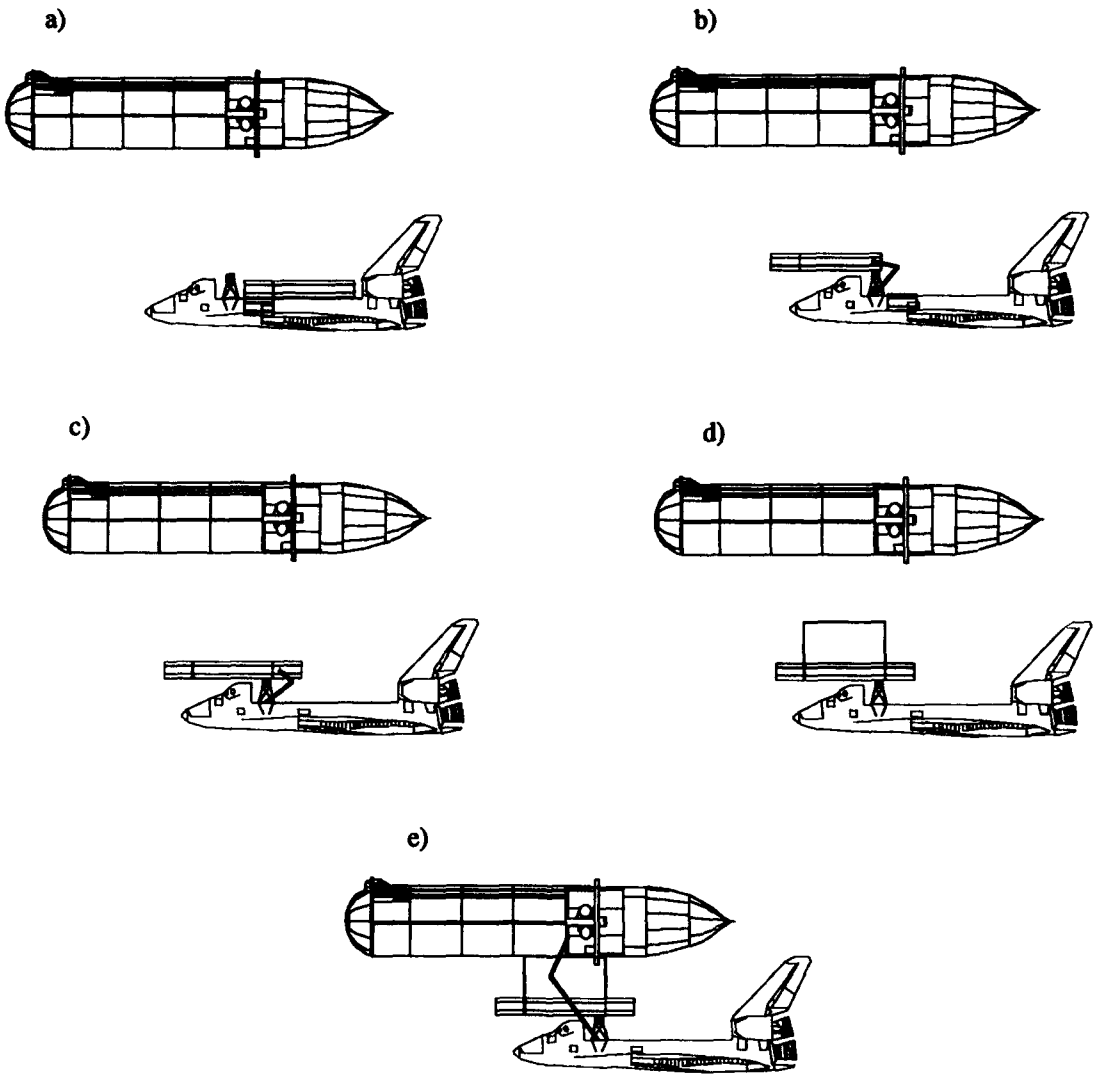

Figure 9.7 Mission 1 to build the SFP. One 17 m section of the main integrated truss and the truss maker's frame, with associated equipment, are brought into space, assembled, and attached to the ASSET vehicle.

shuttle manipulator arm and then translated forward so the 3.5 m section can be attached (see Figure 9.7c). Final attachment is accomplished with remote capture latches and motorized bolts. Once this has been accomplished, EVA astronauts can begin assembling the truss maker (see Figure 9.7d). A complete description of the truss maker can be found in Section 5.3. The truss maker frame is approximately 10 m in length and is built in the center of the 17 m section. After the truss maker assembly is complete, the shuttle is maneuvered to berth with the ASSET facility.

The shuttle must be facing the 'front' of ASSET so its manipulator arm can reach a grapple fixture on the ASSET vehicle. Note that for the purposes of this chapter 'front' relates to the portion of the SFP vehicle where the nose of the external tank is and 'rear' corresponds to the opposite end. Two heavy grapple fixtures have been added to the external tank prior to its launch (this is discussed in Section 4.3). One grapple fixture is located on the intertank structure directly opposite the forward space shuttle mount fixture. The second heavy grapple fixture is offset to the side. Once in position, the shuttle manipulator arm grabs the offset heavy grapple fixture on ASSET and places ASSET onto the SFP docking system located on the top portion of the truss maker assembly (see Section 8.8 for a description of the docking system). Figure 9.7e is an illustration of this task. The shuttle then returns to Earth leaving behind the berthing adapter for future missions.

9.3.2 Mission 2. The payload for mission 2 includes two 13.5 m sections of the main integrated truss. The following discussion refers to Figure 9.8. The shuttle approaches ASSET from the 'rear' and grabs the berthing adapter left behind on the previous mission (see Figure 9.8a). The berthing adapter and the attached vehicle (ASSET and first mission SFP) are maneuvered and placed on the mounting point inside the shuttle bay (see Figure 9.8b). A 13.5 m section of truss is then added to the main integrated truss (see Figure 9.8c). Unfortunately, this section cannot be translated rearward because of the clearance necessary between the shuttle's tail and the rear of ASSET. This situation precludes the shuttle manipulator arm from

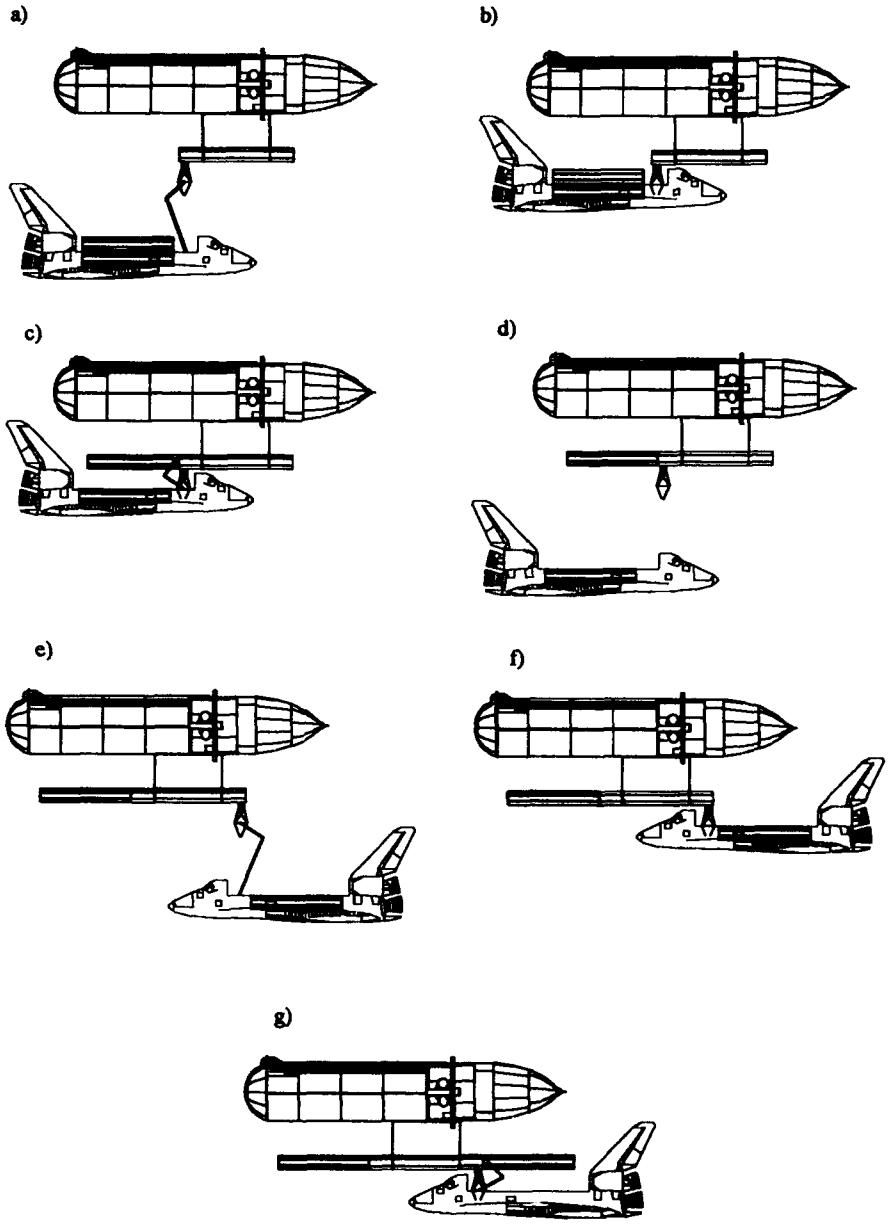

Figure 9.8 Mission 2 to build the SFP. Two 13.5 m segments of the main integrated truss are brought up and attached to either end of the assembled truss.

reaching the front of the main integrated truss and another method has to be found to attach the second 13.5 m section of truss to the 'front'. In order to attach the 13.5 m section to the 'front', the shuttle must release the berthing adapter and reposition to the 'front' of ASSET (see Figure 9.8d and e). While the shuttle is repositioning, the berthing adapter translates to the 'front' portion of the integrated truss. The shuttle then re-berths with the vehicle and adds the final 13.5 m to the 'front' of the integrated truss (see Figure 9.8f and g). At this point, 44 m of the 50 m main integrated truss is complete. Mission 2 is done and the shuttle can return to Earth.

9.3.3 Mission 3. The payload for mission 3 includes the last 6 m of the main integrated truss, the SFP servicing system and the coiled conductor integrated truss. Refer to Section 8.2 for a complete description of the SFP servicing system. The coiled conductor integrated truss is 4.86 m in length and 4.3 m in diameter (a complete description can be found in Section 6.3.9). The following discussion refers to Figure 9.9. The shuttle approaches the vehicle from the 'rear', attaches to the berthing adapter perpendicular to the main integrated truss and places the final 6 m on the main integrated truss (see Figure 9.9a and b). Two independent mobile bases and their associated heavy manipulators are then attached to opposing side rails of the main integrated truss (see Figure 9.9c). This allows them to translate the entire length of the truss. The SFP servicing system is installed prior to the coiled conductor for the purpose of attaching the coiled conductor integrated truss. Space shuttle manipulator arm reach limitations and possible conflicts with the shuttle wingtip clearance makes it necessary for one of the SFP manipulators to attach the coiled conductor integrated truss. As shown in Figure 9.9a, the shuttle must berth perpendicular to the main integrated truss at the 'rear' end of ASSET. Possible interference with the ASSET solar arrays precludes berthing at the 'front' end. Perpendicular berthing also allows easier access to the shuttle bay by the SFP remote manipulator. As shown in Figure 9.9d, e, and f, the SFP manipulator grap-

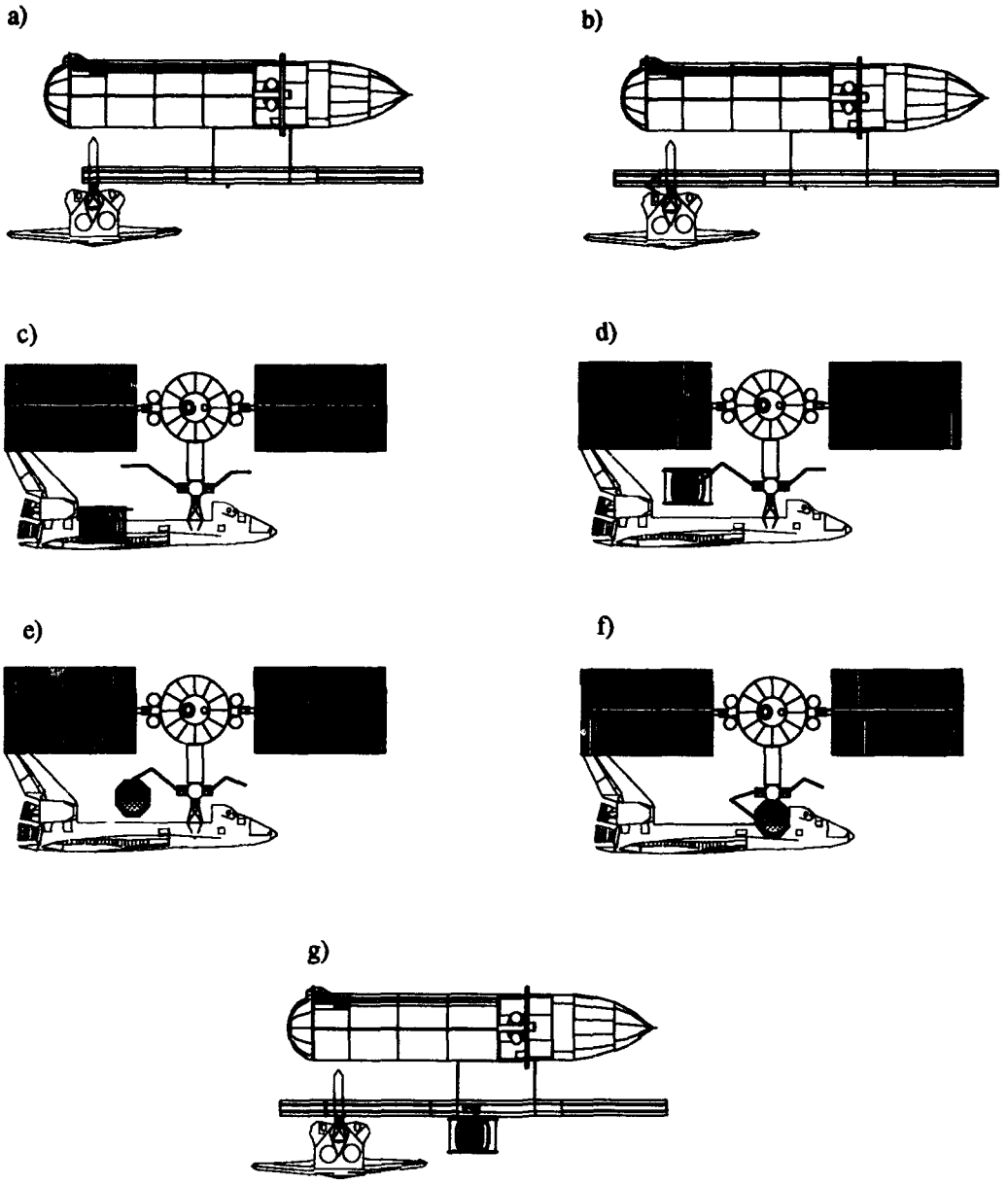

Figure 9.9 Mission 3 to build the SFP. The last 6 m of the main integrated truss is connected. A portion of the SFP servicing system, consisting of two remote heavy manipulators and mobile bases, are placed on either side of the main integrated truss, and the coiled conductor integrated truss is attached.

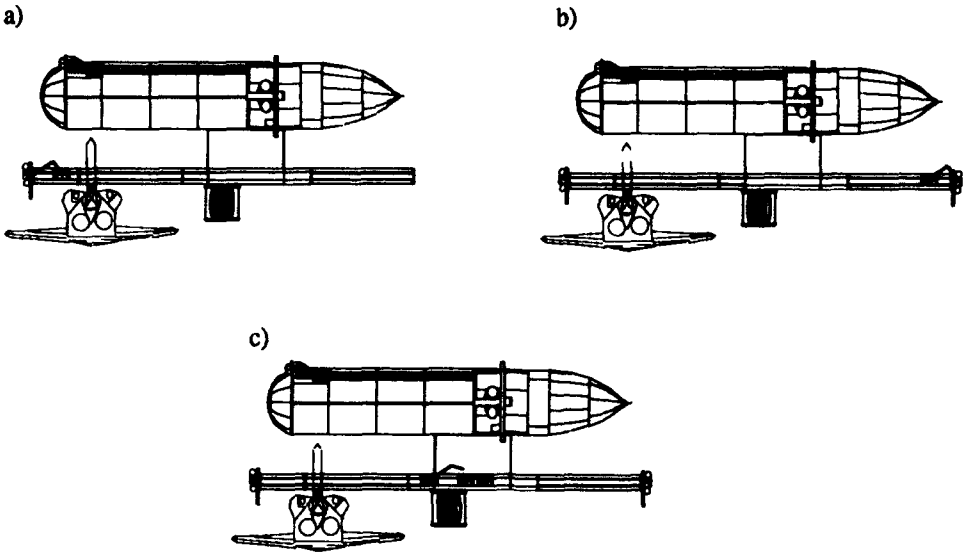

Figure 9.10 Mission 4 to build the SFP. The z-axis augmentation assemblies are attached to either end of the main integrated truss, and the two mobile bases are temporarily placed on the main integrated truss, awaiting the arrival of the appropriate cross integrated truss.

ples the coiled conductor assembly, removes it from the shuttle bay and rotates it parallel to the main truss. The SFP arm then translates forward and attaches the assembly to the midpoint of the main integrated truss (shown in Figure 9.9f and g). Once this connection is made the coiled conductor assembly and the main integrated truss conductors are hooked up to the ASSET power supply and provide a limited attitude control capability as well as some gross orbital motion capability. Once this task is accomplished the mission is complete and the shuttle returns to Earth.

9.3.4 Mission 4. The payload for mission 4 includes the z-axis augmentation thruster assemblies (see Section 6.3.9 for a description) and two mobile bases of the SFP servicing system. Figure 9.10 applies to the following discussion. With the shuttle berthed perpendicular to the main truss, the SFP servicing system is used to install the two sets of augmentation thrusters (see Figure 9.10a and b). The additional two mobile bases are then placed on the main integrated truss. This is

a temporary position since the mobile bases will eventually be placed on the cross integrated trusses.

9.3.5 Mission 5. The payload for mission 5 includes 27 m of cross integrated truss. Figure 9.11 can be referenced for the following discussion. The shuttle bay size causes the truss to be broken into two 13.5 m segments. When connected, the first 25 m of this truss houses the cross conductor, followed immediately by an alpha joint that allows the final section to rotate for the power systems. Once again, for easier access and minimal interference, the shuttle berths perpendicular at the 'rear' of ASSET (Figure 9.11a and b). An SFP heavy manipulator arm then grapples the first 13.5 m segment, translates forward and attaches it to the side of the coiled conductor integrated truss (Figure 9.11b and c). The SFP heavy manipulator arm then removes a mobile base from the main integrated truss and places it on the section of cross integrated truss. The outboard segment, containing the alpha joint, is then attached to the first segment (Figure 9.11d, e and f). With the attachment of the second section, the mission is complete and the shuttle returns to Earth.

9.3.6 Mission 6. The payload for mission 6 is 27 m of cross integrated truss. This mission is a repeat of mission 5 and the same discussion applies. Refer to Figure 9.12 for an overall view of this procedure. After the completion of both cross conductors, they are connected to the ASSET power supply.

9.3.7 Mission 7. The payload for mission 7 includes 6 m of cross integrated truss and the solar dynamic power modules (SDPM). Refer to Figure 9.13 for the following discussion. For accessibility and minimal interference problems, the shuttle berths perpendicular to the 'rear' of the main integrated truss (see Figure 9.13a). The 6 m of truss is broken into two 3 m segments that fit on either end of the cross integrated truss. Once in place these segments complete the 30 m for each cross truss. Due to reach limitations the SFP heavy manipulators must be moved

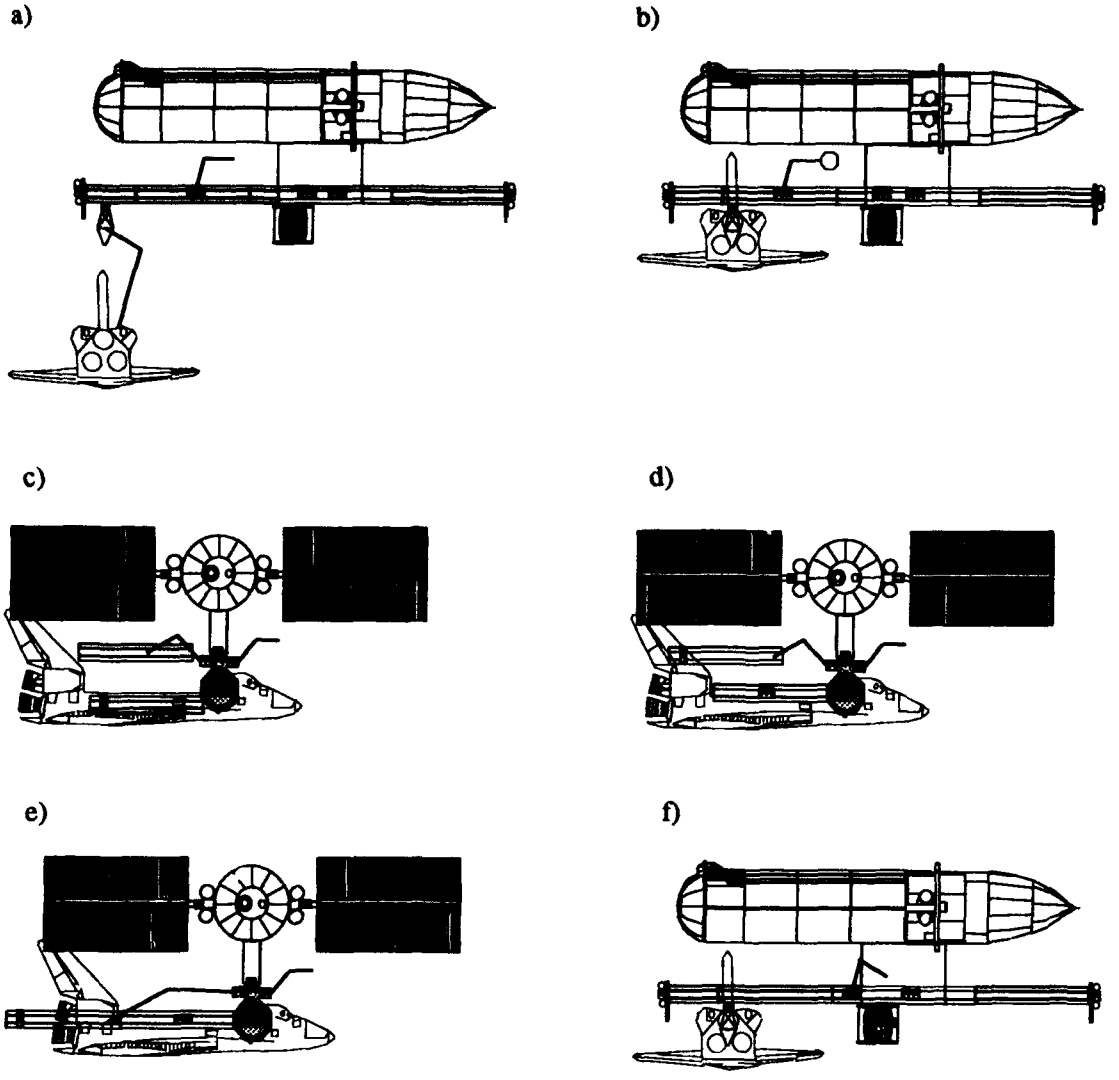

Figure 9.11 Mission 5 to build the SFP. A 27 m section of cross integrated truss is brought up in two equally sized segments. The outboard segment contains the alpha joint.

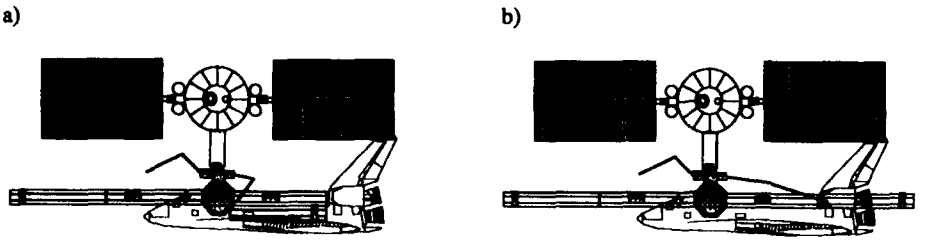

Figure 9.12 Mission 6 to build the SFP. This mission repeats Mission 5.

to the mobile bases on the cross integrated trusses, one allocated to each side (see Figure 9.13a). The SFP heavy manipulators then access the shuttle bay, grapple the 3 *m* section, translate out the cross truss and place the section out-board of the alpha joint (see Figure 9.13b, c and d). Note that an SFP heavy manipulator to SFP heavy manipulator hand-off must be accomplished to pass a 3 *m* section to the side opposing the shuttle.

Once the cross trusses are completed, mission 7 becomes very EVA intensive. The SDPM's must be assembled on the end of each cross truss. Assembly of an SDPM will rely upon both SFP heavy manipulators to transport equipment to the area outboard of the alpha joint on the cross integrated truss. Transport of materials will be controlled by the space shuttle crew using telerobotic commands from inside the shuttle. Space Station Freedom assembly plans called for two EVA crewmen to accomplish the SDPM assembly (73:305). A similar plan is adopted for use on the SFP. Note that assembly takes place so that the concentrator is not positioned on-sun until actual start up is initiated. The entire process encompasses about 20 man hours of EVA (73:306).

A description of the SDPM components can be found in Section 7.2. The EVA crew will first install the beta gimbal, followed by the receiver/radiator assembly and the fine pointing gimbal. The structural and utility connections will be performed by the EVA crew. The concentrator support structure is then attached and assembly of the concentrator itself can begin. The concentrator assembly has a heavy grapple

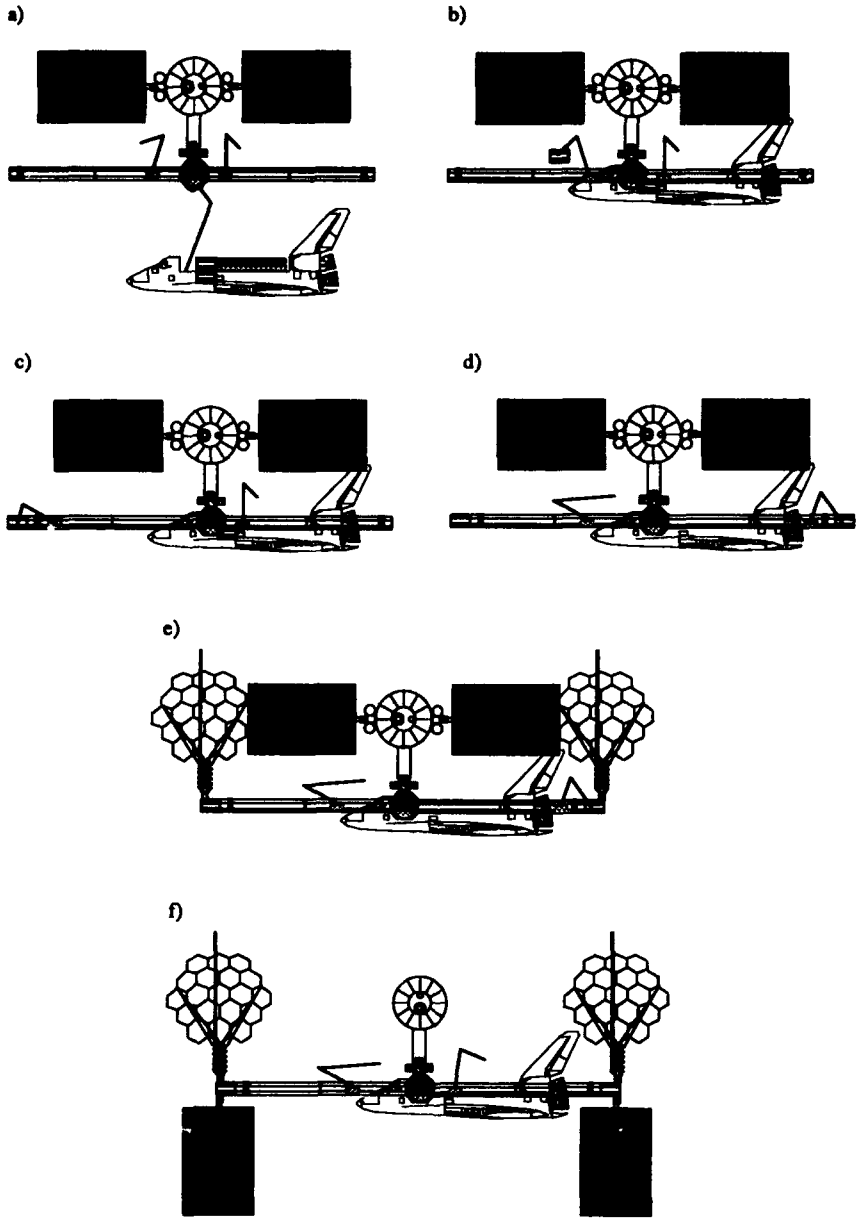

Figure 9.13 Mission 7 to build the SFP. The final 3 m of cross integrated truss is placed on the ends of the assembled truss with the help of the SFP remote manipulators. EVA astronauts then assemble the solar dynamic power modules and move the ASSET power arrays from the ASSET vehicle to the SFP.

fixture mounted on the back side (nonreflective surface) of the central hexagonal panel (73:306). This fixture is grappled by a heavy manipulator on the cross truss and each additional panel (18 remaining) is then latched to the panel above. The wrist joint of the manipulator is rotated as necessary following the latching of each additional panel to provide clearance and prepare for the next panel. After completion of the concentrator, the heavy manipulator places it on the support structure and final connections are made by astronauts.

After the SDPM's are assembled the ASSET photovoltaic arrays are removed and placed at the end of each cross truss (see Figure 9.13f). This involves folding the arrays, moving them and reinstalling them on the cross integrated truss (one panel to each side) opposite the already installed SDPM. This process is accomplished using heavy manipulators on the main truss and the cross truss as well as an EVA crew. Once connected to the cross truss the arrays are redeployed.

9.3.8 Mission 8. The payload for mission 8 includes 27 m of orthogonal integrated truss. Figure 9.14 applies to the following discussion. Similar to previous missions, the truss is brought up in two 13.5 m sections. With the shuttle berthed perpendicular to the main truss as shown in Figure 9.14a, one of the heavy manipulators is moved to a cross truss to assist in the installation of the orthogonal truss. The heavy manipulator on the main truss retrieves the first section of truss and passes it to the manipulator on the cross truss (see Figure 9.14b). The truss segment is then attached to the bottom of the coiled conductor integrated truss (see Figure 9.14c and d). The process is repeated and the second section of 13.5 m truss is attached to the first (see Figure 9.14e and f). Only the heavy manipulator on the cross truss has the reach capability to perform this task. The orthogonal integrated truss also contains the attachment racks for the SFP produced trusses. The attachment racks will have the capability to store a large number of trusses with varying lengths. Refer to Section 5.3.9 for a complete description of the truss rack.

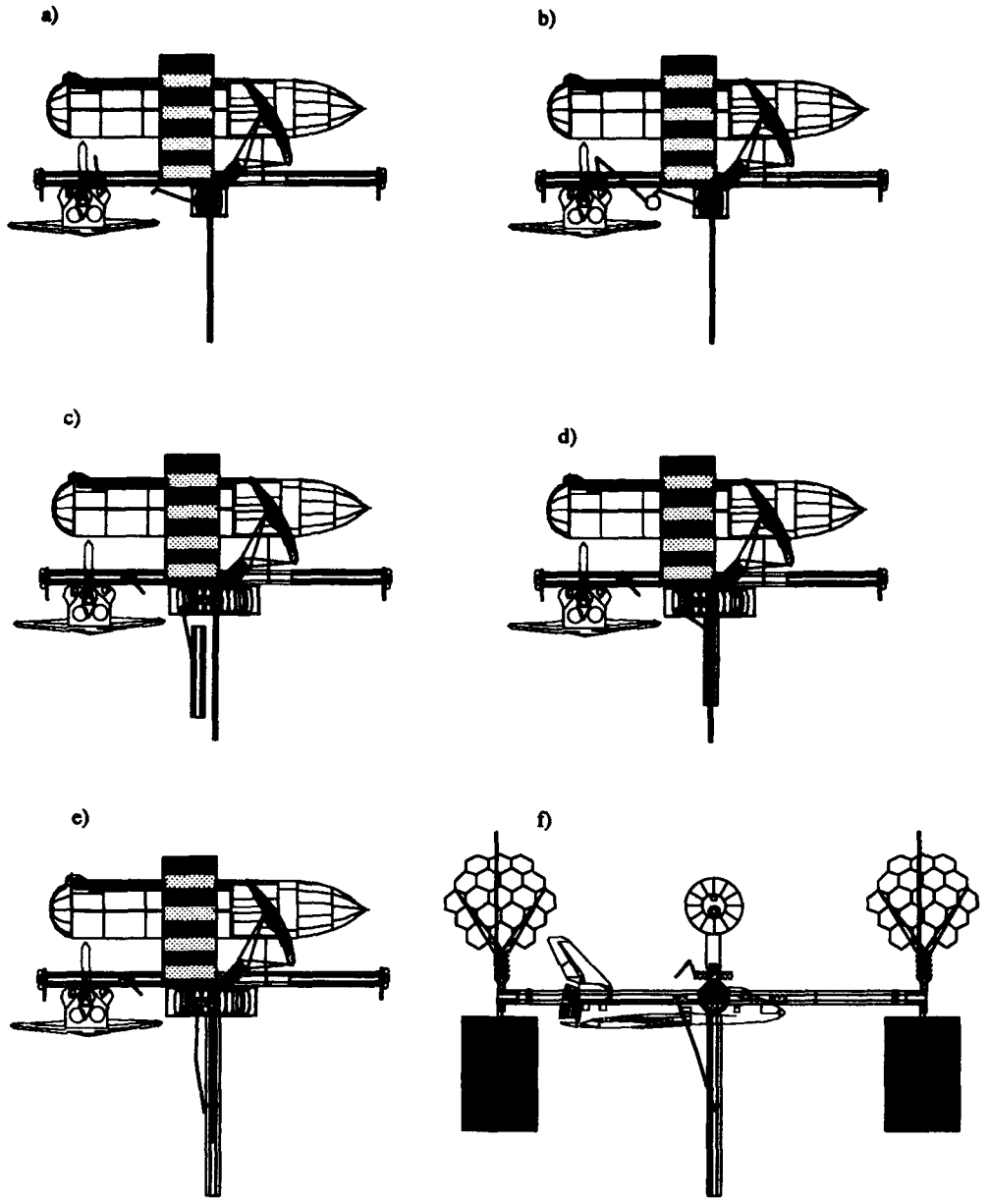

Figure 9.14 Mission 8 to build the SFP. A 27 m section of orthogonal integrated truss is brought up and connected to the coiled conductor integrated truss, completing the construction of the SFP.

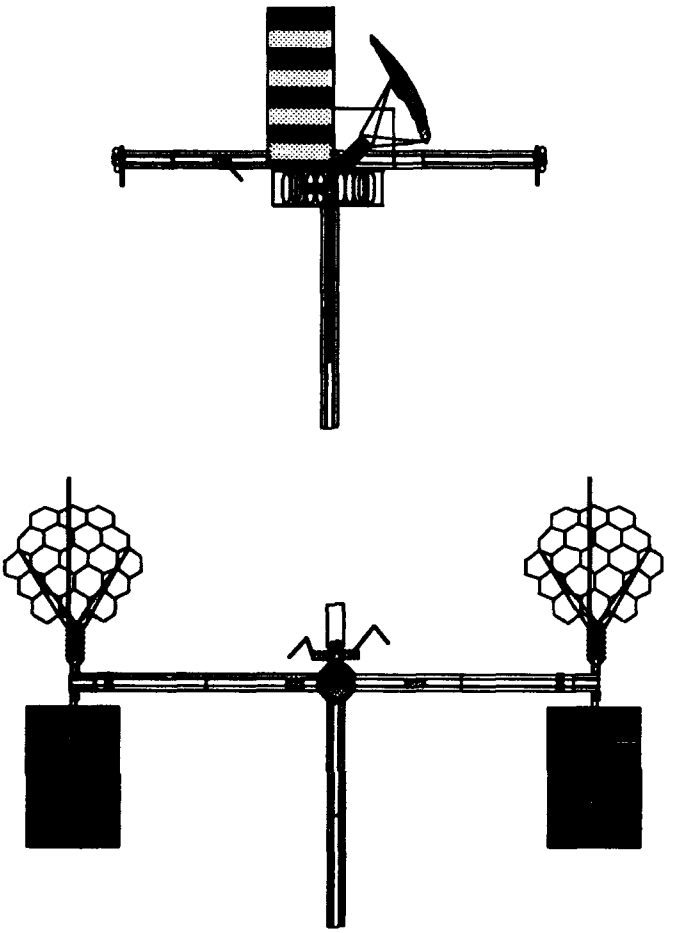

Figure 9.15 A view of the SFP without the shuttle and the external tank attached.

After assembly of the orthogonal truss, all conductors are then connected to the SFP power supply and the SFP is fully operational and can begin manufacturing and delivering trusses. Figure 9.15 shows the completed SFP without the external tank and shuttle attached. This is the configuration the SFP has the majority of its operational time.

X. Operations and Capabilities

The standard SFP mission is a cycle in which the SFP acquires an external tank, reduces it, converts the reduced material into truss, transports/delivers this truss to a user, and then returns to the external tank delivery altitude. (see Figure 10.1). Other missions might include transfer of an intact external tank to a higher orbit, truss fabrication and station keeping at any orbit, or accommodation of other space operations with the SFP's robust and flexible features. The standard SFP mission fully demonstrates the advantages of truss fabrication in space, and the advantages of electrodynamic propulsion. Table 10.1 summarizes the specifications and capabilities of the SFP. Table 10.2 summarizes the specifications and capabilities of the truss product. Both tables represent the culmination of the design effort.

10.1 Standard Mission Event.

The standard SFP mission consists of six major events. These events will be described in detail to provide insight into the various capabilities of the SFP. The major events can be summarized as follows:

Event 1. rendezvous and docking with a space shuttle and its attached external tank

Event 2. reduction of an external tank

Event 3. fabrication of trusses

Event 4. transfer to a higher orbit work site

Event 5. rendezvous and delivery of the truss product

Event 6. return to the external tank delivery orbit altitude

Not included in these six events is orbital maintenance during the possible extended waiting periods. The major events (1–6) of the standard mission will take approximately 38 *days* to complete (see Figure 10.2). This includes 5 *days* for rendezvous/docking and external tank reduction; 13 *days* for truss fabrication

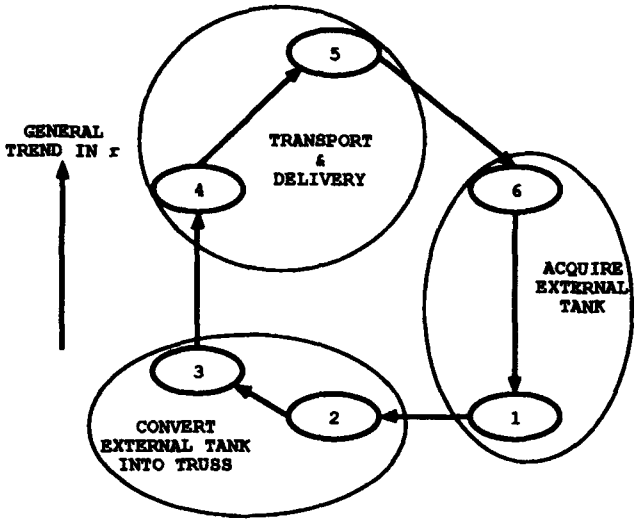

Figure 10.1 A standard SFP mission cycles through six major events. The six events are: 1) rendezvous/docking, 2) external tank reduction, 3) truss fabrication, 4) positive orbit transfer, 5) rendezvous/delivery, and 6) negative orbit transfer.

SFP	
Dimensions	$50.0 \times 64.3 \times 38.3\ m$
Mass	79,309 kg
Primary Propulsion	Electrodynamic
Power Source	Solar Dynamic & Photovoltaic
Permanent Manning Requirement	None
Primary Command and Control Source	Ground
Orbital Altitude Envelope	300–500 km
Orbital Inclination Envelope	0–28.5 °
Maximum Payload	31,300 kg
Maximum Acceleration Rate	$10.3 \times 10^{-5}\ m/s^2$
Minimum Time for 200 km Altitude Change	11.9 $days$
Maximum R-bar Stand-off Range	82 m
Maximum Continuous Usable Power	82 kW
Standard Mission Avg Power	44.9 kW
Propulsion Efficiency	87%

Table 10.1 The final design specifications for the SFP.

Truss Product	
Dimensions	$1.0 \times 1.0 \times$ (variable) m
Mass/Length	$5.25\ kg/m$
Welding Method	Laser
Axial Stiffness	$3.774 \times 10^7\ N$
Bending Stiffness	$9.135 \times 10^6\ N \cdot m^2$
Torsional Stiffness	$1.103 \times 10^6\ N \cdot m^2$
Production Rate	$77\ m/hour$

Table 10.2 Truss Product Specifications.

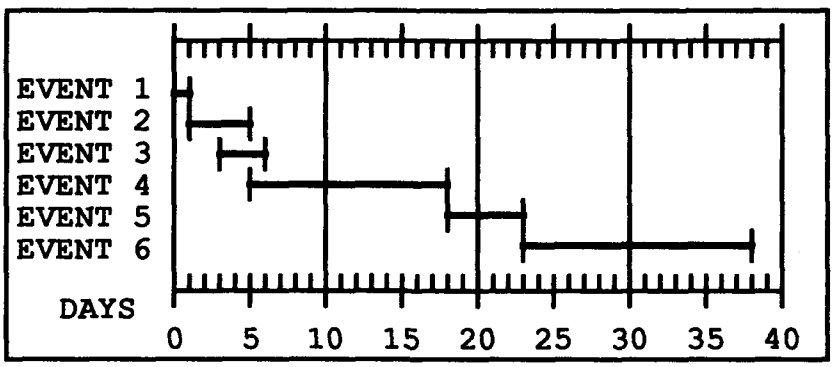

Figure 10.2 A Standard SFP mission lasts for 38 *days*. The figure above shows the chronological order of the six major events for the standard SFP mission.

Average Time between Shuttle Missions *days*	Average Number of Missions per *year*	Average SFP Wait Time *days*	Truss Produced *meters* per *year*
90	4	52	2920
60	6	22	4380
45	8	7	5840
40	9	2	6570
30	12	-	8760

Table 10.3 The average time the SFP must wait for a shuttle launch based upon a standard mission round trip (300 *km* - 500 *km*) time of approximately 38 *days*.

and transfer to higher orbit; 5 *days* for rendezvous/delivery and loiter time at the construction site; and 15 *days* to return to a 300 *km* orbit. In contrast, a mission to transfer an external tank will have a round trip time of 40 *days* (1 *day* rendezvous, 19 *days* transfer, 5 *days* delivery, and 15 *days* return).

The SFP spends the majority of its time in transit between orbits. The reduction and truss making operations of the SFP (events 2 and 3) take approximately 4 *days* to complete. This includes additional time for the setup and breakdown of the reduction equipment, as well as the transfer of materials to the truss maker itself. The setup and breakdown portions of this process necessitate the presence of a space shuttle. EVA astronauts and remotely controlled manipulators are relied upon heavily during these operations.

The amount of time the SFP spends waiting for an external tank will depend mainly on the frequency of space shuttle missions and the round trip time of the SFP (see Table 10.3). Assuming a standard SFP mission, more than nine space shuttle missions a year would have to be launched to exceed the time line capabilities of the SFP. In this event, shuttle missions could be scheduled to maximize the truss production by launching a second shuttle mission just prior to completion of the first external tank reduction. A second external tank would then be available for reduction prior to SFP departure. This would be followed by a 38 day interval

between the next set of launches. The SFP's mission cycle will then follow a modified pattern of events. The reduction of an external tank followed by a few days of truss making and orbit maintenance at 300 *km* will take place, while awaiting the arrival of a second tank for reduction. With the subsequent reduction of a second tank, the SFP would continue its standard event cycle but would arrive at the construction site with a double load of trusses.

10.2 Detailed Mission Events

To provide further insight into the capabilities of the SFP, the six major events of a standard mission are described in detail in the following sections.

10.2.1 Event 1 — Rendezvous and Docking. During this event, the SFP and a space shuttle with the external tank still attached rendezvous. A typical rendezvous will be at an approximate altitude of 300 *km* in a circular orbit of 28.5° inclination. The SFP uses its precision maneuver capability to dock with the orbiter/external tank combination. During docking, the control of the SFP will be executed from the shuttle by remote commands. The SFP will maneuver the extended rigidized docking system to grapple with the heavy grapple fixture on the external tank (refer to Section 8.3 for a complete description of this process). The actual docking is illustrated in Figure 10.3. This event will typically take less than 1 *day*, and the majority of the power will be dedicated to the propulsion system for docking. This *R*-bar maneuver can have 77 *kW* of power available to it. After docking is complete, the external tank will be secured and rigidly attached to the SFP.

Once the external tank is grappled, the shuttle is free to release from it and retreat to a safe standoff distance. From this observation position, the shuttle crew can assist in the tank reduction efforts.

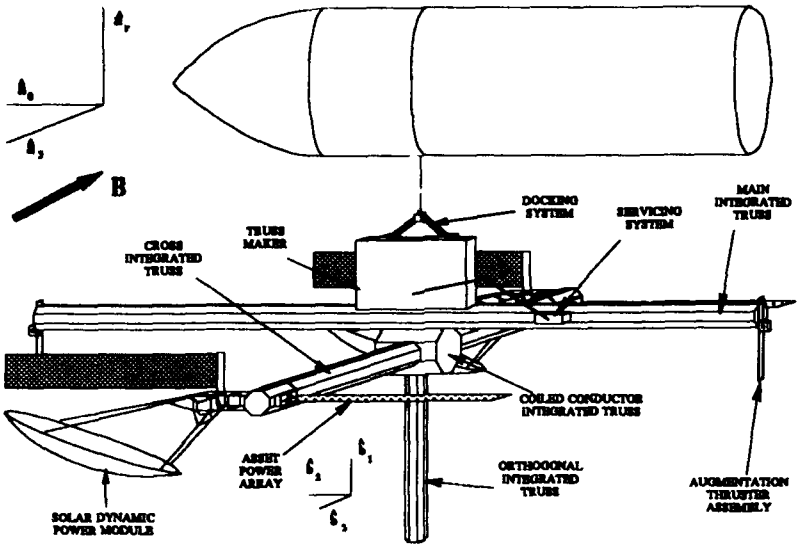

Figure 10.3 A typical docking of the SFP and the external tank. The shuttle orbiter, not shown in this figure, will still be attached to the external tank during this sequence.

10.2.2 Event 2 — External Tank Reduction. The second event involves reduction of the external tank into usable truss making material. It begins with the astronauts performing an EVA to transfer and install reduction equipment into the external tank. This process takes two 8 *hour* EVAs (31:4.2). Astronauts can also carry out any SFP required maintenance during this period, either telerobotically or through further EVAs. Any special cargo for shipment by the SFP could also be transferred from the orbiter to the SFP at this time. The altitude of the SFP will be maintained at 300 *km* with the shielded coil electrodynamic propulsion system which consumes about 15 *kW* of power.

With the reduction equipment in place, reduction of the external tank can begin and the shuttle is free to leave the vicinity and carry out its intended mission. The shuttle returns at the end of its scheduled mission to remove the reduction equipment and storage/feed magazines of the reduced external tank material from the external tank. This is done through EVA and remote manipulators of the SFP

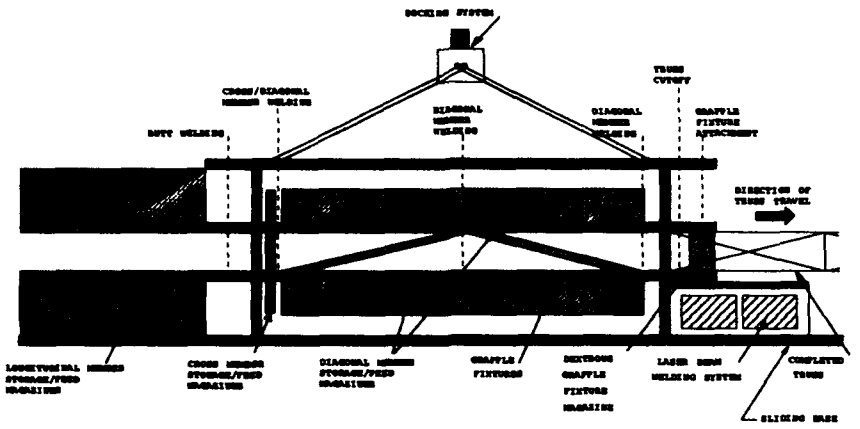

Figure 10.4 The SFP truss maker.

servicing system. Magazines of material are put into place on the truss maker and reduction equipment is stored on the SFP. If the remainder of the reduced external tank is not required, it will be separated via the docking system and allowed to deorbit due to aerodynamic drag. Once material transfer and reduction equipment breakdown has occurred, the shuttle is free to return to Earth.

In addition to orbit maintenance, the typical power requirement for this event includes 12 kW for the salvage operation, 5 kW for base power and 2 kW for the servicing system. The total power consumed during tank reduction is 34 kW.

10.2.3 Event 3 — Truss Making. Because the SFP has 48 kW of excess power during external tank reduction, truss making can begin and run concurrently as soon as sufficient materials are available. Remote manipulators would be used to remove full magazines of material from the partially reduced external tank and load them into the truss maker. Figure 10.4 shows the truss maker producing the truss product. After the end of truss making, the extra and empty magazines are stored on the magazine storage rack on the underside of the main integrated truss. The

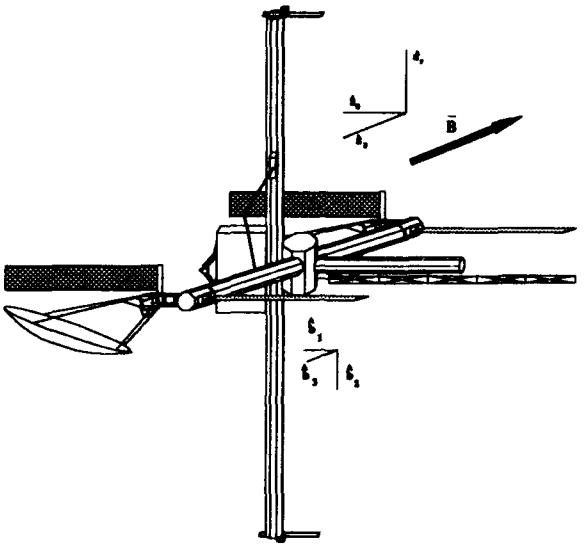

Figure 10.5 During orbit transfer, the SFP main conductors are aligned parallel with the radius vector.

completed trusses are placed on a truss storage rack on the orthogonal integrated truss. The truss storage rack is discussed in Section 5.3.9.

The construction of truss is the primary purpose of the SFP. The truss maker produces truss with an approximate 1 $m \times 1$ m cross section; the length of the trusses produced can be specified by the end user. The material recovered from one external tank will be converted to a total of 730 m of truss in approximately 2 *days*.

10.2.4 Event 4 — Orbit Transfer. With the completion of truss making, the SFP will be rotated to align the main conductors parallel with the radius vector (see Figure 10.5. Current in the main conductor will be increased until power is at a maximum of 77 *kW* and the SFP will begin its transfer to a higher orbit for rendezvous with a space platform under construction or any other user. During this event, the SFP will be teleoperated from ground stations.

The SFP's main conductors, $C1$ and $C2$, are oriented in the radial direction to control the direction of the propulsive force, $\overline{F}_p$. The propulsive force will mainly

be directed to maximize the increase in orbital radius. The SFP will slowly spiral radially outward from the Earth. Occasional redirection of $\overline{F}_p$ will be used to control the orbital elements such as inclination, i, and the longitude of the ascending node, Ω. This will allow the SFP to rendezvous with its target.

If truss making is underway, full power cannot be devoted to propulsion, only 68 kW is available, and the altitude will rise initially at a long term climb rate, $\dot{r}_{LT}$, of 5.0 km/day. With no truss making, 77 kw can be applied to the propulsion system to raise the altitude of the orbit, $\dot{r}_{LT}$ will equal or exceed 10.67 km/day. Both of these rates are for a worst case scenario of a full payload (31,300 kg). If payload is limited to just completed trusses, 77 kW will give a climb rate of 16.7 km/day.

10.2.5 Event 5 — Rendezvous and Delivery. After rendezvous with a target vehicle or platform, astronauts in the vicinity will control the SFP via remote links. At the minimum safe distance to the target vehicle, the SFP will maneuver to place the SFP's working surface toward the target platform. The SFP will use its precision maneuvering capability to position itself and station keep in the most convenient relative location for cargo transfer. Maintaining this relative position may require all available power depending on the stand-off conditions. Delivery will be accomplished with the remote manipulators and the SFP's docking system (see Figure 10.6). Delivery may entail the actual installation or hand-off of truss or other cargo to another space structure.

10.2.6 Event 6 — Return Orbit Transfer. After the delivery of the SFP manufactured trusses, an orbit transfer down to 300 km is necessary to acquire another external tank. The SFP will maneuver to apply the major component of $\overline{F}_p$ in the $-\bar{v}$ direction, and transfer back to a lower orbit to rendezvous with a future shuttle mission. The duration of this event is dependent on the current allowed through the conductor; 100 A drops the SFP from 500 to 300 km altitude in approximately 15 $days$. Control of the SFP will be from ground stations during this event.

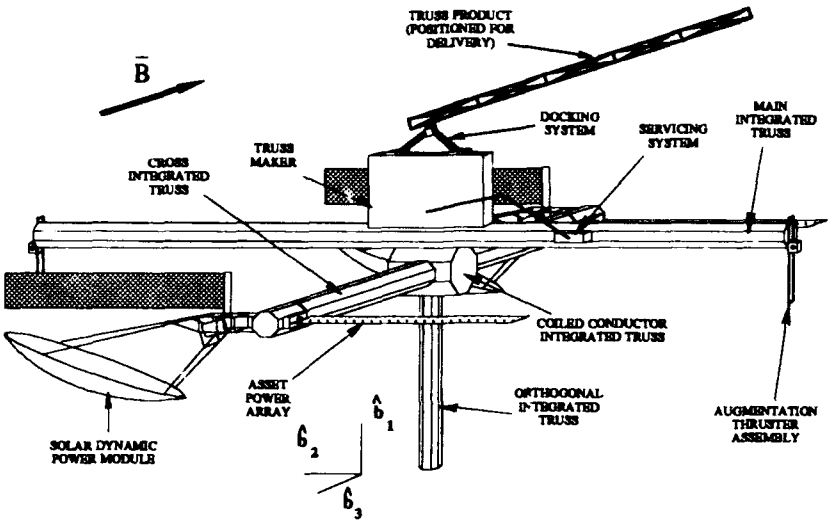

Figure 10.6 The SFP truss maker.

10.2.7 Event 0 — Orbital Maintenance. Orbital maintenance occurs anytime the SFP must remain at a specific altitude. This mainly occurs while waiting for another external tank. In the worst case, a pause at 300 *km* would typically require 15 *kW* to maintain this altitude. Slightly less power is required as the altitude of the orbit increases. A reduction in the drag force reduces the power necessary, but a concurrent reduction in the magnitude of the B-field counters this reduction.

10.3 Advantages of the SFP

The SFP offers three primary capabilities that enhance the construction of large structures in space. The SFP:

- fabricates structural trusses in orbit
- maneuvers with limited expenditure of propellants
- docks with precision

Designing for these capabilities has also resulted in additional capabilities. The large excess in SFP power during periods of limited maneuvering and the SFP's servicing system are important resources that can be exploited. First, the primary capabilities will be addressed.

10.3.1 Fabrication of Trusses. Trusses will provide the basic structure for large structures in space. It can be demonstrated that manufacturing trusses in orbit from expended external tanks is more efficient than launching them from Earth by comparing the amounts of truss that can be brought to orbit by both means.

The dimensions of the payload compartment of a space launch vehicle is the limiting factor on how much truss can be brought to orbit in a single mission. Of the space launch vehicles currently in the U.S. inventory, the space shuttle has the greatest capacity to carry truss. The shuttle cargo bay is a cylinder 4.57 m in diameter, and 18.29 m long (17:13.3). The practical constraints, because of tie-down and handling requirements, are likely 4.5 m diameter and 18 m long in a mission completely dedicated to carrying truss (no unpressurized berthing adapter). The maximum number of 1 $m \times 1$ m square cross section trusses (SFP equivalent) that the orbiter can carry is 10, for a maximum length of 180 m of truss per mission (see Figure 10.7). If the square truss is replaced with hexagonal truss (1 m cross corner to far corner in cross-section) for more efficient packing, the orbiter can carry up to 19 trusses, for 342 m of truss per mission (see Figure 10.7). The hexagonal truss represents the worst case competition for the SFP.

The SFP can produce 730 m of truss from the material provided by the reduction of a single external tank. This exceeds the amount of square or hexagonal truss that can be carried in the shuttle cargo bay. When using the operational SFP, an external tank from a single shuttle mission will be equivalent to over four truss dedicated shuttle missions for a square truss and over two dedicated shuttle missions

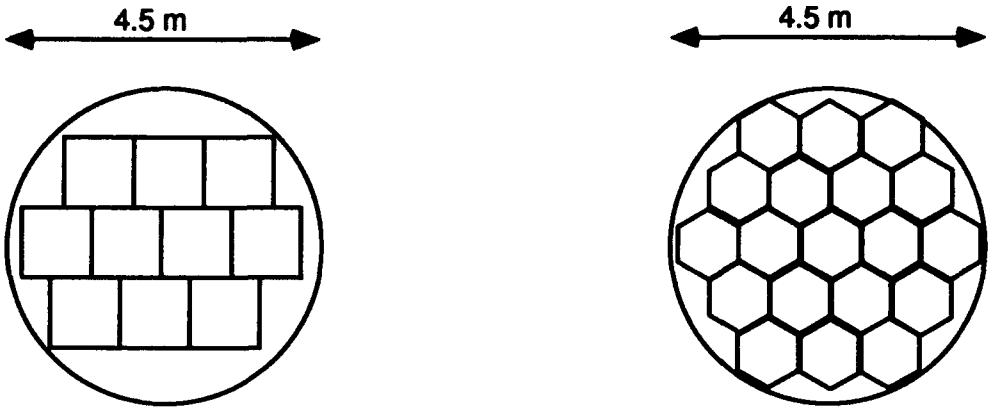

Figure 10.7 A cross-section of trusses in the shuttle cargo bay. The maximum number of SFP equivalent trusses that can be carried in the shuttle orbiter cargo bay.

for a hexagonal truss. In addition, when delivering an external tank to the SFP, the shuttle bay is left empty for other cargo.

If all efforts were dedicated to delivering truss into space — as would be the case for constructing Boeing's Solar Power Satellite — the space shuttle could carry loaded material magazines for the truss maker in its cargo bay. The shuttle can carry the material equivalent to seven reduced external tanks before reaching its maximum payload mass. The resulting mission could produce 5840 m of truss. Without an SFP, 32 dedicated shuttle missions would be required to deliver the same square truss, or 17 mission would be required to deliver similar hexagonal truss. If the shuttle was unable to carry its external tank to orbit, but the SFP already existed, the shuttle could supply the SFP from its cargo bay with enough pre-loaded magazines to produce 5110 r of truss. This is equivalent to over 28 missions carrying the square truss or almost 15 missions carrying the hexagonal truss.

Truss	Break Even	SFP Total Truss	Space Shuttle Total Truss
Square	11	2190 m	1980 m
Hexagonal	16	5840 m	5472 m

Table 10.4 This table gives the number of space shuttle missions required for the SFP to break even against dedicated truss shuttle missions and the resulting amounts of truss.

The cost of the SFP can be considered as the number of missions required to bring the SFP to an operational status (8 assembly missions plus 1 mission for initial salvage setup). After these 9 missions, the SFP can deliver 730 m of truss. If the shuttle had not constructed the SFP during those missions, it could have delivered 1620 m of square truss or 3078 m of hexagonal truss from its cargo bay. After SFP assembly, every external tank from subsequent shuttle missions gets transformed into 730 m of truss while dedicated truss shuttle missions only provide 180 m or 342 m, respectively. A "break even" point occurs at the total mission number where the SFP produces more truss than the shuttle can deliver in its cargo bay. Table 10.4 gives the break even points compared against both the square and hexagonal truss. Remember, on SFP shuttle missions, the cargo bay is completely available for other payloads. If large amounts of truss are required for future orbital applications, it is clear that manufacturing trusses in orbit from expended external tanks is more efficient than manufacturing trusses on Earth.

10.3.2 Maneuvers with Limited Fuel. The electrodynamic propulsion system has another important economical advantage — it only expends propellant for augmented z-axis thrust. Fortunately, z-axis thrust is only mandatory during stand off maneuvers. The ASSET platform was expected to use 5,455 kg of fuel each year just to maintain its orbit. The SFP uses no fuel for orbit maintenance. In addition, the SFP was designed with the capability of transporting large cargoes, such as a complete external tank. It can raise an external tank from a 300 km orbit to a 500 km orbit without expending any fuel. For a comparison, the mass of the

fuel required for the ASSET boost/deboost modules to make the same transfer of an external tank was determined and is presented next.

Using the fuel efficient Hohmann transfer, a total ΔV of 113 m/s is required. The empty external tank mass, m_{ET}, is 31,300 kg. Two boost/deboost modules provide 4,448 N of thrust and have a mass, m_e, of 1,429 kg. Their initial supply of hydrazine fuel has a mass, m_f of 10,884 kg. The engines have an I_{sp} of 230 s, which equates to an engine exhaust velocity, V_e, of 23.47 m/s. Using the rocket equation:

$$\Delta V = V_e \ln \frac{m_0}{m} \tag{10.1}$$

with the initial mass, $m_0 = m_{ET} + m_e + m_f$, the final mass, m, can be determined (93:187). Solving for the change from m_0 to m, the amount of fuel required is 308 kg. The SFP could make 18 equivalent transfers (9 round trips) in one year without expending any hydrazine. A total of 5544 kg of fuel would be saved.

All fuel must be launched from Earth — requiring a significant percentage of the total space launch payload capacity. The advantage of an electrodynamic propulsion system that does not have to expend fuel is apparent.

10.3.3 Precision Docking. As described in Section 8.3, the controllability of the electrodynamic propulsion system and the absence of exhaust plumes make the SFP ideal for docking maneuvers. The problems that have plagued all docking systems to date have been eliminated. This capability would be invaluable for the construction of large structures in space.

10.3.4 Additional SFP Capabilities. In addition to the capabilities directly resulting from the exploited technologies, two additional capabilities are by-products of the SFP design, its abundant electrical power and its remote manipulators.

The SFP has two solar dynamic power units and the ASSET's photovoltaic arrays. These provide more than 62 *kW* of power that can be exploited while the SFP is simply maintaining an orbit. Possible uses for this power include:

- power for work sites
- power for additional fabrication systems that further exploit the material from external tanks
- power for extended duration shuttle missions
- power for science experiments

The SFP has two remote manipulators for the support of truss manufacturing and product delivery. They are a valuable resource, and can be used in a variety of tasks, including construction and maintenance of other space platforms.

10.4 Conclusion

The typical operations and primary capabilities of the SFP have been reviewed. The robust and flexible features of the SFP facilitate the complete or partial accommodation of almost all space operations.

XI. Design Sensitivities

11.1 Introduction

As described in the introduction, this chapter supports the decisions made during the design process. It provides increased detail on a collection of subjects that impacted the study. All of the issues presented arose in the course of the study and were integrated into the overall design of the SFP. They are developed at the end of the report because their level of detail would detract from continuity in the body of the report. The order they are presented in does not reflect a ranking of their importance.

11.2 SFP Design

The final design of the SFP is unquestionably a result of the requirements and constraints levied upon the study at its inception. Early on in the design synthesis, decisions were made that drove the SFP's design to the end seen in this study. The primary factor affecting the design was the conscious decision for the SFP to be capable of performing a steady state R-bar standoff maneuver. This decision, more than any other, drove the design. The final design of the SFP specifically supports the R-bar standoff capability outlined in Section 3.2. If different requirements were levied, the design of the SFP would be different. A number of the components and subsystems of the SFP would change.

First, consider the conceptual requirements for performing the R-bar maneuver. The POTV design proposed by Lawrence used long towers that were assumed to be rigid. The POTV was capable of R-bar standoff, but only at the price of extremely high currents and power requirements. To perform a 50 m R-bar standoff, the POTV required sustained current levels in excess of 400 A. With the conductor circuits closed through the ionosphere, the power levels (estimated to be between 44 kW and 325 kW) and heat transfer problems would be severe. Note that this is

for a vehicle with a total mass of 37,870 kg. The significance of this is that the SFP's total mass is 110,609 kg. The final conductor lengths, at 4950 m, are significantly longer than those used for the POTV. The most significant difference that allows the SFP to be more massive is the concept of shielding portions of the conductors, as discussed in Section 6.2.2.4. This allows the conductor loops to be collapsed and closed on the SFP itself rather than through the ionosphere.

Prior to the incorporation of the shielded loops concept, trusses similar to those outlined by Lawrence (49:D.2), were to be used to house the conductors. When shielding was incorporated, multiple loops were established rather than single conductors closed through the ionosphere with plasma contactor devices. It quickly became apparent that the conductor loops required to support the R-bar requirements would be completely unmanageable due to their size. The main conductors, $C1$ and $C2$, of the final SFP design are 23.16 cm in diameter for each path. There is no way to bring conductor bundles of this size into orbit, except in pieces. This would then require assembling the conductors and towers in space — a task deemed infeasible. This led to the decision to use an integrated truss concept similar to that used by Space Station Freedom. The truss is manufactured on Earth, and has all necessary hardware installed prior to launch. As the design process continued, the sizing of the conductors led to all of the trusses being converted to integrated trusses.

Once the design iterations began, the two primary limiting factors on the size and performance of the SFP were identified to be power and heat transfer. The best power systems identified by the analysis of available systems (see Section 11.8 — solar dynamic power modules — can only provide approximately 82 kW when combined with the ASSET photovoltaic arrays. Of this, only 77 kW is available for propulsion; a power level which falls extremely short of the requirement identified by Lawrence. However, because the shielded loops are closed on the vehicle itself, this power is sufficient for performing the required R-bar maneuver. Using 77 kW as the maximum power available for propulsion, the *orbit history design program* (see Section 6.3.8)

was used iteratively to determine the lightest configuration that could perform the required R-bar maneuver.

Closely related to the power issue is the heat transfer problem. Because of the bundling of the conductors, there is a potential for high temperatures (due to the i^2R heat dissipation term in the power equation). A one dimensional heat transfer analysis was incorporated into the design software to make sure the conductor core temperatures did not exceed the design limit. The design limit was arbitrarily set at a safety factor of 1.5. The power available for propulsion is low enough that for the final design of the SFP, heat transfer is not an issue. However, during orbit transfers from a higher orbit to a lower orbit, additional load resistance must be placed in the circuits. The additional resistance is required to prevent the induced voltage from generating currents that would exceed the conductor's heat transfer capabilities.

Taking all of these concerns into account during the iterative design process, the final design of the SFP is a compromise between performance and power. The optimization of the design was essentially heuristic. Portions of the process were numerically optimized, such as the analysis of the conductor tower size versus the conductor length (see Section 11.11). The overall process was not numerically optimized in its entirety due to the interaction of the linear system control design process with the remainder of the process. A specific design was proposed and then tested. Once the design was near that of the final configuration, the task was to determine the number of turns in each conductor so as to minimize the total vehicle mass.

While the process itself might not change if the requirements were different, the final design would certainly be different. The SFP is designed to perform a steady state R-bar maneuver, not perform optimal orbit transfers, nor any other functions. The sizing of the vehicle, the sizing of the conductors, the placement of the power systems, the placement and maneuverability of the truss maker, and the function of the augmentation thrusters are all oriented toward successfully performing the R-bar maneuver described in Section 3.2.

11.3 SFP Manning and Control

During development of the SFP, it was decided to design the prototype without a habitation module. The primary advantage of this decision is the removal of complications associated with pressurization. Pressurized modules are highly complex and require increased safety considerations (62:187). Pressurized adapters necessary for connecting two pressurized environments, like a habitation module and a space shuttle, also add a high degree of complexity.

The lack of habitation modules on the SFP has two disadvantages: there are no additional pressurized workspaces available for SFP assembly and operations when the space shuttle is on a mission, and there are no permanently manned capabilities for SFP assembly and operations when the space shuttle is away from the SFP. The first disadvantage is an inconvenience and can be overcome with prior planning. The second disadvantage is significant. There will be no on-orbit crew to participate in the SFP processes or react to contingency operations when the space shuttle is away. This deficiency can be countered with an increased emphasis on ground controlled remote manipulators. There are several groups, including SPAR Canada, who contend that ground control should be incorporated into Space Station Freedom (61), (62), and (36).

The Space Station Freedom Program Office anticipates the capability to support 130 *hours/year* of EVA over the life of Space Station Freedom. The Space Station Freedom Task Team estimates the EVA required just to maintain Space Station Freedom will average 3276 *hours/year* (36:76). Ground control of the Space Station Freedom mobile servicing system can make a significant impact on eliminating this dilemma.

Prior to permanently manned capability on Space Station Freedom, ground based control of manipulators is being proposed for many tasks. For example, time consuming processes, like inspections, can be accomplished while the crew is resting between EVA missions or while the space shuttle is away (62:185). Payload

servicing, maintenance tasks, and assembly work are also being considered in these situations (36:80).

Primarily, there are two concerns with ground based control: the performance reliability of the remote manipulators and the time delay associated with space-ground communications (61:338). Reliability is and must continue to be engineered into the proposed manipulator systems. The SFP design includes two complete manipulator systems for its servicing system. This naturally enhances reliability through redundancy. The 4-10 *sec* time delay issue is also receiving attention. Decreasing the time delay has been determined infeasible, so approaches to controlling the manipulators with a time delay are being considered (61:344).

Currently, there are two competing approaches for managing the time delay: time delayed teleoperation and supervised automation (36:79). Tests have shown that whenever a time delay exceeds 0.5 *sec*, time delayed teleoperations reduce to a control strategy where the operator commands a small motion of the manipulator and waits to observe the response at the remote sight (62:189). This strategy is time consuming, fatiguing, and error prone. Also, when tasks require manipulator contact with the environment, the interaction forces are difficult to control. Supervised automation is a more appropriate, but still limited approach (36:81). In this strategy, manipulator actions are carefully pre-planned prior to execution. An accurate world model simulation is required to predict the response of the manipulator system to the commanded action. Operations consist of many short automated sequences strung together. The operator commands the start of a sequence, monitors the progress of the sequence, and verifies the completion of the sequence prior to executing a new sequence. The major limitation is that the planned manipulator tasks must be time invariant. This eliminates operations requiring real time feedback like grasping a moving object.

The SFP will incorporate supervised automation for ground control of the remote manipulators during time invariant tasks, but when time variance is a factor,

controlling will be limited to workstations in the vicinity of the SFP that do not experience a time delay. These concepts extend to the maneuvering control of the SFP as well. Control of the SFP propulsion system will occur from the ground except when operations like docking require real time feedback.

In many of the control scenarios, operators will be unable to physically view the operations they are commanding. Numerous camera and lighting systems — as described in Chapter VIII — are expected to compensate for the limitation. In 1990, the Manipulator Development Facility at NASA Johnson Space Center conducted a study that examined the importance of visual aids during manipulator operations (39). The study concluded that physical viewing was not required for successful manipulator operations. In their scenarios, the runs accomplished with camera viewing instead of physical viewing were actually smoother (39:155). In fact, in the current Space Station Freedom designs, the placement of the habitation module windows virtually eliminates direct viewing of the mobile servicing system (36:81). Manipulator operations can be performed without physically viewing the work site.

11.4 Truss Making Machine Tradeoff

It was originally thought ASSET salvaged flat plate material could be welded together to form continuous flat plates. These continuous flat plates could then be fed into a triangular truss maker similar to General Dynamics and Grumman machines to form longitudinal open cap sections. The cross braces and diagonal braces could be ASSET salvaged I-beam material, cut to appropriate lengths and attached to the formed longitudinal cap sections. Cross brace feed magazines could store and properly place the I-beam material for weld attachment.

A structural analysis performed on the triangular truss described above showed this configuration to be extremely stiff in both bending and torsion for all anticipated loads. This strength was due in part to the thickness of the aluminum material salvaged from the external tank during the ASSET salvage operation. However, the

thickness of the material was one of the reasons the idea of simple modifications to earlier machines was eventually eliminated. Based on discussions with Hobart Welding Company (41), the thickness of the salvaged aluminum was too great to form the material into the desired cap shape.

The inability to form the material into cap sections was not the only reason for dismissing the idea of modifying the General Dynamics and Grumman truss making machines from consideration. Using the I-beam material as cross bracing would have misused material already in a suitable configuration for the longitudinal members. Also, the complexity added to the SFP truss maker through the heating, forming, and cooling processes required to produce the truss was not compatible with minimizing support missions to operate the SFP.

The possibility of making simple modifications to the General Dynamics and Grumman truss makers was eliminated from further consideration as an option for the SFP truss fabrication facility. However, several of the truss construction processes demonstrated as feasible during the General Dynamics and Grumman design studies are incorporated into the SFP final design. The SFP truss fabrication machine design is described in Section 5.3.

11.5 Truss Product and Truss Maker

Modifications to the automated reduction of external tanks accomplished during the ASSET salvage operation are required. These modifications are required to put the ASSET salvaged material into usable SFP truss fabrication form.

The configuration of the SFP truss product was driven by the following:

- product features (strength, ease of joining, ease of handling, etc.)
- reduce excess material/debris when transforming ASSET raw material into usable SFP truss maker form
- minimize modifications to ASSET salvage operations

- reduce ASSET and SFP material handling requirements
- ensure the SFP truss maker fits into the shuttle cargo bay

Based upon these constraints and the material available, an equation was formulated to determine the appropriate length of the diagonal truss member. The final SFP produced truss configuration is based upon using 1.035 m T-beam cross members. This left the length of the truss bay as the only unknown. Justification for the 1.035 m cross member length is discussed next.

11.5.1 Cross Member Length. The webs of the I-beams produced during the ASSET salvage operation are cut lengthwise to produce T-beams. T-beams are used as the longitudinal and cross members of the SFP fabricated truss. The T shape of the longitudinal members lends itself to either a rectangular or square shaped truss. The SFP truss maker produces a truss with a square cross section.

Salvaged T-beam material generated during the salvage operation comes in two basic lengths, 4.14 m and 5.715 m. Quantities of the 5.715 m length material far exceed the 4.14 m length. However, by cutting the 4.14 m length material into four equal length pieces of 1.035 m, an adequate supply of cross member material is produced. By using the shorter material in this manner, the longer material is more efficiently used as the truss longitudinal and diagonal members. This also reduces wasted material and because the entire 4.14 m T-beams are equally divided into fourths, debris is eliminated.

11.5.2 Bay Length. The flat plate material produced during salvage operations is cut lengthwise to produce five equal width strips. These strips are used as diagonal members for the SFP produced truss. The length of the truss diagonals determines the bay length of the truss.

As in the case of the T-beam material generated during the salvage operation, flat plate material can be produced up to the same two basic lengths, 4.14 m and

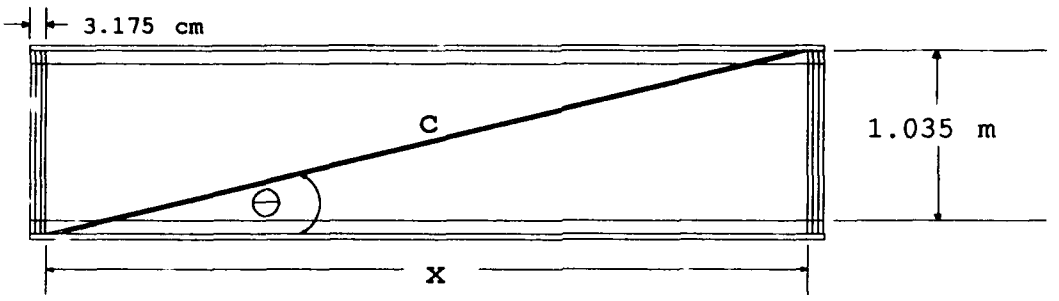

Figure 11.1 Side view of truss bay defining variables used to determine the length of the truss diagonal member.

5.715 m. However, the actual length of the diagonal member will be less because of the modified angle cut performed by the primary cutter. The special cut is necessary to achieve a proper truss diagonal fit and minimize debris. The determination of whether to use the 5.715 m material or the 4.14 m material for the diagonal member reduces to a geometry problem. The 5.715 m material will be addressed to illustrate the problem.

The first step in the problem formulation was to identify appropriate variables (see Figures 11.1 & 11.2). The following variables are defined:

c = SFP truss diagonal length

x = inside bay length

θ = angle between the longitudinal T-beam flange and the diagonal member centerline

y = length of unsalvaged ASSET material

The goal was to solve for length, c, from the 5.715 m of available flat plate material.

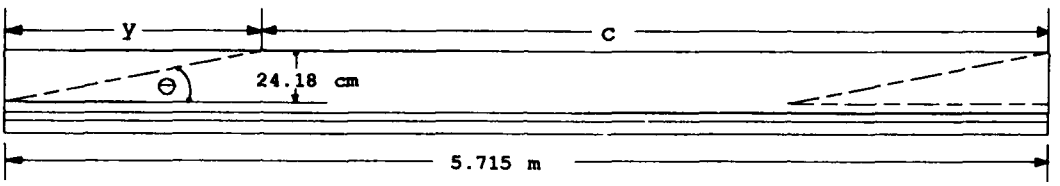

Figure 11.2 Angled cut required by the primary cutter — 5.715 m material

Mathematically this is written:

$$c + y = 5.715 \tag{11.1}$$

Note from Figure 11.1,

$$c = \frac{1.035}{\sin(\theta)}$$

and from Figure 11.2,

$$y = \frac{0.2418}{\tan(\theta)}$$

Plugging these functions into Equation 11.1 and solving for θ produces:

$$\theta = 12.8°$$

The total length of one bay is determined by adding 3.175 cm to the inside bay length variable, x. This accounts for the small length occupied by the cross members. Therefore, the total bay length becomes 4.529 m. A summary of where the material

Member Type	Lengths	Quantities	Bays
Diagonal	4.655 m	1335	166
Cross	1.035 m	748	187
Longitudinal	5.715 m	514	184

Table 11.1 Summary of truss member lengths when using 5.715 m ASSET salvaged material to determine diagonal member lengths.

will be used, the material lengths and quantities, and the possible number of truss bays produceable for each type of material is included in Table 11.1. Using the smallest number of bays possible and a bay length of 4.529 m, provides a 730 m continuous truss. This represents the longest continuous truss possible from the 4.529 m bay configuration.

The main advantages of this configuration are its efficient use of material while minimizing debris, the relatively small quantities of material to be handled, and the intermediate size of the truss maker required to produce this configuration.

The same analysis was performed on the shorter 4.14 m material (see Figure 11.3). Solving for θ produces:

$$\theta = 17.8°$$

The total length of one bay is determined again by adding 3.175 cm to the inside bay length variable, x. The total bay length becomes 3.304 m. A summary of where the material will be used, the material lengths and quantities, and the possible number of truss bays produceable for each type of material is included in Table 11.2. Using the smallest number of bays possible and a bay length of 3.304 m, provides a 700 m continuous truss. This represents the longest continuous truss possible from the 3.304 m bay configuration.

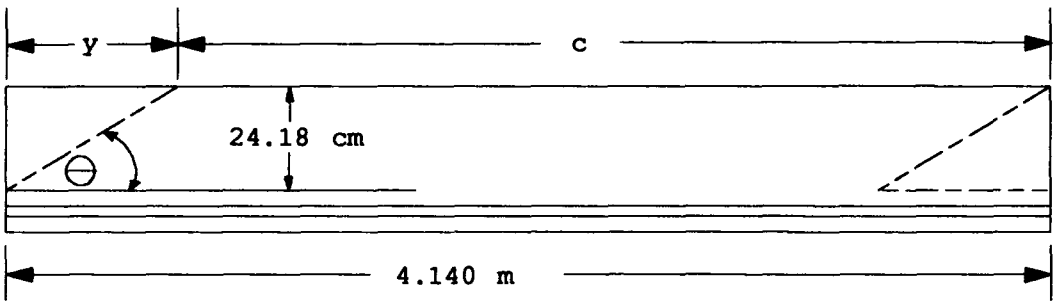

Figure 11.3 Angled cut required by the primary cutter — 4.14 m material.

Member Type	Lengths	Quantities	Bays
Diagonal	3.387 m	1740	217
Cross	1.035 m	848	212
Longitudinal	5.715 m	494	214

Table 11.2 Summary of truss member lengths when using 4.14 m ASSET salvaged material to determine diagonal member lengths.

The main advantage of producing a 3.304 m truss bay is the small SFP truss maker required to fabricate the truss. However, the following disadvantages outweigh this advantage:

- large quantities of individual pieces of material are generated requiring more storage and handling facilities
- large amounts of welding are required due to the increased quantities of individual pieces of material generated
- the primary cutter is required to make a more complex cut on the longer flat plate material in order to size the diagonal members with no debris

Based upon this analysis, the 4.14 m flat plate material salvaged during the ASSET operation was discarded as a candidate for the SFP truss diagonal members. The 5.715 m flat plate material was selected as the best choice for the SFP truss diagonal member.

11.6 Welding Technology Tradeoff Study

Selecting a welding technology capable of welding aluminum in a space environment was a fundamental step in developing a feasible truss making process. A wide variety of welding technologies were reviewed to determine the best welding method for the truss making application. The primary factors used in selecting the welding process were power required, maintainability, and most important, the versatility of the welding system. The goal was to maximize the versatility features of the welding system due to the large number of welds required, minimize the power required, and maximize the welder's maintainability.

11.7 Welding Technologies

On Earth, the welding process can be easily performed by various methods. In space, welding performance is more complicated due to the extraordinary char-

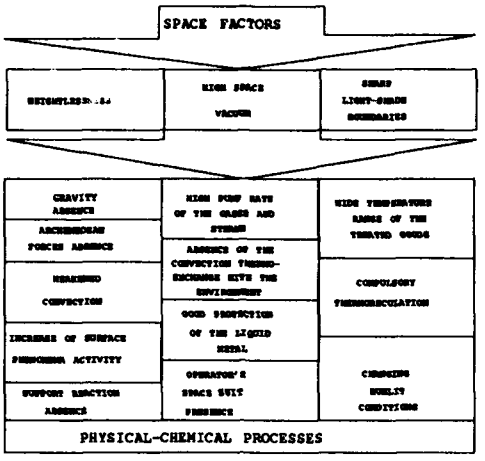

Figure 11.4 Typical Phenomena Caused by Main Factors of Space

acteristics of the space environment. Three main characteristics of space can be distinguished which highly affect the welding process (see Figure 11.4):

- weightlessness
- ultra-high space vacuum
- presence of sharp light-shade boundaries

As can be seen in Figure 11.4 each characteristic changes the nature of physical phenomena occurring in the process of welding. How the space conditions affect the welding process depends largely on the method used for joining of the materials (75:12). The three space characteristics have the least effect on those welding methods which are not accompanied by the use of the liquid phase. Therefore, explosion, diffusion, cold, flash butt, ultrasonic, laser, and electron beam welding are serviceable in the zero gravity conditions (75:12).

11.7.1 Explosion Welding. In explosion welding, the detonation of an explosive is utilized to accelerate one of the components to a high velocity before it collides with the stationary component. At the moment of impact, the kinematic energy of the plate is released as a compressive stress wave on the surface of the components. The collision progresses across the surface of the plates. Surface films are liquefied and jetted out of the interface leaving a perfectly clean surface. Under these conditions, the normal interatomic and intermolecular forces create a bond (92:49). This joining technique was eliminated from further consideration due to the careful preparation and fit-up of the components being treated (75:14) as well as the obvious logistic problems involved in setup and handling of the explosive charges.

11.7.2 Diffusion Welding. Diffusion welding occurs when properly prepared surfaces are in contact under predetermined conditions of time, pressure, and elevated temperature. Diffusion welding was eliminated because components must be specifically designed and carefully processed to produce a joint successfully (92:51).

11.7.3 Cold Welding. Cold welding is a process which uses pressure at room temperature to produce coalescence of metals. Welding is accomplished by using extremely high pressures on extremely clean interfacing surfaces (15:221). This technique was eliminated due to the substantial deformation of the material at the weld and the surface preparation required.

11.7.4 Flash Butt Welding. Flash butt welding is a resistance welding process which produces coalescence simultaneously over the entire area of abutting surfaces by heat obtained from resistance to electric current between the two surfaces and by the application of pressure after heating is substantially completed (15:219). This method of welding was eliminated due to the fact that undesirable molten metal and debris are squeezed out when both components are forced rapidly together to form the weld (92:16).

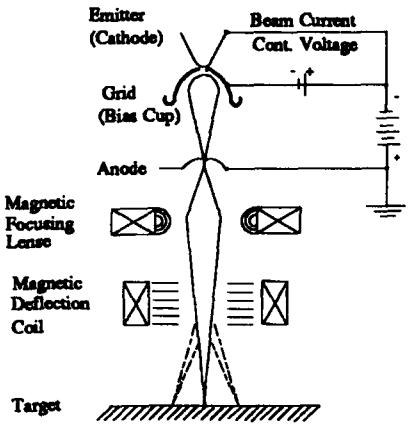

Figure 11.5 Electron Beam Fundamentals

11.7.5 Ultrasonic Welding. Ultrasonic welds are produced by the introduction of high frequency vibratory energy into the weld zone of metals to be joined (92:48). Welding occurs when the ultrasonic tip is clamped against the work pieces and is made to oscillate in a plane parallel to the weld interface. This process is restricted to relatively thin materials normally in the foil thickness range (15:226) and was therefore eliminated as a viable welding option.

11.7.6 Electron Beam Welding. With electron beam welding, some form of an electron gun device (Figure 11.5) is employed to simultaneously accelerate and shape the electron output directly into a negatively charged, high energy particle beam. The beam can then be electromagnetically guided and focused into a very small spot on the workpiece. Generally electron beam processing systems require reasonably good vacuum surroundings (64:25).

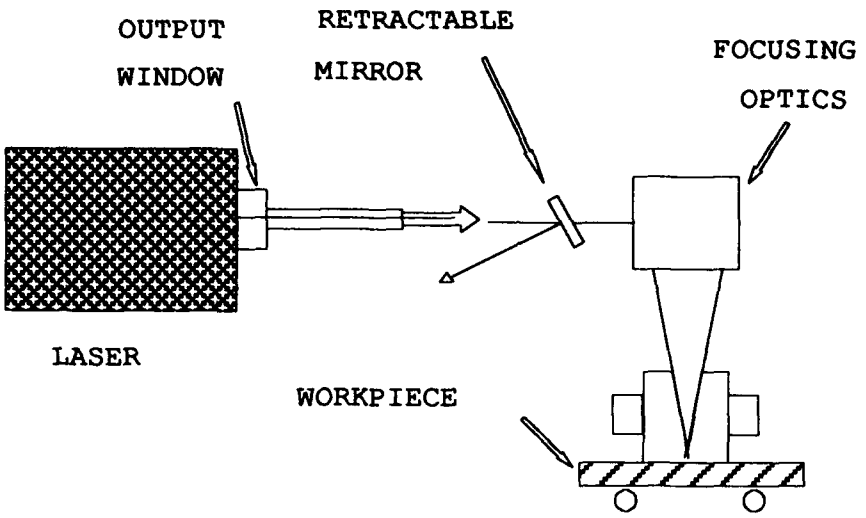

Figure 11.6 Laser Beam Fundamentals

11.7.7 Laser Beam Welding. With laser beam welding (Figure 11.6), a solid, liquid, or gaseous medium is used for providing the lasing action required to produce a coherent, neutrally charged, high-energy light beam. The beam can then be optically guided and focused into a very small spot on the workpiece (64:25).

11.7.8 Electron Beam vs *Laser Beam Welding.* The choice of welding technology was eventually narrowed down to electron beam and laser beam welding.

11.7.8.1 Capabilities. Both processes exhibit the capability for providing the following similar weld action properties:

- very localized heat affected zones
- joining of either thick or thin materials
- minimal thermal distortion during welding
- extremely high-quality autogenous fusion welds
- high depth-to-width ration weld profiles

- very high-speed welding

However, the two tend to exhibit a variety of dissimilar process utilization properties because the fundamental nature of the high energy beam each uses is so radically different. The electron beam generator is a *direct* type of energy conversion device, while a laser beam generator is an *indirect* device; therefore, efficiency achievable with a laser beam welder is lower than can be achieved with an electron beam welding system. Also, the degree of focused beam spot control achievable with an electron beam welder is greater than that attainable with a laser beam welder. However, due to this slightly lower power density of the focused laser beam, the tendency for incomplete fusion by the laser beam welder is less than the electron beam welder (92:22).

The electron beam welder is susceptible to stray electrostatic and magnetic fields adversely affecting the beam's travel path due to the negatively charged particles making up the beam (64:28). The susceptibility to stray electromagnetic fields by the electron beam welding system causes concern due to the electrodynamic propulsion system utilized on the SFP. Because a laser beam welder uses a neutrally charged beam it is not susceptible to stray electrostatic and magnetic fields (64:28).

When an electron beam is impinged on a workpiece, it produces x-rays which require shielding around both the workpiece and the beam generation/transmittal portions to ensure personnel safety (64:26). With a laser beam the possibility exists that some type of laser light reflection might occur. Laser welding has no more eye safety risk than conventional welding (91:4); therefore, the use of some form of simple light shield is needed to ensure personnel safety (64:27).

The reliability of both the welding systems is high. However, the beam generation portion of a laser beam welding system requires relatively low voltages, and therefore uses power supplies, feed cables and cavity discharge electrode designs that allow longer intervals of time between the performance of periodic maintenance (64:29).

The laser beam welding system allows multiplexing or time sharing the output from a single laser into any one of several fiber optic cables. These fibers can extend the distances up to 150 meters over which laser energy can be delivered. Because the fibers are flexible, they can follow any desired route to the workpiece. This makes fiber optic laser beam welding ideal for robotics, since the workpiece may be held stationary during processing (33). The multiplexing capability is ideal for welding at many different workstations, or for one large assembly station requiring the laser beam to be delivered to separate areas (33). With laser beam technology, it is possible to share the energy from one laser beam among several fibers, either alternately or simultaneously (33), which greatly reduces power requirements. An electron beam is not capable of being switched between various workstations (64:27). Fiber optic cabling also eliminates the need to constantly re-align mirrors, thus increasing the stability and accuracy of the process (33).

Comparing electron beam welders with laser beam welders, laser beam welders are the best choice for SFP use. This selection was based upon the high reliability, flexibility in directing power where required, and overall versatility of fiber optic laser beam welding.

11.8 Selection of SFP Power System

The approximate SFP power requirement was initially established as 50-100 kW. The various power alternatives to meet this demand are discussed in Appendix Q. Some of these power supplies can be ruled out immediately. For example, ASSET power (12 kW) can not provide the necessary amount. The ASSET electrical power system was optimized to meet ASSET needs and equipment and must obviously be augmented to provide the necessary power to the SFP. Given that more power is needed an additional source must be provided.

Any type of nuclear driven source can be ruled out on the basis of political consequences and technology issues in the multi-*kilowatt* regime. The issue of shielding

Solar Dynamic System	Efficiency (%)
CBC	35.6
Stirling	42.0
Rankine	15-20

Table 11.3 Solar dynamic power conversion efficiencies for the end user.

the reactor for man tended operation also becomes a large question mark. The shield must reduce the radiation level so that the dose received by the astronauts during rendezvous, fly-by, or EVA is not excessive. This would require a SFP reactor to be completely encased as well as placed up to 30 m away from any equipment or payload (44:159). Also, beamed power can not be counted upon due to the large infrastructure requirements necessary for both lasers and microwaves. This leaves just one source – solar. But, whether photovoltaic or some dynamic option is chosen can not immediately be determined.

11.8.1 Dynamic vs *Photovoltaic.* The most obvious current technology choice to lead the solar dynamic option is the closed Brayton cycle (CBC) design for Space Station Freedom. This was the intended growth mode for Freedom. The free-piston Stirling cycle (FPSE), however, has shown a lot of advantages. In a fairly recent theoretical study between various solar dynamic and two photovoltaic power systems (silicon arrays and a gallium arsenide concentrator) the FPSE was chosen on the basis of lowest area and lowest weight power system for a 35 kW design (89:1). All of these designs were based on Space Station Freedom level of technology. The CBC design ranked second and the alkali-metal Rankine cycle was found to be incapable of achieving the high thermodynamic efficiencies and was eliminated early on in the study (89:17). The efficiencies of the solar dynamic and photovoltaic systems for 35 kW designs are listed in Tables 11.3 and 11.4. The higher predicted cycle efficiency of the FPSE was the main reason it was chosen first. In this study, mass was the primary optimization criteria but the SFP is not so mass critical and other factors such as reliability, safety, technological readiness,

Photovoltaic System	Efficiency (%)
Silicon Array	14.9
Gallium Arsenide Array	22

Table 11.4 Solar photovoltaic array power conversion efficiencies — to the end user.

performance, operability, lifetime and compatibility take on added dimensions. The choice was also based on projected improvements in technology expected to take place. The actual development of the FPSE, however, has lagged that of the Brayton cycle system due to budget cuts within NASA. In fact, performance predictions for the FPSE are believed to be achievable but have yet to be demonstrated whereas the CBC has been demonstrated (89:66). The heat pipe Stirling receiver which passively supplies heat to/from the thermal energy storage and to the free-piston engine is at present no more than a conceptual design (89:24). Also, designs of Stirling engines were more suitable for nuclear power conversion applications (89:64). As such it would seem that a CBC has the advantage in technological maturity, reliability, operability and readiness.

Lower system mass primarily affects transportation to orbit costs. The high efficiencies of the solar dynamic systems allow for smaller array sizes per unit power. This reduces the deployed area perpendicular to orbital motion (drag area) and subsequent re-boost costs. Comparative drag estimates for Space Station Freedom are — solar dynamic power module 266 m^2 versus photovoltaic modules 714 m^2 (85:247). As shown in Section 11.10 this corresponds to a 13.5 km loss in altitude in 4 days for a solar dynamic SFP versus a 31 km loss for a photovoltaic SFP at an initial altitude of 300 km.

An additional advantage to solar dynamics is that energy storage in the heat of fusion of a salt is 97% efficient while battery storage round trip efficiency is on the order of 80% (85:248). Although the solar dynamic system will require more man hours to install than a photovoltaic system, the lower maintenance and resupply

needed for the solar dynamic will quickly overcome the photovoltaic over a lifetime of 30 years (96:779).

Increments of 25 *kW* solar dynamic power modules (SDPM) were to be added to the Space Station Freedom baseline of 75 *kW* (solar arrays) to bring the total power to 325 *kW* (8:321). The most recent cuts to the space station have done away with growth beyond the baseline and the SDPM's were not included in the revised design. Despite this, solar dynamic technology is now ready and NASA is committed to further development through its Office of Aeronautics, Exploration and Technology (96:811). As such, the decision of this design study is to use the closed Brayton cycle solar dynamic power system. A description of this design is included in Section 7.3.

11.9 External Tank Stability

An investigation was undertaken to determine if a separated external tank could be left in orbit by the space shuttle and recovered by the SFP at a later date, and whether it would be sufficiently stable, through passive means, for docking with the SFP. An investigation was also made to determine whether the shuttle could be used to maintain the external tank's attitude if necessary.

It is extremely difficult to dock with an unstabilized spacecraft. An uncontrolled satellite with any initial rotational motion will soon begin to spin about its axis of maximum moment of inertia (45:16). Generally the motion is even more complicated than this rotation because the spacecraft is not a rigid body and a variety of environmental torques are acting upon it. Some form of passive or active attitude control on a spacecraft is required if it is a docking target.

The designed operating altitude for the SFP is 300–500 *km*. The external tank can be placed into an orbit in this range, with increased orbit altitude trading for decreased shuttle fuel/payload mass (58:3). It is believed that 425 *km* is the minimum altitude the external tank can be left for an extended period of time (57:36).

Although a variety of space environmental torques are significant at these altitudes, aerodynamic and gravity gradient are primary. These torques will depend on the shape, construction, and orientation of the spacecraft. Aerodynamic torques typically dominate satellite dynamics below 370 *km* and gravity gradient torques dominate above 555 *km* (95:770). Between these altitudes, both torques can interact to varying degrees with the spacecraft (56:2200). When combined with the dynamic nature of the atmospheric density at these extreme altitudes, it becomes apparent that the applied torque on a separated external tank is difficult to predict. In the long term, the external tank will rotate about its axis of maximum moment of inertia (transverse axis, resulting in an end-over-end rotation) and some unknown angle to the orbital velocity vector (57:28). Coning about this axis is unpredictable.

The above analysis indicates that an unmodified external tank should not be left in orbit for any length of time. If it is, an attitude control system should be added. Possible attitude control systems for an external tank have been studied, and would require installation on every external tank utilized by the SFP (58:4).

An alternative procedure would leave the external tank and shuttle mated during docking so the shuttle could be used to control the external tank's attitude. NASA studies have detailed the required safing procedures to be carried out while the shuttle is still attached (60). Martin Marietta, the manufacturers of the external tank, state that the shuttle has full attitude control capability while the external tank is attached (1). These sources indicate no reason to preclude the use of the shuttle for attitude control of the external tank during docking. This is the SFP's preferred docking method.

11.10 SFP Sensitivity to Aerodynamic Drag

"When the orbit perigee height is below 1,000 *km*, the atmospheric drag becomes increasingly important" (16:213). Without a counteracting propulsive force, a spacecraft will eventually re-enter the atmosphere due to the cumulative effects of

atmospheric drag (30:121). Atmospheric drag is expected to deorbit ASSET from an altitude of 296 *km* in less than 12 *days* (31:5.40). The SFP must operate at the same altitude as ASSET, therefore potential configurations of the SFP must be investigated to determine the effects of atmospheric drag.

The drag force, $\overline{F}_d$, is given by the equation:

$$\overline{F}_d = -\frac{1}{2}\frac{\rho V_r M_{tot}}{\beta}\overline{V}_r \tag{11.2}$$

where ρ is the density of the atmosphere, $\overline{V}_r$ is the velocity of the vehicle relative to the atmosphere, M_{tot} is the vehicle mass, and β is the ballistic coefficient (94:65).

The parameters ρ and $\overline{V}_r$ are discussed in detail in section 6.2.4. The ballistic coefficient is defined as:

$$\beta = \frac{M_{tot}}{C_D A} \tag{11.3}$$

The vehicle mass, M_v, can be estimated from the vehicle design. The coefficient of drag, C_D, depends on the shape and motion of the vehicle, but is commonly assumed to be a constant. References give typical values that vary between 1 and 3, with values greater than 2 considered more realistic (30:127). For this analysis, C_D equals 2.4 — the value chosen by Miner in his analysis of a space shuttle external tank in orbit (57:33). The projected area normal to the flight path (drag area), A, varies because the orientation of the vehicle is constantly changing, and subcomponents, such as photovoltaic arrays, change orientation relative to the body axes. These orientations generally vary sinusoidally in the orbit. In order to simplify computations, this analysis uses the worst case vehicle orientation with respect to the flight path as a constant orientation.

11.10.1 Vehicle Drag Area Comparisons. Estimates of the drag area, A, were made for the likely orbital transfer orientation for a solar dynamic powered SFP (see Table 11.5 and Figure 11.7) and an alternative all photovoltaic powered

Component	Quantity	Area, m^2
External Tank	1	400
ASSET Photovoltaic Array	1	424
Solar Dynamic Power Modules	2	276
Main Integrated Truss	1	6
Cross Integrated Truss	1	50
Total		1432

Table 11.5 SFP drag area estimates — solar dynamic powered.

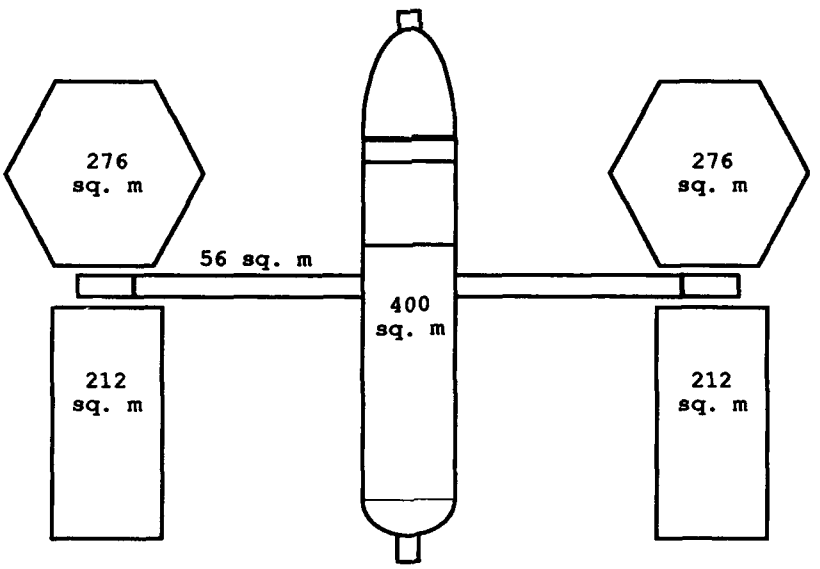

Figure 11.7 SFP drag profile using the worst case drag area of the SFP in the orbital transfer orientation as projected on a plane normal to the flight path.

Component	Quantity	Area, m^2
External Tank	1	400
ASSET Photovoltaic Array	5	424
Main Integrated Truss	1	6
Cross Integrated Truss	1	50
Total		3340

Table 11.6 SFP drag area estimates — photovoltaic powered.

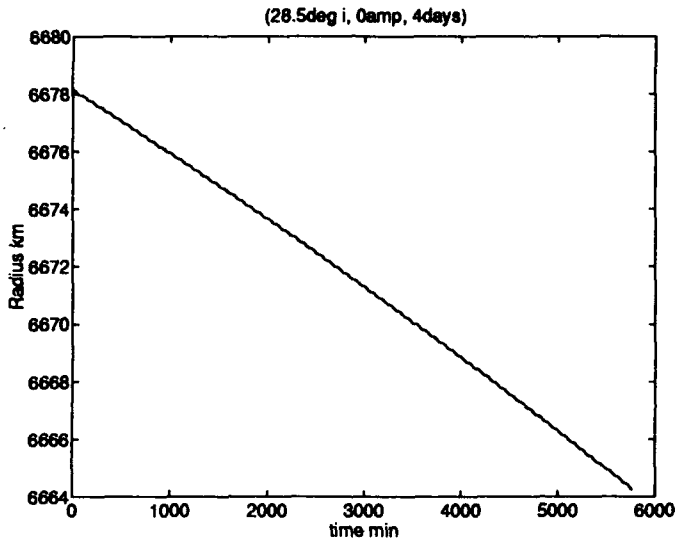

Figure 11.8 Deorbit of a solar dynamic powered SFP without using the propulsion system to maintain orbit. The solar dynamic powered SFP loses 14 *km* altitude in 4 *days*.

SFP (see Table 11.6).

Each of these was used in a numeric integrator without the electrodynamic propulsion system functioning. In 4 *days*, the SFP using solar dynamic power drops approximately 14 *km* in altitude (see Figure 11.8), while the all photovoltaic powered SFP drops 33 *km* (see Figure 11.9). This demonstrates the significance of aerodynamic drag and the significant advantage of solar dynamic power versus photovoltaic power. The decay rate for an SFP powered by all photovoltaic arrays is not acceptable because of its higher associated aerodynamic drag.

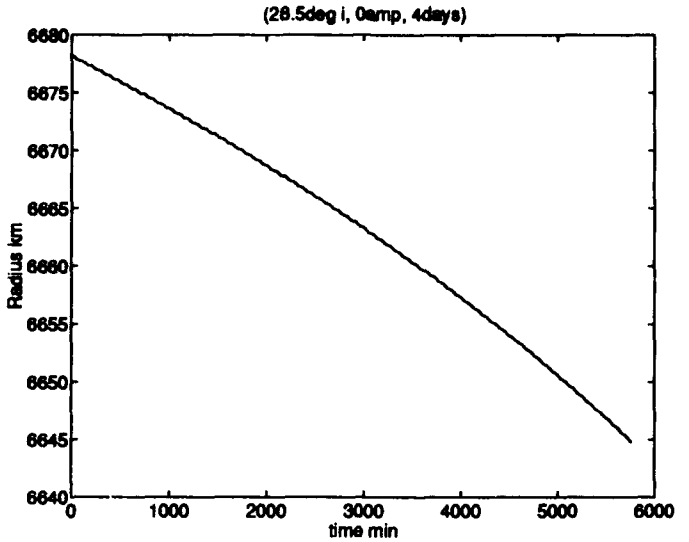

Figure 11.9 Deorbit of a photovoltaic powered SFP. This radius *vs* time plot shows that without using the propulsion system to maintain orbit, the all photovoltaic powered SFP loses 33 *km* altitude in 4 *days*.

11.10.2 Drag and Altitude. At 300 *km* altitude, the loss of 14 *km* in 4 *days* is still cause for concern. It was determined that 11 *kW* is required to overcome the effects of aerodynamic drag in the transfer orientation at an altitude of 300 *km* (see Figure 11.10). This leaves a sufficient surplus of power for external tank reduction and truss fabrication. The power requirements to maintain orbit are reduced as the altitude of the orbit is increased.

Aerodynamic drag decreases with altitude due to the two parameters ρ and V_r. The density of the atmosphere, ρ, and V_r decrease with r. According to Equation 11.2, a decrease in either of these parameters will decrease the aerodynamic drag force. The resulting acceleration on the SFP drops two orders of magnitude (10^{-5} to $10^{-7}\, m/s^2$) as the vehicle rises from 300 *km* to 500 *km* altitude. While the SFP loses 14 *km* altitude in 4 *days* at 300 *km*, at 500 *km* altitude it loses only 3 *km* in the same time period.

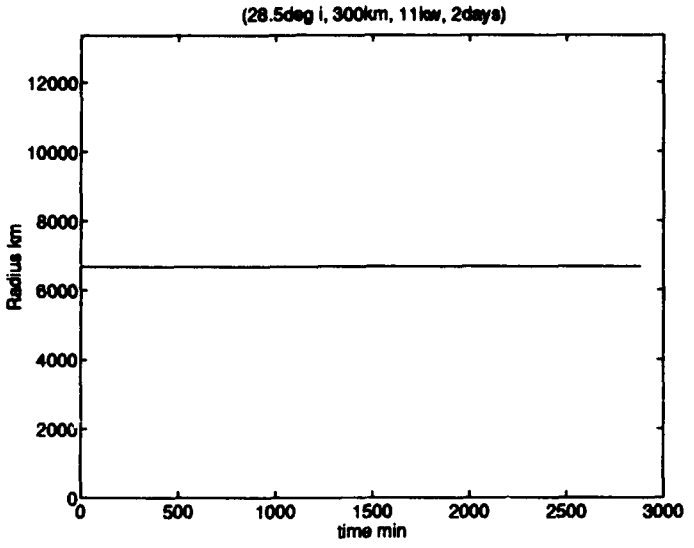

Figure 11.10 Orbit Maintenance. Eleven kW is required to maintain the SFP's 300 km altitude when it is in the transfer orientation.

11.11 SFP Integrated Truss Length vs *Number of Shielded Coils*

The shielded coil electrodynamic propulsion system generates thrust proportional to the effective length of the conductor, L. In a constant relative B-field, with a constant current, i, the magnitude of the thrust force, F, is given by the scalar equation:

$$F = iLB \tag{11.4}$$

Thus, with i and B fixed, the only way to increase F is to increase L. The effective length of the conductor is:

$$L = nl \tag{11.5}$$

There are two ways to increase L; either increase the number of turns, n, or increase the length of the truss, l.

The performance measure chosen for the analysis was vehicle acceleration, a, under fixed conditions. The maximum acceleration under fixed conditions can be directly related to the vehicle performance, in both orbital transfer and docking

maneuvers. Acceleration is simply:

$$a = \frac{F}{M} \tag{11.6}$$

The mass of the vehicle, M, increases with L. With an increase in l, a proportional increase occurs in the mass of the supporting truss, the conductor, and the shield. An increase in n causes a proportional increase in the conductor mass, and a possible increase in shield mass. The equation for the vehicle mass is:

$$M = M_0 + l\,\rho_T + 2nl\,\rho_C + l\;integer(\frac{n}{n_S} + 1)\,\rho_S \tag{11.7}$$

M_0 = the fixed mass of the vehicle

ρ_T = the mass per unit length of the truss

ρ_C = the mass per unit length of the conductor

ρ_S = the mass per unit length of the shield

n_S = the number of turns for which the shield is effective

$integer(\cdot)$ = the greatest integer $\leq$ the value inside $(\cdot)$

Combining the Equations 11.4, 11.5, 11.6, and 11.7 gives:

$$a = \frac{i\,n\,l\,B}{M_0 + l\,\rho_T + 2nl\,\rho_C + l\;integer(\frac{n}{n_S} + 1)\,\rho_S} \tag{11.8}$$

A parametric analysis was carried out by varying the truss length from 1 m to 200 m and the number of turns from 1 to 201. Figure 11.11 shows the resulting surface plot with the acceleration, a, on the vertical axis. The plot shows that an increase in n is generally better than an increase in l for increasing a in regions of practical interest. Note that the plot does not take into account any penalty for increases in size which were a primary concern during the design process because of

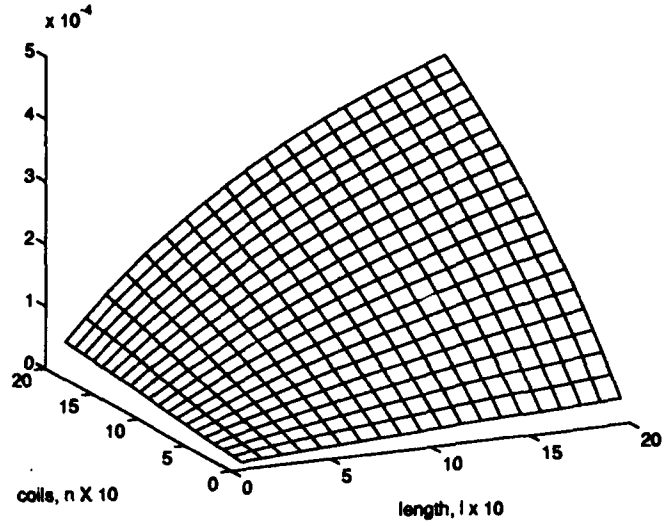

Figure 11.11 The surface plot shows that acceleration, a (vertical axis) increases faster by increasing n than by increasing l.

increased power requirements. This analysis was verified with the use of a non-linear optimization computer package, GINO (51).

The use of shielded conductor loops allows the truss lengths to be virtually any length desired. Because the target payload for the SFP is an external tank, the main integrated truss was required to be at least 50 m to allow for equipment clearances. The analysis of increasing the number of turns or the length of the truss to achieve a given force showed that increasing n was cheaper from a size standpoint than increasing l. As a result, the length of the main integrated truss was set to 50 m and the number of turns was adjusted to achieve the required forces.

XII. Conclusion and Recommendations

12.1 Conclusion

As described in the beginning of this report, the SFP design study focused on establishing the feasibility of a space facility to enhance the construction of other structures in space. The facility was to utilize external tanks from the space shuttle and electrodynamic propulsion. A prototype platform was designed that is capable of reducing external tanks into raw material, fabricating the raw material into trusses, and delivering the trusses anywhere in low inclination, low earth orbit. These capabilities were demonstrated in Chapter X.

12.2 Recommendations

The design study lays the foundation for a space fabrication platform by establishing feasibility. The broad nature of this task required a motivation to address all essential subject areas pertaining to the SFP. During the course of the study, it was recognized that further research in some areas will be essential to the SFP program planning phase. The following list identifies these subject areas:

- The automation required for truss fabrication needs formal design. Working models and simulations are recommended to refine all details of the truss fabrication process. The areas of interest span everything from reducing the external tank to manipulating the completed truss product for delivery.
- Further analysis of the SFP dynamic models is required. Nonlinear, time variant models should be used to refine the performance and control of the SFP. Changes to the current models would impact almost every aspect of the SFP design: propulsion, power, controller, etc.
- The potential for power regeneration and storage in the SFP needs to be readdressed. Utilization of V_{ind} and the forces associated with dragging should

be considered. Energy storage could include batteries, as well as other devices such as capacitors and momentum wheels.

- A review of the materials used throughout the SFP is required. Improvements in material technology should be incorporated. In many areas, the same capabilities may be realized at a lighter weight. For example, composites might replace aluminum in the integrated trusses, or conducting polymers might replace aluminum in the propulsion conductors.
- SFP heat transfer issues need further consideration. An in-depth analysis incorporating all the heat sources associated with the SFP and potential heat transfer methods is required.
- Further analysis of the SFP electromagnetic emission and susceptibility issues is required. Electromagnetic compatibility between the propulsion system, the fabrication equipment, and all other devices must be thoroughly considered in the design of the platform.

Appendix A. Additional ASSET Information

A.1 External Tank

The external tank is 46.9 m long by 8.4 m in diameter. Its mass is approximately 31,300 kg empty and nearly 752,800 kg when fully loaded with propellants. It has three primary structural components, the LO_2 tank, intertank, and LH_2 tank, made primarily of aluminum alloys (see Figure A.1). Its surface is coated with a spray-on foam insulation (SOFI) that helps maintain the temperatures of the propellants before and during launch (31:3.1). The intertank contains instrumentation, range safety components, and a solid rocket booster beam assembly, which distributes thrust loads from the solid rocket boosters. Due to the complexity of the LO_2 and intertank structures, only the LH_2 tank is used for salvage operations.

A.2 ASSET Construction

A dedicated space shuttle mission is required to set up ASSET. Table A.1 lists the cargo required for the mission. The external tank must be carried into orbit. In orbit, the remaining fuel is dumped and the range safety system is safed. Then, long duration EVAs install the boost/deboost modules, photovoltaic arrays, avionics, and reduction equipment. After the set up, external tank salvage operations begin.

A.3 Reduction Equipment

The following are descriptions of the reduction equipment not thoroughly developed in Chapter IV but applicable to the SFP. Figure A.2 provides an overview illustration.

A.3.1 Centerline Track. A pre-installed centerline track allows longitudinal motion of the centerline trolley and primary cutter power truck (31:5.13). The track is made of 15.2x15.2x0.317 cm thick square 2219 aluminum tubing and

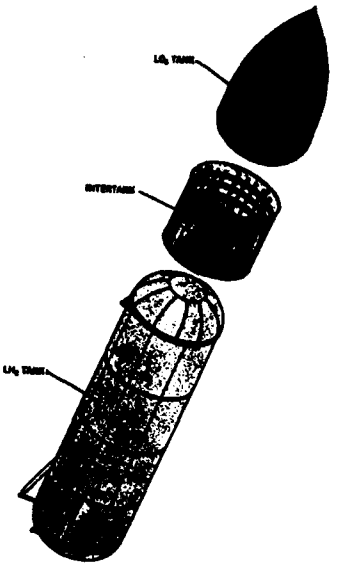

Figure A.1 The external tank is composed of the LO_2 tank, the intertank, and the LH_2 tank.

Item	Mass kg
Solar Photovoltaic Arrays	1000
Thermal Control System	1720
Electrical Power Subsystem	3247
IEA Structure	1228
Subtotal Power	7195
Boost/Deboost Modules	1432
First Year Hypergolics	5455
Second Year Hypergolics	5455
Subtotal Orbital Maintenance	12342
Robot Arm Truck	124
Primary Cutter	91
Spare Cutter	91
Centerline Track	125
External Tank Modifications	261
SOFI Workstation	526
Subtotal Reduction Tools	1218
Communications, Cameras, Lights, Avionics	350
Total First Flight Cargo Mass	21105

Table A.1 The space shuttle cargo manifest required for producing an AS-SET (31:H.9).

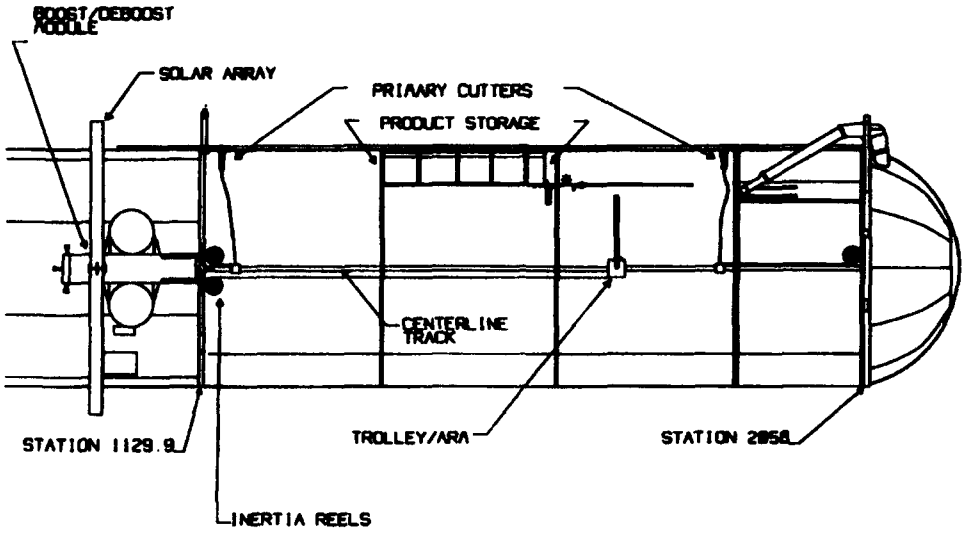

Figure A.2 Side view of the reduction equipment inside an ASSET for salvage operations.

extends from the forward most major ring frame to the aft most major ring frame in the center of the LH_2 tank (23.16 m long).

A.3.2 Centerline Trolley. The centerline trolley consists of an extendible arm with an end effector that can be rotated about the centerline track (see Figure A.3). The whole trolley moves along the track on drive wheels. The trolley allows the transport of material and the primary cutter within the LH_2 tank. Power and control are provided through cables from an inertial reel.

A.3.3 Primary Cutter. The primary cutter moves an electron beam cutter longitudinally and laterally to cut out composite sections of I-beam, flat plate, and SOFI (see Figure A.4(31:5.20). It attaches to pairs of adjacent I-beams and is moved longitudinally by drive wheels positioned below the I-beam flanges. The electron beam cutter is moved laterally by a shaft to permit cross cutting. The primary cutter can be moved by the centerline trolley. Power is provided by a line from a power truck located on the centerline track as shown in Figure A.2.

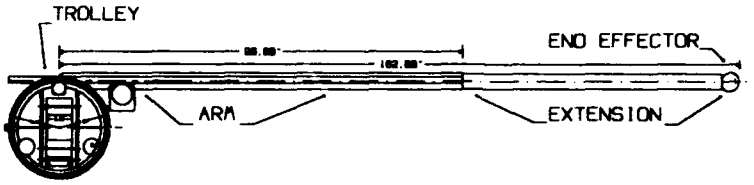

Figure A.3 Cross-section of the centerline trolley. The centerline trolley carries an extendible arm with an end effector.

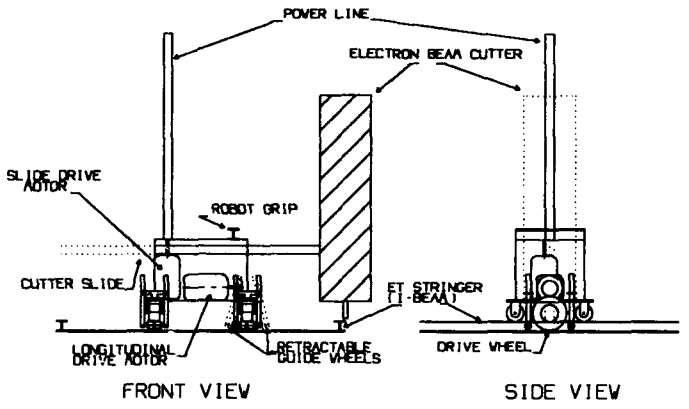

Figure A.4 The primary cutter moves along the LH_2 tank I-beams cutting out sections of the tank skin.

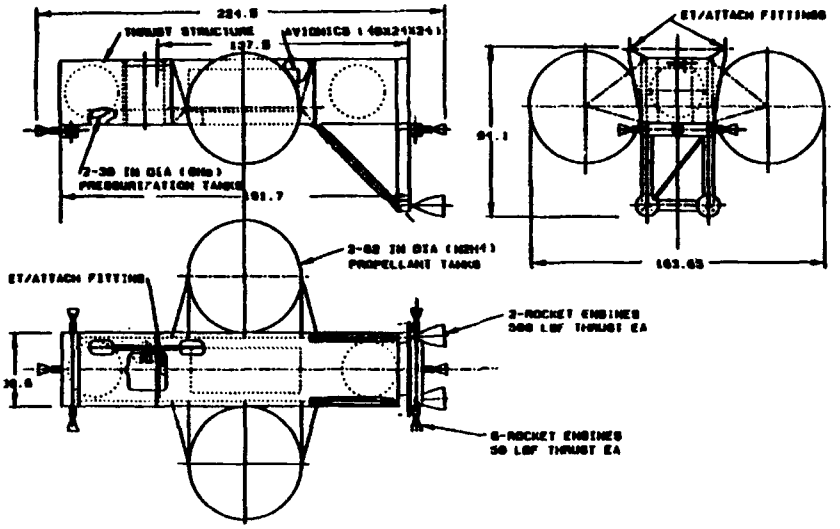

Figure A.5 ASSET uses boost/deboost modules developed for the proposed External Tank Gamma Ray Imaging Telescope for attitude and altitude control.

A.4 External ASSET Equipment

A.4.1 Boost/Deboost Module. ASSET attitude and altitude control is provided by 2 boost/deboost modules attached at the solid rocket booster thrust fittings of the intertank. The boost/deboost modules are based on the design recommendations that Martin Marietta developed for the proposed External Tank Gamma Ray Imaging Telescope (see Figure A.5). Each module has two 2224 N, 230 s specific impulse main thrusters and six 222 N attitude thrusters, all fueled with hydrazine. With ASSET maintained in the minimum drag attitude (nose of the external tank in the velocity vector direction), the initial supply of fuel is estimated to last two years.

A.4.2 Power. ASSET electrical power is provided by two photovoltaic arrays attached, one each, to the boost/deboost modules. The drag area for the entire power system is 424 in^2. The arrays produce 31.13 kW of power. Forty-nine percent of the power is used for charging four NiH_2 batteries. The batteries provide

power during the eclipse periods. Eclipse periods occur for approximately 36 out of every 91 minutes (31:5.23). The remaining 15.88 kW is sent to the electrical equipment subsystem, allowing a 12 kW load.

Appendix B. SFP Produced Truss Properties

B.1 Introduction

The SFP truss maker produces square trusses of varying lengths (see Figure B.1). The SFP truss is composed of three separate entities: Longitudinal, cross, and diagonal members. This appendix documents the material and physical properties of each truss member and the physical properties of the SFP produced truss. These properties can be used by the end user to determine how and when the SFP produced truss can be used in their specific application.

B.2 Truss Member Material Properties

All three SFP truss member types are composed of the same aluminum alloy, Al 2219-T87. The material properties associated with this material are shown in Table B.1.

B.3 Longitudinal and Cross Member Physical Properties

The longitudinal truss members are continuous T-beams with cross section and dimensions shown in Figure B.2. The cross members are 1.035 m long T-beams and are attached orthogonally to either the web or flange of the longitudinal member, depending upon which side of the truss is being viewed. The cross members have the

Young's Modulus (E)	$7.308 \times 10^{10}\ Pa$
Shear Modulus (G)	$2.758 \times 10^{10}\ Pa$
Yield Stress (σ_y)	$4.137 \times 10^{8}\ Pa$
Ultimate Stress (σ_u)	$4.826 \times 10^{8}\ Pa$
Coefficient of Thermal Expansion	$23 \times 10^{-6}/°C$
Mass Density (ρ)	$2851\ kg/m^3$
Poisson's Ratio (ν)	0.33

Table B.1 Material properties of the aluminum alloy, Al 2219-T87.

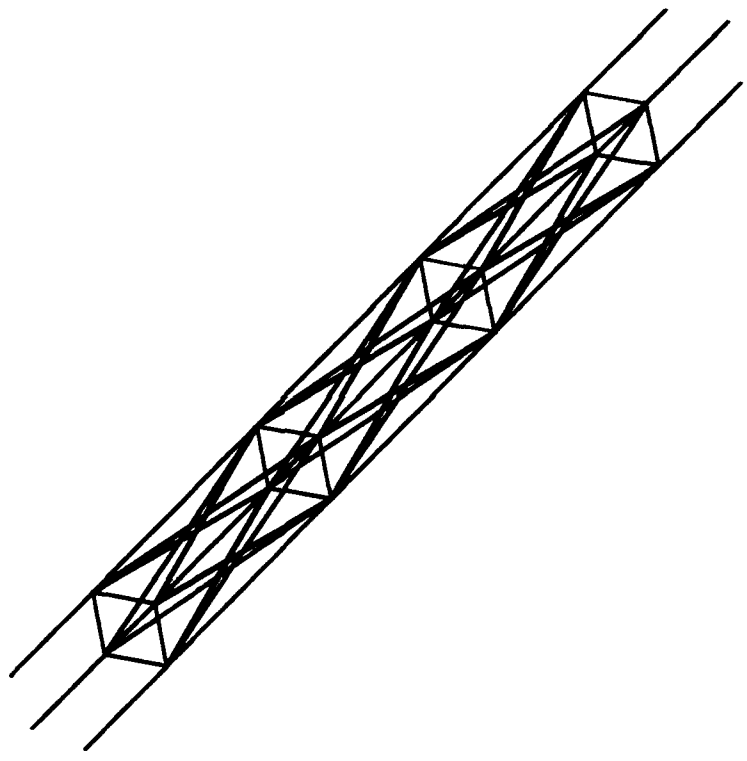

Figure B.1 This view shows three bays of SFP produced truss. The truss is composed of longitudinal, cross, and diagonal members.

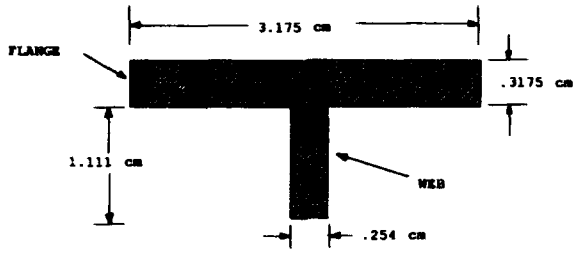

Figure B.2 T-beam cross section for the SFP produced truss longitudinal and cross member.

same cross section as the longitudinal members (see Figure B.2). Section properties for the cross and longitudinal members are shown in Table B.2.

B.4 Diagonal Member Physical Properties

The diagonal truss members are 4.655 m flat strips with cross section and dimensions shown in Figure B.3. The diagonal members are also attached to either the

Length (Longitudinal Member)	Variable
Length (Cross Member)	1.035 m
Flange Length	3.175 cm
Flange Width	0.318 cm
Web Length	1.111 cm
Web Width	0.254 cm
Area	1.291 cm^2
Torsional Constant (K)	0.004 N/cm^2

Table B.2 SFP produced truss longitudinal and cross member section properties.

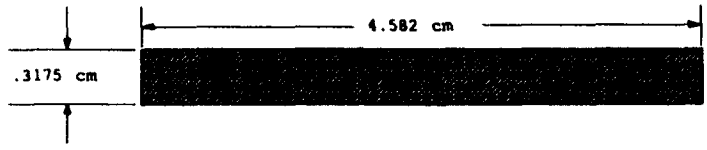

Figure B.3 Cross sectional view of the box beams used to model the main integrated truss.

Length	4.655 m
Width	4.582 cm
Thickness	0.3175 cm
Area	1.455 cm^2
Torsional Constant (K)	0.047 N/cm^2

Table B.3 SFP produced truss diagonal member section properties.

web or flange of the longitudinal truss member. Section properties for the diagonal member are shown in Table B.3.

B.5 Truss Mass Per Unit Length

The mass of the truss is the sum of the masses for all the longitudinal, cross, and diagonal members which make up the truss. By dividing the sum of the member masses by the total length of the truss, the mass per unit length of the truss section can be determined.

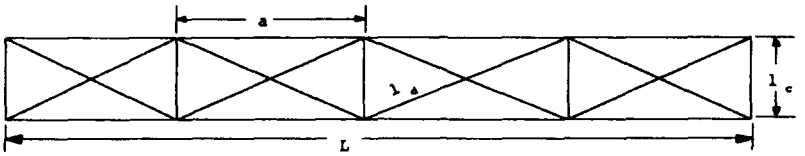

l_d - LENGTH OF DIAGONAL TRUSS MEMBER

l_c - LENGTH OF CROSS TRUSS MEMBER

L - TOTAL LENGTH OF TRUSS

a - LENGTH OF ONE TRUSS BAY

Figure B.4 Side view of SFP produced truss defining dimensions used to calculate the mass per unit length of the truss.

The masses of the truss members are:

$$M_l = 4\rho A_l L \tag{B.1}$$

$$M_c = 4(\frac{L}{a} + 1)\rho A_c l_c \tag{B.2}$$

$$M_d = 8(\frac{L}{a})\rho A_d l_d \tag{B.3}$$

Where M_l, M_c, and M_d are the masses for the longitudinal, cross, and diagonal members, respectively. Figure B.4 defines the remainder of the terms in Equations B.1, B.2, and B.3. The total mass of the truss is then:

$$M_{Tot} = M_l + M_c + M_d \tag{B.4}$$

Therefore, the mass per unit length of any truss section can be found by dividing M_{Tot} by the total truss length, L.

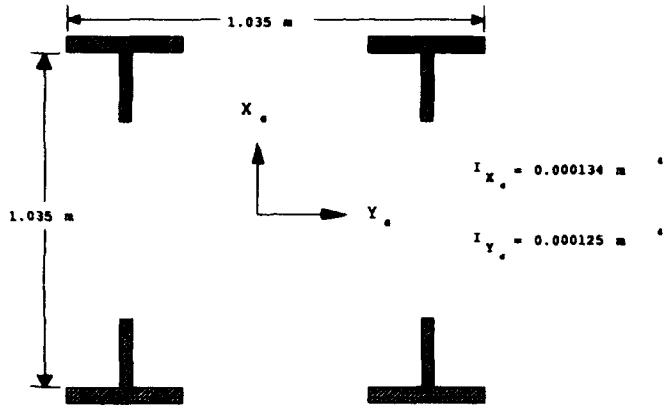

Figure B.5 The intersection of the X and Y axes locates the geometric center of the SFP produced truss. I_X and I_Y were determined for these axes.

B.6 Truss Properties

The product EA is known as the axial stiffness. Where E is Young's Modulus and A is four times the cross sectional area of one longitudinal member. The axial stiffness for the SFP produced truss is then:

$$EA = 4EA_l = 4(7.308 \times 10^{10})(0.0001291) = 3.774 \times 10^7 \, N \qquad \text{(B.5)}$$

The product EI is known as the bending stiffness. Where I is either the moment of inertia about the X or Y axes which run through the geometric center of the cross section (see Figure B.5). The moment of inertia about X_G was determined to be $1.34 \times 10^{-4} \, m^4$ and the moment about Y_G was determined to be $1.25 \times 10^{-4} \, m^4$. Because I_Y is smaller than I_X, the more conservative value, I_Y, is used to determine the bending stiffness for the truss.

$$EI = (7.308 \times 10^{10})(1.25 \times 10^{-4}) = 9.135 \times 10^6 \, N \cdot m^2 \qquad \text{(B.6)}$$

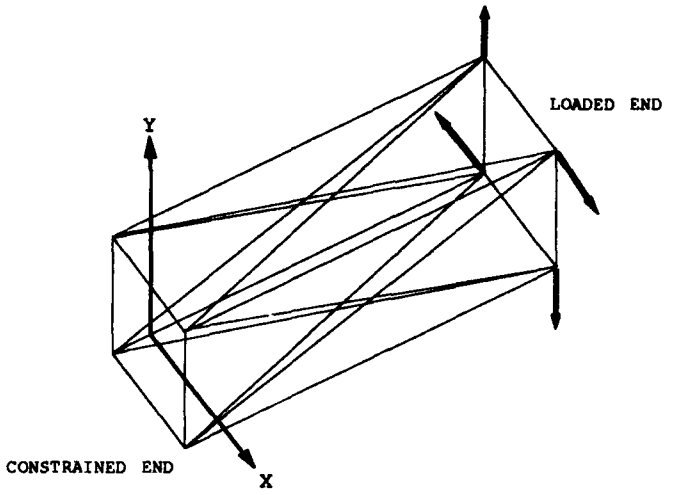

Figure B.6 Finite element model for determining the torsional stiffness of the SFP produced truss.

The product KG is known as the torsional stiffness. Where G is the shear modulus and K is a torsional constant. K is a factor dependent upon the form and dimensions of the cross section. For a circular section, K is the polar moment of inertia J. For non-circular sections, K is less than J and may only be a small fraction of J (12:4.31). A simple expression for K does not exist for the SFP produced truss. However, the torsional stiffness of a bar can be expressed by the general expression:

$$KG = \frac{TL}{\theta} \tag{B.7}$$

where T is a torque applied to the end of the truss, L is the length of the truss, and θ is the resulting rotation due the applied torque, T (12:4.32). The torsional stiffness of the SFP produced truss was determined using Equation B.7 in conjunction with a small finite element model. The general geometry of the finite element model is shown in Figure B.6. The finite element model was one bay long, $L = 4.529\ m$ and was subjected to an arbitrary torque as shown in Figure B.7. The resulting rotation,

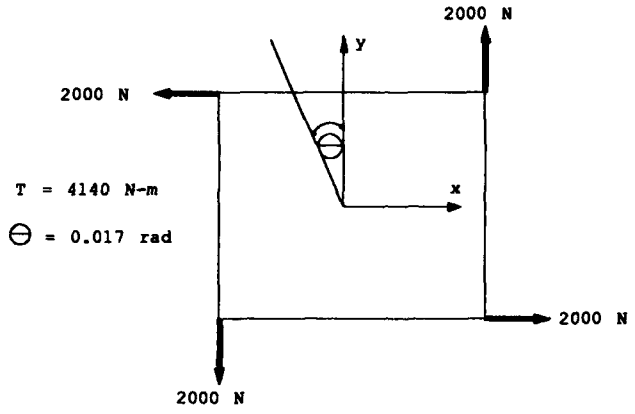

Figure B.7 Finite element model for determining the torsional stiffness for the SFP produced truss.

A	$5.820\ cm^2$
I_X	$1.34 \times 10^{-4}\ m^4$
I_Y	$1.25 \times 10^{-4}\ m^4$
AE	$3.774 \times 10^{7}\ N$
EI	$9.135 \times 10^{6}\ N \cdot m^2$
KG	$1.103 \times 10^{6}\ N \cdot m^2$

Table B.4 SFP produced truss stiffness properties.

θ was found to be

$$\theta = 0.017\ rad \tag{B.8}$$

Plugging the value found for θ into Equation B.7 results in a torsional stiffness of:

$$KG = \frac{TL}{\theta} = \frac{(4140)(4.529)}{0.017} = 1.103 \times 10^{6}\ N \cdot m^2 \tag{B.9}$$

The SFP produced truss stiffness properties are summarized in Table B.4.

Appendix C. Reference Frames

To develop and use the various equations of motion, five coordinate systems are needed. For satellites orbiting the Earth, a suitable inertial reference frame is the geocentric-equatorial coordinate system. Another inertial reference frame, the Earth-centered inertial coordinate system is also used. The use of the dipole model for the Earth's magnetic field requires the use of the Greenwich-equatorial reference frame. An orbital reference frame and body-centered reference frame are required to describe position and orientation.

C.1 Geocentric-Equatorial Coordinate System

The origin of the geocentric-equatorial coordinate system, the $\hat{i}$-frame, is coincident with the Earth's geographic center. The fundamental plane — the plane described by the X and Y directions — is defined by the equator with the positive X-axis pointing in the direction of the vernal equinox (the point in the sky where the sun crosses the equator from south to north on the first day of spring). The positive Z-axis points in the direction of the geographic north pole (coincident with the Earth's spin axis). The positive Y-axis points in the direction to complete the right-handed, orthogonal coordinate system (see Figure C.1). It should be noted that this reference frame is not fixed with respect to the Earth and does not rotate with it. The unit vectors $\hat{i}_1$, $\hat{i}_2$, and $\hat{i}_3$, lie along the X, Y, and Z axes respectively (3:55–56).

C.2 Earth-Centered Inertial Coordinate System

The Earth-centered inertial coordinate system, the $\hat{e}$-frame, is similar to the geocentric-equatorial coordinate system. The origin of the Earth-centered inertial coordinate system is the Earth's geographic center. The positive X_e-axis points in the direction of the line of nodes of the orbit of interest (defined on page C-7), at a specific reference time t_0. Note that the line of nodes changes over time, so the

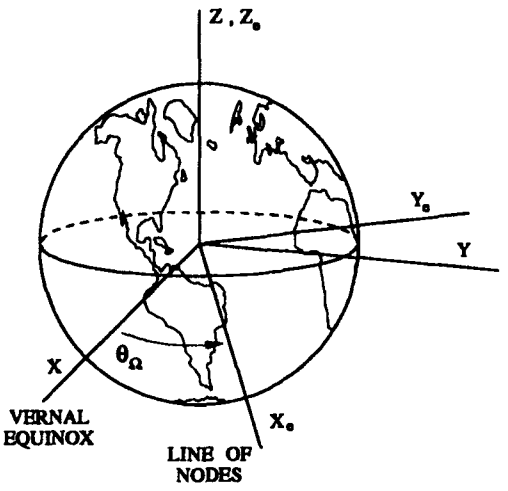

Figure C.1 Geocentric Equatorial Frame: the X-axis points toward the vernal equinox, the Z-axis is coincident with the Earth's spin axis, and the Y-axis completes the basis. Earth Centered Inertial Frame: the X_e-axis points along the line of nodes at a fixed time, the Z_e-axis is coincident with the Earth's spin axis, and the Y_e-axis completes the basis.

reference frame is fixed at t_0. The positive Z_e-axis points in the direction of the geographic north pole (coincident with the Earth's spin axis). The positive Y_e-axis points in the direction to complete the right-handed, orthogonal coordinate system. The unit vectors $\hat{e}_1$, $\hat{e}_2$, and $\hat{e}_3$ lie along the X_e, Y_e, and Z_e axes respectively (see Figure C.1).

To relate the Earth-centered inertial coordinate system to the geocentric-equatorial coordinate system, the angle between $\hat{e}_1$ and $\hat{i}_1$ must be known. This angle, θ_Ω, is the right ascension of the ascending node at a fixed time. To translate a vector from the $\hat{e}$-frame to the $\hat{i}$-frame, a rotation matrix, $R^{ie}(\theta_\Omega)$, can be defined. For this "negative 3-rotation," the rotation matrix is given by Hughes (35:15) as

$$R^{ie}(\theta_\Omega) = \begin{bmatrix} c\theta_\Omega & -s\theta_\Omega & 0 \\ s\theta_\Omega & c\theta_\Omega & 0 \\ 0 & 0 & 1 \end{bmatrix} \tag{C.1}$$

where

$$c \equiv \cos$$

$$s \equiv \sin$$

To translate a vector from the $\hat{i}$-frame to the $\hat{e}$-frame, a reverse-rotation matrix, $R^{ei}(\theta_\Omega)$, can also be defined. The reverse-rotation matrix is the transpose of $R^{ie}(\theta_\Omega)$ and is given by

$$R^{ei}(\theta_\Omega) = \begin{bmatrix} c\theta_\Omega & s\theta_\Omega & 0 \\ -s\theta_\Omega & c\theta_\Omega & 0 \\ 0 & 0 & 1 \end{bmatrix} \tag{C.2}$$

C.3 Greenwich-Equatorial Coordinate System

The Greenwich-equatorial coordinate system, the $\hat{g}$-frame, is the same as the geocentric-equatorial coordinate system except for a rotation about the Z-axis. The Greenwich-equatorial coordinate system is fixed to the Earth and rotates with it. The fundamental plane is defined by the equator with the r_g-axis pointing in the direction of the Greenwich prime meridian (0°E longitude). The positive z_g-axis points in the direction of the geographic north pole. The θ_g-axis points in the direction 90°E longitude to complete the right-handed, orthogonal coordinate system (see Figure C.2). The unit vectors $\hat{g}_r$, $\hat{g}_\theta$, and $\hat{g}_3$, lie along the r_g, θ_g, and z_g axes respectively.

To relate the Greenwich-equatorial coordinate system to the geocentric-equatorial coordinate system, the angle between $\hat{g}_r$ and $\hat{i}_1$ must be known. This angle, Θ_g, is called the *Greenwich sidereal time*. If Θ_{g_0} is known for some particular time t_0, Θ_g at any other time, t, can be determined from

$$\Theta_g = \Theta_{g_0} + \omega_\oplus (t - t_0) \tag{C.3}$$

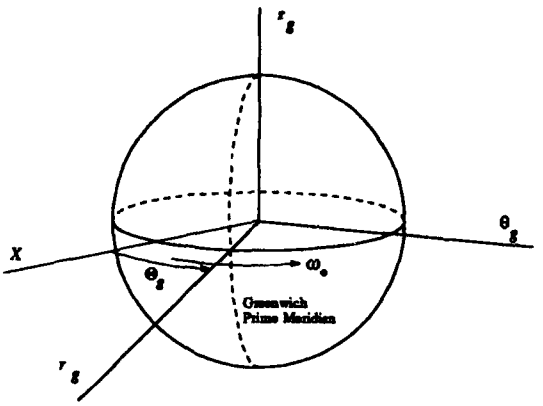

Figure C.2 Greenwich Equatorial Frame: the r_g-axis points toward the Greenwich prime meridian, the z_g-axis is coincident with the Z-axis, and the θ_g-axis completes the basis.

where $\omega_\oplus$ is the angular velocity of the Earth:

$$\omega_\oplus = 7.2921 \times 10^{-5} \frac{rad}{s}$$

Values of Θ_g at 0:00 hours, Universal Time, for each day of the year can be obtained from the *American Ephemeris and Nautical Almanac* (21). To translate a vector from the $\hat{g}$-frame to the $\hat{i}$-frame, a rotation matrix, $R^{ig}(\Theta_g)$, can be defined. For this "negative 3-rotation," the rotation matrix is given by Hughes (35:15) as

$$R^{ig}(\Theta_g) = \begin{bmatrix} c\Theta_g & -s\Theta_g & 0 \\ s\Theta_g & c\Theta_g & 0 \\ 0 & 0 & 1 \end{bmatrix} \tag{C.4}$$

To translate a vector from the $\hat{i}$-frame to the $\hat{g}$-frame, a reverse-rotation matrix, $R^{gi}(\Theta_g)$, can also be defined. The reverse-rotation matrix is the transpose of $R^{ig}(\Theta_g)$

and is given by

$$R^{gi}(\Theta_g) = \begin{bmatrix} c\Theta_g & s\Theta_g & 0 \\ -s\Theta_g & c\Theta_g & 0 \\ 0 & 0 & 1 \end{bmatrix} \tag{C.5}$$

C.4 Orbital Coordinate System

The orbital coordinate system, the $\hat{a}$-frame, is one of the primary reference frames for the work that follows. The origin of the $\hat{a}$-frame is coincident with the center of the Earth. The frame is fixed to a point in a reference orbit; the reference point, and therefore the orbital frame, rotates at orbital rate. This differs from a perifocal coordinate system in that the orbital frame rotates as the vehicle moves through the orbit, while the perifocal frame is fixed with the x-axis (or r-axis) pointing in the direction of the perigee. The fundamental plane of the $\hat{a}$-frame is defined by the plane of the orbit. The r_a-axis points along the line connecting the origins of the $\hat{i}$-frame and the $\hat{a}$-frame, pointing away from the $\hat{i}$-frame origin — this is the R-bar direction. The θ_a-axis points along the tangent to the orbit path (for a reference point in a circular orbit), in the direction of motion — this is the V-bar direction. The positive z_a-axis is normal to the fundamental plane, pointing to complete the right-handed, orthogonal coordinate system — this is the Z-bar direction (see Figure C.3 and C.4). The unit vectors, $\hat{a}_r$, $\hat{a}_\theta$, and $\hat{a}_3$ lie along the r_a, θ_a, and z_a axes respectively.

Before developing the transformation matrix to transform from the $\hat{i}$-frame to the $\hat{a}$-frame, the orbit must be considered further. Six orbit elements make up the classic set used to pinpoint the position of a satellite along the orbit at a particular time. The six elements are given by Wiesel (93:57) as

1. a, the semi-major axis — a constant defining the size of an elliptic orbit. It is defined as one-half the distance from one focus, to a point on the orbit path, to the other focus.

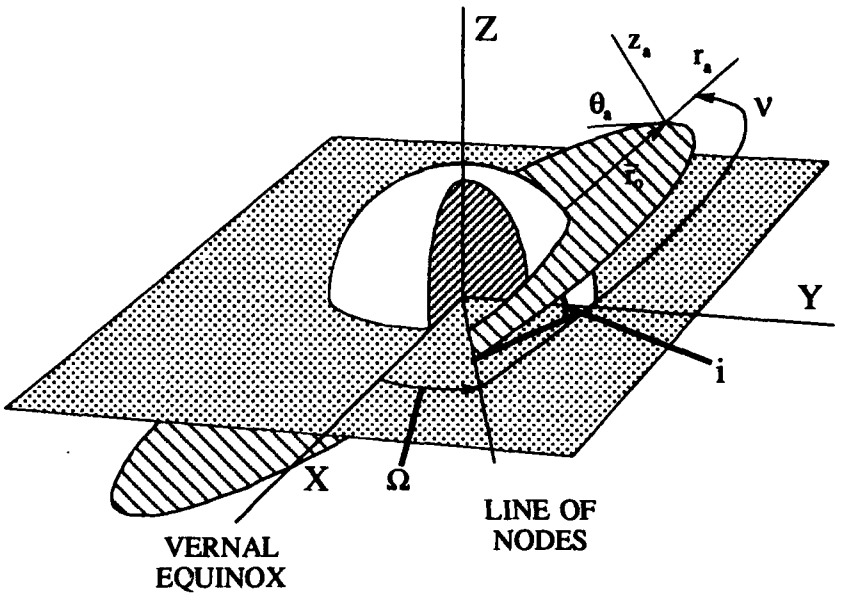

Figure C.3 The orbital reference frame with the origin translated for clarity to a point on the orbit path.

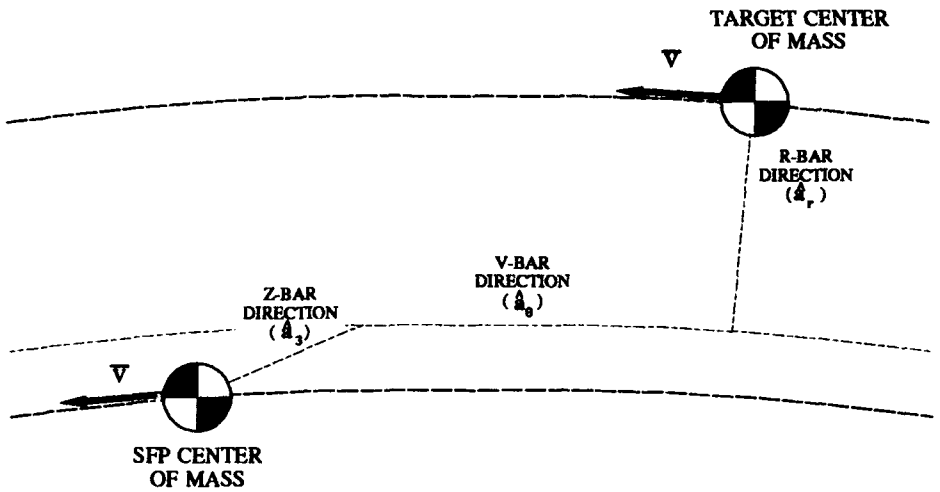

Figure C.4 R-bar is defined along the radial direction, V-bar is defined along the orbit path direction, and Z-bar is defined along the out of plane direction.

2. e, the eccentricity — a constant defining the shape of the conic orbit. If $e = 0$, the orbit is circular (which is a degenerate case of an elliptical orbit with both foci at the center), if $0 < e < 1$, the orbit is elliptical, if $e = 1$, the orbit is parabolic, and if $e > 1$, the orbit is hyperbolic.

3. T_0, the time of perigee passage — the time the orbit vehicle passes the point closest to the Earth's center, thus fixing the position of the vehicle at one instant in time.

4. Ω, the right ascension of the ascending node — the angle measured from the vernal equinox eastward along the equator to the point where the orbit's path crosses the equatorial plane from south to north (the line resulting from the intersection of the planes being the line of nodes). $0 \leq \Omega \leq 180°$.

5. i, the orbital inclination — the angle measured from the equatorial plane to the orbit plane at the ascending node.

6. ω, the argument of perigee — the angle measured from the line of nodes, along the orbit path in the direction of motion, to the perigee point.

Once the position of the vehicle in the orbit is determined, the transformation matrix going from the $\hat{i}$-frame to the $\hat{a}$-frame can be determined. The transformation is carried out by first rotating through Ω, about the Z-axis — this aligns the X-axis with the line of nodes. The second step is to rotate the new reference frame (the $X'Y'Z'$-frame) through i, about the X'-axis (the axis of the new reference frame aligned with the line of nodes) — this rotates the Z'-axis to form the z_a-axis, and brings the Y'-axis into the orbit's fundamental plane. The last step is to rotate the newest reference frame (the $X''Y''z_a$-frame) through ν, the true anomaly (which is the angle measured from the line of nodes, along the orbit path in the direction of motion, to the vehicle's position), about the z_a-axis — this aligns the X''-axis with the r_a-axis. If the transformation was to the perifocal coordinate system, the last rotation would actually be a rotation through ω, thus pointing the r_a-axis toward

the perigee. However, the $\hat{a}$-frame is actually fixed to the orbital vehicle, so ν is time variant. To find the true anomaly, ν, the eccentric anomaly, E, must first be determined. The value of E is obtained for any time, t, from the form of Kepler's equation

$$E - e \sin E = \sqrt{\frac{\mu}{a^3}} (t - T_0) \tag{C.6}$$

where $\mu = G(m_1 + m_2)$ — G is the universal gravitational constant, and m_1 and m_2 are the masses of the orbiting bodies. For artificial satellites in Earth's orbit, $G(m_1 + m_2) \approx GM_\oplus$ and (90:F-175, F-178)

$$\begin{aligned} G &= 6.6720 \times 10^{-11} \frac{N \cdot m^2}{kg^2} \\ M_\oplus &= 5.979 \times 10^{24}\ kg \\ \mu &= 3.9892 \times 10^{14} \frac{m^3}{s^2} \end{aligned}$$

and e, a, and T_0 are from the set of classic orbit elements. Equation C.6 is transcendental and must be solved numerically. Once E is known, the true anomaly, ν, can be determined from:

$$\tan \frac{1}{2}\nu = \sqrt{\frac{1+e}{1-e}} \tan \frac{1}{2}E \tag{C.7}$$

which gives ν without quadrant ambiguity (93:54–65). The rotation matrix which transforms from the $\hat{i}$-frame to the $\hat{a}$-frame can now be determined. This rotation is a classic "3-1-3-rotation" and is given by (35:21):

$$\begin{aligned} R^{ai} &= R_3(\nu)\, R_1(i)\, R_3(\Omega) \\ &= \begin{bmatrix} c\nu & s\nu & 0 \\ -s\nu & c\nu & 0 \\ 0 & 0 & 1 \end{bmatrix} \begin{bmatrix} 1 & 0 & 0 \\ 0 & ci & si \\ 0 & -si & ci \end{bmatrix} \begin{bmatrix} c\Omega & s\Omega & 0 \\ -s\Omega & c\Omega & 0 \\ 0 & 0 & 1 \end{bmatrix} \end{aligned}$$

$$= \begin{bmatrix} c\Omega c\nu - s\Omega cisv & s\Omega c\nu + c\Omega cisv & sisv \\ -c\Omega s\nu - s\Omega cicv & -s\Omega s\nu + c\Omega cicv & sicv \\ s\Omega si & -c\Omega si & ci \end{bmatrix} \tag{C.8}$$

and

$$R^{ia} = R_3(-\Omega) R_1(-i) R_3(-\nu) = R^{ai^T} \tag{C.9}$$

C.5 Body-Centered Coordinate System

The body-centered coordinate system (also known as the principal-body-axis frame), the $\hat{b}$-frame, is the other primary reference frame used in this design study. The $\hat{b}$-frame is attached to the SFP, with the origin located at the platform's center of mass. The basis is aligned so that the moment of inertia tensor is diagonal; the unit vectors describing the reference frame lie along the principal body axes (93:104–106). The orientation of the $\hat{b}$-frame with respect to the $\hat{a}$-frame is described by three angles: yaw, ψ, pitch, θ, and roll, ϕ. The fundamental orientation ($\psi = \theta = \phi = 0°$) of the $\hat{b}$-frame aligns the positive x_b-axis, the positive y_b-axis, and the positive z_b-axis with the positive r_a-axis, the positive θ_a-axis, and the positive z_a-axis respectively. The unit vectors, $\hat{b}_1$, $\hat{b}_2$, and $\hat{b}_3$ lie along the x_b, y_b, and z_b axes respectively. The transformation from the $\hat{a}$-frame to the $\hat{b}$-frame is commonly described by first yawing about the r_a-axis, then pitching about the new lateral axis, and finally rolling about the newest longitudinal axis (93:112). The rotation matrices are given by (35:20):

$$\begin{aligned} R^{ba} &= R_{z_a}(\phi) R_{\theta_a}(\theta) R_{r_a}(\psi) \\ &= R_2(\phi) R_3(\theta) R_1(\psi) \\ &= \begin{bmatrix} c\phi c\theta & c\phi s\theta c\psi + s\phi s\psi & c\phi s\theta s\psi - s\phi c\psi \\ -s\theta & c\theta c\psi & c\theta s\psi \\ s\phi c\theta & s\phi s\theta c\psi - c\phi s\psi & s\phi s\theta s\psi + c\phi c\psi \end{bmatrix} \end{aligned} \tag{C.10}$$

and

$$
\begin{aligned}
R^{ab} &= R_1(-\psi)\, R_3(-\theta)\, R_2(-\phi) \\
&= R^{ba\,T} \\
&= \begin{bmatrix} c\phi c\theta & -s\theta & s\phi c\theta \\ c\phi s\theta c\psi + s\phi s\psi & c\theta c\psi & s\phi s\theta c\psi - c\phi s\psi \\ c\phi s\theta s\psi - s\phi c\psi & c\theta s\psi & s\phi s\theta s\psi + c\phi c\psi \end{bmatrix}
\end{aligned}
\tag{C.11}
$$

Appendix D. Earth's Magnetic Dipole Model

The Earth's magnetic field can be descrbed as:

$$\overline{B} = -\overline{\nabla} V \tag{D.1}$$

where V is the scalar magnetic potential. V, is defined as

$$V = \frac{\overline{M} \cdot \overline{r}}{r^3} \tag{D.2}$$

where $\overline{M}$ is the vector magnetic moment, $\overline{r}$ is the vector distance from the center of the dipole, and r is the magnitude of $\overline{r}$. The magnetic moment vector points toward the austral dipole pole, along the axis of the simple dipole. Expressed in the $\hat{g}$-frame, the magnetic moment vector is given by

$${}^{g}\overline{M} = M \cos \Phi_0 \cos \Lambda_0 \, \hat{g}_r + M \cos \Phi_0 \sin \Lambda_0 \, \hat{g}_\theta + M \sin \Phi_0 \, \hat{g}_3 \tag{D.3}$$

where M is the magnitude of the magnetic dipole, Φ_0 is the latitude and Λ_0 is the longitude of the austral pole of the dipole model:

$$\begin{aligned} M &= 8.05 \times 10^{15} \, T \cdot m^3 \\ \Phi_0 &= 78.5^\circ S \\ \Lambda_0 &= 111.0^\circ E \end{aligned}$$

Using the transformation matrices R^{ig} (Equation C.4) and R^{ai} (Equation C.8), ${}^{g}\overline{M}$ expressed in the $\hat{a}$-frame is

$$\begin{aligned} {}^{a}\overline{M} &= R^{ag}\,{}^{g}\overline{M} \\ &= R^{ai}R^{ig}\,{}^{g}\overline{M} \\ &= M_1\hat{a}_r + M_2\hat{a}_\theta + M_3\hat{a}_3 \end{aligned} \tag{D.4}$$

where, after simplification using various trigonometric identities (6:135–140), M_1, M_2, and M_3 can be expressed as

$$\begin{aligned} M_1 &= M\left\{c\Phi_0\left[c\nu c\left(\Omega-\Theta_g-\Lambda_0\right)-s\nu cis\left(\Omega-\Theta_g-\Lambda_0\right)\right]+s\Phi_0 s\nu si\right\} \quad \text{(D.5)} \\ &\equiv Mm_1 \\ M_2 &= M\left\{c\Phi_0\left[-s\nu c\left(\Omega-\Theta_g-\Lambda_0\right)-c\nu cis\left(\Omega-\Theta_g-\Lambda_0\right)\right]+s\Phi_0 c\nu si\right\} \quad \text{(D.6)} \\ &\equiv Mm_2 \\ M_3 &= M\left\{c\Phi_0 sis\left(\Omega-\Theta_g-\Lambda_0\right)+s\Phi_0 ci\right\} \quad \text{(D.7)} \\ &\equiv Mm_3 \end{aligned}$$

where

$$\begin{aligned} c &\equiv cos \\ s &\equiv sin \end{aligned}$$

and from Appendix C

$$\begin{aligned} \nu &\equiv \text{true anomoly along orbit path} \\ \Omega &\equiv \text{right ascension of the ascending node} \\ \Theta_g &\equiv \text{Greenwich sidereal time} \\ i &\equiv \text{orbit plane inclination} \end{aligned}$$

The vector, $\overline{r}$, describes the position of the reference point, relative to the center of the dipole, in the $\hat{a}$-frame. For the simple dipole model, $\overline{r}$, is given by (93:63)

$$\begin{aligned} {}^{a}\overline{r} &= (r_{\oplus} + r_{alt})\,\hat{a}_r = \frac{a(1-e)}{1+e\cos\nu}\,\hat{a}_r \\ &= r_o\,\hat{a}_r \end{aligned} \tag{D.8}$$

where $r_{\oplus}$ is the radius of the Earth (90:F-175):

$$r_{\oplus} = 6.3713 \times 10^6\, m$$

a is the semi-major axis of an elliptic orbit, e is the eccentricity of a conic orbit, and r_{alt} is the reference point's altitude. This equation shows that the radius vector, in the $\hat{a}$-frame, is time-variant (due to the time dependency of ν). The scalar magnetic potential is obtained from Equation D.2 giving

$$V = \frac{\overline{M}\cdot\overline{r}}{r^3} = \frac{M_1 r_1 + M_2 r_2 + M_3 r_3}{r^3} \tag{D.9}$$

where

$$r = \left(r_1^2 + r_2^2 + r_3^2\right)^{\frac{1}{2}}$$

The vector magnetic potential is then obtained from Equation D.1

$$\begin{aligned} \overline{B} &= -\overline{\nabla} V = -\frac{\partial V}{\partial r_1}\hat{a}_r - \frac{\partial V}{\partial r_2}\hat{a}_\theta - \frac{\partial V}{\partial r_3}\hat{a}_3 \\ \overline{B} &= -\left[\frac{M_1}{r^3} - \frac{3\,(M_1 r_1 + M_2 r_2 + M_3 r_3)\,r_1}{r^5}\right]\hat{a}_r \\ &\quad -\left[\frac{M_2}{r^3} - \frac{3\,(M_1 r_1 + M_2 r_2 + M_3 r_3)\,r_2}{r^5}\right]\hat{a}_\theta \\ &\quad -\left[\frac{M_3}{r^3} - \frac{3\,(M_1 r_1 + M_2 r_2 + M_3 r_3)\,r_3}{r^5}\right]\hat{a}_3 \end{aligned} \tag{D.10}$$

At this point, it is useful to make some simplifications. Assuming the magnetic field is constant in the neighborhood of the reference point, the magnetic moment vector,

$\overline{M}$, and radius vector, $\overline{r}$, can be simplified as follows:

$$
\begin{aligned}
M_1 &= M\,m_1 \qquad r_1 = (r_\oplus + r_{alt}) = r_o \\
M_2 &= M\,m_2 \qquad r_2 = 0 \\
M_3 &= M\,m_3 \qquad r_3 = 0
\end{aligned}
$$

Applying these simplifications to Equation D.10 gives

$$
\overline{B} = \frac{M}{r_o^3}\left[2m_1\,\hat{a}_r - m_2\,\hat{a}_\theta - m_3\,\hat{a}_3\right] \tag{D.11}
$$

remembering that:

$$
\begin{aligned}
m_1 &= c\Phi_0\left[cvc\left(\Omega - \Theta_g - \Lambda_0\right) - svcis\left(\Omega - \Theta_g - \Lambda_0\right)\right] + s\Phi_0 svsi \\
m_2 &= c\Phi_0\left[-svc\left(\Omega - \Theta_g - \Lambda_0\right) - cvcis\left(\Omega - \Theta_g - \Lambda_0\right)\right] + s\Phi_0 cvsi \\
m_3 &= c\Phi_0 sis\left(\Omega - \Theta_g - \Lambda_0\right) + s\Phi_0 ci \\
\overline{r}_o &= \frac{a\left(1-e\right)}{1 + e\cos\nu}\,\hat{a}_r
\end{aligned}
$$

All three elements of $\overline{B}$ are nonlinear and time-variant. The field expressed in the orbital reference frame varies proportionately to the Earth's rotation rate; this is seen by the presence of Θ_g in m_1, m_2, and m_3 in Equations D.5 – D.7. changes occur at orbit rate as well. The presence of ν in the m_1 and m_2 terms indicates these terms vary at orbit velocity. Finally, there is a constant term in m_3, which accounts for the average north/south orientation of $\overline{B}$.

Appendix E. Analysis of SFP Rigid Body Assumption

E.1 Introduction

The SFP integrated trusses are subjected to a variety of loads due to the SFP's shielded coil electrodynamic propulsion system, the augmentation thrusters, and the rotation of the solar power system. The magnitudes of the loads generated by these systems are small and are not considered a threat to the structural integrity of the integrated trusses. However, the equations of motion listed in Section 6.2.4 are based upon the assumption that the SFP is a rigid body. Therefore, an analysis of the integrated truss subjected to the maximum loads is required to demonstrate the validity of the rigid body assumption used to formulate these equations of motion.

E.2 Description of Integrated Truss Loads

The maximum loads applied to the SFP are generated during R-bar standoff and were determined by the *time history program* listed in Section G.1. The maximum distributed forces due to this standoff maneuver are applied to the main integrated truss and are attributed to the SFP's shielded coil electrodynamic propulsion system. The maximum moments possible during this same maneuver are also applied to the main integrated truss and are attributed to moveable augmentation thrusters. The moveable augmentation thrusters produce a maximum thrust of 50 N. The thrusters are attached to both ends of the main integrated truss. These thrusters always fire in the same direction and always perpendicular to the main integrated truss. The farthest distance the augmentation thrusters will ever be from the center of the main integrated truss is 1.65 m. This generates a maximum moment of 82.50 $N \cdot m$ about an axis running lengthwise through the center of the truss.

The moments generated by the rotation of the solar power system were determined in Appendix P. These moments are applied to the ends of the cross integrated truss. However, the magnitude of these moments are minute compared to the mo-

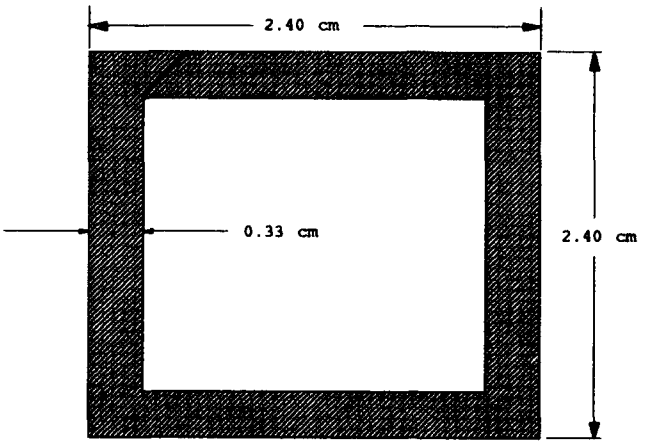

Figure E.1 Cross sectional view of the box beams used to model the main integrated truss.

ments generated by the moveable augmentation thrusters. Also, the distributed forces applied to the cross and orthogonal integrated trusses due to the shielded coil electrodynamic propulsion system are at least an order of magnitude smaller than that applied to the main integrated truss. Therefore, the rigid body analysis will focus on the main integrated truss. If the rigid body assumption can be justified for the main integrated truss, then the rigid body assumption is justified for the cross and orthogonal integrated trusses as well.

E.3 Main Integrated Truss Model

The main integrated truss was modeled using box beams for all the truss members (see Figure E.1). The box beams were connected as shown in Figure E.2 to form the main integrated truss. The dimensions of the box beam (shown in Figure E.1) were chosen so that the mass per unit length of the integrated truss

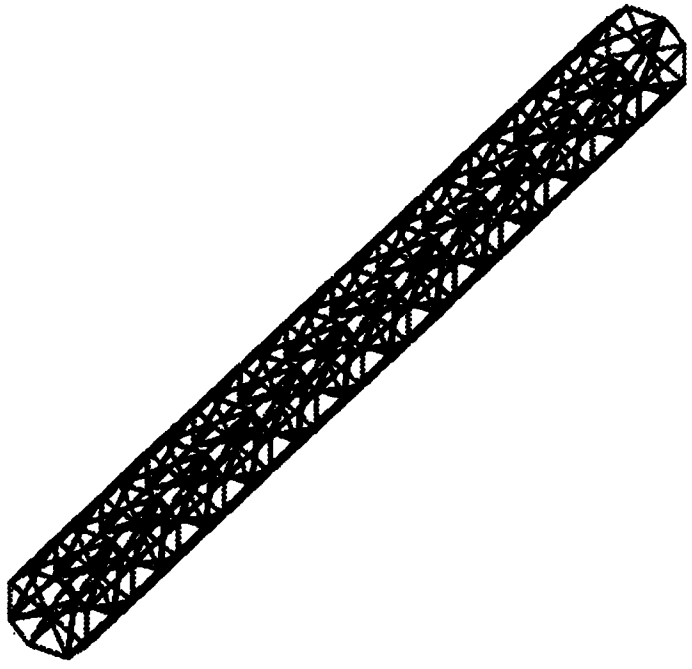

Figure E.2 The main integrated truss was modeled using box beams connected to form a 2 m by 2 m octagonal truss.

was equal to 20 kg/m. This is the value used by all of the design programs listed in Appendix G. The aluminum alloy, Al-2219, was used as the box beam material. This is the same material NASA planned to use for Space Station Freedom's integrated trusses (70:9).

The main integrated truss is 50 m long. Due to the symmetry of the loads applied to the integrated truss and the symmetry of the SFP itself, the truss is modeled as a cantilevered, 26 m long, (due to the 2 m truss bay length) octagonal truss section (see Figure E.2).

The finite element model is made up of 112 nodes and incorporates 324 box beam elements. Each element has 6 degrees of freedom generating a 1944 degree of freedom finite element model.

The load generated by the shielded coil electrodynamic propulsion system is modeled as two orthogonal, distributed forces applied lengthwise to the integrated truss longitudinal members. The 50 N eccentric load applied to the end of the truss is modeled as four 12.5 N individual forces and four individual 20.625 $N \cdot m$ moments. These four forces and moments are applied individually to the two top and bottom nodes at the free end of the truss. See Figure E.3 for the magnitudes and directions of the forces and moments applied to the truss model.

E.4 Analysis Software

A static, linear, finite element analysis was performed on the SFP main integrated truss described in Section E.3. The analysis was accomplished using *I-DEAS Finite Element Modeling Software* produced by *Structural Dynamics Research Corporation.* This software is a computer aided engineering tool that provides the capability to build a complete finite element model, including physical and material properties, loads, and boundary conditions.

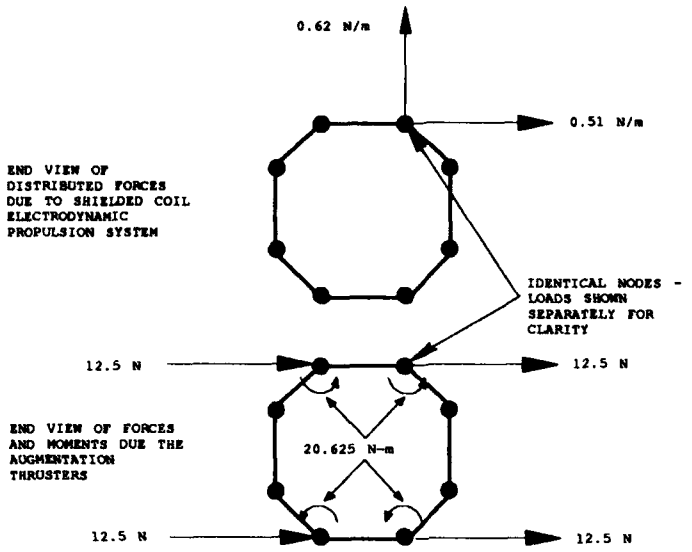

Figure E.3 End view of the maximum loads applied to the main integrated truss.

E.5 Analysis Results

The results of the finite element analysis show very small deflections due to the maximum loads applied to the main integrated truss. The following output shows the raw data generated by the program for this maximum load scenario:

```
%%%%%%%%%%%%%%%%%%%%%%%%%%%%%%%%%%%%%%%%%%%%%%%%%%%%%%%%%%%%%%%%%%%%%%%%%%%%%%%%
                                                                          Page 1

 SDRC  I-DEAS VI.i(s):  FE_Modeling_&_Analysis           22-OCT-93  01:06:02
 Main Integrated Truss - Maximum Loads

 Group ID          : No stored PERMANENT GROUP
 Analysis Dataset  : 1 -  CASE 1,LOAD 1,DISPLACEMENTS
 Report Type       : Deformed Geometry          Units        : SI
 Dataset Type      : Displacements              Load Set     : 1

    Node    Trans-X    Trans-Y    Trans-Z     Rot-X      Rot-Y      Rot-Z

       1  0.000E+00  0.000E+00  0.000E+00  0.000E+00  0.000E+00  0.000E+00
       2  0.000E+00  0.000E+00  0.000E+00  0.000E+00  0.000E+00  0.000E+00
       3  0.000E+00  0.000E+00  0.000E+00  0.000E+00  0.000E+00  0.000E+00
       4  0.000E+00  0.000E+00  0.000E+00  0.000E+00  0.000E+00  0.000E+00
       5  0.000E+00  0.000E+00  0.000E+00  0.000E+00  0.000E+00  0.000E+00
       6  0.000E+00  0.000E+00  0.000E+00  0.000E+00  0.000E+00  0.000E+00
       7  0.000E+00  0.000E+00  0.000E+00  0.000E+00  0.000E+00  0.000E+00
       8  0.000E+00  0.000E+00  0.000E+00  0.000E+00  0.000E+00  0.000E+00
       9  3.588E-07  3.599E-07 -1.013E-07  6.864E-08 -3.087E-07  7.972E-07
      10  3.729E-07  2.652E-07  1.226E-07 -2.129E-08 -2.343E-07 -7.026E-07
      11  7.071E-07 -7.494E-08  1.375E-07  9.174E-09 -2.912E-07  1.924E-07
      12 -2.535E-07 -6.006E-08  3.563E-07  8.667E-08 -4.209E-07 -5.828E-08
      13  2.289E-07  4.277E-07  9.921E-08  8.297E-08 -2.782E-07 -6.754E-07
```

14	2.337E-07	1.974E-07	-1.223E-07	-3.339E-08	-2.053E-07	8.500E-07
15	6.400E-07	-2.053E-07	-1.396E-07	-2.153E-08	-2.772E-07	-7.030E-08
16	-1.856E-07	-1.996E-07	-3.559E-07	5.764E-08	-4.330E-07	2.048E-07
17	1.238E-06	4.037E-07	-2.309E-07	-1.090E-08	-6.020E-07	7.802E-07
18	1.252E-06	3.716E-07	2.214E-07	-4.289E-08	-4.371E-07	-5.262E-07
19	1.469E-06	1.461E-07	3.284E-07	9.899E-08	-4.609E-07	2.796E-07
20	5.860E-07	1.571E-07	6.370E-07	1.473E-07	-7.318E-07	6.283E-09
21	9.679E-07	5.414E-07	2.283E-07	9.722E-10	-5.743E-07	-5.181E-07
22	9.727E-07	2.339E-07	-2.210E-07	-5.491E-08	-4.091E-07	8.134E-07
23	1.332E-06	-1.240E-07	-3.309E-07	7.125E-08	-4.490E-07	-1.728E-08
24	7.237E-07	-1.222E-07	-6.366E-07	1.192E-07	-7.438E-07	2.800E-07
25	2.595E-06	4.335E-07	-3.703E-07	-1.256E-09	-8.257E-07	5.688E-07
26	2.609E-06	5.039E-07	3.065E-07	-3.001E-09	-6.635E-07	-1.707E-07
27	2.641E-06	4.627E-07	5.399E-07	1.390E-07	-6.602E-07	3.238E-07
28	2.015E-06	4.709E-07	8.708E-07	1.620E-07	-9.230E-07	1.009E-07
29	2.185E-06	6.414E-07	3.676E-07	1.088E-08	-7.976E-07	-1.663E-07
30	2.190E-06	2.960E-07	-3.062E-07	-1.498E-08	-6.353E-07	5.984E-07
31	2.434E-06	5.216E-08	-5.426E-07	1.109E-07	-6.481E-07	7.891E-08
32	2.223E-06	5.114E-08	-8.704E-07	1.338E-07	-9.350E-07	3.260E-07
33	4.392E-06	5.417E-07	-5.042E-07	3.199E-08	-1.019E-06	4.320E-07
34	4.406E-06	7.112E-07	3.829E-07	4.194E-08	-8.804E-07	1.085E-07
35	4.299E-06	8.065E-07	7.471E-07	1.587E-07	-8.637E-07	3.703E-07
36	3.835E-06	8.153E-07	1.073E-06	1.691E-07	-1.082E-06	1.931E-07
37	3.841E-06	8.201E-07	5.015E-07	4.415E-08	-9.904E-07	1.117E-07
38	3.845E-06	4.327E-07	-3.826E-07	2.989E-08	-8.520E-07	4.604E-07
39	4.021E-06	2.568E-07	-7.498E-07	1.304E-07	-8.516E-07	1.736E-07
40	4.114E-06	2.543E-07	-1.073E-06	1.407E-07	-1.094E-06	3.750E-07
41	6.582E-06	7.297E-07	-6.247E-07	6.703E-08	-1.190E-06	3.992E-07
42	6.596E-06	9.866E-07	4.520E-07	7.825E-08	-1.076E-06	2.840E-07
43	6.404E-06	1.169E-06	9.370E-07	1.699E-07	-1.056E-06	4.269E-07
44	5.984E-06	1.175E-06	1.251E-06	1.764E-07	-1.231E-06	2.768E-07
45	5.889E-06	1.079E-06	6.219E-07	7.926E-08	-1.161E-06	2.863E-07
46	5.893E-06	6.371E-07	-4.517E-07	6.615E-08	-1.048E-06	4.269E-07
47	6.056E-06	4.751E-07	-9.396E-07	1.415E-07	-1.044E-06	2.588E-07
48	6.333E-06	4.719E-07	-1.250E-06	1.479E-07	-1.243E-06	4.333E-07
49	9.118E-06	9.734E-07	-7.290E-07	9.583E-08	-1.341E-06	4.346E-07
50	9.131E-06	1.310E-06	5.140E-07	1.046E-07	-1.247E-06	3.926E-07

1

SDRC I-DEAS VI.1(e): FE_Modeling_&_Analysis 22-OCT-93 01:06:02
integ2

Node	Trans-X	Trans-Y	Trans-Z	Rot-X	Rot-Y	Rot-Z
51	8.868E-06	1.543E-06	1.106E-06	1.775E-07	-1.229E-06	4.904E-07
52	8.436E-06	1.549E-06	1.406E-06	1.844E-07	-1.369E-06	3.553E-07
53	8.282E-06	1.394E-06	7.262E-07	1.081E-07	-1.312E-06	3.935E-07
54	8.286E-06	8.897E-07	-5.137E-07	9.246E-08	-1.219E-06	4.610E-07
55	8.468E-06	7.072E-07	-1.108E-06	1.490E-07	-1.217E-06	3.379E-07
56	8.857E-06	7.039E-07	-1.404E-06	1.567E-07	-1.381E-06	4.975E-07
57	1.196E-05	1.250E-06	-8.171E-07	1.174E-07	-1.471E-06	5.015E-07
58	1.198E-05	1.666E-06	5.683E-07	1.234E-07	-1.394E-06	4.707E-07
59	1.169E-05	1.934E-06	1.251E-06	1.831E-07	-1.379E-06	5.551E-07
60	1.117E-05	1.940E-06	1.536E-06	1.914E-07	-1.492E-06	4.338E-07
61	1.097E-05	1.742E-06	8.142E-07	1.298E-07	-1.442E-06	4.698E-07
62	1.098E-05	1.174E-06	-5.680E-07	1.112E-07	-1.366E-06	5.263E-07
63	1.120E-05	9.542E-07	-1.254E-06	1.544E-07	-1.366E-06	4.165E-07
64	1.166E-05	9.507E-07	-1.535E-06	1.626E-07	-1.504E-06	5.623E-07
65	1.504E-05	1.543E-06	-8.900E-07	1.334E-07	-1.580E-06	5.786E-07
66	1.505E-05	2.042E-06	6.148E-07	1.367E-07	-1.517E-06	5.396E-07
67	1.475E-05	2.338E-06	1.374E-06	1.865E-07	-1.506E-06	6.176E-07
68	1.415E-05	2.344E-06	1.643E-06	1.966E-07	-1.596E-06	5.155E-07
69	1.391E-05	2.107E-06	8.871E-07	1.458E-07	-1.551E-06	5.367E-07

```
       70  1.392E-05  1.478E-06 -6.146E-07  1.244E-07 -1.488E-06  6.015E-07
       71  1.418E-05  1.214E-06 -1.377E-06  1.577E-07 -1.493E-06  4.979E-07
       72  1.471E-05  1.211E-06 -1.643E-06  1.676E-07 -1.608E-06  6.248E-07
       73  1.833E-05  1.846E-06 -9.491E-07  1.469E-07 -1.668E-06  6.566E-07
       74  1.835E-05  2.429E-06  6.539E-07  1.450E-07 -1.618E-06  6.082E-07
       75  1.801E-05  2.752E-06  1.476E-06  1.872E-07 -1.608E-06  6.810E-07
       76  1.734E-05  2.758E-06  1.728E-06  2.002E-07 -1.676E-06  5.967E-07
       77  1.706E-05  2.483E-06  9.461E-07  1.593E-07 -1.639E-06  6.034E-07
       78  1.707E-05  1.792E-06 -6.538E-07  1.329E-07 -1.589E-06  6.777E-07
       79  1.738E-05  1.484E-06 -1.479E-06  1.581E-07 -1.596E-06  5.792E-07
       80  1.798E-05  1.480E-06 -1.728E-06  1.713E-07 -1.689E-06  6.884E-07
       81  2.180E-05  2.164E-06 -9.961E-07  1.630E-07 -1.737E-06  7.325E-07
       82  2.181E-05  2.810E-06  6.865E-07  1.512E-07 -1.698E-06  6.794E-07
       83  2.144E-05  3.173E-06  1.556E-06  1.838E-07 -1.684E-06  7.635E-07
       84  2.069E-05  3.178E-06  1.789E-06  2.059E-07 -1.734E-06  6.587E-07
       85  2.038E-05  2.873E-06  9.931E-07  1.762E-07 -1.708E-06  6.729E-07
       86  2.039E-05  2.100E-06 -6.865E-07  1.348E-07 -1.671E-06  7.525E-07
       87  2.073E-05  1.759E-06 -1.559E-06  1.553E-07 -1.672E-06  6.419E-07
       88  2.140E-05  1.755E-06 -1.789E-06  1.740E-07 -1.742E-06  7.718E-07
       89  2.540E-05  2.518E-06 -1.033E-06  1.945E-07 -1.791E-06  8.075E-07
       90  2.541E-05  3.157E-06  7.134E-07  1.255E-07 -1.769E-06  7.597E-07
       91  2.496E-05  3.597E-06  1.615E-06  1.812E-07 -1.732E-06  9.063E-07
       92  2.414E-05  3.602E-06  1.827E-06  1.962E-07 -1.739E-06  6.607E-07
       93  2.384E-05  3.301E-06  1.030E-06  2.004E-07 -1.762E-06  7.495E-07
       94  2.384E-05  2.375E-06 -7.134E-07  1.602E-07 -1.723E-06  8.301E-07
       95  2.418E-05  2.037E-06 -1.618E-06  1.440E-07 -1.712E-06  6.358E-07
       96  2.492E-05  2.033E-06 -1.826E-06  1.969E-07 -1.792E-06  9.261E-07
       97  2.911E-05  2.952E-06 -1.062E-06  2.230E-07 -1.840E-06  1.049E-06
       98  2.912E-05  3.421E-06  7.323E-07  5.959E-07 -1.720E-06  1.117E-06
       99  2.851E-05  4.022E-06  1.651E-06  1.305E-07 -1.696E-06  1.100E-06
      100  2.762E-05  4.028E-06  1.843E-06  4.723E-07 -2.104E-06  5.464E-07
      101  2.740E-05  3.808E-06  1.059E-06  2.949E-07 -1.813E-06  1.006E-06
      102  2.741E-05  2.564E-06 -7.325E-07 -2.722E-07 -1.853E-06  1.184E-06
      103  2.766E-05  2.315E-06 -1.654E-06  1.711E-07 -1.755E-06  3.856E-07
      104  2.847E-05  2.311E-06 -1.842E-06 -3.598E-08 -1.447E-06  1.270E-06
      105  3.291E-05  3.515E-06 -1.081E-06  5.410E-07 -1.673E-06  1.012E-05
1

                                                                        Page 3

 SDRC  I-DEAS VI.i(s):  FE_Modeling_&_Analysis                22-OCT-93  01:06:02
 integ2

    Node    Trans-X    Trans-Y    Trans-Z     Rot-X      Rot-Y      Rot-Z

      106  3.291E-05  3.549E-06  7.321E-07  4.874E-08 -1.855E-06  1.104E-05
      107  3.201E-05  4.447E-06  1.666E-06  1.584E-07 -1.744E-06 -1.142E-07
      108  3.107E-05  4.450E-06  1.843E-06  1.965E-07 -1.591E-06 -1.666E-06
      109  3.106E-05  4.443E-06  1.078E-06 -2.884E-08 -1.914E-06  1.012E-05
      110  3.106E-05  2.622E-06 -7.326E-07  1.586E-07 -1.760E-06  1.109E-05
      111  3.110E-05  2.592E-06 -1.670E-06  1.442E-07 -1.672E-06 -1.694E-06
      112  3.198E-05  2.591E-06 -1.842E-06  1.948E-07 -1.875E-06  3.553E-08

                 106        108        108         98          1        110
Maximum    3.291E-05  4.450E-06  1.843E-06  5.959E-07  0.000E+00  1.109E-05

                  12         15        104        102        100        111
Minimum   -2.535E-07 -2.053E-07 -1.842E-06 -2.722E-07 -2.104E-06 -1.694E-06


Average    1.228E-05  1.470E-06 -5.874E-10  1.187E-07 -1.185E-06  7.478E-07
%%%%%%%%%%%%%%%%%%%%%%%%%%%%%%%%%%%%%%%%%%%%%%%%%%%%%%%%%%%%%%%%%%%%%%%%%%%%%%%%
```

A summary of the data appears at the end of the raw data table and shows the maximum deflections and the nodes to which they apply. In this case, the maximum deflections are at the free end of the cantilevered truss as expected. The raw data becomes more pertinent when viewed in graphical form (see Figure E.4). A magnification factor has been applied to the figures deformed geometry case in order to differentiate between the deformed and undeformed geometry. The actual maximum deflection generated by the finite element analysis is approximately 0.000033 m.

E.6 Results

The extremely small deflections due to the maximum loads applied to the main integrated truss are explained by the large mass per unit length of the truss as well as the design of the truss itself.

The analysis performed on the truss model does not take into consideration the dynamic effects of the structure due to starting and stopping of the SFP propulsion system. Even if sporadic firing of the augmentation thrusters and variations in the thrust applied by the shielded coil electrodynamic propulsion system produce vibrations 300 times the maximum truss tip deflection, this is still less than a 1 cm variation in tip deflection. Therefore, based upon the extremely small maximum truss tip deflection and the fact that even large multiples of this deflection are small, the SFP can be considered a rigid body for analysis purposes.

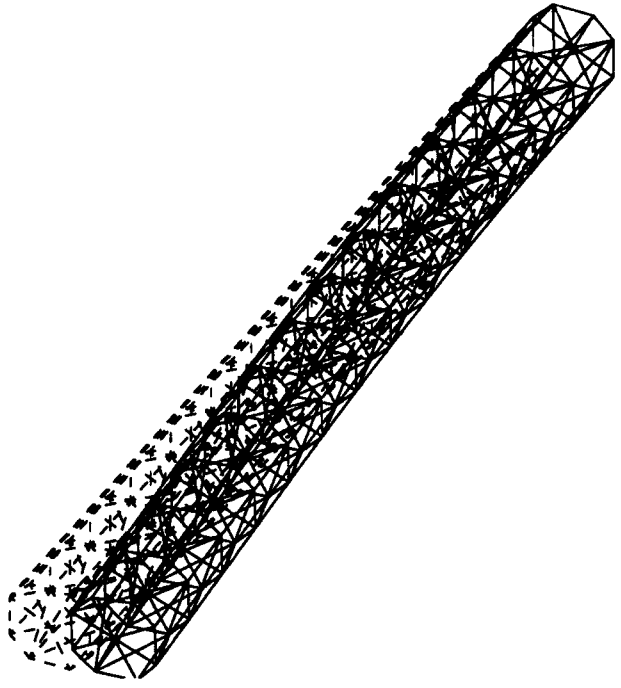

Figure E.4 This figure shows the main integrated truss deformed versus undeformed geometry due to maximum loads. The deformed geometry case has been multiplied by a magnification factor for comparison purposes.

Appendix F. Unforced Equations of Motion Derivation

The design process selected for this study uses an iterative process where, for a proposed design configuration, a linear system controller is developed. The controller is then used during a simulation where current and power requirements are determined for SFP-required R-bar standoff maneuver. To be able to use this process, the SFP's relative equations of motion must be derived for the proposed design. Six equations of motion are required to completely describe the position and orientation of the vehicle. Three of the equations describe the position of the vehicle in inertial space while the other three equations describe the orientation of the vehicle in inertial space. Remembering that the final equations of motion must be linear for the controller design synthesis, anumber of assumptions and linearizations are incorporated into the equations of motion derivation. They include:

- assume the SFP is a rigid body
- assume the true anomoly rate of change is constant
- neglect other than first order terms in the relative position and velocity components
- assume the atmosphere is fixed to the earth and can be described by an exponential model
- assume small angle approximations for yaw, roll, and pitch

The development of the relative equations of motion begins with the development of the translational equations of motion.

F.0.0.1 Translational Equations of Motion. Three of the six equations of motion are translational equations. They describe the movement of the SFP's center of mass relative to the inertial reference frame. While the equations of motion must be derived relative to the inertial frame, it is convenient to express

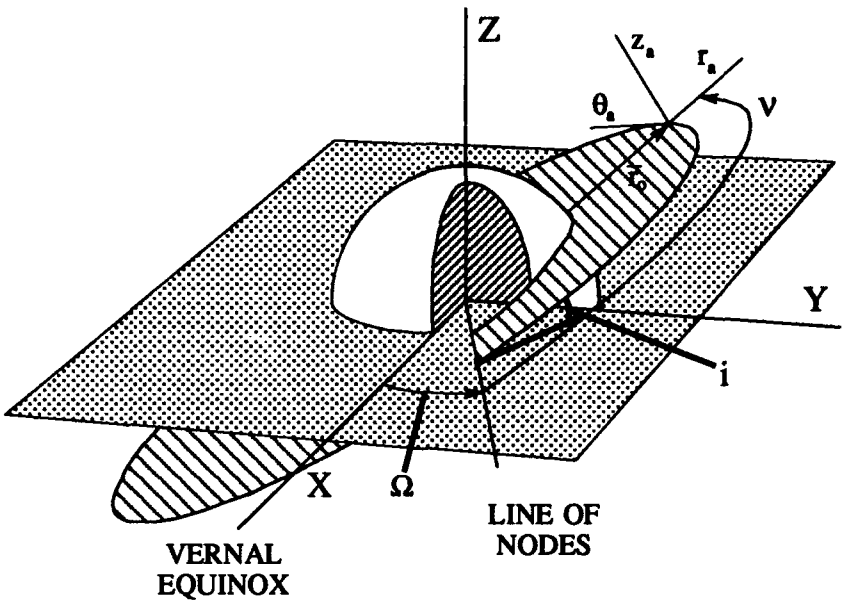

Figure F.1 The orbital reference frame with the origin translated for clarity to a point on the orbit path.

them in the orbital reference frame shown in FigureF.1. The three translation directions are the $\hat{a}_r$, $\hat{a}_\theta$, and the $\hat{a}_z$ directions. Assuming the SFP is a rigid body (see Appendix E), the translational equations of motion are derived from the form of Newton's second law:

$$\overline{F} = M_{tot}\overline{a} \tag{F.1}$$

where $\overline{F}$ is the sum of all external forces acting on the SFP, M_{tot} is the total mass of the SFP, and $\overline{a}$ is the acceleration of the SFP with respect to inertial space (52:406-408). In deriving the expression of Equation F.1 for the SFP, the vehicle's center of mass (i.e. the origin of the $\hat{b}$-frame) will actually be a small distance away from the orbital reference point in the $\hat{a}$-frame. For the scope of this study, the reference point is assumed to be in a circular orbit. This allows for the development of the relative equations of motion for the SFP in the vacinity of a point in a circular reference orbit.

Following the development of the Clohessy-Wiltshire equations outlined by Wiesel (93:78-80), the derivation begins with the SFP's position. The position vector is

$$^{a}\overline{r} = (r_o + \delta r)\,\hat{a}_r + r_o\delta\nu\hat{a}_\theta + \delta z\hat{a}_3 \tag{F.2}$$

where r_o is the distance from the center of the Earth to the reference point (which could be another vehicle with which the SFP is rendezvousing), and δr, $r_o\delta\nu$, and δz describe the relative position of the SFP to the reference point. The relative position components are assumed to be small relative to r_o — i.e. $\delta r \ll r_o$, $r_o\delta\nu \ll r_o$, and $\delta z \ll r_o$. To formulate Equation F.1 properly, the differentiation of $\overline{r}$ to find the acceleration must be carried out with respect to the $\hat{i}$-frame. This process is carried out by applying

$$\frac{^{a}d}{dt}\overline{Z} = \frac{^{d}d}{dt}\overline{Z} + \overline{\omega}^{da} \times \overline{Z} \tag{F.3}$$

where $\overline{\omega}^{da}$ is the angular velocity of the *$\hat{d}$-frame* with respect to the *$\hat{a}$-frame*. This relationship holds for any vector, $\overline{Z}$ (52:109). Applying Equation F.3 to Equation F.2

$$\begin{aligned}
\overline{v} &= \frac{^{i}d}{dt}\overline{r} \\
&= \frac{^{a}d}{dt}\overline{r} + \overline{\omega}^{ai} \times \overline{r} \\
&= (\delta\dot{r})\,\hat{a}_r + (r_o\delta\dot{\nu})\,\hat{a}_\theta + (\delta\dot{z})\,\hat{a}_3 + \\
&\quad (\dot{\nu})\,\hat{a}_3 \times [(r_o + \delta r)\,\hat{a}_r + r_o\delta\nu\hat{a}_\theta + \delta z\hat{a}_3] \\
\overline{v} &= (\delta\dot{r} - \dot{\nu}r_o\delta\nu)\,\hat{a}_r + (r_o\delta\dot{\nu} + \dot{\nu}r_o + \dot{\nu}\delta r)\,\hat{a}_\theta + (\delta\dot{z})\,\hat{a}_3
\end{aligned} \tag{F.4}$$

where $\dot{\nu}$ is the time rate of change of the true anomaly. For a circular orbit, the true anomaly is given by

$$\nu(t) = \nu_0 + \sqrt{\frac{\mu}{r_o^3}}(t - t_0) \tag{F.5}$$

so $\dot{\nu}$ is simply the orbital mean motion

$$\dot{\nu} = n = \sqrt{\frac{\mu}{r_o^3}} \equiv constant \tag{F.6}$$

where

$$\mu = 3.9892 \times 10^{14} \frac{m^3}{s^2}$$

Applying Equation F.3 a second time to find the acceleration:

$$\begin{aligned}
\overline{a} &= \frac{^i d}{dt}\overline{v} \\
&= \frac{^a d}{dt}\overline{v} + \overline{\omega}^{ai} \times \overline{v} \\
&= (\delta\ddot{r} - nr_o\delta\dot{\nu})\,\hat{a}_r + (r_o\delta\ddot{\nu} + n\delta\dot{r})\,\hat{a}_\theta + (\delta\ddot{z})\,\hat{a}_3 + \\
&\quad (n)\,\hat{a}_3 \times [(\delta\dot{r} - nr_o\delta\nu)\,\hat{a}_r + (r_o\delta\dot{\nu} + nr_o + n\delta r)\,\hat{a}_\theta + (\delta\dot{z})\,\hat{a}_3] \\
\overline{a} &= \left(\delta\ddot{r} - 2nr_o\delta\dot{\nu} - n^2 r_o - n^2\delta r\right)\hat{a}_r + \left(r_o\delta\ddot{\nu} + 2n\delta\dot{r} - n^2 r_o\delta\nu\right)\hat{a}_\theta + \\
&\quad (\delta\ddot{z})\,\hat{a}_3
\end{aligned} \tag{F.7}$$

This is the inertial acceleration of the SFP, expressed in the $\hat{a}$-frame. Since the total mass of the SFP is known, the only part of Equation F.1 to determine is the sum of the external forces, $\overline{F}$.

A number of external forces can act on an orbital vehicle. Among these forces are gravity, aerodynamic drag, magnetic field effects, non-spherical Earth effects, radiation pressure, meteoroidal impacts, and non environmental forces, such as mass expulsion; however, this list is not exhaustive. For the purposes of this study, the only external forces that will be included are gravity, aerodynamic drag, and magnetic field effects. Gravity and aerodynamic drag are retarding forces to be overcome, while the magnetic field effects are used for propulsion.

The force of gravity is described by (93:24)

$$\overline{F}_g = -\frac{Gm_1m_2}{r^3}\overline{r} = -\frac{GM_\oplus M_{tot}}{r^3}\overline{r} \tag{F.8}$$

where $\overline{r}$ is the position vector of the SFP relative to the Earth. Substituting Equation F.2 in this equation gives

$$\overline{F}_g = -GM_\oplus M_{tot}\frac{\left[(r_o+\delta r)\,\hat{a}_r + (r_o\delta\nu)\,\hat{a}_\theta + (\delta z)\,\hat{a}_3\right]}{\left[(r_o+\delta r)^2 + (r_o\delta\nu)^2 + (\delta z)^2\right]^{\frac{3}{2}}} \tag{F.9}$$

Approximating the denominator as a binomial expansion (6:295), and neglecting higher order terms of relative position elements $\left(\mathcal{O}\left[|\delta\overline{r}|^2\right]\right)$ (since $\delta\overline{r} \ll \overline{r}_o$)

$$\begin{aligned}
&\left[(r_o+\delta r)^2 + (r_o\delta\nu)^2 + (\delta z)^2\right]^{-\frac{3}{2}} \\
\approx\ & (r_o+\delta r)^{-3} - \frac{3}{2}(r_o+\delta r)^{-5}\left[(r_o\delta\nu)^2 + (\delta z)^2\right] + \mathcal{O}\left[|\delta\overline{r}|^2\right] \\
\approx\ & \left[r_o^{-3} - 3r_o^{-4}\delta r + \mathcal{O}\left[\delta r^2\right]\right] - \frac{3}{2}\left[r_o^{-5} - 5r_o^{-6}\delta r + \mathcal{O}\left[\delta r^2\right]\right]\cdot \\
& \left[\mathcal{O}\left[\delta\nu^2\right] + \mathcal{O}\left[\delta z^2\right] + \mathcal{O}\left[|\delta\overline{r}|^2\right]\right] \\
\approx\ & r_o^{-3} - 3r_o^{-4}\delta r + \mathcal{O}\left[|\delta\overline{r}|^2\right] \\
\approx\ & r_o^{-4}(r_o - 3\delta r)
\end{aligned} \tag{F.10}$$

Substituting this expression back into Equation F.9 and again neglecting $\mathcal{O}\left[|\delta\overline{r}|^2\right]$ terms gives the final expression for the force due to gravity

$$\begin{aligned}
\overline{F}_g &= -\frac{GM_\oplus M_{tot}}{r_o^4}(r_o - 3\delta r)\left[(r_o+\delta r)\,\hat{a}_r + (r_o\delta\nu)\,\hat{a}_\theta + (\delta z)\,\hat{a}_3\right] \\
&= -\frac{GM_\oplus M_{tot}}{r_o^3}\left[(r_o - 2\delta r)\,\hat{a}_r + (r_o\delta\nu)\,\hat{a}_\theta + (\delta z)\,\hat{a}_3\right] \\
&= -M_{tot}n^2\left[(r_o - 2\delta r)\,\hat{a}_r + (r_o\delta\nu)\,\hat{a}_\theta + (\delta z)\,\hat{a}_3\right]
\end{aligned} \tag{F.11}$$

An expression for the force due to aerodynamic drag must also be determined. Below altitudes of 1000 km, aerodynamic drag due to the atmosphere can be impor-

tant (16:213). The forces involved may be relatively small, but will have a significant impact on the SFP design and therefore are included in the analysis. The force due to aerodynamic drag is given by:

$$\overline{F_d} = -\frac{1}{2}\frac{M_{tot}\rho V_r}{\beta}\overline{V_r} \tag{F.12}$$

where ρ is the atmospheric density, $\overline{V}_r$ is the velocity of the SFP relative to the atmosphere, V_r is the magnitude of $\overline{V}_r$, and β is the ballistic coefficient (94:65).

The gross behavior of the density of the upper atmosphere is well established, but the properties are difficult to determine and are highly variable (30:122). However, a reasonable approximation is obtained from a modified exponential model given by:

$$\rho = \rho^* e^{-(r-r^*)/h_s} \tag{F.13}$$

where r^* is the reference altitude, h_s is the scale height, and ρ^* is the atmospheric density at the reference altitude. For this application of Equation F.13, the reference altitude was chosen as $r^* = 300\ km$. Using the *US Standard Atmosphere Table* (30:56), and applying Equation F.13 to the data gives

$$\begin{aligned} \rho^* &= 1.916 \times 10^{-11} \quad \frac{kg}{m^3} \\ h_s &= 50043 \quad km \end{aligned}$$

To find $\overline{V}_r$, the atmosphere is assumed to be fixed to the rotating Earth. $\overline{V}_r$ is then given by (94:65):

$$\overline{V}_r = \overline{v} - (\overline{\omega}_\oplus \times \overline{r}) \tag{F.14}$$

where $\overline{v}$ is the inertial velocity of the SFP, $\overline{\omega}_\oplus$ is the Earth's angular velocity, and $\overline{r}$ is the position of the SFP. To be consistent, all vectors must be expressed in the

$\hat{a}$-frame. Applying Equation C.8 to the Earth's angular velocity gives:

$$\begin{aligned}
\overline{\omega}_{\oplus} &= R^{ai}\left(\overline{\omega}_{\oplus}\hat{i}_3\right) \\
&= \omega_{\oplus} sis\nu\hat{a}_r + \omega_{\oplus} sic\nu\hat{a}_\theta + \omega_{\oplus} ci\hat{a}_3 \\
&= \omega_1\hat{a}_r + \omega_2\hat{a}_\theta + \omega_3\hat{a}_3 \qquad \text{(F.15)}
\end{aligned}$$

Applying this result, Equation F.2, and Equation F.4 to Equation F.14 gives the relative velocity as:

$$\begin{aligned}
\overline{V}_r &= \left[\left(\delta\dot{r} - nr_o\delta\nu\right)\hat{a}_r + \left(r_o\delta\dot{\nu} + nr_o + n\delta r\right)\hat{a}_\theta + \left(\delta\dot{z}\right)\hat{a}_3\right] - \\
&\quad \left(\omega_1\hat{a}_r + \omega_2\hat{a}_\theta + \omega_3\hat{a}_3\right) \times \left[\left(r_o + \delta r\right)\hat{a}_r + r_o\delta\nu\hat{a}_\theta + \delta z\hat{a}_3\right] \\
&= \left[\delta\dot{r} - \delta\omega r_o\delta\nu - \omega_2\delta z\right]\hat{a}_r + \left[\delta\omega\left(r_o + \delta r\right) + r_o\delta\dot{\nu} + \right. \\
&\quad \left.\omega_1\delta z\right]\hat{a}_\theta + \left[\omega_2\left(r_o + \delta r\right) - \omega_1 r_o\delta\nu + \delta\dot{z}\right]\hat{a}_3 \\
&= V_1\hat{a}_r + V_2\hat{a}_\theta + V_3\hat{a}_3 \qquad \text{(F.16)}
\end{aligned}$$

where $\delta\omega = n - \omega_3$. Substituting Equation F.16 into Equation F.12 gives:

$$\overline{F}_d = -\frac{1}{2}\frac{M_{tot}\rho}{\beta}\left[V_1^2 + V_2^2 + V_3^2\right]^{\frac{1}{2}}\left[V_1\hat{a}_r + V_2\hat{a}_\theta + V_3\hat{a}_3\right] \qquad \text{(F.17)}$$

Expanding the V_r term — neglecting second order terms of the relative positions and relative velocities (since $\overline{r}_o \gg \overline{\delta r}$ and $\overline{v} \gg \overline{\delta\dot{r}}$) — gives:

$$\begin{aligned}
V_1^2 &= 0 \\
V_2^2 &= \delta\omega^2 r_o^2 + 2\delta\omega\left[\delta\omega\delta r + r_o\delta\dot{\nu} + \omega_1\delta z\right]r_o \\
V_3^2 &= \omega_2^2 r_o^2 + 2\omega_2\left[\omega_2\delta r - \omega_1 r_o\delta\nu + \delta z\right]r_o
\end{aligned}$$

Assuming $r_o^2 \gg r_o\delta r$, $r_o^2 \gg r_o(r_o\delta\nu)$, and $r_o^2 \gg r_o\delta z$, as well as the terms associated with the relative velocities, the magnitude of $\overline{V}_r$ can be approximated as:

$$\left[V_1^2 + V_2^2 + V_3^2\right]^{\frac{1}{2}} \approx \left[\left(\delta\omega^2 + \omega_2^2\right) r_o^2\right]^{\frac{1}{2}} = r_o\left(\delta\omega^2 + \omega_2^2\right)^{\frac{1}{2}} \tag{F.18}$$

The final term of Equation F.12, the ballistic coefficient is defined as:

$$\beta = \frac{M_{tot}}{C_D A} \tag{F.19}$$

where C_D is the drag coefficient, and A is the projected area normal to the flight path. Based on analysis performed on other vehicles (57:33), the drag coefficient of the SFP is estimated to be $C_D = 2.4$. The projected area is estimated to be $A = 1435\ m^2$ (see Section 11.10.

The final expression for $\overline{F}_d$ can now be found. Substituting back into Equation F.12, the force due to aerodynamic drag can be approximated as:

$$\begin{aligned}\overline{F}_d \;=\; & -\frac{1}{2}C_D A\rho^*\left[e^{-(r_o-r^*)/h_s}\right]\left[r_o\left(\delta\omega^2+\omega_2^2\right)^{\frac{1}{2}}\right]\cdot \\ & \left[\left(\delta\dot{r} - \delta\omega r_o\delta\nu - \omega_2\delta z\right)\hat{a}_r + \left(\delta\omega\left(r_o+\delta r\right) + r_o\delta\dot{\nu} + \omega_1\delta z\right)\hat{a}_\theta + \right. \\ & \left.\left(\omega_2\left(r_o\delta r\right) - \omega_1 r_o\delta\nu + \delta\dot{z}\right)\hat{a}_3\right]\end{aligned} \tag{F.20}$$

Because the magnetic field effects are used for propulsion, they are not included in the homogeneous translational equations of motion. The homogeneous translational equations of motion are obtained by equating the inertial acceleration, given by Equation F.7, with the acceleration due to gravity and aerodynamic drag. However, careful examination of the Equation F.20 shows two constant drag terms ($\delta\omega r_o$ and $\omega_2 r_o$) which act as forcing functions, and thus, the equations are no longer homogeneous. The acceleration due to gravity and aerodynamic drag can be obtained by dividing the sum of Equation F.11 and Equation F.20 by the SFP's total

mass. The relative translation equations of motion are then given by:

$$\hat{a}_r: \quad \delta\ddot{r} - K\delta\dot{r} - 2nr_o\delta\dot{\nu} - 3n^2\delta r + K\delta\omega r_o\delta\nu + K\omega_2\delta z = 0 \qquad \text{(F.21)}$$

$$\hat{a}_\theta: \quad r_o\delta\ddot{\nu} + 2n\delta\dot{r} + Kr_o\delta\dot{\nu} - K\delta\omega\delta r - K\omega_1\delta z - K\delta\omega r_o = 0 \qquad \text{(F.22)}$$

$$\hat{a}_3: \quad \delta\ddot{z} - K\delta\dot{z} - K\omega_2\delta r + K\omega_1 r_o\delta\nu + n^2\delta z - K\omega_2 r_o = 0 \qquad \text{(F.23)}$$

where

$$K = -\frac{C_D A\rho^*}{2M_{tot}}\left[e^{-(r_o-r^*)/h_s}\right]\left[r_o\left(\delta\omega^2+\omega_2^2\right)^{\frac{1}{2}}\right]$$

With the exception of the terms due to aerodynamic drag, these equations are similar to those derived by Wiesel (93:80). It is helpful to consider the solutions to these equations, excluding the drag terms.

Wiesel derives the solutions to Equations F.21 – F.23 (93:80), minus the drag terms, as

$$\delta r(t) = -\left(\frac{2}{n}r_o\delta\dot{\nu}(0) + 3\delta r(0)\right)\cos nt + \frac{\delta\dot{r}(0)}{n}\sin nt + 4\delta r(0) + \frac{2}{n}r_o\delta\dot{\nu}(0) \qquad \text{(F.24)}$$

$$\delta\nu(t) = \delta\nu(0) - \left(3\delta\dot{\nu}(0) + \frac{6n\delta r(0)}{r_o}\right)t + \left(\frac{4\delta\dot{\nu}(0)}{n} + \frac{6\delta r(0)}{r_o}\right)\sin nt + \frac{2\delta\dot{r}(0)}{nr_o}\cos nt - \frac{2\delta\dot{r}(0)}{nr_o} \qquad \text{(F.25)}$$

$$\delta z(t) = \delta z(0)\cos nt + \frac{\delta\dot{z}(0)}{n}\sin nt \qquad \text{(F.26)}$$

These equations form the complete Clohessy-Wiltshire solution. Wiesel notes some phenomena of the solution. The radial motion, $\delta r(t)$, oscillates at orbit rate and describes a slight eccentricity in the SFP's orbit relative to the circular orbit of the reference point. This effect is always present unless the in-plane radial position of the SFP is at the reference radius, and the relative velocity between the SFP and the reference point is zero. The angular motion, $\delta\nu(t)$, is also oscillatory if any

eccentricity is present. The motion also includes a term linear in t. If the SFP is at a different altitude or moving in the angular direction relative to the reference point, it will drift in the track direction. If none of these perturbations are present and the SFP is some distance along the track from the reference point, it will remain at that point. The out-of-plane motion, $\delta z\,(t)$, is completely oscillatory, and oscillates at orbit rate. It is a result of the SFP being at a slightly different inclination from the reference point when the initial out-of-plane position and/or velocity are not zero. These phenomena do not take aerodynamic drag into account. The aerodynamic drag terms can be expected to dampen the motions described above. The magnitude of the aerodynamic drag force is negligible compared to the force due to gravity, and is therefore not expected to significantly affect the gross motion of the SFP in the short term. However, relative to the forces produced by the propulsion system, aerodynamic drag is significant, and cannot be neglected.

F.0.0.2 Rotational Equations of Motion. The remaining three equations of motion are the rotational equations. They describe the rotation of the body about the center of mass. The rotational equations of motion can be found by equating the sum of the applied torques, $\overline{M}$, to the rate of change of the angular momentum, $\overline{H}$ (93:109). Thus, with respect to the inertial frame,

$$\overline{M} = \dot{\overline{H}} \tag{F.27}$$

Assuming the SFP is a rigid body (this assumption is analyzed in Appendix E), the angular momentum is defined by

$$\overline{H} = \tilde{I}\overline{\omega} \tag{F.28}$$

and can be used if the reference frame is attached to the body, thus making the mass moment of inertia tensor, $\tilde{I}$, a constant. However, the time derivative required in

Equation F.27 must be taken with respect to the inertial frame. This requires the application of Equation F.3. Equation F.27 can then be expressed as

$$^{b}\overline{M} = \tilde{I}^{b}\dot{\overline{\omega}}^{bi} + {}^{b}\overline{\omega}^{bi} \times \tilde{I}^{b}\overline{\omega}^{bi} \tag{F.29}$$

where $^{b}\overline{\omega}^{bi} = \omega_a\hat{b}_1 + \omega_b\hat{b}_2 + \omega_c\hat{b}_3$ is the angular velocity of the body frame with respect to the inertial frame. Aligning the $\hat{b}$-frame with the SFP's principal axes results in a diagonal moment of inertia matrix

$$\tilde{I} = \begin{bmatrix} A & 0 & 0 \\ 0 & B & 0 \\ 0 & 0 & C \end{bmatrix}$$

Solving Equation F.29 for the individual elements gives the standard Euler's equations (35:95)

$$\hat{b}_1: \quad A\dot{\omega}_a + (C - B)\omega_b\omega_c = {}^{b}M_1 \tag{F.30}$$

$$\hat{b}_2: \quad B\dot{\omega}_b + (A - C)\omega_a\omega_c = {}^{b}M_2 \tag{F.31}$$

$$\hat{b}_3: \quad C\dot{\omega}_c + (B - A)\omega_a\omega_b = {}^{b}M_3 \tag{F.32}$$

These are coupled, nonlinear, first order differential equations.

Equations F.30 – F.32 can be used to derive the last three equations of motion in terms of the yaw, pitch, and roll of the $\hat{b}$-frame. Thus, the angular velocity of the $\hat{b}$-frame, with respect to the $\hat{i}$-frame, must be defined in terms of ψ, θ, and ϕ. Since angular velocities add, the angular velocity of the $\hat{b}$-frame with respect to the $\hat{i}$-frame is given by

$$\begin{aligned} \overline{\omega}^{bi} &= \overline{\omega}^{ba} + \overline{\omega}^{ai} \\ &= \left(\dot{\psi}\hat{a}_r + \dot{\theta}\hat{a}'_3 + \dot{\phi}\hat{b}_2\right) + \left(\sqrt{\frac{GM_{\oplus}}{r^3}}\hat{a}_3\right) \end{aligned} \tag{F.33}$$

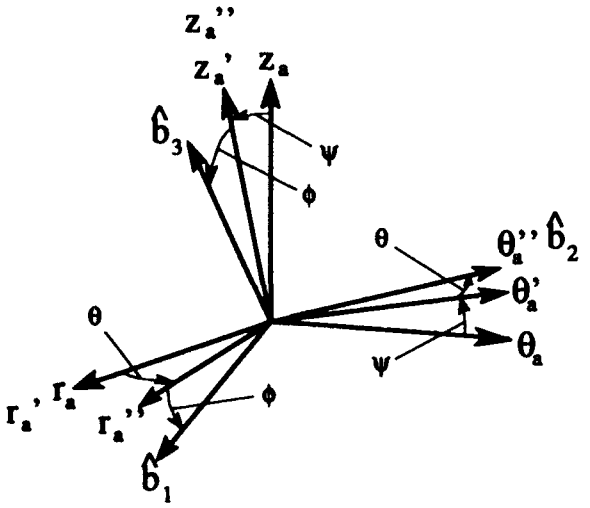

Figure F.2 Rotation of the coordinate axes using the Euler angles for pitch, θ, roll, ϕ, and yaw, ψ.

However, $\overline{\omega}^{bi}$ must be expressed in the $\hat{b}$-frame to be used in Equations F.30 – F.32. Examination of Figure F.2 shows

$$\begin{aligned}
\hat{a}_r &= c\theta c\phi \hat{b}_1 - s\theta \hat{b}_2 + c\theta s\phi \hat{b}_3 \\
\hat{a}'_3 &= -s\phi \hat{b}_1 + c\phi \hat{b}_3 \\
\hat{a}_3 &= (c\phi s\theta s\psi - s\phi c\psi)\,\hat{b}_1 + c\theta s\psi \hat{b}_2 + (s\phi s\theta s\psi + c\phi c\psi)\,\hat{b}_3
\end{aligned}$$

and using a binomial expansion

$$\sqrt{\frac{GM_\oplus}{r^3}} = \sqrt{\frac{GM_\oplus}{r_o^3}}\left(1 - \frac{3}{2}\frac{\delta r}{r_o}\right) = n\left(1 - \frac{3}{2}\frac{\delta r}{r_o}\right) = n_{SFP}$$

Therefore

$$
\begin{aligned}
{}^{b}\overline{\omega}^{bi} &= \omega_a \hat{b}_1 + \omega_b \hat{b}_2 + \omega_c \hat{b}_3 \\
&= \left[\dot{\psi} c\theta c\phi - \dot{\theta} s\phi + n_{SFP}\left(c\phi s\theta s\psi - s\phi c\psi\right)\right] \hat{b}_1 + \\
&\quad \left[-\dot{\psi} s\theta + \dot{\phi} + n_{SFP} c\theta s\psi\right] \hat{b}_2 + \\
&\quad \left[\dot{\psi} c\theta s\phi + \dot{\theta} c\phi + n_{SFP}\left(s\phi s\theta s\psi + c\phi c\psi\right)\right] \hat{b}_3
\end{aligned} \tag{F.34}
$$

Understanding that the last terms in ω_a, ω_b, and ω_c are due to the rotation of the $\hat{a}$-frame, at the center of mass of the SFP, with respect to the $\hat{i}$-frame, Equation F.34 is the same as that derived by Wiesel (93:113).

Equation F.34 is the inertial angular velocity, expressed in the $\hat{b}$-frame. To use Equation F.29, the inertial angula cceleration is also needed. Examination of Equation F.34 shows that $\overline{\omega}^{bi}$ is nonlin ar and coupled in the orientation angles. Since the goal is to obtain three equations of motion describing the orientation of the vehicle in inertial space, the equations resulting from Euler's equations should be in terms of ψ, θ, and ϕ. The application of Equation F.3 to Equation F.34 further compounds the nonlinearities and coupling. For the scope of this study, it is not necessary to solve the complete nonlinear equations. To simplify the problem, $\overline{\omega}^{bi}$ can b linearized about a point. The point selected to linearize about is the fundamental orientation ($\psi = \theta = \phi = 0°$), since this is one of the primary operating orientations for the SFP. Other operating orientations could be chosen, in which case the elements of Equation F.34 would need to be expanded by Taylor series expansions about the point of interest.

To linearize about the point $\psi = \theta = \phi = 0°$, assume the perturbations from this point are small. This allows the use of the small angle assumptions

$$c\theta = c\phi = c\psi \approx 1$$

$$s\theta \approx \theta \qquad s\phi \approx \phi \qquad s\psi \approx \psi$$

It is assumed that the rates of change of the orientation angles are small as well. If the products of small elements are assumed to be negligible, the linearized $\overline{\omega}^{bi}$ can be obtained. Substituting back into Equation F.34 gives

$$\begin{aligned} {}^b\overline{\omega}^{bi} &= \left(\dot{\psi} - n_{SFP}\phi\right)\hat{b}_1 + \left(\dot{\phi} + n_{SFP}\psi\right)\hat{b}_2 + \left(\dot{\theta} + n_{SFP}\right)\hat{b}_3 \\ &= \left(\dot{\psi} - n\phi\right)\hat{b}_1 + \left(\dot{\phi} + n\psi\right)\hat{b}_2 + \left(\dot{\theta} + n - \frac{3}{2}\frac{n\delta r}{r_o}\right)\hat{b}_3 \end{aligned} \tag{F.35}$$

This equation is now easily differentiated to give the linearized inertial angular acceleration in terms of the orientation angles. Differentiating,

$${}^b\dot{\overline{\omega}}^{bi} = \left(\ddot{\psi} - n\dot{\phi}\right)\hat{b}_1 + \left(\ddot{\phi} + n\dot{\psi}\right)\hat{b}_2 + \left(\ddot{\theta} - \frac{3}{2}\frac{n\delta\dot{r}}{r_o}\right)\hat{b}_3 \tag{F.36}$$

Equations F.35 and F.36 can be substituted back into Equations F.30 – F.32 to give the rotational equations of motion in terms of the orientation angles. Again neglecting the products of the orientation angles and/or their rates, the rotational equations of motion are given by

$$\hat{b}_1: \quad A\ddot{\psi} + n\left(C - B - A\right)\dot{\phi} + n^2\left(C - B\right)\psi = {}^bM_1 \tag{F.37}$$

$$\hat{b}_2: \quad B\ddot{\phi} + n\left(A + B - C\right)\dot{\psi} + n^2\left(C - A\right)\phi = {}^bM_2 \tag{F.38}$$

$$\hat{b}_3: \quad C\ddot{\theta} - \frac{3}{2}\frac{nC}{r_o}\delta\dot{r} = {}^bM_3 \tag{F.39}$$

These three equations are the inertial angular accelerations, expressed in the orientation angles, due to the external moment, ${}^b\overline{M}$.

Similar to the case of the translational equations of motion, ${}^b\overline{M}$ is the sum of all external torques acting on the SFP. A number of external forces can contribute to this total torque. As before, gravity, aerodynamic drag, magnetic field effects, and non-environmental forces can all apply torques to an orbiting vehicle. It is reasonable

to expect that if the aerodynamic drag force is strong enough to be considered in the relative translational equations of motion, it should be included in the relative rotational equations as well. However, the SFP's configuration shown in Figure 3.1 is symmetric across the $\hat{b}_1\hat{b}_2$ plane. The majority of the presented area of the SFP is a result of the solar dynamic power modules and the ASSET photovoltaic arrays. Because of symmetry and the fact that the $\hat{b}_2$-axis is essentially aligned with the velocity vector, the aerodynamic drag is assumed to cause no torque about the $\hat{b}_1$-axis in this orientation. The remainder of the area is small and near the center of mass; it is assumed that the drag torque generated by this area is negligible. It is also assumed that there are no drag effects due to assymetries in component drag coefficients. The result is that aerodynamic drag effects are negligable in the relative rotational equations of motion, and for the purposes of this study, gravity and magnetic field effects will be the only forces included in the analysis.

An examination of Equation F.8 shows the force due to gravity changes with the distance between the two bodies. This change can generate a torque on an orbiting vehicle, in this case the SFP. Assuming the SFP's principal body axes are aligned with the $\hat{b}$-frame axes, the approximate component gravitational torques are given by Wiesel (93:146-147) as

$$M_{g_1} = 3\frac{\mu}{r^5}R_2R_3(C-B) \tag{F.40}$$

$$M_{g_2} = 3\frac{\mu}{r^5}R_1R_3(A-C) \tag{F.41}$$

$$M_{g_3} = 3\frac{\mu}{r^5}R_1R_2(B-A) \tag{F.42}$$

where R_1, R_2, and R_3 are the components of $\overline{r}$ expressed in the $\hat{b}$-frame. Transforming $\overline{r}$ (Equation F.2) from the $\hat{a}$-frame to the $\hat{b}$-frame using Equation C.10,

$$
\begin{aligned}
{}^{b}\overline{r} &= R^{baa}\overline{r} \\
&= \begin{bmatrix} c\phi c\theta & c\phi s\theta c\psi + s\phi s\psi & c\phi s\theta s\psi - s\phi c\psi \\ -s\theta & c\theta c\psi & c\theta s\psi \\ s\phi c\theta & s\phi s\theta c\psi - c\phi s\psi & s\phi s\theta s\psi + c\phi c\psi \end{bmatrix} \begin{bmatrix} (r_o + \delta r) \\ r_o \delta\nu \\ \delta z \end{bmatrix} \\
&= [(c\phi c\theta)(r_o + \delta r) + (c\phi s\theta c\psi + s\phi s\psi)(r_o\delta\nu) + (c\phi s\theta s\psi - s\phi c\psi)(\delta z)]\,\hat{b}_1 + \\
&\quad [(-s\theta)(r_o + \delta r) + (c\theta c\psi)(r_o\delta\nu) + (c\theta s\psi)(\delta z)]\,\hat{b}_2 + \\
&\quad [(s\phi c\theta)(r_o + \delta r) + (s\phi s\theta c\psi - c\phi s\psi)(r_o\delta\nu) + \\
&\quad (s\phi s\theta s\psi + c\phi c\psi)(\delta z)]\,\hat{b}_3
\end{aligned}
\tag{F.43}
$$

As can be seen from this expression, the elements of ${}^{b}\overline{r}$ are highly nonlinear in the orientation angles and do not lend themselves to an analytical solution of Euler's equations. If the same assumptions are made as were made for linearizing the angular velocity and acceleration, the expression for the linear ${}^{b}\overline{r}$ becomes

$$
{}^{b}\overline{r} = (r_o + \delta r)\,\hat{b}_1 - r_o(\theta - \delta\nu)\,\hat{b}_2 + (r_o\phi + \delta z)\,\hat{b}_3 \tag{F.44}
$$

so

$$
\begin{aligned}
R_1 &= r_o + \delta r \\
R_2 &= r_o\theta - r_o\delta\nu \\
R_3 &= r_o\phi + \delta z
\end{aligned}
$$

Before the gravity torque equations can be used, the r^{-5} term must be expanded using a binomial expansion

$$\begin{aligned} r^{-5} &= \left[(r_o+\delta r)^2+(r_o\theta-r_o\delta\nu)^2+(r_o\phi+\delta z)^2\right]^{-\frac{5}{2}} \\ &\approx r_o^{-6}(r_o-5\delta r)+\mathcal{O}\left[|\delta\bar{r}|^2\right] \end{aligned}$$

Substituting this expression and the R_i components back into Equations F.40 - F.42 gives the linearized, first order approximation of the gravity torques. The full expressions of components of the gravity torque contain products of position and orientation components. Assuming these terms are small compared to r_o, they can be neglected, and the gravity torque components become:

$$M_{g_1} = 0 \tag{F.45}$$

$$M_{g_2} = 3n^2\left(\phi+\frac{\delta z}{r_o}\right)(A-C) \tag{F.46}$$

$$M_{g_3} = 3n^2(\delta\nu-\theta)(B-A) \tag{F.47}$$

As with the translational equations of motion, the magnetic field effects are used for controlling orientation and are not included in the homogeneous rotational equations of motion. These equations can now be found by substituting Equations F.45 - F.47 into Equations F.37 - F.39. The relative rotational equations of motion are then given as

$$\hat{b}_1: \quad A\ddot{\psi}+n(C-B-A)\dot{\phi}+n^2(C-B)\psi = 0 \tag{F.48}$$

$$\hat{b}_2: \quad B\ddot{\phi}+n(A+B-C)\dot{\psi}+4n^2(C-A)\phi+3n^2\frac{(C-A)}{r_o}\delta z = 0 \tag{F.49}$$

$$\hat{b}_3: \quad C\ddot{\theta}-\frac{3}{2}\frac{nC}{r_o}\delta\dot{r}+3n^2(B-A)\theta-3n^2\frac{(B-A)r_o\delta\nu}{r_o} = 0 \tag{F.50}$$

These are the rotational equations of motion for a reference point in a circular orbit. They are coupled, linear, constant-coefficient, differential equations that can

be used to approxim ·te the rotational motion of the SFP for small perturbations from the condition about which the linearization was performed. They differ from the equations derived by Wiesel (93:148) due to the presence of terms containing relative position components (a result of the SFP being at some other point than, but close to, the reference point) and the orbital frame being fixed to the reference point rather than the SFP. These equations reduce to those derived by Wiesel when the relative positions and velocities are set to zero (i.e. attaching the reference point to the SFP).

F.0.0.3 SFP Relative Equations of Motion. The derivation of the relative equations of motion is now complete. The six equations

$$\delta\ddot{r} - K\delta\dot{r} - 2nr_o\delta\dot{\nu} - 3n^2\delta r + K\delta\omega r_o\delta\nu + K\omega_2\delta z = 0 \quad \text{(F.51)}$$

$$r_o\delta\ddot{\nu} + 2n\delta\dot{r} + Kr_o\delta\dot{\nu} - K\delta\omega\delta r - K\omega_1\delta z - K\delta\omega r_o = 0 \quad \text{(F.52)}$$

$$\delta\ddot{z} - K\delta\dot{z} - K\omega_2\delta r + K\omega_1 r_o\delta\nu + n^2\delta z - K\omega_2 r_o = 0 \quad \text{(F.53)}$$

$$A\ddot{\psi} + n(C - B - A)\dot{\phi} + n^2(C - B)\psi = 0 \quad \text{(F.54)}$$

$$B\ddot{\phi} + n(A + B - C)\dot{\psi} + 4n^2(C - A)\phi + 3n^2\frac{(C - A)}{r_o}\delta z = 0 \quad \text{(F.55)}$$

$$C\ddot{\theta} - \frac{3}{2}\frac{nC}{r_o}\delta\dot{r} + 3n^2(B - A)\theta - 3n^2\frac{(B - A)r_o\delta\nu}{r_o} = 0 \quad \text{(F.56)}$$

completely describe the position and orientation of the SFP, in the neighborhood of the reference point, for small yaw, pitch, and roll angles when *no forcing functions are applied* (such as the propulsion/control system).

F.0.0.4 Steady State Equations of Motion. The primary use of the relative equations of motion is to design a controller to perform steady state tracking relative to a reference point. The controller design is then used to determine specific design parameters for the SFP. Some insight into the platform's required configuration and performance capabilities can be gained by considering the relative

equations of motion under steady state conditions. Under steady state conditions:

$$\delta\dot{r} = \delta\ddot{r} = r_o\delta\dot{\nu} = r_o\delta\ddot{\nu} = \delta\dot{z} = \delta\ddot{z} = 0$$
$$\dot{\psi} = \ddot{\psi} = \dot{\phi} = \ddot{\phi} = \dot{\theta} = \ddot{\theta} = 0$$

Substituting these values into Equations F.51 - F.56 gives:

$$F_{\delta r_{ss}} = M_{tot}\left[-3n^2\delta r + K\delta\omega r_o\delta\nu + K\omega_2\delta z\right] \quad \text{(F.57)}$$

$$F_{r_o\delta\nu_{ss}} = M_{tot}\left[-K\delta\omega\delta r - K\omega_1\delta z - K\delta\omega r_o\right] \quad \text{(F.58)}$$

$$F_{\delta z_{ss}} = M_{tot}\left[-K\omega_2\delta r + K\omega_1 r_o\delta\nu + n^2\delta z - K\omega_2 r_o\right] \quad \text{(F.59)}$$

$$M_{\psi_{ss}} = A\left[n^2(C-B)\psi\right] \quad \text{(F.60)}$$

$$M_{\phi_{ss}} = B\left[4n^2(C-A)\phi + 3n^2\frac{(C-A)}{r_o}\delta z\right] \quad \text{(F.61)}$$

$$M_{\theta_{ss}} = C\left[3n^2(B-A)\theta - 3n^2\frac{(B-A)r_o\delta\nu}{r_o}\right] \quad \text{(F.62)}$$

A few conclusions can be drawn from these equations. First, excluding drag effects, a standoff in the radial direction requires three times as much force as a standoff of the same distance in the out-of-plane direction; a standoff along the orbit path requires no force (when drag is excluded). Second, drag effects require steady forces be applied in both the path and out-of-plane directions to stay at a fixed point, even if the SFP is at the reference radius. Steady state forces are required in the radial direction only if the SFP is not at the reference radius. If the SFP is not at the reference radius, the steady state forces are required due to the vector component of the drag force that is tangent to the orbit path at the SFP's center of mass. Third, steady state moments are required to hold a yaw, roll, and/or pitch attitude. If the SFP is standing off along the orbit path or out-of-plane, steady state moments are required to maintain any fixed attitude.

Appendix G. Platform Design Programs

Several MATLAB (65) computer programs were developed as design tools for the task of sizing the propulsion system. The main design programs are a modified version of the program developed by Lawrence (49:F.1 - F.11). The code was modified to incorporate all differences between Lawrence's POTV and the SFP. The changes included:

- a more detailed breakout of the vehicle mass elements
- a more detailed mass moments of inertia determination
- accounting for specific true anomaly, sidereal time, and inclination data
- accounting for aerodynamic drag
- calculation of all forces and moments generated by individual control elements
- calculation of the total power required, to including induced voltage power requirements
- calculation of the surface and core temperatures of all conductors

The programs determine the currents and thrust required, the state vector and the outputs over a period of time specified when the program is run. The first program places the vehicle at a fixed point in the orbit while time goes forward. The currents required, thrust required, total power required, total voltage required, position and orientation, and forces and moments are all plotted. This program is used to study the time-based performance of the propulsion system at a single fixed point in the orbit. This program can be run at numerous points along the orbit to build a "gain schedule" for the controller. Several subroutines are used to perform specialized tasks such as determining the diameter of a conductor bundle based on the number of individual conductors and checking the surface and core temperatures of the conductors.

G.1 Time-History Design Program

The following MATLAB program is one of the primary tools for performing the detailed design of the SFP. The basic code was developed by Lawrence (49:F.1-F.11). The code was modified to incorporate all differences between the POTV vehicle and the SFP. The changes included:

- a more detailed breakout of the vehicle mass elements
- a more detailed mass moments of inertia determination
- accounting for specific true anomaly, sidereal time, and inclination data
- accounting for aerodynamic drag
- calculation of all forces and moments generated by individual control elements
- calculation of the total power required, to include electromotive forces
- calculation of the surface and core temperatures of all conductors

The program determines the currents and thrust required, the state vector and the outputs over a period of time specified when the program is run. The currents required, thrust required, total required power, total voltage required, position and orientation, and forces and moments are all plotted.

```
%%%%%%%%%%%%%%%%%%%%%%%%%%%%%%%%%%%%%%%%%%%%%%%%%%%%%%%%%%%%%%%%%%%%%%%%%%%%%%%%%%%%
%
%               Program Variables
% -----------------------------------------------------
%
%  A          Total Ixx mass moment of inertia (kg*m^2)
%  a          Matrix containing SFP accelerations (m/s^2)
%  Adrag      SFP Frontal Area (m^2)
%  altitude   SFP altitude
%  area       Conductor wire area (m^2)
%  B          Total Ixx mass moment of inertia (kg*m^2)
%  B1         B field component - b1 direction (T)
%  B2         B field component - b2 direction (T)
%  B3         B field component - b3 direction (T)
%  b1mom1     Conductor C1 moment - b1 direction (N*m)
%  b1mom2     Conductor C2 moment - b1 direction (N*m)
%  b1mom3     Conductor C3 moment - b1 direction (N*m)
%  b1mom4     Conductor C4 moment - b1 direction (N*m)
%  b1mom6     Conductor C6 moment - b1 direction (N*m)
%  b1mom7     Conductor C7 moment - b1 direction (N*m)
%  b1mom8     Conductor C8 moment - b1 direction (N*m)
%  b1mom9     Conductor C9 moment - b1 direction (N*m)
```

```
%  b2mom1     Conductor C1 moment - b2 direction (N*m)
%  b2mom3     Conductor C3 moment - b2 direction (N*m)
%  b2mom4     Conductor C4 moment - b2 direction (N*m)
%  b2mom5     Conductor C5 moment - b2 direction (N*m)
%  b2mom8     Conductor C8 moment - b2 direction (N*m)
%  b2mom9     Conductor C9 moment - b2 direction (N*m)
%  b3mom1     Conductor C1 moment - b3 direction (N*m)
%  b3mom2     Conductor C2 moment - b3 direction (N*m)
%  b3mom3     Conductor C3 moment - b3 direction (N*m)
%  b3mom4     Conductor C4 moment - b3 direction (N*m)
%  b3mom5     Conductor C5 moment - b3 direction (N*m)
%  b3mom6     Conductor C6 moment - b3 direction (N*m)
%  b3mom7     Conductor C7 moment - b3 direction (N*m)
%  b3mom10    Conductor C10 moment - b3 direction (N*m)
%  C          Total Ixx mass moment of inertia (kg*m^2)
%  Cd         SFP Drag Coefficient
%  C0         b-frame to a frame rotation matrix
%  d1         Diameter of conductor C1 (m)
%  d2         Diameter of conductor C2 (m)
%  d3         Diameter of conductor C3 (m)
%  d4         Diameter of conductor C4 (m)
%  d5         Diameter of conductor C5 (m)
%  delr       Commanded delta r relative position (m)
%  delr0      Initial delta r relative position (m)
%  delw       SFP relative angular rate (rad/s) (n-w3)
%  delz       Commanded delta z relative position (m)
%  delz0      Initial r0 delta nu relative position (m)
%  dwire      Wire diameter (m)
%  Fcl        Closed loop system matrix
%  Fsys       Open loop system matrix
%  G          Universal Gravitation Constant (N*m^2/kg^2)
%  Gcl        Closed loop input matrix
%  Gsys       Open loop input matrix
%  hapa       ASSET array center of mass height (m)
%  Hapa       ASSET array effective height (m)
%  Hcl        Closed loop output matrix
%  hs         Scale height (km)
%  Hspm       Power module effective height (m)
%  hspm       Power module center of mass height (m)
%  Hsys       Open loop output matrix
%  Hta        Thruster assembly height (m)
%  Htm        Truss maker height (m)
%  i          Local counter
%  i5ss       Conductor C5 steady state current due to drag
%  incl       Orbit inclination (deg)
%  Ixx(1)     X-axis mass moment of inertia for Payload
%  Ixx(2)     X-axis mass moment of inertia for Truss Maker
%  Ixx(3)     X-axis mass moment of inertia for Main Integrated Truss
%  Ixx(4)     X-axis mass moment of inertia for Thruster Assemblies
%  Ixx(5)     X-axis mass moment of inertia for Cross Integrated Truss
%  Ixx(6)     X-axis mass moment of inertia for Solar Dynamic Cells
%  Ixx(7)     X-axis mass moment of inertia for ASSET Power Arrays
%  Ixx(8)     X-axis mass moment of inertia for Orthogonal Integrated Truss
%  Ixx(9)     X-axis mass moment of inertia for Conductor C1
%  Ixx(10)    X-axis mass moment of inertia for Conductor C2
%  Ixx(11)    X-axis mass moment of inertia for Conductor C3
%  Ixx(12)    X-axis mass moment of inertia for Conductor C4
%  Ixx(13)    X-axis mass moment of inertia for Conductor C5
%  Ixx(14)    X-axis mass moment of inertia for Coiled Conductor Truss Assembly
%  Iyy(1)     Y-axis mass moment of inertia for Payload
%  Iyy(2)     Y-axis mass moment of inertia for Truss Maker
%  Iyy(3)     Y-axis mass moment of inertia for Main Integrated Truss
%  Iyy(4)     Y-axis mass moment of inertia for Thruster Assemblies
%  Iyy(5)     Y-axis mass moment of inertia for Cross Integrated Truss
%  Iyy(6)     Y-axis mass moment of inertia for Solar Dynamic Cells
```

```
%  Iyy(7)     Y-axis mass moment of inertia for ASSET Power Arrays
%  Iyy(8)     Y-axis mass moment of inertia for Orthogonal Integrated Truss
%  Iyy(9)     Y-axis mass moment of inertia for Conductor C1
%  Iyy(10)    Y-axis mass moment of inertia for Conductor C2
%  Iyy(11)    Y-axis mass moment of inertia for Conductor C3
%  Iyy(12)    Y-axis mass moment of inertia for Conductor C4
%  Iyy(13)    Y-axis mass moment of inertia for Conductor C5
%  Iyy(14)    Y-axis mass moment of inertia for Coiled Conductor Truss Assembly
%  Izz(1)     Z-axis mass moment of inertia for Payload
%  Izz(2)     Z-axis mass moment of inertia for Truss Maker
%  Izz(3)     Z-axis mass moment of inertia for Main Integrated Truss
%  Izz(4)     Z-axis mass moment of inertia for Thruster Assemblies
%  Izz(5)     Z-axis mass moment of inertia for Cross Integrated Truss
%  Izz(6)     Z-axis mass moment of inertia for Solar Dynamic Cells
%  Izz(7)     Z-axis mass moment of inertia for ASSET Power Arrays
%  Izz(8)     Z-axis mass moment of inertia for Orthogonal Integrated Truss
%  Izz(9)     Z-axis mass moment of inertia for Conductor C1
%  Izz(10)    Z-axis mass moment of inertia for Conductor C2
%  Izz(11)    Z-axis mass moment of inertia for Conductor C3
%  Izz(12)    Z-axis mass moment of inertia for Conductor C4
%  Izz(13)    Z-axis mass moment of inertia for Conductor C5
%  Izz(14)    Z-axis mass moment of inertia for Coiled Conductor Truss Assembly
%  Jcl        Closed loop feedforward matrix
%  Jsys       Open loop feedforward matrix
%  K          LQR controller constant gain matrix
%  Kd         Drag Factor (1/s)
%  L1         Total length of conductor C1 (m)
%  L2         Total length of conductor C2 (m)
%  L3         Total length of conductor C3 (m)
%  L4         Total length of conductor C4 (m)
%  L5         Total length of conductor C5 (m)
%  L6         Total length of conductor C6 (m)
%  L7         Total length of conductor C7 (m)
%  L8         Total length of conductor C8 (m)
%  L9         Total length of conductor C9 (m)
%  L10        Total length of conductor C10 (m)
%  L1vec      Vector length of conductor C1 in b-frame (m)
%  L2vec      Vector length of conductor C2 in b-frame (m)
%  L3vec      Vector length of conductor C3 in b-frame (m)
%  L4vec      Vector length of conductor C4 in b-frame (m)
%  L5vec      Vector length of conductor C5 in b-frame (m)
%  L1Vind     Conductor C1 induced voltage (v)
%  L2Vind     Conductor C2 induced voltage (v)
%  L3Vind     Conductor C3 induced voltage (v)
%  L4Vind     Conductor C4 induced voltage (v)
%  L5Vind     Conductor C5 induced voltage (v)
%  Lam0       Longitude of austral simple magnetic pole (deg)
%  lapa       ASSET array position on truss (m)
%  LC1        Length of conductor C1 assembly (m)
%  LC2        Length of conductor C2 assembly (m)
%  LC3        Length of conductor C3 assembly (m)
%  LC4        Length of conductor C4 assembly (m)
%  LC5        Length of conductor C5 assembly (m)
%  Lccst      Length of coiled conductor integrated truss (m)
%  Lcit       Cross integrated trusses length (m)
%  Lmit       Integrated truss length (m)
%  Loit       Orthogonal integrated truss length (m)
%  Lpay       Payload length (m)
%  Lsol6      Length of coiled conductor C6 (m)
%  Lsol7      Length of coiled conductor C7 (m)
%  Lsol8      Length of coiled conductor C8 (m)
%  Lsol9      Length of coiled conductor C9 (m)
%  Lsol10     Length of coiled conductor C10 (m)
%  lspm       Power module position on truss (m)
%  Ltm        Truss maker length (m)
```

```
%  M          Magnetic dipole moment of the earth (T*m^3)
%  m1         B-field factor in ar direction
%  m2         B-field factor in atheta direction
%  m3         B-field factor in a3 direction
%  Mapa       Asset array Mass (kg)
%  maxcur     Maximum currents vector (A)
%  Mc         Controllability matrix
%  Mc1        Conductor C1 mass (kg)
%  Mc2        Conductor C2 mass (kg)
%  Mc3        Conductor C3 mass (kg)
%  Mc4        Conductor C4 mass (kg)
%  Mc5        Conductor C5 mass (kg)
%  Mc6        Coiled Conductor C6 mass (kg)
%  Mc7        Coiled Conductor C7 mass (kg)
%  Mc8        Coiled Conductor C8 mass (kg)
%  Mc9        Coiled Conductor C9 mass (kg)
%  Mc10       Coiled Conductor C10 mass (kg)
%  Mccst      Mass of coiled conductor integrated truss (kg)
%  Mcit       Mass of cross integrated truss (kg)
%  Me         Mass of Earth (kg)
%  mm         Local variable - number of rows in matrix
%  Mmit       Mass of main integrated truss (kg)
%  Mo         Observability matrix
%  Moit       Mass of orthogonal integrated truss (kg)
%  Mpay       Mass of payload (kg)
%  Mpf        Constant gain pre-filter matrix
%  Mspm       Mass of solar dynamic power module (kg)
%  Mta        Mass of thruster assembly (kg)
%  Mtm        Mass of truss maker (kg)
%  Mtot       Total mass of SFP (kg)
%  mu6        Mu factor of coiled conductor C1 (m^2)
%  mu7        Mu factor of coiled conductor C2 (m^2)
%  mu8        Mu factor of coiled conductor C3 (m^2)
%  mu9        Mu factor of coiled conductor C4 (m^2)
%  mu10       Mu factor of coiled conductor C5 (m^2)
%  n          Orbital mean motion of reference orbit (rad/s)
%  nn         Local variable - number of columns in matrix
%  n1         Number of turns in conductor C1
%  n2         Number of turns in conductor C2
%  n3         Number of turns in conductor C3
%  n4         Number of turns in conductor C4
%  n5         Number of turns in conductor C5
%  n6         Number of turns in conductor C6
%  n7         Number of turns in conductor C7
%  n8         Number of turns in conductor C8
%  n9         Number of turns in conductor C9
%  n10        Number of turns in conductor C10
%  neg        Vector containing largest negative currents (A)
%  ntinc      Number of time increments
%  nu         True anomaly (deg)
%  Omega      Right ascension of the ascending node (deg)
%  phi        Commanded roll angle (deg)
%  phi0       Initial roll angle (deg)
%  Phi0       Latitude of austral simple magnetic dipole pole (deg)
%  pos        Vector containing largest positive currents (A)
%  pow1       Power required by conductor C1 (kW)
%  pow2       Power required by conductor C2 (kW)
%  pow3       Power required by conductor C3 (kW)
%  pow4       Power required by conductor C4 (kW)
%  pow5       Power required by conductor C5 (kW)
%  pow6       Power required by conductor C6 (kW)
%  pow7       Power required by conductor C7 (kW)
%  pow8       Power required by conductor C8 (kW)
%  pow9       Power required by conductor C9 (kW)
%  pow10      Power required by conductor C10 (kW)
```

```
%  ps1       Linear density of conductor C1 shield (kg/m)
%  ps2       Linear density of conductor C2 shield (kg/m)
%  ps3       Linear density of conductor C3 shield (kg/m)
%  ps4       Linear density of conductor C4 shield (kg/m)
%  ps5       Linear density of conductor C5 shield (kg/m)
%  psi       Commanded yaw angle (deg)
%  psi0      Initial yaw angle (deg)
%  pw1       Linear density of conductor C1 (kg/m)
%  pw2       Linear density of conductor C2 (kg/m)
%  pw3       Linear density of conductor C3 (kg/m)
%  pw4       Linear density of conductor C4 (kg/m)
%  pw5       Linear density of conductor C5 (kg/m)
%  pwcc      Linear density of coiled conductors (kg/m)
%  Q         LQR state weight matrix
%  qwt       Weighting factor of state weight matrix
%  r         Matrix of input vectors
%  r0        Radius of reference orbit (m)
%  R1        Resistance of conductor C1 (ohms)
%  R2        Resistance of conductor C2 (ohms)
%  R3        Resistance of conductor C3 (ohms)
%  R4        Resistance of conductor C4 (ohms)
%  R5        Resistance of conductor C5 (ohms)
%  R6        Resistance of conductor C6 (ohms)
%  R7        Resistance of conductor C7 (ohms)
%  R8        Resistance of conductor C8 (ohms)
%  R9        Resistance of conductor C9 (ohms)
%  R10       Resistance of conductor C10 (ohms)
%  r6        Nominal radius of coiled conductor C6 (m)
%  r7        Nominal radius of coiled conductor C7 (m)
%  r8        Nominal radius of coiled conductor C8 (m)
%  r9        Nominal radius of coiled conductor C9 (m)
%  r10       Nominal radius of coiled conductor C10 (m)
%  rdnu      Commanded ro delta nu relative position (m)
%  rdnu0     Initial delta z relative position (m)
%  re        Mean Equatorial Radius of Earth (m)
%  rho       Resistance of aluminum conductor (ohms/m)
%  rho0      Air density at reference altitude (kg/m^3)
%  RX        LQR Control weighting matrix
%  Rpay      Radius of external tank payload (m)
%  rref      Reference altitude (km)
%  rsol6     Thickness of coiled conductor C6 (m)
%  rsol8     Thickness of coiled conductor C8 (m)
%  rsol10    Thickness of coiled conductor C10 (m)
%  rwire     Radius of individual conductor wire (m)
%  rwt       Weighting factor of control weighting matrix
%  t         Time vector (s)
%  T10       Conductor C1 core temperature (deg C)
%  T20       Conductor C2 core temperature (deg C)
%  T30       Conductor C3 core temperature (deg C)
%  T40       Conductor C4 core temperature (deg C)
%  T50       Conductor C5 core temperature (deg C)
%  T60       Conductor C6 core temperature (deg C)
%  T70       Conductor C7 core temperature (deg C)
%  T80       Conductor C8 core temperature (deg C)
%  T90       Conductor C9 core temperature (deg C)
%  T100      Conductor C10 core temperature (deg C)
%  T11       Conductor C1 Hetic temperature (deg C)
%  T21       Conductor C2 Hetic temperature (deg C)
%  T31       Conductor C3 Hetic temperature (deg C)
%  T41       Conductor C4 Hetic temperature (deg C)
%  T51       Conductor C5 Hetic temperature (deg C)
%  theta     Commanded pitch angle (deg)
%  theta0    Initial pitch angle (deg)
%  Thetag    Sidereal time (deg)
%  thss      Out of plane thrust required due to drag (N)
```

```
%  tleng      Length of time vector
%  tmax       Maximum time in time vector (s)
%  totpow     Total power required by controller (kW)
%  tshield    Metic shield thickness (mm)
%  u          Matrix of control vectors
%  V1         SFP relative velocity - ar direction (rad/s)
%  V2         SFP relative velocity - atheta direction (rad/s)
%  V3         SFP relative velocity - a3 direction (rad/s)
%  VB         Velocity/B-field cross product vector
%  voltage    Total voltage required by controller (V)
%  w1         Earth's angular rotation rate - ar component (rad/s)
%  w2         Earth's angular rotation rate - atheta component (rad/s)
%  w3         Earth's angular rotation rate - a3 component (rad/s)
%  Wapa       ASSET array effective width (m)
%  Wccst      Width of coiled conductor integrated truss (m)
%  Wcit       Width and depth of cross integrated truss (m)
%  we         Earth's angular rotation rate (rad/sec)
%  wire       Diameter of single conductor in cm
%  Wmit       Width and depth of main integrated truss (m)
%  Woit       Width and Depth of orthogonal integrated truss (m)
%  Wspm       Solar dynamic power module effective width (m)
%  Wta        Width and depth of augmentation thruster assemblies (m)
%  Wtm        Width of truss maker (m)
%  x          Matrix containing state vectors
%  X0         State vector initial conditions
%  xforce1    Radial force generated by conductor C1 (N)
%  xforce2    Radial force generated by conductor C2 (N)
%  xforce3    Radial force generated by conductor C3 (N)
%  xforce4    Radial force generated by conductor C4 (N)
%  y          Matrix containing outputs
%  yforce3    In path force generated by conductor C3 (N)
%  yforce4    In path force generated by conductor C4 (N)
%  yforce5    In path force generated by conductor C5 (N)
%  zforce1    Out of plane force generated by conductor C1 (N)
%  zforce2    Out of plane force generated by conductor C2 (N)
%  zforce5    Out of plane force generated by conductor C5 (N)
%
%%%%%%%%%%%%%%%%%%%%%%%%%%%%%%%%%%%%%%%%%%%%%%%%%%%%%%%%%%%%%%%%%%%%%%%%%%%%%%%%%%

disp(' ');
disp('Welcome to the Space Fabrication Platform');
disp('Design Analysis Program');
disp(' ');

format short e

%%%%%%%%%%%%%%%%%%%%%%%%%%%%%%%%%%%%%%%
%
% Define Constants
%
%%%%%%%%%%%%%%%%%%%%%%%%%%%%%%%%%%%%%%%
G=6.67204e-11;     % gravitational constant (N*m^2/kg^2)
Me=5.976e24;       % mass of the earth (kg)
re=6.378e06;       % mean equatorial radius of earth (m)
we=7.2921e-05;     % Earth's Rotation Rate (rad/sec)

M=8.05e15;         % magnetic dipole moment of the earth (T)
Phi0=-78.5*pi/180; % Latitude of austral simple magnetic pole (rad)
Lam0=111*pi/180;   % Longitude of austral simple magnetic pole (rad)

Cd=2.4;            % SFP Drag Coefficient
Adrag=1435;        % SFP Frontal Area (m^2)
rho0=1.916e-11;    % Air Density at Reference Altitude (kg/m^3)
hs=50043;          % Scale Height (km)
rref=300;          % Reference altitude (km)
```

```
%%%%%%%%%%%%%%%%%%%%%%%%%%%%%%%%%%%%%%%%%%%%%%%%%%%%%%%%%%%%%%%%%%%%%%%%%%%%%%%%%%
%
% Platform Dimensions and Operating Regime
%
%%%%%%%%%%%%%%%%%%%%%%%%%%%%%%%%%%%%%%%%%%%%%%%%%%%%%%%%%%%%%%%%%%%%%%%%%%%%%%%%%%

%%%%%%%%%%%%%%%%%%%%%%%%%%%%%%%%%%%%%%%
%
% Payload Data
%
%%%%%%%%%%%%%%%%%%%%%%%%%%%%%%%%%%%%%%%
% Maximum allowable SFP payload = 31,300 kg
Mpay=31300;        % Payload Mass (kg)
Lpay=46.88;        % Payload Length (m)
Rpay=4.206;        % Payload Radius (m)

disp('Payload Mass (kg) = ');,disp(Mpay);

%%%%%%%%%%%%%%%%%%%%%%%%%%%%%%%%%%%%%%%
%
% Truss Maker Mass and Size
%
%%%%%%%%%%%%%%%%%%%%%%%%%%%%%%%%%%%%%%%
% Maximum allowable weight for truss
% maker = 3000 kg
% Size = 5x10x2 (b1xb2xb3)
Mtm=3000;          % Truss Maker Mass (kg)
Ltm=10;            % Truss Maker Length (m)
Wtm=2;             % Truss Maker Width (m)
Htm=5;             % Truss Maker Height (m)

%%%%%%%%%%%%%%%%%%%%%%%%%%%%%%%%%%%%%%%
%
% Main Integrated Truss Mass and Size
%
%%%%%%%%%%%%%%%%%%%%%%%%%%%%%%%%%%%%%%%
% Allow 5000 kg for remote manipulators
% Linear density = 20 kg/m for the truss
% structure
% Allow 2000 kg for ASSET equipment
Lmit=50;                     % Integrated Truss Length (m)
Wmit=2;                      % Main Int Truss Width and Depth (m)
Mmit=5000 + Lmit*20 +...
     2000;                   % Main Int Tr Misc Weight (kg)

%%%%%%%%%%%%%%%%%%%%%%%%%%%%%%%%%%%%%%%
%
% Augmentation Thruster Assemblies
%    Mass and Size
%
%%%%%%%%%%%%%%%%%%%%%%%%%%%%%%%%%%%%%%%
% Allow 1100 kg for augmentation thruster
% assemblies and associated H/W, plus 1000 kg
% for fuel.
Mta=1100 + 1000;   % Thruster Assembly Mass (kg)
Hta=4;             % Thruster Assembly Height (m)
Wta=2;             % TA Width and Depth (m)

%%%%%%%%%%%%%%%%%%%%%%%%%%%%%%%%%%%%%%%
%
% Cross Integrated Truss Mass and Size
%
%%%%%%%%%%%%%%%%%%%%%%%%%%%%%%%%%%%%%%%
% Allow 12000 kg for misc H/W
```

```
% Linear density = 20 kg/m for the truss
% structure
Lcit=30;            % Cross Integrated Trusses Length (m)
Wcit=2;             % Cross Int Truss Width and Depth (m)
Mcit=Lcit*20 +...
     12000;         % Cross Int Tr Misc Weight (kg)

%%%%%%%%%%%%%%%%%%%%%%%%%%%%%%%%%%%%%%%%%%%%%%%%
%
% Solar Dynamic Power Module Data
%
%%%%%%%%%%%%%%%%%%%%%%%%%%%%%%%%%%%%%%%%%%%%%%%%
% Allow 6000 kg/side for Module H/W
% Let Module c.m. be 4m off center of truss
% and 29 m from centerline of SFP
Mspm=6000;          % Solar dynamic Power Module Mass (kg)
Wspm=5;             % Power Module Effective Width (m)
Hspm=10;            % Power Module Effective Height (m)
hspm=4;             % Power Module c.m. Height (m)
lspm=29;            % Power Module Position on Truss (m)

%%%%%%%%%%%%%%%%%%%%%%%%%%%%%%%%%%%%%%%%%%%%%%%%
%
% ASSET Power Array Data
%
%%%%%%%%%%%%%%%%%%%%%%%%%%%%%%%%%%%%%%%%%%%%%%%%
% Allow 2500 kg/side for Array H/W
% Let Array c.m. be 3m off center of truss
% and 29 m from centerline of SFP
Mapa=2500;          % Array Mass (kg)
Wapa=2;             % Array Effective Width (m)
Hapa=7;             % Array Effective Height (m)
hapa=3;             % Array c.m. Height (m)
lapa=29;            % Array Position on Truss (m)

%%%%%%%%%%%%%%%%%%%%%%%%%%%%%%%%%%%%%%%%%%%%%%%%
%
% Orthogonal Integrated Truss Mass and Size
%
%%%%%%%%%%%%%%%%%%%%%%%%%%%%%%%%%%%%%%%%%%%%%%%%
% Allow 12000 kg for misc H/W
% Linear density = 20 kg/m for the truss
% structure
Loit=27;            % Orthogonal Integrated Trusses Length (m)
Woit=2;             % Orthogonal Integrated Truss Width and Depth (m)
Moit=Loit*20 +...
     0;             % Orthogonal Integrated Truss Misc Weight (kg)

%%%%%%%%%%%%%%%%%%%%%%%%%%%%%%%%%%%%%%%%%%%%%%%%
%
% Conductor Wire Diameter
%
%%%%%%%%%%%%%%%%%%%%%%%%%%%%%%%%%%%%%%%%%%%%%%%%
wire=2;             % Wire Diameter (cm)
disp('The diameter of the conductor wire (in cm) = ');,disp(wire);
dwire=wire/100;     % Wire diameter (m)
rwire=wire/200;     % Wire radius (m)
area=pi*rwire^2;    % Wire area (m^2)

tshield=10.14;      % Metic Shield thickness (mm)
disp('The Metic shield thickness (mm) = ');,disp(tshield);
tshield=tshield/1000;

%%%%%%%%%%%%%%%%%%%%%%%%%%%%%%%%%%%%%%%%%%%%%%%%
%
```

```
% Platform Design Dimensions
%
%%%%%%%%%%%%%%%%%%%%%%%%%%%%%%%%%%%%%%%%%%%%%%%%
%%% Conductor 1
LC1=25;
n1=99;
L1=LC1*n1;
disp('Length (LC1) of main conductor tower C1 (m) = ');,disp(LC1);
disp('Number of turns in conductors C1 = ');,disp(n1);
disp('The effective total length (L1) of conductors C1 (m) = ');,disp(L1);

%%% Conductor 2
LC2=LC1;
n2=n1;
L2=L1;
disp('Length (LC2) of main conductor tower C2 (m) = ');,disp(LC2);
disp('Number of turns in conductor C2 = ');,disp(n2);
disp('The effective total length (L2) of conductors C2 (m) = ');,disp(L2);

%%% Conductor 3
LC3=25;
n3=1;
L3=LC3*n3;
disp('Length (LC3) of cross conductor tower C3 (m) = ');,disp(LC3);
disp('Number of turns in conductors C3 = ');,disp(n3);
disp('The effective total length of conductors C3 (m) = ');,disp(L3);

%%% Conductor 4
LC4=LC3;
n4=n3;
L4=L3;
disp('Length (LC4) of main conductor tower C4 (m) = ');,disp(LC4);
disp('Number of turns in conductor C4 = ');,disp(n4);
disp('The effective total length (L4) of conductors C4 (m) = ');,disp(L4);

%%% Conductor 5
LC5=27;
n5=21;
L5=LC5*n5;
disp('Length (LC5) of pole conductor, C5 (m) = ');,disp(LC5);
disp('Number of turns in conductor C5 = ');,disp(n5);
disp('The effective total length of conductor C5 (m) = ');,disp(L5);

%%% Conductor 6
r6=1.9;
n6=137;
Lsol6=ceil((n6/10))*0.02;
if n6<5,
  rsol6=(n6*0.02)/2;
else
  rsol6=0.10;
end
L6=n6*2*pi*(r6-rsol6);
mu6=n6*pi*(r6^2);
disp('Radius (r6) of coiled conductor conductor, C6 (m) = ');,disp(r6);
disp('Length (Lsol6) of coiled conductor, C6 (m) = ');,disp(Lsol6);
disp('Number of turns in conductor coiled conductor C6 = ');,disp(n6);

%%% Conductor 7
r7=r6;
n7=n6;
Lsol7=Lsol6;
L7=L6;
mu7=mu6;
disp('Radius (r7) of coiled conductor conductor, C7 (m) = ');,disp(r7);
```

```
disp('Length (Lsol7) of coiled conductor, C7 (m) = ');,disp(Lsol7);
disp('Number of turns in conductor coiled conductor C7 = ');,disp(n7);

%%% Conductor 8
r8=1.9;
n8=1;
Lsol8=ceil((n8/10))*0.02;
if n8<5,
  rsol8=(n8*0.02)/2;
else
  rsol8=0.10;
end
L8=n8*2*pi*(r8-rsol8);
mu8=n8*pi*(r8^2);
disp('Radius (r8) of coiled conductor conductor, C8 (m) = ');,disp(r8);
disp('Length (Lsol8) of coiled conductor, C8 (m) = ');,disp(Lsol8);
disp('Number of turns in conductor coiled conductor C8 = ');,disp(n8);

%%% Conductor 9
r9=r8;
n9=n8;
Lsol9=Lsol8;
L9=L8;
mu9=mu8;
disp('Radius (r9) of coiled conductor conductor, C9 (m) = ');,disp(r9);
disp('Length (Lsol9) of coiled conductor, C9 (m) = ');,disp(Lsol9);
disp('Number of turns in conductor coiled conductor C9 = ');,disp(n9);

%%% Conductor 10
r10=1.9;
n10=497;
Lsol10=ceil((n10/10))*0.02;
if n10<5,
  rsol10=(n10*0.02)/2;
else
  rsol10=0.10;
end
L10=n10*2*pi*(r10-rsol10);
mu10=n10*pi*(r10^2);
disp('Radius (r10) of coiled conductor conductor, C10 (m) = ');,disp(r10);
disp('Length (Lsol10) of coiled conductor, C10 (m) = ');,disp(Lsol10);
disp('Number of turns in conductor coiled conductor C10 = ');,disp(n10);

%%%%%%%%%%%%%%%%%%%%%%%%%%%%%%%%%%%%%%%%%%%%%%%
%
% Determine Size of Coiled Conductor Support Truss
%
%%%%%%%%%%%%%%%%%%%%%%%%%%%%%%%%%%%%%%%%%%%%%%%
Lccst=Lsol6+Lsol7+max([2*r8 2*r10])+.5;
Wccst=max([2*r6 2*r8 2*r10])+.5;
Mccst=Lccst*40+...
    0;              % Mass of Coiled Conductor Int Truss (kg)
disp('Coiled Conductor Support Truss Length (m) = ');,disp(Lccst);
disp('Coiled Conductor Support Truss Width and Height (m) = ');,disp(Wccst);
disp('Coiled Conductor Support Truss Mass (kg) = ');,disp(Mccst);

%%%%%%%%%%%%%%%%%%%%%%%%%%%%%%%%%%%%%%%%%%%%%%%
%
% Determine Conductor Linear Densities
%    (Includes Shielding)
%
%%%%%%%%%%%%%%%%%%%%%%%%%%%%%%%%%%%%%%%%%%%%%%%
[pw1,ps1,d1]=wireden(rwire,n1,tshield);
[pw2,ps2,d2]=wireden(rwire,n2,tshield);
[pw3,ps3,d3]=wireden(rwire,n3,tshield);
```

```
[pw4,ps4,d4]=wireden(rwire,n4,tshield);
[pw5,ps5,d5]=wireden(rwire,n5,tshield);

pwcc=pi*(rwire)^2*2.699e+003;

%%%%%%%%%%%%%%%%%%%%%%%%%%%%%%%%%%%%%%%%%%%%%%%%
%
% Calculate Mass of Towers and Conductors
%
%%%%%%%%%%%%%%%%%%%%%%%%%%%%%%%%%%%%%%%%%%%%%%%%
Mc1=(2*pw1+ps1)*LC1;                    % Conductor C1 Mass
Mc2=(2*pw2+ps2)*LC2;                    % Conductor C2 Mass

Mc3=(2*pw3+ps3)*LC3;                    % Conductor C3 Mass
Mc4=(2*pw4+ps4)*LC4;                    % Conductor C4 Mass

Mc5=(2*pw5+ps5)*LC5;                    % Conductor C5 Mass

Mc6=pwcc*L6;                             % Coiled Conductor C6 Mass
Mc7=pwcc*L7;                             % Coiled Conductor C7 Mass

Mc8=pwcc*L8;                             % Coiled Conductor C8 Mass
Mc9=pwcc*L9;                             % Coiled Conductor C9 Mass

Mc10=pwcc*L10;                           % Coiled Conductor C10 Mass

Mtot=Mpay+Mtm+Mmit+2*Mta+...
     2*Mcit+2*Mspm+2*Mapa+Mccst+Moit+...
     Mc1+Mc2+Mc3+Mc4+Mc5+...
     Mc6+Mc7+Mc8+Mc9+Mc10;              % Total Platform Mass (kg)

disp('Total Platform Mass = ');,disp(Mtot);
disp(' ');

%%%%%%%%%%%%%%%%%%%%%%%%%%%%%%%%%%%%%%%%%%%%%%%%
%
% Platform Moments of Inertia
%
%%%%%%%%%%%%%%%%%%%%%%%%%%%%%%%%%%%%%%%%%%%%%%%%
% Allow 3m offset for cm of ET and 3m offset
% of cm of truss maker
% Geometric Body Approximation
%   Payload                          = Circular Cylinder
%   Truss Maker                      = Rectangular Prism
%   Main Integrated Truss            = Circular Cylinder
%   Thruster Assemblies              = Rectangular Prism
%   Cross Integrated Truss           = Circular Cylinder
%   Solar Dynamic Cells              = Thin Rectangular Plate
%   ASSET Power Arrays               = Thin Rectangular Plate
%   Conductor C1                     = Circular Cylinder
%   Conductor C2                     = Circular Cylinder
%   Conductor C3                     = Circular Cylinder
%   Conductor C4                     = Circular Cylinder
%   Conductor C5                     = Circular Cylinder
%   Coiled Conductor Truss Assembly = Circular Cylinder
%
Mccst=Mccst+Mc6+Mc7+Mc8+Mc9+Mc10;
%
Ixx(1)=(Mpay/12)*(3*Rpay^2+Lpay^2) +...
       Mpay*(3)^2;                                  % Payload
Ixx(2)=(Mtm/12)*(Wtm^2+Ltm^2) +...
       Mtm*(3)^2;                                   % Truss Maker
Ixx(3)=(Mmit/12)*(3*(Wmit/2)^2+Lmit^2) + 0;         % Main Integrated Truss
Ixx(4)=2*((Mta/12)*(Wta^2+Wta^2) +...
          Mta*((Lmit/2)+(Wta/2))^2);                % Thruster Assemblies
```

```
Ixx(5)=2*((Mcit/12)*(3*(Wcit/2)^2+Lcit^2) +...
          Mcit*((Wccst/2)+(Lcit/2))^2);          % Cross Integrated Truss
Ixx(6)=2*((Mspm/12)*(Wspm^2) +...
          Mspm*((Wccst/2)+lspm)^2);               % Solar Dynamic Cells
Ixx(7)=2*((Mapa/12)*(Wapa^2) +...
          Mapa*((Wccst/2)+lapa)^2);              % ASSET Power Arrays
Ixx(8)=(Moit/2)*(Woit^2) + 0;                    % Orthogonal Integrated Truss
Ixx(9)=2*(((Mc1)/24)*(3*(d1/2)^2+LC1^2) +...
          Mc1*((LC1/2)^2+(Wmit/2)^2));           % Conductor C1
Ixx(10)=2*(((Mc2)/24)*(3*(d2/2)^2+LC2^2) +...
          Mc2*((LC2/2)^2+(Wmit/2)^2));           % Conductor C2
Ixx(11)=2*(((Mc3)/24)*(3*(d3/2)^2+LC3^2) +...
          Mc3*(((Wccst/2)+(LC3/2))^2+...
               (Wcit/2)^2));                     % Conductor C3
Ixx(12)=2*(((Mc4)/24)*(3*(d4/2)^2+LC4^2) +...
          Mc4*(((Wccst/2)+(LC4/2))^2+...
               (Wcit/2)^2));                     % Conductor C4
Ixx(13)=2*(((Mc5)/4)*(d5/2)^2 + Mc5*(.7)^2);     % Conductor C5
Ixx(14)=(Mccst/12)*((3*Wccst/2)^2+Lccst^2);      % Coiled Conductor Truss Assembly
%
Iyy(1)=(Mpay/2)*(Rpay^2) +...
       Mpay*(Htm-0.5+Rpay)^2;                    % Payload
Iyy(2)=(Mtm/12)*(Wtm^2+Htm^2) +...
       Mtm*(Htm/2)^2;                            % Truss Maker
Iyy(3)=(Mmit/2)*(Wmit/2)^2 +...
       Mmit*((Wmit/2)+0.5)^2;                    % Main Integrated Truss
Iyy(4)=2*((Mta/12)*(Hta^2+Wta^2) + 0);           % Thruster Assemblies
Iyy(5)=2*((Mcit/12)*(3*(Wcit/2)^2+Lcit^2) +...
          Mcit*((0.5+Wmit+(Wccst/2))^2+...
                (Lcit/2)^2));                    % Cross Integrated Truss
Iyy(6)=2*((Mspm/12)*(Wspm^2+Hspm^2) +...
          Mspm*(0.5+Wmit+(Wccst/2)-hspm)^2+...
               ((Wccst/2)+lspm)^2);               % Solar Dynamic Cells
Iyy(7)=2*((Mapa/12)*(Wapa^2+Hapa^2) +...
          Mapa*(0.5+Wmit+(Wccst/2)+hapa)^2+...
               ((Wccst/2)+lspm)^2);               % ASSET Power Arrays
Iyy(8)=2*((Moit/12)*(3*(Woit/2)^2+Loit^2) +...
          Moit*(0.5+Wmit+Wccst+(Loit/2))^2);     % Orthogonal Integrated Truss
Iyy(9)=2*(((Mc1)/4)*(d1/2)^2 +...
          Mc1*((0.5+(Wmit/2))^2+(Wmit/2)^2));    % Conductor C1
Iyy(10)=2*(((Mc2)/4)*(d2/2)^2 +...
          Mc2*((0.5+(Wmit/2))^2+(Wmit/2)^2));    % Conductor C2
Iyy(11)=2*(((Mc3)/24)*(3*(d3/2)^2+LC3^2) +...
          Mc3*((0.5+Wmit+(Wccst/2))^2+...
               ((Wccst/2)+(Wcit/2))^2));         % Conductor C3
Iyy(12)=2*(((Mc4)/24)*(3*(d4/2)^2+LC4^2) +...
          Mc4*((0.5+Wmit+(Wccst/2))^2+...
               ((Wccst/2)+(Wcit/2))^2));         % Conductor C4
Iyy(13)=2*(((Mc5)/24)*(3*(d5/2)^2+LC5^2) +...
          Mc5*(0.5+Wmit+Wccst+(LC5/2))^2);       % Conductor C5
Iyy(14)=(Mccst/2)*(Wccst^2) +...
       Mccst*(0.5+Wmit+(Wccst/2))^2;             % Coiled Conductor Truss Assembly
%
Izz(1)=(Mpay/12)*(3*Rpay^2+Lpay^2) +...
         Mpay*((Htm-0.5+Rpay)^2+3^2);            % Payload
Izz(2)=(Mtm/12)*(Htm^2+Ltm^2) +...
       Mtm*((Htm/2)^2+3^2);                      % Truss Maker
Izz(3)=(Mmit/12)*(3*(Wmit/2)^2+Lmit^2) +...
       Mmit*((Wmit/2)+0.5)^2;                    % Main Integrated Truss
Izz(4)=2*((Mta/12)*(Wta^2+Hta^2) +...
          Mta*((Lmit/2)+(Wta/2))^2);             % Thruster Assemblies
Izz(5)=2*((Mcit/2)*(Wcit/2)^2 +...
          Mcit*(0.5+Wmit+(Wccst/2))^2);          % Cross Integrated Truss
Izz(6)=2*((Mspm/12)*Hspm^2 +...
          Mspm*(0.5+Wmit+(Wccst/2)-hspm)^2);       % Solar Dynamic Cells
```

```
Izz(7)=2*((Mapa/12)*Mapa^2 +...
          Mapa*(0.5+Wmit+(Wccst/2)+hapa)^2);    % ASSET Power Arrays
Izz(8)=2*((Moit/12)*(3*(Woit/2)^2+Loit^2) +...
          Moit*(0.5+Wmit+Wccst+(Loit/2))^2);     % Orthogonal Integrated Truss
Izz(9)=2*(((Mc1)/24)*(3*(d1/2)^2+LC1^2) +...
          Mc1*((LC1/2)^2+(0.5+(Wmit/2))^2));    % Conductor C1
Izz(10)=2*(((Mc2)/24)*(3*(d2/2)^2+LC2^2) +...
          Mc2*((LC2/2)^2+(0.5+(Wmit/2))^2));    % Conductor C2
Izz(11)=2*(((Mc3)/4)*(d3/2)^2 +...
          Mc3*((0.5+Wmit+(Wccst/2))^2+...
               (Wcit/2)^2));                    % Conductor C3
Izz(12)=2*(((Mc4)/4)*(d4/2)^2 +...
          Mc4*((0.5+Wmit+(Wccst/2))^2+...
               (Wcit/2)^2));                    % Conductor C4
Izz(13)=2*(((Mc5)/24)*(3*(d5/2)^2+LC5^2) +...
          Mc5*(0.5+Wmit+Wccst+(LC5/2))^2);      % Conductor C5
Izz(14)=(Mccst/2)*(Wccst^2) +...
       Mccst*(0.5+Wmit+(Wccst/2))^2;            % Coiled Conductor Truss Assembly

%%%%%%%%%%%%%%%%%%%%%%%%%%%%%%%%%%%%%%%%%%%%%
%
% Display Principle Moments of Inertia
%
%%%%%%%%%%%%%%%%%%%%%%%%%%%%%%%%%%%%%%%%%%%%%
A=sum(Ixx);
B=sum(Iyy);
C=sum(Izz);
disp('Principle moment of inertia, A - x direction (kg-m^2) =');,...
disp(A);
disp('Principle moment of inertia, B - y direction (kg-m^2) =');,...
disp(B);
disp('Principle moment of inertia, C - z direction (kg-m^2) =');,...
disp(C);

%%%%%%%%%%%%%%%%%%%%%%%%%%%%%%%%%%%%%%%%%%%%%
%
% Get orbital reference information from user
%
%%%%%%%%%%%%%%%%%%%%%%%%%%%%%%%%%%%%%%%%%%%%%
altitude=400;
disp('Altitude of reference orbit (km) = ');,disp(altitude);
r0=re+altitude*1000;          % orbital radius of reference orbit (m)
n=sqrt(G*Me/r0^3);            % orbital mean motion (reference orbit) (rad/s)
disp('Orbital mean motion (rad/s) =');,disp(n);

nu=input('True Anomaly (nu) to work with (deg) = ');
nu=nu*pi/180;                 % Convert to rad

Thetag=input('What is the sidereal time ? ');
Thetag=Thetag*pi/180;         % Convert Sidereal Time to rad

incl=input('What is the orbit inclination ? ');
incl=incl*pi/180;             % Convert Inclination to rad

Omega=input('What is the right ascension of the ascending node = ');
Omega=Omega*pi/180;

%%%%%%%%%%%%%%%%%%%%%%%%%%%%%%%%%%%%%%%%%%%%%
%
% Get reference command information from user
%
%%%%%%%%%%%%%%%%%%%%%%%%%%%%%%%%%%%%%%%%%%%%%
disp('Enter the reference command data');

delr=-60;
```

```
rdnu=0;
delz=0;
psi=0;
phi=0;
theta=0;

disp('What is the value of x to attain and track (m) ? ');,disp(delr);
disp('What is the value of y to attain and track (m) ? ');,disp(rdnu);
disp('What is the value of z to attain and track (m) ? ');,disp(delz);
disp('What is the angle of yaw to attain and track (deg) ? ');,disp(psi);
disp('What is the angle of roll to attain and track (deg) ? ');,disp(phi);
disp('What is the angle of pitch to attain and track (deg) ? ');,disp(theta);

psi=psi*(pi/180);   % Convert degrees to radians
phi=phi*(pi/180);   % Convert degrees to radians
theta=theta*(pi/180);   % Convert degrees to radians

%%%%%%%%%%%%%%%%%%%%%%%%%%%%%%%%%%%%%%%%%%%%%%%
%
% Get initial conditions from user
%
%%%%%%%%%%%%%%%%%%%%%%%%%%%%%%%%%%%%%%%%%%%%%%%
disp(' ')
disp('Enter the initial condition data');

delr0=-60;
rdnu0=0;
delz0=0;
psi0=0;
phi0=0;
theta0=0;

disp('What is the initial value of x (m) ? ');,disp(delr0);
disp('What is the initial value of y (m) ? ');,disp(rdnu0);
disp('What is the initial value of z (m) ? ');,disp(delz0);
disp('What is the initial value of the yaw angle (deg) ? ');,disp(psi0);
disp('What is the initial value of the roll angle (deg) ? ');,disp(phi0);
disp('What is the initial value of the pitch angle (deg) ? ');,disp(theta0);

psi0=psi0*(pi/180);   % Convert degrees to radians
phi0=phi0*(pi/180);   % Convert degrees to radians
theta0=theta0*(pi/180);   % Convert degrees to radians

X0=[delr0 0 rdnu0 0 delz0 0 psi0 0 phi0 0 theta0 0]';

%%%%%%%%%%%%%%%%%%%%%%%%%%%%%%%%%%%%%%%%%%%%%%%
%
% Get time history information from user
%
%%%%%%%%%%%%%%%%%%%%%%%%%%%%%%%%%%%%%%%%%%%%%%%
tmax=5400;
disp('How long of a time response to plot (s) ? ');,disp(tmax);
ntinc=540;
disp('Number of time increments (data points) ? ');,disp(ntinc);

%%%%%%%%%%%%%%%%%%%%%%%%%%%%%%%%%%%%%%%%%%%%%%%
%
% Generate reference command
%
%%%%%%%%%%%%%%%%%%%%%%%%%%%%%%%%%%%%%%%%%%%%%%%
t=0:(tmax/ntinc):tmax;
tleng=length(t);
r=zeros(tleng,6); %construct reference command

r(:,1)=delr*ones(tleng,1);
```

```
r(:,2)=rdnu*ones(tleng,1);
r(:,3)=delx*ones(tleng,1);
r(:,4)=psi*ones(tleng,1);
r(:,5)=phi*ones(tleng,1);
r(:,6)=theta*ones(tleng,1);

%%%%%%%%%%%%%%%%%%%%%%%%%%%%%%%%%%%%%%%%%%%%%%%%
%
% Miscellaneous Calculations
%
%%%%%%%%%%%%%%%%%%%%%%%%%%%%%%%%%%%%%%%%%%%%%%%%
m1=cos(Phi0)*(cos(nu)*cos(Omega-Theta-Lam0)-...
              sin(nu)*cos(incl)*sin(Omega-Theta-Lam0))+...
   sin(Phi0)*sin(nu)*sin(incl);
m2=cos(Phi0)*(-sin(nu)*cos(Omega-Theta-Lam0)-...
              cos(nu)*cos(incl)*sin(Omega-Theta-Lam0))+...
   sin(Phi0)*cos(nu)*sin(incl);
m3=cos(Phi0)*sin(incl)*sin(Omega-Theta-Lam0)+sin(Phi0)*cos(incl);

%%%%%%%%%%%%%%%%%%%%%%%%%%%%%%%%%%%%%%%%%%%%%%%%
%
% Miscellaneous Drag Calculations
%
%%%%%%%%%%%%%%%%%%%%%%%%%%%%%%%%%%%%%%%%%%%%%%%%
w1=we*sin(incl)*sin(nu);     % ar component
w2=we*sin(incl)*cos(nu);     % atheta component
w3=we*cos(incl);             % a3 component

delw=n-w3;

Kd=-((Cd*Adrag*rho0)/(2*Mtot))*exp(-(altitude-rref)/hs)*...
    (r0*sqrt(delw^2+w2^2));   % Drag Factor

i5ss=(Kd*delw*(r0^4)*Mtot)/(M*m3*L5);   % In-path Drag Term
thss=(Kd*w2*r0*Mtot);                   % Out-of-plane Drag Term

%%%%%%%%%%%%%%%%%%%%%%%%%%%%%%%%%%%%%%%%%%%%%%%%
%
% Set Up System Matrices F,G,H,J (open-loop)
%
%%%%%%%%%%%%%%%%%%%%%%%%%%%%%%%%%%%%%%%%%%%%%%%%
% System Matrix, F
Fsys=[0 1 0 0 0 0 0 0 0 0 0 0;
(3*n^2) Kd (-(Kd*delw)) (2*n) (-(Kd*w2)) 0 0 0 0 0 0 0;
0 0 0 1 0 0 0 0 0 0 0 0;
(Kd*delw) (-2*n) 0 (-Kd) (Kd*w1) 0 0 0 0 0 0 0;
0 0 0 0 0 1 0 0 0 0 0 0;
(Kd*w2) 0 (-(Kd*w1)) 0 (-(n^2)) Kd 0 0 0 0 0 0;
0 0 0 0 0 0 0 1 0 0 0 0;
0 0 0 0 0 0 (-(n^2)*(C-B)/A) 0 0 (-n*(-A-B+C)/A) 0 0;
0 0 0 0 0 0 0 0 0 1 0 0;
0 0 0 0 ((3*n^2)*(A-C)/(r0*B)) 0 0 (-n*(A+B-C)/B) ((4*n^2)*(A-C)/B) 0 0 0;
0 0 0 0 0 0 0 0 0 0 0 1;
0 (3*n/(2*r0)) ((3*n^2)*(B-A)/(r0*C)) 0 0 0 0 0 0 ((-3*n^2)*(B-A)/C) 0];

%input matrix
Gsys=(1/r0^3)*([0 0 0 0 0 0 0 0 0 0 0 0;
(-(M*m3*L1)/Mtot) (-(M*m3*L2)/Mtot) ((M*m2*L3)/Mtot) ((M*m2*L4)/Mtot) 0 0 0 0 0 0 0 0;
0 0 0 0 0 0 0 0 0 0 0 0;
0 0 ((2*M*m1*L3)/Mtot) ((2*M*m1*L4)/Mtot) ((M*m3*L5)/Mtot) 0 0 0 0 0 0;
0 0 0 0 0 0 0 0 0 0 0 0;
(-(2*M*m1*L1)/Mtot) (-(2*M*m1*L2)/Mtot) 0 0 (-(M*m2*L5)/Mtot) 0 0 0 0 0 ((r0^3)/Mtot);
0 0 0 0 0 0 0 0 0 0 0 0;
(-(M*m1*L1*LC1)/A) (M*m1*L2*LC2)/A (-(M*m1*L3*LC3)/A) (M*m1*L4*LC4)/A 0 (-(M*m3*mu6)/A) ...
      (-(M*m3*mu7)/A) (M*m2*mu8)/A (M*m2*mu9)/A 0 0;
```

```
0 0 0 0 0 0 0 0 0 0 0;
0 0 (M*m2*L3*LC3)/(2*B) (-(M*m2*L4*LC4)/(2*B)) (-(M*m2*n5*(Wmit+Wccst+LC5/2)*LC5)/B) 0 0 ...
      (2*M*m1*mu8)/B (2*M*m1*mu9)/B (M*m3*mu10)/B 0;
0 0 0 0 0 0 0 0 0 0 0;
(M*m3*L1*LC1)/(2*C) (-(M*m3*L2*LC2)/(2*C)) (-(2*M*m1*n3*(Wmit+Wccst/2)*L3)/C) ...
      (-(2*M*m1*n4*(Wmit+Wccst/2)*L4)/C) (-(M*m3*n5*(Wmit+Wccst+LC5/2)*LC5)/C) ...
      (-(2*M*m1*mu6)/C) (-(2*M*m1*mu7)/C) 0 0 (-(M*m2*mu10)/C) 0]);

%output matrix (selects positions and attitude angles only)
Hsys=[1 0 0 0 0 0 0 0 0 0 0;
0 0 1 0 0 0 0 0 0 0 0;
0 0 0 0 1 0 0 0 0 0 0;
0 0 0 0 0 0 1 0 0 0 0;
0 0 0 0 0 0 0 0 1 0 0;
0 0 0 0 0 0 0 0 0 1 0];

Jsys=zeros(6,11); %no fed-through control signals

%%%%%%%%%%%%%%%%%%%%%%%%%%%%%%%%%%%%%%%%%%%%%%%%
%
% Check Controllability and Observability
%
%%%%%%%%%%%%%%%%%%%%%%%%%%%%%%%%%%%%%%%%%%%%%%%%
%test controllability and observability
disp(' ');
Mc=ctrb(Fsys,Gsys);
if rank(Mc)==12,
        disp('The (Fsys,Gsys) system is completely controllable.');
else
        disp('The (Fsys,Gsys) system has uncontrollable modes!');
end
disp(' ');

Mo=obsv(Fsys,Hsys);
if rank(Mo)==12 ,
        disp('The (Fsys,Hsys) system is completely observable.');
else
        disp('The (Fsys,Hsys) system has unobservable modes!');
end

%%%%%%%%%%%%%%%%%%%%%%%%%%%%%%%%%%%%%%%%%%%%%%%%
%
% Derive LQR Compensator K
%
%%%%%%%%%%%%%%%%%%%%%%%%%%%%%%%%%%%%%%%%%%%%%%%%
% User enters state and control signal weightings

% Normalized state weighting matrix

qwt=1;
disp('Weighting on the state weighting matrix Q = ');,disp(qwt);
%qwt=input('Weighting on the state weighting matrix Q ? ');
Q=qwt*([1 0 0 0 0 0 0 0 0 0 0;
0 1 0 0 0 0 0 0 0 0 0;
0 0 1 0 0 0 0 0 0 0 0;
0 0 0 1 0 0 0 0 0 0 0;
0 0 0 0 1 0 0 0 0 0 0;
0 0 0 0 0 1 0 0 0 0 0;
0 0 0 0 0 0 r0 0 0 0 0;
0 0 0 0 0 0 0 r0 0 0 0;
0 0 0 0 0 0 0 0 r0 0 0;
0 0 0 0 0 0 0 0 0 r0 0;
0 0 0 0 0 0 0 0 0 0 r0]);
```

```
rwt=1;
disp('Weighting on the control weighting matrix R = ');,disp(rwt);
%rwt=input('Weighting on the control weighting matrix R ? ');
RK=rwt*eye(11); % Set up control weighting matrix
RK(1:5,1:5)=1*RK(1:5,1:5);
RK(11,11)=1000*RK(11,11);  % Heavily Penalize Use of Thruster

K=lqr(Fsys,Gsys,Q,RK);

%%%%%%%%%%%%%%%%%%%%%%%%%%%%%%%%%%%%%%%%%%%%%%%%
%
% Derive Non-square Pre-filter Mpf
%
%%%%%%%%%%%%%%%%%%%%%%%%%%%%%%%%%%%%%%%%%%%%%%%%
%Use optimal pseudo-inverse to find Mpf
Mpf=-pinv(Hsys*inv(Fsys-Gsys*K)*Gsys);

%%%%%%%%%%%%%%%%%%%%%%%%%%%%%%%%%%%%%%%%%%%%%%%%
%
% Set Up Closed-Loop Matrices F,G,H,J
%
%%%%%%%%%%%%%%%%%%%%%%%%%%%%%%%%%%%%%%%%%%%%%%%%
Fcl=Fsys-Gsys*K;
Gcl=Gsys*Mpf;
Hcl=Hsys;
Jcl=zeros(6);

[y,x]=lsim(Fcl,Gcl,Hcl,Jcl,r,t,X0); %outputs and states
[mm,nn]=size(y);
for i=1:mm,
  for j=1:nn,
    if abs(y(i,j))<1e-6,
       y(i,j)=0.0;
    end
  end
end

u=(Mpf*r'-K*x')';   % Control vector includes 10 currents and 1 thruster

for i=1:tleng,
  u(i,5)=u(i,5)+i5ss;
  u(i,11)=u(i,11)+thss;
end

[mm,nn]=size(u);
for i=1:mm,
  for j=1:nn,
    if abs(u(i,j))<1e-9,
       u(i,j)=0.0;
    end
  end
end

a=(Gsys*u')';   % Accelerations
[mm,nn]=size(a);
for i=1:mm,
  for j=1:nn,
    if abs(a(i,j))<1e-9,
       a(i,j)=0.0;
    end
  end
end

pos=max(u);
neg=min(u);
```

```
for i=1:11,
  if abs(pos(i))>abs(neg(i))
     maxcur(i)=pos(i);
  else
     maxcur(i)=neg(i);
  end
end

disp(' ');
disp('Maximum current required in conductor C1 (A)= ');,disp(maxcur(1));
disp('Maximum current required in conductor C2 (A)= ');,disp(maxcur(2));
disp('Maximum current required in conductor C3 (A)= ');,disp(maxcur(3));
disp('Maximum current required in conductor C4 (A)= ');,disp(maxcur(4));
disp('Maximum current required in conductor C5 (A)= ');,disp(maxcur(5));
disp('Maximum current required in conductor C6 (A)= ');,disp(maxcur(6));
disp('Maximum current required in conductor C7 (A)= ');,disp(maxcur(7));
disp('Maximum current required in conductor C8 (A)= ');,disp(maxcur(8));
disp('Maximum current required in conductor C9 (A)= ');,disp(maxcur(9));
disp('Maximum current required in conductor C10 (A)= ');,disp(maxcur(10));
disp('Maximum thrust required in thruster (N)= ');,disp(maxcur(11));
disp(' ');

xforce1=((-(M*m3*L1))/(r0^3))*(maxcur(1));
zforce1=(-(2*M*m1*L1)/(r0^3))*(maxcur(1));
xforce2=((-(M*m3*L2))/(r0^3))*(maxcur(2));
zforce2=(-(2*M*m1*L2)/(r0^3))*(maxcur(2));
xforce3=((M*m2*L3)/(r0^3))*(maxcur(3));
yforce3=((2*M*m1*L3)/(r0^3))*(maxcur(3));
xforce4=((M*m2*L4)/(r0^3))*(maxcur(4));
yforce4=((2*M*m1*L4)/(r0^3))*(maxcur(4));
yforce5=((M*m3*L5)/(r0^3))*(maxcur(5));
zforce5=(-(M*m2*L5)/(r0^3))*(maxcur(5));

disp(' ');
disp('Maximum radial force in conductor C1 (N)= ');,disp(xforce1);
disp('Maximum oop force in conductor C1 (N)= ');,disp(zforce1);
disp('Maximum radial force in conductor C2 (N)= ');,disp(xforce2);
disp('Maximum oop force in conductor C2 (N)= ');,disp(zforce2);
disp('Maximum radial force in conductor C3 (N)= ');,disp(xforce3);
disp('Maximum ip lateral force in conductor C3 (N)= ');,disp(yforce3);
disp('Maximum radial force in conductor C4 (N)= ');,disp(xforce4);
disp('Maximum ip lateral force in conductor C4 (N)= ');,disp(yforce4);
disp('Maximum ip lateral force in conductor C5 (N)= ');,disp(yforce5);
disp('Maximum oop force in conductor C5 (N)= ');,disp(zforce5);
disp(' ');

disp(' ');
disp('Distributed radial force in conductor C1 (N)= ');,disp((1/LC1)*xforce1);
disp('Distributed oop force in conductor C1 (N)= ');,disp((1/LC1)*zforce1);
disp('Distributed radial force in conductor C2 (N)= ');,disp((1/LC2)*xforce2);
disp('Distributed oop force in conductor C2 (N)= ');,disp((1/LC2)*zforce2);
disp('Distributed radial force in conductor C3 (N)= ');,disp((1/LC3)*xforce3);
disp('Distributed ip lateral force in conductor C3 (N)= ');,disp((1/LC3)*yforce3);
disp('Distributed radial force in conductor C4 (N)= ');,disp((1/LC4)*xforce4);
disp('Distributed ip lateral force in conductor C4 (N)= ');,disp((1/LC4)*yforce4);
disp('Distributed ip lateral force in conductor C5 (N)= ');,disp((1/LC5)*yforce5);
disp('Distributed oop force in conductor C5 (N)= ');,disp((1/LC5)*zforce5);
disp(' ');

b1mom1=(-(M*m1*L1*LC1)) * (maxcur(1)) * (1/(r0^3));
b3mom1=(M*m3*L1*LC1)/(2) * (maxcur(1)) * (1/(r0^3));
b1mom2=(M*m1*L2*LC2) * (maxcur(2)) * (1/(r0^3));
b3mom2=(-(M*m3*L2*LC2)/(2)) * (maxcur(2)) * (1/(r0^3));
b1mom3=(-(M*m1*L3*LC3)) * (maxcur(3)) * (1/(r0^3));
b2mom3=(M*m2*L3*LC3)/(2) * (maxcur(3)) * (1/(r0^3));
```

```
b3mom3=(-(2*M*m1*n3*(Wmit+Wccst/2)*L3)) * (maxcur(3)) * (1/(r0^3));
b1mom4=(M*m1*L4*LC4) * (maxcur(4)) * (1/(r0^3));
b2mom4=(-(M*m2*L4*LC4)/(2)) * (maxcur(4)) * (1/(r0^3));
b3mom4=(-(2*M*m1*n4*(Wmit+Wccst/2)*L4)) * (maxcur(4)) * (1/(r0^3));
b2mom5=(-(M*m2*n5*(Wmit+Wccst+LC5/2)*LC5)) * (maxcur(5)) * (1/(r0^3));
b3mom5=(-(M*m3*n5*(Wmit+Wccst+LC5/2)*LC5)) * (maxcur(5)) * (1/(r0^3));
b1mom6=(-(M*m3*mu6)) * (maxcur(6)) * (1/(r0^3));
b3mom6=(-(2*M*m1*mu6)) * (maxcur(6)) * (1/(r0^3));
b1mom7=(-(M*m3*mu7)) * (maxcur(7)) * (1/(r0^3));
b3mom7=(-(2*M*m1*mu7)) * (maxcur(7)) * (1/(r0^3));
b1mom8=(M*m2*mu8) * (maxcur(8)) * (1/(r0^3));
b2mom8=(2*M*m1*mu8) * (maxcur(8)) * (1/(r0^3));
b1mom9=(M*m2*mu9) * (maxcur(9)) * (1/(r0^3));
b2mom9=(2*M*m1*mu9) * (maxcur(9)) * (1/(r0^3));
b2mom10=(M*m3*mu10) * (maxcur(10)) * (1/(r0^3));
b3mom10=(-(M*m2*mu10)) * (maxcur(10)) * (1/(r0^3));

disp('The maximum C1 torque around b1 (N-m) = '),;disp(b1mom1);
disp('The maximum C1 torque around b1 (N-m) = '),;disp(b3mom1);
disp('The maximum C2 torque around b1 (N-m) = '),;disp(b1mom2);
disp('The maximum C2 torque around b1 (N-m) = '),;disp(b3mom2);
disp('The maximum C3 torque around b1 (N-m) = '),;disp(b1mom3);
disp('The maximum C3 torque around b1 (N-m) = '),;disp(b2mom3);
disp('The maximum C3 torque around b1 (N-m) = '),;disp(b3mom3);
disp('The maximum C4 torque around b1 (N-m) = '),;disp(b1mom4);
disp('The maximum C4 torque around b1 (N-m) = '),;disp(b2mom4);
disp('The maximum C4 torque around b1 (N-m) = '),;disp(b3mom4);
disp('The maximum C5 torque around b1 (N-m) = '),;disp(b2mom5);
disp('The maximum C5 torque around b1 (N-m) = '),;disp(b3mom5);
disp('The maximum C6 torque around b1 (N-m) = '),;disp(b1mom6);
disp('The maximum C6 torque around b1 (N-m) = '),;disp(b3mom6);
disp('The maximum C7 torque around b1 (N-m) = '),;disp(b1mom7);
disp('The maximum C7 torque around b1 (N-m) = '),;disp(b3mom7);
disp('The maximum C8 torque around b1 (N-m) = '),;disp(b1mom8);
disp('The maximum C8 torque around b1 (N-m) = '),;disp(b2mom8);
disp('The maximum C9 torque around b1 (N-m) = '),;disp(b1mom9);
disp('The maximum C9 torque around b1 (N-m) = '),;disp(b2mom9);
disp('The maximum C10 torque around b1 (N-m) = '),;disp(b2mom10);
disp('The maximum C10 torque around b1 (N-m) = '),;disp(b3mom10);

plot(t,(u(:,1)/1));
title('Conductor 1 (C1) Current');,grid;
xlabel('Time (s)');
ylabel('Current (A)');
print -deps c1current.eps;
pause;

plot(t,(u(:,2)/1));
title('Conductor 2 (C2) Current');,grid;
xlabel('Time (s)');
ylabel('Current (A)');
print -deps c2current.eps;
pause;

plot(t,(u(:,3)/1));
title('Conductor 3 (C3) Current');,grid;
xlabel('Time (s)');
ylabel('Current (A)');
print -deps c3current.eps;
pause;

plot(t,(u(:,4)/1));
title('Conductor 4 (C4) Current');,grid;
xlabel('Time (s)');
ylabel('Current (A)');
```

```
print -deps c4current.eps;
pause;

plot(t,(u(:,5)/1));
title('Conductor 5 (C5) Current');,grid;
xlabel('Time (s)');
ylabel('Current (A)');
print -deps c5current.eps;
pause;

plot(t,(u(:,6)/1));
title('Conductor 6 (C6) Cur. ent');,grid;
xlabel('Time (s)');
ylabel('Current (A)');
print -deps c6current.eps;
pause;

plot(t,(u(:,7)/1));
title('Conductor 7 (C7) Current');,grid;
xlabel('Time (s)');
ylabel('Current (A)');
print -deps c7current.eps;
pause;

plot(t,(u(:,8)/1));
title('Conductor 8 (C8) Current');,grid;
xlabel('Time (s)');
ylabel('Current (A)');
print -deps c8current.eps;
pause;

plot(t,(u(:,9)/1));
title('Conductor 9 (C9) Current');,grid;
xlabel('Time (s)');
ylabel('Current (A)');
print -deps c9current.eps;
pause;

plot(t,(u(:,10)/1));
title('Conductor 10 (C10) Current');,grid;
xlabel('Time (s)');
ylabel('Current (A)');
print -deps c10current.eps;
pause;

plot(t,u(:,11));
title('Z-Axis Thrust Required');,grid;
xlabel('Time (s)');
ylabel('Thrust (N)');
print -deps thrustrqd.eps;
pause;

rho=2.655e-8;
R1=rho*(2*L1/area);
R2=rho*(2*L2/area);
R3=rho*(2*L3/area);
R4=rho*(2*L4/area);
R5=rho*(2*L5/area);
R6=rho*(L6/area);
R7=rho*(L7/area);
R8=rho*(L8/area);
R9=rho*(L9/area);
R10=rho*(L10/area);

disp(' ');
```

```
disp('The resistance of conductor C1 (Ohms)= ');,disp(R1);
disp('The resistance of conductor C2 (Ohms)= ');,disp(R2);
disp('The resistance of conductor C3 (Ohms)= ');,disp(R3);
disp('The resistance of conductor C4 (Ohms)= ');,disp(R4);
disp('The resistance of conductor C5 (Ohms)= ');,disp(R5);
disp('The resistance of conductor C6 (Ohms)= ');,disp(R6);
disp('The resistance of conductor C7 (Ohms)= ');,disp(R7);
disp('The resistance of conductor C8 (Ohms)= ');,disp(R8);
disp('The resistance of conductor C9 (Ohms)= ');,disp(R9);
disp('The resistance of conductor C10 (Ohms)= ');,disp(R10);
disp(' ');
disp('Total Conductor Resistance (Ohms) = ');,disp(R1+R2+R3+R4+R5+R6+R7+R8+R9+R10);

B1=(M/(r0^3))*2*m1;
B2=(M/(r0^3))*(-m2);
B3=(M/(r0^3))*(-m3);

L1vec=[0;L1;0];
L2vec=[0;L2;0];
L3vec=[0;0;L3];
L4vec=[0;0;L4];
L5vec=[L5;0;0];

for i=1:length(t),

  V1=x(i,2)-delw*x(i,3)-w2*x(i,5);
  V2=delw*(r0+x(i,1)) + x(i,4) + w1*x(i,5);
  V3=w2*(r0+x(i,1)) - w1*x(i,3) + x(i,6);

  C0(1,1)=cos(x(i,9))*cos(x(i,11));
  C0(1,2)=-sin(x(i,11));
  C0(1,3)=sin(x(i,9))*cos(x(i,11));
  C0(2,1)=cos(x(i,9))*sin(x(i,11))*cos(x(i,7)) + sin(x(i,9))*sin(x(i,7));
  C0(2,2)=cos(x(i,11))*cos(x(i,7));
  C0(2,3)=sin(x(i,9))*sin(x(i,11))*cos(x(i,7)) - cos(x(i,9))*sin(x(i,7));
  C0(3,1)=cos(x(i,9))*sin(x(i,11))*sin(x(i,7)) - sin(x(i,9))*cos(x(i,7));
  C0(3,2)=cos(x(i,11))*sin(x(i,7));
  C0(3,3)=sin(x(i,9))*sin(x(i,11))*sin(x(i,7)) + cos(x(i,9))*cos(x(i,7));

  VB=[(V2*B3-V3*B2) (V3*B1-V1*B3) (V1*B2-V2*B1)];

  L1Vind(i)=VB*(C0*L1vec);
  L2Vind(i)=VB*(C0*L2vec);
  L3Vind(i)=VB*(C0*L3vec);
  L4Vind(i)=VB*(C0*L4vec);
  L5Vind(i)=VB*(C0*L5vec);

  pow1(i)=((abs(u(i,1)*L1Vind(i)))+(R1*u(i,1)^2))/1000;
  pow2(i)=((abs(u(i,2)*L2Vind(i)))+(R2*u(i,2)^2))/1000;
  pow3(i)=((abs(u(i,3)*L3Vind(i)))+(R3*u(i,3)^2))/1000;
  pow4(i)=((abs(u(i,4)*L4Vind(i)))+(R4*u(i,4)^2))/1000;
  pow5(i)=((abs(u(i,5)*L5Vind(i)))+(R5*u(i,5)^2))/1000;
  pow6(i)=(R6*u(i,6)^2)/1000;
  pow7(i)=(R7*u(i,7)^2)/1000;
  pow8(i)=(R8*u(i,8)^2)/1000;
  pow9(i)=(R9*u(i,9)^2)/1000;
  pow10(i)=(R10*u(i,10)^2)/1000;

  totpow(i)=pow1(i)+pow2(i)+pow3(i)+pow4(i)+pow5(i)+pow6(i)+...
            pow7(i)+pow8(i)+pow9(i)+pow10(i);
  voltage(i)=abs(R1*u(i,1))+abs(R2*u(i,2))+abs(R3*u(i,3))+...
             abs(R4*u(i,4))+abs(R5*u(i,5))+abs(R6*u(i,6))+...
             abs(R7*u(i,7))+abs(R8*u(i,8))+abs(R9*u(i,9))+abs(R10*u(i,10));
end
disp('The maximum power required (kW) = ');,disp(max(totpow));
```

```
disp('The maximum voltage required (V) = ');,disp(max(voltage));
pause

%%%%%%%%%%%%%%%%%%%%%%%%%%%%%%%%%%%%%%%%%%%%%%%%%%%%%%%%%%%%%%%%%%%%%%%%%%%%
%
% Calculate the shield's inner surface temperature and the
% conductor's core temperature.
%
%%%%%%%%%%%%%%%%%%%%%%%%%%%%%%%%%%%%%%%%%%%%%%%%%%%%%%%%%%%%%%%%%%%%%%%%%%%%

[T11,T10]=chktemp1(maxcur(1),LC1,n1,d1,tshield);
[T21,T20]=chktemp1(maxcur(2),LC2,n2,d2,tshield);
[T31,T30]=chktemp1(maxcur(3),LC3,n3,d3,tshield);
[T41,T40]=chktemp1(maxcur(4),LC4,n4,d4,tshield);
[T51,T50]=chktemp1(maxcur(5),LC5,n5,d5,tshield);
[T60]=chktemp2(dwire,maxcur(6),n6,r6,L6,Lsol6);
[T70]=chktemp2(dwire,maxcur(7),n7,r7,L7,Lsol7);
[T80]=chktemp2(dwire,maxcur(8),n8,r8,L8,Lsol8);
[T90]=chktemp2(dwire,maxcur(9),n9,r9,L9,Lsol9);
[T100]=chktemp2(dwire,maxcur(10),n10,r10,L10,Lsol10);

disp('Max allowed shield inner surface temperature (deg C) = 1021');
disp('Max allowed conductor bundle core temperature (deg C) = 438');
disp('');
disp('Conductor C1 shield inner surface and core');
disp('   temperatures: T1, T0 (deg C) = ');,disp([T11 T10]);
disp('   Safety factors = ');,disp([(1532/T11) (657/T10)]);
disp('');
disp('Conductor C2 shield inner surface and core');
disp('   temperatures: T1, T0 (deg C) = ');,disp([T21 T20]);
disp('   Safety factors = ');,disp([(1532/T21) (657/T20)]);
disp('');
disp('Conductor C3 shield inner surface and core');
disp('   temperatures: T1, T0 (deg C) = ');,disp([T31 T30]);
disp('   Safety factors = ');,disp([(1532/T31) (657/T30)]);
disp('');
disp('Conductor C4 shield inner surface and core');
disp('   temperatures: T1, T0 (deg C) = ');,disp([T41 T40]);
disp('   Safety factors = ');,disp([(1532/T41) (657/T40)]);
disp('');
disp('Conductor C5 shield inner surface and core');
disp('   temperatures: T1, T0 (deg C) = ');,disp([T51 T50]);
disp('   Safety factors = ');,disp([(1532/T51) (657/T50)]);
disp('');
disp('Conductor C6 coiled conductor core temperature: T0 (deg C) = ');
disp(T60);
disp('   Safety factor = ');,disp(657/T60);
disp('');
disp('Conductor C7 coiled conductor core temperature: T0 (deg C) = ');
disp(T70);
disp('   Safety factor = ');,disp(657/T70);
disp('');
disp('Conductor C8 coiled conductor core temperature: T0 (deg C) = ');
disp(T80);
disp('   Safety factor = ');,disp(657/T80);
disp('');
disp('Conductor C9 coiled conductor core temperature: T0 (deg C) = ');
disp(T90);
disp('   Safety factor = ');,disp(657/T90);
disp('');
disp('Conductor C10 coiled conductor core temperature: T0 (deg C) = ');
disp(T100);
disp('   Safety factor = ');,disp(657/T100);

plot(t,totpow);
```

```
title('Total Power Required');,grid;
xlabel('Time (s)');
ylabel('Power (kW)');
print -deps power.eps;
pause;

plot(t,voltage);
title('Total Voltage Required');,grid;
xlabel('Time (s)');
ylabel('Voltage (V)');
print -deps voltage.eps;
pause;

plot(t,y(:,1));
title('Radial Position');,grid;
xlabel('Time (s)');
ylabel('Position (m)');
print -deps rposition.eps;
pause;

plot(t,y(:,2));
title('Along-Path Position');,grid;
xlabel('Time (s)');
ylabel('Position (m)');
print -deps nuposition.eps;
pause;

plot(t,y(:,3));
title('Out-of-Plane Position');,grid;
xlabel('Time (s)');
ylabel('Position (m)');
print -deps zposition.eps;
pause;

plot(y(:,2),y(:,1));
title('Along-Path Position vs Radial Position');
xlabel('Along-Path Position (m)');
ylabel('Radial Position (m)');
print -deps x_vs_y.eps;
pause;

plot(y(:,3),y(:,1));
title('Out-of-Plane Position vs Radial Position');
xlabel('Out-of-Plane Position (m)');
ylabel('Radial Position (m)');
print -deps x_vs_z.eps;
pause;

plot(y(:,3),y(:,2));
title('Out-of-Plane Position vs Along-Path Position');
xlabel('Out-of-Plane Position (m)');
ylabel('Along-Path Position (m)');
print -deps y_vs_z.eps;
pause;

plot(t,((180/pi)*y(:,4)));
title('Yaw Orientation');,grid;
xlabel('Time (s)');
ylabel('Orientation (deg)');
print -deps psiorient.eps;
pause;

plot(t,((180/pi)*y(:,5)));
title('Roll Orientation');,grid;
xlabel('Time (s)');
```

```
ylabel('Orientation (deg)');
print -deps phiorient.eps;
pause;

plot(t,((180/pi)*y(:,6)));
title('Pitch Orientation');,grid;
xlabel('Time (s)');
ylabel('Orientation (deg)');
print -deps thetaorient.eps;
pause;

disp(' ');
disp('Maximum vertical (x) force required (N) = ');,disp(max(abs(Mtot*a(:,2))));,...
disp('Maximum horizontal in-plane (y) force required (N) = ');,disp(max(abs(Mtot*a(:,4))));,...
disp('Maximum horizontal out-of-plane (z) force required (N) = ');,disp(max(abs(Mtot*a(:,6))));,...
disp(' '),...
disp('Maximum moment about x required (N-m) = ');,disp(max(abs(A*a(:,8))));,...
disp('Maximum moment about y required (N-m) = ');,disp(max(abs(B*a(:,10))));,...
disp('Maximum moment about z required (N-m) = ');,disp(max(abs(C*a(:,12))));,...
disp(' ');

plot(t,(Mtot*a(:,2)));
title('Force in Radial Direction');,grid;
xlabel('Time (s)');
ylabel('Force (N)');
print -deps rforce.eps;
pause;

plot(t,(Mtot*a(:,4)));
title('Force in Path Direction');,grid;
xlabel('Time (s)');
ylabel('Force (N)');
print -deps nuforce.eps;
pause;

plot(t,(Mtot*a(:,6)));
title('Force in Out-of-Plane Direction');,grid;
xlabel('Time (s)');
ylabel('Force (N)');
print -deps zforce.eps;
pause;

plot(t,(A*a(:,8)));
title('b1-Axis Moment');,grid;
xlabel('Time (s)');
ylabel('Moment (N-m)');
print -deps b1moment.eps;
pause;

plot(t,(B*a(:,10)));
title('b2-Axis Moment');,grid;
xlabel('Time (s)');
ylabel('Moment (N-m)');
print -deps b2moment.eps;
pause;

plot(t,(C*a(:,12)));
title('b3-Axis Moment');,grid;
xlabel('Time (s)');
ylabel('Moment (N-m)');
print -deps b3moment.eps;

%%%%%%%%%%%%%%%%%%%%%%%%%%%%%%%%%%%%%%%%%%%%%%%%%%%%%%%%%%%%%%%%%%%%%%%%%%%%%%%%%%
```

G.2 Wire and Shield Determination Program

This program calls several subroutines to perform specialized tasks. These tasks include calculating the size and linear density of the conductors and their *Netic* shields, calculating the Netic and core temperatures of the long straight conductors, and calculating the core temperatures of the coiled conductors. The following is the routine which determines the linear density of the conductor cables and Netic shielding.

```
%%%%%%%%%%%%%%%%%%%%%%%%%%%%%%%%%%%%%%%%%%%%%%%%%%%%%%%%%%%%%%%%%%%%%%%%%%%%%%%%%%
function [pw,ps,Di]=wireden(r,n,t)
%WIREDEN  Calculate linear mass density for conductor
%         wires for the Space Fabrication Platform.
%         [PW,PS,DI]=WIREDEN(R,N,T) - R is the radius of the
%         individual wire elements in meters; N is the
%         number turns of the conductor;  T is the thickness
%         of the Netic shield; PW is the linear is the
%         mass density of unshielded wire in kg/m;
%         PS linear mass density of unshielded wire in
%         kg/m;  DI is the diameter of the wire bundle.
%         The linear mass density of a shielded
%         wire includes the mass of 5.0 mm of shielding.

% Calculate Density of Wire Alone

Aw=pi*(r)^2;
pw=Aw*n*2.699e+003;

% Calculate Density of Shield

d=2*r;

if (n>0 & n<=1),
  Di=d;
elseif (n>1 & n<=7)
  Di=3*d;
elseif (n>7 & n<=13)
  Di=4.46*d;
elseif (n>13 & n<=19)
  Di=5*d;
elseif (n>19 & n<=31)
  Di=6.29*d;
elseif (n>31 & n<=37)
  Di=7*d;
elseif (n>37 & n<=43)
  Di=7.93*d;
elseif (n>43 & n<=55)
  Di=8.21*d;
elseif (n>55 & n<=61)
  Di=9*d;
elseif (n>61 & n<=73)
  Di=9.72*d;
elseif (n>73 & n<=85)
  Di=10.17*d;
elseif (n>85 & n<=91)
```

```
  Di=11*d;
elseif (n>91 & n<=97)
  Di=11.39*d;
elseif (n>97 & n<=109)
  Di=11.58*d;
elseif (n>109 & n<=121)
  Di=12.14*d;
elseif (n>121 & n<=127)
  Di=13*d;
elseif (n>127 & n<=139)
  Di=13.17*d;
elseif (n>139 & n<=151)
  Di=13.49*d;
elseif (n>151 & n<=163)
  Di=14.11*d;
elseif (n>163 & n<=169)
  Di=14.86*d;
elseif (n>169 & n<=187)
  Di=15*d;
elseif (n>187 & n<=199)
  Di=15.42*d;
elseif (n>199 & n<=211)
  Di=16.10*d;
elseif (n>211 & n<=223)
  Di=16.62*d;
elseif (n>223 & n<=235)
  Di=16.87*d;
elseif (n>235 & n<=241)
  Di=17*d;
elseif (n>241 & n<=253)
  Di=17.37*d;
elseif (n>253 & n<=265)
  Di=18.09*d;
elseif (n>265 & n<=271)
  Di=18.32*d;
elseif (n>271 & n<=283)
  Di=18.44*d;
elseif (n>283 & n<=295)
  Di=18.78*d;
elseif (n>295 & n<=301)
  Di=19*d;
elseif (n>301 & n<=313)
  Di=19.33*d;
elseif (n<0 | n>313)
  error('Density calculation for # of turns is undefined');
end

As=pi*((Di+(2*t))/2)^2 - pi*(Di/2)^2;
ps=7.86e+003*As;

%%%%%%%%%%%%%%%%%%%%%%%%%%%%%%%%%%%%%%%%%%%%%%%%%%%%%%%%%%%%%%%%%%%%%%%%%%%%%%%%
```

G.3 Straight Conductor Temperatures Program

The following routine determines the temperature of the Netic shields and the core temperatures of the long straight conductors.

```
%%%%%%%%%%%%%%%%%%%%%%%%%%%%%%%%%%%%%%%%%%%%%%%%%%%%%%%%%%%%%%%%%%%%%%%%%%%%%%%%%%
function [T1,T0]=chktemp1(i,L,n,d,t)
%  Routine to check to the temperatures of
%  inner surface of the Netic shield for
%  SFP and the core of the conductor bundle.
%  [T1,T0]=chktemp(i,L,n,d,t)
%  The current, i (A), the length
%  of the conductor, L (m), the number of
%  individual conductors in the bundle, n,
%  the diameter of the conductor bundle, d (m),
%  and the thickness of the shield are passed as
%  inputs.  The shield's inner surface
%  temperature, T1 (deg C), and the conductor
%  bundle's core temperature, T2 (deg C), are
%  returned.

R=84e-06;          % Resistance of 2cm aluminum wire (ohms/m)
Tinf=288;          % Temperature of free space (deg K)
sigma=5.669e-08;   % Steffan-Boltzman constant (W/(m deg K))
kshield=49.41;     % Shield thermal conductivity (W/(m deg C))
kcable=.20;        % Asbestos thermal conductivity (W/(m deg C))

% Note: the conductor is modeled as solid asbestos to
%       assess the worst case core temperature.

%%%%%%%%%%%%%%%%%%%%%%%%%%%%%%%%%%%%%%%%%%%%%%%%%%%
%
%  Calculate the heat transfer rate, q
%
%%%%%%%%%%%%%%%%%%%%%%%%%%%%%%%%%%%%%%%%%%%%%%%%%%%

q=(i^2) * (R) * (L) * (n);

%%%%%%%%%%%%%%%%%%%%%%%%%%%%%%%%%%%%%%%%%%%%%%%%%%%
%
%  Calculate the required surface temperature, T2
%
%%%%%%%%%%%%%%%%%%%%%%%%%%%%%%%%%%%%%%%%%%%%%%%%%%%

% Calculate surface area
A2=2 * pi * ((d/2)+t) * (L);

% Calculate T2
T2=((q/(sigma*A2))+Tinf^4)^(.25);

% Convert to celsius
T2=T2-273;

%%%%%%%%%%%%%%%%%%%%%%%%%%%%%%%%%%%%%%%%%%%%%%%%%%%
%
%  Calculate the required shield inner surface
%  temperature, T1
%
%%%%%%%%%%%%%%%%%%%%%%%%%%%%%%%%%%%%%%%%%%%%%%%%%%%

T1=((q*((1/(d/2))-(1/((d/2)+t))))/(4*pi*kshield)) + T2;

%%%%%%%%%%%%%%%%%%%%%%%%%%%%%%%%%%%%%%%%%%%%%%%%%%%
%
%  Calculate the required conductor bundle core
%  temperature, T0
%
%%%%%%%%%%%%%%%%%%%%%%%%%%%%%%%%%%%%%%%%%%%%%%%%%%%

T0=((q/(pi*L))/(4*kcable)) + T1;
```

```
%%%%%%%%%%%%%%%%%%%%%%%%%%%%%%%%%%%%%%%%%%%%%%%%%%%%%%%%%%%%%%%%%%%%%%%%%%%%%%%%%%%%
```

G.4 Coiled Conductor Temperature Program

The following routine determines the core temperatures of the coiled conductors.

```
%%%%%%%%%%%%%%%%%%%%%%%%%%%%%%%%%%%%%%%%%%%%%%%%%%%%%%%%%%%%%%%%%%%%%%%%%%%%%%%%%%%%
function [TO]=chktemp2(d,i,n,r,Lc,Ls)
%  Routine to check to the core temperatures of
%  coiled attitude control elements.
%  [TO]=chktemp2(d,i,n,r,Lc,Ls)
%  The wire diameter, d (m), the current, i (A),
%  the number turns in the coil, n, the radius
%  of the coil, r (m), the length of the
%  conductor, Lc (m), and the length of the coil
%  unit, Ls (m), are passed as inputs.  The coil
%  conductor's core temperature, TO (deg C), is
%  returned.

R=84e-06;         % Resistance of 2cm aluminum wire (ohms/m)
Tinf=288;         % Temperature of free space (deg K)
sigma=5.669e-08;  % Steffan-Boltzman constant (W/(m deg K))
k=1.4;            % Electrically insulated aluminum
                  %     thermal conductivity (W/(m deg C))

% Note: the conductor is modeled as conducting substance
%       with low thermal conductivity to assess the worst
%       case core temperature.

if n<10,
  t=n*d;      % Correct for number of turns
else
  t=.2;           % Assume 10 layers of windings
end

r1=r-t;

%%%%%%%%%%%%%%%%%%%%%%%%%%%%%%%%%%%%%%%%%%%%%%%%%%%%
%
%  Calculate the heat transfer rate, q
%
%%%%%%%%%%%%%%%%%%%%%%%%%%%%%%%%%%%%%%%%%%%%%%%%%%%%

q=(i^2) * (R) * (Lc);

%%%%%%%%%%%%%%%%%%%%%%%%%%%%%%%%%%%%%%%%%%%%%%%%%%%%
%
%  Calculate the required surface temperature, Ts
%
%%%%%%%%%%%%%%%%%%%%%%%%%%%%%%%%%%%%%%%%%%%%%%%%%%%%

% Calculate surface area
A2=2 * pi * (r) * (Ls);
A1=2 * pi * (r1) * (Ls);
```

```
A=A1 + A2;

% Calculate Ts
Ts=((q/(sigma*A))+Tinf^4)^(.25);

% Convert to celsius
Ts=Ts-273;

%%%%%%%%%%%%%%%%%%%%%%%%%%%%%%%%%%%%%%%%%%%%%%%%%%%%%%%%%%%%%%%%%%%%%%%
%
%  Calculate the required core temperature, T0
%
%%%%%%%%%%%%%%%%%%%%%%%%%%%%%%%%%%%%%%%%%%%%%%%%%%%%%%%%%%%%%%%%%%%%%%%

% Calculate qdot
qdot=q/(pi*(r^2-r1^2)*Ls);

% Calculate constants C1 and C2
C1=-(qdot*(r^2-r1^2))/(4*k*log(r1/r));
C2=Ts + (qdot/(4*k))*r1^2 - C1*log(r1);

T0=-((qdot/(4*k))*((r+r1)/2)^2) + C1*log((r+r1)/2) + C2;

% Correct for numerical errors resulting in temperatures
% than Tinf.

if T0<Tinf-273,
   T0=Tinf-273;
   disp('Error trap in CHKTEMP2')
end

%%%%%%%%%%%%%%%%%%%%%%%%%%%%%%%%%%%%%%%%%%%%%%%%%%%%%%%%%%%%%%%%%%%%%%%
```

All other routines called are standard MATLAB routines (65).

G.5 Orbit History Design Programs

As the design process evolved, using the time-history design program to determine and evaluate modifications to the SFP design was found to be cumbersome. A recursive routine was developed to repeatedly call a modified version of the time-history design program to determine and evaluate design modifications at numerous points in an orbit. This new routine — the orbit-history design program — simulates the SFP moving in an orbit and is used to determine the necessary gain scheduling for the controller. To modify the time-history design program, all of the output statements were stripped out of the routine and it was converted to a function. The driver program is used to pass in all orbit, position, and orientation information. Using loops, various parameters can be changed to simulate the SFP's movement through

orbit. The user manually sets the desired parameters within the driver program and then starts the driver. The inputs and outputs can be changed to study how various outputs change over the course of an orbit. The orbit-history design program is not really concerned with determining the stability of a particular design — that is the function of the time-history design program. The orbit-history design program is used to study how parameters such as individual conductor currents, conductor temperatures, power requirements, and thrust of the augmentation thrusters change for changes in the position of the SFP relative to the orbit. The driver program for this recursive calling to the design tool follows:

```
%%%%%%%%%%%%%%%%%%%%%%%%%%%%%%%%%%%%%%%%%%%%%%%%%%%%%%%%%%%%%%%%%%%%%%%%%%%%%%%%%
clear deschk maxP;

inputs(1)=-60;   % Commanded Radial Position (rx)
inputs(2)=0;     % Commanded Orbit Path Position (ry)
inputs(3)=0;     % Commanded Out-of-Plane Position (rz)
inputs(4)=0;     % Commanded Yaw Angle (psi)
inputs(5)=0;     % Commanded Roll Angle (phi)
inputs(6)=0;     % Commanded Pitch Angle (theta)
inputs(7)=-60;   % Initial Radial Position (x0)
inputs(8)=0;     % Initial Orbit Path Position (y0)
inputs(9)=0;     % Initial Out-of-Plane Position (z0)
inputs(10)=0;    % Initial Yaw Angle (psi0)
inputs(11)=0;    % Initial Roll Angle (phi0)
inputs(12)=0;    % Initial Pitch Angle (theta0)
inputs(13)=0;    % True Anomaly (nu)
inputs(14)=0;    % Right Ascension of Ascending Node (Omega)
inputs(15)=0;    % Sidereal Time (Thetag)
inputs(16)=28.5; % Inclination (incl)
inputs(17)=400;  % Orbital Altitude

G=6.67204e-11;         % Universal Gravitational Constant (N*m^2/kg^2)
Me=5.976e24;           % Mass of the earth (kg)
re=6.378e06;           % Mean equatorial radius of earth (m)
ne=7.2921e-05;         % Angular Velocity of the Earth (rad/s)
r0=re+inputs(17)*1000; % orbital radius of reference orbit (m)
no=sqrt(G*Me/r0^3);    % orbital mean motion (reference orbit)

% Change Inclination
%startincl=0;
%stopincl=80;
%stepincl=1;
%steps1=((stopincl-startincl)/stepincl)+1;

%for i=1:steps1

%incl=(i-1)*stepincl+startincl

%inputs(16)=incl;

% Change True Anomaly and Sidereal Time
%startnu=0;
```

```
%stopnu=6000;
%stepnu=60;
%startnu=2000;
%stopnu=3000;
%stepnu=30;
startnu=2300;
stopnu=2660;
stepnu=10;
%startnu=2350;
%stopnu=2400;
%stepnu=5;
steps2=ceil((stopnu-startnu)/stepnu)+1;
startThg=(startnu)*(ne/no)

for j=1:steps2

nu=(j-1)*stepnu+startnu
Thetag=(j-1)*(stepnu*(ne/no))+startThg

inputs(13)=nu;
inputs(15)=Thetag;

[maxcur,temp,maxpow,Mtot,maxforce,maxmom,treq]=deschk3(inputs);

deschk(j,:)=[nu maxcur maxpow temp];
davedat(j,:)=[maxforce maxmom];

tshield(j)=treq;

end  % End j loop

%end  % End i loop

plot(deschk(:,1),deschk(:,13)),grid,title('Total Power');
%print totpow
pause
plot(deschk(:,1),deschk(:,2:12)),grid,title('Conductor Currents');
%print condcur
pause
plot(deschk(:,1),deschk(:,19:28)),grid,title('Max Temps');
pause
%plot(deschk(:,1),deschk(:,19:28)),grid,title('Core Temps');
%print condtemp
%pause
%plot(deschk(:,1),deschk(:,29:38)),grid,title('Conductor Power');
%pause

%max(abs(deschk(:,14:28)))

a=[1:11 1 1:5 1:10];
[Y,I]=max(abs(deschk(:,2:28)));
[a' Y' I']
Mtot
tmax=max(tshield)

%%%%%%%%%%%%%%%%%%%%%%%%%%%%%%%%%%%%%%%%%%%%%%%%%%%%%%%%%%%%%%%%%%%%%%%%%%%%%%%%%%
```

The design tool in its function form follows:

```
%%%%%%%%%%%%%%%%%%%%%%%%%%%%%%%%%%%%%%%%%%%%%%%%%%%%%%%%%%%%%%%%%%%%%%%%%%%%%%%%%%
function [maxcur,maxtemps,maxpow,Mtot,maxforce,maxmom,treq]=deschk3(in)
```

```
%%%%%%%%%%%%%%%%%%%%%%%%%%%%%%%%%%%%%%%%
%
% Breakout Input Data
%
%%%%%%%%%%%%%%%%%%%%%%%%%%%%%%%%%%%%%%%%
rx=in(1);
ry=in(2);
rz=in(3);
rpsi1=in(4);
rpsi2=in(5);
rpsi3=in(6);
x0=in(7);
y0=in(8);
z0=in(9);
psi10=in(10);
psi20=in(11);
psi30=in(12);
nu=in(13);
Omega=in(14);
Thetag=in(15);
incl=in(16);
altitude=in(17);

%%%%%%%%%%%%%%%%%%%%%%%%%%%%%%%%%%%%%%%%
%
% Define Constants
%
%%%%%%%%%%%%%%%%%%%%%%%%%%%%%%%%%%%%%%%%
G=6.67204e-11;          % Universal Gravitational Constant (N*m^2/kg^2)
Me=5.976e24;            % Mass of the earth (kg)
re=6.378e06;            % Mean equatorial radius of earth (m)
we=7.2921e-05;          % Earth's Rotation Rate (rad/sec)

M=8.05e15;              % Magnetic dipole moment of the earth (T m^3)
Phi0=-78.5*pi/180;      % Latitude of austral simple magnetic pole (rad)
Lam0=111*pi/180;        % Longitude of austral simple magnetic pole (rad)

Cd=2.4;                 % SFP Drag Coefficient
Adrag=1435;             % SFP Frontal Area (m^2)
rho0=1.916e-11;         % Air Density at Reference Altitude (kg/m^3)
hs=50043;               % Scale Height (km)
rref=300;               % Reference altitude (km)

%%%%%%%%%%%%%%%%%%%%%%%%%%%%%%%%%%%%%%%%%%%%%%%%%%%%%%%%%%%%%%%%%%%%%%%%%%%%%%%%%%%%
%
% Platform Dimensions and Operating Regime
%
%%%%%%%%%%%%%%%%%%%%%%%%%%%%%%%%%%%%%%%%%%%%%%%%%%%%%%%%%%%%%%%%%%%%%%%%%%%%%%%%%%%%

%%%%%%%%%%%%%%%%%%%%%%%%%%%%%%%%%%%%%%%%
%
% Payload Data
%
%%%%%%%%%%%%%%%%%%%%%%%%%%%%%%%%%%%%%%%%
% Maximum allowable SFP payload = 31,300 kg
Mpay=31300;
Lpay=46.88; % Payload length (m)
Rpay=4.206; % Payload radius (m)

%%%%%%%%%%%%%%%%%%%%%%%%%%%%%%%%%%%%%%%%
%
% Truss Maker Mass and Size
%
%%%%%%%%%%%%%%%%%%%%%%%%%%%%%%%%%%%%%%%%
```

```
% Maximum allowable weight for truss
% maker = 3000 kg
% Size = 5x10x2 (b1xb2xb3)
Mtm=3000;
Ltm=10;  % Length of Truss Maker = 10 m
Wtm=2;   % Width of Truss Maker = 2 m
Htm=5;   % Height of Truss Maker = 5 m

%%%%%%%%%%%%%%%%%%%%%%%%%%%%%%%%%%%%%%%%%%%%%%%%
%
% Main Integrated Truss Mass and size
%
%%%%%%%%%%%%%%%%%%%%%%%%%%%%%%%%%%%%%%%%%%%%%%%%
% Allow 5000 kg for remote manipulators
% Linear density = 20 kg/m for the truss
% structure
% Allow 2000 kg for ASSET equipment
Lmit=50;     % Length of Integrated Truss (m)
Wmit=2;      % Width and Depth of Main Int Truss (m)
Mmit=5000 + Lmit*20 +...
     2000;   % Misc weight of Main Int Tr (kg)

%%%%%%%%%%%%%%%%%%%%%%%%%%%%%%%%%%%%%%%%%%%%%%%%
%
% Augmentation Thruster Assemblies
%    Mass and Size
%
%%%%%%%%%%%%%%%%%%%%%%%%%%%%%%%%%%%%%%%%%%%%%%%%
% Allow 1100 kg for augmentation thruster
% assemblies and associated H/W, plus 1000 kg
% for fuel.
Mta=1100 + 1000;    % Mass of Thrusters (kg)
Hta=4;              % Height of Thruster Assembly (m)
Wta=2;              % Width and Depth of TA (m)

%%%%%%%%%%%%%%%%%%%%%%%%%%%%%%%%%%%%%%%%%%%%%%%%
%
% Cross Integrated Truss Mass and size
%
%%%%%%%%%%%%%%%%%%%%%%%%%%%%%%%%%%%%%%%%%%%%%%%%
% Allow 12000 kg for misc H/W
% Linear density = 20 kg/m for the truss
% structure
Lcit=30;     % Length of Cross Integrated Trusses (m)
Wcit=2;      % Width and Depth of Cross Int Truss (m)
Mcit=Lcit*20 +...
     12000;  % Misc weight of Cross Int Tr (kg)

%%%%%%%%%%%%%%%%%%%%%%%%%%%%%%%%%%%%%%%%%%%%%%%%
%
% Solar dynamic Power Module Mass and Size
%
%%%%%%%%%%%%%%%%%%%%%%%%%%%%%%%%%%%%%%%%%%%%%%%%
% Allow 6000 kg/side for cell H/W
% Let cell cm be 4m off center of truss
% and 29 m from centerline of SFP
Mspm=6000;    % Mass of Solar dynamic Cell (kg)
Wspm=5;       % Effective width of Solar Cell (m)
Hspm=10;      % Effective Height of Solar Cell (m)
hspm=4;       % Height of Solar Cell cm (m)
lspm=29;      % Solar Cell Position on Truss (m)

%%%%%%%%%%%%%%%%%%%%%%%%%%%%%%%%%%%%%%%%%%%%%%%%
%
% ASSET Power Array data
```

```
%
%%%%%%%%%%%%%%%%%%%%%%%%%%%%%%%%%%%%%%%%%%%%
% Allow 2500 kg/side for array H/W
% Let cell cm be 3m off center of truss
% and 29 m from centerline of SFP
Mapa=2500;    % Mass of Solar dynamic Cell (kg)
Wapa=2;       % Effective width of ASSET arrays (m)
Hapa=7;       % Effective height of ASSET arrays (m)
hapa=3;       % Height of Solar Cell cm (m)
lapa=29;      % Array Position on Truss (m)

%%%%%%%%%%%%%%%%%%%%%%%%%%%%%%%%%%%%%%%%%%%%
%
% Orthogonal Integrated Truss Mass and Size
%
%%%%%%%%%%%%%%%%%%%%%%%%%%%%%%%%%%%%%%%%%%%%
% Allow 12000 kg for misc H/W
% Linear density = 20 kg/m for the truss
% structure
Loit=27;           % Orthogonal Integrated Trusses Length (m)
Woit=2;            % Orthogonal Integrated Truss Width and Depth (m)
Moit=Loit*20 +...
     0;            % Orthogonal Integrated Truss Misc Weight (kg)

%%%%%%%%%%%%%%%%%%%%%%%%%%%%%%%%%%%%%%%%%%%%
%
% Diameter of Conductor Wire
%
%%%%%%%%%%%%%%%%%%%%%%%%%%%%%%%%%%%%%%%%%%%%
wire=2;
rwire=wire/200;  % Wire radius (m)
area=pi*rwire^2; % Wire area (m^2)

tshield=10.13;  % Metic Shield thickness (mm)
tshield=tshield/1000;

%%%%%%%%%%%%%%%%%%%%%%%%%%%%%%%%%%%%%%%%%%%%
%
% Platform Design Dimensions
%
%%%%%%%%%%%%%%%%%%%%%%%%%%%%%%%%%%%%%%%%%%%%
%%% Conductor 1
LC1=25;
n1=99;
L1=LC1*n1;

%%% Conductor 2
LC2=LC1;
n2=n1;
L2=L1;

%%% Conductor 3
LC3=25;
n3=1;
L3=LC3*n3;

%%% Conductor 4
LC4=LC3;
n4=n3;
L4=L3;

%%% Conductor 5
LC5=27;
n5=21;
L5=LC5*n5;
```

```
%%% Conductor 6
r6=1.9;
n6=137;
Lsol6=ceil((n6/10))*0.02;
if n6<10,
  rsol6=(n6*0.02)/2;
else
  rsol6=0.10;
end
L6=n6*2*pi*(r6-rsol6);
mu6=n6*pi*(r6^2);

%%% Conductor 7
r7=r6;
n7=n6;
Lsol7=Lsol6;
L7=L6;
mu7=mu6;

%%% Conductor 8
r8=1.9;
n8=1;
Lsol8=ceil((n8/10))*0.02;
if n8<10,
  rsol8=(n8*0.02)/2;
else
  rsol8=0.10;
end
L8=n8*2*pi*(r8-rsol8);
mu8=n8*pi*(r8^2);

%%% Conductor 9
r9=r8;
n9=n8;
Lsol9=Lsol8;
L9=L8;
mu9=mu8;

%%% Conductor 10
r10=1.9;
n10=497;
Lsol10=ceil((n10/10))*0.02;
if n10<10,
  rsol10=(n10*0.02)/2;
else
  rsol10=0.10;
end
L10=n10*2*pi*(r10-rsol10);
mu10=n10*pi*(r10^2);

%%%%%%%%%%%%%%%%%%%%%%%%%%%%%%%%%%%%%%%%%%%%%%%
%
% Coiled Conductor Integrated Truss data
%
%%%%%%%%%%%%%%%%%%%%%%%%%%%%%%%%%%%%%%%%%%%%%%%
% Truss linear density = 40 kg/m
Lccst=Lsol6+Lsol7+max([2*r8 2*r10])+.5;
Wccst=max([2*r6 2*r8 2*r10])+.5;
Mccst=Lccst*40+...
    0;          % Mass of Solenoid Int Truss (kg)

%%%%%%%%%%%%%%%%%%%%%%%%%%%%%%%%%%%%%%%%%%%%%%%
%
% Orthogonal Integrated Truss Mass and size
```

```
%
%%%%%%%%%%%%%%%%%%%%%%%%%%%%%%%%%%%%%%%%%%%%%%
% Allow 0 kg for misc H/W
% Linear density = 20 kg/m for the truss
% structure
Loit=27;      % Length of Bottom Integrated Trusses (m)
Woit=2;       % Width and Depth of Bottom Int Truss (m)
Hoit=Loit*20;

%%%%%%%%%%%%%%%%%%%%%%%%%%%%%%%%%%%%%%%%%%%%%%
%
% Determine Conductor Linear Densities
%    (Includes Shielding)
%
%%%%%%%%%%%%%%%%%%%%%%%%%%%%%%%%%%%%%%%%%%%%%%
[pw1,ps1,d1]=wireden(rwire,n1,tshield);
[pw2,ps2,d2]=wireden(rwire,n2,tshield);
[pw3,ps3,d3]=wireden(rwire,n3,tshield);
[pw4,ps4,d4]=wireden(rwire,n4,tshield);
[pw5,ps5,d5]=wireden(rwire,n5,tshield);

pws=pi*(rwire)^2*2.699e+003;

%%%%%%%%%%%%%%%%%%%%%%%%%%%%%%%%%%%%%%%%%%%%%%
%
% Calculate Mass of Towers and Conductors
%
%%%%%%%%%%%%%%%%%%%%%%%%%%%%%%%%%%%%%%%%%%%%%%
Mc1=(2*pw1+ps1)*LC1;                % Mass of conductor C1 truss
Mc2=(2*pw2+ps2)*LC2;                % Mass of conductor C2 truss

Mc3=(2*pw3+ps3)*LC3;                % Mass of conductor C3 truss
Mc4=(2*pw4+ps4)*LC4;                % Mass of conductor C4 truss

Mc5=(2*pw5+ps5)*LC5;                % Mass of conductor C5 truss

Mc6=pws*L6;                         % Mass of coil C6
Mc7=pws*L7;                         % Mass of coil C7

Mc8=pws*L8;                         % Mass of coil C8
Mc9=pws*L9;                         % Mass of coil C9

Mc10=pws*L10;                       % Mass of coil C10

Mtot=Mpay+Mtm+Mmit+2*Mta+...
     2*Mcit+2*Mspm+2*Mapa+Mccst+Moit+...
     Mc1+Mc2+Mc3+Mc4+Mc5+...
     Mc6+Mc7+Mc8+Mc9+Mc10;          % Total Platform Mass (kg)

%%%%%%%%%%%%%%%%%%%%%%%%%%%%%%%%%%%%%%%%%%%%%%
%
% Platform Moments of Inertia
%
%%%%%%%%%%%%%%%%%%%%%%%%%%%%%%%%%%%%%%%%%%%%%%
% Allow 3m offset for cm of ET and 3m offset
% of cm of truss maker
% Geometric Body Approximation
%   Payload                 = Circular Cylinder
%   Truss Maker             = Rectangular Prism
%   Main Integrated Truss   = Circular Cylinder
%   Thruster Assemblies     = Rectangular Prism
%   Cross Integrated Truss  = Circular Cylinder
%   Solar Dynamic Cells     = Thin Rectangular Plate
%   ASSET Power Arrays      = Thin Rectangular Plate
%   Conductor C1            = Circular Cylinder
```

```
%   Conductor C2            = Circular Cylinder
%   Conductor C3            = Circular Cylinder
%   Conductor C4            = Circular Cylinder
%   Conductor C5            = Rectangular Prism
%   Solenoid Truss Assembly = Circular Cylinder
%
Mccst=Mccat+Mc6+Mc7+Mc8+Mc9+Mc10;
%
Ixx(1)=(Mpay/12)*(3*Rpay^2+Lpay^2) +...
       Mpay*(3)^2;                          % Payload
Ixx(2)=(Mtm/12)*(Wtm^2+Ltm^2) +...
       Mtm*(3)^2;                           % Truss Maker
Ixx(3)=(Mmit/12)*(3*(Wmit/2)^2+Lmit^2) + 0;  % Main Integrated Truss
Ixx(4)=2*((Mta/12)*(Wta^2+Wta^2) +...
          Mta*((Lmit/2)+(Wta/2))^2);        % Thruster Assemblies
Ixx(5)=2*((Mcit/12)*(3*(Wcit/2)^2+Lcit^2) +...
          Mcit*((Wccst/2)+(Lcit/2))^2);     % Cross Integrated Truss
Ixx(6)=2*((Mspm/12)*(Wspm^2) +...
          Mspm*((Wccst/2)+lspm)^2);         % Solar Dynamic Cells
Ixx(7)=2*((Mapa/12)*(Wapa^2) +...
          Mapa*((Wccst/2)+lapa)^2);         % ASSET Power Arrays
Ixx(8)=(Moit/2)*(Woit^2) + 0;               % Orthogonal Integrated Truss
Ixx(9)=2*(((Mc1)/24)*(3*(d1/2)^2+LC1^2) +...
          Mc1*((LC1/2)^2+(Wmit/2)^2));      % Conductor C1
Ixx(10)=2*(((Mc2)/24)*(3*(d2/2)^2+LC2^2) +...
          Mc2*((LC2/2)^2+(Wmit/2)^2));      % Conductor C2
Ixx(11)=2*(((Mc3)/24)*(3*(d3/2)^2+LC3^2) +...
          Mc3*(((Wccst/2)+(LC3/2))^2+...
               (Wcit/2)^2));                % Conductor C3
Ixx(12)=2*(((Mc4)/24)*(3*(d4/2)^2+LC4^2) +...
          Mc4*(((Wccst/2)+(LC4/2))^2+...
               (Wcit/2)^2));                % Conductor C4
Ixx(13)=2*(((Mc5)/4)*(d5/2)^2 + Mc5*(.7)^2);  % Conductor C5
Ixx(14)=(Mccst/12)*((3*Wccst/2)^2+Lccst^2);   % Solenoid Truss Assembly
%
Iyy(1)=(Mpay/2)*(Rpay^2) +...
       Mpay*(Htm-0.5+Rpay)^2;               % Payload
Iyy(2)=(Mtm/12)*(Wtm^2+Htm^2) +...
       Mtm*(Htm/2)^2;                       % Truss Maker
Iyy(3)=(Mmit/2)*(Wmit/2)^2 +...
       Mmit*((Wmit/2)+0.5)^2;               % Main Integrated Truss
Iyy(4)=2*((Mta/12)*(Hta^2+Wta^2) + 0);      % Thruster Assemblies
Iyy(5)=2*((Mcit/12)*(3*(Wcit/2)^2+Lcit^2) +...
          Mcit*((0.5+Wmit+(Wccst/2))^2+...
                (Lcit/2)^2));               % Cross Integrated Truss
Iyy(6)=2*((Mspm/12)*(Wspm^2+Hspm^2) +...
          Mspm*(0.5+Wmit+(Wccst/2)-hspm)^2+...
               ((Wccst/2)+lspm)^2);           % Solar Dynamic Cells
Iyy(7)=2*((Mapa/12)*(Wapa^2+Hapa^2) +...
          Mapa*(0.5+Wmit+(Wccst/2)+hapa)^2+...
               ((Wccst/2)+lspm)^2);           % ASSET Power Arrays
Iyy(8)=2*((Moit/12)*(3*(Woit/2)^2+Loit^2) +...
          Moit*(0.5+Wmit+Wccst+(Loit/2))^2);  % Orthogonal Integrated Truss
Iyy(9)=2*(((Mc1)/4)*(d1/2)^2 +...
          Mc1*((0.5+(Wmit/2))^2+(Wmit/2)^2)); % Conductor C1
Iyy(10)=2*(((Mc2)/4)*(d2/2)^2 +...
          Mc2*((0.5+(Wmit/2))^2+(Wmit/2)^2)); % Conductor C2
Iyy(11)=2*(((Mc3)/24)*(3*(d3/2)^2+LC3^2) +...
          Mc3*((0.5+Wmit+(Wccst/2))^2+...
               ((Wccst/2)+(Wcit/2))^2));      % Conductor C3
Iyy(12)=2*(((Mc4)/24)*(3*(d4/2)^2+LC4^2) +...
          Mc4*((0.5+Wmit+(Wccst/2))^2+...
               ((Wccst/2)+(Wcit/2))^2));      % Conductor C4
Iyy(13)=2*(((Mc5)/24)*(3*(d5/2)^2+LC5^2) +...
          Mc5*(0.5+Wmit+Wccst+(LC5/2))^2);  % Conductor C5
```

```
Iyy(14)=(Mccst/2)*(Wccst^2) +...
       Mccst*(0.5+Wmit+(Wccst/2))^2;              % Solenoid Truss Assembly
%
Izz(1)=(Mpay/12)*(3*Rpay^2+Lpay^2) +...
         Mpay*((Htm-0.5+Rpay)^2+3^2);          % Payload
Izz(2)=(Mtm/12)*(Htm^2+Ltm^2) +...
       Mtm*((Htm/2)^2+3^2);                    % Truss Maker
Izz(3)=(Mmit/12)*(3*(Wmit/2)^2+Lmit^2) +...
       Mmit*((Wmit/2)+0.5)^2;                  % Main Integrated Truss
Izz(4)=2*((Mta/12)*(Wta^2+Hta^2) +...
          Mta*((Lmit/2)+(Wta/2))^2);           % Thruster Assemblies
Izz(5)=2*((Mcit/2)*(Wcit/2)^2 +...
          Mcit*(0.5+Wmit+(Wccst/2))^2);          % Cross Integrated Truss
Izz(6)=2*((Mspm/12)*Hspm^2 +...
          Mspm*(0.5+Wmit+(Wccst/2)-hspm)^2);      % Solar Dynamic Cells
Izz(7)=2*((Mapa/12)*Hapa^2 +...
          Mapa*(0.5+Wmit+(Wccst/2)+hapa)^2);    % ASSET Power Arrays
Izz(8)=2*((Moit/12)*(3*(Woit/2)^2+Loit^2) +...
          Moit*(0.5+Wmit+Wccst+(Loit/2))^2);     % Orthogonal Integrated Truss
Izz(9)=2*(((Mc1)/24)*(3*(d1/2)^2+LC1^2) +...
          Mc1*((LC1/2)^2+(0.5+(Wmit/2))^2));  % Conductor C1
Izz(10)=2*(((Mc2)/24)*(3*(d2/2)^2+LC2^2) +...
          Mc2*((LC2/2)^2+(0.5+(Wmit/2))^2));  % Conductor C2
Izz(11)=2*(((Mc3)/4)*(d3/2)^2 +...
          Mc3*((0.5+Wmit+(Wccst/2))^2+...
               (Wcit/2)^2));                   % Conductor C3
Izz(12)=2*(((Mc4)/4)*(d4/2)^2 +...
          Mc4*((0.5+Wmit+(Wccst/2))^2+...
               (Wcit/2)^2));                   % Conductor C4
Izz(13)=2*(((Mc5)/24)*(3*(d5/2)^2+LC5^2) +...
          Mc5*(0.5+Wmit+Wccst+(LC5/2))^2);    % Conductor C5
Iyy(14)=(Mccst/2)*(Wccst^2) +...
       Mccst*(0.5+Wmit+(Wccst/2))^2;              % Solenoid Truss Assembly

%%%%%%%%%%%%%%%%%%%%%%%%%%%%%%%%%%%%%%%%%%%%%%%
%
% Display Principle Moments of Inertia
%
%%%%%%%%%%%%%%%%%%%%%%%%%%%%%%%%%%%%%%%%%%%%%%%
A=sum(Ixx);
B=sum(Iyy);
C=sum(Izz);

%%%%%%%%%%%%%%%%%%%%%%%%%%%%%%%%%%%%%%%%%%%%%%%
%
% Get orbital reference information from user
%
%%%%%%%%%%%%%%%%%%%%%%%%%%%%%%%%%%%%%%%%%%%%%%%
r0=re+altitude*1000;  % orbital radius of reference orbit (m)
n=sqrt(G*Me/r0^3);    % orbital mean motion (reference orbit)

nu=nu*pi/180;           % Convert True Anomaly rad
Omega=Omega*pi/180;     % Convert Right Ascension to rad
Thetag=Thetag*pi/180;   % Convert Sidereal Time to rad
incl=incl*pi/180;       % Convert Inclination to rad

%%%%%%%%%%%%%%%%%%%%%%%%%%%%%%%%%%%%%%%%%%%%%%%
%
% Prepare Reference Command Information
%
%%%%%%%%%%%%%%%%%%%%%%%%%%%%%%%%%%%%%%%%%%%%%%%
rpsi1=rpsi1*(pi/180);   % Convert to rad
rpsi2=rpsi2*(pi/180);   % Convert to rad
rpsi3=rpsi3*(pi/180);   % Convert to rad
```

```
psi10=psi10*(pi/180);   % Convert to rad
psi20=psi20*(pi/180);   % Convert to rad
psi30=psi30*(pi/180);   % Convert to rad

X0=[x0 0 y0 0 z0 0 psi10 0 psi20 0 psi30 0]';

%%%%%%%%%%%%%%%%%%%%%%%%%%%%%%%%%%%%%%%%%%%%%%%%
%
% Get time history information from user
%
%%%%%%%%%%%%%%%%%%%%%%%%%%%%%%%%%%%%%%%%%%%%%%%%
tmax=2;
ntinc=2;

%%%%%%%%%%%%%%%%%%%%%%%%%%%%%%%%%%%%%%%%%%%%%%%%
%
% Generate reference command
%
%%%%%%%%%%%%%%%%%%%%%%%%%%%%%%%%%%%%%%%%%%%%%%%%
t=0:(tmax/ntinc):tmax;

tleng=length(t);
r=zeros(tleng,6); %construct reference command

r(:,1)=rx*ones(tleng,1);
r(:,2)=ry*ones(tleng,1);
r(:,3)=rz*ones(tleng,1);
r(:,4)=rpsi1*ones(tleng,1);
r(:,5)=rpsi2*ones(tleng,1);
r(:,6)=rpsi3*ones(tleng,1);

%%%%%%%%%%%%%%%%%%%%%%%%%%%%%%%%%%%%%%%%%%%%%%%%
%
% Miscellaneous Calculations
%
%%%%%%%%%%%%%%%%%%%%%%%%%%%%%%%%%%%%%%%%%%%%%%%%
m1=cos(Phi0)*(cos(nu)*cos(Omega-Thetag-Lam0)-...
              sin(nu)*cos(incl)*sin(Omega-Thetag-Lam0))+...
   sin(Phi0)*sin(nu)*sin(incl);
m2=cos(Phi0)*(-sin(nu)*cos(Omega-Thetag-Lam0)-...
              cos(nu)*cos(incl)*sin(Omega-Thetag-Lam0))+...
   sin(Phi0)*cos(nu)*sin(incl);
m3=cos(Phi0)*sin(incl)*sin(Omega-Thetag-Lam0)+sin(Phi0)*cos(incl);

%%%%%%%%%%%%%%%%%%%%%%%%%%%%%%%%%%%%%%%%%%%%%%%%
%
% Miscellaneous Drag Calculations
%
%%%%%%%%%%%%%%%%%%%%%%%%%%%%%%%%%%%%%%%%%%%%%%%%
w1=we*sin(incl)*sin(nu);     % ar component
w2=we*sin(incl)*cos(nu);     % atheta component
w3=we*cos(incl);             % a3 component

delw=n-w3;

Kd=-((Cd*Adrag*rho0)/(2*Mtot))*exp(-(altitude-rref)/hs)*...
    (r0*sqrt(delw^2+w2^2));   % Drag Factor

i5ss=(Kd*delw*(r0^4)*Mtot)/(M*m3*L5);   % In-Path Drag Term
thss=(Kd*w2*r0*Mtot);                   % Out-of-plane Drag Term

%Set Up System Matrices F,G,H,J (open-loop)

% System Matrix, F
Fsys=[0 1 0 0 0 0 0 0 0 0 0 0;
```

```
(3*n^2) Kd (-(Kd*delw)) (2*n) (-(Kd*w2)) 0 0 0 0 0 0 0;
0 0 0 1 0 0 0 0 0 0 0 0;
(Kd*delw) (-2*n) 0 (-Kd) (Kd*w1) 0 0 0 0 0 0 0;
0 0 0 0 0 1 0 0 0 0 0 0;
(Kd*w2) 0 (-(Kd*w1)) 0 (-(n^2)) Kd 0 0 0 0 0 0;
0 0 0 0 0 0 0 1 0 0 0 0;
0 0 0 0 0 0 (-(n^2)*(C-B)/A) 0 0 (-n*(-A-B+C)/A) 0 0;
0 0 0 0 0 0 0 0 0 1 0 0;
0 0 0 0 ((3*n^2)*(A-C)/(r0*B)) 0 0 (-n*(A+B-C)/B) ((4*n^2)*(A-C)/B) 0 0 0;
0 0 0 0 0 0 0 0 0 0 0 1;
0 (3*n/(2*r0)) ((3*n^2)*(B-A)/(r0*C)) 0 0 0 0 0 0 ((-3*n^2)*(B-A)/C) 0];

%input matrix
Gsys=(M/(r0^3))*([0 0 0 0 0 0 0 0 0 0 0 0;
(-(m3*L1)/Mtot) (-(m3*L2)/Mtot) ((m2*L3)/Mtot) ((m2*L4)/Mtot) 0 0 0 0 0 0 0;
0 0 0 0 0 0 0 0 0 0 0 0;
0 0 ((2*m1*L3)/Mtot) ((2*m1*L4)/Mtot) ((m3*L5)/Mtot) 0 0 0 0 0 0;
0 0 0 0 0 0 0 0 0 0 0 0;
(-(2*m1*L1)/Mtot) (-(2*m1*L2)/Mtot) 0 0 (-(m2*L5)/Mtot) 0 0 0 0 0 (r0^3)/(M*Mtot);
0 0 0 0 0 0 0 0 0 0 0 0;
(-(m1*L1*LC1)/A) (m1*L2*LC2)/A (-(m1*L3*LC3)/A) (m1*L4*LC4)/A 0 (-(m3*mu6)/A) ...
      (-(m3*mu7)/A) (m2*mu8)/A (m2*mu9)/A 0 0;
0 0 0 0 0 0 0 0 0 0 0 0;
0 0 (m2*L3*LC3)/(2*B) (-(m2*L4*LC4)/(2*B)) (-(m2*n5*(0.5+Wmit+Wccst+LC5/2)*LC5)/B) ...
      0 0 (2*m1*mu8)/B (2*m1*mu9)/B (m3*mu10)/B 0;
0 0 0 0 0 0 0 0 0 0 0 0;
(m3*L1*LC1)/(2*C) (-(m3*L2*LC2)/(2*C)) (-(2*m1*n3*(0.5+Wmit+Wccst/2)*L3)/C) ...
      (-(2*m1*n4*(0.5+Wmit+Wccst/2)*L4)/C) (-(m3*n5*(0.5+Wmit+Wccst+LC5/2)*LC5)/C) ...
      (-(2*m1*mu6)/C) (-(2*m1*mu7)/C) 0 0 (-(m2*mu10)/C) 0]);

%output matrix (selects positions and attitude angles only)
Hsys=[1 0 0 0 0 0 0 0 0 0 0 0;
0 0 1 0 0 0 0 0 0 0 0 0;
0 0 0 0 1 0 0 0 0 0 0 0;
0 0 0 0 0 0 1 0 0 0 0 0;
0 0 0 0 0 0 0 0 1 0 0 0;
0 0 0 0 0 0 0 0 0 0 1 0];

Jsys=zeros(6,11); %no fed-through control signals

%test controllability and observability
Mc=ctrb(Fsys,Gsys);
if rank(Mc)==12,
      % disp('The (Fsys,Gsys) system is completely controllable.');
else
      % disp('The (Fsys,Gsys) system has uncontrollable modes!');
end

Mo=obsv(Fsys,Hsys);
if rank(Mo)==12 ,
      % disp('The (Fsys,Hsys) system is completely observable.');
else
      % disp('The (Fsys,Hsys) system has unobservable modes!');
end

%derive LQR compensator K
%user enters state and control signal weightings

%normalized state weighting matrix

qwt=1;
Q=qwt*([1 0 0 0 0 0 0 0 0 0 0 0;
0 1 0 0 0 0 0 0 0 0 0 0;
0 0 1 0 0 0 0 0 0 0 0 0;
0 0 0 1 0 0 0 0 0 0 0 0;
```

```
0 0 0 0 1 0 0 0 0 0 0 0;
0 0 0 0 0 1 0 0 0 0 0 0;
0 0 0 0 0 0 r0 0 0 0 0 0;
0 0 0 0 0 0 0 r0 0 0 0 0;
0 0 0 0 0 0 0 0 r0 0 0 0;
0 0 0 0 0 0 0 0 0 r0 0 0;
0 0 0 0 0 0 0 0 0 0 r0 0;
0 0 0 0 0 0 0 0 0 0 0 r0]);

rwt=1;
R=rwt*eye(11); % Set up control weighting matrix
R(1:5,1:5)=1*R(1:5,1:5);
R(11,11)=1000*R(11,11);  % Heavily Penalize Use of Thruster

K=lqr(Fsys,Gsys,Q,R);

%derive non-square pre-filter Hpf using optimal pseudo-inverse
Hpf=-pinv(Hsys*inv(Fsys-Gsys*K)*Gsys);

% Setup closed-loop system matrices

Fcl=Fsys-Gsys*K;
Gcl=Gsys*Hpf;
Hcl=Hsys;
Jcl=zeros(6);

[y,x]=lsim(Fcl,Gcl,Hcl,Jcl,r,t,X0); %outputs and states

[m,n]=size(y);
for i=1:m,
  for j=1:n,
    if abs(y(i,j))<1e-6,
       y(i,j)=0.0;
    end
  end
end

u=(Hpf*r'-K*x')'; % Control vector includes 10 currents and 1 thruster

for i=1:tleng
  u(i,5)=u(i,5)+i5ss;
  u(i,11)=u(i,11)+thss;
end

[m,n]=size(u);
for i=1:m,
  for j=1:n,
    if abs(u(i,j))<1e-9,
       u(i,j)=0.0;
    end
  end
end

a=(Gsys*u')';   % Accelerations
[m,n]=size(a);
for i=1:m,
  for j=1:n,
    if abs(a(i,j))<1e-9,
       a(i,j)=0.0;
    end
  end
end
```

```
pos=max(u);
neg=min(u);
for i=1:11,
  if abs(pos(i))>abs(neg(i))
     maxcur(i)=pos(i);
  else
     maxcur(i)=neg(i);
  end
end

rho=2.655e-8;
R1=rho*(2*L1/area);
R2=rho*(2*L2/area);
R3=rho*(2*L3/area);
R4=rho*(2*L4/area);
R5=rho*(2*L5/area);
R6=rho*(L6/area);
R7=rho*(L7/area);
R8=rho*(L8/area);
R9=rho*(L9/area);
R10=rho*(L10/area);

B1=(M/(r0^3))*2*m1;
B2=(M/(r0^3))*(-m2);
B3=(M/(r0^3))*(-m3);

L1vec=[0;L1;0];
L2vec=[0;L2;0];
L3vec=[0;0;L3];
L4vec=[0;0;L4];
L5vec=[L5;0;0];

for i=1:length(t),

  V1=x(i,2)-delw*x(i,3)-w2*x(i,5);
  V2=delw*(r0+x(i,1)) + x(i,4) + w1*x(i,5);
  V3=w2*(r0+x(i,1)) - w1*x(i,3) + x(i,6);

  C(1,1)=cos(x(i,9))*cos(x(i,11));
  C(1,2)=-sin(x(i,11));
  C(1,3)=sin(x(i,9))*cos(x(i,11));
  C(2,1)=cos(x(i,9))*sin(x(i,11))*cos(x(i,7)) + sin(x(i,9))*sin(x(i,7));
  C(2,2)=cos(x(i,11))*cos(x(i,7));
  C(2,3)=sin(x(i,9))*sin(x(i,11))*cos(x(i,7)) - cos(x(i,9))*sin(x(i,7));
  C(3,1)=cos(x(i,9))*sin(x(i,11))*sin(x(i,7)) - sin(x(i,9))*cos(x(i,7));
  C(3,2)=cos(x(i,11))*sin(x(i,7));
  C(3,3)=sin(x(i,9))*sin(x(i,11))*sin(x(i,7)) + cos(x(i,9))*cos(x(i,7));

  VB=[(V2*B3-V3*B2) (V3*B1-V1*B3) (V1*B2-V2*B1)];

  L1Vind(i)=VB*(C*L1vec);
  L2Vind(i)=VB*(C*L2vec);
  L3Vind(i)=VB*(C*L3vec);
  L4Vind(i)=VB*(C*L4vec);
  L5Vind(i)=VB*(C*L5vec);

  pow1(i)=((abs(u(i,1)*L1Vind(i)))+(R1*u(i,1)^2))/1000;
  pow2(i)=((abs(u(i,2)*L2Vind(i)))+(R2*u(i,2)^2))/1000;
  pow3(i)=((abs(u(i,3)*L3Vind(i)))+(R3*u(i,3)^2))/1000;
  pow4(i)=((abs(u(i,4)*L4Vind(i)))+(R4*u(i,4)^2))/1000;
  pow5(i)=((abs(u(i,5)*L5Vind(i)))+(R5*u(i,5)^2))/1000;
  pow6(i)=(R6*u(i,6)^2)/1000;
  pow7(i)=(R7*u(i,7)^2)/1000;
  pow8(i)=(R8*u(i,8)^2)/1000;
  pow9(i)=(R9*u(i,9)^2)/1000;
```

```
  pow10(i)=(R10*u(i,10)^2)/1000;

  totpow(i)=pow1(i)+pow2(i)+pow3(i)+pow4(i)+pow5(i)+pow6(i)+...
            pow7(i)+pow8(i)+pow9(i)+pow10(i);
  voltage(i)=abs(R1*u(i,1))+abs(R2*u(i,2))+abs(R3*u(i,3))+...
             abs(R4*u(i,4))+abs(R5*u(i,5))+abs(R6*u(i,6))+...
             abs(R7*u(i,7))+abs(R8*u(i,8))+abs(R9*u(i,9))+abs(R10*u(i,10));
end

pow(1)=(R1*maxcur(1)^2)/1000;
pow(2)=(R2*maxcur(2)^2)/1000;
pow(3)=(R3*maxcur(3)^2)/1000;
pow(4)=(R4*maxcur(4)^2)/1000;
pow(5)=(R5*maxcur(5)^2)/1000;
pow(6)=(R6*maxcur(6)^2)/1000;
pow(7)=(R7*maxcur(7)^2)/1000;
pow(8)=(R8*maxcur(8)^2)/1000;
pow(9)=(R9*maxcur(9)^2)/1000;
pow(10)=(R10*maxcur(10)^2)/1000;

%%%%%%%%%%%%%%%%%%%%%%%%%%%%%%%%%%%%%%%%%%%%%%%%%%%%%%%%%%%%%%%%%%%%%%%%%%%
%
% Calculate the shield's inner surface temperature and the
% conductor's core temperature.
%
%%%%%%%%%%%%%%%%%%%%%%%%%%%%%%%%%%%%%%%%%%%%%%%%%%%%%%%%%%%%%%%%%%%%%%%%%%%

[maxtemps(1),maxtemps(6)]=chktemp1(maxcur(1),LC1,n1,d1,tshield);
[maxtemps(2),maxtemps(7)]=chktemp1(maxcur(2),LC2,n2,d2,tshield);
[maxtemps(3),maxtemps(8)]=chktemp1(maxcur(3),LC3,n3,d3,tshield);
[maxtemps(4),maxtemps(9)]=chktemp1(maxcur(4),LC4,n4,d4,tshield);
[maxtemps(5),maxtemps(10)]=chktemp1(maxcur(5),LC5,n5,d5,tshield);
[maxtemps(11)]=chktemp2((wire/100),maxcur(6),n6,r6,L6,Lsol6);
[maxtemps(12)]=chktemp2((wire/100),maxcur(7),n7,r7,L7,Lsol7);
[maxtemps(13)]=chktemp2((wire/100),maxcur(8),n8,r8,L8,Lsol8);
[maxtemps(14)]=chktemp2((wire/100),maxcur(9),n9,r9,L9,Lsol9);
[maxtemps(15)]=chktemp2((wire/100),maxcur(10),n10,r10,L10,Lsol10);

maxpow=max(totpow);

maxforce(1)=((-(M*m3*L1))/(r0^3))*(maxcur(1));
maxforce(2)=(-(2*M*m1*L1)/(r0^3))*(maxcur(1));
maxforce(3)=((-(M*m3*L2))/(r0^3))*(maxcur(2));
maxforce(4)=(-(2*M*m1*L2)/(r0^3))*(maxcur(2));
maxforce(5)=((M*m2*L3)/(r0^3))*(maxcur(3));
maxforce(6)=((2*M*m1*L3)/(r0^3))*(maxcur(3));
maxforce(7)=((M*m2*L4)/(r0^3))*(maxcur(4));
maxforce(8)=((2*M*m1*L4)/(r0^3))*(maxcur(4));
maxforce(9)=((M*m3*L5)/(r0^3))*(maxcur(5));
maxforce(10)=(-(M*m2*L5)/(r0^3))*(maxcur(5));

b1mom1=(1/(r0^3))*(-(M*m1*L1*LC1)) * (maxcur(1));
b3mom1=(1/(r0^3))*(M*m3*L1*LC1)/(2) * (maxcur(1));
b1mom2=(1/(r0^3))*(M*m1*L2*LC2) * (maxcur(2));
b3mom2=(1/(r0^3))*(-(M*m3*L2*LC2)/(2)) * (maxcur(2));
b1mom3=(1/(r0^3))*(-(M*m1*L3*LC3)) * (maxcur(3));
b2mom3=(1/(r0^3))*(M*m2*L3*LC3)/(2) * (maxcur(3));
b3mom3=(1/(r0^3))*(-(2*M*m1*n3*(0.5+Wmit+Wccst/2)*L3)) * (maxcur(3));
b1mom4=(1/(r0^3))*(M*m1*L4*LC4) * (maxcur(4));
b2mom4=(1/(r0^3))*(-(M*m2*L4*LC4)/(2)) * (maxcur(4));
b3mom4=(1/(r0^3))*(-(2*M*m1*n4*(0.5+Wmit+Wccst/2)*L4)) * (maxcur(4));
b2mom5=(1/(r0^3))*(-(M*m2*n5*(0.5+Wmit+Wccst+LC5/2)*LC5)) * (maxcur(5));
b3mom5=(1/(r0^3))*(-(M*m3*n5*(0.5+Wmit+Wccst+LC5/2)*LC5)) * (maxcur(5));
b1mom6=(1/(r0^3))*(-(M*m3*mu6)) * (maxcur(6));
b3mom6=(1/(r0^3))*(-(2*M*m1*mu6)) * (maxcur(6));
```

```
b1mom7=(1/(r0^3))*(-(M*m3*mu7)) * (maxcur(7));
b3mom7=(1/(r0^3))*(-(2*M*m1*mu7)) * (maxcur(7));
b1mom8=(1/(r0^3))*(M*m2*mu8) * (maxcur(8));
b2mom8=(1/(r0^3))*(2*M*m1*mu8) * (maxcur(8));
b1mom9=(1/(r0^3))*(M*m2*mu9) * (maxcur(9));
b2mom9=(1/(r0^3))*(2*M*m1*mu9) * (maxcur(9));
b2mom10=(1/(r0^3))*(M*m3*mu10) * (maxcur(10));
b3mom10=(1/(r0^3))*(-(M*m2*mu10)) * (maxcur(10));

maxmom(1)=b1mom1;
maxmom(2)=b3mom1;
maxmom(3)=b1mom2;
maxmom(4)=b3mom2;
maxmom(5)=b1mom3;
maxmom(6)=b2mom3;
maxmom(7)=b3mom3;
maxmom(8)=b1mom4;
maxmom(9)=b2mom4;
maxmom(10)=b3mom4;
maxmom(11)=b2mom5;
maxmom(12)=b3mom5;
maxmom(13)=b1mom6;
maxmom(14)=b3mom6;
maxmom(15)=b1mom7;
maxmom(16)=b3mom7;
maxmom(17)=b1mom8;
maxmom(18)=b2mom8;
maxmom(19)=b1mom9;
maxmom(20)=b2mom9;
maxmom(21)=b2mom10;
maxmom(22)=b3mom10;

% Calculate required shield thickness

Be=5.4e-5;
Bw1=((2e-7)*(maxcur(1))*(n1))/(d1/2);
Bw2=((2e-7)*(maxcur(1))*(n1))/(2.0-(2*d1));
Bsol=((2e-7)*(max(maxcur(6:10)))*(10))/(2.0);

treq=10*((1.571e-6)*(d1*100)*((Be+Bw1+Bw2+Bsol)/(pi*4e-7))/1.375);

%%%%%%%%%%%%%%%%%%%%%%%%%%%%%%%%%%%%%%%%%%%%%%%%%%%%%%%%%%%%%%%%%%%%%%%%%%%%%%%%%
```

Appendix H. Analysis of Center of Mass Shifts for the SFP

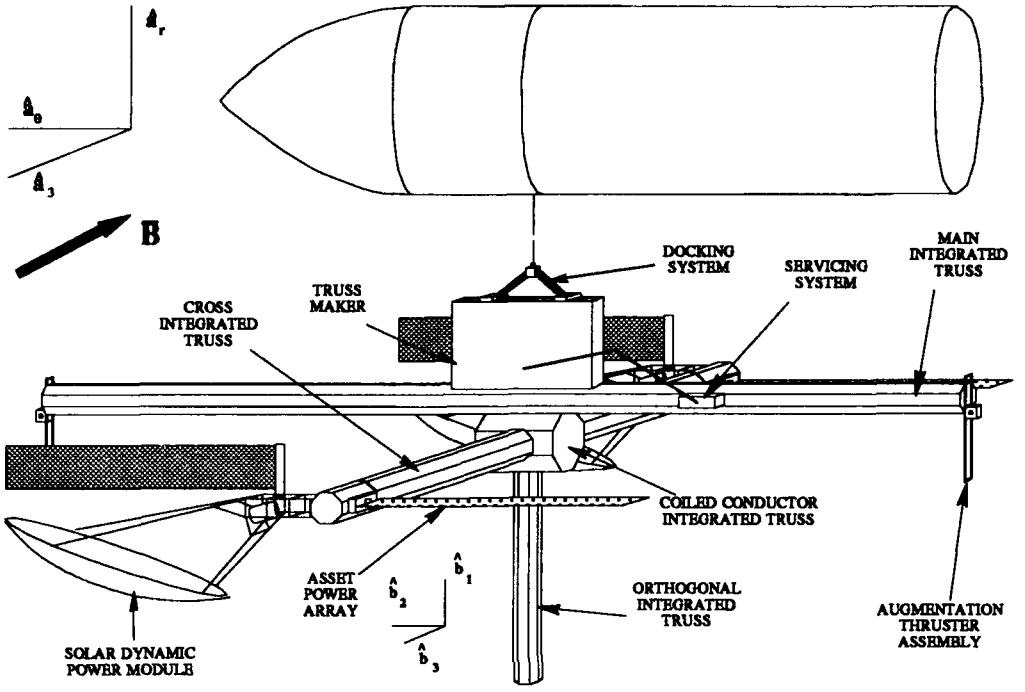

Figure H.1 SFP reference.

Figure H.1 is essential to this analysis. In the figure, a reference point is defined as the intersection between the orthogonal integrated truss axis and the top of the main integrated truss. Under most conditions, the mass distribution of the SFP is symmetric about the main and orthogonal integrated truss plane. When payload variations and power system rotations are considered, mass distribution asymmetries about the main and cross integrated truss plane, as well as the cross and orthogonal integrated truss plane, occur. To assist the controller, the SFP incorporates translating augmentation thrusters (in the $\hat{b}_1$ direction) and a translating truss maker (in the $\hat{b}_2$ direction).

H.1 Augmentation Thrusters

To insure that the augmentation thrusters do not generate undesirable moments, they are able to track the center of mass of the platform. It is therefore necessary to determine the range over which the center of mass will move in the $\hat{b}_1$ direction. The SFP has two configurations that define the high and low limits of the vehicle's mass. The center of mass for these two configurations — one with the maximum allowed payload, and one with no payload — determine the required range of the augmentation thrusters in the $\hat{b}_1$ direction.

Modeling the SFP as a system of particles, an approximation of the position of the center of mass can be calculated from

$$\overline{r}_c = \frac{1}{M}(\sum_i m_i \overline{r}_i) \tag{H.1}$$

$\overline{r}_c$ is the position of the center of mass relative to the fixed reference point
m_i is the mass of each particle
$\overline{r}_i$ is the position of each particle relative to the reference point
M is the total mass of the system (74:302-303)

Table H.1 shows the data for the external tank payload with the solar dynamic power modules oriented in the $\hat{b}_1$ direction. Applying Equation H.1 to the data in Table H.1 gives:

$$\overline{r}_{c1} = 0.65\ \hat{b}_1\ m$$

Table H.2 shows the data for the case of no payload with the solar dynamic concentrators oriented in the -$\hat{b}_1$ direction. The position of the center of mass for this case is then:

$$\overline{r}_{c2} = -3.62\ \hat{b}_1\ m$$

SFP Component	Position (m)	Mass (kg)
Payload/Truss Maker Assembly	8.61 $\hat{b}_1$	34,300
Main Integrated Truss	-1.00 $\hat{b}_1$	12,200
Conductors $C_1 + C_2$	-1.40 $\hat{b}_1$	11,418
Power System	-1.90 $\hat{b}_1$	17,000
Conductors $C_3 + C_4$	-3.50 $\hat{b}_1$	462
Cross Integrated Truss	-3.90 $\hat{b}_1$	25,200
Coiled Conductor Integrated Truss	-3.90 $\hat{b}_1$	195
Conductors $C_6 + C_7 + C_8 + C_9 + C_{10}$	-3.90 $\hat{b}_1$	7,414
Orthogonal Integrated Truss and Conductor C_5	-13.80 $\hat{b}_1$	2420
	Total	110,609

Table H.1 SFP component mass and position data with an external tank payload and the solar dynamic concentrators oriented in the $\hat{b}_1$ direction.

SFP Component	Position (m)	Mass (kg)
Truss Maker Assembly	2.50 $\hat{b}_1$	3,000
Main Integrated Truss	-1.00 $\hat{b}_1$	12,200
Conductors $C_1 + C_2$	-1.40 $\hat{b}_1$	11,418
Power System	-6.10 $\hat{b}_1$	17,000
Conductors $C_3 + C_4$	-3.50 $\hat{b}_1$	462
Cross Integrated Truss	-3.90 $\hat{b}_1$	25,200
Coiled Conductor Integrated Truss	-3.90 $\hat{b}_1$	195
Conductors $C_6 + C_7 + C_8 + C_9 + C_{10}$	-3.90 $\hat{b}_1$	7,414
Orthogonal Integrated Truss and Conductor C_5	-13.80 $\hat{b}_1$	2,420
	Total	79,309

Table H.2 SFP component mass and position data without an external tank payload and the solar dynamic concentrators oriented in the -$\hat{b}_1$ direction.

$\bar{r}_{c1}$ and $\bar{r}_{c2}$ represent the approximate required range for the augmentation thrusters in the $\hat{b}_1$ direction.

H.2 Truss Maker

The truss maker translates along the top rail of the main integrated truss so that the center of mass of the combined truss maker/payload assembly remains symmetric about the cross and orthogonal integrated truss plane. Because of the SFP's robust payload capabilities, the truss maker was designed with a full range of motion along the main integrated truss.

H.3 Conclusion

To assist the controller, translating augmentation thrusters reduce undesirable moments, and a translating truss maker keeps the SFP center of mass on the orthogonal integrated truss axis.

Appendix I. Variable Thrust Augmentation Thrusters

Electrodynamic propulsion lacks the capability to produce thrust parallel to $\overline{B}$. The necessary thrust profile for an R-bar maneuver is seen in Figure I.1. The SFP needs a thruster with variable output of 0–44 N. Using an upper bound of 50 N, to ensure coverage, rules out any type of electric thruster — most electric thrusters produce less than 1 N of thrust. Numerous thrusters would be required to achieve 50 N. Multiple thrusters would only be able to discretize the shown profile, and the size and weight of such a system could be quite extensive. This leaves chemical thrusters as the only alternative. Most liquid propellant rocket engines have been designed for constant thrust operation; however, it is possible to design an engine capable of variable thrust.

Given the following set of equations (83:83):

$$T = \dot{m} v_e + (P_e - P_a) A_e \tag{I.1}$$

$$T = C_F P_c A_t \tag{I.2}$$

$$v_e = \sqrt{\frac{2k}{k-1}\frac{\overline{R}}{M}T_c\left(1 - \left(\frac{P_e}{P_c}\right)^{\left(\frac{k-1}{k}\right)}\right)} \tag{I.3}$$

$$C_F = \sqrt{\frac{2k^2}{k-1}\left(\frac{2}{k+1}\right)^{\left(\frac{k+1}{k-1}\right)}\left(1 - \left(\frac{P_e}{P_c}\right)^{\left(\frac{k-1}{k}\right)}\right)} + \frac{P_e - P_a}{P_c}\frac{A_e}{A_t} \tag{I.4}$$

where

T = thrust

$\dot{m}$ = mass flow rate

v_e = nozzle exit velocity

P_e = nozzle exit pressure

P_a = ambient pressure

A_e = nozzle exit area

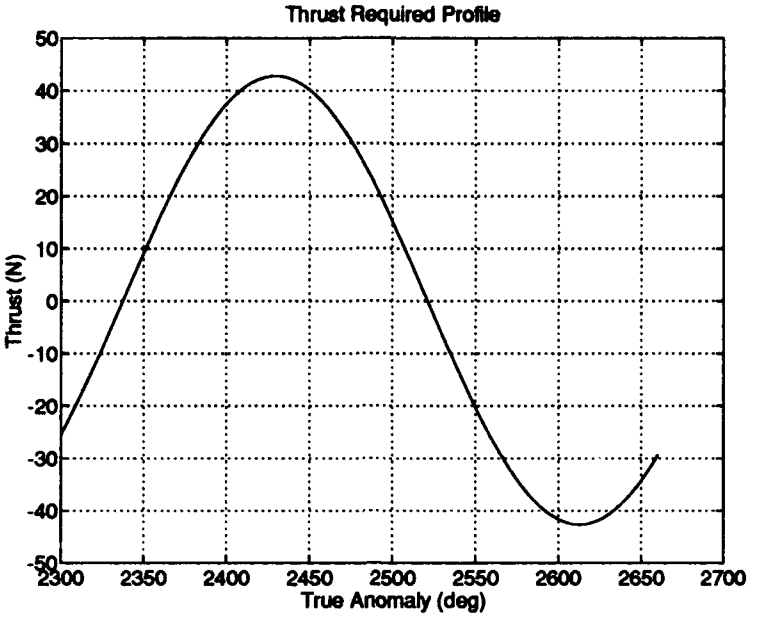

Figure I.1 The out-of-plane thrust required to perform an R-bar standoff of -60 m.

C_F = coefficient of thrust

P_c = chamber pressure

A_t = throat area

k = specific heat ratio

$\overline{R}$ = universal gas constant

M = molecular weight

T_c = chamber temperature

It is easily seen that T is proportional to A_t, P_c, $\dot{m}$, and $\sqrt{T_c/M}$. These equations show how variations in thrust can affect other factors.

A method of varying thrust is to change A_t while simultaneously throttling the flow (accomplished by inserting a movable, tapered plug into the nozzle)(83:82). In this case, P_c can remain constant, as well as T_c, M and the specific impulse, I_{sp}. This

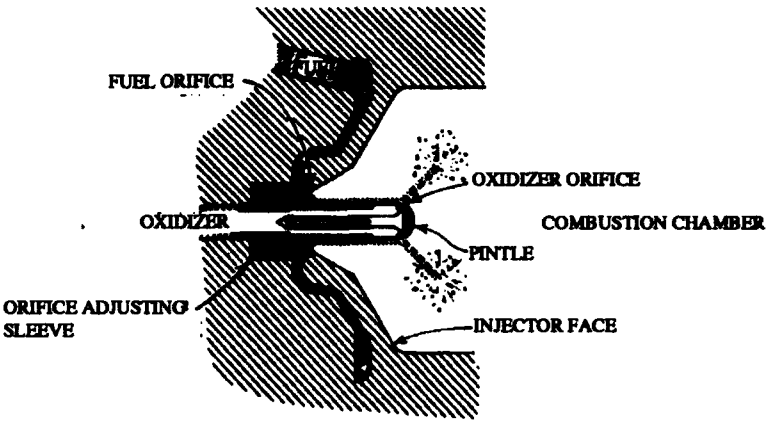

Figure I.2 A variable thrust injector with movable sleeves to vary the amounts of fuel and oxidizer entering the chamber.

has been done experimentally but the mechanism is complex, heavy and difficult to cool.

For liquid propellant rockets, the flow to the chamber can be decreased by throttling valves/injectors in the propellant feed system, while chamber geometry and A_t are held constant (83:82). This results in a linear decrease in P_c, with a slight decrease in T_c and I_{sp}. In other words, there is a small penalty for throttled thrust.

A typical throttleable injector, with variable injection slot areas, is shown in Figure I.2. This is an effective means of controlling the propellant flows and injector pressure drops at various engine thrust levels. The addition of moving parts does cause some design complications, but this is a proven method that was used on the lunar lander with a throttling ratio of 10:1 (83:82). The McDonnell Douglas Delta Clipper (experimental single stage to orbit vehicle) also relies on throttleable valves for thrust variation from 30% to 100% (47:55).

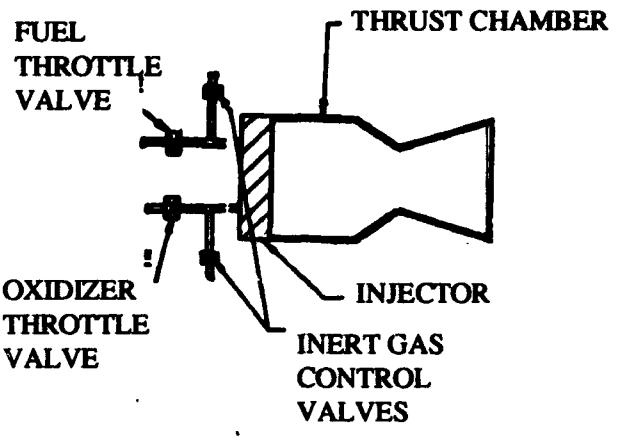

Figure I.3 A variable thrust injector introduces an inert gas to reduce thrust by varying the propellant/gas mixture ratio.

A second approach to a throttleable injection system is the "aeration method" shown in Figure I.3. An inert gas is introduced into the injector propellant manifold to reduce thrust levels by variation of the propellant/gas mixture ratio. This effectively varies the propellant density to achieve any desired thrust level without affecting combustion stability. The inert gas can be supplied by the same source used to pressurize the propellant tanks. This method makes it possible to achieve a throttling ratio of 100:1 (37:127).

For the SFP, 50 N of thrust can be achieved by a relatively small liquid propellant thruster and can easily be handled by a set of two 40 N thrusters for each side of the SFP. The total of four thrusters are mounted in opposing pairs, on stanchions at the ends of the main integrated truss. With a throttling ratio of 10:1, these thrusters will easily achieve the variable out-of-plane thrust requirement depicted in Figure I.1.

The augmentation thrusters must also track shifts in the center of mass — shifts due to the changes in payload and rotation of the power systems. This tracking is required to eliminate undesirable moments that would be caused by the thrusters.

This is discussed in Appendix H. In other words, the thrusters must translate along the $\hat{b}_1$ direction to provide the thrust through the axis of the shifting center of mass. Two movable thruster assemblies on stanchions have been selected for the task. These thruster assemblies are located at the ends of the main integrated truss, and are designed to thrust in the $\hat{b}_3$ direction. The two assemblies will each consist of a stanchion and movable platform. The platform will house the thruster assemblies and positioning motor. The thruster assembly will consist of the thruster and any necessary fuel. These components are powered and controlled by a flexible umbilical connected to the main integrated truss.

Appendix J. Linear System Controller Development

The detailed derivation of the equations of motion provides a model of the SFP's behavior that can be used to develop an SFP design that gives full control over the equations of motion while achieving the operational capability goals. The method chosen to combine these two tasks was to use the controller design process outlined in the POTkV study (81:4–5) in an iterative scheme. First, a design for the SFP is proposed. The equations of motion for the design are derived. They are then converted to a state space representation. The state space representation is checked for controllability and observability. Based on the state space representation, a two degree of freedom controller is designed using a linear quadratic regulator and a prefilter. The state space open loop system is then converted to a closed loop system using full state feedback. A linear simulation using the closed loop system is then run to generate the currents and thrust required by the control elements to achieve the desired performance. This data is then used to evaluate power, temperature, and performance. If changes to the design are required, then updates are made, and the process is repeated. The process repeats until an acceptable design is achieved. An acceptable design would allow the platform to precisely fly a desired trajectory and maintain a desired attitude during maneuvering.

J.1 State Space Equations of Motion

The first step of the design process — deriving the equations of motion — has been carried out in the preceding sections. The SFP equations of motion can now be written as a state space representation. However, before this can be done, the constant aerodynamic drag terms in Equations 6.20 and 6.21 must be removed. Since the orientation angles are assumed to be small, the control elements that will be expected to compensate for the aerodynamic drag can be predicted. The forces due to the constant drag terms will be calculated separately in the control design process.

Their power and thrust requirements will be added back in prior to evaluation of the design. This makes the aerodynamic drag part of the equilibrium state for the controller.

Once the constant terms are removed, the conversion to a state space representation can occur. In order to convert the equations, the coupling of the currents and attitude terms in Equations 6.38 - 6.40 and 6.46 - 6.48 must be eliminated. This decoupling can be performed by linearizing the equations of motion. The linearization assumes products of the states and controls are small relative to the other terms in the equations of motion. For this system, the states are the relative position and attitude components, and the controls are the conductor currents and the thrust of the augmentation thrusters. Making this assumption, and dividing both sides of the equations by the appropriate mass terms, Equations 6.38 - 6.40 and 6.46 - 6.48 simplify to give:

$$\hat{a}_r : \cdots = \frac{M}{M_{tot} r_o^3} \left[-\left(niL_1 + niL_2\right) m_3 + \left(niL_3 + niL_4\right) m_2 \right] \tag{J.1}$$

$$\hat{a}_\theta : \cdots = \frac{M}{M_{tot} r_o^3} \left[2\left(niL_3 + niL_4\right) m_1 + \left(niL_5\right) m_3 \right] \tag{J.2}$$

$$\hat{a}_3 : \cdots = \frac{M}{M_{tot} r_o^3} \left[-2\left(niL_1 + niL_2\right) m_1 - \left(niL_5\right) m_2 \right] + \frac{F_{th}}{M_{tot}} \tag{J.3}$$

$$\hat{b}_1 : \cdots = \frac{M}{A r_o^3} \left[\left(-n_1 i_1 L_1^2 + n_2 i_2 L_2^2 - n_3 i_3 L_3^2 + n_4 i_4 L_4^2 \right) m_1 - \left(niA_6 + niA_7\right) m_3 + \left(niA_8 + niA_9\right) m_2 \right] \tag{J.4}$$

$$\hat{b}_2 : \cdots = \frac{M}{B r_o^3} \left[\left(\frac{n_3 i_3 L_3^2}{2} - \frac{n_4 i_4 L_4^2}{2} - n_5 i_5 L_5 \left(h_{mit} + h_{ccit} + \frac{L_5}{2} \right) \right) m_2 + 2\left(niA_8 + niA_9\right) m_1 + \left(niA_{10}\right) m_3 \right] \tag{J.5}$$

$$\hat{b}_3 : \cdots = \frac{M}{C r_o^3} \left[\left(\frac{n_1 i_1 L_1^2}{2} - \frac{n_2 i_2 L_2^2}{2} - n_5 i_5 L_5 \left(h_{mit} + h_{ccit} + \frac{L_5}{2} \right) \right) m_3 - 2\left(n_3 i_3 L_3 - n_4 i_4 L_4 \left(h_{mit} + \frac{h_{ccit}}{2} \right) \right) m_1 - 2\left(niA_6 + niA_7\right) m_1 - \left(niA_{10}\right) m_2 \right] \tag{J.6}$$

These are now linear, second order differential equations. These equations can now be used to perform the second step in the iterative design process.

The linear equations of motion can be converted to a state space representation by defining a new set of variables as described by Franklin, et al (26:362 - 363). The process yields 12 first order differential equations that are described by the matrix equations:

$$\dot{\overline{x}} = F\overline{x} + G\overline{u} \tag{J.7}$$

$$\overline{y} = H\overline{x} \tag{J.8}$$

where $\overline{x}$ is the *state vector*, F is the *system matrix*, G is the *input matrix*, $\overline{u}$ is the *input vector*, $\overline{y}$ is the *output vector*, and H is the *output matrix*. The state vector contains the relative position components, the orientation angles, and their rates:

$$\overline{x} = \left[\delta r \quad \delta\dot{r} \quad r_o\delta\nu \quad r_o\delta\dot{\nu} \quad \delta z \quad \delta\dot{z} \quad \psi \quad \dot{\psi} \quad \phi \quad \dot{\phi} \quad \theta \quad \dot{\theta}\right]^T \tag{J.9}$$

The system matrix is formed from the coefficients of the left hand side terms of the converted 12 first order differential equations. This process results in the system matrix, F:

$$F = \begin{bmatrix} F_1 & 0 \\ F_2 & F_3 \end{bmatrix} \tag{J.10}$$

where

$$F_1 = \begin{bmatrix} 0 & 1 & 0 & 0 & 0 & 0 \\ 3n^2 & K & -K\delta\omega & 2n & -K\omega_2 & 0 \\ 0 & 0 & 0 & 1 & 0 & 0 \\ K\delta\omega & -2n & 0 & -K & K\omega_1 & 0 \\ 0 & 0 & 0 & 0 & 0 & 1 \\ K\omega_2 & 0 & -K\omega_1 & 0 & -n^2 & K \end{bmatrix}$$

$$F_2 = \begin{bmatrix} 0 & 0 & 0 & 0 & 0 & 0 \\ 0 & 0 & 0 & 0 & 0 & 0 \\ 0 & 0 & 0 & 0 & 0 & 0 \\ 0 & 0 & 0 & 0 & 3n^2\frac{C_3}{Br_o} & 0 \\ 0 & 0 & 0 & 0 & 0 & 0 \\ 0 & \frac{3n}{2r_o} & 3n^2\frac{C_4}{Cr_o} & 0 & 0 & 0 \end{bmatrix}$$

$$F_3 = \begin{bmatrix} 0 & 1 & 0 & 0 & 0 & 0 \\ -n^2\frac{C_1}{A} & 0 & 0 & -n\frac{C_2}{A} & 0 & 0 \\ 0 & 0 & 0 & 1 & 0 & 0 \\ 0 & n\frac{C_2}{B} & 4n^2\frac{C_3}{B} & 0 & 0 & 0 \\ 0 & 0 & 0 & 0 & 0 & 1 \\ 0 & 0 & 0 & 0 & -3n^2\frac{C_4}{C} & 0 \end{bmatrix}$$

and

$$C_1 = (C - B) \qquad C_3 = (A - C)$$
$$C_2 = (-A - B + C) \qquad C_4 = (B - A)$$

The input vector consists of the currents of the ten conductors and the thrust of the augmentation thrusters:

$$\overline{u} = [\, i_1 \;\; i_2 \;\; i_3 \;\; i_4 \;\; i_5 \;\; i_6 \;\; i_7 \;\; i_8 \;\; i_9 \;\; i_{10} \;\; F_{th} \,]^T \qquad \text{(J.11)}$$

The coefficients of the conductor currents and the thruster terms in the linearized equations of motion are assigned to the input matrix. The input matrix, G, is then:

$$G = \begin{bmatrix} G_1 & G_2 \end{bmatrix} \qquad \text{(J.12)}$$

where

$$G_1 = \begin{bmatrix} 0 & 0 & 0 & 0 & 0 \\ -\frac{M_3 n_1 L_1}{M_{tot} r_o^3} & -\frac{M_3 n_2 L_2}{M_{tot} r_o^3} & \frac{M_2 n_3 L_3}{M_{tot} r_o^3} & \frac{M_2 n_4 L_4}{M_{tot} r_o^3} & 0 \\ 0 & 0 & 0 & 0 & 0 \\ 0 & 0 & \frac{2M_1 n_3 L_3}{M_{tot} r_o^3} & \frac{2M_1 n_4 L_4}{M_{tot} r_o^3} & \frac{M_3 n_5 L_5}{M_{tot} r_o^3} \\ 0 & 0 & 0 & 0 & 0 \\ \frac{2M_1 n_1 L_1}{M_{tot} r_o^3} & -\frac{2M_1 n_2 L_2}{M_{tot} r_o^3} & 0 & 0 & -\frac{M_2 n_5 L_5}{M_{tot} r_o^3} \\ 0 & 0 & 0 & 0 & 0 \\ -\frac{M_1 n_1 L_1^2}{A r_o^3} & \frac{M_1 n_2 L_2^2}{A r_o^3} & -\frac{M_1 n_3 L_3^2}{A r_o^3} & \frac{M_1 n_4 L_4^2}{A r_o^3} & 0 \\ 0 & 0 & 0 & 0 & 0 \\ 0 & 0 & \frac{M_2 n_3 L_3^2}{2B} & -\frac{M_2 n_4 L_4^2}{2B} & -\frac{M_2 n_5 L_5^*}{B} \\ 0 & 0 & 0 & 0 & 0 \\ \frac{M_3 n_1 L_1^2}{2C} & -\frac{M_3 n_2 L_2^2}{2C} & -\frac{2M_1 n_3 L_3^*}{C} & -\frac{2M_1 n_4 L_4^*}{C} & -\frac{M_3 n_5 L_5^*}{C} \end{bmatrix}$$

$$G_2 = \begin{bmatrix} 0 & 0 & 0 & 0 & 0 & 0 \\ 0 & 0 & 0 & 0 & 0 & 0 \\ 0 & 0 & 0 & 0 & 0 & 0 \\ 0 & 0 & 0 & 0 & 0 & 0 \\ 0 & 0 & 0 & 0 & 0 & 0 \\ 0 & 0 & 0 & 0 & 0 & \frac{1}{M_{tot}} \\ 0 & 0 & 0 & 0 & 0 & 0 \\ -\frac{M_3 \mu_6}{A r_o^3} & -\frac{M_3 \mu_7}{A r_o^3} & \frac{M_2 \mu_8}{A r_o^3} & \frac{M_2 \mu_9}{A r_o^3} & 0 & 0 \\ 0 & 0 & 0 & 0 & 0 & 0 \\ 0 & 0 & \frac{2M_1 \mu_8}{B} & \frac{2M_1 \mu_9}{B} & \frac{M_3 \mu_{10}}{B} & 0 \\ 0 & 0 & 0 & 0 & 0 & 0 \\ -\frac{2M_1 \mu_6}{C} & -\frac{2M_1 \mu_7}{C} & 0 & 0 & -\frac{M_2 \mu_{10}}{C} & 0 \end{bmatrix}$$

and $L_3^* = L_3\left(h_{mit} + \frac{1}{2}h_{ccit}\right)$, $L_4^* = L_4\left(h_{mit} + \frac{1}{2}h_{ccit}\right)$, and $L_5^* = L_5\left(h_{mit} + h_{ccit} + \frac{L_5}{2}\right)$. Note that due to the presence of the B-field terms in G, it is actually time variant

at orbit rate. This makes the control problem linear and time variant. The output vector consists of the three relative positions and the orientation angles:

$$\overline{y} = [\, \delta r \quad r_o \delta \nu \quad \delta z \quad \psi \quad \phi \quad \theta \,]^T \tag{J.13}$$

The output matrix is then:

$$H = \begin{bmatrix} 1 & 0 & 0 & 0 & 0 & 0 & 0 & 0 & 0 & 0 & 0 & 0 \\ 0 & 0 & 1 & 0 & 0 & 0 & 0 & 0 & 0 & 0 & 0 & 0 \\ 0 & 0 & 0 & 0 & 1 & 0 & 0 & 0 & 0 & 0 & 0 & 0 \\ 0 & 0 & 0 & 0 & 0 & 0 & 1 & 0 & 0 & 0 & 0 & 0 \\ 0 & 0 & 0 & 0 & 0 & 0 & 0 & 0 & 1 & 0 & 0 & 0 \\ 0 & 0 & 0 & 0 & 0 & 0 & 0 & 0 & 0 & 0 & 1 & 0 \end{bmatrix} \tag{J.14}$$

The goal of the SFP design process is to design a platform that is capable of controlling all six outputs. This can be achieved by designing the SFP so it is fully controllable and fully observable from a multivariable control standpoint.

J.2 Controllability and Observability

A system is completely controllable if and only if the system can be transferred from any initial state, x_i, at any initial time, t_i, to any final state, $x(t_f) = x_f$, within a finite time, $t_f - t_i$ (68·2.42). Complete controllability implies that all poles of the system can be moved using feedback. A simple test to check a system's controllability uses the controllability matrix, M_c, given by:

$$M_c = \left[\, G \;\; | \;\; FG \;\; | \;\; F^2G \;\; | \;\; \cdots \;\; | \;\; F^{n-1}G \, \right] \tag{J.15}$$

where n is the number of states in the system. If the rank of M_c is equal to n, then the system is completely controllable. If the rank is less than n, the system is not

completely controllable, and the rank defect of M_c $(n - rank(M_c))$ tells how many system poles are uncontrollable.

A system is said to be completely observable if every initial state $x(t_i)$ can be exactly determined from the measurements of the output $y(t)$ over a finite interval of time $t_i \leq t \leq t_f$. Complete observability implies every state $x(t)$ affects the output $y(t)$. A simple test to check a system's controllability uses the controllability matrix, M_o, given by:

$$M_o = \left[H^T \mid F^T H^T \mid \left(F^T\right)^2 H^T \mid \cdots \mid \left(F^T\right)^{n-1} H^T \right] \qquad \text{(J.16)}$$

If the rank of M_o is equal to n, then the system is completely observable. If the rank is less than n, the system is not completely observable, and the rank defect of M_o $(n - rank(M_o))$ tells how many system poles are unobservable.

Since G is time variant, the controllability matrix must have full rank for all time for the system to be completely controllable. Inspection of G shows there to be control elements containing M_3 for each of the controlled state equations. Because of the constant term in M_3, and if the system resulting from this design configuration is controllable at any time, t, it will be controllable for all time. This must be true since the M_i terms are the only time varying terms in G. As a result, the design proposed by Equations J.7 - J.14 is completely controllable.

J.3 Linear Quadratic Regulator Controller Design

Once a design passes the controllability check, a suitable controller must be designed. A two degree of freedom controller, using a linear quadratic regulator and a prefilter, will allow for tracking a reference point at a fixed distance and orientation and good disturbance rejection. The tracking of the reference point — *set-point tracking* — is needed to achieve the precision docking and delivery capa-

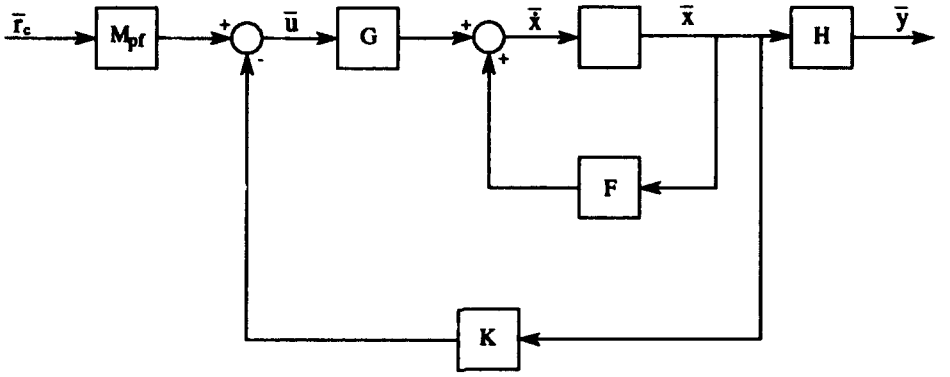

Figure J.1 Top level block diagram of the SFP control system. K is the linear quadratic regulator gain matrix which uses full state feedback. M_{pf} is the prefilter matrix.

bilities required of the SFP. Good disturbance rejection is needed to compensate for the inherent fluctuations of the B-field as well as other environmental disturbances.

Figure J.1 is a block diagram of the closed loop system. As can be seen from the diagram, the controller uses full state feedback; if this were not the case, a linear quadratic estimator could be included in the feedback path to build an estimate of the full state. The linear quadratic regulator uses the standard quadratic control cost function which combines the weighted states and weighted controls to generate the constant gain matrix, K, to be used by the control law:

$$\bar{u} = -K\bar{x} \tag{J.17}$$

The gain matrix will be optimal, and has guaranteed closed loop stability margins (68:6.1 - 6.5,7.1).

When the feedback loop is closed, the closed loop system equations become:

$$\begin{aligned}
\dot{\bar{x}} &= F\bar{x} + G\bar{u} \\
&= F\bar{x} + G(M_{pf}\bar{r}_c - K\bar{x}) \\
&= (F - GK)\bar{x} + GM_{pf}\bar{r}_c \qquad \text{(J.18)} \\
\bar{y} &= H\bar{x} \qquad \text{(J.19)}
\end{aligned}$$

Assuming there is no noise, this set of equations can be used to derive an optimal prefilter. Under the assumption of no noise, the desired performance of the controller provides set point tracking. This implies that under steady state conditions, the state does not change over time, and thus $\dot{\bar{x}} = \bar{0}$. This concept can be used to derive the prefilter:

$$\begin{aligned}
\dot{\bar{x}} &= (F - GK)\bar{x} + GM_{pf}\bar{r}_c \\
\bar{0} &= (F - GK)\bar{x}_{ss} + GM_{pf}\bar{r}_c \\
\bar{x}_{ss} &= -(F - GK)^{-1} GM_{pf}\bar{r}_c \qquad \text{(J.20)}
\end{aligned}$$

With some reference command, $\bar{r}_c$, if the set point tracking is error-free, the steady state output, $\bar{y}_{ss}$, should match the reference command perfectly (i.e. $\bar{y}_{ss} = \bar{r}_c$). Substituting Equation J.20 back into Equation J.19 and rearranging gives the optimal prefilter:

$$\begin{aligned}
\bar{y}_{ss} &= \bar{x}_{ss} \\
&= -H(F - GK)^{-1} GM_{pf}\bar{r}_c \\
\bar{y}_{ss} &= -H(F - GK)^{-1} GM_{pf}\bar{y}_{ss} \qquad \text{(J.21)}
\end{aligned}$$

For this to be true, the coefficient of the right hand side must be an identity matrix. Using a pseudo inverse, the prefilter matrix can be found:

$$\begin{aligned} -H(F-GK)^{-1}GM_{pf} &= U \\ M_{pf} &= \left[-H(F-GK)^{-1}G\right]^{-p} \end{aligned} \tag{J.22}$$

where $[\cdot]^{-p}$ denotes the pseudo inverse operator. In the absence of noise, this prefilter matrix will insure the controller tracks a reference command perfectly.

Appendix K. Heat Transfer Analysis of Translational and Attitude Control Elements

A shielded 99 conductor cable is the thickest conductor loop in the electrodynamic propulsion system of the SFP. A one dimensional heat transfer analysis of the cable was performed to insure the heat transfer is sufficient. The designed cable consists of 99 individual 2 *cm* aluminum conductors bundled in a hexagonal packing scheme with each conductor completely insulated by asbestos. All spaces between the conductors are filled with asbestos as well. The cable has a 23.16 *cm* diameter. A 10.14 *mm* thick cylinder of *Netic* magnetic shielding material surrounds the cable (see Figure K.1). This provides 19.78 m^2 of surface area from which the heat transfer must occur for the shielded section of the conductor. The heat transfer model of the shielded cable has the same dimensions, but the 99 aluminum conductors are completely replaced with asbestos to simulate a worst case thermal conductivity for the cable heat source (see Figure K.2). The thermal conductivities for the materials used in the shielded cable are listed in Table K.1.

All the power generated in the cable is dissipated into space by conducting outward from the core of the cable to the surface of the shield and then radiating to the space environment. If the shielded cable is not designed correctly, the core temperature could exceed the melting points of the materials of which it is made. The correct design is influenced by many variables. Only the most influential variables were considered in this analysis and any uncertainty was compensated for by

Material	Thermal Conductivity (k)–$W/m \cdot °C$
Aluminum Conductor	204.00
Asbestos Insulation	0.20
Netic Magnetic Shield	49.41
Pyrex Glass	1.40

Table K.1 Thermal conductivities of the materials used in the shielded cable.

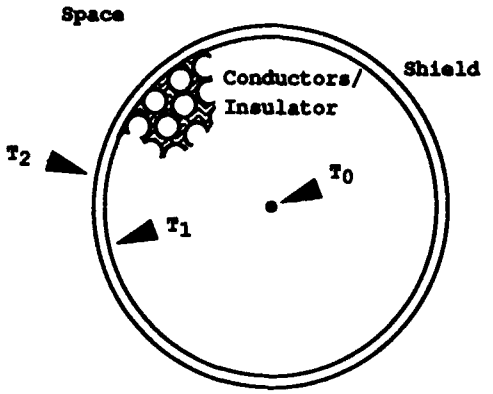

Figure K.1 The designed shielded cable with 99 aluminum conductors insulated by asbestos.

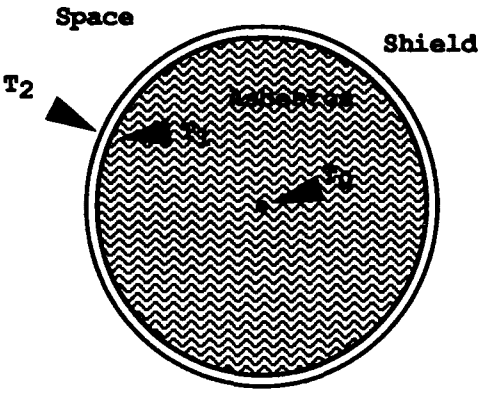

Figure K.2 The modeled shielded cable with low thermal conductivity asbestos completely replacing the conductors

implementing a large safety factor. The methodology of the analysis was to determine the worst case temperature at the core of the cable by back-propagating the temperature from outside the shielded cable into the core.

The external shield is coated with a spectrally selective material (76:146–152). This coating is highly reflective at the shorter wavelengths associated with the Sun, and highly emissive at the longer wavelengths associated with heat emission. White paint is a popular coating (76:152). With an emissivity near 1, the radiation of the power from the surface of the shield is governed by the equation (34:15):

$$i^2R = q \approx \sigma A_2(T_2^4 - T_\infty^4) \tag{K.1}$$

q = the heat transfer rate

σ = the Steffan-Boltzmann constant ($5.669 \times 10^{-8} W/m^2 \cdot {}^\circ K^4$)

A_2 = the surface area of the shielded cable

T_2 = the surface temperature of the shield

T_∞ = the approximate temperature of space at an orbital altitude of 400 km ($288\,^\circ K$) (77:3–5)

Incident radiation from the Sun is assumed reflected and not considered.

A maximum current of 261.5 A in each conductor of the cable creates the worst case power dissipation requirement:

$$i^2R_{max} = 14,217\ W$$

From Equation K.1, the surface temperature of the shield (T_2) can be determined:

$$T_2 = 374.0\,^\circ K = 101.0\,^\circ C$$

The temperature between the cable and the shield (T_1) is determined with the equation for heat transfer through a cylinder (34:32):

$$q = \frac{4\pi k_{shield}(T_1 - T_2)}{\frac{1}{r_1} - \frac{1}{r_2}} \tag{K.2}$$

k_{shield} = thermal conductivity of the shield

r_1 = inner radius of the shield

r_2 = outer radius of the shield

$$T_1 = 116.9\,^{\circ}C$$

Under steady state conditions for this one dimensional analysis, the temperature at the core of the cable is approximated with the equation (38:97):

$$T_0 = \frac{q^* r_1^2}{4k_{cable}} + T_1 \tag{K.3}$$

where, q^* = the heat transfer rate per unit volume, and:

$$T_0 = 343.1\,^{\circ}C$$

Note, the lower thermal conductivity of an all asbestos cable was used to simulate a worst case core temperature. Actual aluminum conductors would decrease the core temperature significantly. Even with the thermal conductivity of asbestos, the maximum temperature anywhere in the shielded conductor under the maximum load is $343.1\,^{\circ}C$. This is 1.91 times less than the melting point of aluminum ($657\,^{\circ}C$) and 4.47 times less than the melting point of Netic ($1532\,^{\circ}C$). It is therefore assumed that a heat transfer problem does not exist with the SFP's translational conductor design.

The same type of process as above must also be carried out for the attitude control coiled conductors. Because of the difference in geometry, several changes

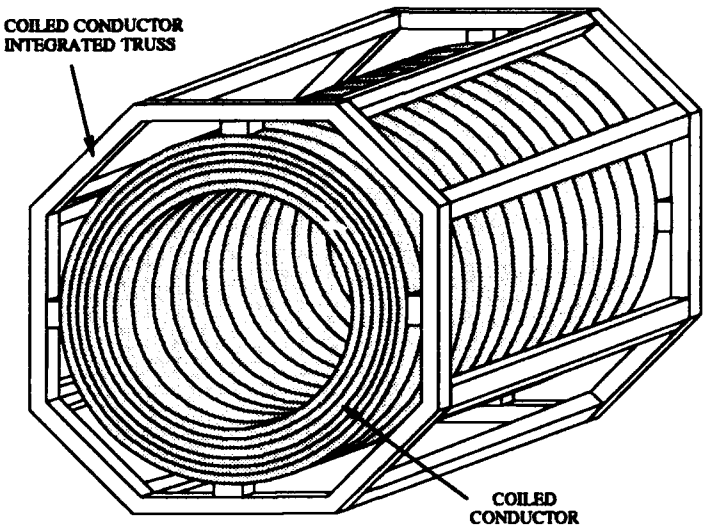

Figure K.3 The portion of the coiled conductor integrated truss showing the configuration of an attitude control coiled conductor.

must be made to the analysis process. The worst case analysis is of a 137 turn coiled conductor, wrapped in ten layers. Each wire is coated with insulation such as Pyrex glass (see Table K.1). The coiled conductor has the geometry of a hollow cylinder (see Figure K.3). The outer radius is 1.9 m and the inner radius is 1.7 m. For analysis purposes, the thermal conductivity is assumed to be uniform and equal to that of the Pyrex glass.

In heat transfer, the power dissipated by each surface is assumed to be proportional to the surface area. For example, if the inner surface were one third of the total radiating surface area, it would dissipate one third of the power. Thus, the inner and outer surface temperatures are the same.

As before, the external coating is assumed to have a high emmisivity, so the radiation of the power is governed by Equation K.1. The worst case power dissipation requirement is a result of a maximum current of 334.8 A in the 137 turn coiled

conductor. The power is then

$$i^2 R_{max} = 14,588.6\ W$$

and from applying Equation K.1, the surface temperature of the coiled conductor is found to be

$$T_1 = 466.9°K = 193.9°C$$

The core temperature is found by applying the temperature distribution across a hollow cylinder (38:99)

$$T(r) = -\frac{\dot{q}}{4k_{cable}} r^2 + C_1 \ln r + C_2 \qquad \text{(K.4)}$$

where C_1 and C_2 are constants of integration determined by applying the initial conditions $T(1.7) = T(1.9) = 193.9°C$. Solving Equation K.4 with the initial conditions for the radius of the center of the cylinder wall gives

$$T_0 = 276.2°C$$

As before, even when assuming less than ideal heat transfer conditions, the maximum core temperature of any coiled conductor is $276.2°C$. This is 2.4 times less than the melting point of aluminum. Based on this analysis, the heat transfer problem does not exist for the attitude control elements of the SFP.

Appendix L. Determination of Magnetic Shield Thickness

The required thickness of the magnetic shielding material can be easily determined from the strength of the B-fields that must be blocked. The thickness was determined by following the instructions for an "off-the-shelf" shielding material manufactured by the Magnetic Shield Corporation (54). The procedure consists of determining the strength of the B-field, and then calculating the required thickness to block a field of that strength. The maximum magnetic fields are created when the two main conductors are operating at their maximum currents. These two 99 turn, 22.78 cm diameter, conductors reach their maximum currents of 261.5 A during a steady-state R-bar maneuver at a distance of -60 m.

The B-fields associated with the Earth (B_e), the shielded portion of the conductor cable (B_{sl}), the unshielded portion of the conductor cable (B_{ul}), and the coiled conductors (B_{cc}) were considered for shielding requirements. For analysis, the contributions of the B-fields, in terms of their strengths, H, were determined. The strength of a B-field is calculated by applying the relation (24:3):

$$H = \frac{B}{\mu} \tag{L.1}$$

where B is the sum of the fields under consideration, and μ is the permeability of the medium containing the field. The units for H are A/m. In this analysis, the B-fields emanate from their sources to the shield in free space. The free space permeability constant, μ_o, was used. The B-fields for the conductor sources are calculated using:

$$B = \frac{\mu_0 i}{2\pi r}$$

and are estimated to be

$$
\begin{aligned}
B_e &= 5.40 \times 10^{-5}\ T \\
B_{sl} &= \frac{(4\pi \times 10^{-7}\ (T \cdot m)/A)(261.5\ A/turn)(99\ turns)}{2\pi(.1158\ m)} &= 4.47 \times 10^{-2}\ T \\
B_{ul} &= \frac{(4\pi \times 10^{-7}\ (T \cdot m)/A)(261.5\ A/turn)(99\ turns)}{2\pi(1.5368\ m)} &= 3.36 \times 10^{-3}\ T \\
B_{cc} &= \frac{(4\pi \times 10^{-7}\ (T \cdot m)/A)(1.2\ A/turn)(10\ turns)}{2\pi(2.0947\ m)} &= 1.09 \times 10^{-6}\ T
\end{aligned}
$$

Summing these B-fields gives

$$H = \frac{4.81 \times 10^{-2}\ T}{4\pi \times 10^{-7}\ (T \cdot m)/A} = 38,289\ \frac{A}{m}$$

With the field strength calculated, the magnetic flux capacity (B_{shield}) for a shield of a given thickness, t, can be determined. Again, the relation of Equation L.1 is applied; however, the permeability, μ, is that of the shield, not free space. The Magnetic Shield Corporation's instructions approximate μ with (54):

$$\mu = \frac{(1.571 \times 10^{-6})D}{t} \tag{L.2}$$

where D is the diameter of the shell and t is the thickness of the shield. The maximum desired magnetic flux capacity is 1.375 T. Combining equations and rearranging to find t:

$$t = \frac{(1.571 \times 10^{-6}\ (T \cdot m)/A)DH}{B_{shield}} \tag{L.3}$$

$$= \frac{(1.571 \times 10^{-6}\ (T \cdot m)/A)(231.6\ mm)(38,289\ A/m)}{1.375\ T} \tag{L.4}$$

$$t = 10.13\ mm \tag{L.5}$$

The Magnetic Shield Corporation produces four types of magnetic shielding material (54). One type, *Netic*, is rated to 2.10 T and has the lowest specific gravity (7.86).

An additional check was accomplished to insure the outer most conductor of the cable did not exceed the flux capacity of the designed shield because of its small distance from the shield. A 2 cm aluminum conductor, with a current of 261.5 A, has a 4162 A/m field strength at its surface. A conductor cable made up of 99 individual 2 cm aluminum conductors under the same conditions has a 38,289 A/m field strength on its surface. The contribution from the outermost conductor is less than that of the entire cable and does not saturate the shield.

To achieve the desired shielding capability for the electrodynamic propulsion system, a 10.14 mm thick *Netic* shield was chosen. This shield will be used for all shielding applications on the SFP.

Appendix M. Tracking and Performance

The MATLAB programs generate a wide variety of data that can be used to analyze the SFP's design and performance. The *time history design program* generates data over time for a specific point in the orbit. The data shows the time based stability of the controller. If the outputs versus time are straight, flat lines, the controller was assumed to be stable over time. The *orbit history design program* generates data for a short time slice at multiple points around an orbit. Once a stable design and controller have been designed, the *time history design program* is called recursively — for very short time intervals — using initial conditions and reference command inputs for numerous points around an orbit, so as to simulate the SFP moving through its orbit. This data can be used to show how controller gains would have to be scheduled to correct for the changing B-field as the SFP orbits the Earth.

M.1 Time-History Program Outputs

M.1.1 Numerical Output Data. The following output shows the final SFP design performance data output generated by the program for the specific R-bar maneuver for which the SFP was designed to accomplish:

```
%%%%%%%%%%%%%%%%%%%%%%%%%%%%%%%%%%%%%%%%%%%%%%%%%%%%%%%%%%%%%%%%%%%%%%%%%%%%%%

                      Space Fabrication Platform
                       Design Analysis Program

Payload Mass (kg) = 31300

The diameter of the conductor wire (in cm) = 2
The Metic shield thickness (mm) = 1.0140e+001

Length (LC1) of main conductor tower C1 (m) = 25
Number of turns in conductors C1 =  99
The effective total length (L1) of conductors C1 (m) = 2475

Length (LC2) of main conductor tower C2 (m) = 25
Number of turns in conductor C2 = 99
The effective total length (L2) of conductors C2 (m) = 2475

Length (LC3) of cross conductor tower C3 (m) = 25
Number of turns in conductors C3 = 1
The effective total length of conductors C3 (m) = 25
```

```
Length (LC4) of main conductor tower C4 (m) = 25
Number of turns in conductor C4 = 1
The effective total length (L4) of conductors C4 (m) = 25

Length (LC5) of pole conductor, C5 (m) = 27
Number of turns in conductor C5 = 21
The effective total length of conductor C5 (m) = 567

Radius (r6) of coiled conductor conductor, C6 (m) = 1.9000e+000
Length (Lsol6) of coiled conductor, C6 (m) = 2.8000e-001
Number of turns in conductor coiled conductor C6 = 137

Radius (r7) of coiled conductor conductor, C7 (m) = 1.9000e+000
Length (Lsol7) of coiled conductor, C7 (m) = 2.8000e-001
Number of turns in conductor coiled conductor C7 = 137

Radius (r8) of coiled conductor conductor, C8 (m) = 1.9000e+000
Length (Lsol8) of coiled conductor, C8 (m) = 2.0000e-002
Number of turns in conductor coiled conductor C8 = 1

Radius (r9) of coiled conductor conductor, C9 (m) = 1.9000e+000
Length (Lsol9) of coiled conductor, C9 (m) = 2.0000e-002
Number of turns in conductor coiled conductor C9 = 1

Radius (r10) of coiled conductor conductor, C10 (m) = 1.9000e+000
Length (Lsol10) of coiled conductor, C10 (m) = 1
Number of turns in conductor coiled conductor C10 = 497

Coiled Conductor Support Truss Length (m) = 4.8600e+000
Coiled Conductor Support Truss Width and Height (m) = 4.3000e+000
Coiled Conductor Support Truss Mass (kg) = 1.9440e+002

Total Platform Mass = 1.1061e+005

Principle moment of inertia, A - x direction (kg-m^2) =4.1001e+007
Principle moment of inertia, B - y direction (kg-m^2) =1.3802e+007
Principle moment of inertia, C - z direction (kg-m^2) =2.0756e+007

Altitude of reference orbit (km) = 400
Orbital mean motion (rad/s) =1.1316e-003

True Anomaly (nu) to work with (deg) =  2630
What is the sidereal time ? 169.4830
What is the orbit inclination ? 28.5
What is the right ascension of the ascending node = 0
Enter the reference command data
What is the value of x to attain and track (m) ? -40
What is the value of y to attain and track (m) ? 40
What is the value of z to attain and track (m) ? 40
What is the angle of yaw to attain and track (deg) ? 5
What is the angle of roll to attain and track (deg) ? -5
What is the angle of pitch to attain and track (deg) ? -5

Enter the initial condition data
What is the initial value of x (m) ? -40
What is the initial value of y (m) ? 40
What is the initial value of z (m) ? 40
What is the initial value of the yaw angle (deg) ? 5
What is the initial value of the roll angle (deg) ? -5
What is the initial value of the pitch angle (deg) ? -5

How long of a time response to plot (s) ? 5400
Number of time increments (data points) ? 540

The (Fsys,Gsys) system is completely controllable.
```

```
The (Fsys,Hsys) system is completely observable.
Weighting on the state weighting matrix Q = 1
Weighting on the control weighting matrix R = 1

Maximum current required in conductor C1 (A)= 1.7173e+002
Maximum current required in conductor C2 (A)= 1.7434e+002
Maximum current required in conductor C3 (A)= -1.4076e+000
Maximum current required in conductor C4 (A)= -1.2470e+001
Maximum current required in conductor C5 (A)= 1.5419e+002
Maximum current required in conductor C6 (A)= 5.2323e+001
Maximum current required in conductor C7 (A)= 5.2323e+001
Maximum current required in conductor C8 (A)= -1.6934e-001
Maximum current required in conductor C9 (A)= -1.6934e-001
Maximum current required in conductor C10 (A)= -8.1211e+001
Maximum thrust required in thruster (N)= -2.1490e+001

Maximum radial force in conductor C1 (N)= 8.4348e+000
Maximum oop force in conductor C1 (N)= 1.3486e+001

Maximum radial force in conductor C2 (N)= 8.5628e+000
Maximum oop force in conductor C2 (N)= 1.3691e+001

Maximum radial force in conductor C3 (N)= -1.6808e-004
Maximum ip lateral force in conductor C3 (N)= 1.1166e-003

Maximum radial force in conductor C4 (N)= -1.4890e-003
Maximum ip lateral force in conductor C4 (N)= 9.8916e-003

Maximum ip lateral force in conductor C5 (N)= -1.7349e+000
Maximum oop force in conductor C5 (N)= -4.1758e-001

Distributed radial force in conductor C1 (N)= 3.3739e-001
Distributed oop force in conductor C1 (N)= 5.3945e-001

Distributed radial force in conductor C2 (N)= 3.4251e-001
Distributed oop force in conductor C2 (N)= 5.4764e-001

Distributed radial force in conductor C3 (N)= -6.7233e-006
Distributed ip lateral force in conductor C3 (N)= 4.4663e-005

Distributed radial force in conductor C4 (N)= -5.9561e-005
Distributed ip lateral force in conductor C4 (N)= 3.9566e-004

Distributed ip lateral force in conductor C5 (N)= -6.4257e-002
Distributed oop force in conductor C5 (N)= -1.5466e-002

The maximum C1 torque around b1 (N-m) = 1.6858e+002
The maximum C1 torque around b1 (N-m) = -1.0543e+002

The maximum C2 torque around b1 (N-m) = -1.7114e+002
The maximum C2 torque around b1 (N-m) = 1.0704e+002

The maximum C3 torque around b1 (N-m) = -1.3957e-002
The maximum C3 torque around b1 (N-m) = -2.1010e-003
The maximum C3 torque around b1 (N-m) = -4.6337e-003

The maximum C4 torque around b1 (N-m) = 1.2364e-001
The maximum C4 torque around b1 (N-m) = 1.8613e-002
The maximum C4 torque around b1 (N-m) = -4.1050e-002

The maximum C5 torque around b1 (N-m) = -8.2681e+000
The maximum C5 torque around b1 (N-m) = 3.4352e+001

The maximum C6 torque around b1 (N-m) = 1.6133e+000
The maximum C6 torque around b1 (N-m) = 2.5795e+000
```

```
The maximum C7 torque around b1 (N-m) = 1.6133e+000
The maximum C7 torque around b1 (N-m) = 2.5795e+000

The maximum C8 torque around b1 (N-m) = -9.1731e-006
The maximum C8 torque around b1 (N-m) = 6.0937e-005

The maximum C9 torque around b1 (N-m) = -9.1731e-006
The maximum C9 torque around b1 (N-m) = 6.0937e-005

The maximum C10 torque around b1 (N-m) = 9.0839e+000
The maximum C10 torque around b1 (N-m) = 2.1864e+000

Maximum vertical (x) force required (N) = 1.6996e+001
Maximum horizontal in-plane (y) force required (N) = 1.7239e+000
Maximum horizontal out-of-plane (z) force required (N) = 5.2696e+000

Maximum moment about x required (N-m) = 7.7715e-001
Maximum moment about y required (N-m) = 8.3250e-001
Maximum moment about z required (N-m) = 4.3252e+001

The resistance of conductor C1 (Ohms)= 4.1833e-001
The resistance of conductor C2 (Ohms)= 4.1833e-001
The resistance of conductor C3 (Ohms)= 4.2256e-003
The resistance of conductor C4 (Ohms)= 4.2256e-003
The resistance of conductor C5 (Ohms)= 9.5836e-002
The resistance of conductor C6 (Ohms)= 1.3094e-001
The resistance of conductor C7 (Ohms)= 1.3094e-001
The resistance of conductor C8 (Ohms)= 1.0036e-003
The resistance of conductor C9 (Ohms)= 1.0036e-003
The resistance of conductor C10 (Ohms)= 4.7503e-001

Total Conductor Resistance (Ohms) = 1.6799e+000

The maximum power required (kW) = 7.5190e+001
The maximum voltage required (V) = 2.1189e+002

Max allowed shield inner surface temperature (deg C) = 1021
Max allowed conductor bundle core temperature (deg C) = 438

Conductor C1 shield inner surface and core
   temperatures: T1, T0 (deg C) = 6.7208e+001  1.6479e+002
                 Safety factors = 2.2795e+001  3.9868e+000

Conductor C2 shield inner surface and core
   temperatures: T1, T0 (deg C) = 6.8542e+001  1.6911e+002
                 Safety factors = 2.2351e+001  3.8850e+000

Conductor C3 shield inner surface and core
   temperatures: T1, T0 (deg C) = 1.5001e+001  1.5001e+001
                 Safety factors = 1.0213e+002  4.3798e+001

Conductor C4 shield inner surface and core
   temperatures: T1, T0 (deg C) = 1.5046e+001  1.5051e+001
                 Safety factors = 1.0182e+002  4.3652e+001

Conductor C5 shield inner surface and core
   temperatures: T1, T0 (deg C) = 3.4588e+001  5.1275e+001
                 Safety factors = 4.4293e+001  1.2813e+001

Conductor C6 coiled conductor core temperature: T0 (deg C) = 2.6877e+001
                                                Safety factor = 2.4444e+001

Conductor C7 coiled conductor core temperature: T0 (deg C) = 2.6877e+001
                                                Safety factor = 2.4444e+001
```

```
Conductor C8 coiled conductor core temperature: T0 (deg C) = 1.5000e+001
                                             Safety factor = 4.3800e+001

Conductor C9 coiled conductor core temperature: T0 (deg C) = 1.5000e+001
                                             Safety factor = 4.3800e+001

Conductor C10 coiled conductor core temperature: T0 (deg C) = 4.2528e+001
                                              Safety factor = 1.5448e+001

%%%%%%%%%%%%%%%%%%%%%%%%%%%%%%%%%%%%%%%%%%%%%%%%%%%%%%%%%%%%%%%%%%%%%%%%%%%%%%%%%%%
```

M.1.2 Graphical Output Data. This section shows the data plotted by the *time-history design program* for the SFP final design configuration. The following plots correspond to the data listed in the previous section. The flat lines on the plots show the controller is stable. The flat lines on the position plots show that the controller can precisely track the reference position.

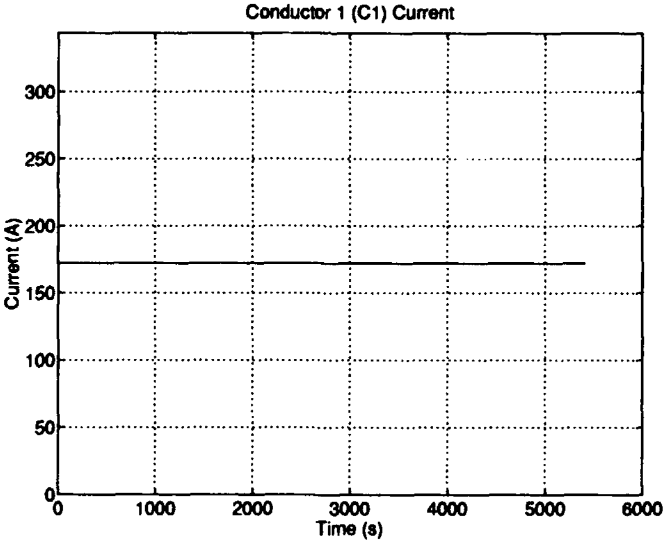

Figure M.1 Time history of current $C1$.

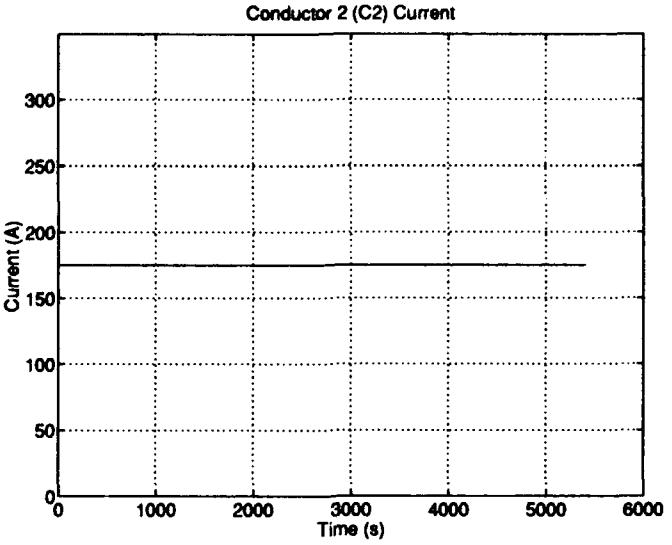

Figure M.2 Time history of current $C2$.

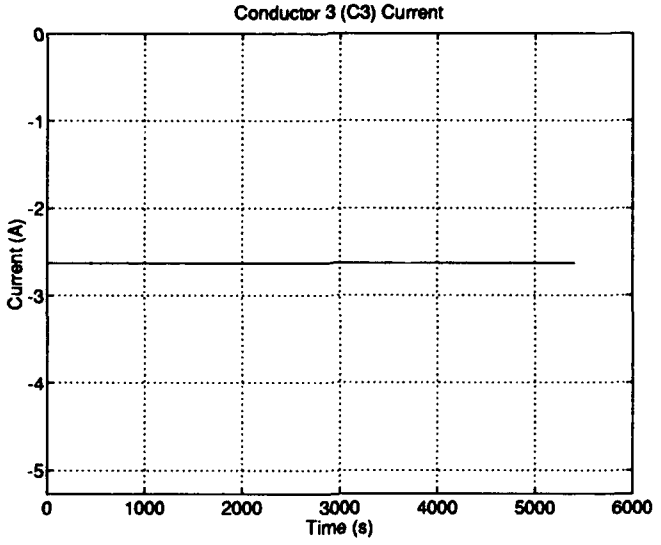

Figure M.3 Time history of current $C3$.

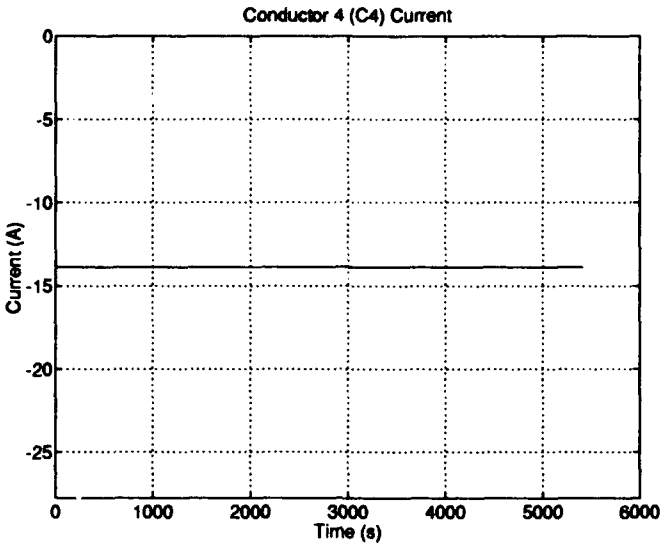

Figure M.4 Time history of current $C4$.

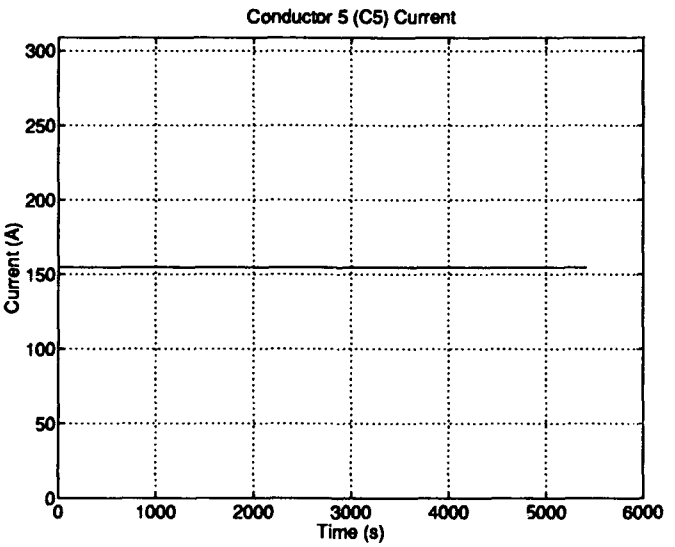

Figure M.5 Time history of current $C5$.

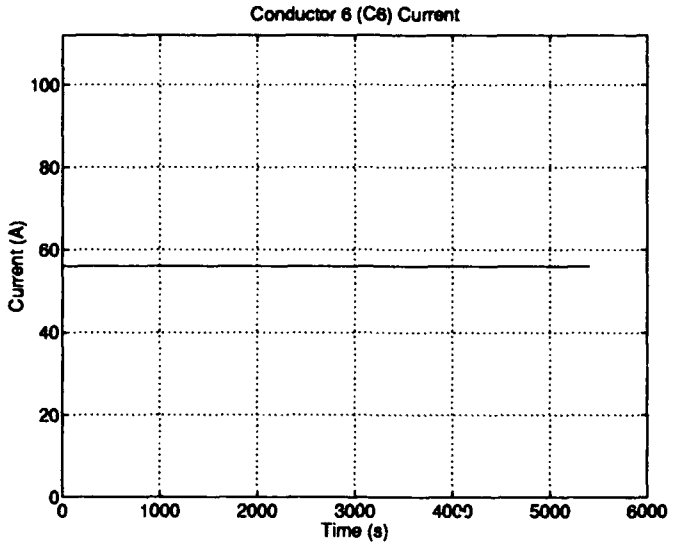

Figure M.6 Time history of current $C6$.

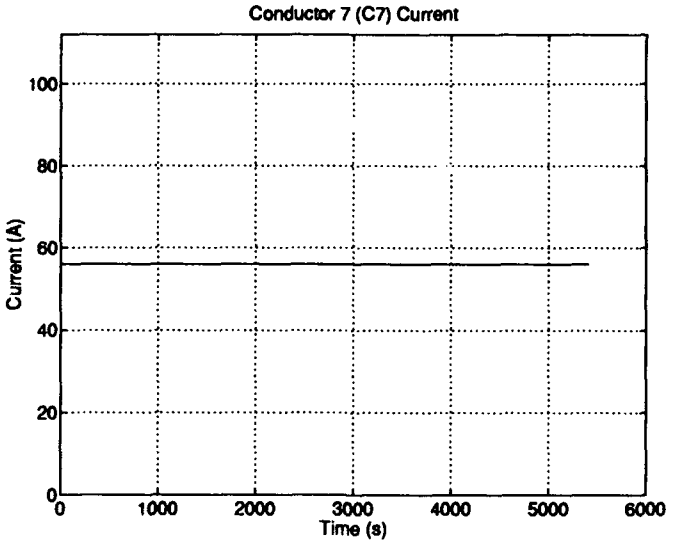

Figure M.7 Time history of current $C7$.

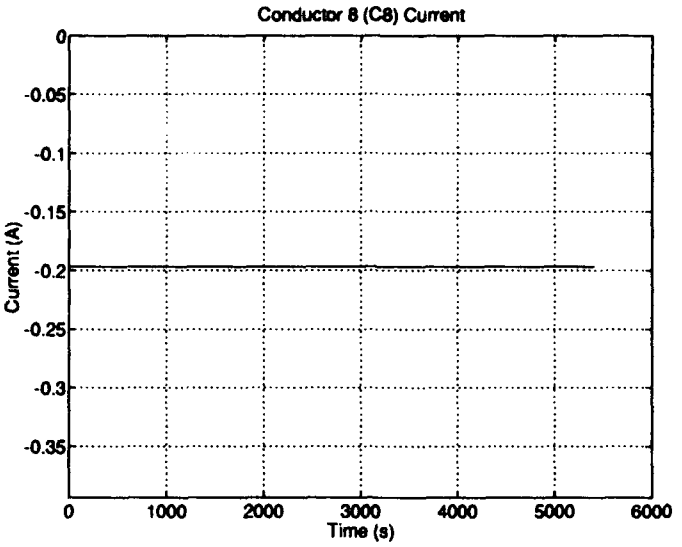

Figure M.8 Time history of current $C8$.

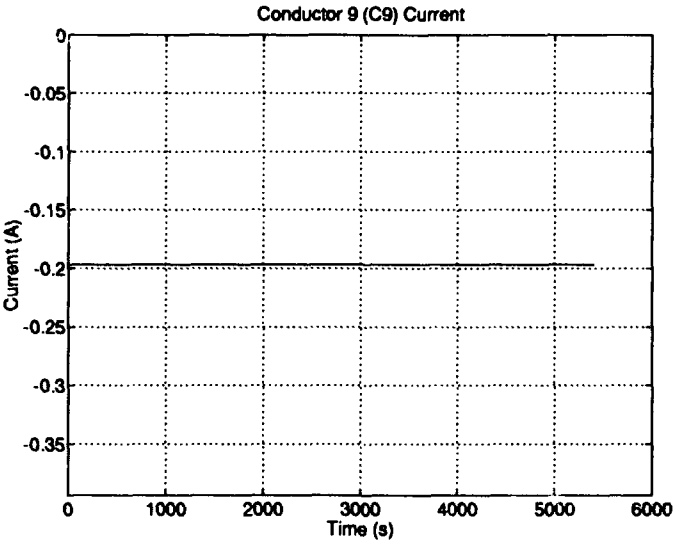

Figure M.9 Time history of current $C9$.

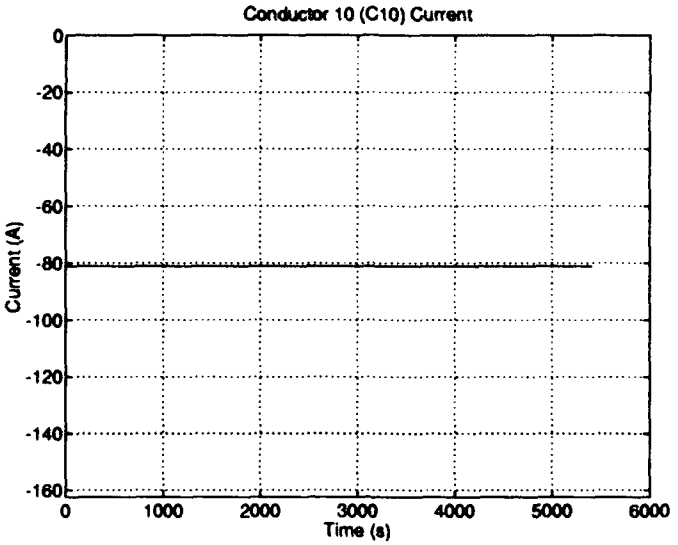

Figure M.10 Time history of current $C10$.

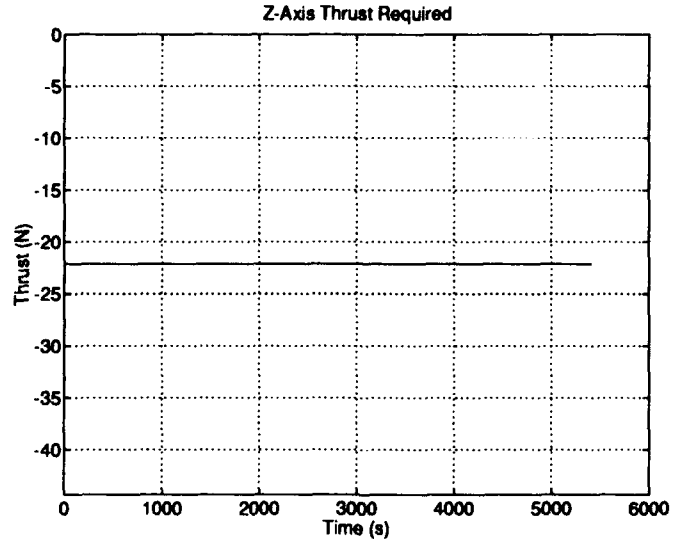

Figure M.11 Time history of the z-axis thrust required.

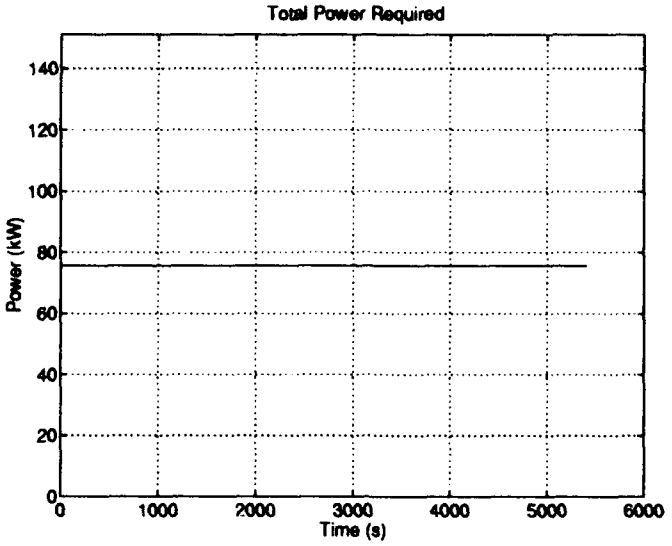

Figure M.12 Ti.ne history of the total power required.

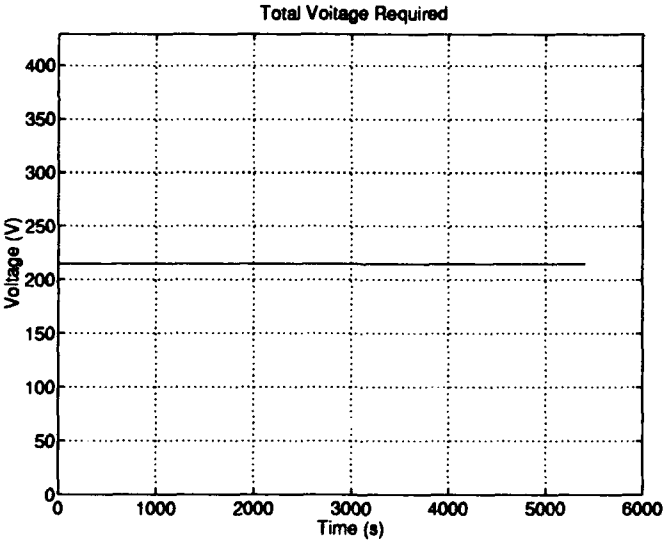

Figure M.13 Time history of the total voltage required.

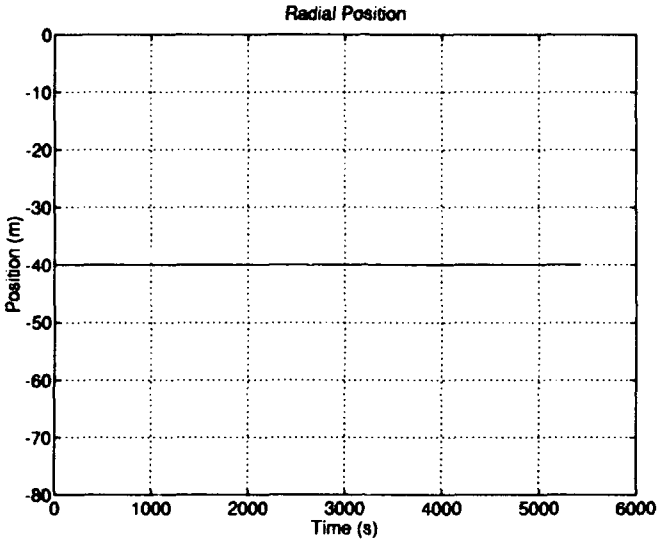

Figure M.14 Time history of the tracking of the desired radial position.

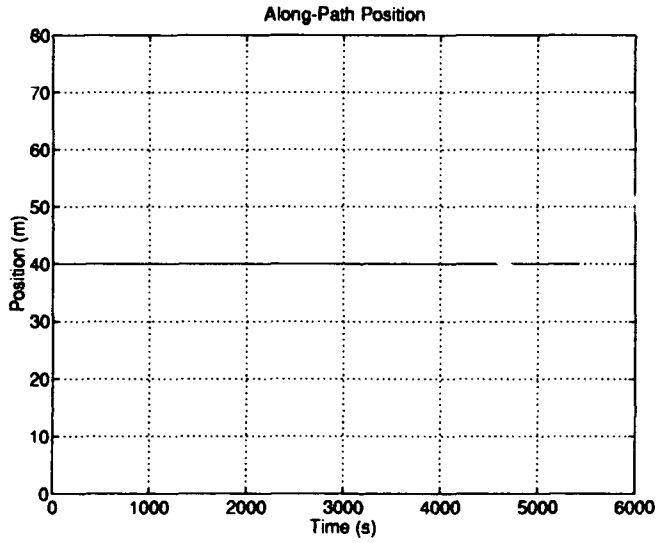

Figure M.15 Time history of the tracking of the desired in-path position.

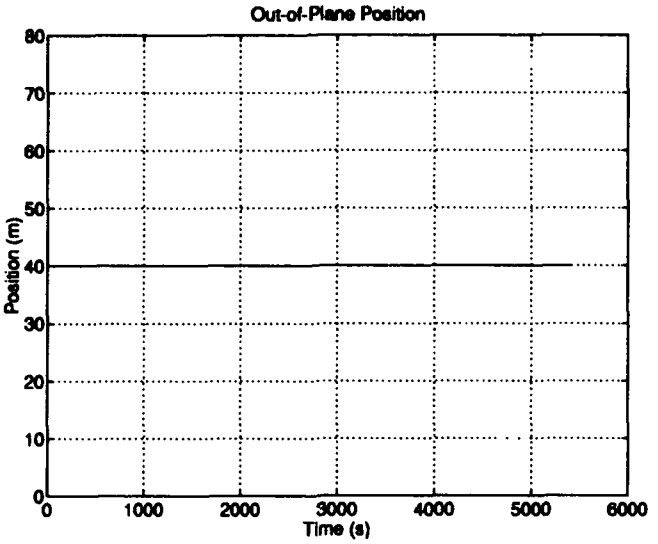

Figure M.16 Time history of the tracking of the desired out-of-plane position.

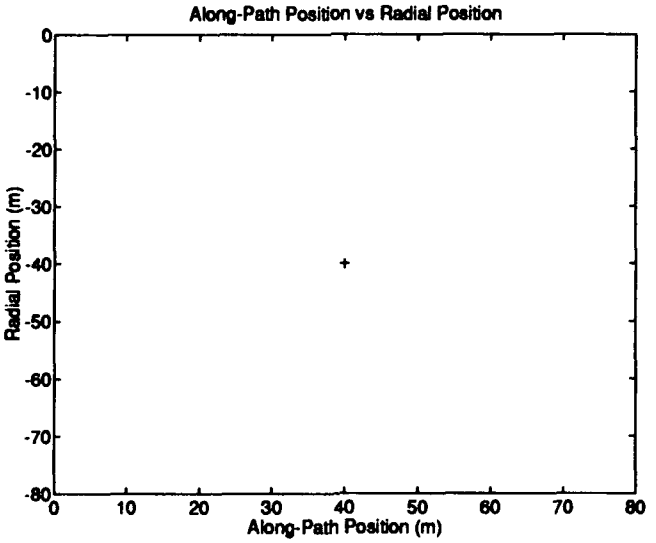

Figure M.17 Time history of the tracking of the desired radial position versus the path position.

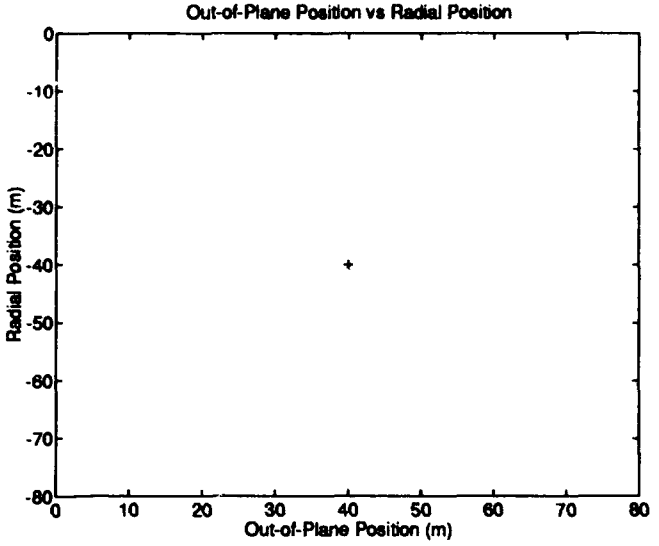

Figure M.18 Time history of the tracking of the desired radial position versus the out-of-plane position.

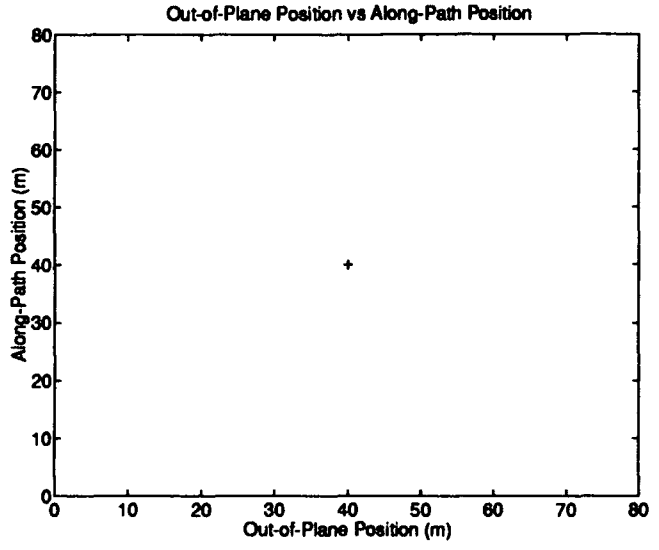

Figure M.19 Time history of the tracking of the desired path position versus the out-of-plane position.

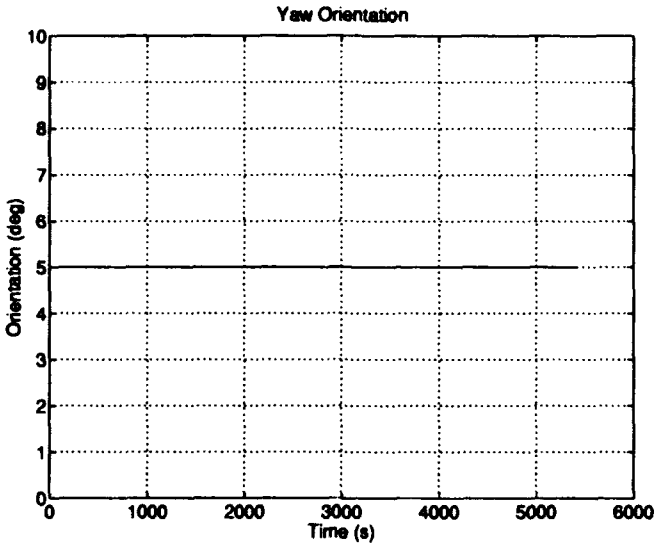

Figure M.20 Time history of the tracking of the desired yaw orientation.

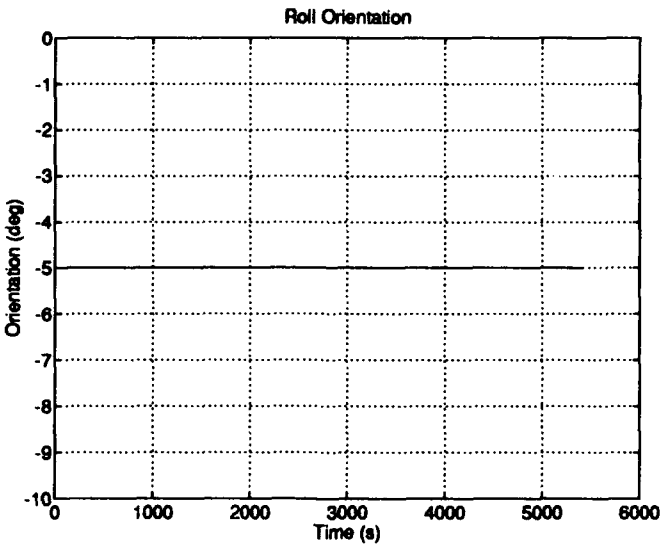

Figure M.21 Time history of the tracking of the desired roll orientation.

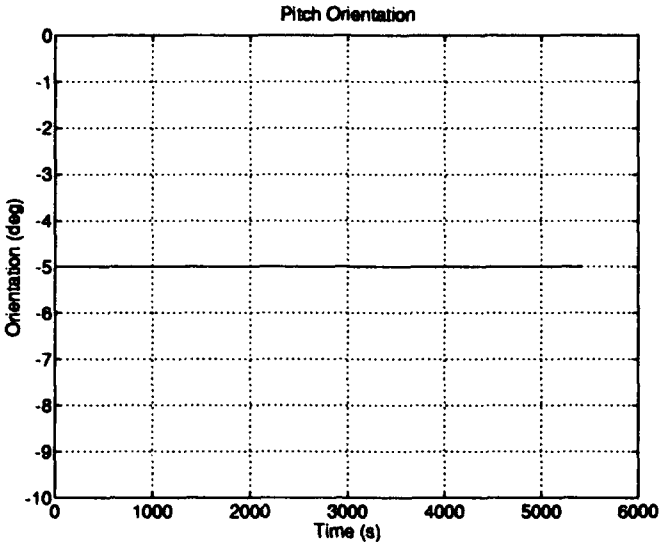

Figure M.22 Time history of the tracking of the desired pitch orientation.

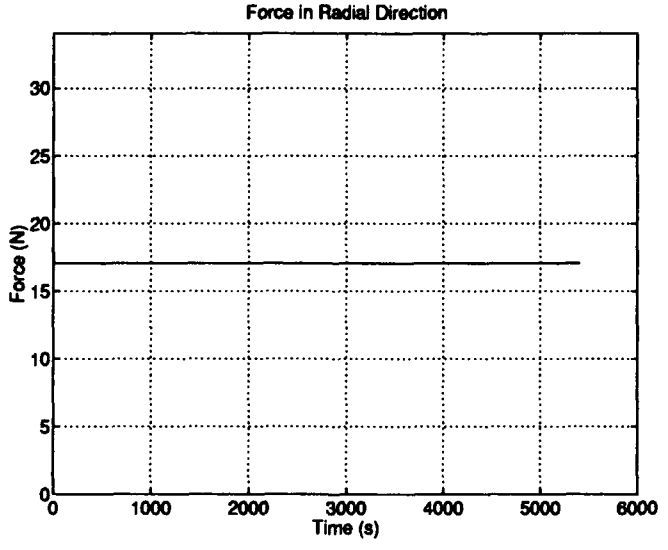

Figure M.23 Time history of the radial force required to track the desired position.

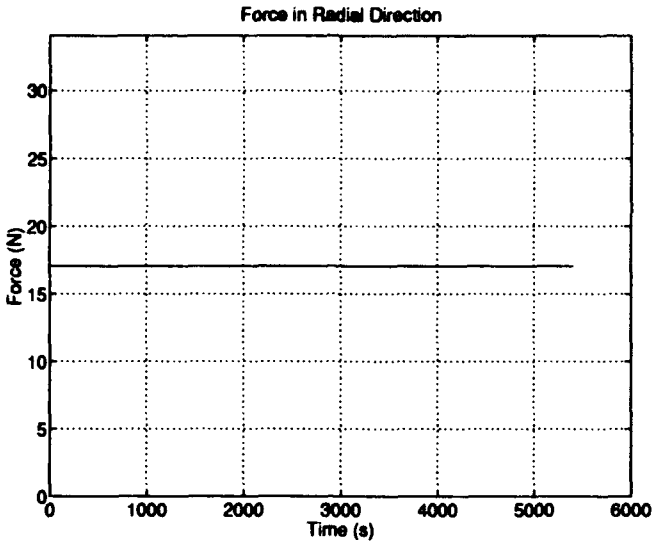

Figure M.24 Time history of the in-path force required to track the desired position.

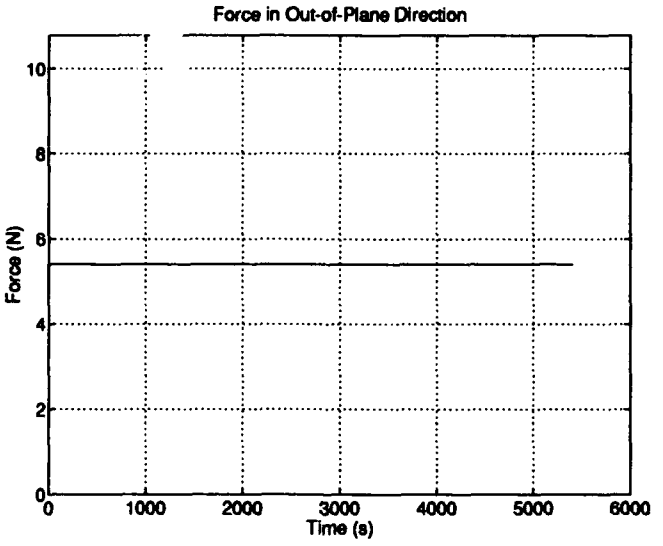

Figure M.25 Time history of the out-of-plane force required to track the desired position.

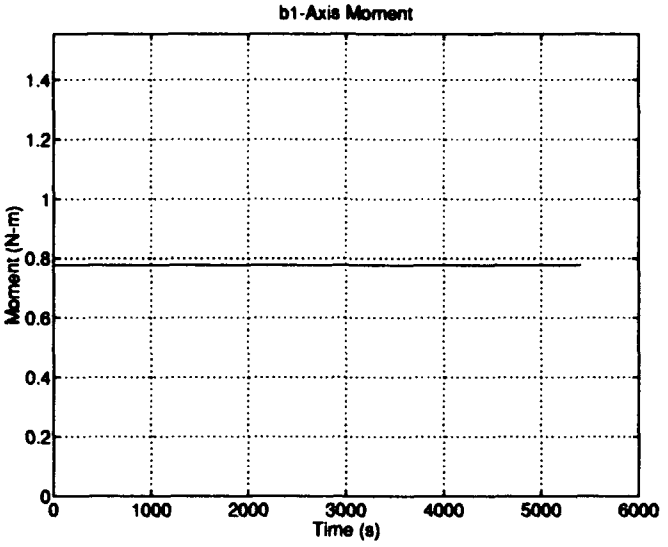

Figure M.26 Time history of the moment about $\hat{b}_1$-axis required to track the desired orientation.

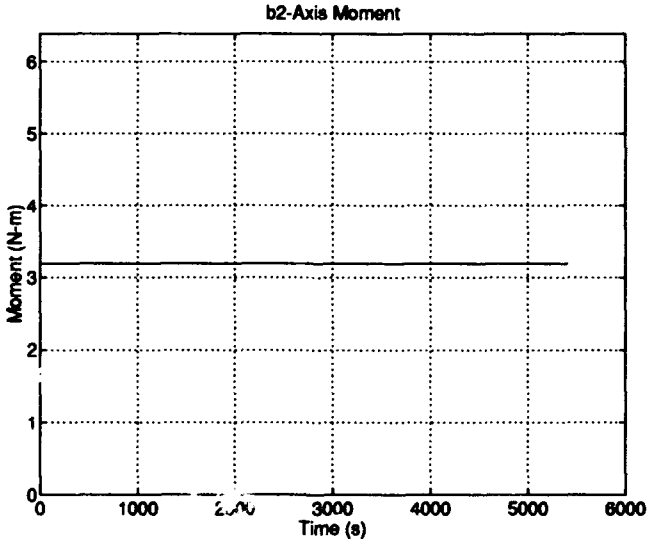

Figure M.27 Time history of the moment about $\hat{b}_2$-axis required to track the desired orientation.

Figure M.28 Time history of the moment about $\hat{b}_3$-axis required to track the desired orientation.

M.2 Orbit-History Program Outputs

M.2.1 Multiple Orbit - Design R-Bar Standoff. The following plots show the total power required, the currents in each of the conductors, the thrust required from the augmentation thrusters, and the core temperatures of the conductors using high current. The data for conductors $C8$ and $C9$ is not included — these conductors are almost completely unused by the controller, and their currents are nearly zero. The plots emulate the gain scheduling required over the period of one revolution of the earth:

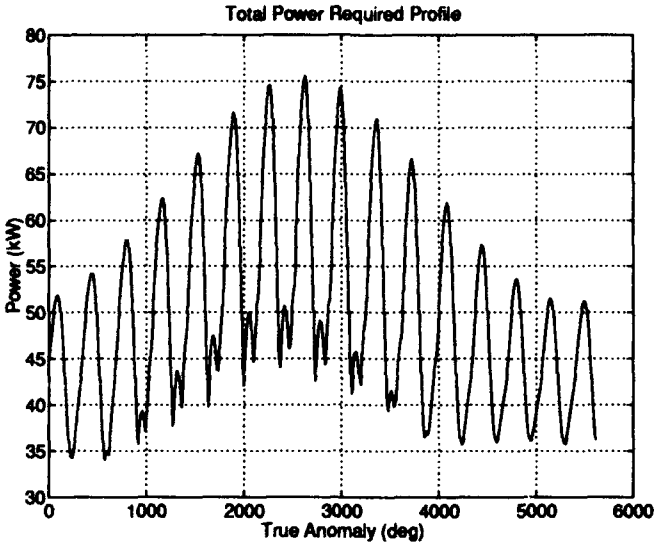

Figure M.29 Orbit history of power required.

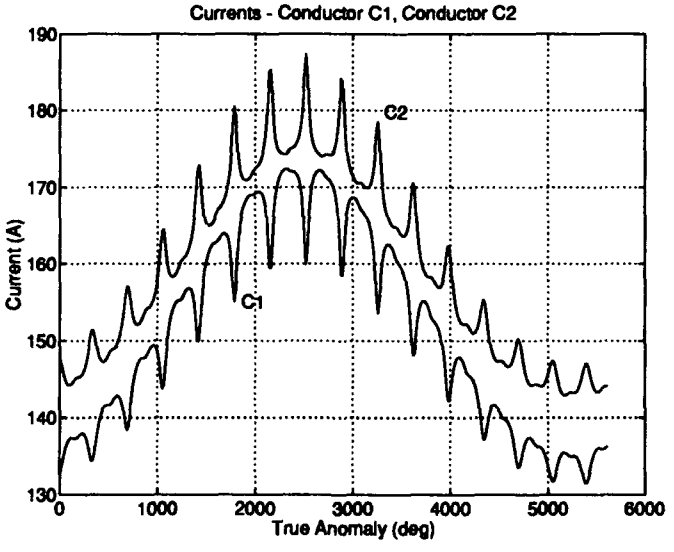

Figure M.30 Orbit history of $C1$ and $C2$ currents required.

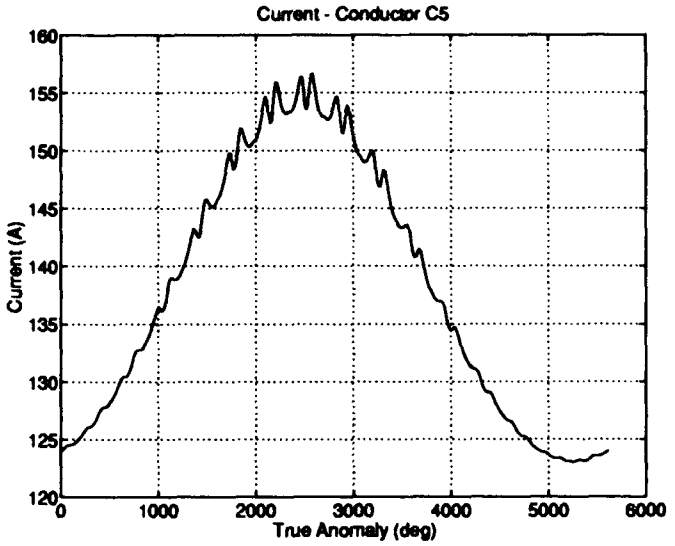

Figure M.31 Orbit history of $C5$ current required.

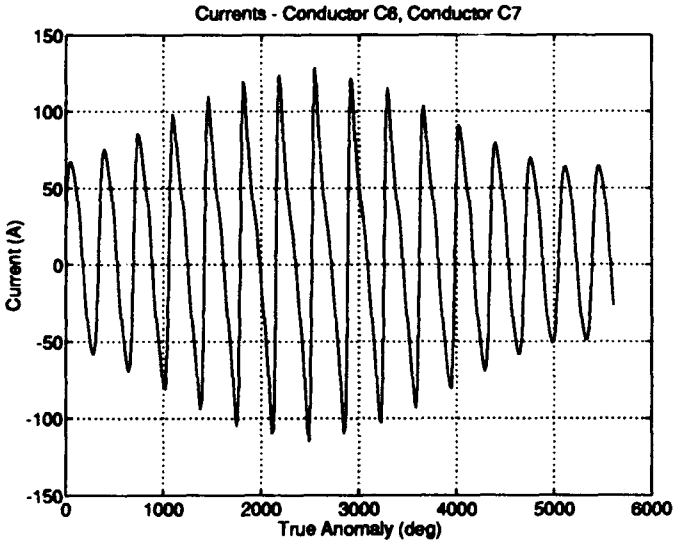

Figure M.32 Orbit history of $C6$ and $C7$ currents required.

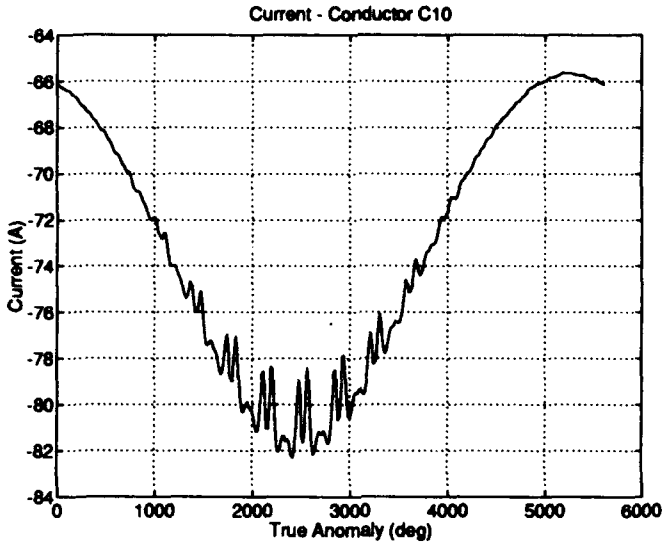

Figure M.33 Orbit history of $C10$ current required.

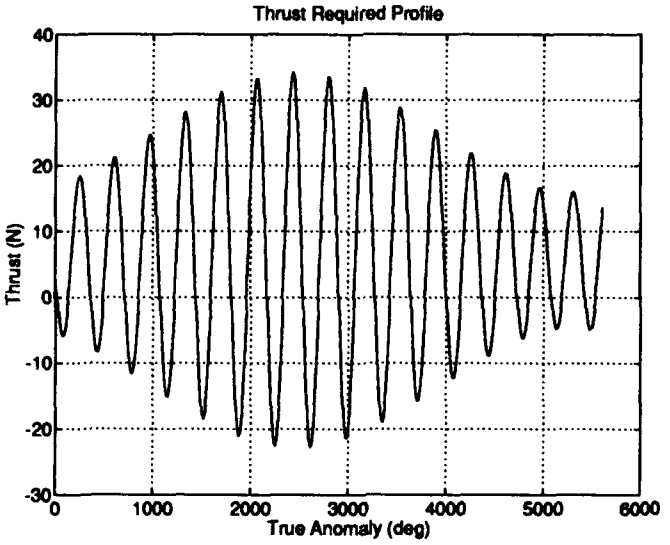

Figure M.34 Orbit history of thrust required from the augmentation thrusters.

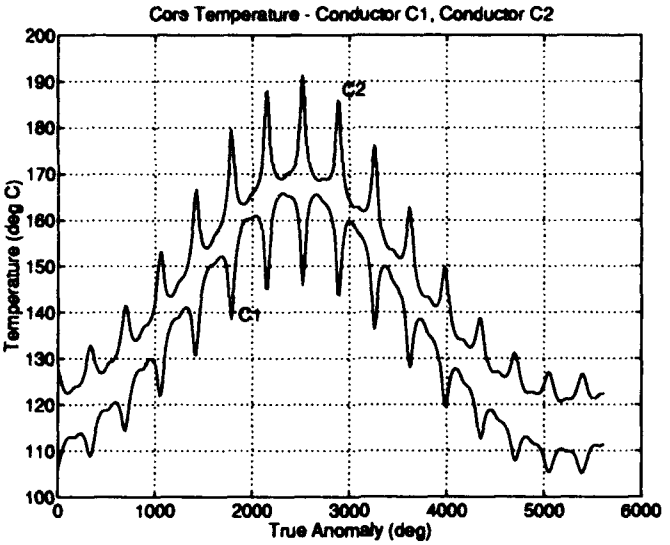

Figure M.35 Orbit history of $C1$ and $C2$ core temperatures .

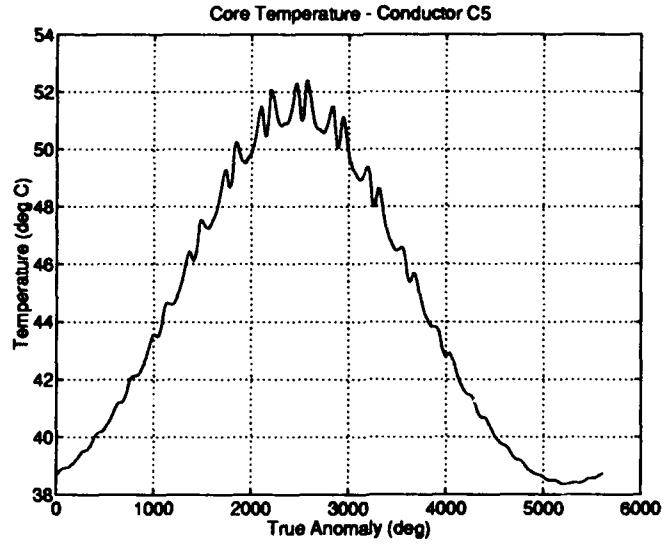

Figure M.36 Orbit history of $C5$ core temperature.

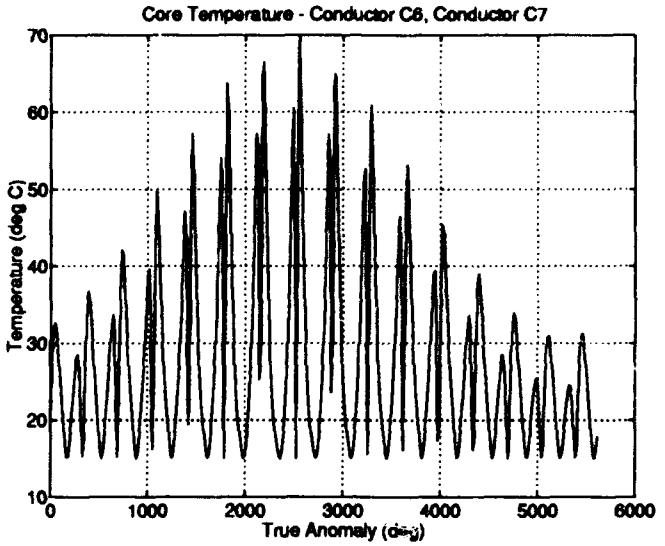

Figure M.37 Orbit history of $C6$ and $C7$ core temperatures.

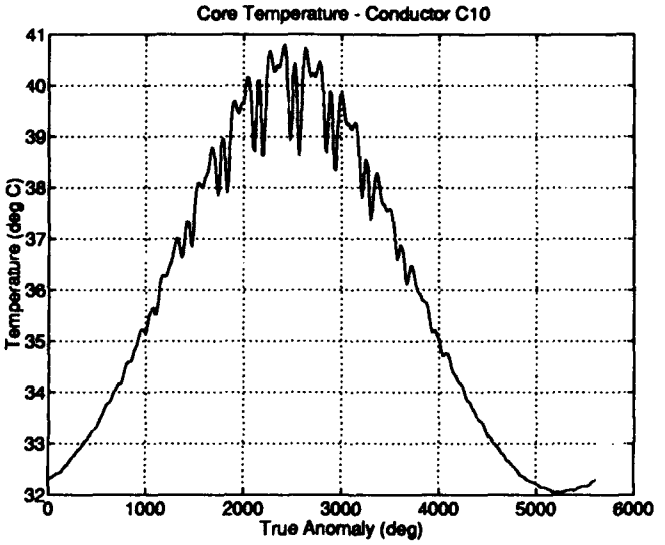

Figure M.38 Orbit history of conductor $C10$ core temperature.

M.2.2 Single Orbit - Design R-Bar Standoff. By changing the range over which the true anomaly changes, the plots can be refined to a narrow window. These types of plots were used extensively when the final design was being evaluated since they quickly show when power, current, and/or temperature constraints are exceeded. The following plots show the gain scheduling required for one orbit:

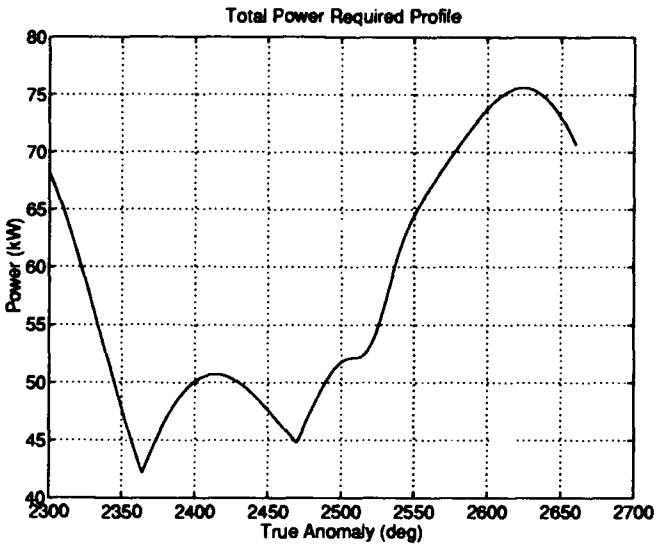

Figure M.39 Orbit history of total power required.

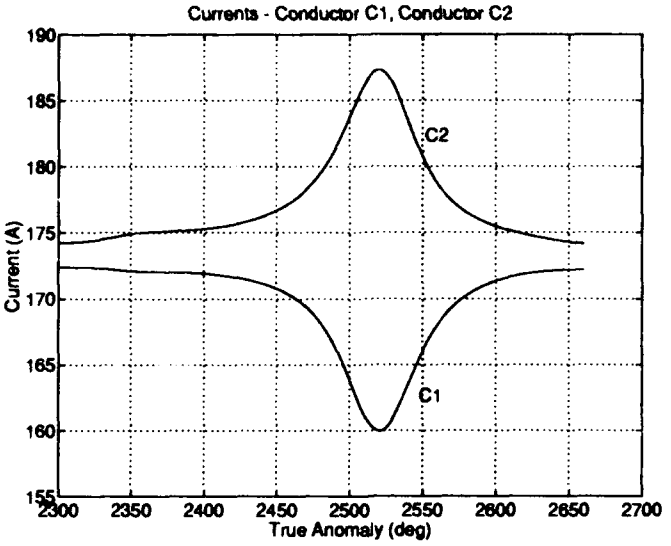

Figure M.40 Orbit history of $C1$ and $C2$ currents.

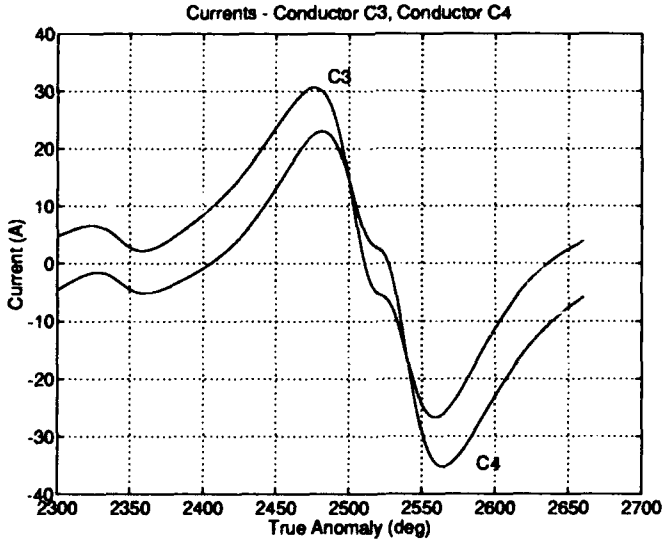

Figure M.41 Orbit history of $C3$ and $C4$ currents.

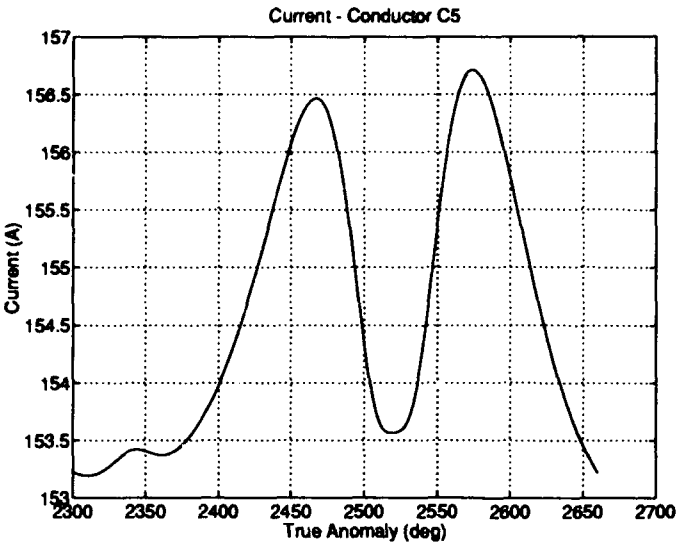

Figure M.42 Orbit history of conductor $C5$ current.

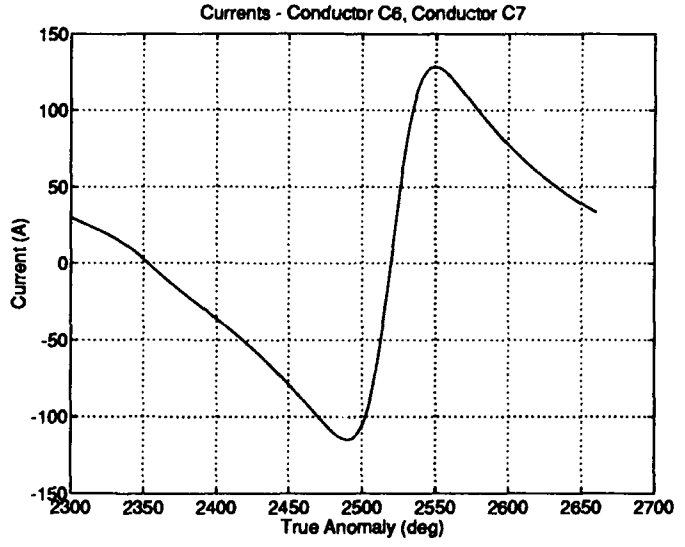

Figure M.43 Orbit history of $C6$ and $C7$ currents.

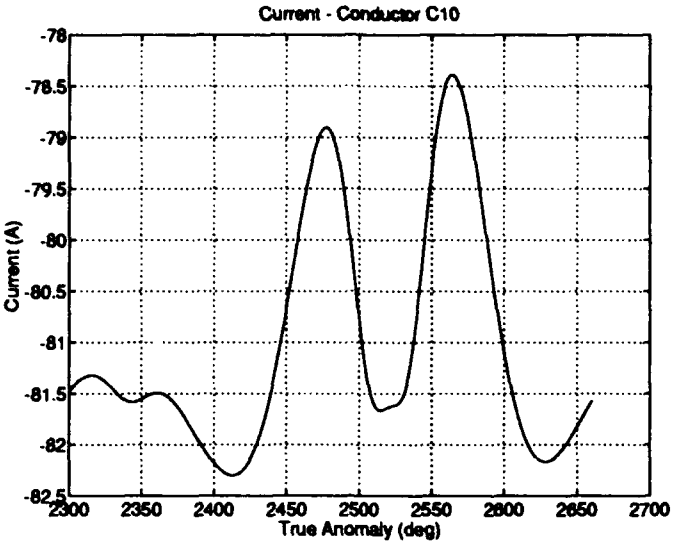

Figure M.44 Orbit history of $C10$ current.

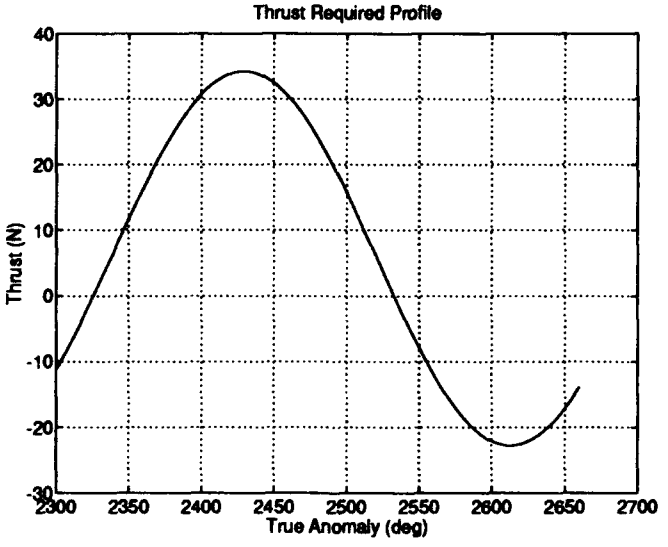

Figure M.45 Orbit history of the thrust required from the augmentation thrusters.

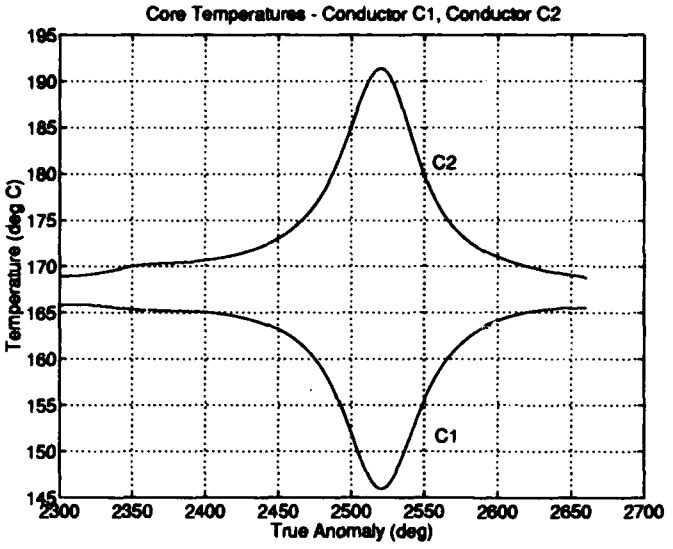

Figure M.46 Orbit history of $C1$ and $C2$ core temperatures.

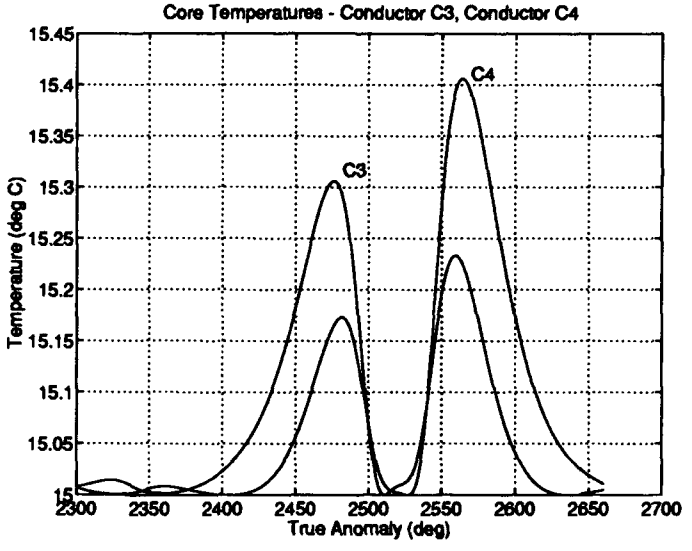

Figure M.47 Orbit history of $C3$ and $C4$ core temperatures.

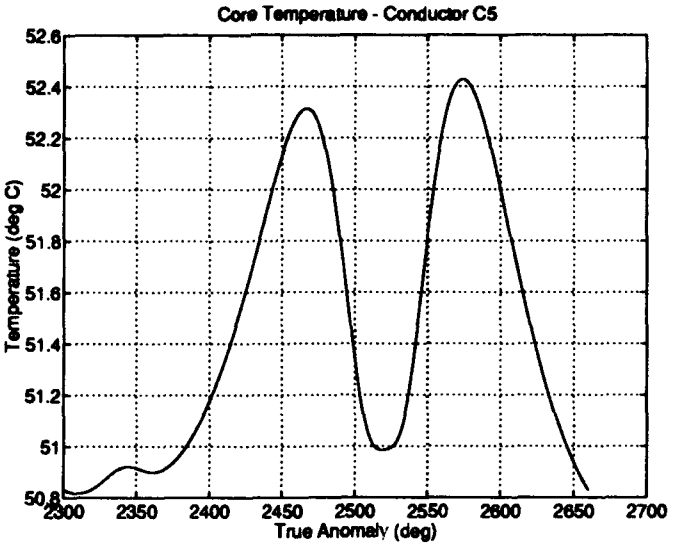

Figure M.48 Orbit history of conductor $C5$ core temperature.

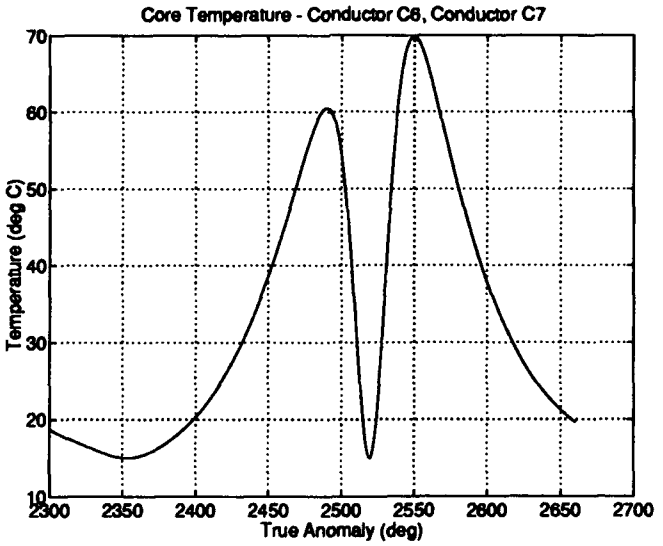

Figure M.49 Orbit history of $C6$ and $C7$ core temperatures.

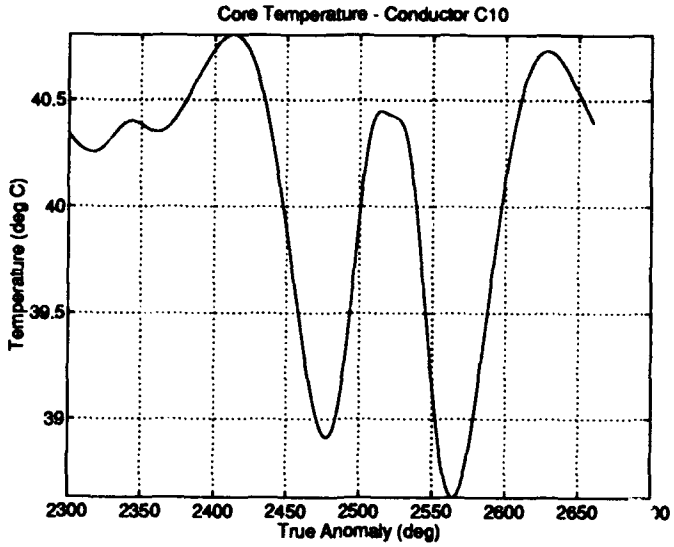

Figure M.50 Orbit history of $C10$ core temperature.

M.2.3 Single Orbit - Maximum R-Bar Standoff. The following plots show the single orbit requirements for the maximum capability R-bar standoff. The interval chosen includes the peak power requirement, the peak current requirement, and maximum temperature reached during propulsion system operations. The interval is one orbit of the SFP:

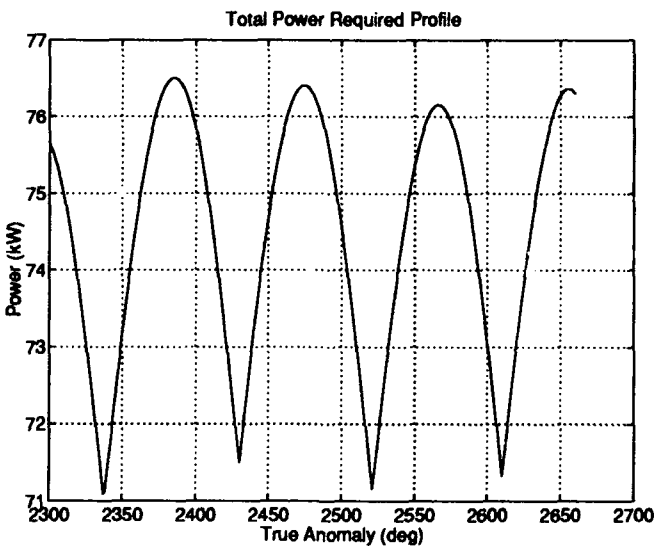

Figure M.51 Orbit history of total power required.

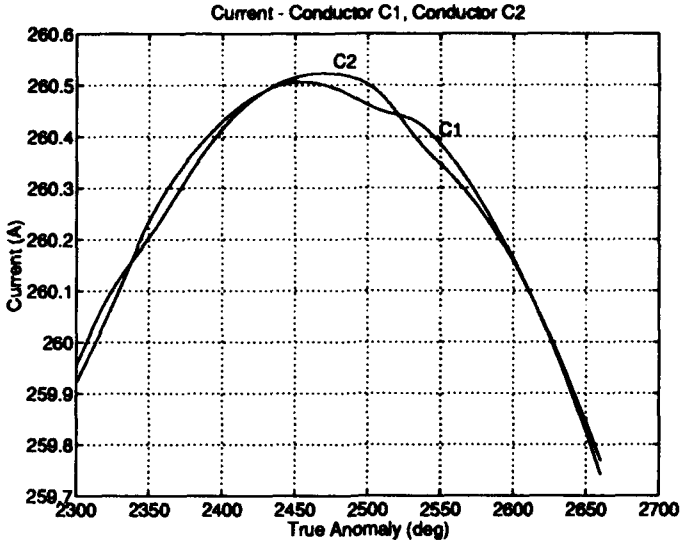

Figure M.52 Orbit history of $C1$ and $C2$ currents.

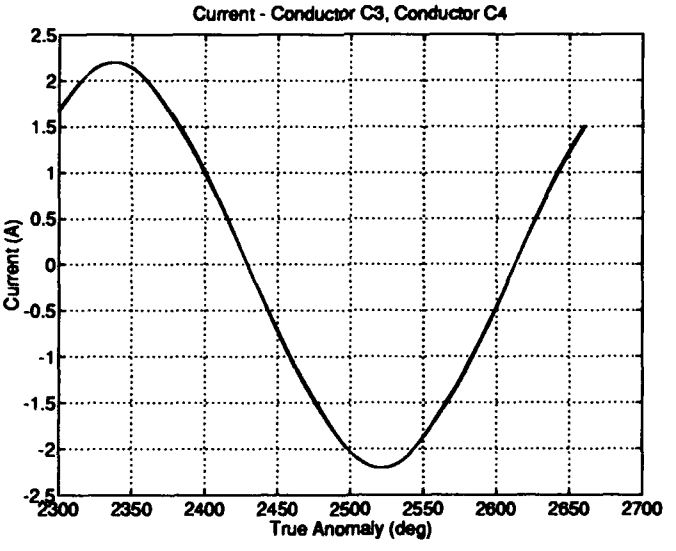

Figure M.53 Orbit history of $C3$ and $C4$ currents.

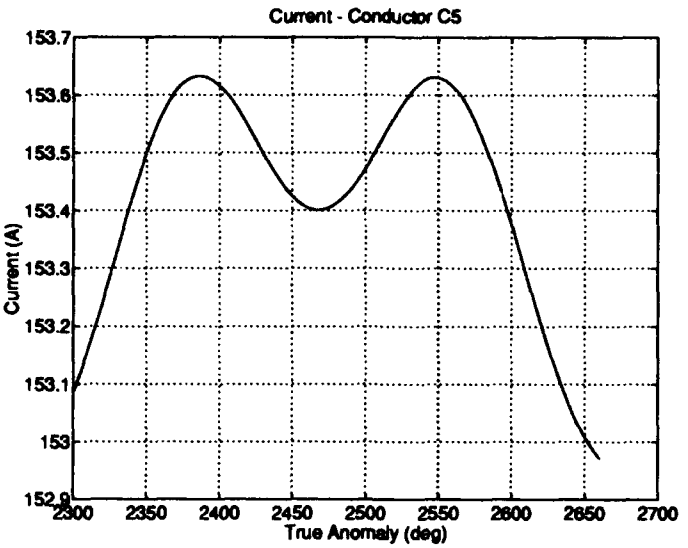

Figure M.54 Orbit history of conductor $C5$ current.

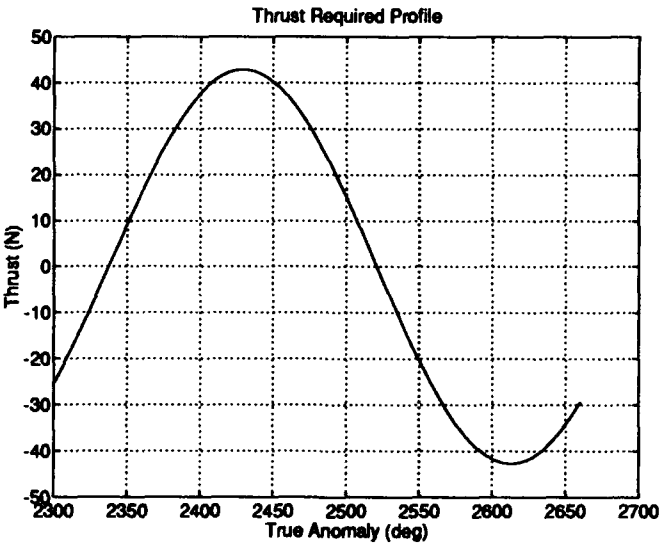

Figure M.55 Orbit history of the thrust required from the augmentation thrusters.

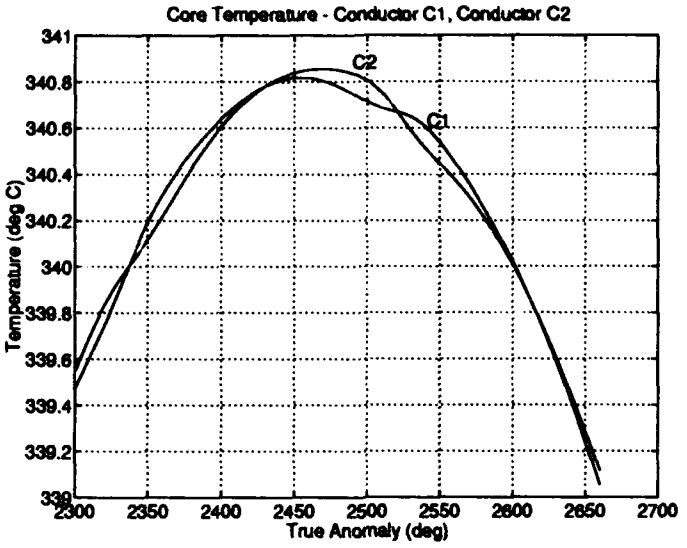

Figure M.56 Orbit history of $C1$ and $C2$ core temperatures.

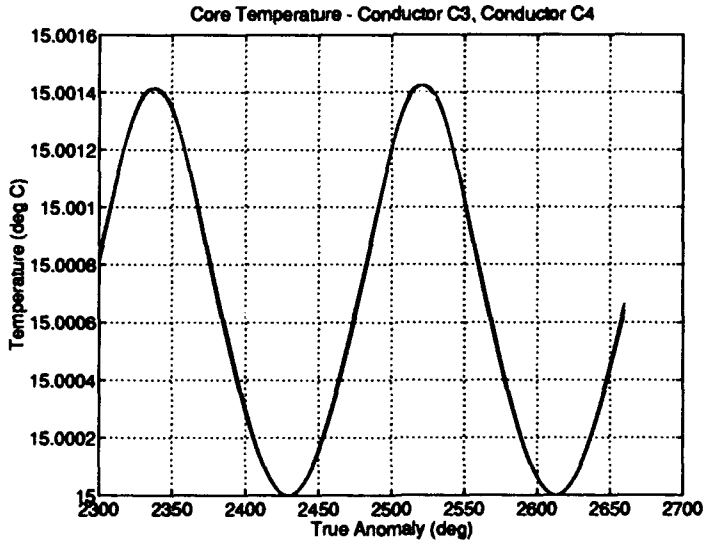

Figure M.57 Orbit history of $C3$ and $C4$ core temperatures.

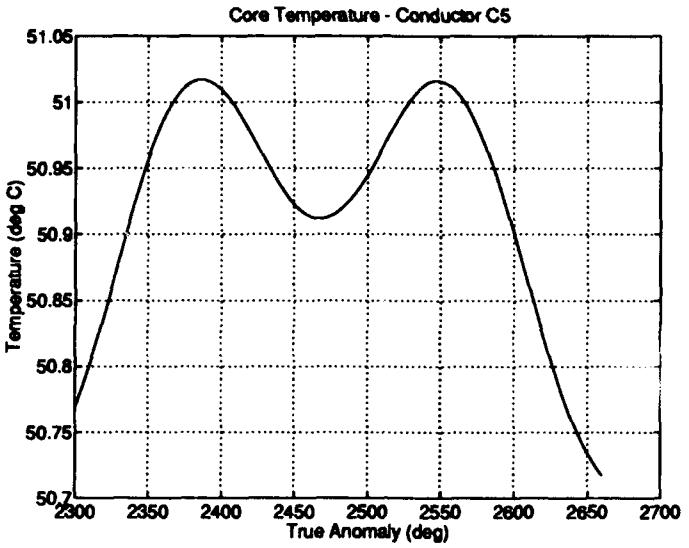

Figure M.58 Orbit history of conductor $C5$ core temperature.

Appendix N. Comparison of Conductor Orientations with the B Field

N.1 Introduction

In Section 6.3.10 two methods of orbit transfer were defined: Method 1, track a fixed average B-field magnitude and direction with the SFP conductors, and Method 2, track a time-varying B-field with the SFP conductors. Method 2 was concluded to be most efficient. This appendix justifies the conclusion.

N.2 Comparison of Method 1 and Method 2

To compare the two methods, both were implemented with the starting conditions:

$$\begin{aligned} r &= 300\ km \\ i &= 28.5^\circ \\ Power\ (P) &= 77\ kW \\ \Delta t &= 2\ hours \end{aligned}$$

The results were then compared. The total acceleration profiles due to $\overline{F_p}$ are similar, but Method 2 has a higher minimum and maximum acceleration (see Figure N.1).

A comparison of the component accelerations in the velocity vector direction shows that over a 2 *hour* interval, Method 2 provides more acceleration than Method 1 (see Figure N.2). Figure N.2 also graphically shows the difference between assuming a constant orientation versus changing the orientation to track the B-field. During the oscillations of the B-field, the vehicle's orientation resulting from the application of Method 2 transitions through the vehicle's orientation resulting from the application of Method 1 using the constant B-field assumption. At these points, the two methods produce the same thrust. The long term increase in Method 1's useful

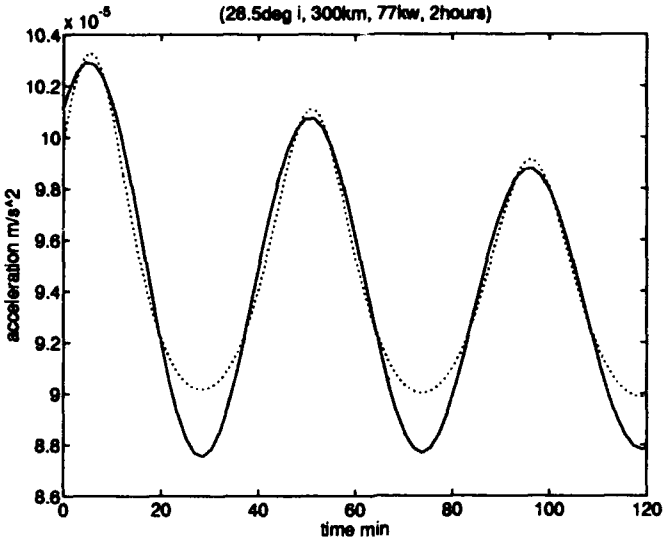

Figure N.1 Acceleration versus time for Method 1 (—) and Method 2 (· · ·). Method 2 has a higher minimum and maximum acceleration.

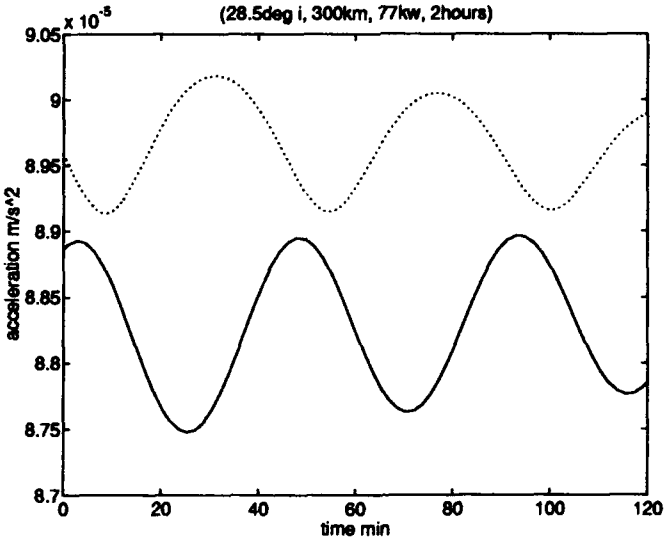

Figure N.2 Method 1 (—) provides less acceleration along the velocity vector than does Method 2 (· · ·).

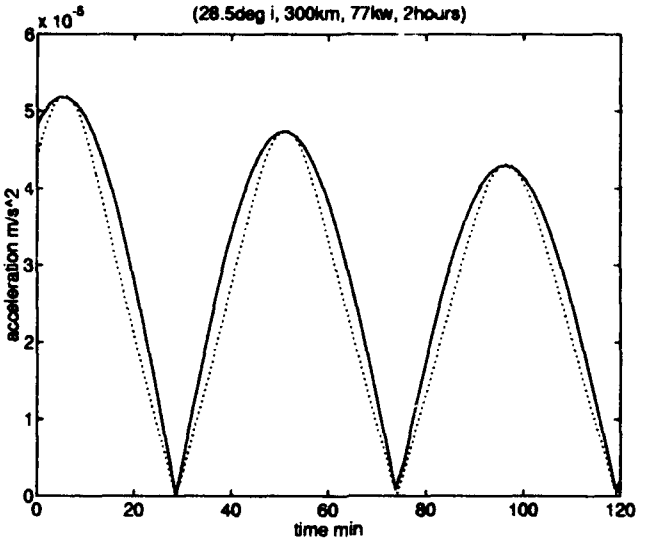

Figure N.3 Method 2 ($\cdots$) provides less useless acceleration in the out-of-plane direction than does Method 1 (—).

acceleration during this period results from Earth's rotation changing the B-field's orientation. The out-of-plane acceleration profiles are almost identical. However, the peaks under Method 1 are broader, indicating more time is spent thrusting out-of-plane. This out-of-plane is wasted acceleration (see Figure N.3). A comparison of the percentage of the total acceleration contributing to an acceleration along the velocity vector indicates Method 2 is slightly more efficient. This is characterized by the broader peaks in Figure N.4.

Because the forces generated by the propulsion system are small, and the vehicle's mass is large, the actual performance differences between Method 1 and Method 2 is small. After 2 *hours*, the increase in orbital radius of the SFP using Method 2 is only slightly greater than when using Method 1 (see Figure N.5). The major difference in the two methods is the induced changes in inclination and line of nodes. Method 1 causes larger changes in both inclination and the line of nodes (see Figures N.6 and N.7). Using Method 2 will require less effort to counter the undesired out-of-plane accelerations.

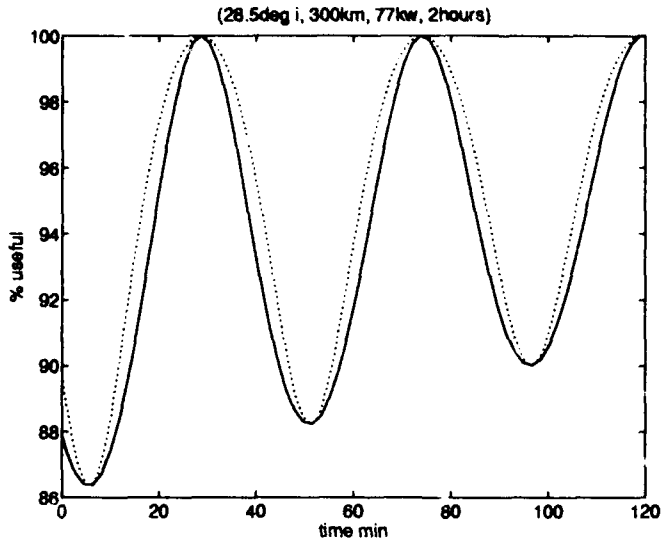

Figure N.4 Method 2 ($\cdots$) has a higher percentage of the total acceleration contributing to increasing velocity along the velocity vector than Method 1 (—).

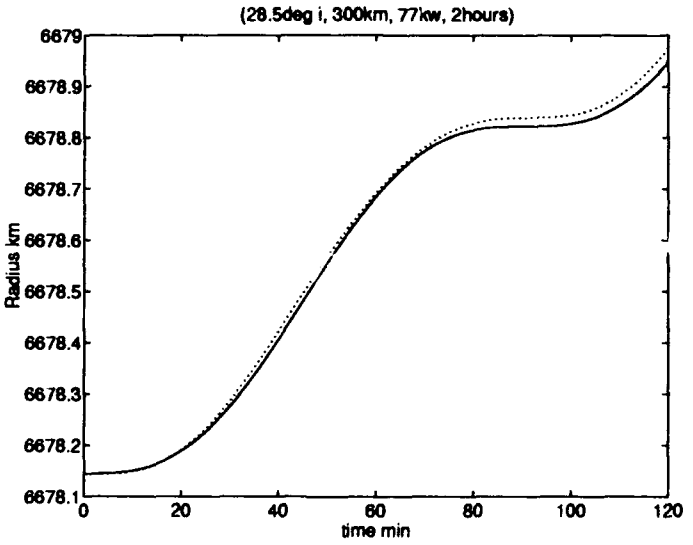

Figure N.5 Method 1 (—) increases the SFP's altitude by 0.77 *km* in 2 *hours* while Method 2 ($\cdots$) increases the altitude by 0.82 *km* in the same time.

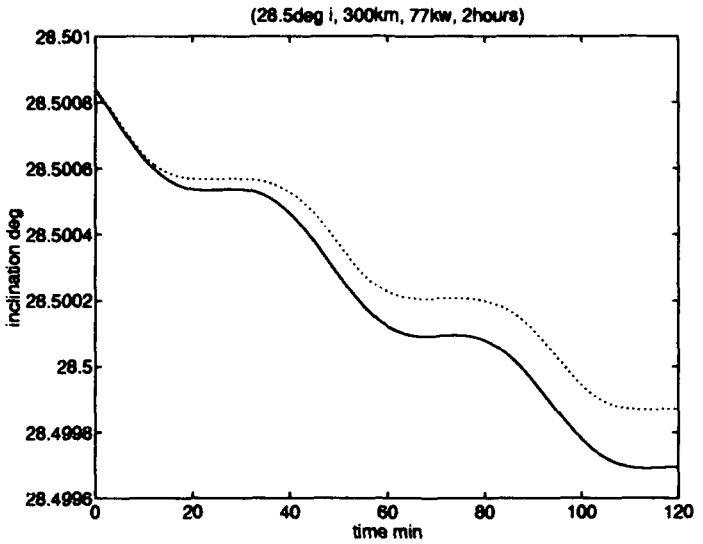

Figure N.6 Method 1 (—) decreases the inclination by 0.00114° in 2 *hours* while the decrease by Method 2 (···) is 0.00097°.

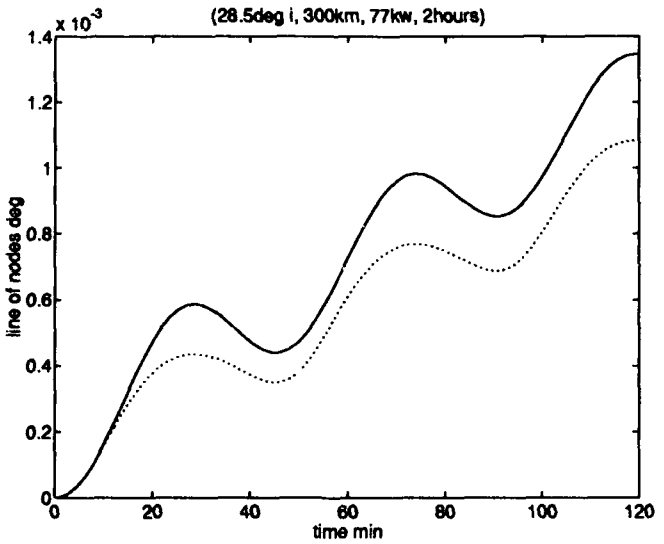

Figure N.7 Method 1 (—) increases Ω by 1.35×10^{-3}° in 2 *hours*; Method 2 (···) causes an increase of only 1.18×10^{-3}°.

These same trends exist for longer time periods. Applying 77 kW for 2 *days* shows the same general trends, although changes in the line of nodes are cyclic over the course of a day. Based on the results of the comparison, reorienting the SFP to account for the time-variations in the B-field will provide the best performance during an orbit transfer.

N.2.1 Current and Power. It is apparent from the equation:

$$\overline{F_p} = i\overline{L} \times \overline{B} \tag{N.1}$$

the current should be maximized to maximize the propulsive force. However, the power available to generate the current is limited. The power required is given by the equation:

$$P = i\left(\left(\overline{v} \times \overline{B}\right) \cdot \overline{L}\right) + i^2 R \tag{N.2}$$

where $\overline{v}$ is the relative velocity of the SFP with respect to the B-field and R is the resistance of the conductor. The first term on the right hand side is the induced voltage due to the movement of a current carrying conductor through a magnetic field. Method 2 will nearly maximize the power required for a given current because of the induced voltage.

To gain an insight on power requirements for the orbital transfer, the current was fixed at $i = 50\ A$ while the orbital parameters were the same as those previously defined. The amount of power required to produce a constant current was highly variable during a 2 *day* run. The best way to use the SFP's power resources is to maintain a constant level of applied power, at the maximum level available, and vary the current so the power required does not exceed the power available.

The maximum power available for propulsion is 77 kW. The current must be modulated so that it is maximized without the power required exceeding 77 kW. Equation N.2 is a quadratic with respect to the current. The current can be solved

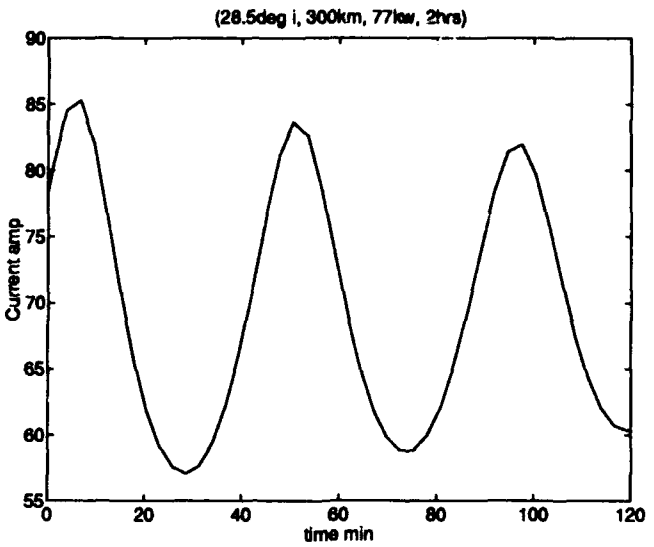

Figure N.8 The regulated current varies greatly due to the changing B-field.

for by finding the roots of the quadratic. However, the computational efficiency of the numerical integration routines can be improved by using the following approximation for the regulated current, i_R:

$$i_R = \frac{P_{max}}{\left(\left(\overline{v} \times \overline{B}\right) \cdot \overline{L}\right) + i_{lmax} R} \tag{N.3}$$

with i_{lmax} an estimate of the maximum current. Figure N.8 shows the resulting current profile for a 2 day integration. Figure N.9 demonstrates that power was near, but below, the 77 kW limit. The variation in the power level is a result of approximating i_R. Using the full quadratic solution for i_R makes the power used constant. However, the difference in the two solution methods is small (see Figure N.10). Approximating i_R results in slightly shorter time-to-climb data, but showed better computational efficiency.

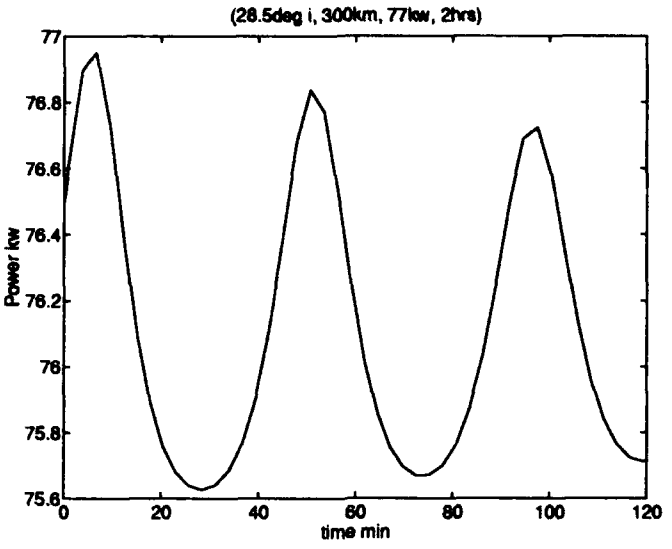

Figure N.9 The power applied to the electrodynamic propulsion system during orbit transfer is kept below 77 kW.

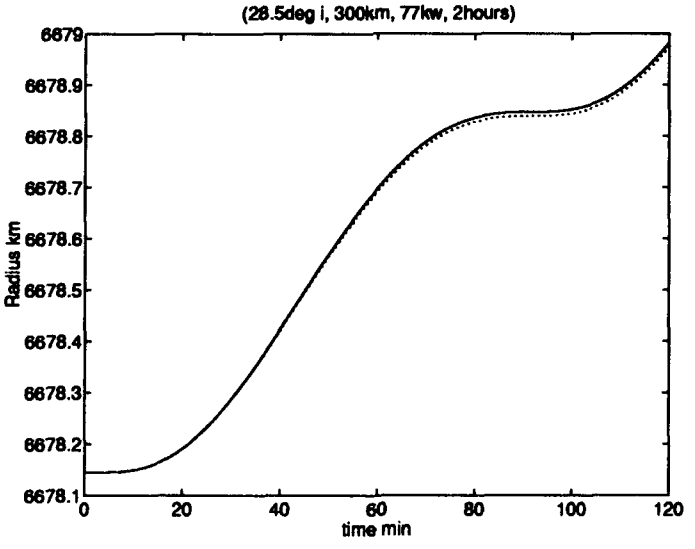

Figure N.10 The difference between the increase in orbital radius using the true solution for i (—) and the approximation, i_R ($\cdots$) is small.

Appendix O. Orbital Transfer Performance Analysis

O.1 Orbital Transfer Performance Analysis Program

The orbital transfer analysis program was created for MATLAB. The program implements first order models for the Earth's gravity and magnetic field as well as an exponential model of Earth's atmosphere. These models were used to determine the accelerations due to gravity, shielded coil electrodynamic propulsion, and aerodynamic drag. A vector function $Xd(t)$, containing the sum of these accelerations and the vehicle velocity, is numerically integrated using fourth and fifth order Runge-Kutta formulas. The result is a vector, $X(t)$, representing the location and velocity of the SFP, in Earth-centered inertial coordinates, at time, t.

The program is in two parts: the main program and the integrator. The main program defines the initial conditions and calls the integrator. $X(t)$ is used to calculate a variety of performance parameters (power, inclination, etc.), which are plotted versus time. The main program is *empvb.m*:

```
%%%%%%%%%%%%%%%%%%%%%%%%%%%%%%%%%%%%%%%%%%%%%%%%%%%%%%%%%%%%%%%%%%%%%%%%%%%%%%%%%%%

%  This routine establishes the IC’s
%  and integrates the functions
%  The result is a vector X as a function of time, t,
%  where X = [ x
%              xdot
%              y
%              ydot
%              z
%              zdot ]
%  The program computes various performance parameters
%  and then makes performance plots.
%
     F     = 'emdragp';
     t0    = 0;                         % initial time
     tf    = 1440*2;                    % final time min
     X0    = [6678145; 0;
                   0; 6789.53269*60;
                   0; 3686.41547*60]; % IC‘s
     tol   = 1.0e-6;                    % tolerance
     trace = 0;                         % diplatimestep
     [t,X] = ode45(F,t0,tf,X0,tol,trace);
%
% different IC‘s
% 300 28.5 [ 6678145; 0; 0; 6789.53269*60; 0; 3686.41547*60]
% 400 28.5 [ 6778145; 0; 0; 6739.26259*60; 0; 3659.12103*60]
% 500 28.5 [ 6878145; 0; 0; 6600.09281*60; 0; 3632.42402*60]
```

```
% 300 15    [ 6678145; 0; 0; 7462.51396*60; 0; 1999.57459*60]
% 300 45    [ 6678145; 0; 0; 5462.93937*60, 0; 5462.93937*60]
% 300 5     [ 6678145; 0; 0; 7696.36409*60; 0; 673.34461*60]
% 300 0     [ 6678145; 0; 0; 7725.76295*60; 0; 0*60]
%
%  IC's for calcs
%
      Mu = 3.986012*10^14;        % Earth's Grav Coef, m^3/s^2
      omega = 60*7.292115856e-5; % Earth's spin rate, rad/min
      L = 50*99;                  % Effect conductor length, m DESIGN
      mag = 8.05*10^(15);         % Earth's mag dipole strength, Tm^3
      Res = 84e-6;                % resistance/m, ohms/m
      rhoref = 1.916e-11;         % Air Density at ref radius, kg/m^3
      Rref = 6678145;             % ref radius, m
      HI = 0.00001998284;         % inverse scale ht, 1/m
      Cd = 2.4;                   % Drag Coef. DESIGN
      M = 110609;                 % Platform mass, kg  DESIGN
      A = 1435;                   % effect drag area, m^2  DESIGN
      Pow = 77000;                % Power limit, watts
      IGuess = 35;                % max est current, A
%
% vehicle masses
% transfer with ET 1430
% transfer w/o ET  1200
% transfer w ET SV 3340
%
% Variable Defn's
%
%   r = magnitude of radius vector
%   mx,my,mz = x,y,z components of Earth's dipole moment
%   Bx,By,Bz = x,y,z components of B vector
%   B = magnitude of B vector
%   uBx,uBy,uBx = unit x,y,z components of B vector
%   v = magnitude of velocity vector
%   uxd,uyd,uzd = unit x,y,z components of velocity vector
%   vrx,vry,vrz = x,y,z components of relative velocity vector
%   Lx,Ly,Lz = x,y,z components of conductor direction
%   LL = magnitude of conductor direction
%   uLx,uLy,uLz = unit x,y,z components of conductor direction
%   V1,V2,V3 = subcomponents of back EMF
%   LN = number of output state vectors
%   wun = col vector of 1's
%   RR = quadratics matrix
%   II = Roots matrix
%   III = vector of max roots
%   I = current
%   P = power
%   xddp,yddp,zddp = x,y,z components of acceleration due to propulsion
%   aemp = magnitude of acceleration due to propulsion
%   Rad = r in km.
%   Vel = v in m/s.
%   Vc = circular orbit velocity
%   rho = atmospheric density
%   Vr = magnitude of relative velocity vector
%   Beta = vehicle Beta value
%   xddd,yddd,zddd = x,y,z components of acceleration due to drag
%   adrag = magnitude of acceleration due to drag
%   hx,hy,hz = x,y,z components of angular momentum vector
%   nx,ny = x,y components of lin-of-nodes
%   inclin = inclination angle
%   nodes = magnitude of line-of-nodes angle
%   nullx,nully,nullz = x,y,z components of v cross accel due to propulsion
%   badx,bady,badz = x,y,z components of wasted accel due to propulsion
%   bad = magnitude of wasted accel due to propulsion
%   ubadx,ubady,ubadz = unit x,y,z components of wasted accel
```

```
%   good = magnitude of v
%   ugoodx,ugoody,ugoodz = unit x,y,z components of v
%   gooda = magnitude of useful accel due to propulsion
%   bada = magnitude of wasted accel due to propulsion
%   goodprcnt = percent of useful accel due to propulsion
%   UP = useful power
%   effic = efficiency
%
%
%  Calc Performance parameters
%
     r = ( X(:,1).^2 + X(:,3).^2 + X(:,5).^2 ).^0.5;
     mx = mag*cos(1.3701)*cos(omega*t);
     my = mag*cos(1.3701)*sin(omega*t);
     mz = -mag*sin(1.3701);
     Bx = -(mx./r.^3 - 3*(mx.*X(:,1)
          + my.*X(:,3) + mz.*X(:,5)).*X(:,1)./r.^5);
     By = -(my./r.^3 - 3*(mx.*X(:,1)
          + my.*X(:,3) + mz.*X(:,5)).*X(:,3)./r.^5);
     Bz = -(mz./r.^3 - 3*(mx.*X(:,1)
          + my.*X(:,3) + mz.*X(:,5)).*X(:,5)./r.^5);
     B = (Bx.^2 + By.^2 + Bz.^2).^(.5);
     uBx = Bx./B; uBy = By./B; uBz = Bz./B;
     v = (X(:,2).^2 + X(:,4).^2 + X(:,6).^2).^(.5);
     uxd = X(:,2)./v; uyd = X(:,4)./v; uzd = X(:,6)./v;
     vrx = (X(:,2) + omega*X(:,3))/60;
     vry = (X(:,4) - omega*X(:,1))/60;
     vrz = (X(:,6))/60;
     Lx = (uBy.*uzd - uBz.*uyd);
     Ly = (uBz.*uxd - uBx.*uzd);
     Lz = (uBx.*uyd - uBy.*uxd);
     LL = (Lx.^2 + Ly.^2 + Lz.^2).^(.5);
     uLx = Lx./LL; uLy = Ly./LL; uLz = Lz./LL;
%
     V1 = (vry.*Bz - vrz.*By).*(uLx);
     V2 = (vrz.*Bx - vrx.*Bz).*(uLy);
     V3 = (vrx.*By - vry.*Bx).*(uLz);
%
%     LN = length(V1);
%     wun = ones(LN,1);
%     RR = [(2*L*Res*wun) (abs(L*(V1 + V2 + V3))) -Pow*wun];
%     for NN = 1:LN;
%        II = (roots(RR(NN,:)))';
%        III(NN) = max(II);
%     end;
%     I = III';
%
     I = Pow./(abs(L*(V1 + V2 + V3)) + (IGuess)*2*L*Res);
     P = (abs(L*I.*(V1 + V2 + V3)) + (I.^2)*2*L*Res)/1000;
%
     xddp = (L/M)*I.*(uLy.*Bz - uLz.*By);
     yddp = (L/M)*I.*(uLz.*Bx - uLx.*Bz);
     zddp = (L/M)*I.*(uLx.*By - uLy.*Bx);
     aemp = (xddp.^2 + yddp.^2 + zddp.^2).^(.5);
%
     Rad = r./1000;
     Vel = v./60;
     Vc = (Mu*(r.^(-1))).^0.5;
%
     rho = rhoref*exp(-HI*(r - Rref));
     Vr = (vrx.^2 + vry.^2 + vrz.^2).^.5;
     Beta = M/(Cd*A);
     xddd = -.5*rho.*Vr*(1/Beta).*vrx;
     yddd = -.5*rho.*Vr*(1/Beta).*vry;
     zddd = -.5*rho.*Vr*(1/Beta).*vrz;
```

```
     adrag = ( xddd.^2 + yddd.^2 + zddd.^2 ).^0.5;
%
     hx = (X(:,3).*X(:,6)-X(:,5).*X(:,4));
     hy = (X(:,5).*X(:,2)-X(:,1).*X(:,6));
     hz = (X(:,1).*X(:,4)-X(:,3).*X(:,2));
     nx = -hy;  ny = hx;
     inclin = (acos(hz./((hx.^2 + hy.^2 + hz.^2).^0.5)))
              *(180/3.1415);
     nodes = (acos(nx./((nx.^2 + ny.^2).^0.5)))*(180/3.1415);
%
     nullx = (X(:,4).*zddp-X(:,6).*yddp);
     nully = (X(:,6).*xddp-X(:,2).*zddp);
     nullz = (X(:,2).*yddp-X(:,4).*xddp);
     badx = (nully.*X(:,6)-nullz.*X(:,4));
     bady = (nullz.*X(:,2)-nullx.*X(:,6));
     badz = (nullx.*X(:,4)-nully.*X(:,2));
     bad = ( badx.^2 + bady.^2 + badz.^2 ).^0.5;
     ubadx = badx./bad; ubady = bady./bad; ubadz = badz./bad;
     good = ( X(:,2).^2 + X(:,4).^2 + X(:,6).^2 ).^0.5;
     ugoodx = X(:,2)./good;
     ugoody = X(:,4)./good;
     ugoodz = X(:,6)./good;
     gooda = (xddp.*ugoodx + yddp.*ugoody + zddp.*ugoodz);
     bada = (xddp.*ubadx + yddp.*ubady + zddp.*ubadz);
     goodprcnt = 100*gooda./aamp;
%
     UP = (abs(L*I.*(V1 + V2 + V3)).*(goodprcnt/100))/1000;
     Effic = 100*UP./P;
%
%  Plots
%
     clg;
      plot(t,P),xlabel('time min'),ylabel('Power kW'),
           title('(28.5deg i, 300km, 16kW, 2days)');
     print -deps <m2RP2d>;
%
     clg;
      plot(t,I),xlabel('time min'),ylabel('Current A'),
           title('(28.5deg i, 300km, 16kW, 2days)');
     print -deps <m2RI2d>;
%
     clg;
      plot(t,Rad),xlabel('time min'),ylabel('Radius km'),
            title('(28.5deg i, 300km, 16kW, 2days)');
    print -deps <m2r2d>;
%
     clg;
      plot(t,B),xlabel('time min'),ylabel('B-field'),
           title('(28.5deg i, 300km, 16kW, 2days)');
     print -deps <m2B2d>;
%
     clg;
      plot(t,Vel,'+',t,Vc,':'),xlabel('time min'),
           ylabel('Velocity m/s'),
           title('(28.5deg i, 300km, 16kW, 2days)');
     print -deps <m2vel2d>;
%
     clg;
      plot(t,inclin),xlabel('time min'),
           ylabel('inclination deg'),
           title('(28.5deg i, 300km, 16kW, 2days)');
     print -deps <m2i2d>;
%
     clg;
      plot(t,nodes),xlabel('time min'),
```

```
          ylabel('line of nodes deg'),
          title('(28.5deg i, 300km, 16kW, 2days)');
     print -deps <m2lon2d>;
%
     clg;
      plot(t,aemp),xlabel('time min'),
          ylabel('acceleration m/s^2'),
          title('(28.5deg i, 300km, 16kW, 2days)');
     print -deps <m2ap2d>;
%
     clg;
      plot(t,adrag),xlabel('time min'),
          ylabel('acceleration m/s^2'),
          title('(28.5deg i, 300km, 16kW, 2days)');
     print -deps <m2Fd2d>;
%
     clg;
      plot(t,gooda),xlabel('time min'),
          ylabel('acceleration m/s^2'),
          title('(28.5deg i, 300km, 16kW, 2days)');
     print -deps <m2useap2d>;
%
     clg;
      plot(t,bada),xlabel('time min'),
          ylabel('acceleration m/s^2'),
          title('(28.5deg i, 300km, 16kW, 2days)');
     print -deps <m2wastap2d>;
%
     clg;
      plot(t,goodprcnt),xlabel('time min'),
          ylabel('percent useful accel'),
          title('(28.5deg i, 300km, 16kW, 2days)');
     print -deps <m2prcnt2d>;
%
     clg;
      plot(t,Effic),xlabel('time min'),
          ylabel('Percent Efficiency'),
          title('(28.5deg i, 300km, 16kW, 2days)');
     print -deps <m2E2d>;
%
%%%%%%%%%%%%%%%%%%%%%%%%%%%%%%%%%%%%%%%%%%%%%%%%%%%%%%%%%%%%%%%%%%%%%%%%%%%%%%%
```

The second program is a subroutine defining the vector function $Xd(t)$ that is called for integration. The equations of motion and their supporting environment models and controllers are in the program *emdragp.m*:

```
%%%%%%%%%%%%%%%%%%%%%%%%%%%%%%%%%%%%%%%%%%%%%%%%%%%%%%%%%%%%%%%%%%%%%%%%%%%%%%%%

%  Shielded EM propulsion with aerodynamic drag
%
%  The function is integrated in empvb.m
%  Xd consists of [ xdot
%                   xdotdot (f1)
%                   ydot
%                   ydotdot (f2)
%    zdot
%    zdotdot (f3) ]
%  Where x, y, and z are ECI cartesian coordinates.
%
    function Xd = emdragp(t,X)
%
    Mu = 3.986012*10^14;        % Earth's Grav. Coef., m^3/s^2
```

```
      omega = 60*7.292115856e-5; % Earth's spin rate, rad/min
      rhoref = 1.916e-11;        % Air Density at ref radius, kg/m^3
      Rref = 6678145;            % reference radius, m
      HI = 0.00001998284;        % inverse scale ht, 1/m
      Cd = 2.4;                  % Drag Coef. DESIGN
      M = 110609;                % Platform mass, kg  DESIGN
      A = 1435;                  % effect. drag area, m^2  DESIGN
      P = 77000;                 % Power limit, watts
      L = 50*99;                 % Effect conductor length, m DESIGN
      mag = 8.05*10^(15);        % Earth's mag dipole strength, Tm^3
      Res = 84e-6;               % resistance/m, ohms/m
      IGuess = 35;               % max est current, A
%
% vehicle masses
% transfer with ET 1430
% transfer w/o ET  1200
% transfer w ET SV 3340
%
      x = X(1);  xd = X(2);  y = X(3);  yd = X(4);
      z = X(5);  zd = X(6);
%
%  The supporting functions
%
%  gravity
%   r = magnitude of radius vector
%   xddg,yddg,zddg = x,y,z components of acceleration due to gravity
%
      r = ( x^2 + y^2 + z^2 )^0.5;
      xddg = -x*(Mu/(r^3))*3600;
      yddg = -y*(Mu/(r^3))*3600;
      zddg = -z*(Mu/(r^3))*3600;
%
%  aerodynamic drag
%   rho = atmospheric density
%   vrx,vry,vrz = x,y,z components of relative velocity vector
%   V = magnitude of relative velocity vector
%   Beta = vehicle Beta value
%   xddd,yddd,zddd = x,y,z components of acceleration due to drag
%
      rho = rhoref*exp(-HI*(r - Rref));
      vrx = (xd + y*omega);
      vry = (yd - x*omega);
      vrz = (zd);
      V = (vrx^2 + vry^2 + vrz^2)^.5;
      Beta = M/(Cd*A);
      xddd = -.5*rho*V*(1/Beta)*vrx;
      yddd = -.5*rho*V*(1/Beta)*vry;
      zddd = -.5*rho*V*(1/Beta)*vrz;
%
%  em propulsion
%   mx,my,mz = x,y,z components of Earth's dipole moment
%   Bx,By,Bz = x,y,z components of B vector
%   B = magnitude of B vector
%   uBx,uBy,uBz = unit x,y,z components of B vector
%   v = magnitude of velocity vector
%   uxd,uyd,uzd = unit x,y,z components of velocity vector
%   Lx,Ly,Lz = x,y,z components of conductor direction
%   LL = magnitude of conductor direction
%   uLx,uLy,uLz = unit x,y,z components of conductor direction
%   V1,V2,V3 = subcomponents of back EMF
%   RR = quadratics matrix
%   II = Roots matrix
%   I = current
%   xddp,yddp,zddp = x,y,z components of acceleration due to propulsion
%
```

```
     mx = mag*cos(1.3701)*cos(omega*t);
     my = mag*cos(1.3701)*sin(omega*t);
     mz = -mag*sin(1.3701);
     Bx = -(mx/r^3 - 3*(mx*x + my*y + mz*z)*x/r^5);
     By = -(my/r^3 - 3*(mx*x + my*y + mz*z)*y/r^5);
     Bz = -(mz/r^3 - 3*(mx*x + my*y + mz*z)*z/r^5);
     B = (Bx^2 + By^2 + Bz^2)^(.5);
     uBx = Bx/B; uBy = By/B; uBz = Bz/B;
     v = (xd^2 + yd^2 + zd^2)^(.5);
     uxd = xd/v; uyd = yd/v; uzd = zd/v;
     Lx = (uBy*uzd - uBz*uyd);
     Ly = (uBz*uxd - uBx*uzd);
     Lz = (uBx*uyd - uBy*uxd);
     LL = (Lx^2 + Ly^2 + Lz^2)^(.5);
     uLx = Lx/LL; uLy = Ly/LL; uLz = Lz/LL;
%
     V1 = (vry*Bz - vrz*By)*(uLx)/60;
     V2 = (vrz*Bx - vrx*Bz)*(uLy)/60;
     V3 = (vrx*By - vry*Bx)*(uLz)/60;
%
%     RR = [(2*L*Res) (abs(L*(V1 + V2 + V3))) -P];
%     II = roots(RR);
%     I = max(II);
%
     I = P/(abs(L*(V1 + V2 + V3)) + (IGuess)*2*L*Res);
%
     xddp = (I*L/(M))*(uLy*Bz - uLz*By)*3600;
     yddp = (I*L/(M))*(uLz*Bx - uLx*Bz)*3600;
     zddp = (I*L/(M))*(uLx*By - uLy*Bx)*3600;
%
%  combining the accels up
%
     f1 = xddg + xddp + xddd; %
     f2 = yddg + yddp + yddd; %
     f3 = zddg + zddp + zddd; %
%
%  the actual function to be integrated
%
     Xd = [ X(2);
            f1;
            X(4);
            f2;
            X(6);
            f3 ];
%
%%%%%%%%%%%%%%%%%%%%%%%%%%%%%%%%%%%%%%%%%%%%%%%%%%%%%%%%%%%%%%%%%%%%%%%%%%%%%%%
```

O.2 SFP Performance Analysis

Once the configuration of the SFP was established, the vehicle's orbital transfer performance was determined. The equations of motion were numerically integrated using the above programs with a variety of initial conditions and vehicle states. In each case, the integration was stopped at a final time, t_f, of 2 *days*. This Appendix contains the plotted data from this performance analysis.

The majority of the program executions were made with only one initial condition or state varied from an arbitrary standard. This arbitrary standard was used to ease analysis. The standard initial condition was a 28.5° inclination circular orbit with an altitude of 300 *km*. This is the likely inclination for Space Station Freedom. The altitude is also the approximate ASSET work altitude. This orbit represents the typical starting conditions for an orbit transfer of the SFP. The worst case state chosen for analysis was 77 *kW* of power for propulsion while carrying a external tank as payload. 77 *kW* is the maximum amount of sustained power available for propulsion, and is the expected operating level during most of a transfer. The external tank represents the design specification payload, and is expected to be the worst case for the SFP total mass and drag area.

O.2.1 Baseline SFP Performance Analysis.

O.2.1.1 300 km Altitude Initial Condition. This program execution uses the standard initial conditions and vehicle states. It establishes the baseline performance for the SFP (see Figures O.1 through O.8). The baseline trends are discussed in Section 6.3.10.4.

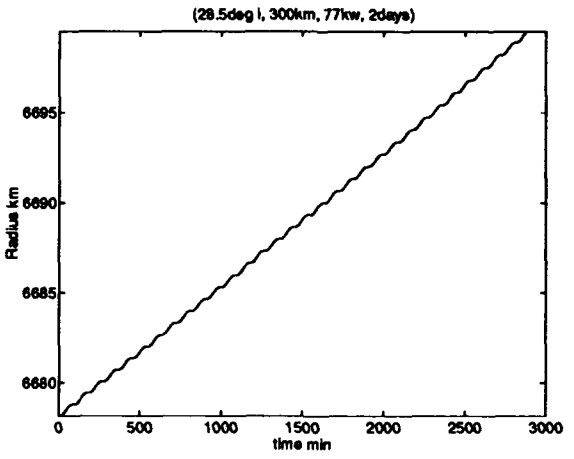

Figure O.1 The SFP rises 21.33 *km* in 2 *days*.

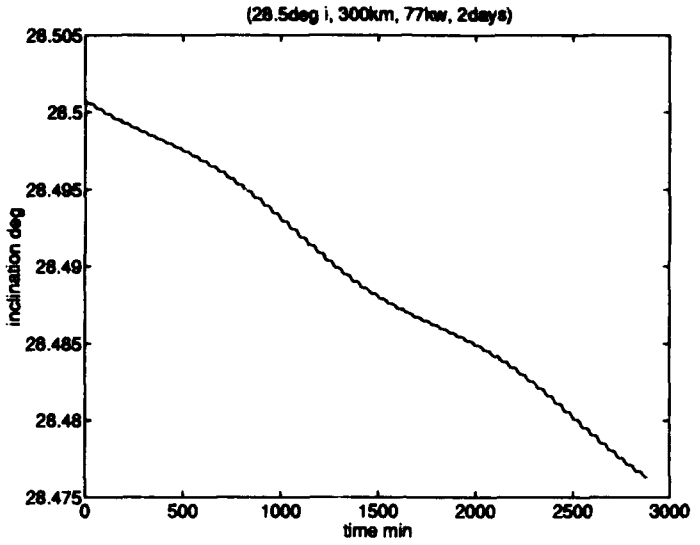

Figure O.2 The SFP's inclination decreases 0.024° in 2 *days*.

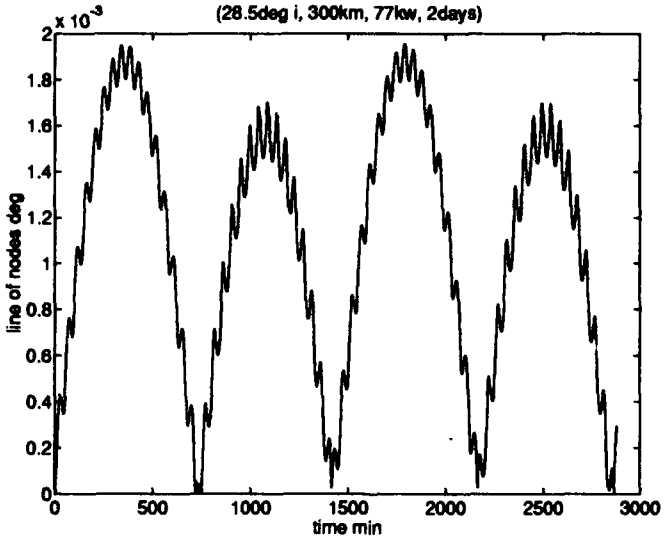

Figure O.3 The maximum $|\Omega|$ is less than 2×10^{-3}°.

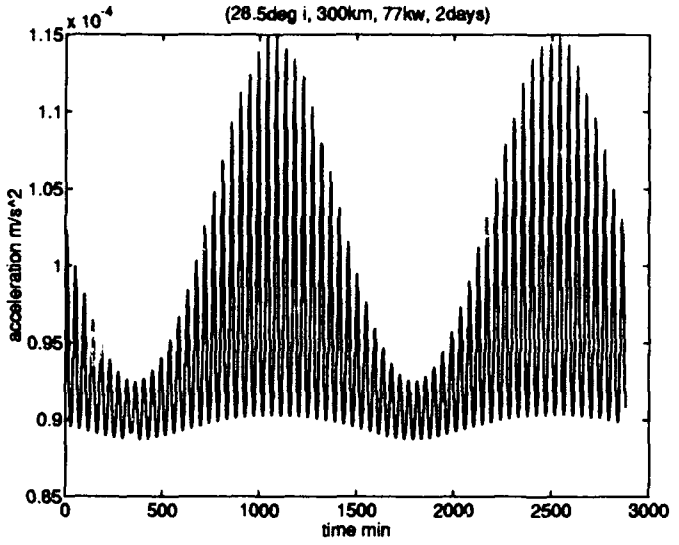

Figure O.4 The total a_p varies between 0.88×10^{-4} and $1.16 \times 10^{-4}\, m/s^2$.

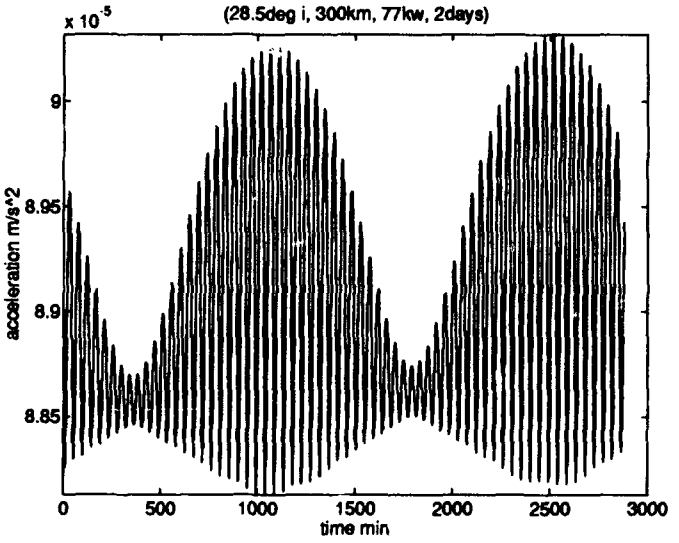

Figure O.5 The useful a_p varies between 8.81×10^{-5} and $9.03 \times 10^{-5}\, m/s^2$.

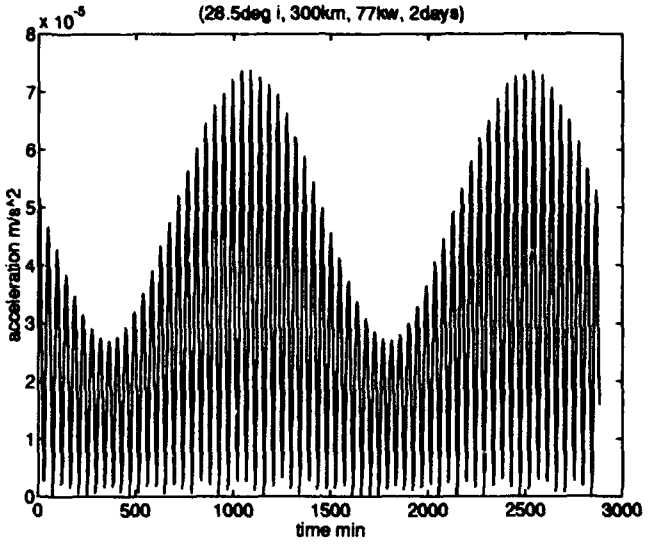

Figure O.6 The wasted a_p varies between 0 and 7.3 $\times$ $10^{-5}\, m/s^2$.

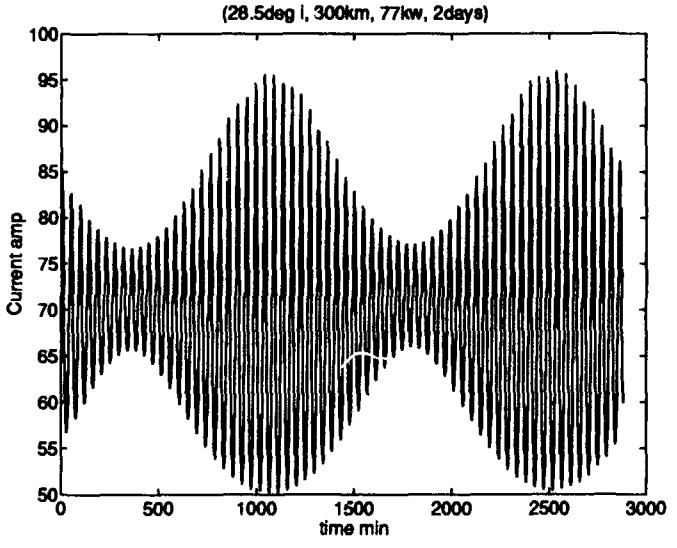

Figure O.7 The regulated current varies between 50 and 95 A.

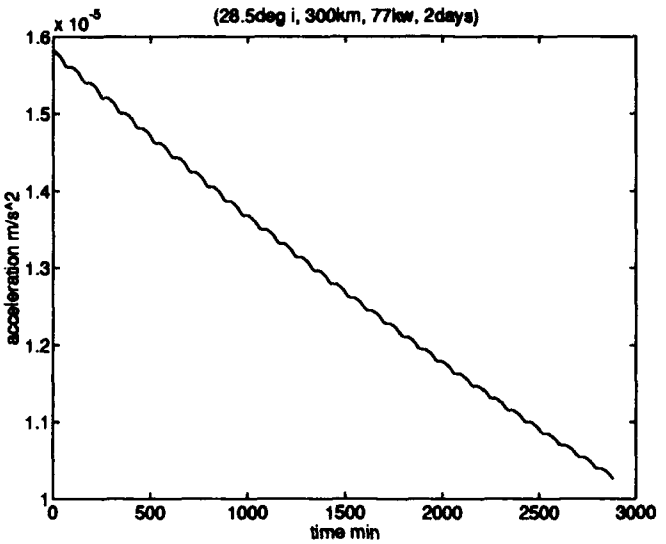

Figure O.8 The maximum acceleration due to aerodynamic drag, a_d, is 1.59 $\times$ $10^{-5}\, m/s^2$.

O.2.1.2 400 km Altitude Initial Condition. With the vehicle initial orbit at an altitude of 400 km, a program execution was made to verify the trends demonstrated in the baseline (see Figures O.9 through O.16). During the SFP's upward spiral, the vehicle is always close to circular orbit conditions. Therefore, the 400 km circular orbit is a good approximation of the vehicles orbital state at that altitude. The baseline trends were verified by this run.

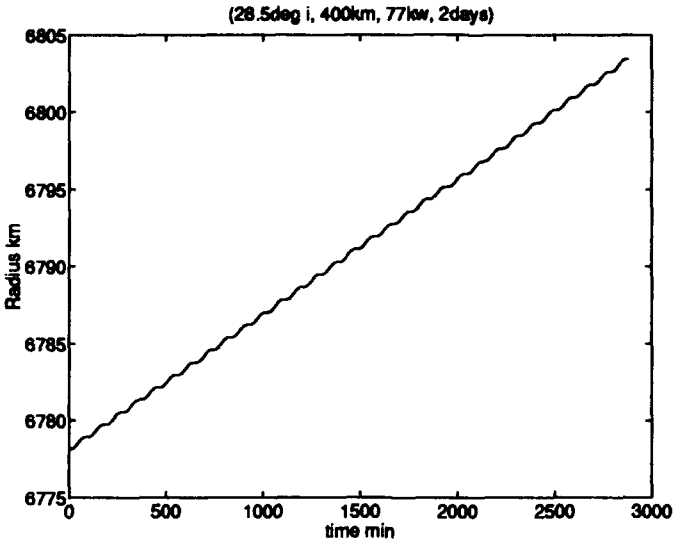

Figure O.9 The SFP rises 25.4 *km* in 2 *days*; note that the long term climb rate has increased relative to the baseline conditions.

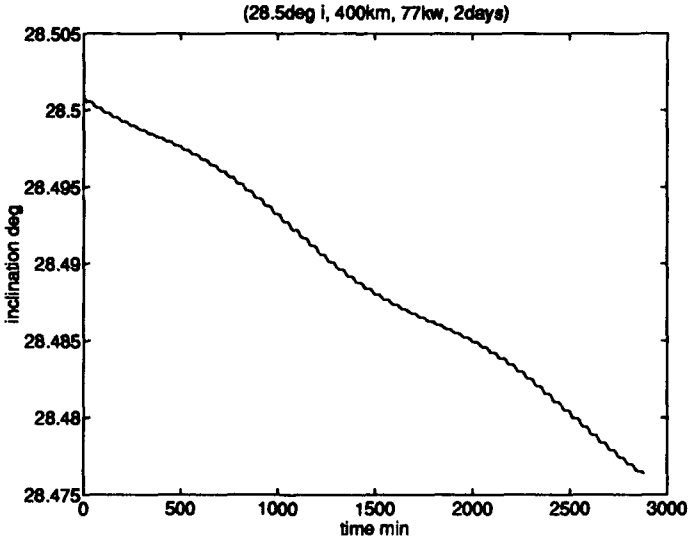

Figure O.10 The SFP's inclination decreases 0.024° in 2 *days*; note that the long term decrease has remained relatively constant.

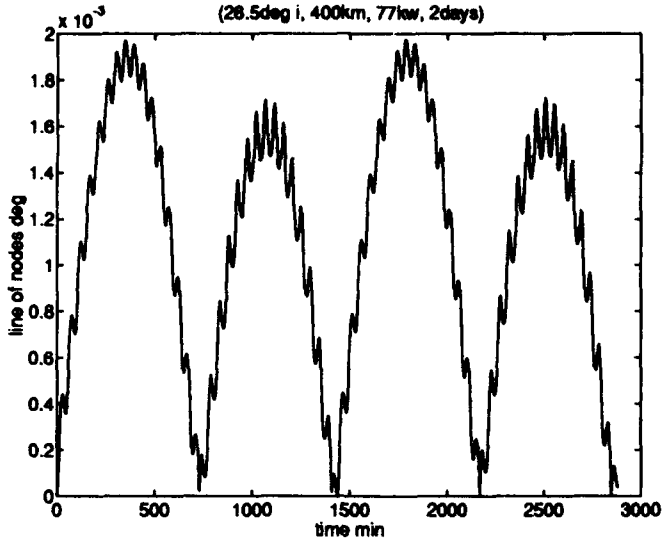

Figure O.11 The maximum $|\Omega|$ is less than 2×10^{-3}°; note that the profile is nearly unchanged relative to the baseline.

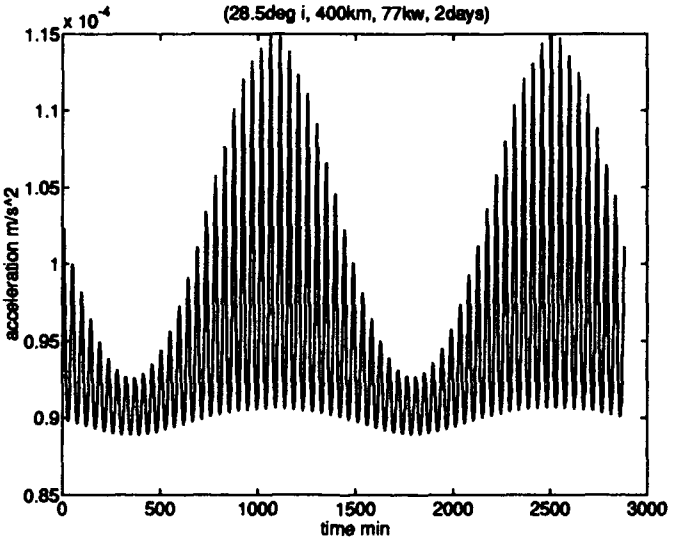

Figure O.12 The total a_p varies between 0.88×10^{-4} and $1.16 \times 10^{-4}\, m/s^2$; note that the profile is nearly unchanged relative to the baseline.

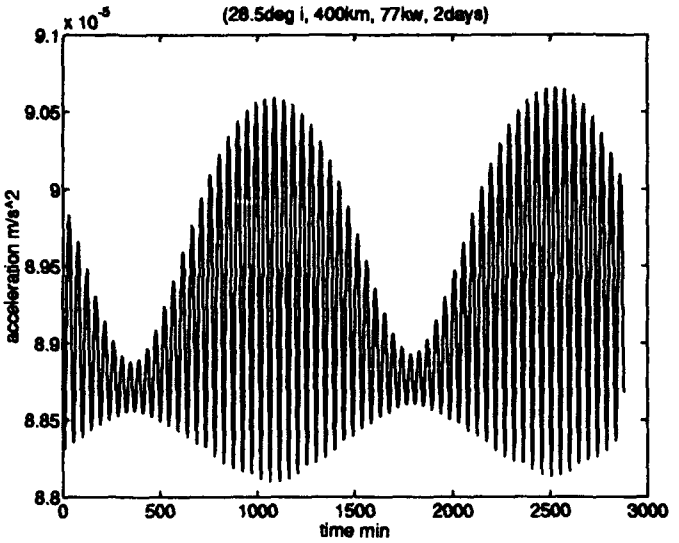

Figure O.13 The useful a_p varies between 8.81×10^{-5} and $9.06 \times 10^{-5}\, m/s^2$; note that the maximum useful a_p has increased slightly.

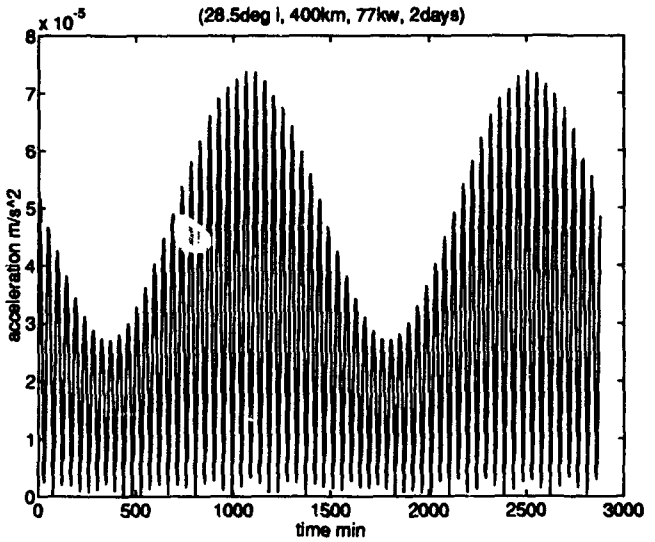

Figure O.14 The wasted a_p varies between 0 and $7.3 \times 10^{-5}\, m/s^2$; note that the profile is nearly unchanged relative to the baseline.

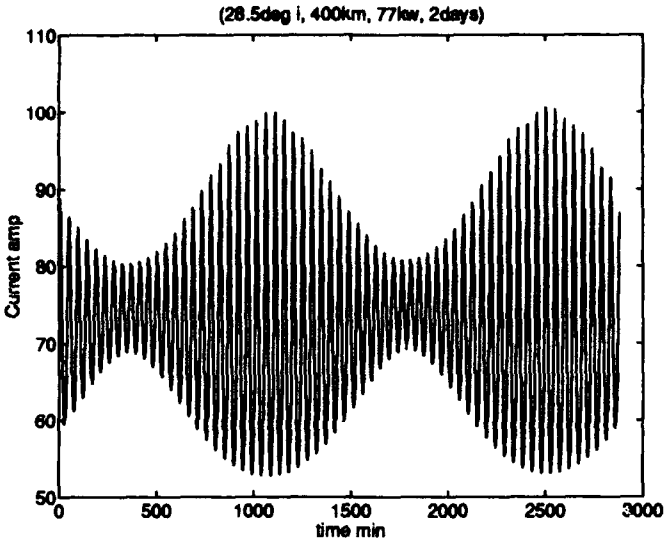

Figure O.15 The current varies between 53 and 101 A; note that the average current has increased.

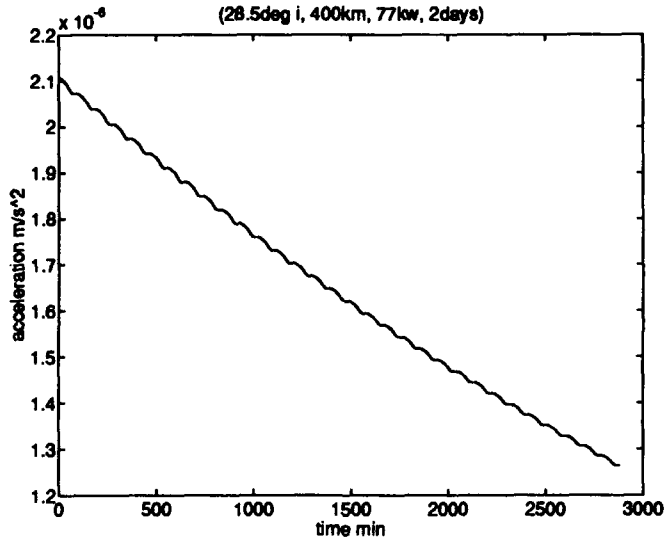

Figure O.16 The maximum acceleration due to aerodynamic drag, a_d, is 2.1 $\times$ 10^{-6} m/s^2; note that the aerodynamic drag has dropped with altitude.

O.2.1.3 500 km Altitude Initial Condition. The trends of the baseline were further confirmed by starting the SFP at 500 *km* (see Figures O.17 through O.23). Again, the baseline trends were confirmed.

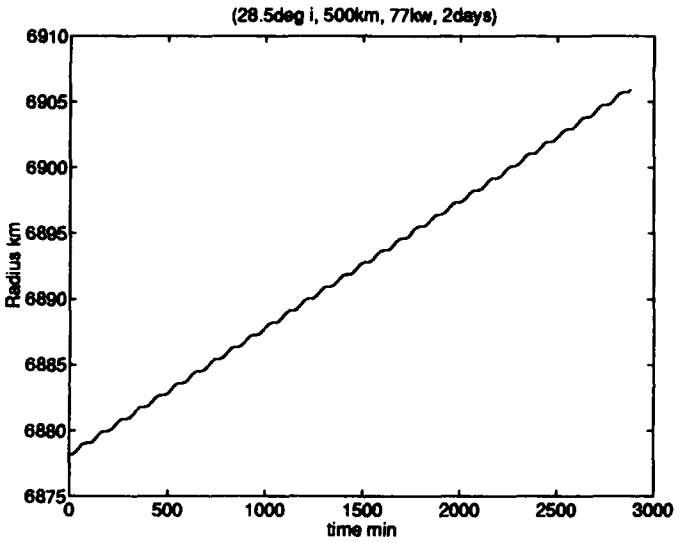

Figure O.17 The SFP rises 28.0 *km* in 2 *days*; note that the long term climb rate has increased relative to the baseline conditions.

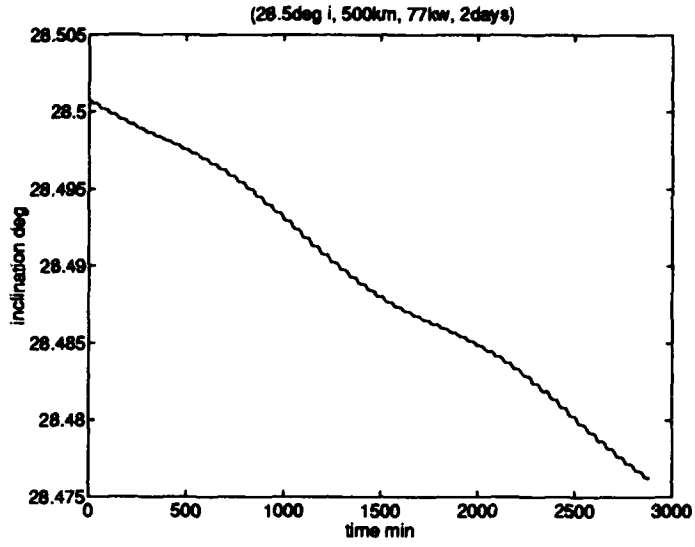

Figure O.18 The SFP's inclination decreases 0.024° in 2 *days*; note that the long term decrease has remained relatively constant.

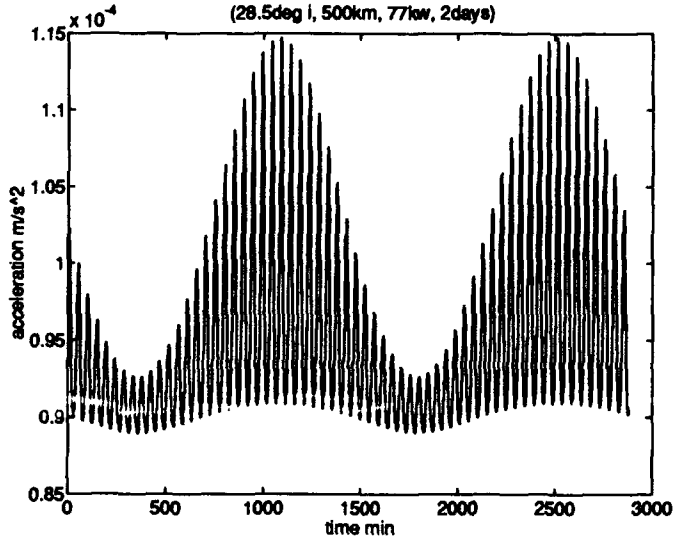

Figure O.19 The total a_p varies between 0.88×10^{-4} and $1.16 \times 10^{-4} m/s^2$; note that the profile is nearly unchanged relative to the baseline.

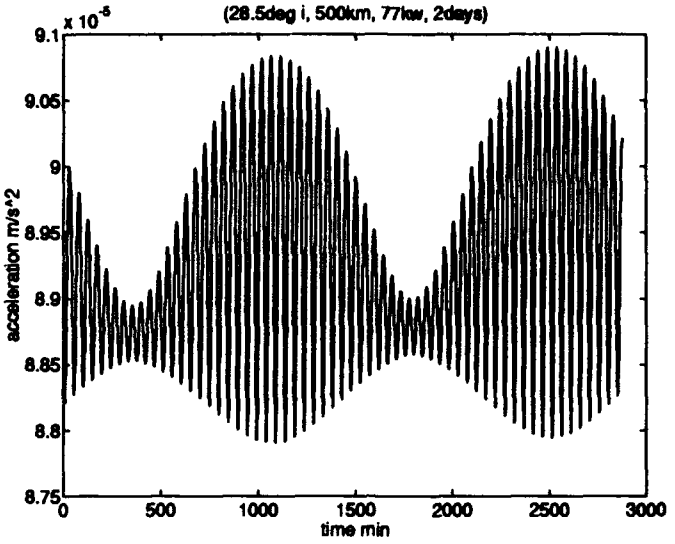

Figure O.20 The useful a_p varies between 8.81×10^{-5} and $9.08 \times 10^{-5}\, m/s^2$; note that the maximum useful a_p has increased slightly.

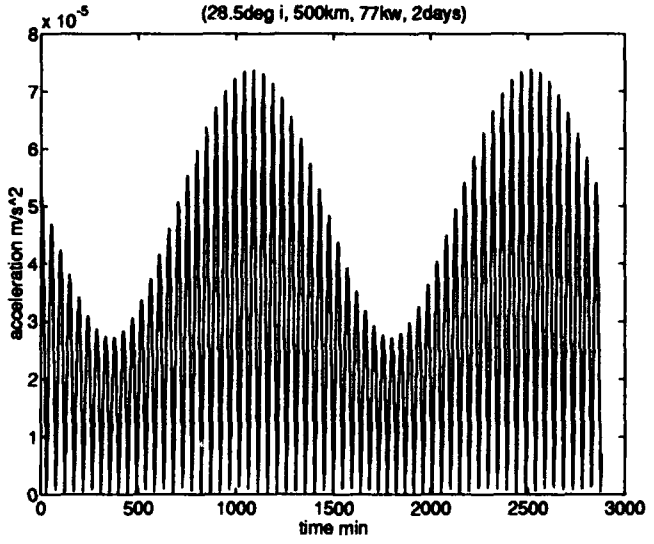

Figure O.21 The wasted a_p varies between 0 and $7.3 \times 10^{-5}\, m/s^2$; note that the profile is nearly unchanged relative to the baseline.

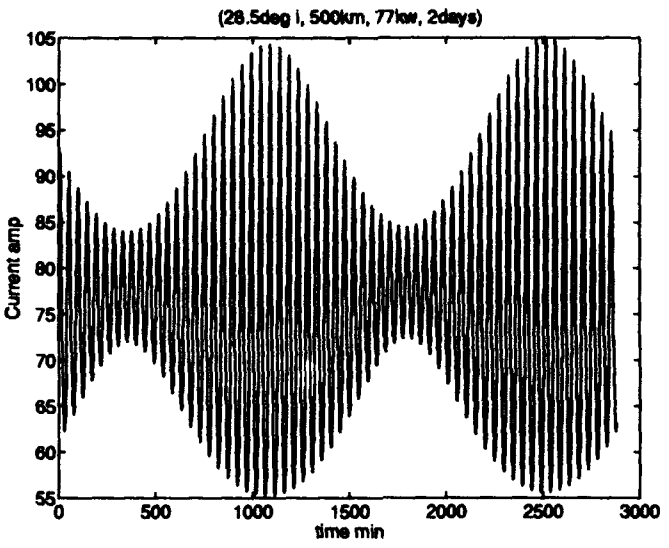

Figure O.22 The current varies between 55 and 105 A; note that the average current has continued to increase.

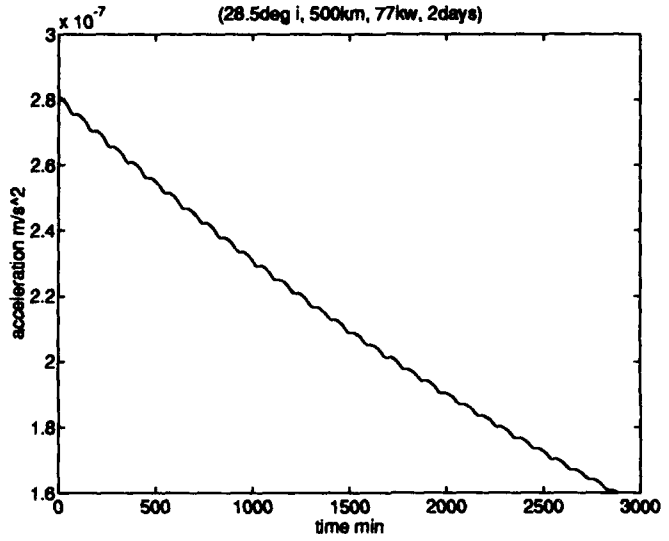

Figure O.23]

The maximum acceleration due to aerodynamic drag, a_d, is $2.8 \times 10^{-7} m/s^2$; note that the aerodynamic drag has continued to drop with altitude.

O.2.2 Reduced Power Performance Analysis. The SFP has sufficient power to perform an orbital transfer while the truss builder and remote manipulators are in operation, but the power available for propulsion is reduced (see Figures O.24 through O.28). This analysis was made to determine the SFP's orbital transfer performance under this condition. The propulsion power was reduced by the combined peak power load of the truss maker and remote manipulators (9 kW) to 68 kW. The results are as follows:

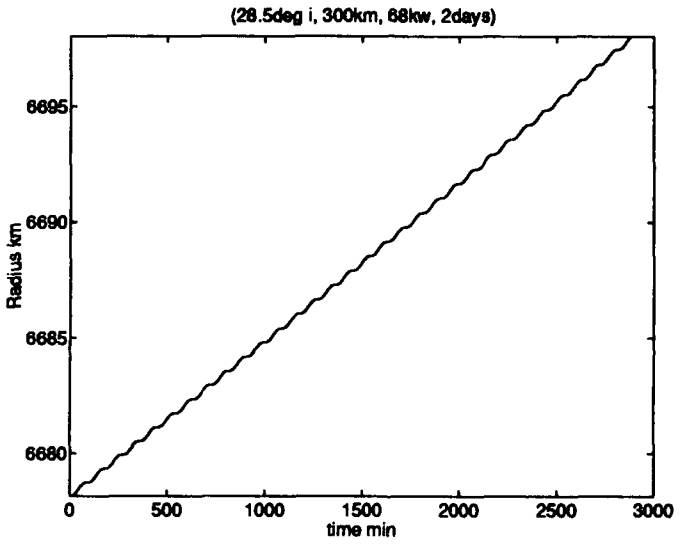

Figure O.24 The SFP rises 10.0 km in 2 *days*; with a reduction of only 9 kW, the long term climb rate is less than half the baseline's climb rate.

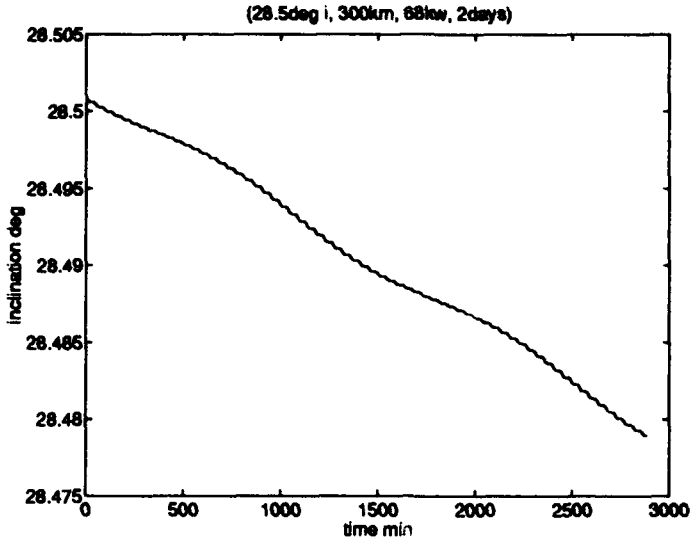

Figure O.25 The SFP's inclination decreases 0.022° in 2 *days*; the change is smaller than the baseline's inclination change.

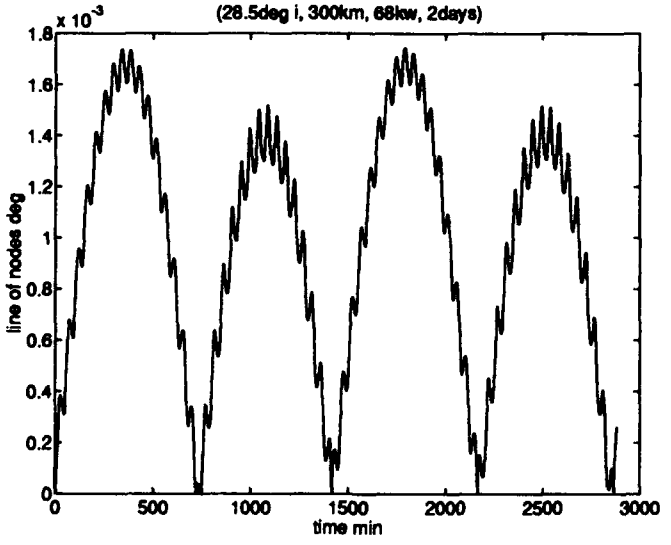

Figure O.26 The maximum $|\Omega|$ is less than 1.68×10^{-3}°; the change is smaller than the baseline's line-of-node change.

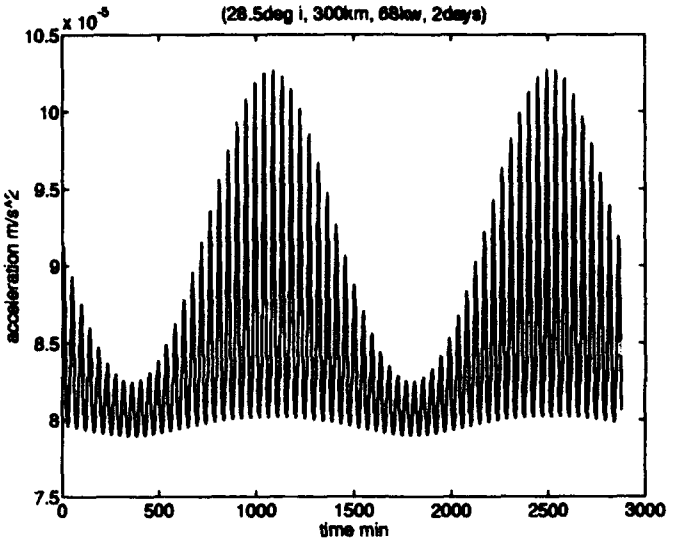

Figure O.27 The total a_p varies between 7.9 $\times$ 10^{-5} and 10.3 $\times$ $10^{-5}\, m/s^2$; the average is smaller than the baseline's average a_p.

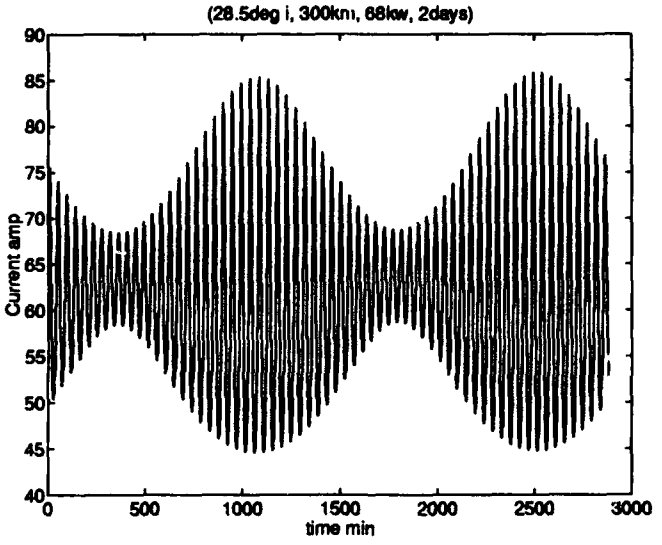

Figure O.28 The current varies between 45 and 86.3 A.

O.2.3 No Payload Performance Analysis. To determine the *best* performance of the SFP, the external tank payload was removed. Without the external tank, the vehicle mass is 79,309 kg, and the vehicle drag area is reduced to 1,196 m^2. The standard initial condition orbit was used, and the full 77 kW applied (see Figures O.29 through O.33).

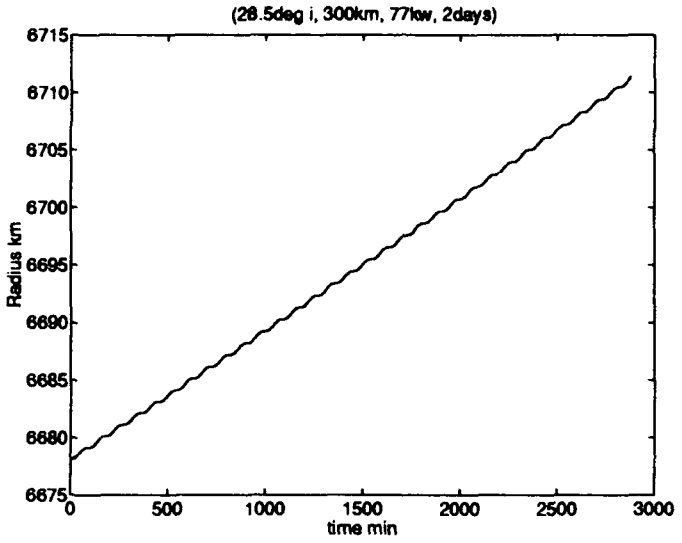

Figure O.29 The SFP rises 33.4 km in 2 *days*; this is the SFP's best climb performance.

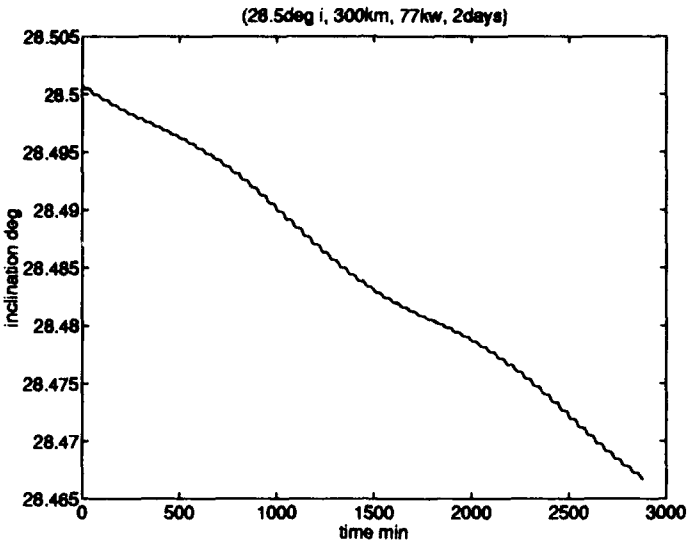

Figure O.30 The SFP's inclination decreases 0.034° in 2 *days*; note the long term decrease rate has increased.

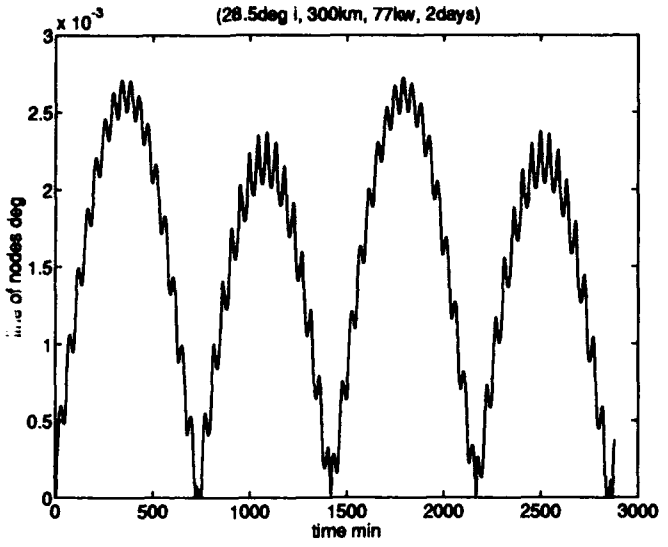

Figure O.31 The maximum $|\Omega|$ is less than 2.7×10^{-3}°, also greater than the baseline's.

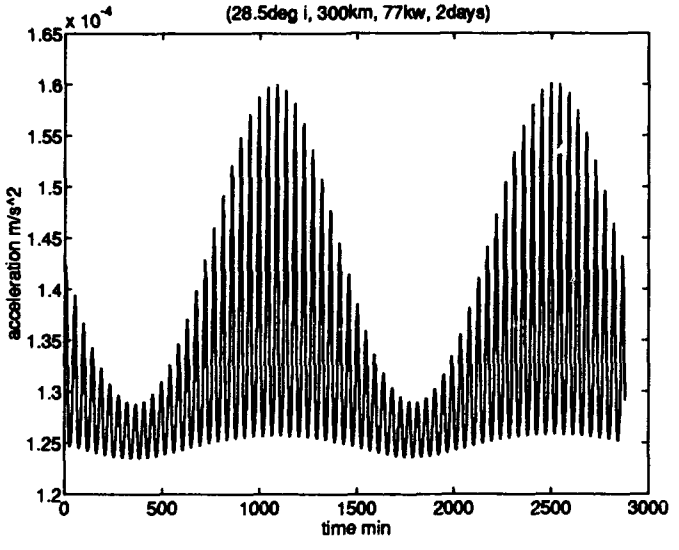

Figure O.32 The total a_p varies between 1.24×10^{-4} and $1.6 \times 10^{-4}\, m/s^2$, a significant increase from the baseline.

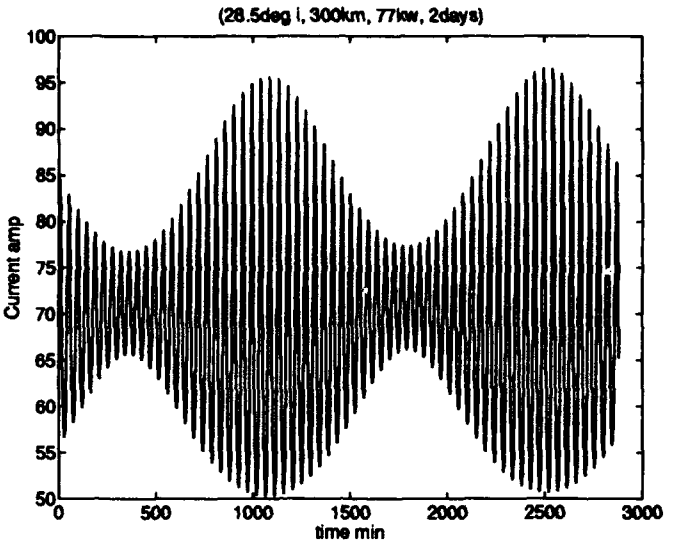

Figure O.33 The current varies between 50 and 96 A, essentially the same as baseline.

O.2.4 Analysis of Inclination Changes on Performance.

O.2.4.1 5° *Inclination Orbit.* The method used to direct the propulsive force, $\overline{F_p}$, depends on the $\overline{B}$ being nearly orthogonal to $\overline{v}$. The angle between $\overline{F_p}$ and $\overline{v}$ is dependent on the vehicles position and time. Generally, the angle will be closer to 90° in lower inclination orbits. The inclination of the initial orbit was changed to 5° to study the effects of inclination on the the SFP's orbital transfer (see Figures O.34 through O.37).

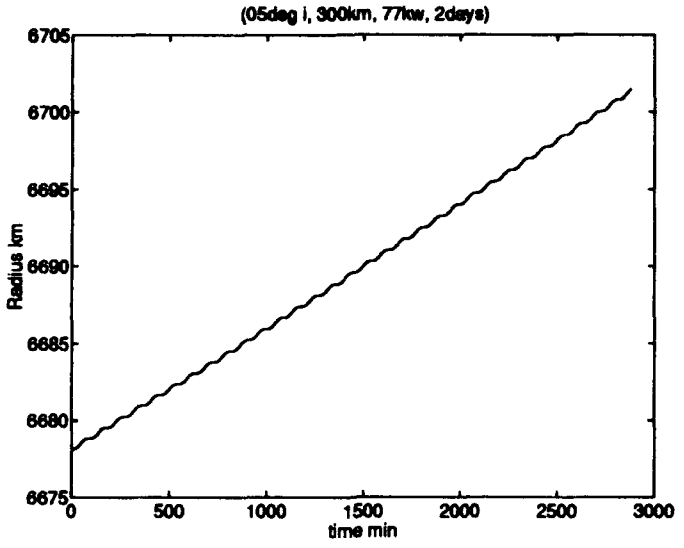

Figure O.34 The SFP rises 23.3 *km* in 2 *days*; note that the SFP's long term climb rate is superior at the lower inclination.

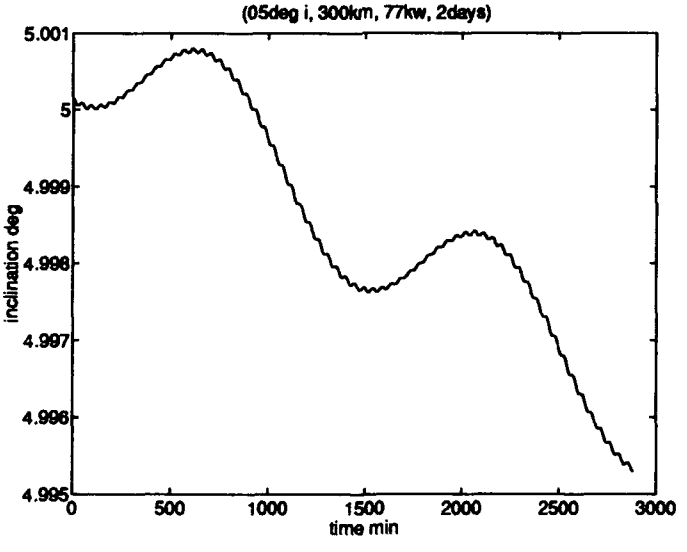

Figure O.35 The SFP's inclination decreases 0.0048° in 2 *days*; this is an order of magnitude less than the baseline.

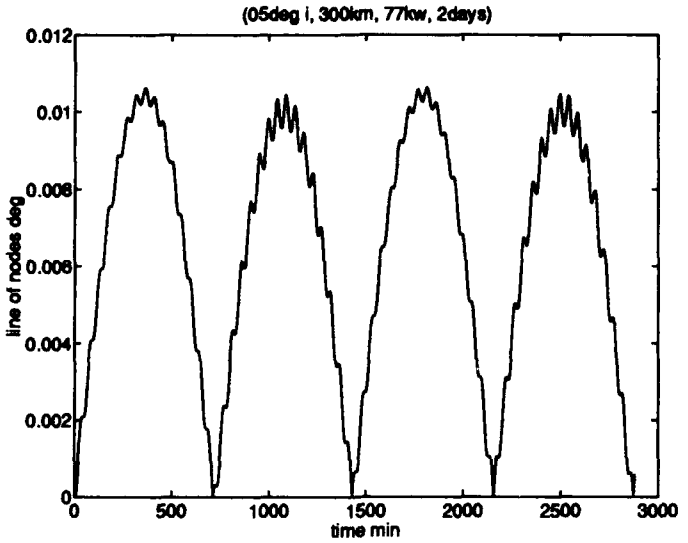

Figure O.36 The maximum $|\Omega|$ is less than 0.0105°; this is an order of magnitude worse than the baseline.

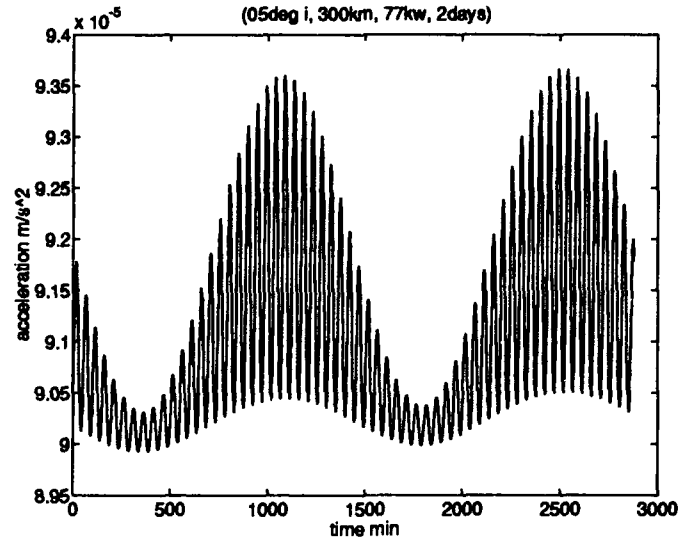

Figure O.37 The total a_p varies between 9.00×10^{-5} and $9.37 \times 10^{-5}\, m/s^2$, a smaller variation in acceleration.

O.2.4.2 15° *Inclination Orbit.* Continuing the study of the effects of inclination on the SFP's orbital transfer, the inclination of the initial orbit was changed to 15° (see Figures O.38 through O.41).

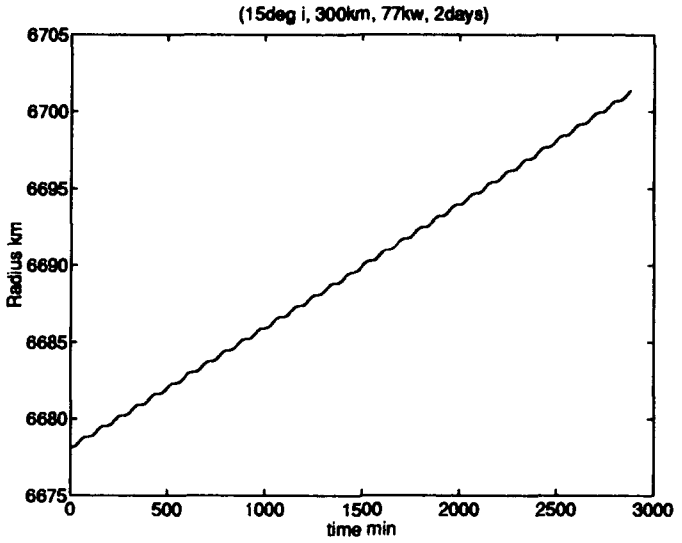

Figure O.38 The SFP rises 23.28 *km* in 2 *days*; note that the SFP's long term climb rate is superior at the lower inclination.

O.2.5 Descending Orbit Transfers. The program was executed to study the performance of the SFP in transfers from 500 *km* to lower altitude orbits. A thrust in the $-\overline{v}$ direction is achieved by reversing the direction of current flow through the conductor. In the code, this is implemented by using a "negative" current. The analysis was made with the vehicle in the 'no payload' configuration.

A run was made with a current of 300 *A*. Figure O.42 shows that the SFP can reach a 300 *km* altitude in less than 3 days. Figure O.43 shows that the shielded coil electrodynamic propulsion system *produces* power when the vehicle lowers its orbit.

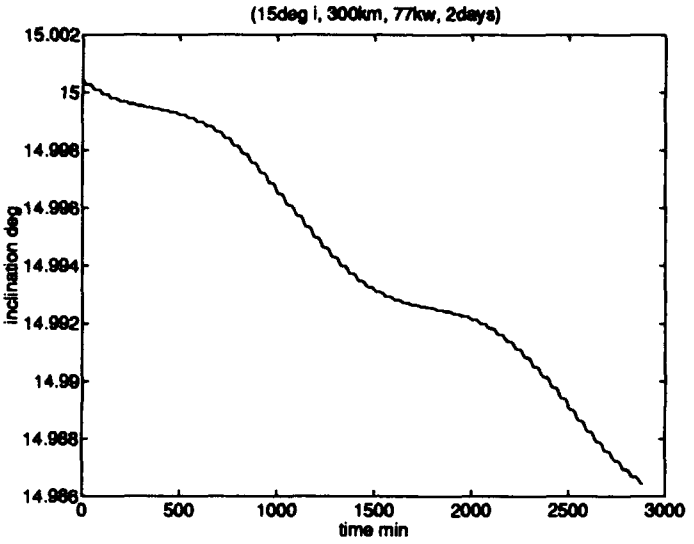

Figure O.39 The SFP's inclination decreases 0.0014° in 2 *days*; this is an order of magnitude less than the baseline.

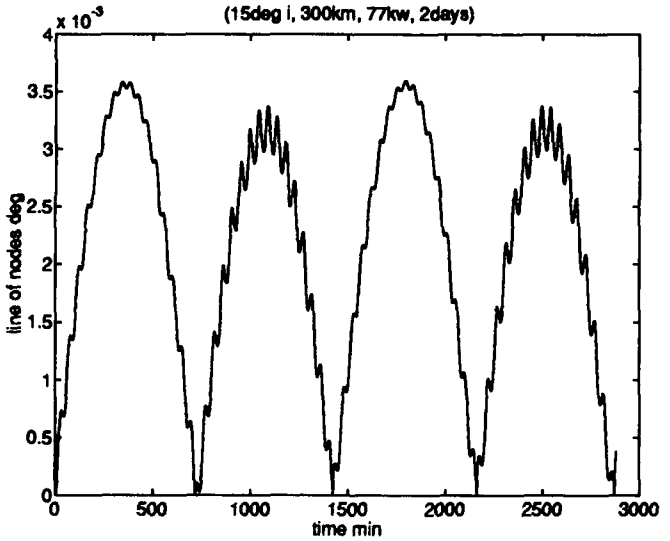

Figure O.40 The maximum $|\Omega|$ is less than 3.6×10^{-3}°; this is roughly double the baseline max $|\Omega|$.

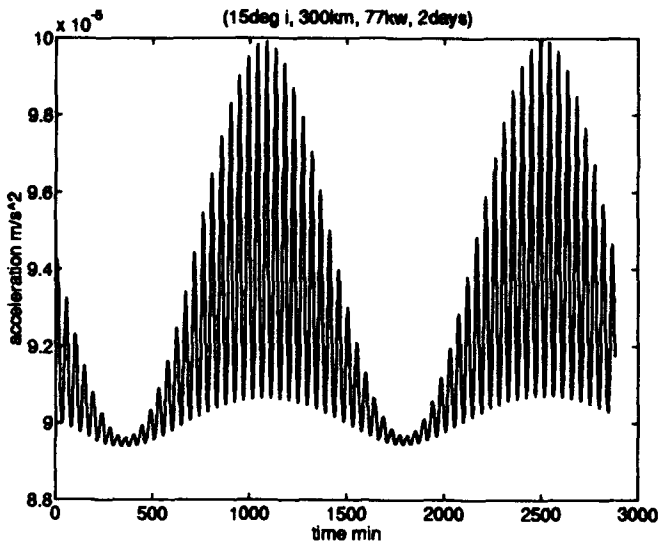

Figure O.41 The total a_p varies between 8.94×10^{-5} and $10.00 \times 10^{-5}\, m/s^2$, a smaller variation in acceleration.

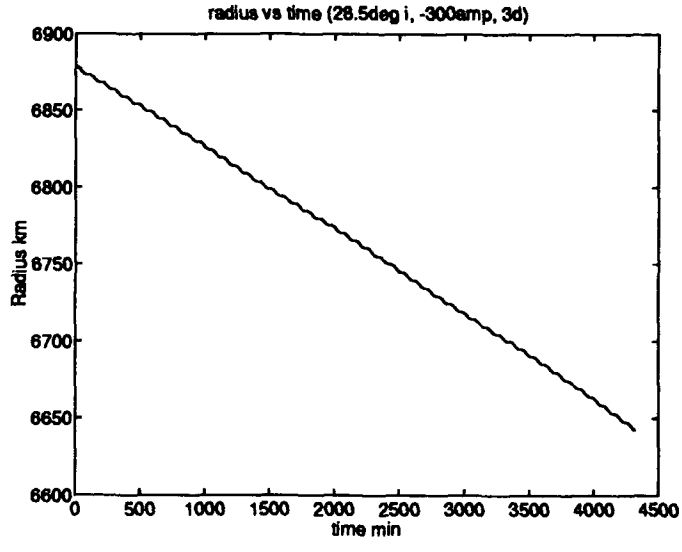

Figure O.42 The SFP can drop over 200 km is 3 days when 300 A are allowed to flow through the main conductor.

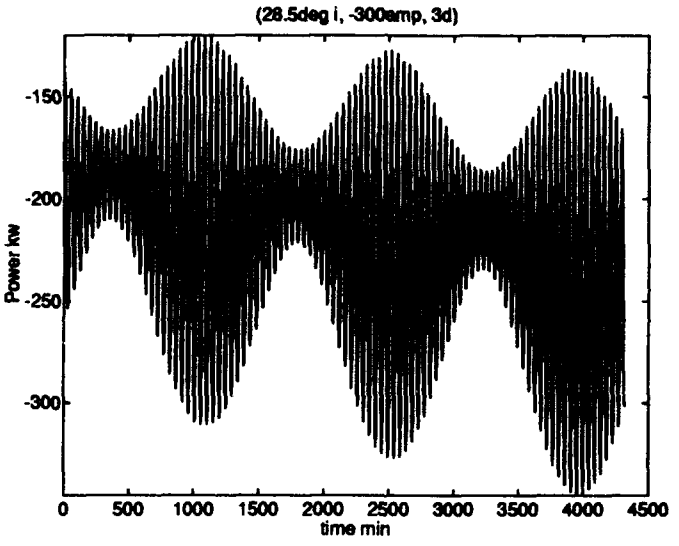

Figure O.43 The *negative* power in this figure shows that the shielded coil electrodynamic propulsion system generates power when the vehicle drops in altitude.

Appendix P. Integrated Truss Moments

P.1 Introduction

The integrated truss components are subjected to a variety of moments. The majority of moments are induced by maneuvering. The control system will be programmed to inhibit commanded moments that exceed the strength of the truss. The moments generated by the solar power system, at the ends of the cross integrated trusses, fall under different considerations. They must rotate at orbit rate to remain oriented with the sun. An analysis was accomplished to insure the moments due to the rotating power system's center of mass not being aligned with the rotation axis did not exceed the strengths of the cross integrated trusses. The rotation of the solar power system occurs mostly about the $\hat{b}_3$ axis at approximately 1.1335×10^{-3} rad/sec (see Figure P.1).

Some off axes rotations of individual solar power components do occur because of inclination changes. Like the majority of moments, these rotations are a function of controlled maneuvering. They will be categorized as commanded moments and not a part of this analysis.

P.2 Solar Power Component Models

The primary components on one end of a cross integrated truss are also illustrated in Figure P.1. They are the concentrator, the power generation assembly, the ASSET photovoltaic array, and the radiator. The component's moments of inertia, I, were modeled by a spherical cap, a cylinder, and two thin plates respectively. Table P.1 identifies the primary masses, I parameters, and Cartesian distances from the truss center mounting point, q, on the SFP to the center of masses, CM, for each of the primary components.

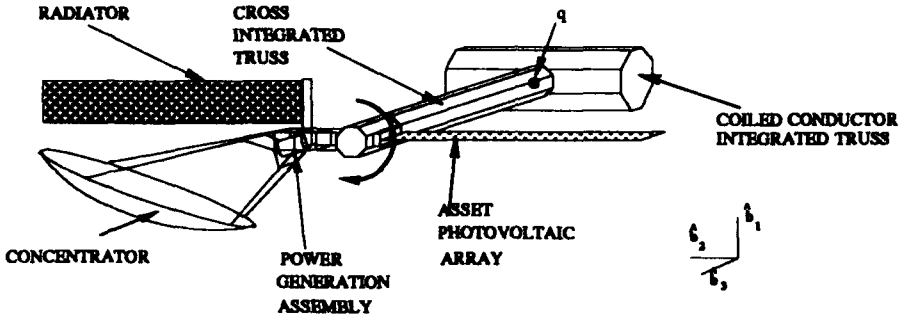

Figure P.1 The solar power system of the SFP on the end of one cross integrated truss. The primary components are labeled.

Component	Mass, kg	I parameters, m	distance q to CM, m
Concentrator	845.0	r = 25.0 (sphere) h = 2.0 (depth)	$\hat{b}_1$ = 15.5 $\hat{b}_2$ = -7.5 $\hat{b}_3$ = 28.0
Power Generation Assembly	2265.0	r = 1.0 h = 4.0	$\hat{b}_1$ = 4.5 $\hat{b}_2$ = -2.2 $\hat{b}_3$ = 28.0
ASSET Photovoltaic Array	2419.0	b = 10.3 h = 13.4	$\hat{b}_1$ = -8.7 $\hat{b}_2$ = 0.0 $\hat{b}_3$ = 28.0
Radiator	1471.0	b = 8.0 h = 18.4	$\hat{b}_1$ = 12.2 $\hat{b}_2$ = 4.0 $\hat{b}_3$ = 28.0

Table P.1 The specifications for calculating the moment contributions of the primary solar power components. The concentrator is oriented in the $\hat{b}_1$ direction.

P.3 MATLAB Program

The MATLAB program that follows was used to calculate the moments of inertia for each of the primary components, rotate their axes to align with the $\hat{b}$-axes (if necessary), and translate their inertias to the point q (52:421–443). The code finishes with a calculation of the total moments experienced by one cross integrated truss due to the primary solar component rotating at orbit rate.

```
%%%%%%%%%%%%%%%%%%%%%%%%%%%%%%%%%%%%%%%%%%%%%%%%%%%%%%%%%%%%%%%%%%%%%%%%%%%%%%%%

% Moment calculations on one cross truss due to the moments
% of inertia of the solar power system rotating at orbit rate.

% Concentrator (modeled as a spherical cap)

  mc = 845;   % mass
  rc = 25;    % radius of spherical cap
  hc = 2;     % depth of spherical cap
  b1c = 15.5; % Cartesian distance form q to CM
  b2c = -7.5;
  b3c = 28;
  thc = .35;  % off axis angle in radians

  % Rotation matrix for a 20 degree rotation

  Cc = [cos(thc) 0 -sin(thc);
           0     1    0    ;
        sin(thc) 0 cos(thc)];

  % Moment of inertia about CM

  Icmtrx = [(rc - hc./3)      0              0        ;
                0       (rc./2 - hc./12)     0        ;
                0             0        (rc./2 - hc./12)];

  Icprime = mc .* hc .* Icmtrx;

  Ic = Cc' * Icprime * Cc;

  skewc = [0 -b1c  b3c;
           b1c  0 -b2c;
          -b3c b2c  0];

  % Moment of inertia about q

  Icq = Ic - mc .* skewc * skewc

% Power Generation Assembly (modeled as a cylinder)

  ra = 1;     % radius
  ha = 4;     % height
  ma = 2265;  % mass
  b1a = 4.5;  % Cartesian distance from q to CM
  b2a = -2.2;
  b3a = 28;
  tha = .61;  % off axis angle in radians

  % Rotation matrix for a 35 degree rotation
```

```
  Ca = [cos(tha) 0 -sin(tha);
          0     1    0     ;
        sin(tha) 0 cos(tha)];

  % Moment of inertia about CM

  Iamtrx = [(ra^2./2 + ha^2./6)          0              0  ;
                    0           (ra^2./2 + ha^2./2)    0  ;
                    0                    0           ra^2];

  Iaprime = ma./2 .* Iamtrx;

  Ia = Ca * Iaprime * Ca';

  skewa = [0 -b1a   b3a;
           b1a  0  -b2a;
          -b3a b2a   0];

  % Moment of inertia about q

  Iaq = Ia - ma .* skewa * skewa

% ASSET photovoltaic array (modeled as a thin plate)

  bp = 10.3;  % base
  hp = 13.4;  % height
  mp = 2419;  % mass
  b1p = -8.7; % Cartesian distance from q to CM
  b2p = 0;
  b3p = 28;

  % Moment of inertia about CM

  Ipmtrx = [(bp^2 + hp^2)  0    0   ;
                0       hp^2  0   ;
                0        0   bp^2];

  Ip = mp./12 .* Ipmtrx;

  skewp = [0 -b1p   b3p;
           b1p  0  -b2p;
          -b3p b2p   0];

  % Moment of inertia about q

  Ipq = Ip - mp .* skewp * skewp;

% Radiator (modeled as a thin plate)

  br = 8;     % base
  hr = 18.4;  % height
  mr = 1471;  % mass
  b1r = 12.2; % Cartesian distance from q to CM
  b2r = 4;
  b3r = 28;

  % Moment of inertia about CM

  Irmtrx = [hr^2       0         0  ;
              0   (br^2 + hr^2)   0  ;
              0         0       br^2];

  Ir = mr./12 .* Irmtrx;
```

```
  skewr = [0 -b1r   b3r;
          b1r  0  -b2r;
         -b3r b2r   0];

  Irq = Ir - mr .* skewr * skewr

% Total moment of inertia about q

  Itotq = Icq + Ipq + Iaq + Irq

% Moment calculations

  omega = [    0    ;
          .0011336 ;
             0    ];

  skewomega = [     0       -omega(3,1)   omega(2,1) ;
               omega(3,1)       0        -omega(1,1) ;
              -omega(2,1)  omega(1,1)        0      ];

  M = skewomega * Itotq * omega
%%%%%%%%%%%%%%%%%%%%%%%%%%%%%%%%%%%%%%%%%%%%%%%%%%%%%%%%%%%%%%%%%%%%%%%%%%%%%%%%
```

P.4 Results

The moments experienced by a cross integrated truss due to the orbit rate rotations of the primary solar power components about the b axes are listed in Table P.2.

b axis	Moment, $N \cdot m$
$\hat{b}_1$	-0.1956
$\hat{b}_2$	-0.7264
$\hat{b}_3$	0

Table P.2 The moments experienced by a cross integrated truss due to the orbit rate rotations of the primary solar power components about the b axis.

Appendix Q. Power System Literature Survey

Q.1 Introduction

What follows is an extensive literature search that outlines the available space power systems. The discussion is not intended to be all encompassing but rather, give an overview of currently available technologies.

Q.2 Energy Sources

There are only three on-board input sources of energy available to support spacecraft. They are direct solar energy, stored chemical energy, and nuclear energy. A possible off-board solution is beamed power. There is a wide variety of both static and dynamic energy conversion systems that can be combined with these heat sources to form an overall space power system. The interrelationships of the energy sources and conversion systems is illustrated in Figure Q.1 (46:343). Possible static conversion systems shown in the figure include batteries, fuel cells, photovoltaic, thermoelectric, and thermionic devices. The dynamic systems consist of either turbine or reciprocating engines coupled to electric generators (17:4.2). The engines operate on thermal energy derived from the sun, nuclear reactors, isotopes, or the combustion of chemicals. A review of the choices shown in Figure Q.1 is essential in determining the electrical power system design for the SFP.

Q.2.1 Solar. The most frequently used power system to date has been solar arrays. At the Earth's orbit, the solar power available is about 1400 W/m^2 (19:90). Solar arrays convert the Sun's energy directly to electrical energy by means of photovoltaic cells. Planar solar arrays have been powering spacecraft since the 1960's and generally come in two types: rigid and flexible. Rigid planar arrays are fabricated on sandwiched panels constructed by bonding two thin face sheets to either side of a honeycomb core material. Flexible blanket arrays use coated Kapton as the

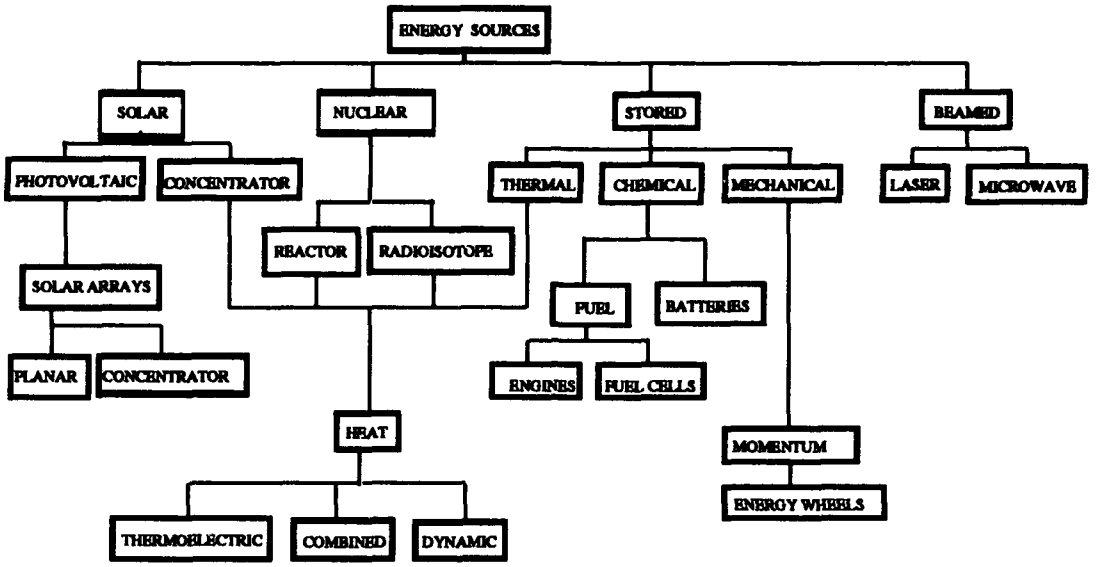

Figure Q.1 Energy sources and their associated derivatives available to power the SFP (46).

substrate (89:158). Most arrays are of the planar variety and were initially silicon based. Gallium arsenide, $GaAs$, cells are the current trend with greater power to weight ratios and increased radiation resistance (23:318–319). All solar cells vary in thickness, resistivity and purity and as a result vary in efficiency, cost, and output characteristics. In fact, most solar arrays continue to be custom designed for specific needs. Disadvantages of solar arrays include the need for sun tracking mechanisms, large surface areas, and batteries or some other storage device. Storage devices are required to provide power during eclipse portions of the orbit. Solar arrays also need replacing during long duration missions (typically every 15 years).

A concentrator array uses either imaging or non-imaging concentrators to provide a concentration of sunlight on cells. Imaging systems include simple lenses, Fresnel lenses, reflectors, and parabolic reflectors. Non-imaging systems include parabolic mirrors operated out of focus, heliostat fields, and compound parabolic collectors (23:507). Using concentrators results in a smaller array (less than 2/3 of a planar) thereby providing a considerable drag and mass advantage (46:343). Other

advantages of concentrator arrays are a superior radiation tolerance (concentrator optics shield the cells) and a possible early application of advanced cells, such as the multi-band gap and indium phosphide, InP (27:362). The draw backs of concentrators are an increased sun tracking requirement and a lack of compressibility for launch packaging.

Q.2.2 Chemical. Chemical power systems are a transportable source of energy where the actual energy is stored in chemical bonds. At their best, chemical bonds provide just a few electron volts of energy. The sheer mass of chemicals needed for time periods greater than one day eliminates them from consideration as the sole source of energy (19:75).

Q.2.3 Nuclear. Obviously there are enormous implications in putting a nuclear system in space, especially in low earth orbit. A space nuclear power system must undergo a highly politicized and very uncertain environmental review and approval process. Completing this process might not even be achievable for a facility that calls for man tended operations. Operating nuclear systems emit copious amounts of gamma rays and neutrons. This requires that the system be shielded to protect humans and equipment. For space applications, achieving low radiation levels would require an extremely high shield mass — possibly great enough to make it infeasible (44:219). The system itself must also be shielded from possible meteoroid damage.

The Systems for Nuclear Auxiliary Power (SNAP) program was initiated in the late 1950's to develop compact, lightweight, reliable energy units and electrical power conversion devices for space, sea, and land use (17:4–8). To date the U.S. has successfully flown 38 nuclear power systems (37 radioisotope thermoelectric generators (RTGs) and 1 reactor). These range from the 2.7 W SNAP-3B to the 500 W SNAP-10A and the 300 W GPHS-RTG (5:23). Current reactor concepts (out-of-core thermionic, in-core thermionic, thermoelectric, dynamic, etc.) provide no compelling

reason to choose one over the other at power levels below 40 kW (5:23). It is suggested to use thermoelectrics with a radioisotope heat source below 2 kW and to us some type of dynamic conversion system (Brayton, Rankine or Stirling) with radioisotopes from 2–10 kW. The latter suggestion is based on mass considerations and technological maturity. Nuclear reactors become the lower mass power source at approximately 10–15 kW. It is thought that for 40 kW and greater, the best concept near term would be a liquid metal cooled fast reactor with a closed Brayton cycle.

The advantages of nuclear power systems are: adjustable power levels and long life operation. The disadvantages include: actual fabrication, launch considerations, a more demanding safety analysis and testing, uncertainties in technological development, and reentry nuclear safety considerations.

Q.2.4 Beamed Power. Beaming power from the Earth to the spacecraft represents an external source of energy. There are currently two methods being pursued, namely microwave and laser.

Q.2.4.1 Microwave. Earth based stations could be built to relay power via microwave to an orbiting platform (the reverse of the Solar Power Satellite concept). A vehicle with a microwave receptor (rectenna) area of 50,000 m^2 could absorb enough beam energy to convert it to 20 MW of power (11:1239). The receptor captures the microwave power and converts it to dc power with an overall capture and conversion efficiency of 85% (11:1243). A 1 kg/kW specific mass for the rectenna — compared to a 30 kg/kW specific mass nuclear reactor — provides a great reduction in mass. The major drawback in such a system is that it has only been proposed for equatorial orbits. Twenty-four or more power stations on the equator would be necessary to support a 42,000 kg platform in orbit (11:1249). An infeasible arrangement to propose for powering the SFP.

Q.2.4.2 Laser. Similar to microwaves, it is possible to beam lasers from Earth to space. Beamed laser photovoltaic power has three fundamental advantages: 1) Laser wavelength is 10,000 times shorter than microwaves allowing for smaller power and receiver apertures. 2) Conversion efficiency of laser photovoltaic cells can be three to four times greater than solar cells (60% versus 15%) because the band-gap energy of the semiconductor material can be closely matched to the photon energy of the laser. And 3) laser cells operating at 800 *nm* (near infrared region) can be subjected to more than five times the natural solar energy without requiring active cooling (67:166). There are other less obvious advantages to laser beaming. For example, there is an inherent backup of using the laser array to collect solar energy. However, the technological maturity must be increased — specifically large aperture optics. There is also the same problem of numerous ground stations necessary to support a low Earth orbiting vehicle.

It has been suggested that a constellation of 12 satellites in equatorial orbits ranging from 24,000–32,000 *km* could relay power to a vehicle in low Earth orbit (2:117). This is an infeasible infrastructure undertaking just to support the SFP (but an undertaking the proposed SFP could assist with). NASA plans currently call for testing of limited laser power transmission to existing satellites by 1995 (67:95).

Q.3 Conversion Cycles

A review of the conversion cycles associated with the solar, chemical and nuclear heat sources is provided in the following sections. Major components and how they relate to the heat source are described as well as currently available versions.

Q.3.1 Organic Rankine Cycle. Organic Rankine cycle (ORC) systems are similar to conventional steam power plants and can be coupled to various heat sources (isotopes, chemical combusters, solar collectors, or reactors). The major system components as shown in Figure Q.2 consist of a boiler, turbopump generator,

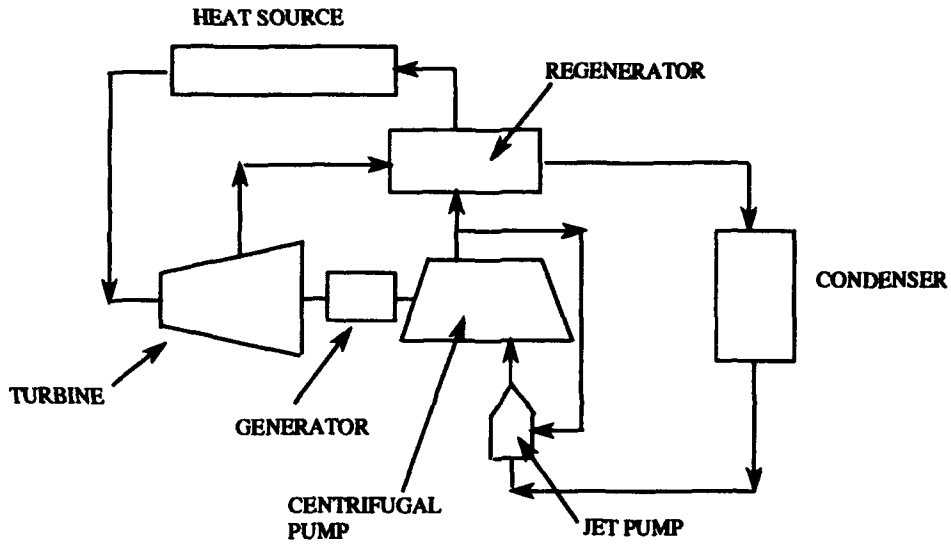

Figure Q.2 Typical organic Rankine cycle showing the system components — heat source, generator, regenerator and radiator (14).

regenerator, and a radiator in addition to the given heat source. Organic working fluids such as toluene and RC-1 are used instead of steam to achieve high cycle efficiencies at moderate temperatures. Current efficiencies are from 18–25% with the main limitations being zero g operation, possible decomposition of organic fluids, heat source availability, cost, and safety (14:579).

Space Station Freedom studies provided an emphasis for a solar powered ORC in the 23–40 kW range (14:582). An additional requirement is a lithium hydroxide, $LiOH$, thermal energy storage subsystem to provide a heat source during the eclipse portions of the orbit. Other major issues in the solar dynamic power system are collector concentration ratio, pointing accuracy, peak and partial load operating characteristics, receiver aperture optimization, and structural dynamic interactions (14:583). Currently available derivatives include a 3 kW solar dynamic mercury Rankine cycle from TRW and a 15 kW solar dynamic rubidium Rankine cycle from Sunstrand Corporation.

An isotope, $Pu - 238$, powered ORC could be a candidate for a 1–10 kW output range. A 1.3 kW demonstration model was developed by Sunstrand Corp. for the Department of Energy (14:579). For operations of greater than 50 kW the only alternative heat source would be a nuclear reactor. A good base of technology already exists for these systems (3 kW SNAP2 and the 35–50 kW SNAP8). A 25 kW ORC with a compact nuclear power source is currently under development by Los Alamos National Laboratory (LANL) with cycle efficiencies predicted at 30%. LANL is also working on a 100–300 kW lithium cooled reactor for the SP-100 program.

Q.3.2 Liquid-metal Potassium Rankine Cycle. The liquid-metal potassium Rankine cycle (LMKRC) is similar to an ORC except that potassium is the working fluid. This allows for high turbine inlet temperatures and a greater heat rejection capability (reducing the size of the radiator) (14:605). In the 1960's, General Electric and Pratt and Whitney carried out preliminary research and development on a SNAP-50 300 kW version, but due to a lack of a specific mission and high temperature corrosion problems, the project was canceled (14:605). Several companies are conceptualizing designs based upon Strategic Defense Initiatives (SDI). A nuclear heat source would seem to be the only viable option for continuous power.

Q.3.3 Closed Brayton Cycle. A closed Brayton cycle (CBC) system is similar to a gas turbine heat engine, but the working fluid is recirculated rather than emitted as exhaust to the environment (14:585). A CBC system includes a combined rotating unit (turbine-compressor and alternator), recuperator, radiator, and gas management system in addition to the heat source (chemical, solar, nuclear reactor, or isotope). A typical CBC is shown in Figure Q.3. The working fluid can be any number of gases but for a space application a helium-xenon, $He - Xe$, mixture has been found to be satisfactory.

If a CBC uses a solar collector as its heat source than practical size limitations give a power level of 10–50 kW. Once again, a thermal energy storage for eclipse

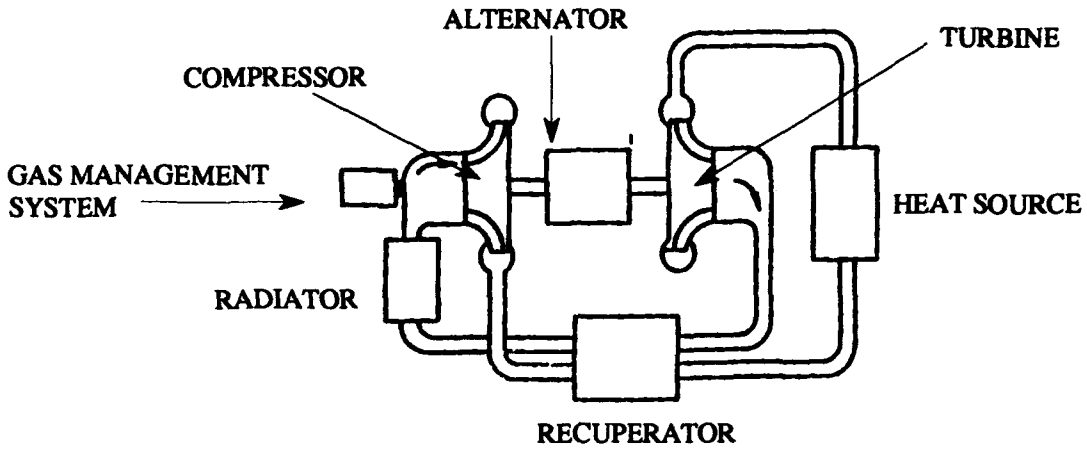

Figure Q.3 Typical closed Brayton cycle showing the system components (14).

periods is necessary. A 35 kW CBC Solar Dynamic system uses latent heat of fusion of lithium fluoride, LiF, to maintain the cycle turbine inlet temperature (14:587). Space Station Freedom plans call for a solar dynamic CBC system in Phase II which has a specific power to weight ratio of 70 kg/kW.

Isotope driven CBCs have demonstrated power levels of 1–10 kW. For continuous power (7–20 *years*) in the 75 kW range, a fast high temperature reactor would be the recommended heat source for a CBC. Typical concepts have included the nuclear engine for rocket vehicle applications derivative reactor, gas and liquid-metal cooled compact reactors, and gas cooled particle bed reactors.

Q.3.4 Free-Piston Stirling Engine. Free-Piston Stirling engine (FPSE) power systems are akin to a closed cycle piston engine with cyclic re-circulation of the working fluid (14:596). After some initial problems the FPSEs have become a more attractive candidate for space applications because they weigh less and have a smaller volume than other cycles. They operate without physical linkages; relying instead on internal gas pressures to impart the motion to reciprocating elements. Figure Q.4 illustrates a typical FPSE. Mechanical Technology Inc. has developed a

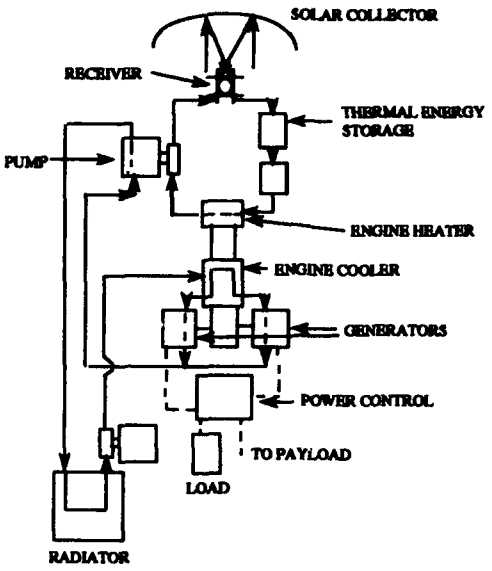

Figure Q.4 Typical free-piston Stirling engine with a solar heat source. It relies on internal pressures to impart motion to reciprocating elements rather than physical linkages (14).

12.5 kW FPSE (designated the space power demonstration engine (SPDE)) which can easily be configured with isotope, solar, or reactor input sources (14:596).

Two SPDEs in a back to back configuration united with a lithium fluoride, LiF, thermal energy storage subsystem driven by a solar collector can achieve an output power of 25 kW (14:598). Higher power levels are possible through the use of multiple systems. This is dependent on the deployability and erectability of multiple collectors. Mechanical Technologies Inc. and Sunflower Inc. are developing a 25 kW space Stirling engine that relies on a nuclear source (89:64).

A $Pu - 238$ isotope heat source is capable of efficiencies in the 28–35% range when attached to an SPDE operating at 12.5 kW. For higher power systems (greater than 50 kW) a reactor heat source is needed to reduce weight. Rockwell International is studying a 100 kW design that uses sodium potassium, NaK, heat pipe exchangers connected to five SPDEs (14:598).

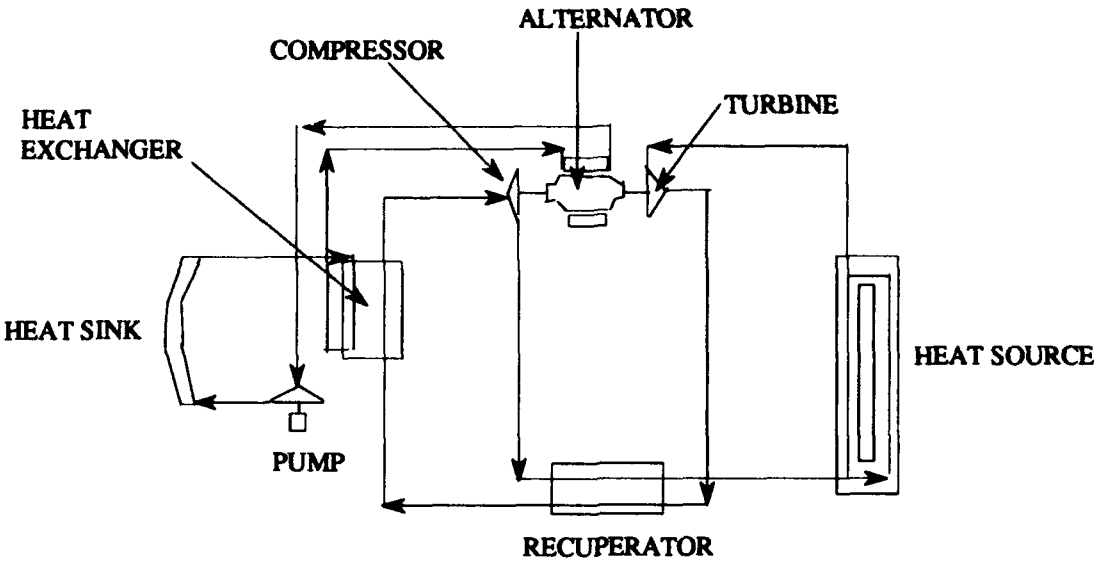

Figure Q.5 Typical supercritical cycle. Components are similar to other cycles but are operating at higher temperatures and pressures (14).

Q.3.5 Supercritical Cycle. A thermodynamic cycle that avoids many of the problems associated with the Rankine, Brayton or Stirling cycles is the supercritical cycle shown in Figure Q.5. So named because it operates in the supercritical pressure region of the working fluid (that region above the fluids critical temperature and pressure). In this region the density of the liquid and the vapor at any point is the same. The problems of boiling and condensing in a zero g environment are eliminated (14:605). Common working fluids include carbon dioxide, CO_2, sulfur dioxide, SO_2, and ammonia, NH_3. Since it is a high pressure cycle, it has performance characteristics that are not suitable for power levels below 25 kW. This generally rules out isotope heat sources but leaves solar and reactor heat sources.

Q.3.6 Thermoelectric Conversion. Thermoelectric conversion (TEC) cycles have had the most extensive application in space power systems. They are compatible with all the previously mentioned heat sources but are typically driven by isotope sources due to reliability considerations. Thermoelectric systems utilize

the Seebeck effect in a circuit for power generation, and their efficiencies are related to the Carnot cycle efficiency and material properties (19:117).

The SP-100 will most probably end up as a TEC system. This is due to lower development risks and the extensive flight experience of TECs. A possible choice could be the alkali metal thermal to electric conversion (AMTEC), also referred to as the sodium heat engine, which is a thermally regenerative electrochemical device for direct thermal to electric conversion. AMTEC has a specific power to weight ratio of 18 W/kg and an efficiency of 20% (14:159).

Q.3.7 Thermionic Conversion. Thermionic conversion is based on the use of a vacuum diode utilizing a temperature difference and employing electrons as the working fluid (19:118). Similar to TECs it is subject to Carnot cycle efficiency limitations (generally the maximum temperature of the source and sink). Essentially the electrons are given off at a heated emitter (cathode) and collector (anode) then pass through the external load back to the emitter. A thermionic device is shown in Figure Q.6. Thermionic systems connected to nuclear reactors have received the most attention, and there are two basic approaches to such systems: in-core or out-of-core. The Soviet TOPAZ reactor is an in-core version and can reportedly deliver 6–10 kW (5:24). GA technologies is currently studying a space thermionic auxiliary reactor for SP-100 applications. So far producing a reliable, long life, in-core, thermionic fuel element has been elusive for the United States (5:24).

Q.4 Energy Storage

In using solar energy, a form of energy storage is necessary because all low inclination orbits have eclipse periods. Also, inherent to electrodynamic propulsion systems, there is the possibility of reversing the current and generating power. If it is chosen to store energy from these sources, an energy storage device is necessary. An illustration of all energy storage methods for the space environment is provided

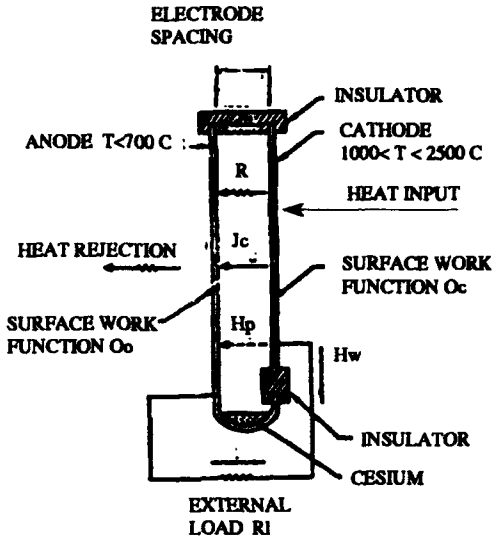

Figure Q.6 A thermionic conversion unit. Electrons are given off at the emitter (cathode) and collector (anode) and then pass through the external load back to the emitter (14).

in Figure Q.7. A review of the most promising energy storage devices —rechargeable batteries and reversible fuel cells (46:343) — is provided in the following sections.

Q.4.1 Batteries. A battery converts the chemical energy contained in its active materials into electrical energy through an electrochemical oxidation-reduction reaction. Nickel-cadmium, $NiCd$, batteries are the industry's current standard for energy storage. They are relatively heavy but can be recharged over many cycles. Lifetime is a complicated function of operating temperature, depth of discharge (DOD), charge and discharge rates, overcharge, number of cycles, recycling strategy, and a variety of other factors.

Battery sizing is determined by the voltage desired (the number in series) and by energy storage requirements in $apmere \cdot hours$, $A \cdot H$, capacity. $A \cdot H$ requirements are determined by the load, eclipse time, and chosen DOD. The number of cycles is determined by the mission time and the number of orbits per day.

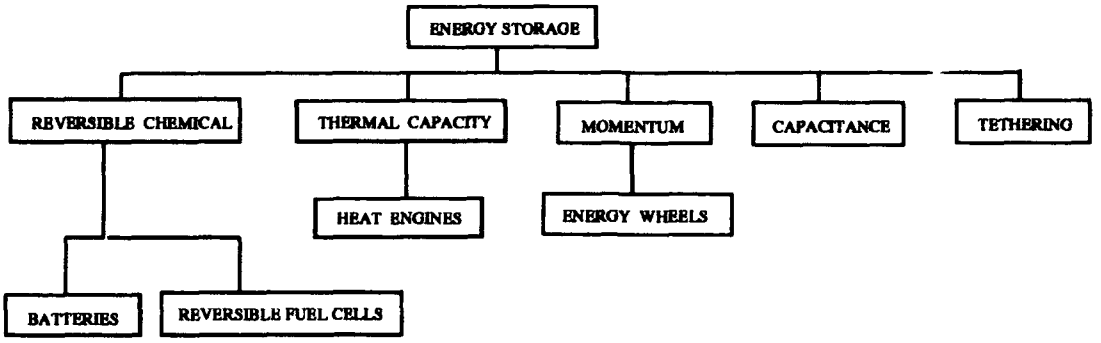

Figure Q.7 Typical energy storage devices available for use on the SFP (46).

Batteries may be deeply discharged to save on the weight of additional batteries. Life cycle trade studies indicate that low temperature, $0°C$, operation with moderate (20–30%) DOD and higher than minimum initial battery weight is the best system approach. Batteries must be charged under controlled conditions so that the charge rate is not too high and overcharge does not occur. Charge and discharge cycles result in a net inefficiency and in the production of waste heat.

Nickel-hydrogen, NiH_2, is the more recent battery technology. It has a slightly higher DOD than $NiCd$ and can tolerate over-charging better. For example, NiH_2 batteries at 40% DOD have lasted greater than 18,000 cycles while $NiCd$ batteries at 25% DOD last between 14,000–15,000 *cycles* (46:135). NiH_2 batteries are 15% lighter but are 40% larger in volume than $NiCd$ batteries

Current research is being done on a high energy density rechargeable battery (HEDRB) with a goal of a 110 $\frac{Watt \cdot hour}{kg}$ battery with a 10 year life (14:572). Two technologies have been identified to meet this goal, lithium iron di-sulfide, $LiFeS_2$, and sodium sulfur, NaS. The HEDRB could reduce battery weight by 80% compared to $NiCd$ batteries and 60% compared to NiH_2 batteries (14:572). These batteries are also projected to have greater DOD — 75% for NaS and 40–80% for $LiFeS_2$ (14:579).

Q.4.2 Reversible Fuel Cell. The operation of a fuel cell is similar to a battery except that one or both of the reactants are not permanently contained in the

electrochemical cell but are fed to it from an external source when power is desired. Reversible fuel cell (RFC) systems convert hydrogen fuel and an oxidizer, O_2, into electrical energy and water during the eclipse portion of the orbit. An electrolysis unit is used to electrolyze the water (using electrical energy from the source) back into H_2 and O_2 during sunlight. This is obviously an inefficient process and has not been perfected yet. Lifetime of the system is a function of operating temperature; pressure; and the reliability of the necessary pumps, compressors, valves, and regulators. Recent work has dealt with proton membrane exchange RFCs to meet long life applications for the lunar surface or Mars.

Bibliography

1. Baillif, Faye F. Telephone interview. Martin Marietta Manned Space Systems, New Orleans, LA, 15 July 1993.
2. Bamberger, Judith Ann. "A Power Beaming Based Infrastructure for Space Power." *26th Intersociety Energy Conversion Engineering Conference*. 116–121. American Nuclear Society, 1991.
3. Bate, Roger R. and others. *Fundamentals of Astrodynamics*. New York: Dover Publications, 1971.
4. Bell, Allen J. Telephone interview. Lockheed Engineering and Sciences Company, Houston, TX, 2 September 1993.
5. Bennet, Gary L. "Toward the Last Frontier: A Strategy for the Evolutionary Development of Space Nuclear Power Systems." *27th Intersociety Energy Conversion Engineering Conference*. 23–33. Society of Automotive Engineers, 1992.
6. Beyer, William, editor. *CRC Standard Mathematical Tables, 27th Edition*. Boca Raton, FL: CRC Press, 1984.
7. Bodle, J.G. and Others. "Progress in Composite Structure and Space Construction Systems Technology." *Proceedings of the 2nd AIAA Conference on Large Space Platforms*. 1981.
8. Boyle, R. V. and others. "Solar Dynamic Power Option for the Space Station." *23rd Intersociety Energy Conversion Engineering Conference*. 319–328. American Society of Mechanical Engineers, 1988.
9. Brand, Vince D. and others. "Assembling a Space Station in Orbit," *Acta Astronautica, Vol. 29, No. 4*:317–323 (1993).
10. Britton, W. R. and others. *Structural Attachments for Large Space Structures*. Technical Report N78-30168, Martin Marietta Corp., July 1978.
11. Brown, William C. "Beamed Microwave Power Transmission and It's Application to Space," *IEEE Transaction on Microwave Theory and Techniques, 40*:1239–1250 (June 1992).
12. Browning, Lee and Others. *Space Construction Automated Fabrication Experiment Definition Study (SCAFEDS) Volume II, Study Results*. Technical Report N78-25112, General Dynamics Convair Division, 1978.
13. Butler, George V. *Working in Space*. New York: AIAA Press, 1981.
14. Cantafio, Leopold J. *Space Based Radar Handbook*. Norwood, MA: Artech House, 1989.
15. Cary, Howard B., editor. *Modern Welding Technology*. Prentice Hall, 1979.

16. Chobotov, Vladimir A., editor. *Orbital Mechanics*. Washington, D.C.: American Institute of Aeronautics and Astronautics, 1991.

17. Cocharan, Curtis D. Lt Col and others. *Space Handbook*. Maxwell AFB, Alabama: Air University Press, 1985.

18. Cook, John and David Wicks. "Space Station Rendezvous and Berthing," *Simulation*, 26–30 (July 1991).

19. Corliss, William R. *Propulsion Systems for Space Flight*. New York: McGraw Hill, 1960.

20. Croft, Terrell. *American Electricians Handbook*. New York: McGraw Hill, 1961.

21. Department of the Navy. *American Ephemeris and Nautical Almanac*. Technical Report. Washington, D.C.: U.S. Government Printing Office, 1980.

22. Drell, S. D. and others. "Drag and Propulsion of Large Satellites in the Ionosphere: An Alfven Propulsion Engine in Space," *Journal of Geophysical Research, Vol. 70, No. 13*:3131–3145 (July 1965).

23. Fahrenburch, Alan L. and Richard Bube. *Fundamentals of Solar Cells*. New York: Academic Press, 1983.

24. Fitzgerald, A. E. and others. *Electric Machinery*. New York: McGraw Hill, 1983.

25. Fluegel, Kari. "JSC Researchers Evaluate Electrodynamic Tether System that Holds Promise for Power Management, Propulsion," *NASA JSC: Space News Roundup* (July 1993).

26. Franklin, Gene F. and others. *Feedback Control of Dynamic Systems*. New York: Addison-Wesley Publishing Company, 1991.

27. Gee, James M. and Robert W. Francis. "Space Concentrator Photovoltaic Technology: Workshop Summary." *Proceedings of the 9th Space Photovoltaic Research and Technology Conference*. 361–363. 1988.

28. Gimarc, Alex J. *Report on Space Shuttle External Tank Applications*. New Jersey: Space Studies Institute, 1985.

29. Gould, Charles L. "New Roles for Manned Space." *Proceedings of the 2nd AIAA Conference on Large Space Platforms*. 1–8. February 1981.

30. Griffin, Michael D. and James R. French. *Space Vehicle Design*. Washington, DC: AIAA Press, 1991.

31. Haislip, Capt James N. and others. *An Aluminum Salvage Station for the External Tank (ASSET)*. MS thesis, AFIT/GSE/ENY/90D-02, School of Engineering, Air Force Institute of Technology (AU), Wright-Patterson AFB OH, December 1990 (AD-A230841).

32. Halliday, David and Robert Resnick. *Fundamentals of Physics*. New York: John Wiley & Sons, 1981.

33. *Hobart High Powered CW Nd:YAG Laser*. Product Application Guide NWSA: 460-A. May 1993.

34. Holman, Jack P. *Heat Transfer*. New York: McGraw Hill, 1986.

35. Hughes, Peter C. *Spacecraft Attitude Dynamics*. New York: John Wiley & Sons, 1986.

36. Hunter, David G. and others. "Time-Delayed Remote Operation and Maintenance of Space Station Freedom," *Acta Astronautica*, *Vol. 28*:73–84 (1992).

37. Huzel, Dieter K. and David H Huang. *Design of Liquid Propellant Rocket Engines*. Washington, D.C.: NASA, 1967.

38. Incropera, Frank P. and David P. Dewitt. *Fundamentals of Heat Transfer*. New York: John Wiley & Sons, 1981.

39. Jackson, Stewart W. and Frank G. Gallo. "The Resupply Interface Mechanism RMS Compatibililty Test," *The 24th Aerospace Mechanisms Symposium*, 143–156 (April 1990).

40. Janson, S. W. "The On-Orbit Role of Electric Propulsion." *Proceedings of the AIAA/SAE/ASME/ASEE 29th Joint Propulsion Conference and Exhibit*. June 1993.

41. Johnson, William. Personal interview. Hobart Welding Co., Troy, OH, 4 August 1993.

42. Jones, Andrew S. and others. "The Mobile Servicing System — A System Description." *26th Space Congress*. 7.1–7.9. April 1989.

43. Kellock, Brian. "Roll Forming That's Out of This World," *Machinery and Production Engineering*, 34–35 (June 1981).

44. Keshishian, Vahe and others. "Space Reactor Shield Technology." *23rd Intersociety Energy Conversion Engineering Conference*. 218–228. American Society of Mechanical Engineers, 1988.

45. King-Hele, Desmond. *Theory of Satellite Orbits in an Atmosphere*. London: Butterworths, 1964.

46. Kline, Richard and others. "Potential Designs of Space Stations and Platforms." *Space Stations and Space Platforms — Concepts, Design, Infrastructure, and Uses*, edited by Ivan Bekey. New York: AIAA Press, 1985.

47. Kolcum, Edward. "Delta Clipper Partners Set Goal For Single-Stage-To-Orbit Vehicle," *Aviation Week and Space Technology*, 55–56 (February 1992).

48. Ladouceur, Maj Richard J. R. *Feasibility Study of Electrodynamic Propulsion in Space Using a Closed Loop Circuit*. MS thesis, AFIT/GOR/ENY/93D, School of Engineering, Air Force Institute of Technology (AU), Wright-Patterson AFB OH, (TBA).

49. Lawrence, Capt Richard E. *An Electromagnetically Controlled Precision Orbital Tracking Vehicle (POTV).* MS thesis, AFIT/GA/ENY/92D-05, School of Engineering, Air Force Institute of Technology (AU), Wright-Patterson AFB OH, December 1992 (TBA).

50. Leahy, Micheal B., Jr. Class notes in EENG 540, Robotic Fundamentals. School of Engineering, Air Force Institute of Technology (AU), Wright-Patterson AFB OH, September 1992.

51. Liebman, Judith and others. *GINO.* Chicago: LINDO Systems, 1989.

52. Likins, Peter. *Elements of Engineering Mechanics.* New York: McGraw Hill, 1973.

53. Mager, Albrecht J. "Magnetic Shields," *IEEE Transactions on Magnetics, Vol. 6, No. 1*:67–74 (March 1972).

54. Magnetic Shield Corporation. *Magnetic Shielding Lab Kit with AC Probe.* Product Application Guide LK-2G. Bensenville, Illinois, 1991.

55. Martinez-Sanchez, Manuel and D.E. Hastings. "A Systems Study of a 100 KW Electrodynamic Tether." *Advances in the Astronautical Sciences Vol. 62: Tethers in Space.* 341–366. American Astronautical Society, 1987.

56. Meirovitch, L. and F. B. Wallace Jr. "On the Effect of Aerodynamic and Gravitational Torques on Attitude Stability of Satellites," *AIAA Journal, Vol. 4*:2196–2202 (December 1966).

57. Miner, Dennis D., Major USAF. *Orbital Analysis of a STS External Tank in Low Earth Orbit.* MS thesis, AFIT/GA/AA/87D-4, School of Engineering, Air Force Institute of Technology (AU), Wright-Patterson AFB OH, December 1987 (TBA).

58. Nein, Max E. and John C. Fikes. "Potential Orbital Use of the Space Shuttle External Tanks." *Proceedings of the AIAA/SAE/ASME/ASEE 26th Joint Propulsion Conference.* July 1990.

59. Nobles, William. "Electrodynamic Tethers for Energy Conversion." *Advances in the Astronautical Sciences Vol. 62: Tethers in Space.* 453–471. American Astronautical Society, 1987.

60. *Preliminary Data for On-Orbit Utilization of the External Tank.* Technical Report, Huntsville, AL: NASA: Marshal Space Flight Center, April 1988.

61. Parrish, Joseph C. "Opportunities for Space Station Assembly Operations During Crew Absence," *Journal of Spacecraft, Vol. 27, No. 3*:338–345 (May-June 1990).

62. Parrish, Joseph C. *Ground Controlled Robotic Assembly Operations for Space Station Freedom.* Technical Report N91-20665, Reston, VA: NASA: Space Station Freedom Program Office, 1991.

63. Penzo, Paul A. and Paul W. Ammann. *Tethers in Space Handbook-Second Edition*. Arlington: SRS Technologies, 1989.

64. Powers, D.E. and G.R. LaFlamme. "EBW vs. LBW - A Comparative Look at the Cost and Performance Traits of Both Processes," *Welding Journal*, 25–31 (March 1988).

65. *PRO-MATLAB user's Guide*. South Natick, MA: MathWorks, 1989.

66. Quinn, Roger D. and Thomas W. Keslake. "Solar Dynamic Modules for Space Station Freedom: The Relationship Between Fine Pointing Control and Thermal Loading of the Aperture Plate." *Proceedings of the International Solar Energy Conference*. April 1992.

67. Rather, John D. G. "Advantages of Ground to Space Laser Power Beaming." *AIAA International Communication Satellite Systems Conference 14*. 1660–1670. June 1992.

68. Ridgely, D. Brett and Siva S. Banda. *Introduction to Multivariable Control*. Government AFWAL-TR-85-3102, Wright-Patterson Air Force Base, Ohio: Air Force Wright Aeronautical Laboratories, February 1986 (AD-A165891).

69. Riel, F. D. and G. Markus. "Pre-Integrated Truss Assemblies for Space Station Freedom." *Proceedings of the 42nd Congress of the International Astronautical Federation*. October 1991.

70. Riel, F. D. and L. P. Morata. "Space Station Freedom Pre-Integrated Truss Configuration." *Proceedings of the AIAA Space Programs and Technologies Conference*. March 1992.

71. Ross, Mike. "The Long Arm of CAD/CAE," *Aerospace America*, 34–35 (June 1993).

72. Sage, Andrew P. *Methodology for Large-Scale Systems*. New York: McGraw Hill, 1977.

73. Secunde, Richard R. and others. "Solar Dynamic Power Module Design." *23rd Intersociety Energy Conversion Engineering Conference*. 299–307. IEEE Press, 1989.

74. Shames, Irving H. *Engineering Mechanics: Statics and Dynamics*. Englewood Cliffs, FL: Prentice Hall, 1980.

75. Shulym. V. F. and Others. "Peculiarities and Future Development of Space Welding." *Welding in Space and the Construction of Space Vehicles by Welding*. September 1991.

76. Siegel, Robert. *Thermal Radiation Heat Transfer*. Washington, DC: Hemisphere, 1981.

77. Smith, Robert E. and George S. West. *Space and Planetary Environment Criteria Guidelines for Use in Space Vehicle Development, 1982 Revision (Volume*

1). Technical Report NTM-82478, Huntsville, AL: NASA: Marshal Space Flight Center, 1983.

78. Sours, T. and others. *Photovoltaic Module On-Orbit Assembly for Space Station Freedom*. Technical Report N89-26887, Cleveland, OH: NASA: Lewis Research Center, 1989.

79. *System Requirements Document: Special Purpose Dexterous Manipulator*. Technical Report TSS-30699, Ottawa: Canadian Space Agency, December 1992.

80. Spenny, C. and others. "An Aluminum Salvage station for External Tanks of the Space Shuttle," *Acta Astronautica, Vol. 29, No. 5*:379–397 (1993).

81. Spenny, C. and Richard E. Lawrence Jr. "A Precision Orbital Tracking Vehicle (POTkV)." *AIAA/SAE/ASME/ASEE 29th Joint Propulsion Conference and Exhibit*. June 1993.

82. *U. S. Space Station Manned Base to Mobile Servicing System*. Technical Report SSP-42003, Reston, VA: NASA: Space Station Freedom Program Office, April 1991.

83. Sutton, George P. *Rocket Propulsion Elements: An Introduction to the Engineering of Rockets*. New York: John Wiley And Sons, 1992.

84. Tascione, Thomas F. *Introduction to the Space Environment*. Malabar, FL: Orbit Book Company, 1988.

85. Thomas, Ronald L. and George J. Hallinan. "Design of the Space Station Freedom Power System." *24th Intersociety Energy Conversion Engineering Conference*. 245–250. IEEE Press, 1989.

86. "Let There Be Light," *Time* (February 15 1993).

87. Vallejo, J. J. Gonzalez. "Concept Design for Hermes Docking/Berthing Mechanism." *ESA, Fourth European Space Mechanisms and Tribology Symposium*. 13–18. March 1990.

88. Veerasamy, Sam P. E. "Berthing Simulator for Space Station and Orbiter." *NASA, Lyndon B. Johnson Space Center, Fourth Annual Workshop on Space Operations, Applications, and Research*. 120–125. January 1991.

89. Wallin, Wayne E. and Jerry M. Friefeld. *Solar Dynamic Power System Definition Study*. Contract N88-24864, Cleveland, OH: NASA: Lewis Research Center, March 1988.

90. Weast, Robert, editor. *CRC Handbook of Chemistry and Physics, 59th Edition*. Boca Raton, FL: CRC Press, 1978.

91. Webber, Tim. "Welding With Lasers," *The Fabricator* (December 1991).

92. Weisman, Charlotte, editor. *Welding Handbook* (Seventh Edition), *One*. American Welding Society, 1976.

93. Wiesel, William E. *Spaceflight Dynamics*. New York: McGraw Hill, 1989.

94. Wiesel, William E. *Advanced Astrodynamics*. Wright Patterson AFB, OH: AFIT, 1992.

95. Wiggins, Lyle E. "Relative Magnitudes of Space-Environment Torques on a Satellite," *AIAA Journal*, *Vol. 2, No. 4*:770–771 (April 1964).

96. Zernic, Michael J. "Solar Dynamic Technology Status for Space Station Freedom Application." *Proceedings of the Space Station Evolution Symposium*. 765–811. Washington D.C.: NASA, 1992.

Vita

Captain James A. Bessel was born March 2, 1966 in Rockville Centre, New York. He graduated from high school in Freeport, New York in June of 1984. He then attended the United States Air Force Academy where he obtained a Bachelor of Science degree in Astronautical Engineering on 1 June 1988. He was commissioned a second lieutenant and attended Undergraduate Navigator Training at Mather AFB, California. After attending training in the F-4E at George AFB, California, he transitioned to the RF-4C and was assigned to the 91st TRS, Bergstrom AFB, Texas. He entered the Graduate School of Engineering, Air Force Institute of Technology, in May of 1992. Captain Bessel and his wife Elizabeth were married on January 14, 1989. They have two children: Sarah and Maggie.

Permanent Address: 227 Lexington Avenue
Freeport, NY 11520

Captain James M. Ceney was born April 2, 1965 in Hillsboro, Illinois. He graduated from Hillsboro High School in June of 1983, and then attended the University of Illinois, Urbana-Champaign. He obtained a Bachelor of Science degree in Aeronautical and Astronautical Engineering and was commissioned a second lieutenant in May 1987. He entered active duty in January 1988 and was assigned as an astronautical engineer to the Foreign Technology Division, Wright Patterson AFB, OH. He entered the Graduate School of Engineering, Air Force Institute of Technology, in May of 1992.

Permanent Address: Kinkead Road RR2
Hillsboro, IL 62049

Captain David M. Crean was born July 31, 1957 in Salamanca, New York. He graduated from high school in Olean, New York, in June of 1976 and entered the civilian work force. On August 22, 1982, he entered the Air Force as a Telephone Switching Technician assigned to the 2149th Communications Squadron, F. E. Warren AFB. Upon his selection to the Airmen's Education and Commissioning Program, he attended the University of Illinois where he obtained a Bachelor of Science degree in Aeronautical and Astronautical Engineering. After receiving his commission through Officer Training School, he was assigned to Headquarters, Tactical Air Command, Langley AFB, Virginia where he worked as a project engineer in the Communications/Computers Directorate. He entered the Graduate School of Engineering, Air Force Institute of Technology, in May 1992. Capt Crean and his wife Lisa were married in August 1977 and have two children: Bethany and Amanda.

Permanent Address: 427 Second Avenue
Olean, NY 14760

Captain Edward A. Ingham was born June 30, 1962 in Seattle, Washington. He graduated from high school in Edmonds, Washington in June of 1980. He then attended the United States Air Force Academy where he obtained a Bachelor of Science degree in Engineering Sciences on 30 May 1984. He was commissioned a second lieutenant and attended Undergraduate Pilot Training at Williams AFB, Arizona. After training, he continued at Williams as a first assignment instructor pilot in the T-37. In May of 1988, he upgraded to the F-16C and was assigned to the 14th Fighter Squadron, Misawa Air Base, Japan. He entered the Graduate School of Engineering, Air Force Institute of Technology, in May of 1992. Captain Ingham and his wife Renee were married in 1985. They have two sons: Connan and Dillon.

Permanent Address: 8512 224th South West
Edmonds, WA 98025

Captain David J. Pabst was born November 5, 1963 at Wright Patterson AFB, Ohio. He graduated from Doherty High School, Colorado Springs, Colorado, in May 1982. In 1986, he graduated from Rensselaer Polytechnic Institute where he earned a Bachelor of Science degree in Aeronautical Engineering. Through the Reserve Officer Training Corps program, he was commissioned a Second Lieutenant. In 1987, he was assigned to the Training Systems Management Division at Hill AFB. He served as engineer and program manager for F-4 and F-111 training systems, and later as Deputy Branch Chief for Strategic, Cargo, and Special Operations Forces Training Systems. He entered the Graduate School of Engineering, Air Force Institute of Technology, in May of 1992. Captain Pabst and his wife Vickie were married on August 7, 1993.

Permanent Address: 6600 River Downs Drive, Apartment 2C
Centerville, OH 45459